First Principle Studies on Ground and Excited Electronic States: Chemical Bonding in Main–Group Molecules, Molecular Systems with Diffuse Electrons, and Water Activation using Transition Metal Monoxides

by

Isuru Rangana Ariyarathna

A dissertation submitted to the Graduate Faculty of
Auburn University
in partial fulfillment of the
requirements for the degree of
Doctor of Philosophy

Auburn, Alabama
May 1, 2021

Keywords: quantum chemistry, chemical bonding, solvated electrons

Approved by

Evangelos Miliordos, Chair, J. E. Land Assistant Professor of Chemistry and Biochemistry
Michael McKee, Professor Emeritus of Chemistry and Biochemistry
J. Vincent Ortiz, Ruth W. Molette Professor of Chemistry and Biochemistry
Konrad Patkowski, Professor of Chemistry and Biochemistry
Andrew J. Adamczyk, Assistant Professor of of Chemical Engineering

Abstract

Potential energy profiles can be used to investigate the origins of chemical bonding of molecules. Such profiles were adopted to show the propagation of lone pair electrons of $N_2(X^1\Sigma_g^+)$ to the vacant orbital of $O(^1D)$ or $NH(a^1\Delta)$ to produce $N_2O(\tilde{X}^1\Sigma^+)$ or $N_3H(\tilde{X}^1A')$ molecules, respectively. Similarly, the combination of $N_2(X^1\Sigma_g^+)$ + $2O(^1D)$ or $N_2O(\tilde{X}^1\Sigma^+)$ + $O(^1D)$ generates N_2O_2 molecule. Using multi-reference potential energy profiles chemical bonding patterns of ground and excited states of series of metal-ligand molecules were rationalized. Ground states of $Li(CO)_{1-3}$, LiNO, $Be(CO)_{1-3}$, and BeNO originate from some excited state of the metal. In contrast, similar metal-ammonia molecules emerge from ground state fragments. The $Be\cdots NH_3$ interaction guided us to propose the **:**Be$\leftarrow$**:**Be + Be**:**$\rightarrow$Be**:** resonance chemical bonding pattern for Be_2 dimer. The Be−Be bond can be significantly strengthened by ammonia ligation (e.g. $NH_3Be-BeNH_3$ and $(NH_3)_2Be-Be(NH_3)_2$). Even though $[Be-Be]^{2+}$ dimer is metastable, $[NH_3Be-BeNH_3]^{2+}$ and $[(NH_3)_2Be-Be(NH_3)_2]^{2+}$ create stable minima.

Ammonia and water solvate loosely bound valence electrons of metals. In such neutral or partially oxidized complexes solvated electrons orbit in a diffuse atomic s-type orbital. Fascinatingly, diffuse electrons of these complexes tend to populate quasi p-, d-, f-orbitals in low-lying electronic states. Such complexes were dubbed *"solvated electron precursors"* (SEPs) where an SEP is a *"complex that displaces one or more electrons from its coordinated metal atom to the periphery of its ligands"*. The SEPs of the simplest $M(NH_3)_4$ (M = Li, Na) bear one peripheral electron that orbits around $M(NH_3)_4{}^+$ core. Based on the shapes of the orbitals and the excitation energies of $M(NH_3)_4$, the 1s, 1p, 1d, 2s, 2p Aufbau principle of SEPs were introduced. $Be(NH_3)_4$ and $Be(H_2O)_4$ bear two outer electrons, hence their excited state spectra show substantial multi-reference characters. Similarly, several Mg and Ca-ammine (or aqua) complexes behave as SEPs. The M (≡Metal): cc-pVTZ,

N/O: cc-pVTZ, and H: d-aug-cc-pVTZ basis set was proven to represent excited states of these species accurately and efficiently. Ammonia or water does not solvate the inner 3d electrons of titanium but solvates the valence 4s electrons which promote to higher-angular momentum p- and d-type orbitals. Two SEPs bind together to form a stable dimer. By linking two SEPs with an adjustable carbon chain, its singlet-triplet gap can be tuned into a desirable value. Twelve or twenty-four ammonia molecules can occupy the second solvation shell of a tetrahedral metal-ammine SEP (e.g. $M(NH_3)_4@nNH_3$; n = 12, 24) and follow a similar Aufbau order (1s, 1p, 1d, 1f, 2s, 2p, 1g, 2d). Geometries of such clusters (species with solvated electrons and H−bonds) can be represented accurately using density functional theory with CAM-B3LYP functional.

Implementation of the correct active space in multi-reference calculations is critical for accurate description of ground and excited electronic states of transition metal monoxides. Low-lying electronic states of ZrO^+ can be represented by probing a larger number of electronic states into $2p_{/O}$, $5s_{/Zr}$, $4d_{/Zr}$ CASSCF active space. Interestingly, its state specific calculations tend to use $3p_{x/O}$ and $3p_{y/O}$ orbitals instead of $4d_{xz/Zr}$ and $4d_{yz/Zr}$ in the active space and provide rather inaccurate descriptions of electronic states. This error can be overcome by applying a larger active space that contains twelve orbitals ($2p_{/O}$, $5s_{/Zr}$, $4d_{/Zr}$, and $3p_{/O}$) at CASSCF level. A similar dilemma occurs in MoO^- and RuO^-. Even though nine active orbitals ($2p_{/O}$, $5s_{/Zr}$, $4d_{/Zr}$) can treat low-lying electronic states of NbO^+, MoO^+, MoO^{2+}, RuO, RuO^+, and RuO^{2+} accurately, the use of three more CASSCF orbitals ($2p_{/O}$, $5s_{/Mo,Ru}$, $4d_{/Mo,Ru}$, $5p_{/Mo,Ru}$) is critically important to obtain the correct order of electronic states and energetics of MoO^- and RuO^-. Using suitable active spaces, high-level multi-reference configuration interaction calculations were performed to unravel chemical bonding patterns and spectroscopic constants of their low-lying electronic states. Water activation potential of these second-row transition metal monoxides were tested, and it was observed that in general anions are more suitable for the thermodynamically favorable water activation process compared to their neutral or cationic counterparts. Furthermore, a better understanding of the electronic structures of transition metal monoxides allows us to design more practical molecular complexes for efficient water activation.

Acknowledgments

First, I would like to thank Dr. Evangelos Miliordos for being an excellent advisor. He guided me through research problems and gave me the free rein to grow. It has been a great pleasure working him and I am grateful for his patience and enthusiasm.

Next, I would like to thank my committee members: Prof. Michael McKee, Prof. Vincent Ortiz, Prof. Konrad Patkowski, and Prof. Andrew Adamczyk for their valuable comments on improving this work.

I thank Prof. Vincent Ortiz for his fascinating research ideas and allowing me to gain experience on navigating through collaborative research projects. I would also like to acknowledge Prof. Kit H. Bowen Jr. and Prof. Anne E. V. Gorden for their collaborations that allowed me to combine my results with experiment.

I am grateful to the Auburn University for supporting me with financial assistance to carry out my research.

My life at Auburn would not have been half as productive and pleasant if it wasn't for loving Pradeepa. I am truly grateful for her constant impetus that propelled me through during the last seven years.

I am forever indebted to my parents for being an endless source of motivation and for all the sacrifices they made in order to provide me a better life.

Contents

List of Figures

List of Tables

List of Abbreviations

HOMO	Highest Occupied Molecular Orbital
IE	Ionization Energy
EA	Electron Affinity
DFT	Density Functional Theory
MP2	Møller–Plesset Second-order Perturbation Theory
CASSCF	Complete Active Space Self–Consistent Field Theory
CASPT2	Complete Active Space Second–order Perturbation Theory
MRCI	Multi–Reference Configuration Interaction Theory
CCSD(T)	Coupled–Cluster Singles and Doubles plus approximate Triples
PEC	Potential Energy Curve
$\boldsymbol{D_e}$	Binding Energy
vbL	valence–bond–Lewis
XZ	cc–pVXZ; X = D, T, Q
AXZ	aug–cc-pVXZ; X = D, T, Q
DAXZ	d–aug–cc–pVXZ; X = D, T, Q
TAXZ	t–aug–cc–pVXZ; X = D, T, Q

Chapter 1

Introduction

1.1 Computational chemistry

Computational chemistry is a relatively young area of chemistry investigating chemical phenomena by means of computers. The rapid improvement of the performance of modern supercomputing systems has placed computational chemistry in the frontier of chemistry research. Often, computational chemistry is used to obtain geometric parameters of a molecule, calculate energies of a reaction pathway, understand the mechanism and performance of a reaction, explain spectroscopic fractures, guide drug designing, and in material science.[1] In computational chemistry molecular mechanics, molecular dynamics, *ab initio*, semiempirical, and density functional tools are being used.[1] In molecular mechanics atoms and bonds are considered as balls and springs while laws of motions are being applied to molecules in molecular dynamics.[1] Molecular mechanics and molecular dynamics are much faster compared to the *ab initio*, semiempirical, and density functional calculations.[1] The *ab initio*, semiempirical, and density functional calculations are based on the Schrödinger equation proposed almost a century ago.[2] Even though *ab initio* calculations are substantially more demanding compared to others, it provides highly accurate results. The thesis research described here is mainly focused on *ab initio* multi−reference methodologies applied to a series of molecules with unusual electronic structure with the goal to unveil their chemical behavior.

1.2 Multi–reference calculations

A comprehensive account of multi–reference techniques has been compiled by Szala et al.[3] This introduction provides a general idea about multi–reference approaches for non–specialized readers to follow the methodologies and concepts described in later sections.

Hartree–Fock (HF) is the simplest *ab initio* method. The HF wavefunction is written as one determinant using spatial orbitals and electron spins. For example, the HF wavefunction of a six electron closed–shell system (electron configuration of Figure 1.1D_1) can be written in the form of Equation 1.1 (ψ is the orbital, the α and β corresponds to the spin–up and spin–down electron configurations, $1/\sqrt{6!}$ is the normalization constant).

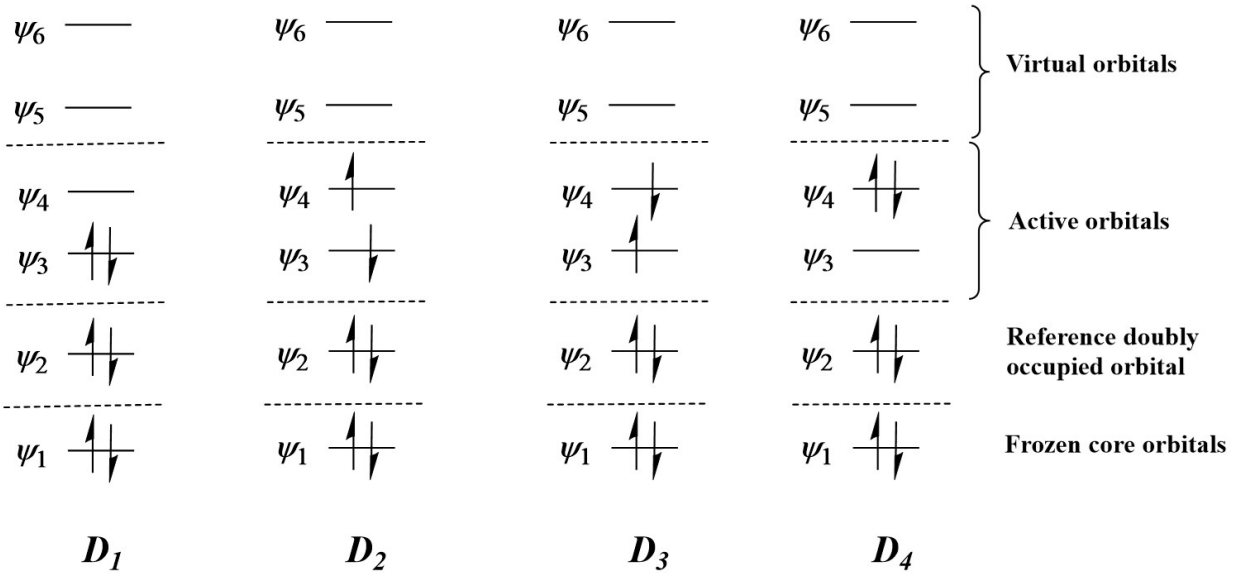

Figure 1.1: Configuration interaction determinants. D_1 is the Hartree–Fock determinant. D_2 and D_3 are determinant for single electron promotions from D_1. D_4 corresponds to the double electron promotion from D_1.

$$\Psi_{HF} = \frac{1}{\sqrt{6!}} \begin{vmatrix} \psi_1(1)\alpha(1) & \psi_1(1)\beta(1) & \psi_2(1)\alpha(1) & \psi_2(1)\beta(1) & \psi_3(1)\alpha(1) & \psi_3(1)\beta(1) \\ \psi_1(2)\alpha(2) & \psi_1(2)\beta(2) & \psi_2(2)\alpha(2) & \psi_2(2)\beta(2) & \psi_3(2)\alpha(2) & \psi_3(2)\beta(2) \\ \psi_1(3)\alpha(3) & \psi_1(3)\beta(3) & \psi_2(3)\alpha(3) & \psi_2(3)\beta(3) & \psi_3(3)\alpha(3) & \psi_3(3)\beta(3) \\ \psi_1(4)\alpha(4) & \psi_1(4)\beta(4) & \psi_2(4)\alpha(4) & \psi_2(4)\beta(4) & \psi_3(4)\alpha(4) & \psi_3(4)\beta(4) \\ \psi_1(5)\alpha(5) & \psi_1(5)\beta(5) & \psi_2(5)\alpha(5) & \psi_2(5)\beta(5) & \psi_3(5)\alpha(5) & \psi_3(5)\beta(5) \\ \psi_1(6)\alpha(6) & \psi_1(6)\beta(6) & \psi_2(6)\alpha(6) & \psi_2(6)\beta(6) & \psi_3(6)\alpha(6) & \psi_3(6)\beta(6) \end{vmatrix} \tag{1.1}$$

The HF energy can be obtained by the Equation 1.2, where Ψ^* is the complex conjugate of Ψ, $\hat{H}$ is the Hamiltonian operator, $d\tau$ indicates integration with respect to spin and spatial coordinates. Minimization of this quantity provides the atomic or molecular orbitals ψ in terms of a set of known functions called basis set.

$$E_{HF} = \frac{\int \Psi^* \hat{H} \Psi \, d\tau}{\int \Psi^* \Psi \, d\tau} \tag{1.2}$$

Multi−reference wavefunction is created by considering all possible electron configurations of a selected active space. The total orbital space can be divided into four categories: (1) frozen core orbitals (2) reference doubly occupied orbitals (3) active orbitals (4) virtual orbitals. These categories are illustrated in Figure 1.1. In the example given in Figure 1.1 only two active orbitals, ψ_3 and ψ_4, are used to build the complete active space self−consistent field theory (CASSCF) wavefunction. Within the two−orbital active space only four possible electronic configurations are possible (*D_1, D_2, D_3, and D_4* of Figure 1.1). The *D_2/D_3* and *D_4* correspond to single and double electron promotions from the HF determinant, respectively. For example, the expression of the *D_2* determinant is given in Equation 1.3.

The CASSCF wavefunction for the case illustrated in Figure 1.1 can be written as Equation 1.4. The c_1, c_2, c_3, and c_4 are the coefficients of the determinants.

$$D_2 = \frac{1}{\sqrt{6!}} \begin{vmatrix} \psi_1(1)\alpha(1) & \psi_1(1)\beta(1) & \psi_2(1)\alpha(1) & \psi_2(1)\beta(1) & \psi_3(1)\beta(1) & \psi_4(1)\alpha(1) \\ \psi_1(2)\alpha(2) & \psi_1(2)\beta(2) & \psi_2(2)\alpha(2) & \psi_2(2)\beta(2) & \psi_3(2)\beta(2) & \psi_4(2)\alpha(2) \\ \psi_1(3)\alpha(3) & \psi_1(3)\beta(3) & \psi_2(3)\alpha(3) & \psi_2(3)\beta(3) & \psi_3(3)\beta(3) & \psi_4(3)\alpha(3) \\ \psi_1(4)\alpha(4) & \psi_1(4)\beta(4) & \psi_2(4)\alpha(4) & \psi_2(4)\beta(4) & \psi_3(4)\beta(4) & \psi_4(4)\alpha(4) \\ \psi_1(5)\alpha(5) & \psi_1(5)\beta(5) & \psi_2(5)\alpha(5) & \psi_2(5)\beta(5) & \psi_3(5)\beta(5) & \psi_4(5)\alpha(5) \\ \psi_1(6)\alpha(6) & \psi_1(6)\beta(6) & \psi_2(6)\alpha(6) & \psi_2(6)\beta(6) & \psi_3(6)\beta(6) & \psi_4(6)\alpha(6) \end{vmatrix} \tag{1.3}$$

$$\Psi_{CASSCF} = c_1 D_1 + c_2 D_2 + c_3 D_3 + c_4 D_4 \tag{1.4}$$

The general form of the CASSCF wavefunction is $\Psi_{\mathrm{CASSCF}} = c_1 D_1 + c_2 D_2 + c_3 D_3 + \cdots + c_{\mathrm{i}} D_{\mathrm{i}}$ (the i is the i^{th} determinant corresponds to its i^{th} electron configuration). The CASSCF energy is given by Equation 1.5. In this case energy minimization provides the atomic or molecular orbitals ψ and coefficients.

$$E_{CASSCF} = \frac{\int \Psi^*_{CASSCF} \hat{H} \Psi_{CASSCF} \, d\tau}{\int \Psi^*_{CASSCF} \Psi_{CASSCF} \, d\tau} \tag{1.5}$$

The energy difference between E_{HF} and E_{CASSCF} is called static electron correlation (also known as strong correlation) and it is extremely important in cases such as transition metal compounds, where multiple configurations involving s and d orbitals contribute to the wavefunction. Although CASSCF improves the wavefunction considerably, a more advanced methodology is needed for accurate results. The multi−reference configuration interaction (MRCI) is one of these methods. The technically possible MRCISD variant allows single and double electron promotions from all electrons (except the frozen core ones) to the virtual orbitals and corresponding coefficients are obtained by minimizing the energy.

The total energy of two monomers, *E(A) + E(B)*, obtained by calculating *E(A)* and *E(B)* separately, should be equal to the total energy of the monomers obtained by keeping them in a larger distance *E(A + B)*. This is known as size-consistency.[1] However for MRCI the *E(A + B) ≠ E(A) + E(B)*, hence not size-consistent. Davidson correction (MRCI+Q) is being used to overcome the size-consistency errors of MRCI. The Davidson correction is calculated

form the Equation 1.6.[4] E_{DC} is the Davidson correction, c_0 is the combined coefficients of the MRCI wavefunction, and ΔE is the correlation energy.

$$E_{DC} = (1 - c_0^2)\Delta E \tag{1.6}$$

Usually, the active space is the valence space of an atom or a molecule. Often computational cost restricts the selection of the full valence space, hence only important orbitals of a specific process are included. For example, both the bonding and anti−bonding orbital are vital for correct bond dissociations, especially at infinite distances of a potential energy profile.

1.3 Electronically excited states of molecules

Promotion of one or few electrons from an orbital to another orbital creates excited states of a molecule. Electron promotion changes the $c_1 - c_4$ coefficients in the CASSCF wavefunction i.e. $c_2/c_3/c_4$ are larger for the excited states compared to the c_1 (see Section 1.2). Molecules bear bound excited states with respect to electron ionization. Since electrons are much lighter than nucleus their rearrangement is much more rapid compared to the nuclear motion of the molecule (Frank−Condon principle).[5] Because of this reason electron excitation energies govern the absorption spectrum of a molecule.[6]

Excited state of a molecule can behave completely differently compared to the ground state. For example, the $^3\Sigma_g^-$ ground state of O_2 is inert compared to its $^1\Delta_g$ first excited state.[7,8] The formation of the ground state of molecules from excited states of their fragments or constituent atoms is very often in chemistry, maybe more often than the formation from the ground state fragments. Because of that better appreciation of excited state electronic structures is vital to understand or to interpret properties or phenomena in chemical, biological, and material science (e.g. photosynthesis, photocatalysts, and light−harvesting processes).[9,10]

To this end, computational tools are extremely useful to describe the excited states of molecules. There are series of methodologies are available to analyze ground state of a molecule. In contrast, studying excited states of a molecule is not that straightforward. Ap-

plication of proper computational methodology is crucial for accurate description of excited states.[4]

1.4 Potential energy curves

Potential energy curves (PECs) are useful to understand and visualize the relationship between molecular geometry and potential energy.[1] Using multi−reference PECs ground and excited states of molecules can be analyzed efficiently. The depth of a potential well represents the stability and the energy minimum corresponds to the equilibrium geometry of the electronic state.[1] By approximating a potential well to a harmonic potential well, spectroscopic constants of an electronic state of a diatomic molecule can be computed.[1] Furthermore, PECs can be utilized to propose origins of chemical bonding patterns of a molecule.[11] In some cases, molecules result from excited state fragments and show avoided crossings in the energy profile. In a potential energy profile curves with same spins and same symmetry are not allowed to cross, instead such curves produce avoided crossings (see the Figure 1.2).[12] These are also known as, intended crossings, non−crossings, and anti−crossings. Avoided crossings can be detected using full PECs. This helps us to introduce their accurate bonding patterns. Avoided crossing point possesses mixed electronic configurations of the two crossing PECs. Only multi−reference methods can describe avoided crossings accurately. In overall the ground state PEC shown in Figure 1.2 originate from the excited state fragments and ground state fragments are repulsive in nature.

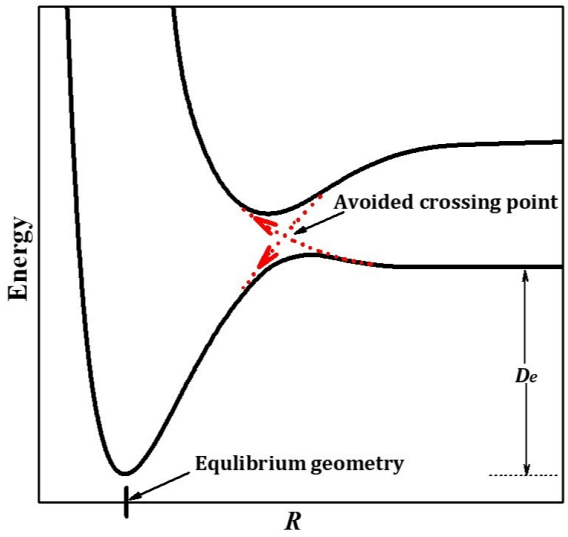

Figure 1.2: An illustration of avoided crossing. Two potential energy curves have identical spin and symmetry. D_e is the binding energy of the species with respect to ground state fragments. R is the reaction coordinate.

Full PECs of a diatomic molecule can be created by combining the wavefunctions of the ground and excited electronic states of the two fragments using multi−reference calculations. For example, the mixing of the three lowest energy fragment combinations produces the four lowest energy electronic states of BeO.[13] In this case lowest energy channel is Be(^{1}S) + O(^{3}P). Since the first excitation energy of oxygen is lower than that of Be (~16,000 vs 22,000 cm^{-1}), the next lowest energy asymptote becomes the Be(^{1}S) + O(^{1}D).[13,14] The ground state of BeO($X^1\Sigma^+$) origin from this channel. The following combination is Be(^{3}P) + O(^{3}P), because the first excitation energy of beryllium atom is smaller compared to the third excited state of oxygen.[13] These three combinations produce three triplet, five singlet, and nine(singlet + triplet + quintet) electronic states for BeO. By considering all these electronic states that arise from these three lowest energy fragments full potential energy profile can be obtained. This methodology is ideal to study excited states of a molecule since all the low energy states of a molecule are accounted into the calculation. Using this approach excited states of series of molecules were investigated in this thesis work.

1.5 Carbon monoxide and metal carbonyls

Carbon monoxide is the strongest ligand in the spectrochemical series.[15] The ground state of CO is a $X^1\Sigma^+$ bear triple bonds. The valence−bond−Lewis (vbL) diagram of CO($X^1\Sigma^+$) is given in Figure 1.3. Its first excited state, $a^3\Pi$, lies 48686.7 cm^{-1} above the ground state.[14] To create the excited state one electron promotes to π^* of CO and hence its bond length is expected to be longer compared to the ground state. As expected $X^1\Sigma^+$ and $a^3\Pi$ of CO have 1.128 and 1.206 Å bond lengths, respectively.

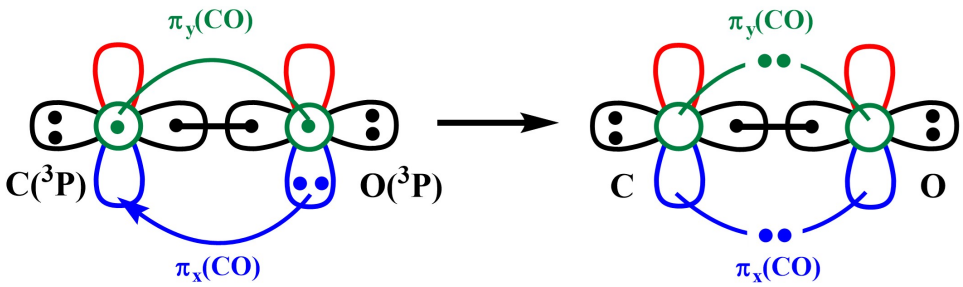

Figure 1.3: vbL diagrams of the CO molecule.

The two electrons at the carbon terminal are more basic compared to the lone pair at the oxygen end and make bonds with more electro−positive metals efficiently. Generally, metal−CO bonds are dative in nature. A M←:CO dative bond tends to develop a δ^+ charge on the carbon of CO and this induces the π−accepter strength of CO.[16] Its vacant two π^* orbitals are another reason for its excellent π−acidity. In metal−carbonyls π−backdonation is common. The π−backdonation weakens the CO bond but strengthen the M−C bond of MCO. The bigger the π−backdonation the weaker the CO becomes. Cotton and Wilkinson identify the chemical bonding of metal−carbonyls as resonance $M^-{-}C^+{\equiv}O: \longleftrightarrow M{=}C{=}\ddot{O}:$ form. In general, CO bond is weaker in metal−carbonyls compared to a free CO.[16] However, in some cationic metal−carbonyl complexes the C−O bond is found to be stronger compared to free CO (e.g. $M(CO)_{1,2}^+$ (M = Cu, Ag, Au)). Frenking et al. identify such species as non−classical metal−carbonyls .[17]

Even though oxygen is more electronegative than carbon, the CO has $C(\delta^-)O(\delta^+)$ charge distribution. The dipole moment of CO is 0.122 D.[18] Replacing the oxygen with an isovalent S, Se, Te increases the dipole moment and creates much stronger bonds with metals.[19]

Chemical bonding of NO($X^2\Pi$) ground state is somewhat similar to CO($X^1\Sigma^+$). Both has triple bonds but the π^* orbitals of NO is occupied by an electron. π^* orbitals are vacant in CO. Similar to CO, NO prefers to bind with metals from N terminal i.e. linearly. But NO also creates bent M−NO and side−bonded M[NO] due to its π^* electron. In NO all these three electrons (two sigma electrons in N terminal and the π^* electron) contribute for the chemical bonding.[16] Similar to heavy analogs of CO (e.g. CS, CSe, CTe), such counterparts of NO (i.e. NS, NSe, NTe) create stronger chemical bonds with metals.[20]

1.6 Molecules with diffuse electrons

Atoms and molecules populate diffuse orbitals at high excited states. Such electronic states are commonly known as Rydberg excited states.[21,22] However, molecules that bear diffuse electrons at ground states are rare. Several such anionic systems have been identified. For example, a free electron in water or ammonia is heavily diffuse in nature.[23,24] These less−stable electrons in a solvent are called *"solvated electrons"*. Solvated electrons can be produced by reacting some metals with water or ammonia. Alkali metals are ideal for this purpose due to their lower ionization potentials. Interestingly, solvated electrons in lithium−ammonia are significantly more stable compared to solvated electrons in water.[23,25] To understand the lithium−ammonia interactions a comprehensive molecular level study has been conducted by Hoffman et al.[24] They identified tetrahedral $Li(NH_3)_4$ as a major species that is present in a lithium−ammonia solution.[24] This molecule possesses a diffuse electron in the periphery. Fascinatingly, this electron cloud is spherical in shape as an s−type atomic orbital. Furthermore, in the first excited state of $Li(NH_3)_4$ an atomic p−type orbital is occupied. Hoffman et al. mooted $Li(NH_3)_4$ as a *"superatom"* that mimics a H−atom. Other metals such as Na, Be, Mg, and Ca also can create such molecular species with diffuse electrons.[26–29] Similar to Hoffman's finding they tend to populate p−, d−, f−type heavily diffuse orbitals in excited states. We dubbed such species as *"solvated electron precursors"* (SEPs).[26]

SEPs are somewhat different from traditional superatoms. Superatom is a molecule that mimics an atom.[30] Metal clusters often behave as superatoms and follows a specific superatomic Aufbau orbital order.[30] For example, the twenty valence electrons of the Al_7^+

cluster shows $1s^2 1p^6 1d^{10} 2s^2$ superatomic electron configuration[31] (see the orbital plots in Figure 1.4). Note that this superatomic Aufbau order has been introduced by counting only and all valence electrons of the cluster i.e. electrons in superatoms are in the valence space of the atoms.[31] In contrast to such superatoms, all valence electrons of SEPs do not occupy atomic type orbitals. What makes a SEP unique is its atomic s−type HOMO and populating atomic−type orbitals in excited states.[26]

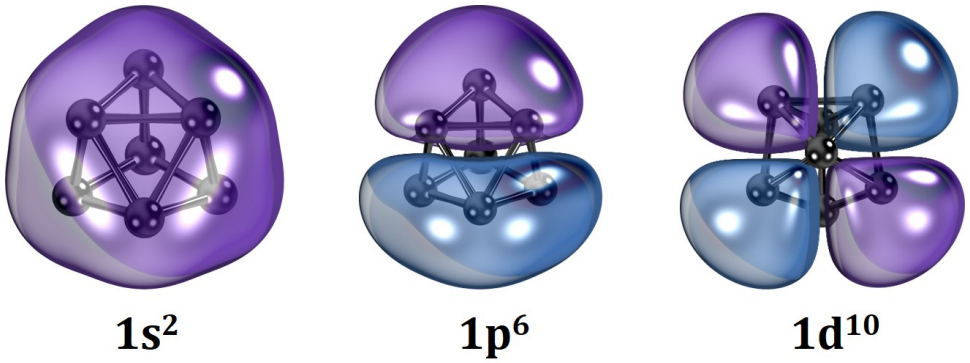

Figure 1.4: Superatomic orbitals of Al_7^+.

Superhalogens and superalkalis are also superatoms. A superhalogen is a molecule that possess a greater electron affinity (EA) compared to the Cl atom and tends to mimic halogens.[30] On the other hand, a superalkali bears a lower ionization potential than Cs atom imitating alkali metals.[30,32] Interestingly, several SEPs have lower ionization energy (IE) than Cs and also can be categorized as superalkalis.

1.7 Beryllium molecules

Beryllium is one of the most chemically rich main group elements in the periodic table.[33,34] Involvement in ionic, covalent, and dative bonds clearly shows the *"chameleon−like"* chemical nature of beryllium.[19,33–35] This versatility of beryllium arises by its dual acidic and basic properties.[33,36,37] Experimental studies on beryllium compounds are limited due to its high−toxicity.[33,36,38] Because of that insight on properties of beryllium species have mostly gained via theoretical studies.

Sometimes, theoretical studies on beryllium containing molecules are challenging due

to their multi−reference electronic nature.[35] Furthermore, beryllium bears several low−lying electronic states that readily participate in chemical bonding.[14] The ground state of beryllium has a closed shell $1s^2 2s^2$ configuration.[14] By the promotion of one $2s^2$ electron to the vacant valence 2p orbitals beryllium gives birth to its first excited state $^3P(1s^2 2s^1 2p^1)$ at ~22,000 cm^{-1}. The corresponding $^1P(1s^2 2s^1 2p^1)$ is high in energy (at 42,565 cm^{-1}) which follows the *"Hund's rule"* which is *"the maximum multiplicity of a particular electronic configuration is the lowest in energy"*.[14,15] The next two states ^3S (at 52,081 cm^{-1}) and ^1S (at 54,677 cm^{-1}) are Rydberg states with $1s^2 2s^1 3s^1$ configuration.[14] Even the high energy $^1D(1s^2 2p^2$; 56,8883 cm^{-1}) state gives birth to ground states of molecules (e.g. $Be(CO)_3$).[14,19] So, it is absolutely important to consider these important low−lying electronic states in chemical bonding studies of beryllium molecules.

During my thesis research I performed theoretical studies on series of beryllium containing molecules. Specifically, chemical bonding, potential energy profiles, and excited states of $Be(O)_{1-2}$, $Be(CO)_{1-3}$, BeNO, $Be(PH_3)_3$, $Be(H_2O)_{1-4}$, $Be(NH_3)_{1-4}$, and $[Be(NH_3)_{1-4}]_2$ are discussed. A detailed discussion about these molecules is reported in Chapters 2 and 3.

1.8 Transition metal monoxides (TMMO)

In general, transition metals (TMs) have a plethora of low−lying electronic states stacked very close in energy. Interaction of these electronic states of TMs with oxygen gives rise to manifolds of electronic states of TMMOs. Because of this reason theoretical studies on transition metal−monoxides are challenging. It is almost impossible to make predictions on spin or electronic configuration of a ground state of a TMMO based on chemical intuition. Even though it is an arduous task to study TMMOs, their fundamental knowledge can be very valuable not only to explain and predict their catalytic potency but also to design better catalysts.

Symmetry does not allow all d−orbitals of a TM to mix with an oxygen atom. The d_{z^2}, d_{xz}, and d_{yz} connect with p_z, p_x, and p_y orbitals of oxygen, respectively. The δ orbitals (d_{xy} and $d_{x^2-y^2}$) of a TM do not participate in TM−O chemical bonding. The orbital arrangement between TM and O is illustrated in Figure 1.5.

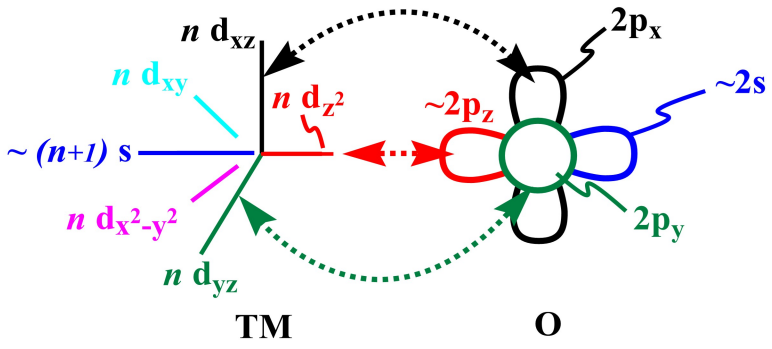

Figure 1.5: A typical vbL diagram for a TMMO.

1.9 Outline

Chapter 2 is devoted to the chemical bonding analysis of several small molecules. The implementation of PECs has allowed us to introduce their chemical bonding patterns, their origins, and to obtain an accurate description for their excited states. This chapter summarizes the most important findings reported in the six articles published as a partial fulfilment of my thesis research. See Appendix A for full copies of their reprints.

Chapters 3 and 4 introduce a new class of molecular entities dubbed *"solvated electron precursors"* (SEPs) that possess diffuse electrons in the periphery. Several metal−ammine (Chapter 3) and metal−aqua (Chapter 4) complexes can be identified as SEPs. In their ground states the electron cloud mimics an s-type orbital and promotes to higher−angular momentum p−, d−, f−, and g−type orbitals. Based on the shapes of the orbitals and excitation energies their Aufbau principles were disclosed. The results given in Chapters 3 and 4 are based on the published papers included in the Appendices B and C, respectively.

Chapter 5 discusses ground and excited electronic structures of transition metal monoxides and their water and hydrogen sulfide activation strengths. Specifically, ZrO^+, NbO^+, $MoO^{+,2+,-}$, and $RuO^{+,0,-}$ diatomics were examined. Their chemical bonding patterns are also discussed. The reprints of the papers related to this area of research are included in the Appendix D.

Chapter 2

Chemical bonding of main–group molecules

It is not an exaggeration to say that chemical bonding is the heart of chemistry. A better understanding of chemical bonds (or corresponding electron arrangements) often provides us with a fundamental knowledge that can explain or predict chemical and physical phenomena of a molecule or molecular cluster. Recently, especially for main−group molecules, the field of chemical bonding has gained a special interest.[11,39–43] Ionic bonds are common for main−group metals even though they occasionally engage in covalent and dative bonds as well.[11,39] Often, quantum calculations are performed to uncover chemical bonding patterns of molecules.[11,39] Specifically, multi−reference methods are ideal to represent complicated electronic structures of ground and excited states of molecules.[4] Multi−reference methods can break bonds accurately, hence can be used to produce full potential energy profiles of ground and excited states of molecules.[4] Often, we use multi−reference potential energy curves to explore origins of chemical bonds of molecules. In this chapter findings related to chemical bonding analysis of several small molecules are discussed.

2.1 Chemical bonding analysis of N_2O, N_2O_2, N_3H, and NH_3O

N_2O, N_2O_2, N_3H, and NH_3O molecules are often being used in elementary−level chemical bonding teaching purpose. Even though, their equilibrium ground state electronic structures are well documented such studies disclose their origins are not.[7,44–47] Because of this reason full potential energy profiles were used to unveil their origins.

MRCI PECs of N_2O are produced as a function of N−O distance considering $N_2(X^1\Sigma_g^+)$ + $O(^3P)$ and $N_2(X^1\Sigma_g^+)$ + $O(^1D)$ interactions (see Figure 2.1). The former and latter channels produce $^3\{\Pi, \Sigma^-\}$ and $^1\{\Sigma^+, \Pi, \Delta\}$ states, respectively. All valence orbitals are occupied in the ^3P state of oxygen, restricting dative bond formation with two−electron donor ligands such as N_2. Hence, $^3\Pi$ and $^3\Sigma^-$ PECs arising from $N_2(X^1\Sigma_g^+)$ + $O(^3P)$ are repulsive. The $^1\Sigma^+$ originating from $N_2(X^1\Sigma_g^+)$ + $O(^1D)$ is attractive and produces the ground state of N_2O. In the $O(^1D)$ state one 2p orbital is empty which allows formation of a dative bond with the lone electron pair of $N_2(X^1\Sigma_g^+)$. This interaction is pictorially described in the Figure 2.2. At CCSD(T) (coupled−cluster singles and doubles plus approximate triples) level, the optimal N−N and N−O distances of N_2O are 1.133 and 1.190 Å, respectively. The bond distance of naked N_2 molecule is 1.098 Å. Compared to the N_2 molecule the N−N length of the N_2O is ∼0.1 Å longer.

In the N_2O molecule the N−terminal possess a lone pair electron. These two electrons interact with another $O(^1D)$ to create the N_2O_2 molecule. Similarly, two $O(^1D)$ atoms can bind with $N_2(X^1\Sigma_g^+)$ simultaneously to produce N_2O_2. It should be noted that N_2O_2 can easily dissociate in to two NO molecules.[45] Here we only studied the origin of N_2O_2 molecule by creating PECs as a function of N−O, where (1) one oxygen atom approaches the N−terminal of N_2O (2) two oxygen atoms simultaneously approach the N_2 colinearly from opposite directions. PECs for these two interactions are given in the Figure 2.1. After $N_2O(\tilde{X}^1\Sigma_g^+)$ + $O(^1D)$ or $N_2(X^1\Sigma_g^+)$ + $2O(^1D)$ interaction, it passes via a conical intersection to produce a C_{2h} molecule. This phenomenon is described for the isoelectronic $(CH_2)_2N_2$ molecule by Khan et al. in 2019.[48] The electron arrangements of the linear $N_2(X^1\Sigma_g^+)$ + $2O(^1D)$ interaction and C_{2h} molecule are illustrated in Figure 2.2.

NH is isoelectronic to oxygen atom. Similar to oxygen the 2p orbitals of N of NH is

occupied in the $^3\Sigma^-$ ground state. Its first excited state ($a^1\Delta$) bears a vacant ~2p orbital at the N and binds with a N_2 ligand. See the PECs of the Figure 2.1. Proposed vbL diagrams for the formation of the ground state are given in the Figure 2.2. Its optimal N−N−N and N−N−H angles are 171.6 and 108.3 degrees, respectively. The N_x−N_y, N_y−N_z, and N_z−H parameters of the $N_xN_yN_zH$ are 1.136, 1.247, and 1.018 Å, respectively.

Formation of NH_3O molecule is similar to the N_2O. In this case the empty 2p of O(^{1}D) binds with the lone pair of the NH_3 molecule. The PECs of NH_3O and vbL diagram for the $NH_3O(\tilde{X}^1A_1)$ are shown in the Figures 2.1 and 2.2, respectively. The N−O bond length of the NH_3O is 1.370 Å. The D_e of the molecule with respect to $NH_3(\tilde{X}^1A_1)$ + O(^{1}D) fragments is 67.6 kcal/mol.

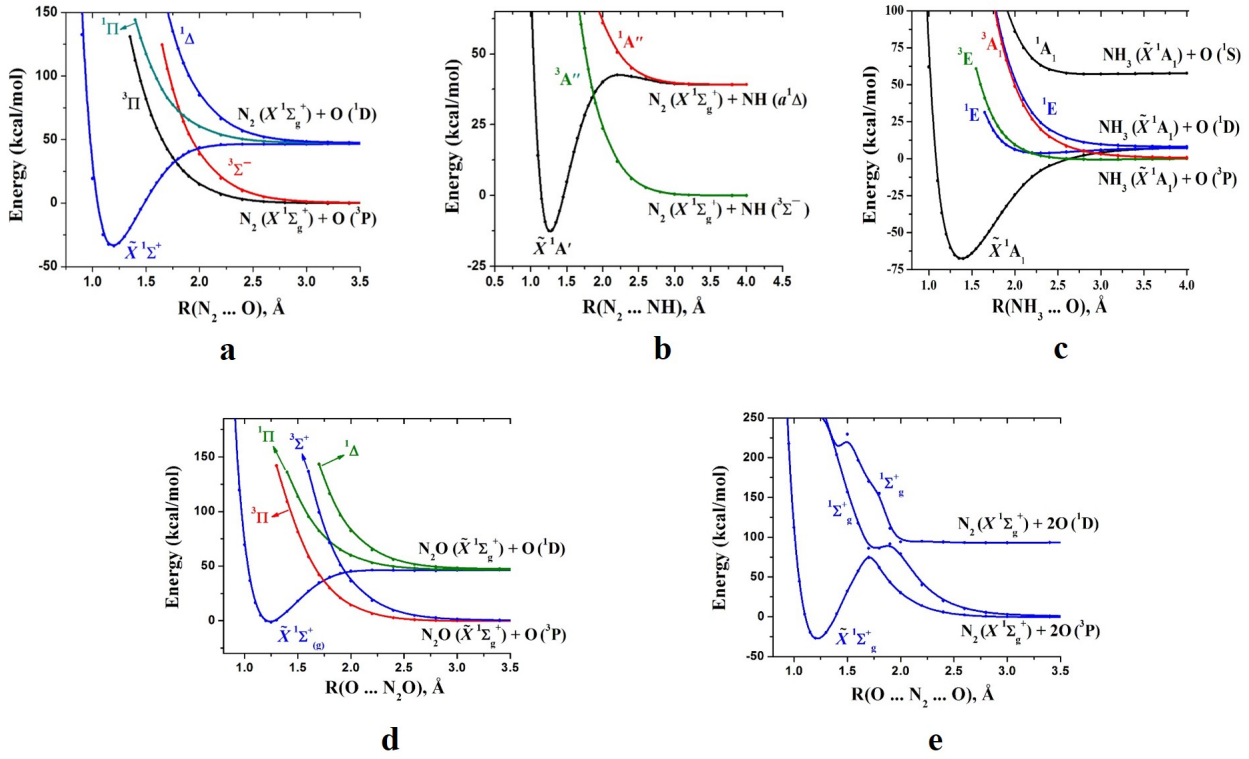

Figure 2.1: MRCI PECs of the (a) N_2O as a function of N−O (b) N_3H as a function of N_2−NH (c) NH_3O as a function of N−O (d) N_2O_2 as a function of N−O for the colinear approach of oxygen towards the N−terminal of N_2O (e) N_2O_2 as a function of N−O for the simultaneous approach of two oxygen atoms towards N_2 colinearly in opposite directions. In cases (a), (b), and (e) N−N distance is kept fixed to the experimental N_2 distance of 1.098 Å. In case (c) N−H lengths are kept fixed to the ground state geometry of $NH_3(\tilde{X}^1A_1)$. In (d) N−N and N−O bonds of N_2O are kept fixed to the ground state geometry of $N_2O(\tilde{X}^1\Sigma_g^+)$.

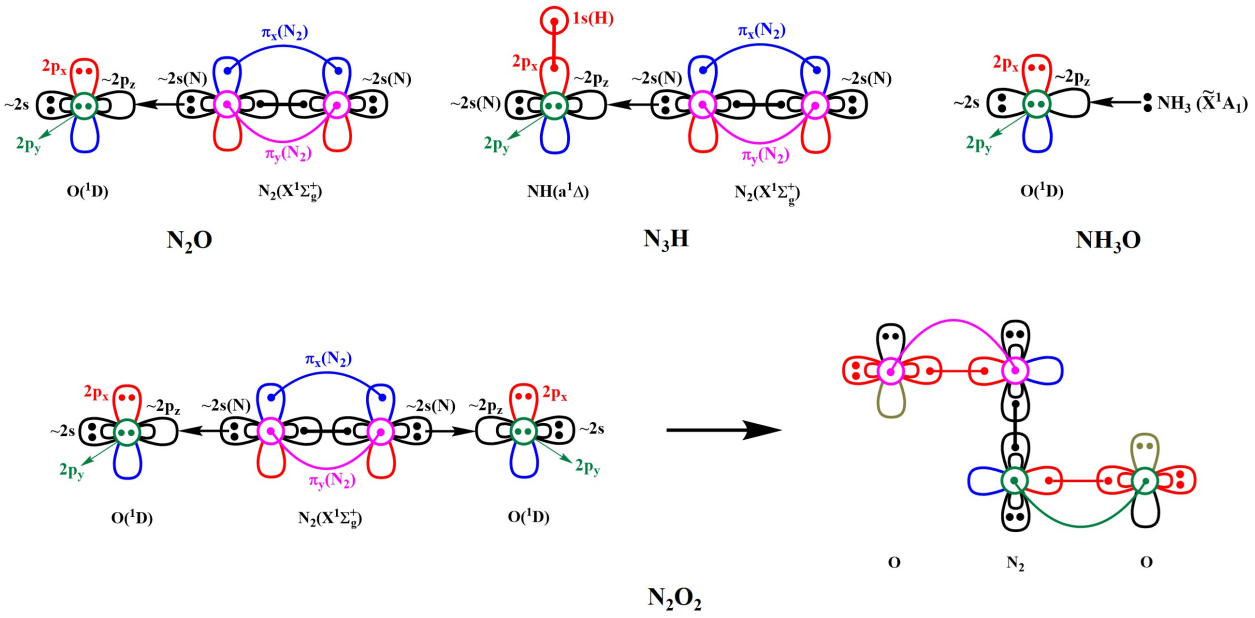

Figure 2.2: vbL diagrams of N_2O, N_3H, NH_3O, and N_2O_2.

2.2 Chemical bonding of analysis of metal carbonyls

2.2.1 Neutral and anionic $M(CX)_{n=1-3}$ [M = Li, Na and X = O, S, Se, Te, Po] and $[Li(CO)_3]_2$ dimer

In this section most important findings reported in following paper[49] given in Appendix A are summarized. Reprints were made with permission from JOHN WILEY & SONS, INC.

Ariyarathna, I. R.; Miliordos, E. *J. Comput. Chem.* **2019**, *40*, 1344–1351.

LiCO is the simplest metal carbonyl molecule that can exist. Interaction between Li and CO has been studied by Kalemos et al.[50] The $^2\Pi$ ground state of LiCO is metastable with respect to Li(^{2}S) + CO($X^1\Sigma^+$) fragments. The attack of two CO ligands to Li creates a stable $Li(CO)_2$ molecule that bears 8.8 kcal/mol D_e with respect to Li(^{2}S) + 2CO($X^1\Sigma^+$) fragments. Linear and bent structures are stable minima on the of $Li(CO)_2$ potential energy surface. The bent $\tilde{X}^2B_1$ structure is slightly lower in energy (by ~2 kcal/mol) compared to the linear $^2\Pi_u$ structure. Li(^{2}P) + 2CO($X^1\Sigma^+$) fragments give birth to both $\tilde{X}^2B_1$ and $^2\Pi_u$ structures of $Li(CO)_2$. Note that the ^{2}P is the first excited state of Li which carries a $1s^22p^1$

electronic configuration. In both structures the $2p^1$ electron of Li back−donates to the π^* of CO ligands (see Figure 2.3). Similar to $Li(CO)_2$, all $Li(CX)_2$ (X = S, Se, Te, Po) molecules are generated from the first excited state of Li. Analogous to $Li(CO)_2$, the bent isomer of $Li(CS)_2$ is slightly stabilized (only by 0.5 kcal/mol) compared to the linear structure. $Li(CSe)_2$, $Li(CTe)_2$, and $Li(CPo)_2$ have only linear structures for the ground state. Going from X = Li to Po the D_e of $Li(CX)_2$ rises. D_es of $Li(CX)_3$ are higher than $Li(CX)_2$. Each $Li(CX)_3$ carries a planer geometry with $\tilde{X}^2A_2''$ ground state. Similar to $Li(CX)_2$, $Li(CX)_3$ is produced by the ^2P state of Li and the $2p^1$(Li) electron back−donates to π^* of three CO.

$Na(CX)_{n=2,3}$ species behave similar to $Li(CX)_{n=2,3}$. Both linear and bent ground states of $Na(CO)_2$ are metastable with respect to their ground state fragments. Similarly, $Na(CO)_3$ has a negative D_e. All other $Na(CX)_{n=2,3}$ show positive but smaller D_es, compared to $Li(CX)_{n=2,3}$ molecules.

All MCX^-, $M(CX)_2{}^-$, and $M(CX)_3{}^-$ (M = Li, Na) are stable with respect to their neutral molecules, except for the $Na(CO)_3{}^-$. MCX^- species have $^3\Pi$ ground state with the additional electron placed in the empty slightly polarized 2s of Li. The two same spin electrons of $^3\Sigma^-$ ground state of $M(CX)_2{}^-$ reside in the two perpendicular π−orbitals. On the other hand, $M(CX)_3{}^-$ are closed shell singlets, with two electrons in the π−frame. Electron affinities of $Li(CX)_{n=1-3}$ increase going from X = O to Po. $Li(CX)_3$ have electron affinities bigger than LiCX, but lower compared to $Li(CX)_2$.

Two $Li(CO)_3$ molecules bind together to make a stable $[Li(CO)_3]_2$ dimer by coupling the two π−electron of two $Li(CO)_3$ monomers. The HOMO of the dimer is given in the Figure 2.3. These type of chemical bonds are known as *"Pancake chemical bonds"*.[51] The D_e of the dimer with respect to $2Li(CO)_3(\tilde{X}^2A_2'')$ monomers is 27.2 kcal/mol at MP2(Møller−Plesset Second−order Perturbation Theory)[52] level. The dimer has staggered and eclipsed isomers, but the former is 1.7 kcal/mol more stable than the latter. The eclipsed−to−staggered interconversion energy barrier is only 2.7 kcal/mol.

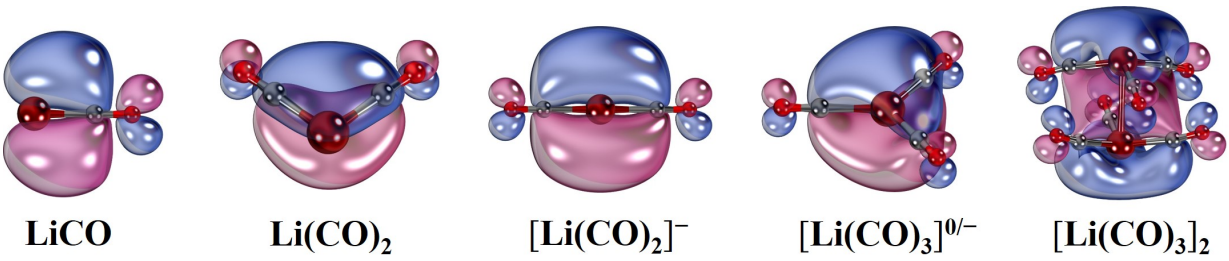

Figure 2.3: HOMOs LiCO, $Li(CO)_2^{0,-}$, $Li(CO)_3^{0,-}$, and $[Li(CO)_3]_2$.

2.2.2 $Be(CO)_{n=1-2}$

In this section most important findings related to $Be(CO)_{n=1-2}$ species reported in following paper[35] given in Appendix A are summarized. Reprints were made with permission from American Chemical Society.

Ariyarathna, I. R.; Miliordos, E. *J. Phys. Chem. A* **2017**, *121*, 7051–7058.

The ^{1}S ground state of beryllium bears a $1s^22s^2$ closed shell configuration. Its first two excited states, ^{3}P and ^{1}P, that show $1s^22s^12p^1$ electron configuration lie 21,980 and 42,565 cm^{-1} above the ground state. Third and fourth excited states of beryllium are Rydberg states.[14] They are followed by a ^{1}D($1s^22p^2$) state.[14]

The interaction between Be(^{1}S) and CO($X^1\Sigma^+$) is expected to be repulsive, due to their closed shell nature. The PEC results from these fragments indeed show repulsive behavior proving the aforementioned prediction (see Figure 2.4). The 2s to 2p electron promotion opens the Be core for a favorable CO attack. The Be(1^3P) + CO($X^1\Sigma^+$) produces the metastable $^3\Pi$ ground state of BeCO. This might be the reason for unavailable experimental data on BeCO.[53] The electron arrangement of BeCO($^3\Pi$) is shown in Figure 2.5. The attractive PEC arising from Be(1^1P) + CO($X^1\Sigma^+$) is the first excited state ($^1\Pi$) of BeCO.

Unlike BeCO, the ground state of $Be(CO)_2$ is stable with respect to ground state fragments. The Be(^{1}S) + 2CO($X^1\Sigma^+$) interaction is initially repulsive but turn attractive around 2.1 Å. This interaction is caused by the attractive $^1\Sigma_g^+$ PEC coming from high−energy Be(^{1}D) + 2CO($X^1\Sigma^+$) channel (See Figure 2.4). Observe that the interaction of 2^3P of Be with CO($X^1\Sigma^+$) gives birth to the third excited state ($^3\Sigma^-$) of BeCO, but the ground state of $Be(CO)_2$ originate from the same 2^3P state of Be. The vbL diagram of the $Be(CO)_2$ ($^3\Sigma^-$)

is illustrated in the Figure 2.5. The Be–C and C–O distances of BeCO ($^3\Sigma^-$) are 1.539 and 1.181 Å, respectively. The corresponding bond lengths of $Be(CO)_2$ ($^3\Sigma_g^-$) are 1.612 and 1.157 Å, respectively. This is a direct result of stronger π back donation from Be→CO in BeCO compared to $Be(CO)_2$.

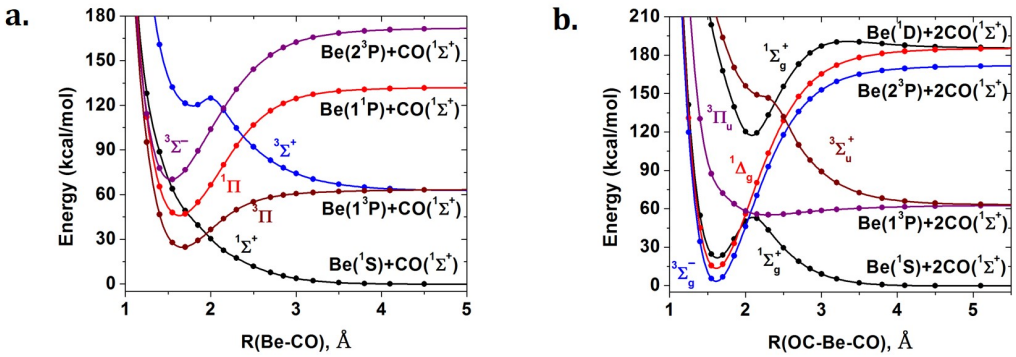

Figure 2.4: MRCI PECs of (a) BeCO and (b) $Be(CO)_2$ as a function of Be–C distance. Two CO ligands approach Be atom simultaneously in $Be(CO)_2$ case.

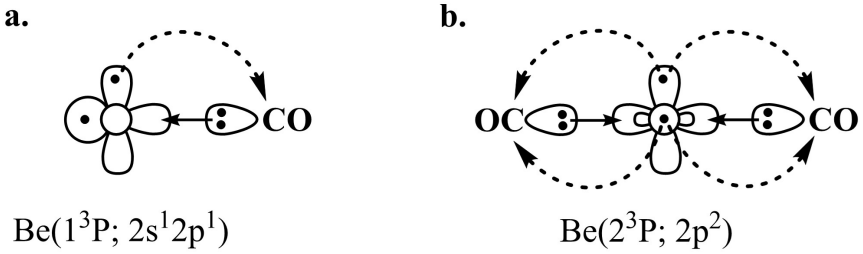

Figure 2.5: vbL diagrams of (a) BeCO($^3\Pi$) and (b) $Be(CO)_2$($^3\Sigma_g^-$).

2.2.3 $Be(CX)_3$ [X = O, S, Se, Te, Po]

In this section most important findings reported in following paper[19] given in Appendix A are summarized. Reprints were made with permission from JOHN WILEY & SONS, INC.

Ariyarathna, I. R.; Miliordos, E. *Int. J. Quantum Chem.* **2018**, *118*, e25673.

Similar to BeCO and $Be(CO)_2$ the interaction between Be and 3CO molecules were studied producing PECs (see Figure 2.6). Be(^{1}S; $1s^2 2s^2$) interaction between 3CO($X^1\Sigma^+$)

is initially repulsive but becomes attractive to produce the ground state of the molecule. Similar to $Be(CO)_2$ this sudden shift around 2.4 Å of the $^1A_1'$ ground state curve is an outcome of an avoided crossing that is caused by the $^1A_1'$ PEC arising from $Be(^1D)$ + $3CO(X^1\Sigma^+)$. $Be(^1D)$ has a $1s^22p^2$ electronic configuration. The three vacant orbitals of $Be(^1D)$ allows it to bind with 3CO ligands via dative bonds. In the ground state $2p^2$ electrons of Be back–donate to π^* of 3CO (see Figure 2.7). Compared to free CO, the C–O bonds of $Be(CO)_3$ are 0.013 Å longer. This is an outcome of the metal–to–ligand π–back donation. $Be(CO)_3$ is isoelectronic to the $Li(CO)_3^-$ and have same type of π–back donation. The Li–C in $Li(CO)_3$ are 0.36 Å longer than Be–C of $Be(CO)_3$. Chemical bonding of all $Be(CS)_3$, $Be(CSe)_3$, $Be(CTe)_3$, $Be(CPo)_3$ are the same as $Be(CO)_3$. D_e increases in the $Be(CO)_3$ < $Be(CS)_3$ < $Be(CSe)_3$ < $Be(CTe)_3$ < $Be(CPo)_3$ order.

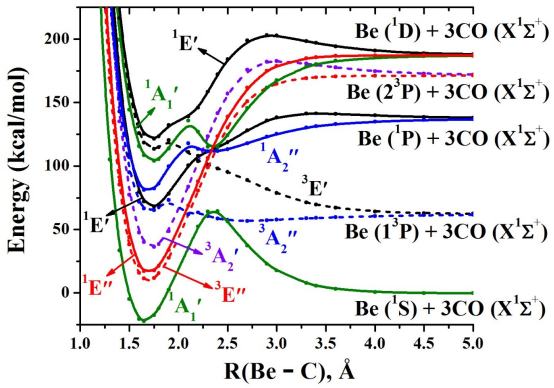

Figure 2.6: MRCI PECs of $Be(CO)_3$ as a function of Be–C distance. Be atom approached by all three CO ligands simultaneously.

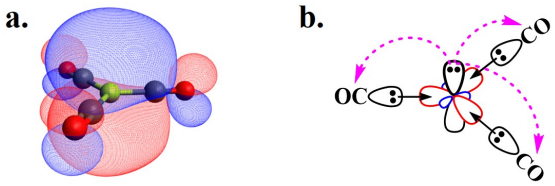

Figure 2.7: (a) The HOMO and the (b) bonding pattern of $Be(CO)_3(\tilde{X}^1A_1')$.

2.2.4 ThCO

In this section most important findings reported in following paper[54] given in Appendix A are summarized. Reprints were made with permission from Royal Society of Chemistry.

Ariyarathna, I. R.; Miliordos, E. *Phys. Chem. Chem. Phys.* **2019**, *21*, 24469–24477.

Computational studies on actinide species are computationally challenging due to their higher number of valence electrons and rich multi−reference characters.[55] Even though Th is recognized as an actinide it does not carry f−electrons in several low−lying electronic states, which is encouraging for computational studies on Th. Specifically, the first three (^{3}F, ^{3}P, ^{1}D) and fourth (^{5}F) electronic states of Th bear $6d^27s^2$ and $6d^37s^1$ electronic configurations, respectively.[14]

Before studying Th interactions with CO, we probed three different active spaces to study excited states of Th atom. The used CASSCF active spaces are, (1) 7s, 6d, 7p, 5f, (2) 7s, 6d, 7p, and (3) 7s, 6d. At MRCI level four valence electrons and the 6s and 6p electrons are correlated. According to our values the 2nd active space (7s, 6d, 7p) represents low−lying electronic structures of Th more accurately, providing most comparable results with the experimental values. Hence, this active space was used to study ThCO molecule. PECs were produced considering the interaction between the ^{3}F, ^{3}P, ^{1}D, ^{5}F of Th with CO($X^1\Sigma^+$). The constructed MRCI PECs of ThCO are given in Figure 2.8.

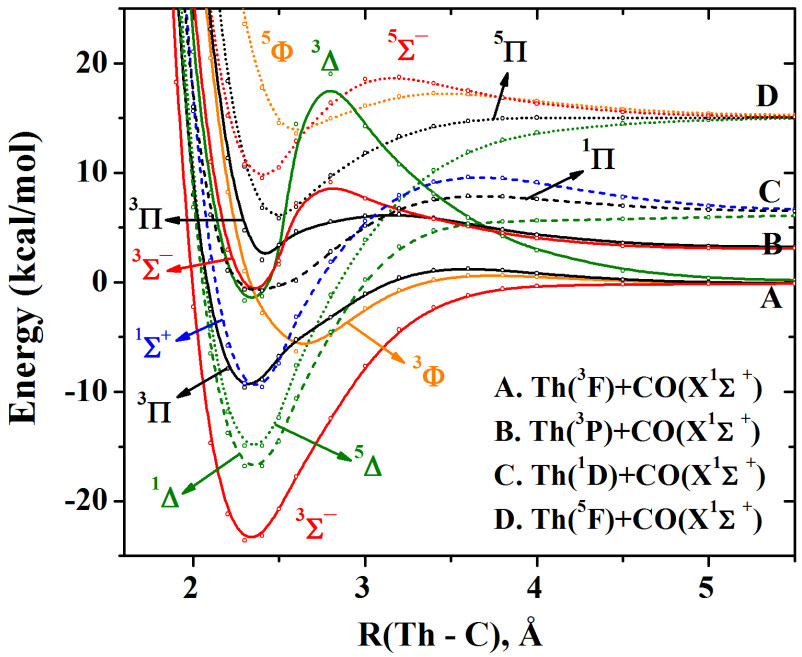

Figure 2.8: MRCI PECs of ThCO as a function of Th−C. The CO length kept fixed to 1.128 Å which is the experimental CO distance.

The $^3\Sigma^-$ ground state of ThCO is produced from the Th(^{3}F) + CO($X^1\Sigma^+$) asymptote. To create the ground state, the $7s^2$ electrons of Th polarize away from the approaching CO ligand. The $6d^2$ electrons of Th back−donate to π_x^* and π_y^* of CO. Th(^{3}F) + CO($X^1\Sigma^+$) asymptote also creates $^3\Pi$ and $^3\Phi$, of ThCO. Its first and second excited states, $^1\Delta$ and $^5\Delta$, smoothly dissociate into Th(^{1}D) + CO($X^1\Sigma^+$) and Th(^{5}F) + CO($X^1\Sigma^+$) fragments, respectively. Overall, the first seven electronic states of ThCO are $^3\Sigma^-$, $^1\Delta$, $^5\Delta$, $^1\Sigma^+$, $^3\Pi$, $^3\Phi$, and $^1\Pi$ in energy order. Based on the dominant electronic configurations at the equilibrium bond distances vbL diagrams are proposed for the first four electronic states of ThCO (see Figure 2.9). These four electronic states show Th=C double bond character with ~2.3 Å lengths. Electron back donation from Th to CO elongate their C−O lengths by ~0.1 Å.

Th atom can cleave CO molecule to create O−Th−C molecule. In 1999 both ThCO and OThC species have been experimentally detected by Andrews et al.[56] ThCO is ~4 kcal/mol stable compared to OThC. The energy barrier lies in between ThCO and OThC is ~30 kcal/mol. The $^3A'$ ground state of O−Th−C has O^{2-}−Th^{4+}−C^{2-} ionic nature as depicted in the Figure 2.9.

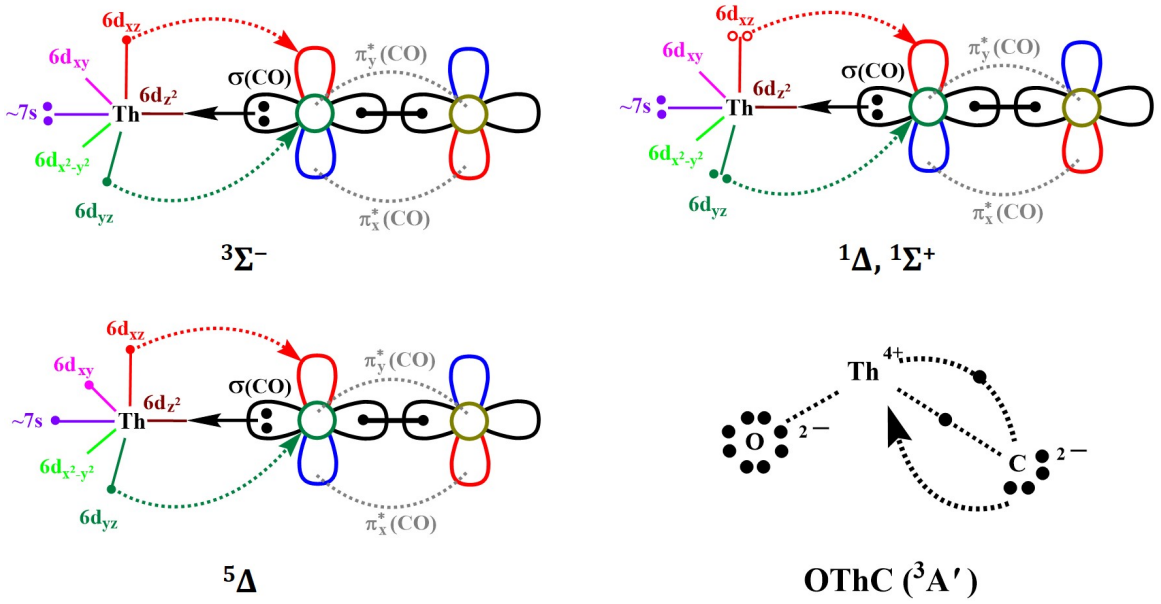

Figure 2.9: Proposed vbL diagrams for the four low−lying electronic states of ThCO and the ground state of OThC. The $^1\Delta$ and $^1\Sigma^+$ bear $-0.59(16\sigma^2 10\pi_y{}^2) + 0.59(16\sigma^2 10\pi_x{}^2)$ and $0.58(16\sigma^2 10\pi_y{}^2) + 0.58(16\sigma^2 10\pi_x{}^2)$ multi−reference electronic characters, respectively. The $(10\pi_x)^2 \pm (10\pi_y)^2$ electron combinations of $^1\Delta$ and $^1\Sigma^+$ are depicted by solid and open circles

2.3 Chemical bonding analysis of neutral and anionic MNX [M = Li, Na, Be and X = O, S, Se, Te]

In this section most important findings reported in following paper[20] given in Appendix A are summarized. Reprints were made with permission from JOHN WILEY & SONS, INC.

Ariyarathna, I. R.; Miliordos, E. *J. Comput. Chem.* **2019**, *40*, 1740–1751.

NO (nitric oxide) ligand is somewhat similar to CO. Both NO and CO are σ−donors and π−acceptors.[16] In the ground state π^* orbitals of CO are empty, but one π^* of NO is occupied by one electron. NO can bind to a metal in linear or oblique fashion.[16] The linear and oblique interactions between NO with Li were studied making potential energy profiles.

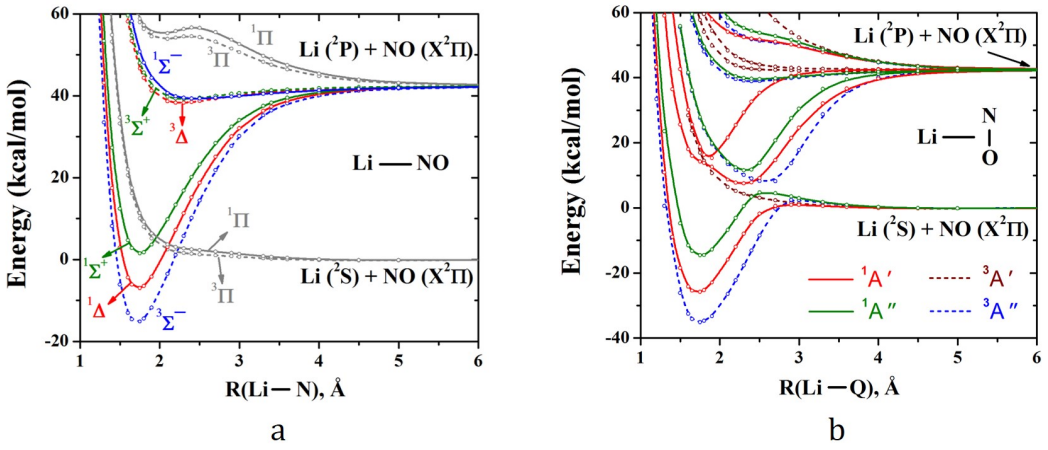

Figure 2.10: MRCI PECs of LiNO (a) as a function of Li−N (b) as a function of Li−Q (Q is the central point of N−O bond). In each case the N−O length kept fixed to its experimental bond distance (1.151 Å).[7]

PECs arising from the Li(^{2}S) + NO($X^2\Pi$) and Li(^{2}P) + NO($X^2\Pi$) interactions are depicted in the Figure 2.10. The linear Li←NO attack produces two repulsive PECs from Li(^{2}S) + NO($X^2\Pi$) asymptote. This is caused by the electron−electron repulsion between $2s^1$(Li) and lone electron pair on N−terminal of NO. This electron−electron repulsion is absent in the Li(^{2}P) + NO($X^2\Pi$) interaction. This combination gives rise to the three lowest energy states of LiNO ($^3\Sigma^-$, $^1\Delta$, $^1\Sigma^+$). The $^3\Sigma^+$, $^3\Delta$, $^1\Sigma^-$ states arising from the same combination are slightly attractive around 2.2 Å. All the $^{1,3}\Pi$ PECs are repulsive. The $^3\Sigma^-$ ground state has a 32.8 kcal/mol D_e with respect to Li(^{2}S) + NO($X^2\Pi$) fragments. The $^3\Sigma^-$ of LiNO is significantly ionic in nature (see Figure 2.11). The two unpaired electrons of the molecule primarily lie in the perpendicular π^* orbitals of NO of the molecule. The oblique fashioned interaction between Li and NO creates a more stable ^{3}A″ structure than the linear $^3\Sigma^-$. Proposed vbL diagrams of linear and bent structures are shown in Figure 2.11. The bent (^{3}A′) structure has a 1.7 kcal/mol higher D_e than the linear ($^3\Sigma^-$) structure. The NO distance of the bent structure is ~0.06 Å longer compared to the linear one. The linear structures of LiNS, LiNSe, and LiNTe are more stable than corresponding bent isomers. Overall, D_e increase in LiNO < LiNS < LiNSe < LiNTe order.

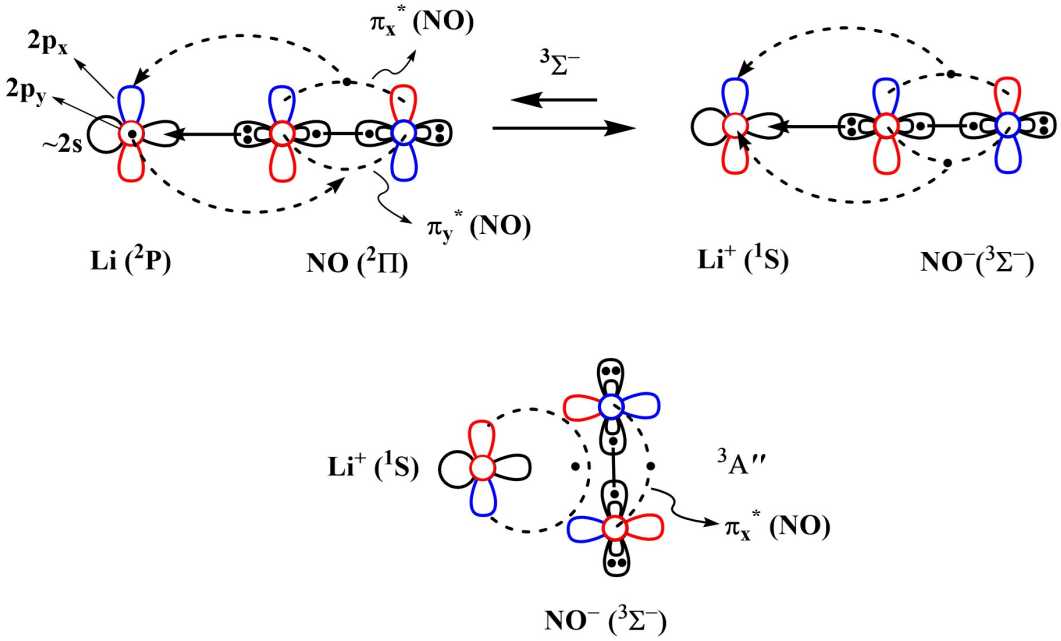

Figure 2.11: vbL diagrams of linear (top) and bent (bottom) LiNO.

The linear $LiNO^-$ isomer is 1.4 kcal/mol stable than bent isomer. The placement of an additional electron in the polarized 2s of Li of linear $LiNO(^3\Sigma^-)$ creates $^4\Sigma^-$ and $^2\Sigma^-$ states of $LiNO^-$. Interestingly, both these states are stable compared to the ground state of LiNO. The $^4\Sigma^-$ ground state of $LiNO^-$ has 0.51 eV electron affinity. All $LiNS^-$, $LiNSe^-$, and $LiNTe^-$ have $^4\Sigma^-$ ground state which is followed by $^2\Sigma^-$ excited state. The electron affinities increase in the LiNO < LiNS < LiNSe < LiNTe order.

$LiNO^-$ is isoelectronic to BeNO. The first four electronic states of BeNO ($^4\Sigma^-$, $^2\Sigma^-$, $^2\Delta$, $^2\Sigma^+$) are produced from $Be(^3P)$ + $NO(X^2\Pi)$. The $^4\Sigma^-$ ground state has an electronic structure identical to $^4\Sigma^-$ of $LiNO^-$. The $^2A'$ ground state of bent BeNO is 7.5 kcal/mol higher than the $^4\Sigma^-$ state of linear BeNO. D_es increase going from BeNO to BeNTe. All BeNO, BeNS, BeNSe, and BeNTe has positive electron affinities and they increase in the same order. Interestingly, both linear and bent isomers are possible for these anions. The electron affinity of both linear and bent isomers of BeNO is 0.99 eV. In BeNS, BeNSe, and BeNTe the linear isomer is more stable.

2.4 Chemical bonding analysis of BeO_2 and $Be(O_2)_2$

In this section most important findings related to $Be(O_2)_{n=1-2}$ species reported in following paper[35] given in Appendix A are summarized. Reprints were made with permission from American Chemical Society.

Ariyarathna, I. R.; Miliordos, E. *J. Phys. Chem. A* **2017**, *121*, 7051–7058.

The most stable isomer of BeO_2 is the linear O−Be−O structure over side bonded $Be(O_2)$. The simpler $BeO(X^1\Sigma^+)$ molecule has been assigned to have ionic Be^+O^- structure.[13] Similar to BeO, the $^3\Sigma_g^-$ ground state of linear OBeO bear ionic $O^-Be^{2+}O^-$ skeleton. The linear interaction of $O(^3P)$ + $Be(^1S)$ + $O(^3P)$ gives birth to $^{1,5}\{\Sigma_g^+, \Sigma_g^+, \Sigma_u^-, \Pi_g, \Pi_u, \Delta_g\}$ and $^3\{\Sigma_u^+, \Sigma_u^+, \Sigma_g^-, \Pi_g, \Pi_u, \Delta_u\}$ states. The attractive singlet and triplet PECs of aforementioned states are given in the Figure 2.12. The $^3\Sigma_g^-$, $^1\Delta_g$, $^1\Sigma_u^-$, $^1\Sigma_g^+$, $^3\Delta_u$, $^3\Sigma_u^+$ states are nearly degenerate in energy. Similarly the states of $[^3\Pi_u, ^1\Pi_g, ^3\Pi_g, ^1\Pi_u]$ and $[2^1\Sigma_g^+, 2^3\Sigma_u^+]$ sets are almost same in energy.

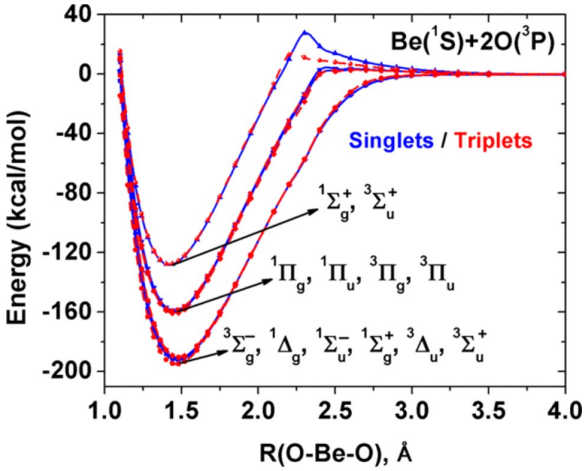

Figure 2.12: MRCI PECs of OBeO as a function of O−Be−O for the simultinious approach of two oxygen atoms towards Be.

$Be(O_2)_2$ has D_{2d} symmetry. The PECs of $Be(O_2)_2$ are given in Figure 2.13. The ground state of $Be(O_2)_2$ is a $^1B_2$. Notice that $^1B_2$ and $^3B_2$ of $Be(O_2)_2$ are almost degenerate in energy. PECs of both these states dissociate to the $Be(O_2)(b^3B_2)$ + $O_2(X^3\Sigma_g^-)$ fragments. However, these two PECs undergo avoided crossings with $^1B_2$ and $^3B_2$ PECs that arise from

$Be(O_2)(c^3B_2)$ + $O_2(X^3\Sigma_g^-)$. The $^{1,3}B_2$ states of $Be(O_2)_2$ bear $O_2^-Be^{2+}O_2^-$ skeleton. The proposed chemical bonding pattern for the $^{1,3}B_2$ is shown in Figure 2.14.

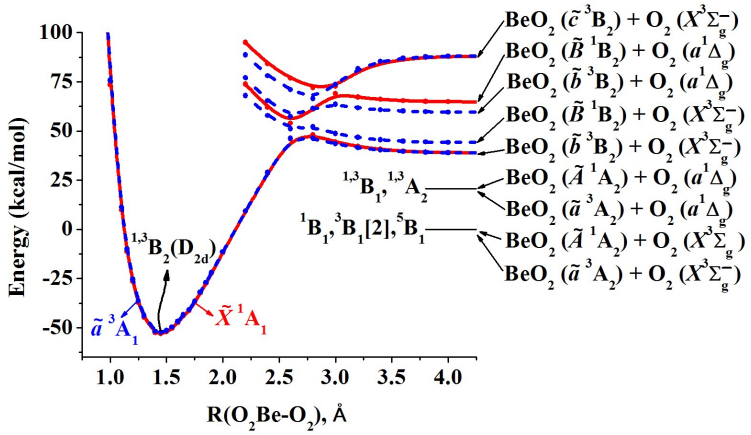

Figure 2.13: MRCI full PECs of $^{1,3}A_1$ states of $Be(O_2)_2$ as a function of the $O_2Be{-}O_2$ distance.

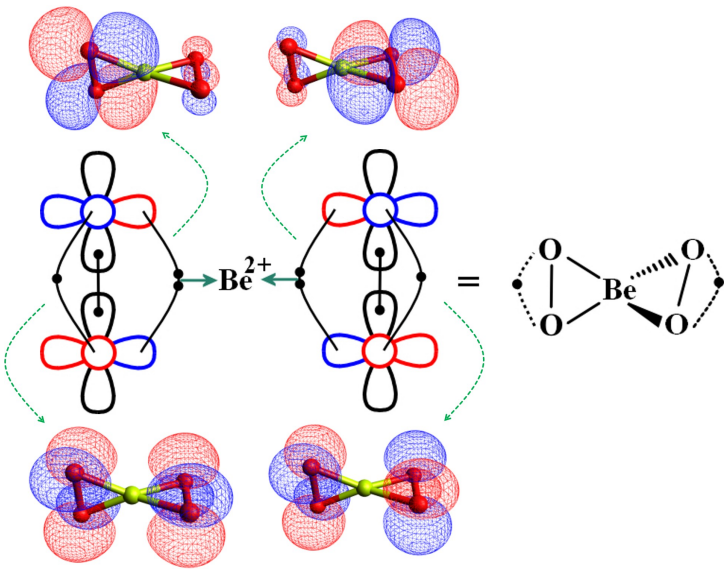

Figure 2.14: Chemical bonding pattern of $Be(O_2)_2$.

2.5 Chemical bonding analysis of $Be(NH_3)_n^{0,+}$ (n = 1–3) and their dimers

In this section most important findings reported in following paper[37] given in Appendix A are summarized. Reprints were made with permission from American Chemical Society.

Ariyarathna, I. R.; Miliordos, E. *J. Phys. Chem. A* **2020**, *124*, 9783–9792.

2.5.1 $Be(NH_3)_{n=1-3}$

Interaction between $nNH_3(\tilde{X}^1A_1)$ + $Be(^1S)$ (n = 1–3) is expected to produce a repulsive PEC owing to their closed shell electronic configurations similar to $Be(CO)_{1-3}$. As predicted, they are initially repulsive but become attractive < 2.5 Å distances (see Figure 2.15). Compared to $Be(NH_3)_{n=2,3}$ the initial repulsion and the proceeding attraction of $BeNH_3(\tilde{X}^1A_1)$ is minor. For $BeNH_3$ it creates a shallow minimum around 1.8 Å with a 6.7 kcal/mol D_e at CCSD(T) level. The interaction between Be and one NH_3 can be used to understand the chemical bonding of Be–Be dimer. But the Be–NH_3 bond length is shorter compared to the bond length of Be_2 dimer (2.45 Å).[57] Be_2 has a 1.35 kcal/mol D_e at the same level of theory. At MRCI+Q/aug–cc–pCV7Z level Be–Be distance (2.444 Å) and D_e (2.639 kcal/mol) are in excellent agreement with the 2.45 Å and 2.658 kcal/mol experimental values.[57,58] The $2s^2$ electrons of Be polarize away from the approaching NH_3. Similarly, the $2s^2$ electrons of each atom of Be_2 repel each other. The $2\sigma_g$ and $2\sigma_u$ of Be_2 (see Figure 2.16) are doubly occupied with $2\sigma_g{}^2 2\sigma_u{}^2$; 79% electronic configuration. The stability of Be_2 dimer is caused by the $2\sigma_g{}^2 3\sigma_g{}^2$; 7% configuration. Based on these configurations the introduced Lewis diagram is depicted in Figure 2.17.

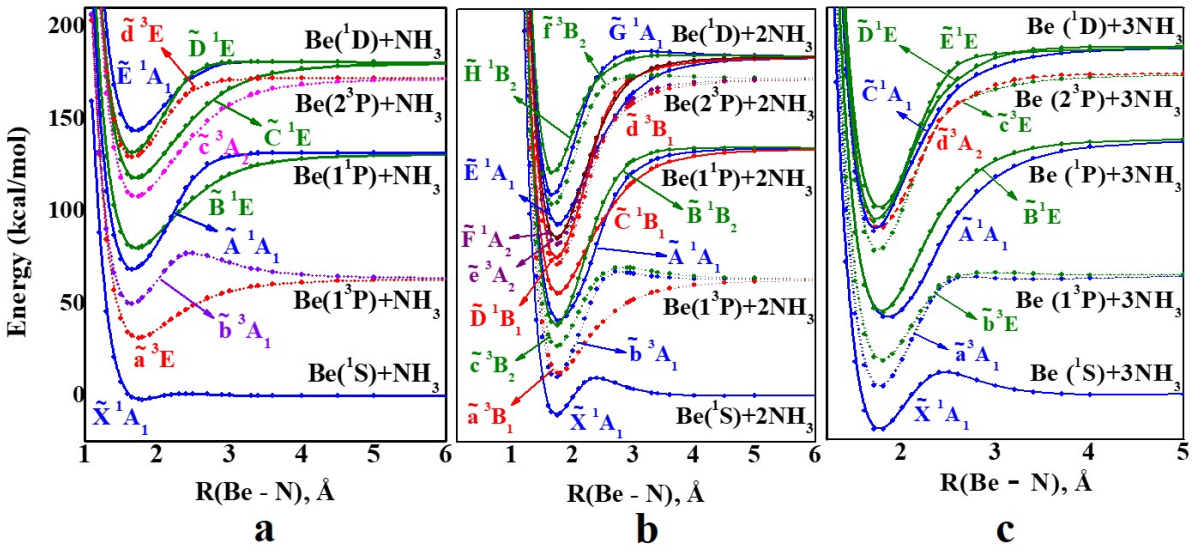

Figure 2.15: MRCI PECs of (a) $BeNH_3$, (b) $Be(NH_3)_2$, and (c) $Be(NH_3)_3$ as a function of Be–N. All other parameters kept fixed to those of the ground state geometries. For all dissociations NH_3 is in its $\tilde{X}^1A_1$ ground state.

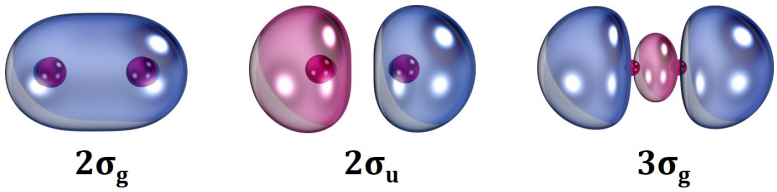

Figure 2.16: Selected molecular orbitals of Be_2

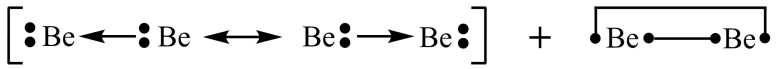

Figure 2.17: Lewis structures for the Be–Be bonding in Be_2.

The CCSD(T) D_es of $Be(NH_3)_2(\tilde{X}^1A_1)$ and $Be(NH_3)_3(\tilde{X}^1A_1)$ are 16.6 and 33.2 kcal/mol, respectively. Interestingly, as n grows the energy barrier of $nNH_3(\tilde{X}^1A_1)$ + $Be(^1S) \rightarrow Be(NH_3)_n$ reaction increases (see Figure 2.15). As ammonia approaches $Be(^1S)$ its $2s^2$ electron cloud polarizes away from ammonia to produce the ground state (See the HOMOs of

$Be(NH_3)_{n=1-3}$ given in Figure 2.18). In $Be(NH_3)_2(\tilde{X}^1A_1)$ a slight electron solvation was observed. Electron solvation is significant in $Be(NH_3)_3(\tilde{X}^1A_1)$.

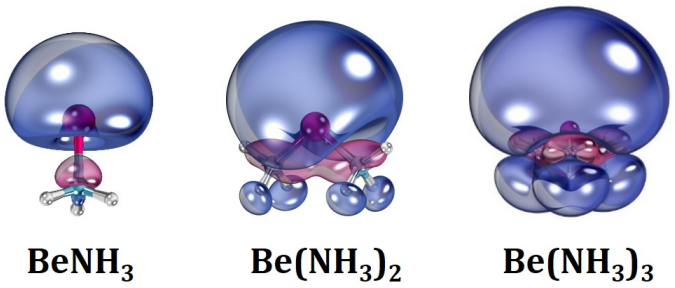

Figure 2.18: HOMOs of $Be(NH_3)_{n=1-3}$.

Excitation energies, optimal parameters [for $BeNH_3$ and $Be(NH_3)_2$], and electronic configurations of the several low−lying electronic states of $BeNH_3$, $Be(NH_3)_2$, and $Be(NH_3)_3$ are listed in Ref[37] of Appendix A.

2.5.2 $Be(NH_3)_{1-3}^+$

The $\tilde{X}^2A_1$ ground state PECs of $Be(NH_3)_{1-3}^+$ are strongly attractive compared to their neutral molecules because of the electrostatic attraction between $Be^+(^2S)$ + $nNH_3(\tilde{X}^1A_1)$ fragments (Figure 2.19). Similar to $Be(NH_3)_n$ the D_e of $Be(NH_3)_n^+$ increases with n. The CCSD(T) D_es of $Be(NH_3)_n^+$ are 78.3, 129.4, and 167.7 kcal/mol, with respect to $Be^+(^2S)$ + $nNH_3(\tilde{X}^1A_1)$ dissociations. Similar to $Be(NH_3)_{1-3}$ the HOMOs of $Be(NH_3)_{1-3}^+$ are mostly the polarized 2s of beryllium (see Figure 2.18). As expected bond lengths of $Be(NH_3)_{1-3}^+$ are shorter compared to $Be(NH_3)_{1-3}$ (by ∼0.12 Å for $Be(NH_3)^+$, 0.02 Å for $Be(NH_3)_2^+$, and 0.03 Å for $Be(NH_3)_3^+$. The Be−N lengths of $Be(NH_3)$, $Be(NH_3)_2^+$, $Be(NH_3)_3^+$ are 1.682, 1.724, 1.765 Å, respectively.

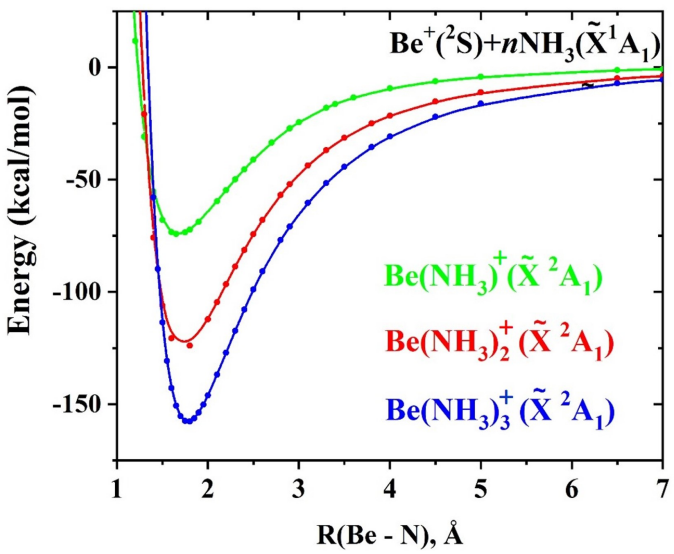

Figure 2.19: MRCI PECs of the ground electronic states of $Be(NH_3)_{1-3}{}^+$ as a function of the Be–N distance.

2.5.3 $[Be(NH_3)_{n=1-2}]_2$ dimers

$[BeNH_3]_2$ dimer

Several low–lying PECs of $[BeNH_3]_2$ are shown in Figure 2.20a. To make PECs of the dimer three lowest energy channels of $BeNH_3$ are considered. These channels are: (1) $BeNH_3(\tilde{X}^1A_1)$ + $BeNH_3(\tilde{X}^1A_1)$, (2) $BeNH_3(\tilde{X}^1A_1)$ + $BeNH_3(\tilde{a}^3E)$, and (3) $BeNH_3(\tilde{a}^3E)$ + $BeNH_3(\tilde{a}^3E)$ in the order of energy. Each channel produces one–singlet, four–triplets, and four (singlets + triplets + quintets), respectively. The ground state of the dimer (^1A_g) smoothly dissociates into two $BeNH_3(\tilde{X}^1A_1)$ fragments.

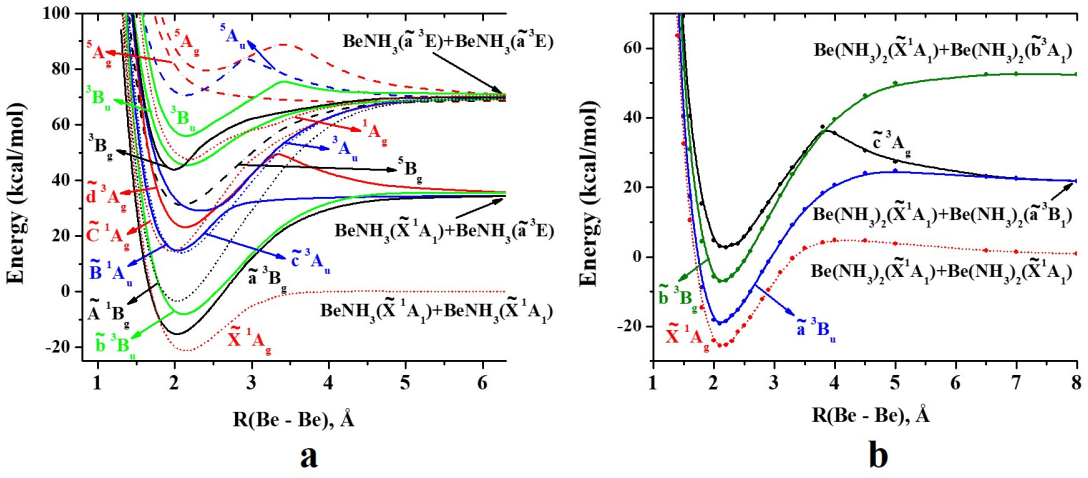

Figure 2.20: MRCI PECs of the (a) $[BeNH_3]_2$ and (b) $[Be(NH_3)_2]_2$ dimers as a function of Be–Be. All other parameters kept fixed to their optimal ground state values.

The interaction of two $BeNH_3$ creates a significantly stronger Be–Be bond in $[BeNH_3]_2$ dimer. The CCSD(T) D_e of $[BeNH_3]_2$ dimer with respect to two $BeNH_3$ is 25.8 kcal/mol. Remember that the D_e of Be_2 is 1.35 kcal/mol under the same level of theory. Interestingly, the bonding mechanisms in Be_2 and $[BeNH_3]_2$ dimers are similar. See the orbitals and electronic configurations of $[BeNH_3]_2$ given in the Figure 2.21 and Table 2.1. The ground state configuration of $[BeNH_3]_2$ is $6a_g{}^2 6b_u{}^2$; 79% + $6a_g{}^2 7a_g{}^2$; 13%. Note that the second configuration is almost doubled in $[BeNH_3]_2$ compared to Be_2 causing a stronger Be–Be bond in the former.

Be–Be, Be–N distances, and Be–Be–N angles of the $[BeNH_3]_2(\tilde{X}^1A_g)$ dimer are 2.125 Å, 1.769 Å, and 120.3 degrees, respectively. Calculated vertical excitation energies and electronic configurations of several low–lying states of the dimer are given in the Table 2.1.

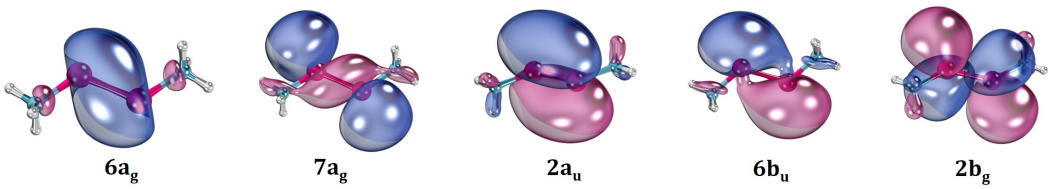

Figure 2.21: Selected orbitals of $[BeNH_3]_2$ dimer.

Table 2.1: Vertical excitation energies T_e (cm^{-1}) and dominant electronic configurations for several low−lying electronic states of $[BeNH_3]_2$ dimer.

State (C_{2h})	Method	T_e	Electronic configuration					
			Coef.	$6a_g$	$7a_g$	$2a_u$	$6b_u$	$2b_g$
$\tilde{X}^1A_g$	MRCI	0	0.89	2	0	0	2	0
			−0.36	2	2	0	0	0
	MRCI+Q	0						
$\tilde{a}^3B_g$	MRCI	1,584	0.94	2	0	α	α	0
	MRCI+Q	1,770						
$\tilde{b}^3B_u$	MRCI	4,670	0.96	2	α	0	α	0
	MRCI+Q	4,665						
$\tilde{a}^1B_g$	MRCI	6,381	0.65	2	0	β	α	0
			−0.65	2	0	α	β	0
	MRCI+Q	5,955						
$\tilde{c}^3A_u$	MRCI	12,785	0.96	2	α	α	0	0
	MRCI+Q	12,838						
$\tilde{b}^1A_u$	MRCI	12,861	0.56	2	α	β	0	0
			−0.56	2	β	α	0	0
	MRCI+Q	12,950						
$\tilde{c}^1A_g$	MRCI	13,513	0.89	2	0	2	0	0
	MRCI+Q	13,180						

$[Be(NH_3)_2]_2$ dimer

The D_e of $[Be(NH_3)_2]_2$ is 29.4 kcal/mol with respect to two $Be(NH_3)_2$ fragments at CCSD(T)/TZ level. Its electronic configurations are $7a_g{}^2 7b_u{}^2$; 83% + $7a_g{}^2 8a_g{}^2$; 12% (Figure 2.22). Note that its first component is bigger than $[BeNH_3]_2$ by 4% and in principle its Be−Be bond should be weaker than $[BeNH_3]_2$. But observe that the $7b_u$ shows a significant π delocalization in $[Be(NH_3)_2]_2$ and this might cause for an improved D_e in $[Be(NH_3)_2]_2$ compared to the $[BeNH_3]_2$. The PECs of $[Be(NH_3)_2]_2$ are given in Figure 2.20b. The

ground state PEC ($\tilde{X}^1A_g$) is initially slightly repulsive but become attractive starting at ~4 Å.

Be–Be and Be–N distances, Be–Be–N and N–Be–N angles, and N–Be–Be–N dihedral angle of the $[Be(NH_3)_2]_2$ dimer are 2.135 Å, 1.866 Å, 117.3 degrees, 98.3 degrees, and 63.4 degrees, respectively. The first excited state PEC ($\tilde{a}^3B_u$) smoothly dissociates into the second lowest energy asymptote. The other triplet state ($\tilde{c}^3A_g$) that originates from the same fragments is initially repulsive but becomes attractive after 4 Å due to an avoided crossing. The third excited state ($\tilde{b}^3B_g$) comes from the $Be(NH_3)_2(\tilde{X}^1A_1)$ + $Be(NH_3)_2$ ($\tilde{b}^3A_1$) combination. The vertical excitation energies and electronic configurations of the first three states of $[Be(NH_3)_2]_2$ are listed in Table 2.2.

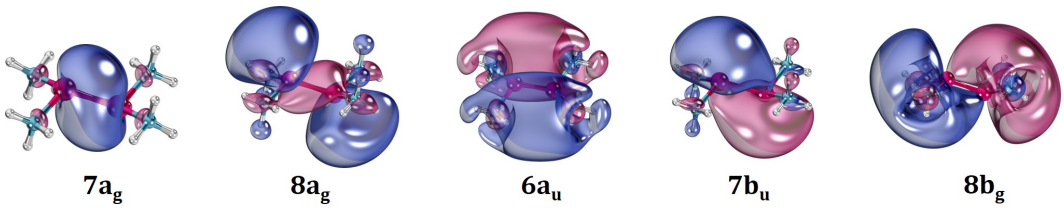

Figure 2.22: Selected orbitals of $[Be(NH_3)_2]_2$ dimer.

Table 2.2: Vertical excitation energies T_e (cm^{-1}) and dominant electronic configurations for several low–lying electronic states of $[Be(NH_3)_2]_2$ dimer.

State (C_{2h})	Method	T_e	Electronic configuration					
			Coef.	$7a_g$	$8a_g$	$6a_u$	$7b_u$	$8b_g$
$\tilde{X}^1A_g$	MRCI	0	0.91	2	0	0	2	0
			−0.34	2	2	0	0	0
	MRCI+Q	0						
$\tilde{a}^3B_u$	MRCI	2359	0.97	2	α	0	α	0
	MRCI+Q	2505						
$\tilde{b}^3B_g$	MRCI	6483	0.96	2	0	α	α	0
	MRCI+Q	6233						

2.5.4 $[Be(NH_3)_{1,2}]_2^{2+}$ dimers

Be_2^{2+} dimer is metastable by ~50 kcal/mol with respect to $Be^+(^2S)$ + $Be^+(^2S)$ fragments. Interestingly, $[BeNH_3]_2^{2+}$ and $[Be(NH_3)_2]_2^{2+}$ have 16.2 and 22.9 kcal/mol D_es at CCSD(T)/cc−pVTZ level of theory, respect to their two $Be(NH_3)_{1-2}^+$ fragments. Their PECs are shown in Figure 2.23. All three PECs are initially repulsive but turn attractive. The energy barrier of $[BeNH_3]_2^{2+}$ is greater compared to the $[Be(NH_3)_2]_2^{2+}$ (~42 vs 35 kcal/mol).

The two Be centers of each $[Be(NH_3)_{0,1,2}]_2^{2+}$ dimer are connected via a two electron sigma bond. The $[BeNH_3]_2^{2+}$ and $[Be(NH_3)_2]_2^{2+}$ dimers have D_{3h} and C_1 symmetries, respectively. The Be−Be/Be−N distances of the $[BeNH_3]_2^{2+}$ and $[Be(NH_3)_2]_2^{2+}$ are 2.086/1.665 and 2.172/1.769 Å. Note that the Be−Be length of $[BeNH_3]_2^{2+}$ is shorter by 0.04 Å, compared to $[BeNH_3]_2$ and that of $[Be(NH_3)_2]_2^{2+}$ is longer by 0.04 Å, compared to $[Be(NH_3)_2]_2$.

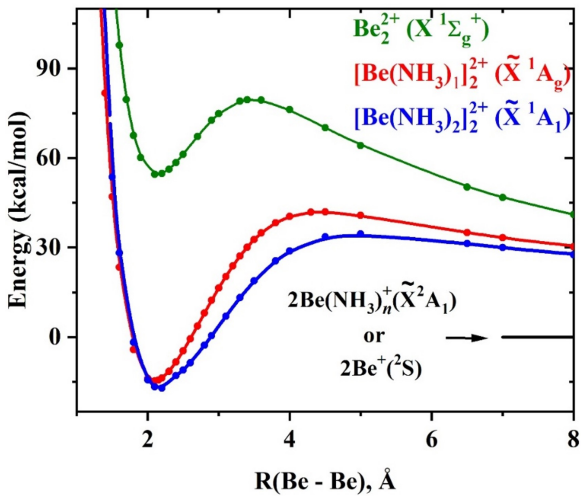

Figure 2.23: MRCI PECs of $[Be(NH_3)_{0,1,2}]_2^{2+}$ as a function of the Be−Be distance. All other parameters kept fixed to their optimal values of the ground state geometry.

2.6 Conclusions

The excited ^{1}D state of O atom is used to generate N_2O molecules. A lone electron pair from one terminal of $N_2(X^1\Sigma_g^+)$ participates on a dative bond with the empty orbital of $O(^1D; M_L=0)$. Its isoelectronic $N_3H(\tilde{X}^1A')$ and $NH_3O(\tilde{X}^1A_1)$ have similar chemical bonding

patterns to N_2O. In the $N_3H(\tilde{X}^1A')$ case the electron transfer occurs from $:N_2(X^1\Sigma_g^+)$ to the empty orbital of $NH(a^1\Delta)$. The remaining lone electron pair of the other end of the N_2 can also engage in dative bonds (e.g. N_2O_2; $O(^1D)\leftarrow:N\equiv N:\rightarrow O(^1D)$).

Ground states of $Li(CO)_{n=1-3}$ originate from $Li(^2P)$ + $nCO(X^1\Sigma^+)$ fragments. In these cases, empty three orbitals of $Li(^2P;\ 2p^1)$ allow for dative attacks by CO ligands. The electron occupying the 2p orbital of Li back−donates to π^* orbitals of CO. Even though LiCO is metastable, $Li(CO)_2$ and $Li(CO)_3$ are well bound with respect ground state fragments. The ground state of $LiNO(^3\Sigma^-)$ also originates from ^2P state of Li. LiNO has an ionic frame (Li^+NO^-) unlike $Li(CO)_n$ species. The two radical electrons of $LiNO(^3\Sigma^-)$ occupy the perpendicular π^* orbitals. The linear $LiNO(^3\Sigma^-)$ surpasses ∼5 kcal/mol barrier and transforms to its bent $^3A''$ global minimum that is stabilized by 1.7 kcal/mol compared to the $^3\Sigma^-$ one. However, the linear structures are more stable for its isovalent LiNS, LiNSe, and LiNTe molecules.

BeCO is metastable with respect to ground state fragments similar to LiCO and uses an excited state of Be to produce the $^3\Pi$ ground state. The ground state of BeCO originate from $Be(1^3P)$ + $CO(X^1\Sigma^+)$ fragments. $Be(CO)_2$ and $Be(CO)_2$ also use excited states of Be to create ground states that are well bound with respect to ground state fragments. Specifically, they result from $Be(2^3P)$ + $2CO(X^1\Sigma^+)$ and $Be(^1D)$ + $3CO(X^1\Sigma^+)$, respectively. The D_es of $Be(CO)_n$ vary in BeCO < $Be(CO)_2$ < $Be(CO)_3$ order. The replacement of O with a heavier isovalent atom such as S, Se, Te, Po significantly increases the D_e of the $Be(CX)_3$ molecule. Specifically, D_es vary in the $Be(CO)_3$ < $Be(CS)_3$ < $Be(CSe)_3$ < $Be(CTe)_3$ order.

BeO, OBeO, and $Be(O_2)_2$ molecules are ionic with Be^+O^-, $O^-Be^{2+}O^-$, $O_2{}^-Be^{2+}O_2{}^-$ skeletons, respectively. Ground states of BeO, OBeO, and $Be(O_2)_2$ are $^1\Sigma^+$ ($C_{\infty v}$), $^3\Sigma_g^-$ ($D_{\infty h}$), and $^1B_2$ (D_{2d}), respectively.

Ground states of $Be(NH_3)_n$ (n = 1−3) are produced by $Be(^1S)$ + $nNH_3(\tilde{X}^1A_1)$ fragments. Interaction between $Be(^1S)$ + $nNH_3(\tilde{X}^1A_1)$ (n = 1−3) is initially repulsive but turn attractive at distances < 2.5 Å. The ground state PEC for n = 1 has a shallow minimum with 6.69 kcal/mol D_e. Two valence electrons of Be polarize away from the approaching NH_3 ligand ($:Be\leftarrow:NH_3$) to create $BeNH_3$ molecule. Be_2 dimer bears a similar bonding mechanism as $:Be\leftarrow:NH_3$. The major electronic configuration of Be_2 dimer (79%) is resonance $:Be\leftarrow:Be$ + $Be:\rightarrow Be:$.

Moving from n = 1 to 3 the D_e increases for $Be(NH_3)_n$. The polarization of two valence electrons of n = 2, 3 structures are greater compared to $BeNH_3$. The polarization is far too great in $Be(NH_3)_3$ and the two electrons of Be delocalize in the periphery. The D_es of $Be(NH_3)_n{}^+$ (n = 1–3) are greater compared to corresponding neutral species, due to the electrostatic interaction between Be^+ and nNH_3. Electron solvation was observed in $Be(NH_3)_3{}^+$ similar to $Be(NH_3)_3$.

Two $BeNH_3$ molecules binds together to produce a stable dimer. The $NH_3Be–BeNH_3$ bond is much stronger compared to that of Be_2 dimer. The D_es of $[BeNH_3]_2$ and Be_2 with respect to ground state fragments are 25.8 and 1.35 kcal/mol at CCSD(T) level. The D_e of $[Be(NH_3)_2]_2$ is bigger than $[BeNH_3]_2$ by 3.6 kcal/mol. $[BeNH_3]_2$ and $[Be(NH_3)_2]_2$ bear multi–reference ($6a_g{}^2 6b_g{}^2$; 79% + $6a_g{}^2 7a_g{}^2$; 13%) and ($7a_g{}^2 7b_u{}^2$; 83% + $7a_g{}^2 8a_g{}^2$; 12%) configurations. Even though, $Be_2{}^{2+}$ is metastable, $[BeNH_3]_2{}^{2+}$ and $[Be(NH_3)_2]_2{}^{2+}$ create stable minima with 16.2 and 22.9 kcal/mol D_es, respectively.

Chapter 3

Superatomic nature of ground and excited states of neutral and partially oxidized metal–ammine complexes

The first study on metal interaction with ammonia traces back to Sir Humphry Davy's work in 1808.[59] He observed that heating alkali metals such as sodium and potassium in gaseous ammonia produces a *"fine blue color"*. 56 years after Davy's discovery, W. Weyl studied the interactions of sodium with ammonia in solution phase and suggested that the blue color is caused by $NaNH_3$ species.[24] Later in 1916, Gibson and Argo confirmed that the brilliant blue color arises from the free electrons present in ammonia.[60] Today these electrons are known as *"solvated electrons"*.[24] The relatively longer lifetime of $Li(NH_3)_4$ has aided solid−state experimentalists to unravel its chemistry.[61,62] However, even after two centuries of research following Davy's discovery, these metal−ammine systems are poorly understood.[24] Hence, we have focused our attention towards metal−ammine complexes. This chapter discusses our findings of ground and excited electronic states of several metal−ammine systems that can be identified as solvated electron precursors.

3.1 Group I metal–ammine complexes

In this section most important findings reported in following paper[26] given in Appendix B are summarized. Reprints were made with permission from Royal Society of Chemistry.

Ariyarathna, I. R.; Pawłowski, F.; Ortiz, J. V.; Miliordos, E. *Phys. Chem. Chem. Phys.* **2018**, *20*, 24186–24191.

Hoffmann et al. claims solid $Li(NH_3)_4$ as the *"lowest melting point metal"* which crystallizes at 90 K.[63] Molecular $Li(NH_3)_4$ possesses a diffuse electron in the periphery of the tetrahedral $Li(NH_3)_4{}^+$ core.[24] The HOMO of $Li(NH_3)_4$ has been identified as a Rydberg−like orbital by Sommerfeld and Dreux.[64] According to their study approximately 6% density of this electron is closely associated with the atoms. The remaining 94% corresponds to the pseudo spherical superatomic s−type orbital (see Figure 3.1). Fascinatingly, this diffuse electron promotes to higher angular momentum p−, d−, f−shaped orbitals. To account for the diffuse nature of this electron, it is remarkably important to use diffuse basis functions on the basis set. Specifically, M (≡Metal): TZ, N: TZ and H: DATZ basis set has proven to provide very accurate results for such systems efficiently. Calculated excitation energies using the aforementioned basis set for $Li(NH_3)_4$ and $Na(NH_3)_4$ are given in the Table 3.1. Corresponding orbitals for the electron transitions of $Li(NH_3)_4$ are shown in Figure 3.1.

Hashimoto and Daigoku calculated MRCI/6−311++G(2d,2p) excitation energies correspond to $1^2A_1 \rightarrow 1^2T_1$ and $1^2A_1 \rightarrow 2^2A_1$ transitions of of $Li(NH_3)_4$ and the values are 0.58 and 1.50 eV, respectively.[65] Notice that the MRCI first excitation energy is very close to our CASSCF value, but their $1^2A_1 \rightarrow 2^2A_1$ transition is similar to our complete active space second−order perturbation theory (CASPT2) value (1.50 vs 1.52 eV). The only experimentally reported transition of $Li(NH_3)_4$ ($1^2A_1 \rightarrow 1^2T_1$ = 0.74 eV) is almost identical to our CASPT2 value.[65]

Orbitals of $Na(NH_3)_4$ have identical shapes to $Li(NH_3)_4$. According to excitation energies, both $Li(NH_3)_4$ and $Na(NH_3)_4$ follow 1s, 1p, 1d, 2s, 2p superatomic Aufbau principle. Importantly, this hydrogenic orbital series is very different from the orbital order of atomic Li or Na. Specifically, in the first seven excited states Li populates 2p (1.848 eV), 3s (3.373 eV), 3p (3.834 eV), 3d (3.879 eV), 4s (4.341 eV), 4p (4.522 eV), 4d (4.541 eV) orbitals, while

it is 3p (2.102 eV), 4s (3.191 eV), 3d (3.617 eV), 4p (3.753), 5s (4.116 eV), 4d (4.283 eV), 4f (4.288 eV) for Na.[14] It is interesting to notice that the $Li(NH_3)_4$ and $Na(NH_3)_4$ have many low−lying electronic states compared to Li and Na.

Hashimoto and Daigoku computed the vertical first ionization energy (IE1) of $Li(NH_3)_4$ at MP2 level, and it is 2.81 eV.[66] The experimental value is 2.85 eV.[67] These numbers are in excellent agreement with the values provided by high−level electron propagator methods[68–70] (D2 = 2.83 eV, P3 = 2.84 eV, P3+ = 2.84 eV).[26]

The CCSD(T) adiabatic IE1s of $Li(NH_3)_4$ and $Na(NH_3)_4$ are 2.92 and 2.79 eV, respectively. The IE1 of $Li(NH_3)_4$ and $Na(NH_3)_4$ are significantly smaller compared to Li (5.392 eV) and Na (5.139 eV).[71] This is a consequence of weaker attraction between M^+ and the distant e^- of $M(NH_3)_4$ complexes. Notice that the IE1 of each $Li(NH_3)_4$ and $Na(NH_3)_4$ is lower than the IE1 of Cs atom (IE1 of Cs = 3.89 eV).[71] This is important because a molecule that possesses a lower IE1 than Cs atom is generally recognized as a *"superalkali"*. Hence, both $Li(NH_3)_4$ and $Na(NH_3)_4$ are superalkalis. Loosely bound electrons of such species can easily migrate to the solvent and becomes a powerful reducing agent that is strong enough to reduce an aromatic ring.[72] Further such metal−ammine solutions have been proposed as potential high−temperature superconductors.[73]

The experimental EAs of Li and Na are 0.618 and 0.548 eV, respectively.[71] Experimental electron affinities of $Li(NH_3)_4$ and $Na(NH_3)_4$ are 0.45 and 0.42 eV, respectively.[74,75] The MRCI value of $Na(NH_3)_4$ calculated by Hashimoto et al. at MRCI level is 0.39 eV.[76] Both $Li(NH_3)_4$ and $Na(NH_3)_4$ has 0.45 eV adiabatic EA at CCSD(T) level of theory. Anions possess two peripheral electrons with $1s^2$ superatomic electronic configuration. Excited states of anions are not bound.

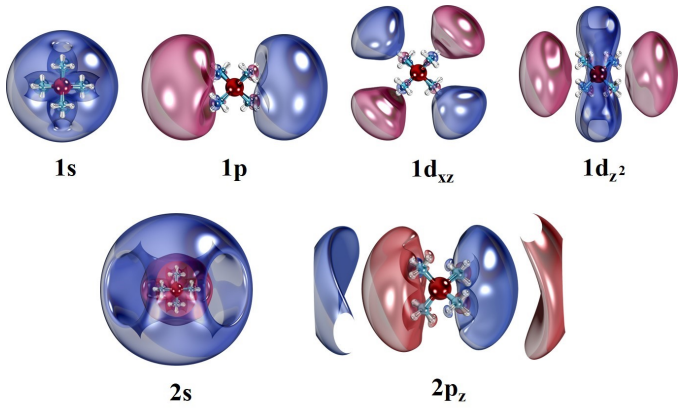

Figure 3.1: Contours of selected outer orbitals of $Li(NH_3)_4$.

Table 3.1: Superatomic electronic configurations and vertical excitation energies (eV) of $Li(NH_3)_4$ and $Na(NH_3)_4$.

State (T_d)	S.E.C.[a]	$Li(NH_3)_4$		$Na(NH_3)_4$	
		CASSCF	CASPT2	CASSCF	CASPT2
1^2A_1	$1s^1$	0.00	0.00	0.00	0.00
1^2T_2	$1p^1$	0.55	0.72	0.51	0.65
2^2T_2	$1d^1$	1.12	1.40	1.06	1.31
1^2E	$1d^1$	1.13	1.43	1.06	1.33
2^2A_1	$2s^1$	1.28	1.52	1.22	1.43
3^2T_2	$2p^1$	1.53	1.79	1.43	1.67
1^2T_1		1.61	1.96	1.52	1.83
4^2T_2		1.88	2.14	1.82	2.05
2^2E		1.94	2.22	1.87	2.12
5^2T_2		2.12	2.40	2.03	2.27

[a]S.E.C. stands for superatomic electronic configuration.

3.2 Group II metal–ammine complexes

3.2.1 $Be(NH_3)_4^{0,+,-}$

In this section most important findings reported in following paper[27] given in Appendix B are summarized. Reprints were made with permission from American Chemical Society.

Ariyarathna, I. R.; Khan, S. N.; Pawłowski, F.; Ortiz, J. V.; Miliordos, E. *J. Phys.Chem. Lett.* **2018**, *9*, 84–88.

Similar to $Li(NH_3)_4$, its isoelectronic $Be(NH_3)_4^+$ possesses a diffuse electron in the periphery of the tetrahedral $Be(NH_3)_4^{2+}$ which promotes to superatomic p−, d−, f−shaped orbitals.[27] Since it is important to find a suitable basis set that represent these species we studied excited states of $Be(NH_3)_4^+$ probing series of basis sets. Specifically, (1) Be: TZ, N: TZ, H:TZ (2) Be: TZ, N: TZ, H:ATZ (3) Be: TZ, N: TZ, H: DATZ (4) Be:ATZ, N:DATZ, H: DATZ (5) Be: TZ, N: TZ, H: DAQZ (6) Be: TZ, N: TZ, H: TATZ (7) Be: TZ, N: TZ, H: QATZ basis sets were used.[77–79] P3+ results provided by the Filip Pawłowski and Joseph Vincent Ortiz are in excellent agreement with the CASPT2 data. The Be: TZ, N: TZ, H: DATZ combination provides the best accuracy−efficiency compromise. Going from this basis set to bigger (4), (5), (6), or (7) basis sets only changes the excitation energies by less than 0.07 eV. Importantly, going to aforementioned bigger basis sets does not change the superatomic orbital model in the excited states. Based on the shapes of the orbitals and the excitation energies the superatomic Aufbau principle of $Be(NH_3)_4^+$ was discovered and it is 1s, 1p, 1d, 2s, 1f, 2p, 2d.

In $Be(NH_3)_4$, two electrons orbit around the $Be(NH_3)_4^{2+}$ core. $Be(NH_3)_4$ has 64.1 kcal/mol D_e with respect to $Be(^1S) + 4NH_3(\tilde{X}^1A_1)$ fragments with an 18.2 kcal/mol energy barrier that separates them. For the $Be(NH_3)_3(\tilde{X}^1A_1) + NH_3(\tilde{X}^1A_1) \rightarrow Be(NH_3)_4(\tilde{X}^1A_1)$ reaction this energy barrier is less than 2.0 kcal/mol. Synchronically, the Be−N bonds stretch and N−H bonds shorten going from $Be(NH_3)_4$ to $Be(NH_3)_4^+$ or from $Be(NH_3)_4^+$ to $Be(NH_3)_4^{2+}$. It can be pictured as if the outer electron cloud pushes the electron negative N−atoms towards Be, while the electron positive H−atoms get attracted towards the electron cloud.

Excited state calculations of the $Be(NH_3)_4$ were performed using the previously benchmarked Be: TZ, N: TZ, H: DATZ basis set. Excited state calculations on $Be(NH_3)_4$ are computationally challenging owing to its multi−reference electronic character. The first excited state of $Be(NH_3)_4$ (^3P; $1s^1 1p^1$, 0.81 eV) is formed by promoting one electron from $1s^2$ ground state to the 1p shell. The ^1P state is a mixture of several electronic states with major $1s^1 1p^1$ character and lies around 1.62 eV. The third excited state, ^1D ($^1T_2$; 1.65 eV, ^1E; 1.82 eV), is a combination of $1s^1 1d^1$ and $1p^2$ configurations. This is followed by ^3D; $1s^1 1d^1$ ($^3T_2$; 1.93 eV, ^1E; 2.10 eV) state. The ^3S ($1s^1 2s^1$), The ^1S ($1s^1 2s^1$), $2^3P(1p^2)$ states lie very close to each other at 2.24−2.30 eV. Beyond this point the spectrum becomes heavily multi−reference.

Interestingly, $Be(NH_3)_4$ possesses 0.26 eV electron affinity even though Be^- is not stable. Notice that the electron affinities of Li and Na are greater compared to their SEPs (see Section 3.1). The addition of an extra electron to $Be(NH_3)_4$ distorts its T_d geometry to D_{2d}. The $Be(NH_3)_4{}^-$ has $1s^2 1p^1$ superatomic electronic configuration.

3.2.2 $Mg(NH_3)_{n=4-6}{}^{0,+}$

All three $Mg(NH_3)_{n=4-6}{}^{0,+}$ complexes can be identified as superatoms due to their diffuse valence electron(s). Specifically, one and two electrons orbit in the periphery in cationic and neutral complexes, respectively. n = 4, n = 5, and n = 6 complexes are T_d, C_1, and C_s in symmetry with tetrahedral, trigonal bipyramidal, and octahedral shapes, respectively. Do $Mg(NH_3)_{n=4-6}{}^{0,+}$ follow the same orbital series as its isovalent $Be(NH_3)_4{}^{0,+}$? To answer this question excited states of these complexes were analyzed. Figure 3.2 illustrates the CASPT2 vertical excitation energies of $Mg(NH_3)_{n=4-6}{}^+$ complexes. The calculated $1^2A_1 \rightarrow 1^2T_1$ (or $1s^1 \rightarrow 1p^1$) transition is 1.21 eV agrees very well with the experimental value reported by Yoshida et al. which is ~1.24 eV.[80] The observed Aufbau shell model of $Mg(NH_3)_4{}^+$ is 1s, 1p, 1d, 2s, 2p, 1f, 2d and it is not identical to the $Be(NH_3)_4{}^+$. In the $Be(NH_3)_4{}^+$, 1f shell appears before 2p. Exited state calculations on $Mg(NH_3)_5{}^+$ is challenging due to its lower symmetry, hence only the first (1s→1p) and second excitations (1s→1d) were computed. The orbital series of $Mg(NH_3)_6{}^+$ (1s, 1p, 1d, 2p, 2s, 1f, 2p, 2d) is different from both $Be(NH_3)_4{}^+$ and $Mg(NH_3)_4{}^+$.

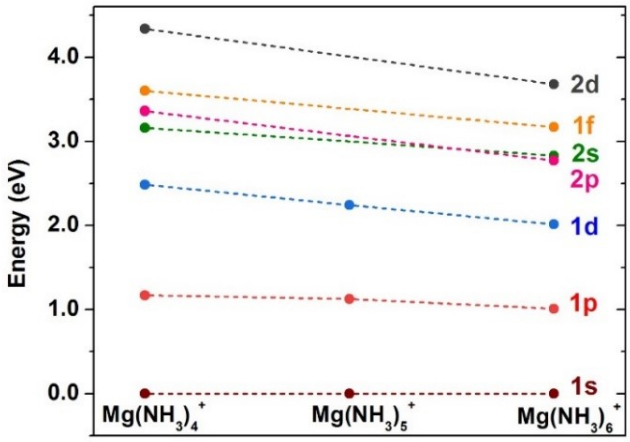

Figure 3.2: State average CASPT2 vertical excitation energies of $Mg(NH_3)_4{}^+$, $Mg(NH_3)_5{}^+$, and $Mg(NH_3)_6{}^+$.

Electronic configurations and excitation energies of several excited states of $Mg(NH_3)_{4-6}$ complexes are listed in the Table 3.2. A selected set of superatomic orbitals are illustrated in Figure 3.3. The electronic structures of low−lying states of $Mg(NH_3)_4$ is identical to the $Be(NH_3)_4$. However, the excitation energies of $Mg(NH_3)_4$ are lower compared to $Be(NH_3)_4$ by 0.05−0.20 eV. The lower symmetry (C_s) of $Mg(NH_3)_5$ induces the multi−reference character in its excited electronic states. Because of this, superatomic configurations could not be assigned for the states that lie beyond 1^3P state. Excitation energies of $Mg(NH_3)_6$ are lower compared to both $Mg(NH_3)_4$ and $Mg(NH_3)_5$.

Table 3.2: Superatomic electronic configurations and vertical excitation energies (eV) of $Mg(NH_3)_{4-6}$ at CASPT2 and C−CASPT2 (values in brackets)[a] levels of theory.

State	S.E.C.[b]	$Mg(NH_3)_4$	$Mg(NH_3)_5$	$Mg(NH_3)_6$
1^1S	$1s^2$	0.00 (0.00)	0.00 (0.00)	0.00 (0.00)
1^3P	$1s^1 1p^1$	0.72 (0.70)	0.70 (0.67)	0.58 (0.57)
1^1P	$1s^1 1p^1$	1.56 (1.52)		1.28 (1.28)
1^1D	$1s^1 1d^1/1p^2$	1.62 (1.59)		1.30 (1.30)
1^3D	$1s^1 1d^1$	1.99 (1.95)		1.62 (1.62)
2^3P	$1p^2$	2.10 (2.05)		1.72 (1.69)
1^3S	$1s^1 2s^1$	2.16 (2.14)		1.96 (1.97)
2^1S	$1s^1 2s^1$	2.21 (2.19)		1.98 (1.99)
1^3F	$1s^1 1f^1/1p^1 1d^1$	2.64 (2.59)		2.13 (2.12)

[a]C−CASPT2: Inner $3s^2 3p^6$ electrons of Mg atom are correlated.

[b]S.E.C. stands for superatomic electronic configuration.

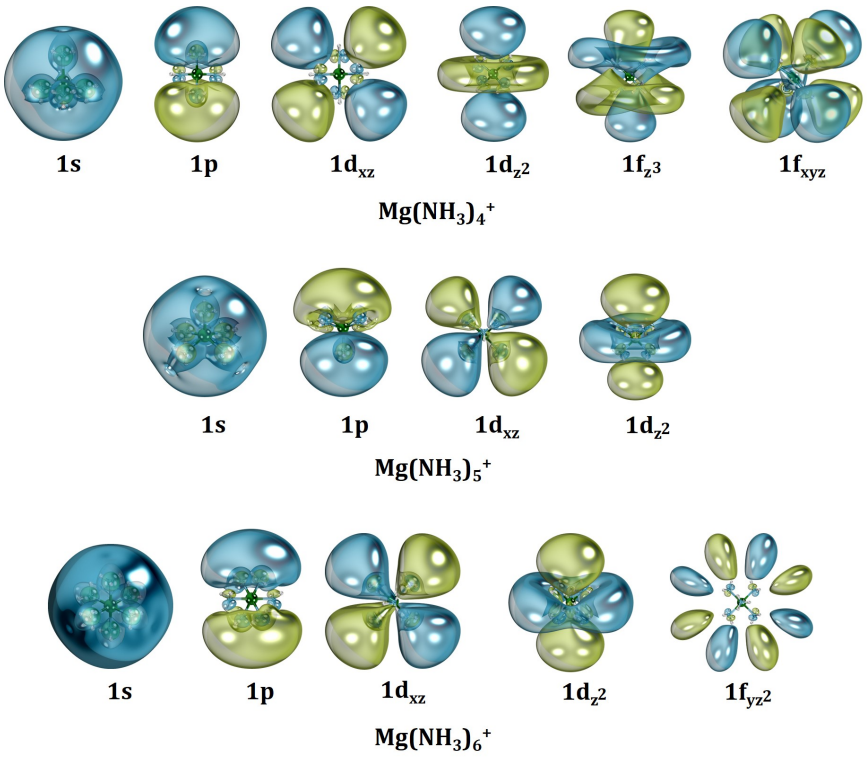

Figure 3.3: Selected outer orbitals of $Mg(NH_3)_4^+$, $Mg(NH_3)_5^+$, and $Mg(NH_3)_6^+$.

3.2.3 $Ca(NH_3)_{n=6-8}^{0,+}$

In this section most important findings reported in following paper[28] *given in Appendix B are summarized. Reprints were made with permission from American Chemical Society.*

Ariyarathna, I. R.; Almeida, N. M. S.; Miliordos, E. *J. Phys. Chem. A* **2019**, *123*, 6744–6750.

Ca creates SEPs similar to Be and Mg. Owing to larger atomic radius Ca accommodates up to eight ammonia molecules in the first solvation shell.[81] The main IR peak belonging to N−H stretches of $Ca(NH_3)_{n=1-8}$ moves to lower frequencies going from n = 1 to n = 5, but shifts towards higher frequencies moving from n = 5 to n = 8. In $Ca(NH_3)_{n=6-8}^+$ and $Ca(NH_3)_{n=6-8}$ one and two electrons are fully solvated in the periphery, respectively. The Aufbau orbital series observed for $Ca(NH_3)_6^+$ is 1s, 1p, 1d, 2s, 1f, 2p. But in the $Ca(NH_3)_8^+$ the 1f populates before the 2s. Several excited states of neutral Ca SEPs are multi−reference in nature. The order of the states of $Ca(NH_3)_6$, 1^1S, 1^3P, 1^1P, 1^1D, 1^3D, 2^3P, is identical to

$Mg(NH_3)_6$, but excitation energies of $Ca(NH_3)_6$ are 0.1−0.5 eV lower compared to $Mg(NH_3)_6$ at C−CASPT2 level. The order of the states of $Ca(NH_3)_7$ and $Ca(NH_3)_8$ is (1^1S, 1^3P, 1^1D, 1^1P, 2^3P, 1^3D) slightly different from $Ca(NH_3)_6$. A complete list of excitation energies of cations and neutral species can be found in the Ref[28] in Appendix B.

3.3 Transition metal–ammine complexes

3.3.1 $Ti(NH_3)_6^{0,+}$

Valence s−electrons of alkali and alkaline−earth metals solvate by ammonia to create Li−, Na−, Be−, Mg−, and Ca−SEPs. Similarly, ammonia ligate with scandium, vanadium, and yttrium transition metals to produce SEPs.[82–84] Only the valence 4s valence electrons of Scandium and vanadium atoms solvate by ammonia whereas inner d electrons stay intact. Interestingly, ammonia solvate all valence electrons of yttrium ($4d^15s^2$ electrons) in the periphery.[84] Does ammonia solvate all $3d^24s^2$ electrons or only $4s^2$ electrons of titanium? Electronic structures of $Ti(NH_3)_{n=1-6}^{+,0}$ were studied to answer this question.

The ground states of Ti^+ and Ti are $^4F(3d^24s^1)$ and $^3F(3d^24s^2)$, respectively.[14] $Ti^{0,+}$ can accommodate six ammonia molecules in the first shell. Importantly, all n = 1−6 species are stable with respect to $Ti(NH_3)_n^{0,+} \rightarrow Ti(NH_3)_{n-1}^{0,+} + NH_3$ dissociation. Six ammonia molecules complete the micro−solvation process by solvating 4s electron(s) $Ti^{0,+}$. The transformation of atomic 4s of Ti to the superatomic 1s of the $Ti(NH_3)_6$ are shown in the Figure 3.4. But the inner d electrons of $Ti^{0,+}$ remain intact. The ground state of $Ti(NH_3)_6^+$ and $Ti(NH_3)_6$ has $t_{2g}^2s^1$ (quartet) and $t_{2g}^2s^2$ (triplet) electronic configurations, respectively (see Figure 3.5 for orbitals). In the first excited state, two t_{2g} electrons of $Ti(NH_3)_6^+$ couple to produce a doublet $t_{2g}^2s^1$ state. The next two excited states of the cation are produced by 1s→1p electron transitions. The first state that occupies e_g orbitals appears around 1.5 eV. In the $Ti(NH_3)_6$ the first excited state is a quintet with $t_{2g}^2s^1p^1$ configuration. This state is followed by its corresponding triplet and singlet states, respectively. The fourth excited state is a mixture of $t_{2g}^2p^2$ and $t_{2g}^2s^1d^1$.

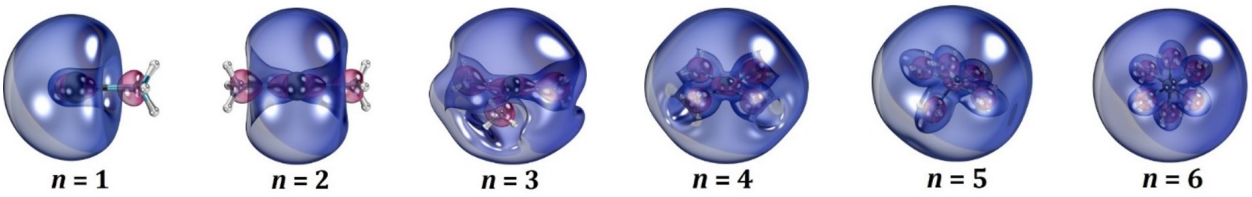

Figure 3.4: Orbital contours of the $Ti(NH_3)_{n=1-6}$ species, which gradually transform from 4s of Ti to the superatomic 1s of $Ti(NH_3)_6$.

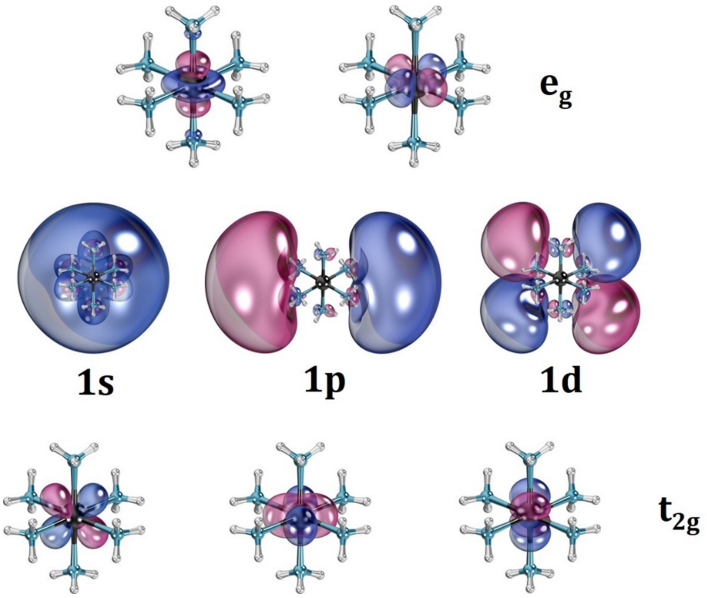

Figure 3.5: t_{2g}, e_g, and selected superatomic orbitals of $Ti(NH_3)_6^+$.

3.4 SEPs dimers

3.4.1 $[Li(NH_3)_4]_2$ and $[Na(NH_3)_4]_2$

In this section most important findings related to $[Li(NH_3)_4]_2$ and $[Na(NH_3)_4]_2$ molecules reported in following paper[26] given in Appendix B are summarized. Reprints were made with permission from Royal Society of Chemistry.

Ariyarathna, I. R.; Pawłowski, F.; Ortiz, J. V.; Miliordos, E. *Phys. Chem. Chem. Phys.* **2018**, *20*, 24186–24191.

Two $Li(NH_3)_4$ or $Na(NH_3)_4$ monomers can bind together to make a stable dimer. The D_es of $[Li(NH_3)_4]_2$ and $[Na(NH_3)_4]_2$ at DFT/B3LYP with respect to the ground state fragments are 9.1 and 9.5 kcal/mol. The constructed PECs for $[Li(NH_3)_4]_2$ are shown in Figure 3.6 (green box). We optimized all possible orientations that two monomers might interact and found that the global minimum of both dimers are staggered−like structures (see Figure 3.6 red box).

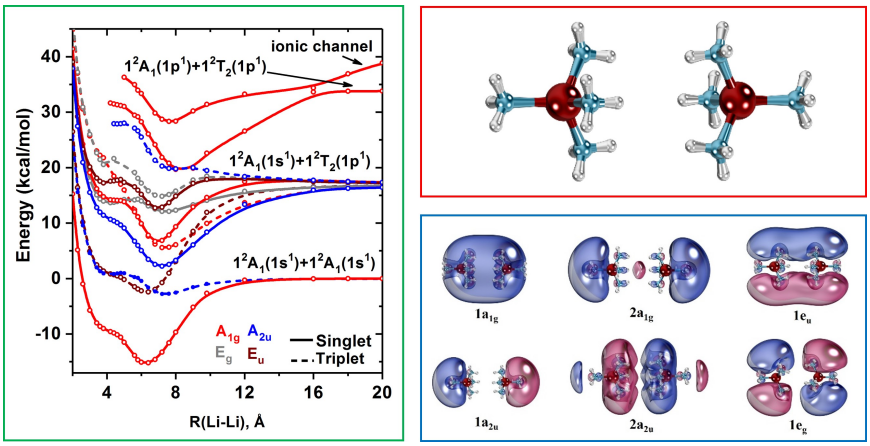

Figure 3.6: PECs (green box), equilibrium geometry (red box), and selected molecular orbitals (blue box) of the $[Li(NH_3)_4]_2$ dimer.

The ground state of $[Li(NH_3)_4]_2$ dimer results from the interaction of ground states of two $Li(NH_3)_4$ monomers: $1^2A_1(1s^1)$ + $1^2A_1(1s^1)$. The D_e of the $[Li(NH_3)_4]_2$ dimer at CASPT2 level of theory is 14.7 kcal/mol. Ground state potential energy curve shows a minimum around 6 Å. The Li$\cdots$Li distance of the CASPT2 optimized structure is 6.365 Å. The shoulder around 4 Å of the ground state curve may be caused by $Li(NH_3)_4^-$ + $Li(NH_3)_4^+$ interaction. At the ground state of the dimer, two electrons occupy $1a_{1g}$ orbital (Figure 3.6 blue box). $1a_{1g}$ orbital is singly occupied in the first eight excited states of the dimer and the other electron is promoted to the $1a_{2u}$, $1e_u$, $2a_{1g}$, and $1e_g$ orbitals. A complete list of vertical excitation energies and electron configurations of $[Li(NH_3)_4]_2$ and $[Na(NH_3)_4]_2$ are listed in the Ref.[26] given in Appendix B.

3.4.2 $[Be(NH_3)_3]_2$ and $[Be(NH_3)_3]_2^{2+}$

$[Be(NH_3)_3]_2$ and $[Be(NH_3)_3]_2^{2+}$ dimers have D_{3d} point groups and used C_{2h} highest

Abelian point group for calculations. Geometry optimizations and frequency calculations for $[Be(NH_3)_3]_2$ and $[Be(NH_3)_3]_2{}^{2+}$ dimers were carried out under MP2/ATZ level. Their D_es were calculated at the same level of theory. MP2 optimized geometry was used to perform vertical excited states calculations for $[Be(NH_3)_3]_2$ under CASSCF and CASPT2 levels of theory. Four electrons in ten active orbitals were used at CASSCF level and thirty−two orbitals were kept closed. The active orbitals are five−a_g, one−a_u, two−b_u, two−b_g and closed orbitals are ten−a_g, six−a_u, ten−b_u, six−b_g at C_{2h} symmetry. At D_{3d} point group the closed orbitals are five−a_{1g}, one−a_{2g}, one−a_{1u}, five−a_{2u}, ten−e_u, ten−e_g. All valence electrons were correlated at CASPT2 level. The used level−shift and IPEA values for CASPT2 calculations are 0.02 and 0.02, respectively. Excited state calculations were performed using Be: DZ, N: DZ, and H: DADZ basis set.

$Be(NH_3)_3$ and $Be(NH_3)_3{}^+$ has two and one diffuse electrons in the periphery similar to $Be(NH_3)_4$. However the HOMO of $Be(NH_3)_3{}^{0,+}$ is not as spherical as the HOMO of $Be(NH_3)_4{}^{0,+}$ (see Section 2.5 for more details). The D_e of $[Be(NH_3)_3]_2$ is 35.0 kcal/mol with respect to two $Be(NH_3)_3(\tilde{X}^1A_1)$ fragments. Its Be−Be and Be−N lengths are 2.178 and 1.804 Å, respectively. The ground state of the $[Be(NH_3)_3]_2$ is a $^1A_{1g}$. In the ground state two electrons occupy a quasi−spherical superatomic s−orbital (see $2a_{1g}$ of Figure 3.7). These two electrons can be pictured as two electrons that orbit in the periphery of the $[Be(NH_3)_3]_2{}^{2+}$ core. Interestingly, in excited states electrons populate higher−angular momentum p− and d−shaped orbitals. For example, in the first excited state superatomic 1s ($2a_{1g}$) and 1p ($1e_u$) orbitals are occupied by one electron (see Figure 3.7 and Table 3.3). This excitation only requires 0.23 eV at CASPT2 level. To excite both $1s^2$ superatomic electrons at least 0.73 eV are required which creates the ^1E_g ($1p^11p^1$) superatomic state. The first 1s→1d transition requires 1.24 eV that produces the $^3A_{1g}$ ($1s^11d^1$) state. Table 3.3 lists all the states that span within 0−1.57 eV (at CASPT2). Each of these states contain a doubly occupied $1a_{1g}{}^2$ orbital. It is interesting to notice that $[Be(NH_3)_3]_2{}^{2+}$ has 7.1 kcal/mol D_e with respect to two $Be(NH_3)_3{}^+(\tilde{X}^2A_1)$ fragments. In $[Be(NH_3)_3]_2{}^{2+}$ two electrons are shared between the two Be atoms (in $1a_{1g}$ orbital) and diffuse outer electrons are absent. Its Be−Be (2.326 Å) and Be−N (1.819 Å) distances are longer compared to the neutral dimer.

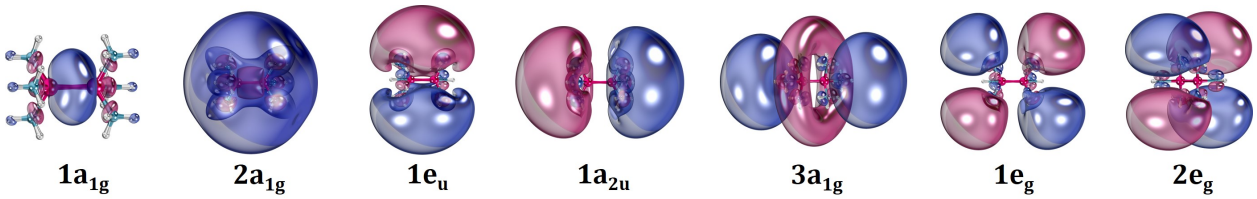

Figure 3.7: Selected molecular orbitals of $[Be(NH_3)_3]_2$ dimer.

Table 3.3: CASSCF and CASPT2 vertical excitation energies (eV) and dominant electronic configurations for several low−lying electronic states of $[Be(NH_3)_3]_2$ dimer.

State (D_{3d})	E.C.[a]	S.E.C.[b]	Excitation energy	
			CASSCF	CASPT2
1^1A_{1g}	$2a_{1g}{}^2$	$1s^2$	0.00	0.00
1^3E_u	$2a_{1g}{}^1 1e_u{}^1$	$1s^1 1p^1$	0.21	0.23
1^3A_{2u}	$2a_{1g}{}^1 1a_{2u}{}^1$	$1s^1 1p^1$	0.26	0.33
1^1E_u	$2a_{1g}{}^1 1e_u{}^1$	$1s^1 1p^1$	0.78	0.70
1^1E_g	$1e_u{}^1 1e_u{}^1$	$1p^1 1p^1$	0.66	0.73
1^1A_{2u}	$2a_{1g}{}^1 1a_{2u}{}^1$	$1s^1 1p^1$	0.76	0.74
1^3A_{2g}	$1e_u{}^1 1e_u{}^1$	$1p^1 1p^1$	0.83	0.78
2^1A_{1g}	$1a_{2u}{}^2$	$1p^2$	0.69	0.80
2^1E_g	$1e_u{}^1 1a_{2u}{}^1$	$1p^1 1p^1$	0.72	0.81
1^3E_g	$1e_u{}^1 1a_{2u}{}^1$	$1p^1 1p^1$	0.88	0.91
1^3A_{1g}	$2a_{1g}{}^1 3a_{1g}{}^1$	$1s^1 1d^1$	1.25	1.24
2^3E_g	$2a_{1g}{}^1 2e_g{}^1$	$1s^1 1d^1$	1.41	1.30
3^3E_g	$2a_{1g}{}^1 1e_g{}^1$	$1s^1 1d^1$	1.39	1.36
1^3A_{1u}	$2e_g{}^1 1e_u{}^1$	$1p^1 1d^1$	1.42	1.49
2^3E_u	$2e_g{}^1 1e_u{}^1$	$1p^1 1d^1$	1.41	1.50
3^3E_u	$3a_{1g}{}^1 1e_u{}^1 / 1a_{2u}{}^1 1e_g{}^1$	$1p^1 1d^1$	1.42	1.52
4^3E_u	$1e_g{}^1 1e_u{}^1$	$1p^1 1d^1$	1.46	1.56
2^1E_u	$3a_{1g}{}^1 1e_u{}^1$	$1p^1 1d^1$	1.46	1.57

[a]E.C. stands for electronic configuration.

[b]S.E.C. stands for superatomic electronic configuration.

3.4.3 $[Be(NH_3)_4]_2$

In this section most important findings related to [Be(NH3)4]2 molecule reported in following paper[37] given in Appendix A are summarized. Reprints were made with permission from

American Chemical Society.

Ariyarathna, I. R.; Miliordos, E. *J. Phys. Chem. A* **2020**, *124*, 9783–9792.

To create PECs of the $[Be(NH_3)_4]_2$ dimer three different combinations were used. They are (1) $Be(NH_3)_4(\tilde{X}^1A_1/^1S)$ + $Be(NH_3)_4(\tilde{X}^1A_1/^1S)$, (2) $Be(NH_3)_4(\tilde{X}^1A_1/^1S)$ + $Be(NH_3)_4$ $(\tilde{A}^3A_1/^3P)$, and (3) $Be(NH_3)_4(\tilde{A}^3A_1/^3P)$ + $Be(NH_3)_4(\tilde{A}^3A_1/^3P)$. Each combination produces one, six, and nine electronic states, respectively. Interaction between two $Be(NH_3)_4$ $(\tilde{X}^1A_1/^1S)$ monomers produces the $\tilde{X}^1A_1'$ ground state of $[Be(NH_3)_4]_2$ dimer (see Figure 3.8). Its D_e with respect to ground state fragments are 5.6 kcal/mol under CASPT2 level. In the ground state four electrons populate diffuse $1a_1'$ bonding orbital and $1a_2''$ antibonding orbital (see Figure 3.8 and Table 3.4). In the first excited state ($1^3A_2''$) two electrons occupy $1a_1'$ and one in each $2a_1'$ and $1a_2''$ orbital. Both first and second excited states of the dimer result from the interaction between $Be(NH_3)_4(\tilde{X}^1A_1/^1S)$ + $Be(NH_3)_4(\tilde{A}^3A_1/^3P)$. Third excited state is a $^1E''$ originates from $Be(NH_3)_4(\tilde{A}^3A_1/^3P)$ + $Be(NH_3)_4(\tilde{A}^3A_1/^3P)$.

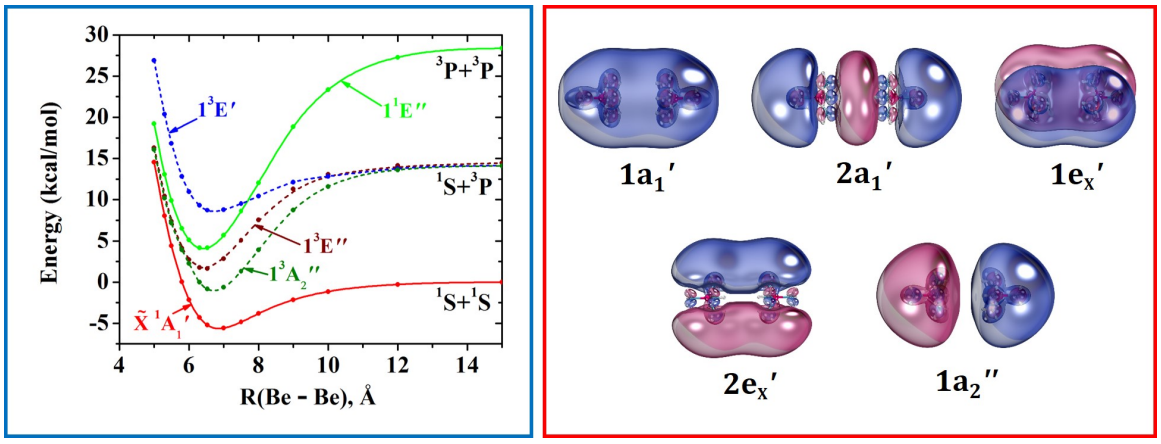

Figure 3.8: CASPT2 PECs of the $[Be(NH_3)_4]_2$ dimer as a function of Be–Be distance (blue box) and selected molecular orbitals at the equilibrium geometry (red box).

Table 3.4: CASSCF and CASPT2 vertical excitation energies (cm^{-1}) and dominant electronic configurations for few low−lying electronic states of $[Be(NH_3)_4]_2$ dimer.

State (D_{3h})	Excitation energy		E.C.[a]					
	CASSCF	CASPT2	Coeff.[b]	$1a_1'$	$2a_1'$	$1a_2''$	$1e_x'$	$1e_y'$
$\tilde{X}^1A_1'$	0	0	0.82	2	0	2	0	0
			–0.34	2	2	0	0	0
$1^3A_2''$	1564	1557	0.92	2	α	α	0	0
$1^3E''$	2567	2579	0.85	2	0	α	α	0
$1^1E''$	3679	3537	0.59	2	0	α	0	β
			–0.59	2	0	β	0	α
$1^3E'$	4693	4772	0.68	α	0	2	α	0
			0.43	2	α	0	α	0

[a]E.C. stands for electronic configuration.

[b]Coeff. stands for CASSCF coefficient.

3.5 Singlet–triplet gaps of linked SEPs

Electrons of two hydrogen atoms produce singlet and triplet spins. At closer distances two electrons become paired to produce a more stable singlet spin state (H_2 molecule) but the triplet is repulsive. When two hydrogen atoms are placed at a far distance, the singlet and triplet states are degenerate. Similarly each end of the $(NH_3)_3Li{-}NH_2(CH_2)_nNH_2{-}Li(NH_3)_3$ chain has one electron and for bigger n values the singlet and triplet states are degenerate. Specifically, for n = 3–6 the singlet−triplet energy gap is almost zero. As n becomes smaller, the two electrons pair up to form a stable singlet state. For n = 1, 2 the singlet−triplet gaps are 2980 and 860 cm^{-1}, respectively.

$(NH_3)_3Be{-}(CH_2)_n{-}Be(NH_3)_3$ is similar to $(NH_3)_3Li{-}NH_2(CH_2)_nNH_2{-}Li(NH_3)_3$. Each species bears two diffuse electrons on the chain. For $(NH_3)_3Be{-}(CH_2)_n{-}Be(NH_3)_3$; n = 6 and 7 chains singlet and the triplet states are almost degenerate. Interestingly, for n = 4 and 5 the triplet structure is slightly more stable than the singlet. Moving to

smaller n values (n = 1–3) singlets are becoming more stable than triplets similar to the $(NH_3)_3Li–NH_2(CH_2)_nNH_2–Li(NH_3)_3$ (see Figure 3.9). The energy gaps for n = 1–3 structures are 3200, 227, and 129 cm^{-1}, respectively. Geometry optimizations were performed at CAM–B3LYP under TZ(Li, C, N) and ATZ(H) basis set. Using the same basis set singlet–triplet energy gaps were evaluated by performing vertical excited state calculations at CASPT2 level of theory. In all cases two electrons at eight active orbitals were placed at reference CASSCF level. All valence electrons are correlated at CASPT2 level except those that correspond to Li–N, N–C, C–C bonds of $(NH_3)_3Li–NH_2(CH_2)_nNH_2–Li(NH_3)_3$ and Be–N, Be–C, C–C of $(NH_3)_3Be–(CH_2)_n–Be(NH_3)_3$.

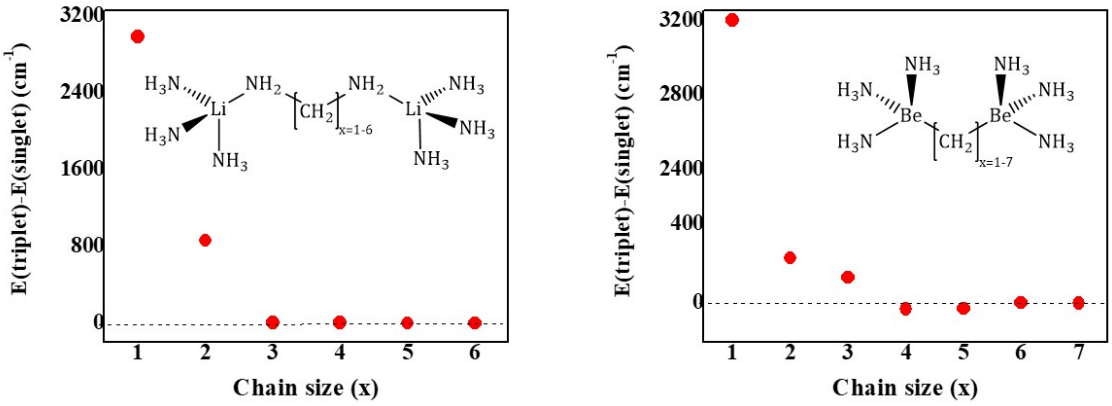

Figure 3.9: singlet–triplet gaps of $(NH_3)_3Li–NH_2(CH_2)_nNH_2–Li(NH_3)_3$ for n = 1–6 and $(NH_3)_3Be–(CH_2)_n–Be(NH_3)_3$ for n = 1–7 chains.

3.6 Second solvation shell of SEPs: $M(NH_3)_4@nNH_3$ (M = Li, Be^+, B^{2+} and n = 12, 24)

In this section most important findings reported in following paper[85] given in Appendix B are summarized. Reprints were made with permission from American Chemical Society.

Ariyarathna, I. R.; Pawłowski, F.; Ortiz, J. V.; Miliordos, E. *J. Phys. Chem. A* **2020**, *124*, 505–512.

Twelve ammonia molecules can bind to the $M(NH_3)_4$ (M = Li, Be^+, B^{2+}) via H–bonds.

These interactions are shown in the Figure 3.10. The $M(NH_3)_4@12NH_3$ (M = Li, Be^+, B^{2+} clusters belong to the T point group. The outer twelve NH_3 molecules withdraw the valence electron of M further away from $M(NH_3)_4$. To accurately describe the structures of these clusters, the diffuse nature of the electron and the H−bonding strength between ammonia molecules should be taken into account. To this end, several density functionals were tested and CAM−B3LYP[86] was found to provide accurate geometries for such clusters.

The ground state of each $M(NH_3)_4@12NH_3$ (M = Li, Be^+, B^{2+} has one electron occupying a more extended quasi spherical s−type orbital similar to $M(NH_3)_4$ (see Figure 3.1). Interestingly, this electron populates superatomic p−, d−, f−, and g−orbitals in excited states, similar to their monomers (see the orbitals of Figure 3.11). Specifically, $M(NH_3)_4@12NH_3$ (M = Li, Be^+, B^{2+} follow the 1s, 1p, 1d, 1f, 2s, 2p, 1g, 2d Aufbau principle.

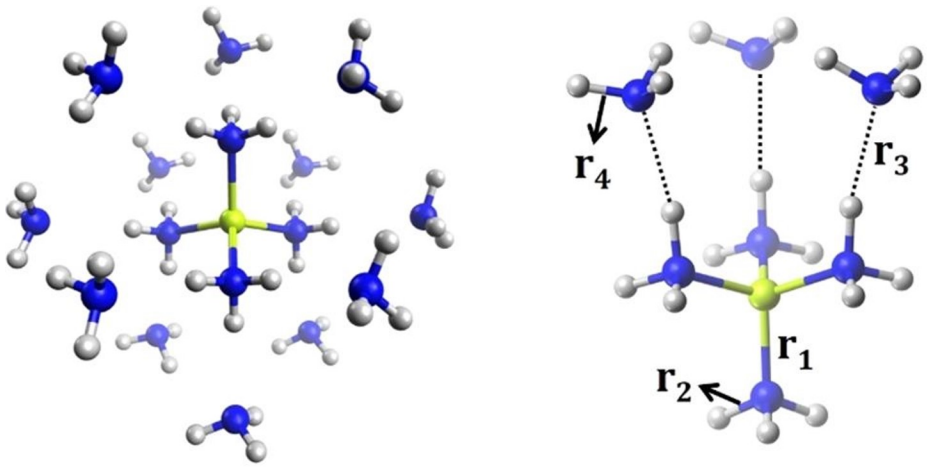

Figure 3.10: Optimized geometry of $Be(NH_3)_4@12NH_3{}^+$ (left figure) and H−bonds between inner and outer ammonia molecules shown in dashed lines (only three outer NH_3 molecules are shown for clarity) (right figure).

Twelve more ammonia molecules can fit into the cavities of $M(NH_3)_4@12NH_3$ (M = Li, Be^+). In these two cases, twenty−four ammonia molecules rest in the second solvation shell. However, in the M = B^{2+} case the cavities are not large enough to accommodate twelve more ammonia molecules in the second shell. The peripheral electron of $M(NH_3)_4@24NH_3$ (M = Li, Be^+) also populates p−, d−, f−shaped orbitals in their excited states (see the Figure 3.11). Their superatomic Aufbau principle is identical to the $M(NH_3)_4@12NH_3$, but

excitation energies are lower by 0−0.5 eV.

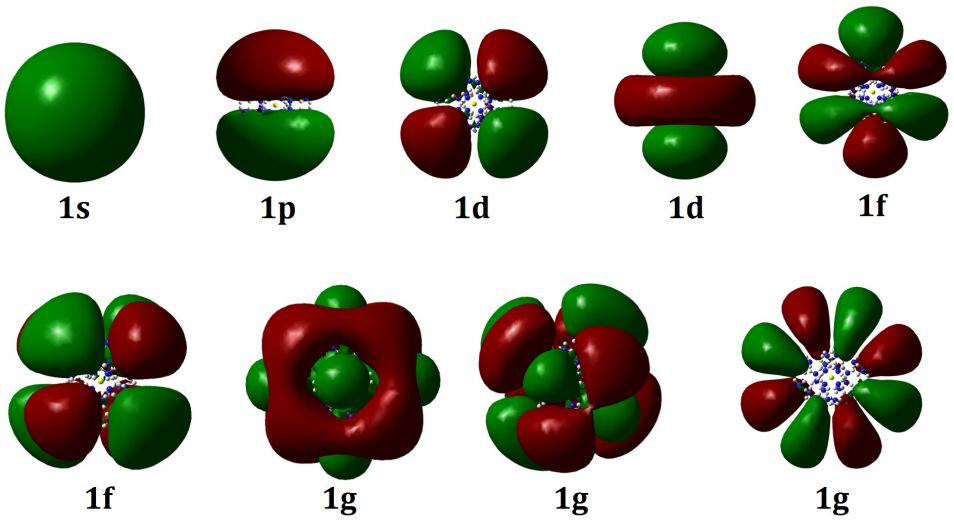

Figure 3.11: Superatomic 1s, 1p, 1d, 1f, and 1g orbitals of $Be(NH_3)_4@24NH_3{}^+$. Orbitals of $Li(NH_3)_4@24NH_3$ and $M(NH_3)_4@12NH_3{}^+$ (M = Li, Be^+, B^{2+}) have same shapes.

3.7 Conclusions

The solvation process is complete in $Li(NH_3)_4$, $Na(NH_3)_4$, $Be(NH_3)_4{}^{0,+}$, $Mg(NH_3)_4{}^{0,+}$, $Ca(NH_3)_6{}^{0,+}$, and $Ti(NH_3)_6{}^{0,+}$ complexes. Even though the electron solvation is complete in $Mg(NH_3)_4{}^{0,+}$, magnesium can bind up to six ammonia molecules. Similarly, $Ca(NH_3)_7{}^{0,+}$ and $Ca(NH_3)_8{}^{0,+}$ complexes are stable. In $Li(NH_3)_4$/$Na(NH_3)_4$ the solvated electron occupies a quasi−spherical s−type orbital that rests around the $Li(NH_3)_4{}^+$/$Na(NH_3)_4{}^+$ core. We identify such species as SEPs. In $Be(NH_3)_4$, $Mg(NH_3)_4$, and $Ca(NH_3)_6$ cases, two electrons occupy the pseudo s orbital. In their cations only one electron occupies the superatomic 1s orbital similar to the $Li(NH_3)_4$. The outer electrons of SEPs promote to higher angular momentum p−, d−, f−, g−type orbitals. The exact Aufbau model of $Li(NH_3)_4$ and $Na(NH_3)_4$ is 1s, 1p, 1d, 2s, 2p. The order of $Be(NH_3)_4{}^+$ is 1s, 1p, 1d, 2s, 1f, 2p, 2d. The series of $Mg(NH_3)_4{}^+$ is (1s, 1p, 1d, 2s, 2p, 1f, 2d) slightly different from $Be(NH_3)_4{}^+$. In the case of $Mg(NH_3)_6{}^+$ the orbital series is 1s, 1p, 1d, 2p, 2s, 1f, 2p, 2d. The Aufbau principle of $Ca(NH_3)_6{}^+$ is identical to the one of $Be(NH_3)_4{}^+$. In $Ca(NH_3)_8{}^+$, 1f falls in between 1d and 2s (1s, 1p, 1d, 1f, 2s, 2p).

Two $Be(NH_3)_3$ or $Be(NH_3)_4$ monomers bind to create dimers. In both $[Be(NH_3)_3]_2$ and $[Be(NH_3)_4]_2$ dimers solvated electrons are present. Two solvated electrons orbit around the $[Be(NH_3)_3]_2{}^{2+}$ core in the $[Be(NH_3)_3]_2$ dimer. In the excited states of $[Be(NH_3)_3]_2$ electrons populate superatomic p−, d−type orbitals similar to SEPs. $[Be(NH_3)_4]_2$ has four electrons in the periphery, two in each of superatomic σ and σ^* orbitals. In the case of $[Li(NH_3)_4]_2$ only two solvated electrons are present in the diffuse σ orbital. The D_e of $[Li(NH_3)_4]_2$ is greater than that of $[Be(NH_3)_4]_2$.

By linking two SEPs via an adjustable carbon chain their singlet−triplet gaps can be tuned. $(NH_3)_3Li{-}NH_2(CH_2)_nNH_2{-}Li(NH_3)_3$ and $(NH_3)_3Be{-}(CH_2)_n{-}Be(NH_3)_3$ have degenerate singlet−triplet splittings for bigger n values. The singlet−triplet gaps for n = 1 and 2 of $(NH_3)_3Li{-}NH_2(CH_2)_nNH_2{-}Li(NH_3)_3$ are 2980 and 860 cm^{-1}, respectively. Its n = 3−6 singlet and triplet structures are almost degenerate. For $(NH_3)_3Be{-}(CH_2)_n{-}Be(NH_3)_3$; n =1−3 the gaps are 3200, 227, and 129 cm^{-1}, respectively. The triplet structures are slightly more stable than singlet ones for n = 4, 5. For each n = 6, 7 the singlet−triplet gap is almost zero.

$M(NH_3)_4$ (M = Li, Be^+, B^{2+}) can accommodate $12NH_3$ molecules in the second solvation shell. They are bound to the ammonia molecules in the first shell via H−bonds. The peripheral electron of $M(NH_3)_4$ (M = Li, Be^+, B^{2+}) is further withdrawn by the outer $12NH_3$ molecules. Similar to their monomers, the diffuse electron of $M(NH_3)_4@12NH_3$ (M = Li, Be^+, B^{2+}) occupies a pseudo 1s orbital and is excited in to superatomic p−, d−, f−orbitals. The orbital series observed is 1s, 1p, 1d, 1f, 2s, 2p, 1g, 2d. $M(NH_3)_4$ (M = Li, Be^+) can pack up to $24NH_3$ molecules in the second solvation shell. The additional $12NH_3$ molecules move into the vacancies of $M(NH_3)_4@12NH_3$. The orbital series of $M(NH_3)_4@24NH_3$ is identical to the orbital series of $M(NH_3)_4@12NH_3$.

Chapter 4

Superatomic nature of ground and excited states of neutral and partially oxidized metal–aqua complexes

Solvated electrons in aqueous media are commonly known as *"hydrated electrons"*.[23,87,88] Even though hydrated electrons were detected about a half a century after the discovery of ammoniated electrons, the field of hydrated electrons is much more evolved compared to the latter.[23] When generated in low concentrations, an electron has a lifetime of ~300 μs in neutral water.[89] These highly reactive electrons reduce water and produce gaseous hydrogen. Due to this rapid reaction, experimental characterization of solvated electrons in aqueous media is highly challenging and theoretical studies are encouraged.[23,90–92] Reactions between certain metals and water produce solvated electrons.[93–97] Do neutral or partially oxidized metal−aqua complexes behave similar to metal−ammonia SEPs? This chapter is devoted to answering this question by focusing on ground and excited electronic structures of metal−aqua complexes.

4.1 $Be(H_2O)_{n=1-4}^{+,0}$

In this section most important findings related to beryllium aqua complexes reported in following paper[29] given in Appendix C are summarized. Reprints were made with permission from Royal Society of Chemistry.

Ariyarathna, I. R.; Miliordos, E. *Phys. Chem. Chem. Phys.* **2019**, *21*, 15861–15870.

The only experimental gas phase study reported on Be interaction with H_2O is on Be^+–H_2O.[98] $Be^{+,0}$ can bind up to four water molecules to complete the first solvation shell. The $Be(H_2O)_{n=1-4}^+$ has significantly higher D_es compared to their neutral counterparts. For cationic species the D_e drops as n goes from 1 to 4, with respect to $Be(H_2O)_n^+ \rightarrow Be(H_2O)_{n-1}^+ + H_2O$ reaction. Specifically, the D_es for n = 1, 2, 3, and 4 are 59.4, 39.8, 25.9, and 18.7 kcal/mol, respectively. This pattern is opposite for neutral species. The D_es of n = 1, 2, 3, and 4 neutral species are 1.2, 5.8, 14.1, and 20.0 kcal/mol, respectively.

In each $Be(H_2O)_{n=1-3}^{+,0}$, the 2s atomic orbital of Be polarizes away from electron rich H_2O ligands to minimize electrostatic repulsion and/or overlap with the ammonia lone pairs. The attack of another H_2O molecule to the $Be(H_2O)_3^{+,0}$ forces its valence electron cloud to the periphery to create $Be(H_2O)_4^{+,0}$ species. This is the same phenomenon that was observed in $Be(NH_3)_4^{+,0}$. However, the diffuse electron cloud of $Be(H_2O)_4^{+,0}$ is not perfectly symmetric as in $Be(NH_3)_4^{+,0}$ due to its C_1 symmetry.

$Be(H_2O)_4$ is less stable compared to $Be(NH_3)_4$ and dissociates to $Be(H_2O)_2(OH)_2 + H_2$ fragments easily. The $Be(H_2O)_4 \rightarrow Be(H_2O)_2(OH)_2 + H_2$ reaction is a single step process, where two H atoms dissociate simultaneously from two H_2O ligands. The transition state barrier for this one–step reaction is only 8 kcal/mol. On the other hand, H_2 dissociation is a two–step process for $Be(NH_3)_4$. In the first step a H atom cleaves from an NH_3 to generate the $Be(NH_3)_3NH_2\cdots H$ intermediate. In the next step, another H atom departs from $Be(NH_3)_3NH_2$ to produce $Be(NH_3)_2(NH_2)_2 + H_2$. The first process is the rate determining step of the $Be(NH_3)_4 \rightarrow Be(NH_3)_2(NH_2)_2 + H_2$ reaction with a ~24 kcal/mol energy barrier. The full energy landscape of these reactions is given in Figure 4.1.

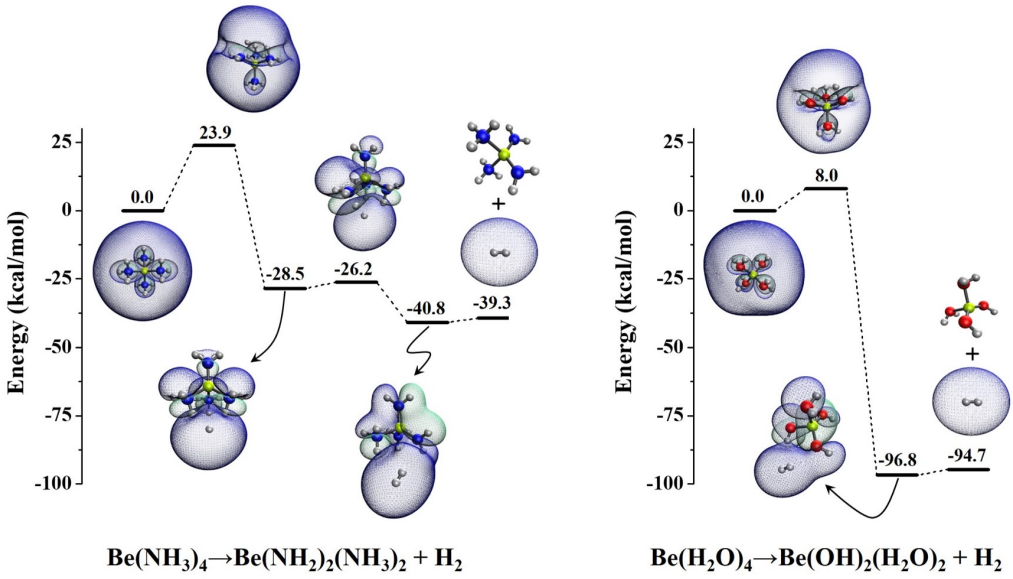

Figure 4.1: H_2 dissociation landscape of $Be(NH_3)_4$ and $Be(H_2O)_4$ at CCSD(T) level and corresponding HOMOs.

Similar to metal ammonia SEPs, the outer electron(s) of $Be(H_2O)_4{}^{+,0}$ populate p−, and d−shaped orbitals. Due to the low symmetry of $Be(H_2O)_4{}^{+,0}$ the three p or five d states are no longer degenerate. For example, the three 1s→1p and five 1s→1d transitions of $Be(H_2O)_4{}^{+}$ span within 1.3−1.8 and 2.5−3.5 eV regions, respectively. Excitation energies of $Be(H_2O)_4{}^{+}$ are comparable to those of $Be(NH_3)_4{}^{+}$, where 1s→1p and 1s→1d transitions of $Be(NH_3)_4{}^{+}$ require approximately 1.4 and 2.4 eV, respectively. The excited states of $Be(H_2O)_4$ are heavily multi−referenced. More details regarding $Be(H_2O)_4{}^{0,+}$ are reported in the Ref[29] of Appendix C.

4.2 $Mg(H_2O)_6{}^{+/0}$

In this section most important findings related to magnesium aqua complexes reported in following paper[29] given in Appendix C are summarized. Reprints were made with permission from Royal Society of Chemistry.

Ariyarathna, I. R.; Miliordos, E. *Phys. Chem. Chem. Phys.* **2019**, *21*, 15861–15870.

The 3s atomic orbital of each $Mg(H_2O)_{n=1-5}{}^{+,0}$ species stays contacted with the Mg atom

but polarized away from the ligands, and hence are categorized as quasi−valence type structures.[99,100] Six water molecules can saturate the first solvation spheres of $Mg^{+,0}$. $Mg(H_2O)_6{}^+$ and $Mg(H_2O)_6$ have one and two diffuse electrons in the periphery of $Mg(H_2O)_6{}^{2+}$, respectively.

The $Mg(H_2O)_6{}^+$ is T_h in symmetry. Because of the high symmetry it is an ideal system to study a plethora of excited states probing the suitability of various basis sets. The tested basis sets are, (1) Mg:TZ, O: TZ, H: DATZ (2) Mg:TZ, O: TZ, H: DAQZ (3) Mg:TZ, O: TZ, H: TATZ (4) Mg:TZ, O: TZ, H: TAQZ. Under all four basis sets the observed shell model of $Mg(H_2O)_6{}^+$ is 1s, 1p, 1d, 2s, 2p, 1f, 2d, 3s, 1g. This is the first time we observed a g−superatomic orbital for a SEP. Several superatomic orbitals of $Mg(H_2O)_6{}^+$ are illustrated in the Figure 4.2. The excitation energy difference between our smallest basis set (1) and biggest basis set (4) is less than 0.2 eV for all states. Excited state calculations under basis set (4) is associated with insurmountable technical difficulties, hence only several excitations were evaluated. Excitation energies calculated under basis sets (1)−(3) under CASPT2 and C−CASPT2 are depicted in Figure 4.2. Overall, the basis set (1) provides very accurate results efficiently. Furthermore, basis set (1) was used to compute excitation energies at EOM−EA−CCSD[101] level of theory. EOM−EA−CCSD and CASPT2 numbers agree very well and the energy discrepancy is less than 0.07 eV. Compared to $Be(H_2O)_4{}^+$, $Mg(H_2O)_6{}^+$ has lower excitation energies. The same pattern was observed going from $Be(NH_3)_4{}^+$ to $Mg(NH_3)_6{}^+$.

$Mg(H_2O)_6$ is C_1 in symmetry. By imposing C_s symmetry to the $Mg(H_2O)_6$ molecule we were able to minimize the computational cost associated with excited state calculations, significantly. The energy difference between C_1 vs C_s structures is only 1.18 kcal/mol. The $1s^2$ ground state and the first three excited states with $1s^1 1p^1$ character (0.66−0.74 eV) show clean electronic configurations. Excited states beyond this point have rather mixed electronic characters.

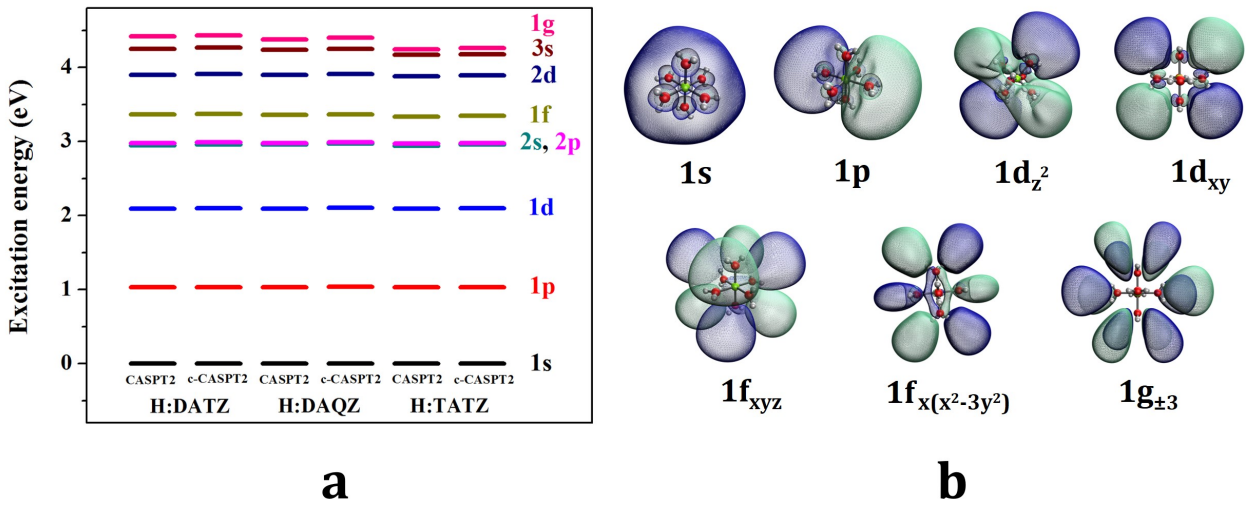

Figure 4.2: (a) Excited states of $Mg(H_2O)_6^+$ with different basis sets. The DATZ, DAQZ, and TATZ represent excitation energies calculated with (1) Mg:TZ, O: TZ, H: DATZ, (2) Mg:TZ, O: TZ, H: DAQZ, and (3) Mg:TZ, O: TZ, H: TATZ basis sets, respectively. (b) Contours of selected 1s, 1p, 1d, 1f, and 1g orbitals of $Mg(H_2O)_6^+$.

4.3 $Ca(H_2O)_{6,8}^+$ and $Ca(H_2O)_6@12H_2O^+$

In this section most important findings reported in following paper[102] *given in Appendix C are summarized. Reprints were made with permission from Royal Society of Chemistry.*

Ariyarathna, I. R.; Miliordos, E. *Phys. Chem. Chem. Phys.* **2020**, *22*, 22426–22435.

Similar to $Mg(H_2O)_6^+$, $Ca(H_2O)_6^+$ has T_h symmetry with one peripheral electron around the $Ca(H_2O)_6^{2+}$ core. $Ca(H_2O)_6^+$ has a lower D_e compared to $Mg(H_2O)_6^+$. But, Ca^+ accommodates up to eight H_2O molecules in the first solvation shell whereas for Mg^+ the limit is six molecules. The M: (≡Metal):TZ, O: TZ, H: DATZ basis set has been proven to provide very accurate results efficiently for metal ammonia or metal aqua SEPs, and hence adopted for this work. The Aufbau principle observed for the $Ca(H_2O)_6^+$ is 1s, 1p, 1d, 2s, 1f, 2p, 2d, 1g, 3s. This is slightly different from $Mg(H_2O)_6^+$, where the 2p and 3s are populated before the 1f and 1g. Compared to $Mg(H_2O)_6^+$, excitation energies of $Ca(H_2O)_6^+$ are lower.

$Ca(H_2O)_7^+$ cannot be identified as a SEP due to its quasi−valence type structure. On the other hand, $Ca(H_2O)_8^+$ has an S_8 symmetry with one peripheral electron that promotes to higher angular momentum 1p, 1d, 2s, 1f, 2p orbitals. Compared to $Ca(H_2O)_6^+$ the excitation energies of $Ca(H_2O)_8^+$ are 0.23−0.32 eV lower, but follow the same Aufbau shell model.

Twelve H_2O molecules bind to $Ca(H_2O)_6^+$ via H−bonds (see Figure 4.3) to produce $Ca(H_2O)_6@12H_2O^+$. This cluster has S_6 symmetry. Electronic structures of such transition metal−aqua clusters are reported in the literature [e.g. $M(H_2O)_6(H_2O)_{12}$, M = Ti^{3+}, V^{3+}, Cr^{3+}, Mn^{2+}, Fe^{3+}, Fe^{2+}, Co^{3+}, Ni^{2+}, Ru^{3+}].[103,104] In $Ca(H_2O)_6@12H_2O^+$ the outer twelve H_2O molecules displace the valence electron of Ca^+ even further and solvate around the $Ca(H_2O)_6^{2+}@12H_2O$. Excited states of $Ca(H_2O)_6@12H_2O^+$ are studied only up to 1d level. The excitation energies of $Ca(H_2O)_6@12H_2O^+$ are approximately half of that of $Ca(H_2O)_6^+$.

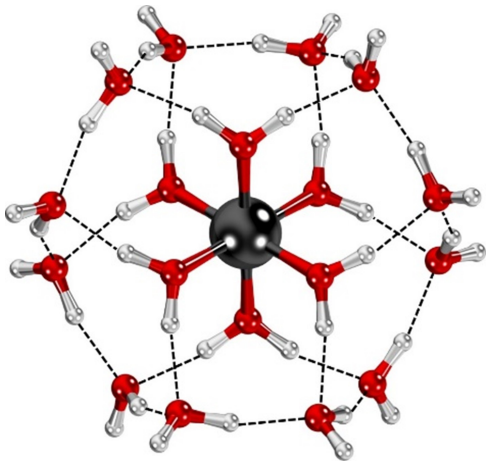

Figure 4.3: Optimized geometry of $Ca(H_2O)_6@12H_2O^+$. H−bonds between H_2O molecules are denoted by black dashed lines.

4.4 $Ti(H_2O)_6^{3+,2+,+,0}$

In the ground state $Ti(H_2O)_6^{3+}$ has an electron in a t_{2g} orbital at T_h symmetry. Since t_{2g} orbitals are unevenly occupied the complex undergoes Jahn−Teller distortion from T_h to C_i.[105] However, the distortion is weak and the splitting of t_{2g} set is a mere 0.07 eV. This electron promotes to $d_{x^2-y^2}$ and d_{z^2} orbitals by absorbing 1.86 and 2.10 eV, respectively. But what would be the next electron transition? At CASPT2 level the next excitation requires

9.11 eV. Fascinatingly, the electron of this metastable state occupies a pseudo atomic s−type orbital. Upon further excitations, this electron moves to atomic type 1p, 1d, 1f, 2s, 2p orbitals.

In $Ti(H_2O)_6^{2+}$ the first quasi−s orbital can be populated by supplying 4.52 eV, which is significantly lower than in $Ti(H_2O)_6^{3+}$ case. This 1s superatomic orbital occupies in the ground states of $Ti(H_2O)_6^{+}$ and $Ti(H_2O)_6$. The electronic configurations and excitation energies of $Ti(H_2O)_6^{+}$ and $Ti(H_2O)_6$ are listed in Tables 4.1 and 4.2, respectively.

The ground state of $Ti(H_2O)_6^{+}$ is a quartet with two electrons in t_{2g} orbitals and one in superatomic s orbital. The same electronic configuration also produces a doublet. This doublet state lies only 0.04 eV above the ground state. The next excited state is created by promoting one t_{2g} electron to e_g shell creating quartet (at 0.70 eV) and a doublet (at 0.75 eV) state with $t_{2g}^1e_g^1s^1$ configuration. The next several electronic states have $t_{2g}^2p^1$ character (1.00−1.05 eV). The superatomic 1s orbital populates in the next four states that lies in between 1.30−1.59 eV. A manifold of states with $t_{2g}^2d^1$ configuration appears around 1.72−2.24 eV.

The 1^3T_g ground state of $Ti(H_2O)_6$ is created by adding one electron to the singly occupied s orbital of the 1^4T_g ($t_{2g}^2s^1$) ground state of $Ti(H_2O)_6^{+}$. Compared to $Ti(H_2O)_6^{+}$ the spectrum of $Ti(H_2O)_6$ is dense. For example, all triplets, quintets, and singlets with the $t_{2g}^2s^1p^1$ configuration are stacked around 0.51−0.62 eV. From 1.19−2.24 eV a plethora of states were observed. All these states bear at least one electron in a diffuse superatomic orbital.

Table 4.1: Electronic configurations and state average CASPT2 excitation energies (eV) of $Ti(H_2O)_6{}^+$.

E.C.[a]	State (T_h)	Excitation energy
$t_{2g}{}^2s^1$	1^4T_g	0.00
$t_{2g}{}^2s^1$	1^2T_g	0.04
$t_{2g}{}^1e_g{}^1s^1$	2^4T_g	0.70
$t_{2g}{}^1e_g{}^1s^1$	2^2T_g	0.75
$t_{2g}{}^2p^1$	1^4T_u, 2^4T_u, 1^4A_u, 1^4E^u	1.00–1.05
$t_{2g}{}^2p^1$	1^2T_u, 2^2T_u, 1^2A_u, 1^2E^u	1.01–1.05
$t_{2g}{}^2s^1$	3^2T_g	1.30
$t_{2g}{}^2s^1$	1^2E_g	1.35
$e_g{}^2s^1$	1^4A_g	1.53
$e_g{}^2s^1$	1^2A_g	1.59
$t_{2g}{}^1e_g{}^1p^1$	2^4A_u, 3^4T_u, 4^4T^u, 2^4E_u	1.74–1.75
$t_{2g}{}^1e_g{}^1p^1$	2^2A_u, 3^2T_u, 4^2T^u, 2^2E_u	1.74–1.75
$t_{2g}{}^2d^1$	3^4T_g, 4^4T_g, 5^4T_g, 6^4T^g, 2^4A_g, 1^4E_g	1.72–2.24
$t_{2g}{}^2d^1$	4^2T_g, 5^2T_g, 6^2T_g, 7^2T^g 2^2A_g, 2^2E_g	1.78–2.21
$t_{2g}{}^1e_g{}^1s^1$	7^4T_g	2.07
$t_{2g}{}^1e_g{}^1s^1$	8^2T_g	2.15

[a]E.C. stands for electronic configuration.

Table 4.2: Electronic configurations and state average CASPT2 excitation energies (eV) of $Ti(H_2O)_6$.

E.C.[a]	State (T_h)	Excitation energy
$t_{2g}{}^2s^2$	1^3T_g	0.00
$t_{2g}{}^2s^1p^1$	1^3T_u, 1^3A_u, 2^3T_u, 1^3E_u	0.51–0.57
$t_{2g}{}^2s^1p^1$	1^5T_u, 2^5T_u, 1^5E_u, 1^5A_u	0.51–0.60
$t_{2g}{}^2s^1p^1$	1^1T_u, 1^1A_u, 2^1T_u, 1^1E_u	0.55–0.62
$t_{2g}{}^2p^2/t_{2g}{}^2s^1d^1$	2^3T_g, 3^3T_g, 1^3E_g, 4^3T_g, 1^3A_g, 5^3T_g	1.19–1.39
$t_{2g}{}^2s^2$	1^1T_g, 1^1E_g	1.30–1.35
$t_{2g}{}^2p^2$	6^3T_g, 2^3A_g, 2^3E_g, 7^3T_g	1.36–1.67
$t_{2g}{}^2s^2/t_{2g}{}^2s^1d^1$	2^1T_g, 3^1T_g	1.42–1.47
$t_{2g}{}^2s^1d^1$	1^5T_g, 2^5T_g, 1^5A_g, 3^5T_g, 1^5E_g, 4^5T_g	1.50–1.81
$t_{2g}{}^1e_g{}^1s^2$	8^3T_g	1.55
$t_{2g}{}^2p^2$	1^1A_g, 2^1E_g, 4^1T_g, 5^1T_g	1.59–1.67
$t_{2g}{}^2p^2$	2^5A_g, 2^5E_g, 5^5T_g, 6^5T_g	1.62–1.70
$t_{2g}{}^1e_g{}^1s^1p^1$	3^3T_u, 2^3E_u, 2^3A_u, 4^3T_u	1.71–1.82
$t_{2g}{}^1e_g{}^1s^1p^1$	3^5T_u, 2^5E_u, 2^5A_u, 4^5T_u	1.71–1.84
$t_{2g}{}^1e_g{}^1s^1p^1/t_{2g}{}^1s^1p^1d^1$	3^1T_u, 2^1E_u, 4^1T_u	1.76–1.87
$t_{2g}{}^2s^1d^1$	3^3E_g	1.80
$t_{2g}{}^2p^1d^1$	5^5T_u, 6^5T_u, 3^5E_u, 7^5T_u, 8^5T_u	2.07–2.22
$t_{2g}{}^2p^1d^1$	5^3T_u, 3^3A_u, 6^3T_u, 4^3A_u, 7^3T_u, 8^3T_u	2.08–2.22
$t_{2g}{}^2e_g{}^1p^1/t_{2g}{}^2p^1d^1$	5^1T_u, 6^1T_u, 7^1T_u	2.11–2.21
$t_{2g}{}^2p^1d^1$	8^1T_u	2.24

[a]E.C. stands for electronic configuration.

4.5 Conclusions

Neutral or partially oxidized metal aqua complexes bear diffuse electrons in the periphery similar to metal ammonia SEPs. For example $Be(H_2O)_4$, $Mg(H_2O)_6$, $Ca(H_2O)_6$, $Ca(H_2O)_8$

and their cationic complexes have two and one peripheral electrons, respectively. The excited state spectra of $Be(H_2O)_4$, $Mg(H_2O)_6$, are $Ca(H_2O)_6$ are heavily multi−referenced in nature due to their C_1 symmetry. The Aufbau shell model of the cations are similar to the orbital order of their corresponding metal ammonia SEPs.

The high symmetry of $Mg(H_2O)_6{}^+$ (T_h) helped us to expand the previously introduced Aufbau rule of SEPs beyond the 2d level. All four basis sets; (1) Mg:TZ, O: TZ, H: DATZ (2) Mg:TZ, O: TZ, H: DAQZ (3) Mg:TZ, O: TZ, H: TATZ (4) Mg:TZ, O: TZ, H: TAQZ predicted an identical 1s, 1p, 1d, 2s, 2p, 1f, 2d, 3s, 1g superatomic Aufbau shell model for $Mg(H_2O)_6{}^+$. The Mg:TZ, O: TZ, H: DATZ basis set provides accurate excitation energies efficiently. The $Mg(NH_3)_6{}^+$ SEP discussed in the Chapter 3 populates 2p before 2s and 1f prior to the 2p.

The shell model of $Ca(H_2O)_6{}^+$ is 1s, 1p, 1d, 2s, 1f, 2p, 2d, 1g, 3s and is slightly different from $Mg(H_2O)_6{}^+$. Overall excitation energies decrease moving from $Be(H_2O)_4{}^+$ to $Mg(H_2O)_6{}^+$ and $Mg(H_2O)_6{}^+$ to $Ca(H_2O)_6{}^+$. $Ca(H_2O)_6{}^+$ can accommodate twelve H_2O molecules in the second shell that are H−bonded to the inner six H_2O molecules. The second solvation shell shifts the unpaired electron further away from the Mg^{2+} center. Similar to $Ca(H_2O)_6{}^+$, the $Ca(H_2O)_6@12H_2O^+$ cluster populates p−, d−type orbitals in excited states. Excitation energies of $Ca(H_2O)_6{}^+$ decrease approximately by half by implementing the second solvation shell.

$Ti(H_2O)_6{}^{3+}$ and $Ti(H_2O)_6{}^{2+}$ have one and two d electrons in their ground state. Interestingly, these d electrons populate diffuse s−, p−, d−shaped orbitals in their excited states. Specifically, $Ti(H_2O)_6{}^{3+}$ and $Ti(H_2O)_6{}^{2+}$ require 9.11 and 4.52 eV excitation energies to occupy the 1s type diffuse orbital. The 1s superatomic orbital is occupied in the ground states of $Ti(H_2O)_6{}^+$ and $Ti(H_2O)_6$. The ^4T_g ground state of $Ti(H_2O)_6{}^+$ has $t_{2g}{}^2s^1$ electronic configuration. The ^3T_g ($t_{2g}{}^2s^2$) ground state bears two electrons in the superatomic 1s orbital. These complexes give birth to a plethora of low−lying electronic states due to various electronic transfers such as $t_{2g}\rightarrow e_g$, $t_{2g}\rightarrow$1s, 1s$\rightarrow$1p, and 1s$\rightarrow$1d.

Chapter 5

Ab initio investigations of ground and excited states of transition metal monoxides and their catalytic strengths towards water and hydrogen sulfide activation

Transition metal oxides exhibit a wide range of industrial applications.[106,107] Primarily, they are excellent heterogeneous catalysts due to their uniquely rich redox and acid−base chemistries.[108,109] Transition metal oxide molecular clusters are being studied in gas phase as model catalysts to understand the catalytic processes that exist on surfaces.[110] It is also a common practice to predict efficiency of a potential metal oxide molecular catalyst computationally prior to its laboratory synthesis.[111,112] This approach can save millions of dollars and abate environmental pollution. High−level quantum mechanical calculations provide a profound electronic structure understanding that can help us to optimize the efficiency by tuning metal identity and the nature of ligands to create superior catalysts.[110] Multi−reference methods have been employed to understand electron arrangements of ground and excited states of first−row transition metal monoxides.[113–115] Such studies on second−row transition metal monoxides are limited. Because of this reason we performed a series of high−level *ab*

initio studies on several neutral and charged second−row transition metal monoxides and explored their water and hydrogen sulfide activation strengths. Our findings are discussed in this chapter.

5.1 Ground and excited electronic states of ZrO^+ and NbO^+ and their water and hydrogen sulfide activation strengths

Water splitting is an endothermic reaction that can be catalyzed by transition metal based catalysts.[116] Generally, Ru, Co, Ir, and Pt based catalysts are known to be efficient in water splitting.[117] But the search for an ideal catalyst capable of water splitting with the required efficiency for practical use is an ongoing process. Unlike water its isovalent hydrogen sulfide is a toxic gas. Industrially it is crucial to separate H_2S from petroleum, natural gas, or waste gas produce from chemical plants.[118,119] Due to this, desulfurization of H_2S to produce elemental sulfur and hydrogen gas has gained a particular interest.[119,120] This section focuses on ground and excited electronic structures of MO^+ (M = Zr, Nb), $MO^+ + H_2X$ (M = Zr, Nb and X = O, S) reactions, and contains an attempt to model complexes that activate H_2O and H_2S efficiently.

5.1.1 Electronic structures of ZrO^+ and NbO^+

In this section most important findings reported in following paper[121] given in Appendix D are summarized. Reprints were made with permission from Elsevier.

Ariyarathna, I. R.; Miliordos, E. *J. Quant. Spectrosc. Radiat. Transf.* **2020**, *255*, 107265.

We tested two different CASSCF active spaces to study ZrO^+. In the first active space we used 7 electrons in 9 active orbitals ($2p_{/O}$, $5s_{/Zr}$, $4d_{/Zr}$). These are $4a_1$, $2b_1$, $2b_2$, $1a_2$ under C_{2v} symmetry. State average calculations were found to keep these selected orbitals in the active space at each Zr−O distance of the potential energy profile. However, state specific calculations of low−lying electronic states were found to insert $3p_{x/O}$ and $3p_{y/O}$

orbitals instead of the required $4d_{xz/Zr}$ and $4d_{yz/Zr}$. We overcame this problem by increasing the active space by three more orbitals in the CASSCF active space. This is our second active space: 7 electrons in 12 active orbitals ($5a_1$, $3b_1$, $3b_2$, $1a_2$). We used the bigger second active space to collect energetics of ZrO^+ species.

The first three electronic states of ZrO^+ are $X^2\Delta$, $1^2\Sigma^+$, and $1^2\Pi$. They have ~168, 158, 117 kcal/mol D_es with respect to the $Zr^+(^4F)$ + $O(^3P)$ fragments. They bear 1.724, 1.712, and 1.775 Å bonds at MRCI+Q level of theory, respectively. At equilibrium distances $X^2\Delta$, $1^2\Sigma^+$, $1^2\Pi$ have $1\sigma^2 1\pi^4 1\delta^1$, $1\sigma^2 2\sigma^1 1\pi^4$, $1\sigma^2 1\pi^4 2\pi^1$ electronic configurations, respectively. These states bear $Zr^{3+}O^{2-}$ oxo character with triple bonds. Their chemical bonding patterns are described in the vbL diagrams given in Figure 5.1. The $1^2\Pi$ state is followed by the closely arranged $1^2\Phi$, $2^2\Pi$, $1^4\Pi$, $1^4\Phi$, $3^2\Pi$, $2^4\Pi$, $4^2\Pi$, $1^4\Delta$, $2^2\Delta$, $2^4\Delta$ electronic states and they bear ~2 Å equilibrium bond lengths. All these states show $Zr^{2+}O^{\bullet-}$ oxyl electronic configurations.

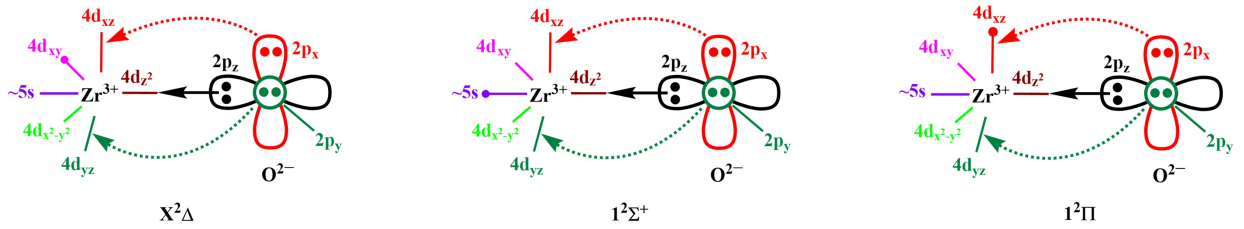

Figure 5.1: vbL diagrams for the three lowest energy states of ZrO^+.

It is not necessary to use a bigger active space to study NbO^+ and the *CAS(8,9)* (8 electrons in 9 active orbitals ($2p_{/O}$, $5s_{/Nb}$, $4d_{/Nb}$)) space is sufficient. Similar to the ZrO^+, the NbO^+ has ionic $M^{3+}O^{2-}$ character. The ground state electronic structure of $NbO^+(X^3\Sigma^-)$ can be created by placing an electron in the empty δ orbital of $ZrO^+(X^2\Delta)$. Similarly, coupling these two delta electrons into a singlet, the ($1^1\Gamma$, $1^1\Sigma^+$) states with $1\sigma^2 1\pi^4 1\delta^2$ configuration are created. Overall, the order of the states for NbO^+ is $X^3\Sigma^-$, $1^1\Gamma$, $1^1\Sigma^+$, $1^3\Delta$, $1^1\Delta$, $1^3\Phi$, $1^3\Pi$, $1^1\Pi$, $1^1\Phi$, $2^3\Pi$, $2^1\Sigma^+$, $1^5\Sigma$, $2^1\Pi$, $1^5\Pi$, $1^5\Delta$, $3^3\Pi$. The vbL diagrams proposed for the first five electronic states of NbO^+ are illustrated in the Figure 5.2. All five states possess triple bonds with ~1.66 Å lengths.

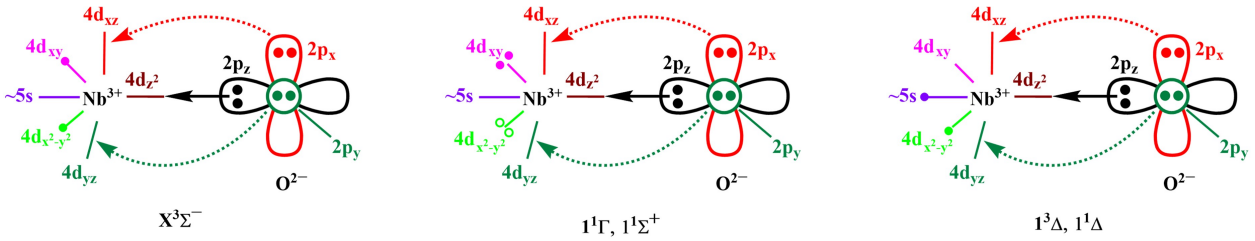

Figure 5.2: vbL diagrams for five lowest energy states of NbO^+. The $(4d_{xy})^2 \pm (4d_{x^2-y^2})^2$ electron combinations of $^1\Gamma$ and $^1\Sigma^+$ states are illustrated by solid and open circles (The $1^1\Gamma$ and $1^1\Sigma^+$ have $(4d_{xy})^2 - (4d_{x^2-y^2})^2$ and $(4d_{xy})^2 + (4d_{x^2-y^2})^2$ configurations, respectively). Two unpaired electrons of $1^3\Delta$ and $1^1\Delta$ have same and opposite spins, respectively.

5.1.2 Water and hydrogen sulfide activation by ZrO^+ and NbO^+

In this section most important findings reported in following paper[122] given in Appendix D are summarized. Reprints were made with permission from Royal Society of Chemistry.

Ariyarathna, I. R.; Miliordos, E. *Phys. Chem. Chem. Phys.* **2021**, *23*, 1437–1442.

The H_2X (X = O, S) activation process by MO^+ (M = Zr, Nb) can be partitioned into three major processes: (1) Formation of the $[H_2X\cdots MO]^+$ interacting complex, (2) Surpass the transition state barrier that involves H–X bond cleavage of metal bound H_2X, (3) $[HX–M–OH]^+$ product formation. First, we optimized geometries of several low–lying electronic states of interacting complexes (IC), transition states (TS), and final products (P) of $MO^+ + H_2X$ (M = Zr, Nb and X = O, S) reactions at MRCI level of theory. The reference CASSCF wave functions of these calculations consist of seven active orbitals with five and six electrons in M = Zr and M = Nb cases, respectively. At MRCI level of theory all valence electrons are correlated. The used basis set for O and H atoms are cc–pVDZ and aug–cc–pVDZ, respectively.[79] For the metal atom cc–pVDZ–PP basis set with Stuttgart relativistic pseudopotential that replace 28 inner electrons was used.[123]

These structures were adopted to perform single–point MRCI+Q calculations at bigger cc–pVTZ–PP: M, cc–pVTZ: H, aug–cc–pVTZ: O basis set to obtain more accurate energies. We selected the $X^2\Delta$, $1^2\Sigma^+$, $1^2\Pi$, $1^4\Pi$ of ZrO^+ and $X^3\Sigma^-$, $1^1\Gamma$, $1^1\Sigma^+$, $1^3\Delta$, $1^5\Sigma^-$ states of NbO^+ to study the $MO^+ + H_2X \rightarrow [HX–M–OH]^+$ reactions and the constructed energy

landscapes are shown in Figure 5.3. Notice that the degenerate $^2\Pi$ electronic state of naked ZrO^+ is nearly degenerate in $ZrO^+ + H_2O$ reactants, due to the implementation of smaller active space. The $MO^+ + H_2O$ reaction causes these doubly degenerate electronic states of naked MO^+ to lift their degeneracies by splitting into two components creating two different energy pathways. Geometric parameters of IC, TS, and P of the lowest spin state of each reaction are depicted in the Figures 5.4 and 5.5.

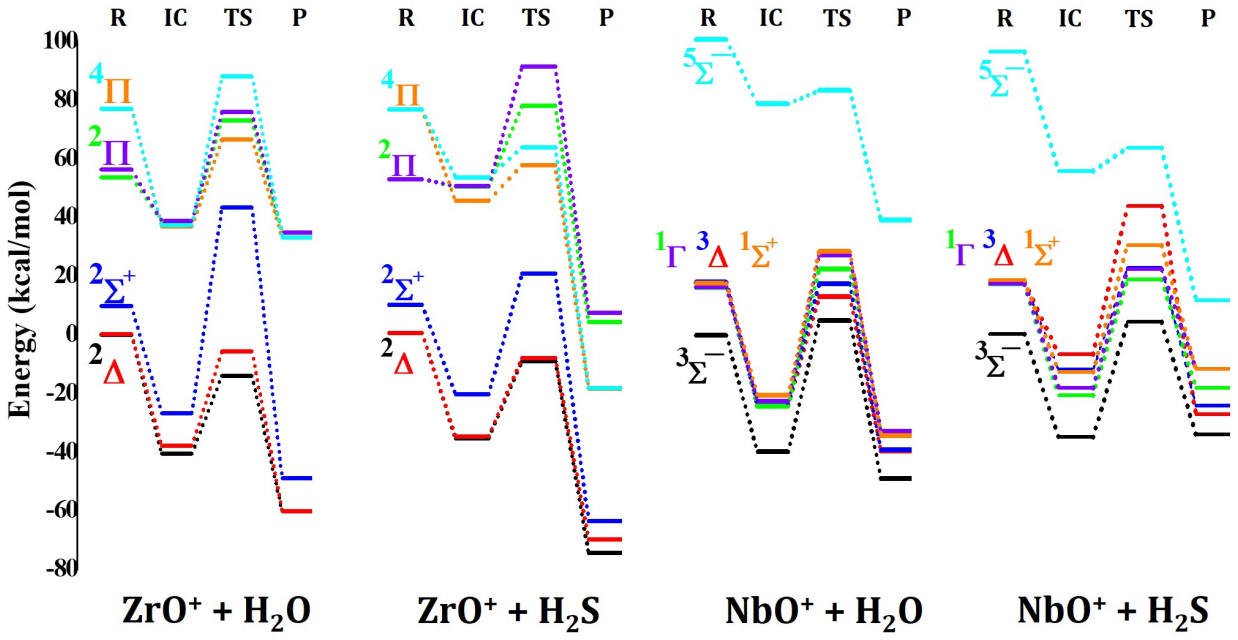

Figure 5.3: MRCI+Q energy landscape of $MO^+ + H_2X \rightarrow [HX{-}M{-}OH]^+$ (M = Zr, Nb and X = O, S) reactions.

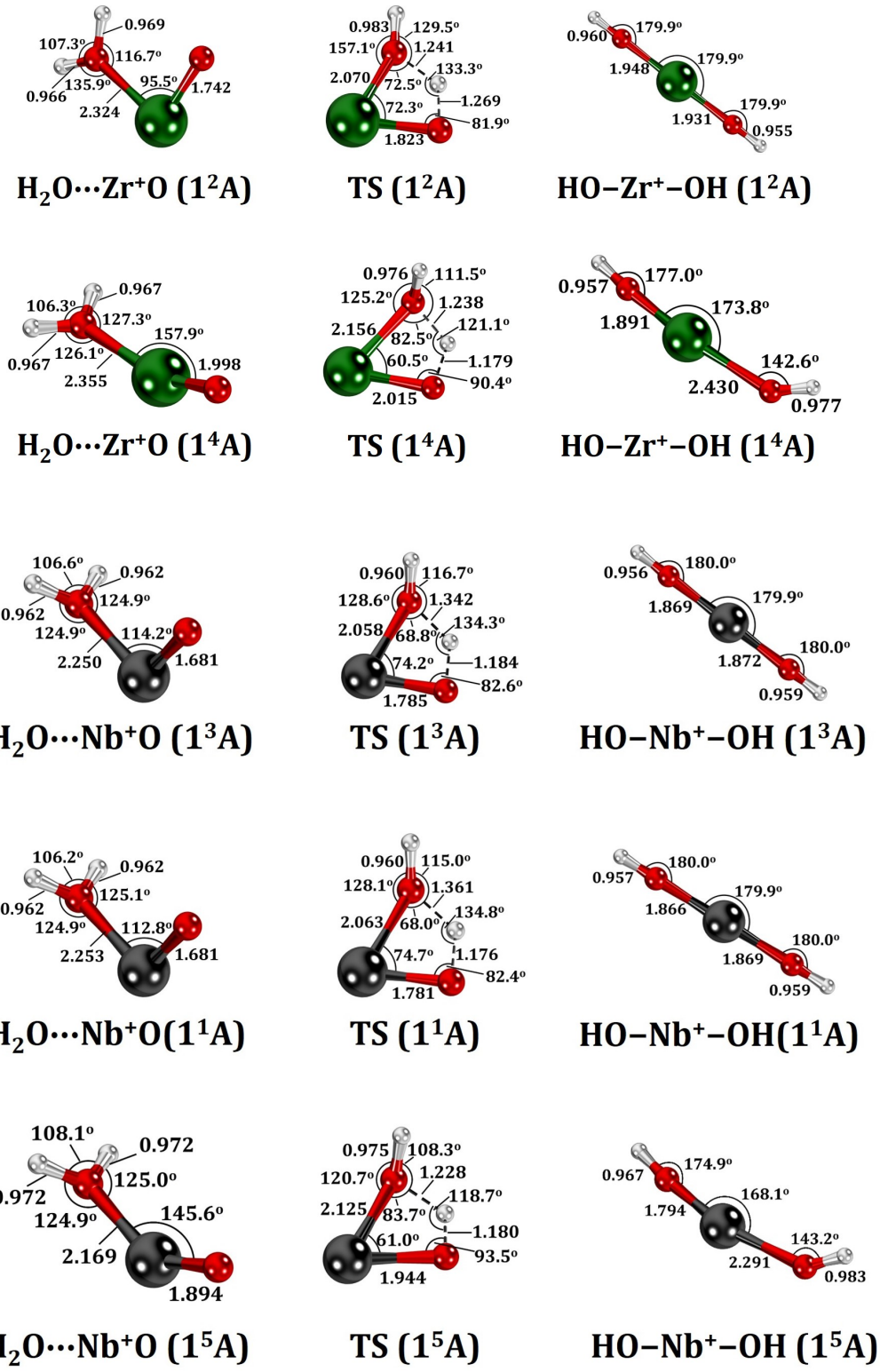

Figure 5.4: Equilibrium structures for the ground and excited states for the $ZrO^+ + H_2O$ and $NbO^+ + H_2O$ reactions at MRCI level of theory.

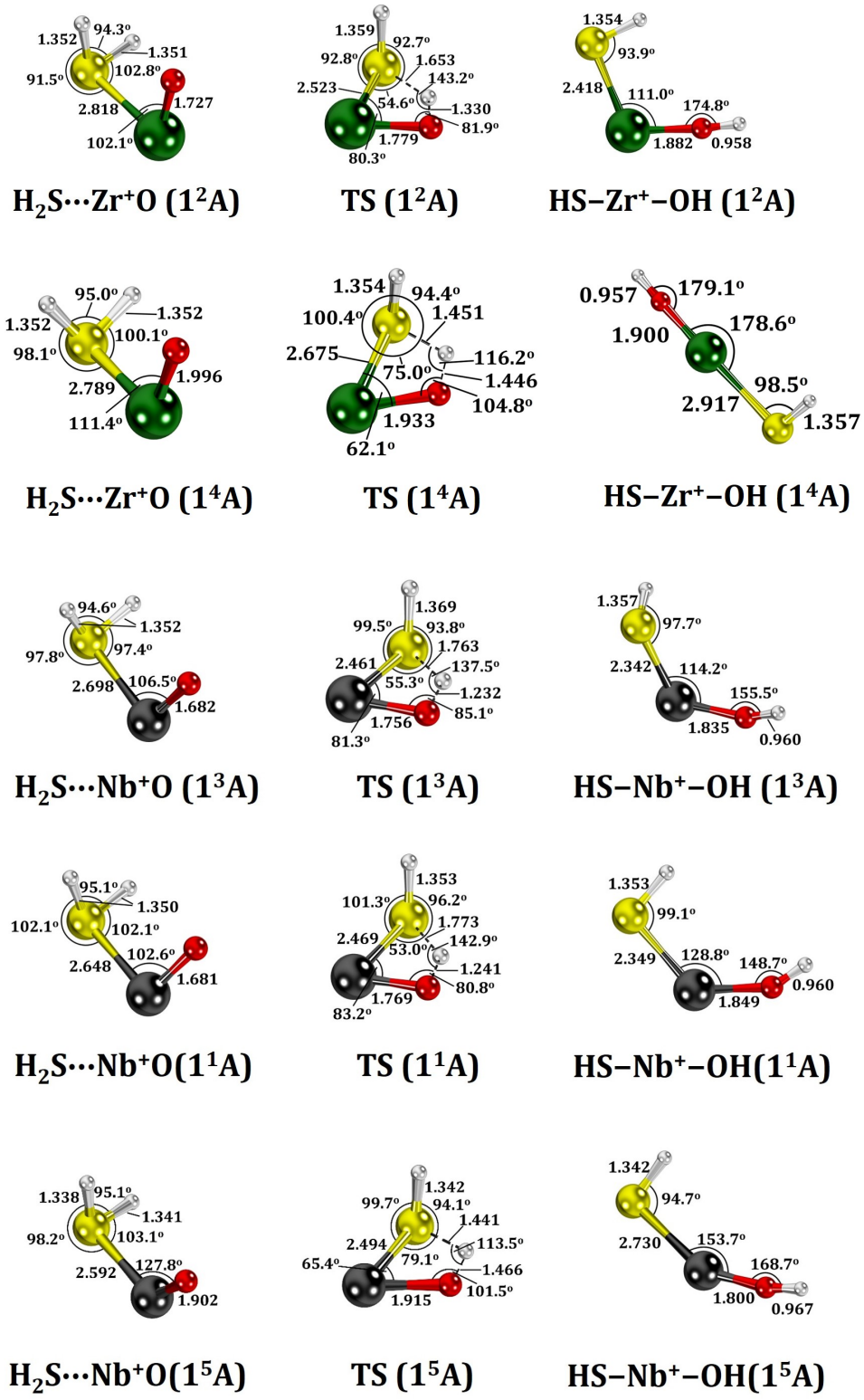

Figure 5.5: Equilibrium structures for the ground and excited states for the ZrO^+ + H_2S and NbO^+ + H_2S reactions at MRCI level of theory.

In all instances formation of IC is exothermic with respect to their reactants. Specifically, in $ZrO^+ + H_2O$, $ZrO^+ + H_2S$, $NbO^+ + H_2O$, and $NbO^+ + H_2S$ cases, the formation of IC ground state is exothermic by 40.7, 35.8, 40.5, and 35.3 kcal/mol, respectively. The TS barriers of the lowest energy pathways of $ZrO^+ + H_2O$ and $ZrO^+ + H_2S$ reactions are lower in energy compared to the infinitely separated reactants, hence expected to reach products exothermically. These TS barriers are higher in energy than the reactants of $NbO^+ + H_2O$ and $NbO^+ + H_2S$ cases (by ~5 kcal/mol). The $[HS{-}Zr{-}OH]^+$ product formation is more favorable compared to the formation of $[HO{-}Zr{-}OH]^+$. This is opposite for the NbO^+ case, where $[HO{-}Nb{-}OH]^+$ is more stable than $[HS{-}Nb{-}OH]^+$. For high−spin ZrO^+ ($^4\mathbf{\Pi}$) and NbO^+ ($^5\mathbf{\Sigma}^-$) cases transition state barriers of the $MO^+ + H_2X \rightarrow [HX{-}M{-}OH]^+$ reactions are significantly smaller. Is it possible for us to exploit these excited high−spin states of MO^+ with oxyl character to design molecular complexes that activate H_2O or H_2S efficiently?

To answer this question as a first step we re−optimized lowest energy state of each spin of R, IC, P, and TS of $MO^+ + H_2X \rightarrow [HX{-}M{-}OH]^+$ (M = Zr, Nb and X = O, S) reactions at DFT/MN15 level. For these spin states DFT/MN15 and MRCI+Q show similar qualitative features in the energy landscape (compare Figure 5.6 and Figure 5.3). Hence, we can use DFT/MN15 to study energy landscapes of bigger single−reference complexes made up of ZrO^+ and NbO^+. Going one step further, we investigated $MO^+ + CH_4$ reactions at DFT/MN15 level (Figure 5.6).

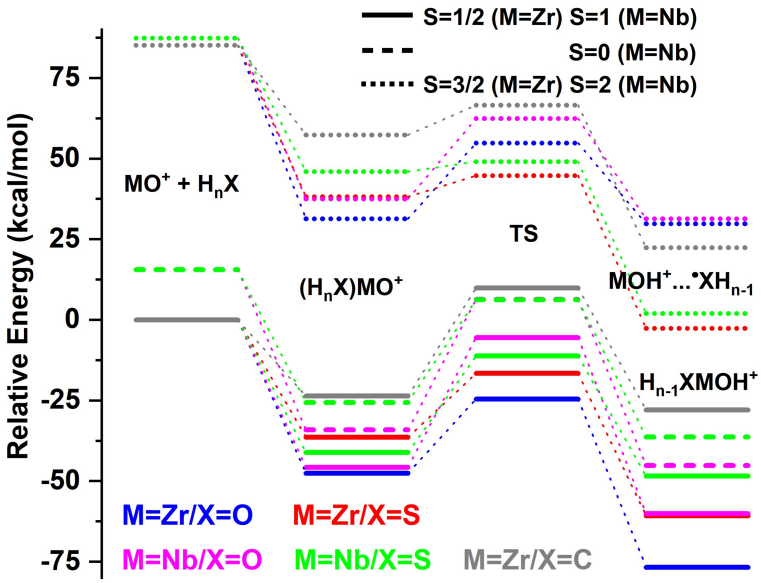

Figure 5.6: DFT/MN15 energy landscape of MO^+ + $H_2O/H_2S/CH_4$ reactions (M = Zr, Nb).

Attachment of two X (≡ H, F, Cl, CH_3) to the $ZrO^+(^4\Pi)$ produces X_2ZrO^+ with doublet spin. Such two systems (e.g. H_3ZrO and F_3ZrO) has been tested for methane to methanol conversion in the past and a much favorable energy pathway has been observed in the case of F_3ZrO.[124] In this work we coupled $ZrO^+(^4\Pi)$ with two Cl atoms to test the energy pathway. The IC, TS, and P of the Cl_2ZrO^+ + H_2S reaction is slightly destabilized compared to the corresponding species of $ZrO^+(^4\Pi)$ + H_2S reaction (see Figure 5.7). It is interesting to notice that the TS barriers of H_2S activation become less than 6.5 kcal/mol once Cl_2ZrO^+ is ligated with ammonia. Likewise, we can use $(NH_3)_nCl_2ZrO^+$ (n = 1–3) complexes for efficient H_2O activation. Employing the same approach, we designed Nb based molecular catalysts for H_2O and H_2S activation. For that we coupled $^5\Sigma^-$ oxyl state of NbO^+ with three Cl atoms to create a doublet spin ground state for the Cl_3NbO^+. Again, by ammonia ligation we can design more practical $(NH_3)_nCl_3NbO^+$ (n = 1–2) for H_2O and H_2S activation.

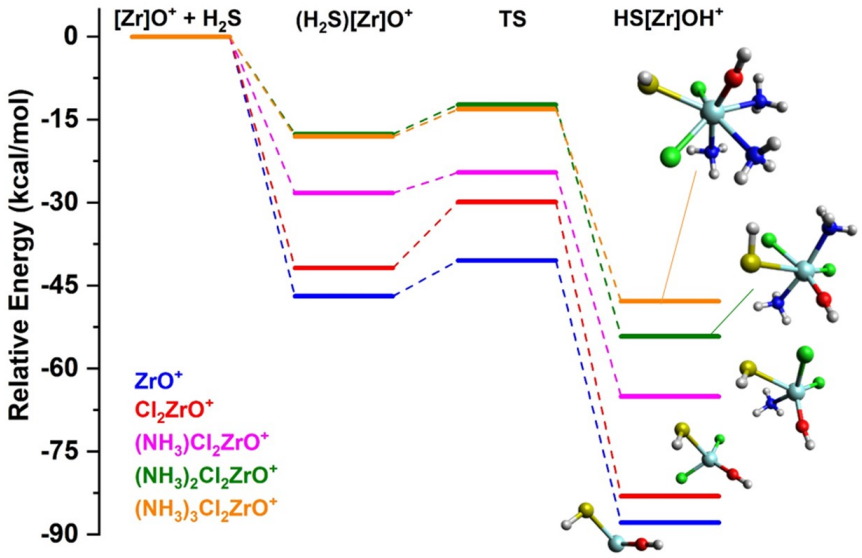

Figure 5.7: DFT/MN15 energy landscape of $(NH_3)_mCl_nZrO^+$ + H_2S reactions for (m,n = 0,0; 0,2; 1,2; 2,2; 3,2). For m,n = 0,0 case quartet spin is shown.

5.2 Ground and excited states of $MoO^{+,2+,-}$ and their water activation strengths

In this section most important findings reported in following paper[125] given in Appendix D are summarized. Reprints were made with permission from Royal Society of Chemistry.

Ariyarathna, I. R.; Miliordos, E. *Phys. Chem. Chem. Phys.* **2018**, *20*, 12278–12287.

5.2.1 MoO^+

The $^4\Sigma^-$ ground state of MoO^+ has ~110 kcal/mol D_e with respect to $Mo^+(^6S)$ + $O(^3P)$ ground state fragments. It is followed by the $^2\Delta$ and $^4\Pi$ electronic states, respectively. Both $^4\Sigma^-$ and $^4\Pi$ smoothly dissociate to $Mo^+(^6S)$ + $O(^3P)$ fragments while, the $^2\Delta$ originate from either $Mo^+(^4G)$ + $O(^3P)$ or $Mo^+(^4P)$ + $O(^3P)$. The origin of $^2\Delta$ is inconclusive since $Mo^+(^4G)$ + $O(^3P)$ or $Mo^+(^4P)$ + $O(^3P)$ asymptotes are very close in energy. Proposed vbL diagrams for $^4\Sigma^-$, $^2\Delta$, and $^4\Pi$ states, based on their dominant electronic configurations at equilibrium geometries are shown in Figure 5.8). Equilibrium structures of $^4\Sigma^-$, $^2\Delta$, and

$^4\Pi$ have $Mo^{2+}O^-$ skeleton. Both $^4\Sigma^-$ and $^2\Delta$ have triple bonds with 1.64 and 1.62 Å bond lengths, respectively. Compared to the first two states $^4\Pi$ bears a slightly longer bond length (1.69 Å) caused by its double bond nature. These three electronic states lie well separated from series of congested excited states. Fifteen more excited states of MoO^+ were analyzed at MRCI and MRCI+Q levels. In overall the order of the electronic states of MoO^+ is $X^4\Sigma^-$, $a^2\Delta$, $A^4\Pi$, $1^2\Gamma$, $2^2\Sigma^-$, $1^2\Pi$, $1^2\Sigma^+$, 1^2H, $1^2\Phi$, $2^2\Pi$, $1^4\Phi$, $2^4\Pi$, $1^4\Delta$, $1^6\Sigma^-$, $1^6\Pi$, $1^4\Sigma^+$, $3^2\Pi$, and $4^2\Pi$.

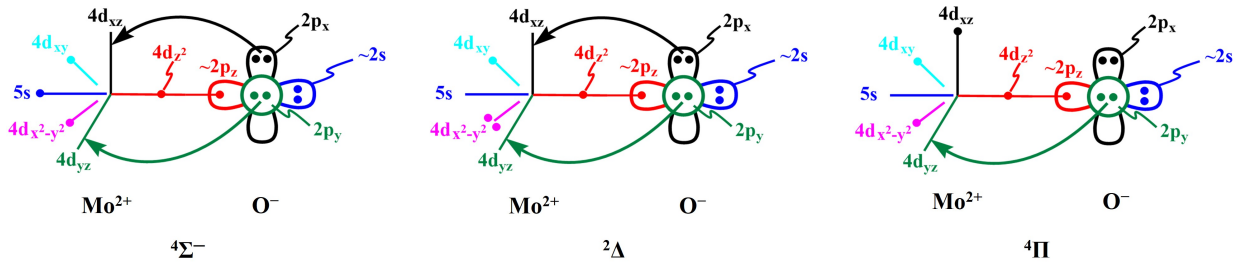

Figure 5.8: vbL diagrams of three lowest energy electronic states of MoO^+. Only one component of $^2\Delta$ and $^4\Pi$ states are depicted. The other component of $^2\Delta$ and $^4\Pi$ have have $(4d_{xy})^2(4d_{x^2-y^2})^1$ and $(4d_{xz})^0(4d_{yz})^1$ configurations, respectively.

5.2.2 MoO^{2+}

Similar to MoO^+ the lowest three electronic states of MoO^{2+} settle well separated from others. The $^3\Sigma^-$ ground state of MoO^{2+} originate from $Mo^{2+}(^5D)$ + $O(^3P)$ asymptote. It is important to note that the $Mo^+(^6S)$ + $O^+(^4S)$ fragments are more stable compared to $Mo^{2+}(^5D)$ + $O(^3P)$, but only produce repulsive potential energy curves due to the electrostatic repulsion between Mo^+ and O^+. The first and second excited states of MoO^{2+} are $^1\Gamma$ and $^1\Sigma^+$, respectively. The proposed vbL diagrams of these three states are given in Figure 5.9. Notice that both $^1\Gamma$ and $^1\Sigma^+$ have the same electronic configuration, but with different components. Specifically, the configurations of $^1\Gamma$ and $^1\Sigma^+$ are $0.67(1\sigma^2 1\pi_x{}^2 1\pi_y{}^2 \delta_{xy}{}^2)$ – $0.67(1\sigma^2 1\pi_x{}^2 1\pi_y{}^2 \delta_{x^2-y^2}{}^2)$ and $0.67(1\sigma^2 1\pi_x{}^2 1\pi_y{}^2 \delta_{xy}{}^2)$ + $0.67(1\sigma^2 1\pi_x{}^2 1\pi_y{}^2 \delta_{x^2-y^2}{}^2)$, respectively. All three electronic states have triple bonded $Mo^{2+}O$ electronic structures with ~1.60 Å bond distance. The observed order of the first fourteen electronic states of MoO^{2+} are $X^3\Sigma^-$, $a^1\Gamma$, $a^1\Sigma^+$, $1^3\Phi$, $1^3\Pi$, $1^3\Delta$, $1^1\Pi$, $1^5\Sigma^-$, $1^1\Phi$, $1^1\Delta$, $1^5\Delta$, $1^7\Sigma^-$, $2^3\Sigma^-$, and $1^5\Sigma^+$.

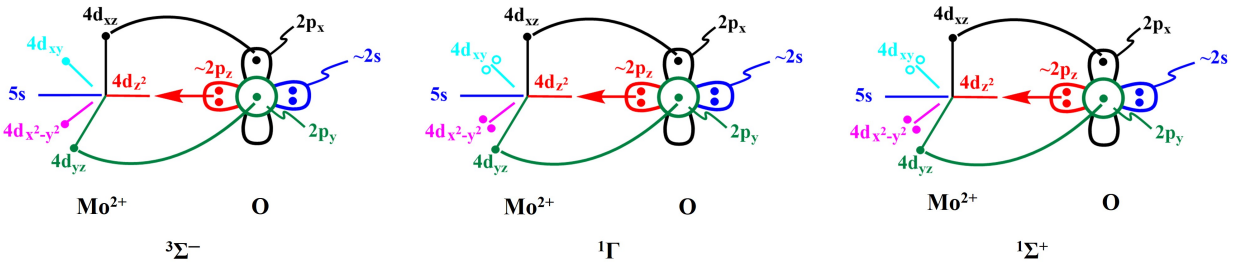

Figure 5.9: vbL diagrams of three lowest energy electronic states of MoO^{2+}. The $(4d_{xy})^2$ ± $(4d_{x^2-y^2})^2$ combinations of $^1\Gamma$ and $^1\Sigma^+$ states are represented by electron pairs with solid and open circles.

5.2.3 MoO^-

Five electronic states of MoO^- are stable compared to the $X^5\Pi$ ground state of MoO. According to the CCSD(T) calculations they are $X^4\Pi$, $1^2\Delta$, $1^6\Sigma^+$, $1^4\Sigma^-$, and $1^6\Pi$ in energy order. For multi−reference calculations we used two different active spaces at reference CASSCF level; (1) 11 electrons in 9 active orbitals ($2p_{/O}$, $5s_{/Mo}$, $4d_{/Mo}$) (2) 11 electrons in 12 active orbitals ($2p_{/O}$, $5s_{/Mo}$, $4d_{/Mo}$, $5p_{/Mo}$). Note that the number of orbitals in (1) is the same as the number of orbitals in MoO^+ and MoO^{2+}. At active space (1) the ground and first excited state of MoO^- are $^6\Sigma^+$ and $^4\Pi$, respectively, which disagree with CCSD(T). However, the bigger (2) active space provides identical order of states as CCSD(T). We further calculated EA of MoO using the aforementioned two active spaces. Calculated MRCI/MRCI+Q EA of MoO under (1) and (2) active spaces are 0.05/−0.01 and 0.87/1.07 eV, respectively. The EA under CCSD(T) (1.20 eV) agrees very well with the experimental value reported by Gunion et al (1.290 ± 0.006 eV).[126] In overall $(2)^{nd}$ active space provides much better results compared to the small $(1)^{st}$ active space. Because of this reason electronic structures and energetics of ground and excited states of MoO^- were studied using bigger $(2)^{nd}$ active space.

Both $Mo(^7S)$ + $O^-(^2P)$ and $Mo^-(^6S)$ + $O(^3P)$ are stable compared to the $Mo(^7S)$ + $O(^3P)$ fragments. The $Mo^-(^6S)$ + $O(^3P)$ gives birth to the $X^4\Pi$ and $1^4\Sigma^-$ states of MoO^-. The $1^6\Sigma^+$ and $1^6\Pi$ come from $Mo(^7S)$ + $O^-(^2P)$. The $Mo^-(^4G)$ + $O(^3P)$ combination is higher in energy than $Mo(^7S)$ + $O(^3P)$ and produces the $1^2\Delta$ state of MoO^-. The $1^2\Delta$ and

$1^6\Sigma^+$ and $1^4\Sigma^-$ and $1^6\Pi$ are very close in energy. According to MRCI, the ground state of MoO^- is the $^6\Sigma^+$ following $^2\Delta$ and $^4\Pi$ states, but MRCI+Q reorders them as does CCSD(T). Proposed vbL diagrams for the first three electronic states of MoO^- are depicted in Figure 5.10.

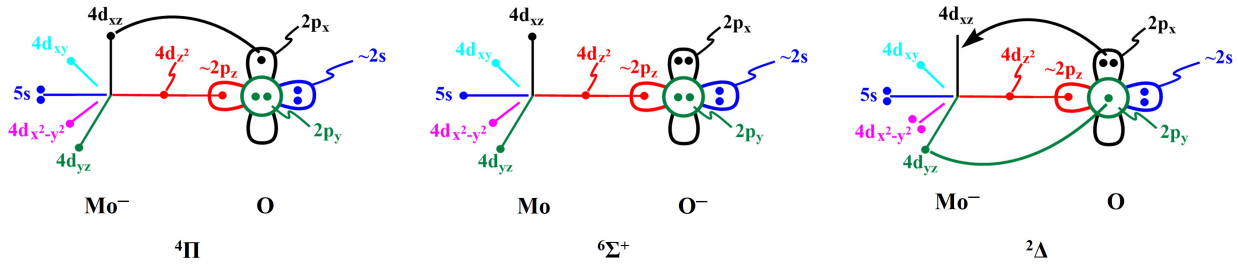

Figure 5.10: vbL diagrams of three lowest energy electronic states of MoO^-. Only one component of $^4\Pi$ and $^2\Delta$ states are depicted. The other component of $^4\Pi$ and $^2\Delta$ have $2p_x{}^2 2p_y{}^1$ and $(4d_{x^2-y^2})^1(4d_{xy})^2$ configurations, respectively.

5.2.4 Water activation from $MoO^{2+,+,-}$

$MoO^{2+,+,-} + H_2O \rightarrow Mo(OH)_2{}^{2+,+,-}$ reactions were investigated for several low–lying electronic states of $MoO^{2+,+,-}$. Both MoO^{2+} and MoO^+ react with H_2O similar to the MO^+ (M = Zr or Nb). Specifically, electronegative oxygen end of H_2O binds to the $MoO^{2+,+}$ to create $H_2O\cdots MoO^{2+,+}$ IC that undergoes H–O bond cleavage to produce $[HO–Mo–OH]^{2+,+}$. The lowest energy IC, TS, P structures of $MoO^+\cdots H_2O$ reaction are illustrated in Figure 5.11. Their excited states have approximately similar structures. Structures of ground and excited IC, TS, P of $MoO^{2+}\cdots H_2O$ reaction also have geometries similar to those of $MoO^+\cdots H_2O$ reaction.

MoO^- reacts with H_2O in a different fashion. One H atom of H_2O interacts with oxygen of MoO^- to produce the $MoO^-\cdots H–OH$ IC (see Figure 5.11). But, the transition state of this reaction has a similar structure as $MoO^{2+,+}$ cases.

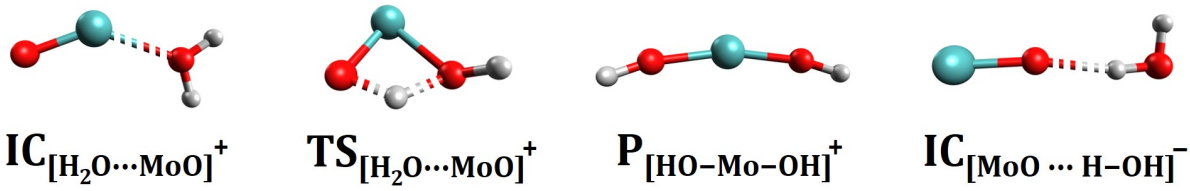

Figure 5.11: Lowest energy IC, TS, P structures of $MoO^{+}\cdots H_2O$ reaction and ground state IC produce from MoO^{-} + H_2O reaction.

Each of the lowest energy R, IC, TS, and P of $MoO^{+}\cdots H_2O$ reaction are quartets. They are triplets for the MoO^{2+} + H_2O reaction. Interestingly the MoO^{-} + H_2O reaction proceeds via a spin crossover. Specifically, the R, I, and P of the reaction are quartets, but the lowest energy TS is a sextet. The ICs of $MoO^{-}\cdots H_2O$ reaction is slightly stabilized compared to the MoO^{+} and MoO^{2+} cases. Explicitly, the lowest energy ICs of $MoO^{-}\cdots H_2O$, $MoO^{+}\cdots H_2O$, and $MoO^{2+}\cdots H_2O$ have approximately 15, 45, and 130 kcal/mol D_es with respect to ground state fragments, respectively (see Figure 5.12). They have to surpass ~90, 45, 15 kcal/mol TS barriers to reach products, respectively. The $[HO–Mo–OH]^{+}$ product is more stable compared to $[HO–Mo–OH]^{-}$ but less stable than $[HO–Mo–OH]^{2+}$. Overall, the anionic system is the best candidate for water activation since it has a lower activation energy barrier and produces a more stabilized P than IC.

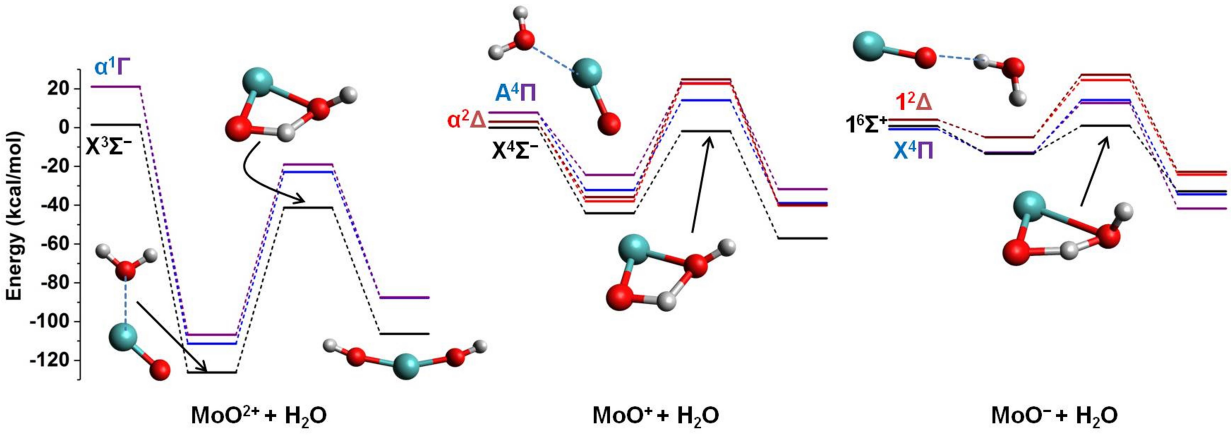

Figure 5.12: MRCI+Q energy landscape for the $MoO^{2+,+,-}$ + $H_2O \rightarrow Mo(OH)_2^{2+,+,-}$ reactions.

5.3 Ground and excited states of $RuO^{+,0,-}$ and their water activation strengths

In this section most important findings reported in following paper[127] given in Appendix D are summarized. Reprints were made with permission from Royal Society of Chemistry.

Ariyarathna, I. R.; Almeida, N. M. S.; Miliordos, E. *Phys. Chem. Chem. Phys.* **2020**, *22*, 16072–16079.

5.3.1 RuO^+

Potential energy curves belonging to the lowest sixteen electronic states of RuO^+ dissociates into $Ru^+(^4F)$ + $O(^3P)$ fragments. Those states of RuO^+ are $X^2\Pi$, $1^4\Delta$, $1^6\Sigma^+$, $1^4\Phi$, $1^4\Pi$, $1^2\Sigma^+$, $1^2\Gamma$, $1^2\Delta$, $1^2\Sigma^-$, $2^2\Sigma^+$, $1^2\Phi$, $2^2\Pi$, $1^4\Sigma^+$, $2^2\Delta$, $2^4\Delta$, and $1^6\Phi$ in energy order. The $X^2\Pi$ and $1^4\Delta$ states lie very close in energy. They are separated by less than 2 kcal/mol under all levels of theory. According to MRCI, MRCI+Q, C−MRCI, C−MRCI+Q, and C−CCSD(T) levels the ground state of RuO^+ is the $^2\Pi$, but CCSD(T) predicted $^4\Delta$ to be more stable compared to $^2\Pi$. Similarly, $1^6\Sigma^+$, $1^4\Phi$, $1^4\Pi$ states are nearly degenerate separating only within 1.5 kcal/mol. According to generalized valence bond (GVBCI) level of theory a different order of states ($^4\Delta$, $^2\Gamma$, $^2\Delta$, $^2\Sigma^+$, $^2\Sigma^-$, $^2\Delta$) has been predicted for RuO^+ in 1988 by Carter and Goddard.[128]

Equilibrium structures of all $X^2\Pi$, $1^4\Delta$, $1^6\Sigma^+$, $1^4\Phi$, $1^4\Pi$ states have $Ru^{2+}O^-$ ionic skeleton. Their dominant electronic configurations at equilibrium geometries are listed in the Table 5.1. Proposed vbL diagrams for these states are shown in Figure 5.13. Selected set of valence molecular orbitals of RuO^+ are also included to the Figure 5.13. $X^2\Pi$ has a double bond with one electron in π^*_{RuO}. Both $1^4\Delta$ and $1^6\Sigma^+$ have single bonds and two π^* electrons. Hence bond lengths of $1^4\Delta$ and $1^6\Sigma^+$ are expected to be longer compared to the $X^2\Pi$ state. Indeed, this is true, where the CCSD(T) bond lengths of $X^2\Pi$, $1^4\Delta$, and $1^6\Sigma^+$ are 1.609, 1.665, and 1.741 Å, respectively.

Table 5.1: Dominant electronic configurations for the first five electronic states of RuO^+.

State	Coef.	2σ	3σ	$1\pi_x$	$2\pi_x$	$1\pi_y$	$2\pi_y$	$1\delta_{x^2-y^2}$	$1\delta_{xy}$
$X^2\Pi$	0.89	2	0	2	α	2	0	2	2
$1^4\Delta$	0.95	2	0	2	α	2	α	2	α
$1^6\Sigma^+$	0.94	2	α	2	α	2	α	α	α
$1^4\Phi$	0.66	2	α	2	0	2	α	2	α
	−0.66	2	α	2	α	2	0	α	2
$1^4\Pi$	0.66	2	α	2	0	2	α	2	α
	0.66	2	α	2	α	2	0	α	2

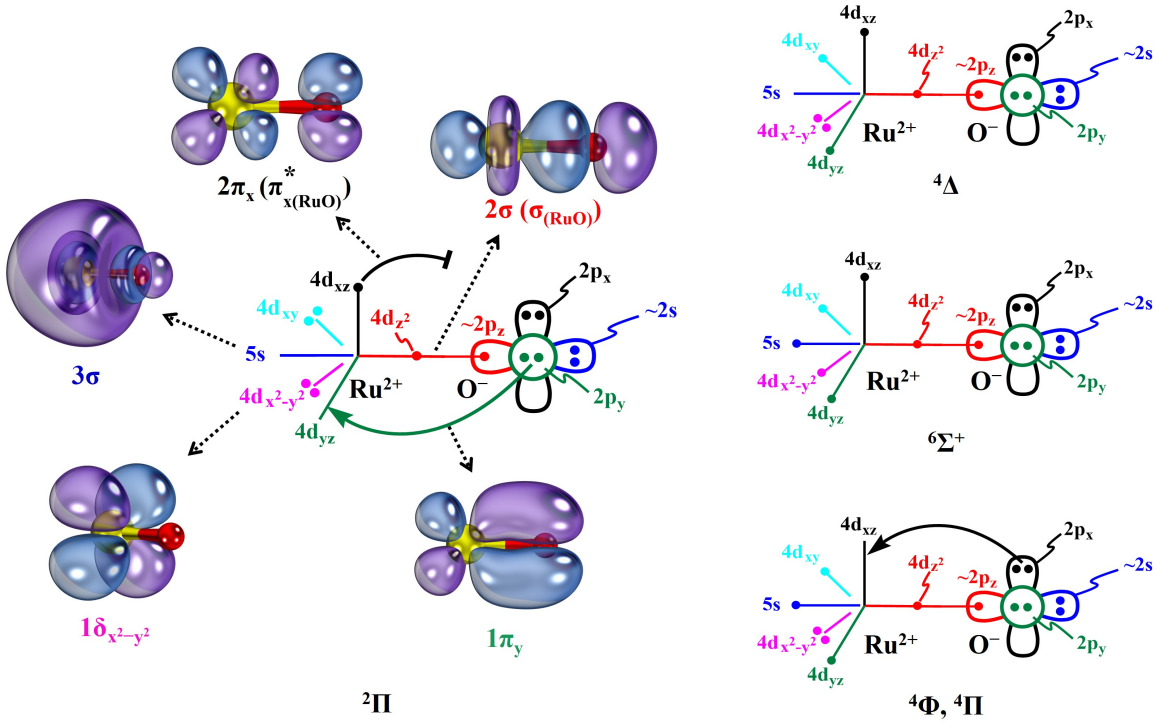

Figure 5.13: vbL diagrams for five lowest energy electronic states of RuO^+. Set of selected valence molecular orbitals of RuO^+ are shown with the $X^2\Pi$ diagram. Only one component of $X^2\Pi$ and $1^4\Delta$ states are depicted. Only one configuration of each $1^4\Phi$ and $1^4\Pi$ is shown. The other one has $(4d_{x^2-y^2})^1(4d_{xy})^2 + (4d_{xz})^1(4d_{yz})^0$ configuration.

5.3.2 RuO

The $X^5\Delta$ ground state of RuO has ~115 kcal/mol D_e with respect to Ru(^{5}F) + O(^{3}P) fragments. Its first two excited states, $1^3\Pi$ and $1^3\Delta$, are ~14 and 23 kcal/mol (at MRCI) high in energy than $X^5\Delta$, respectively. Next eleven electronic states of RuO stack very closely within 10.5 kcal/mol. Overall the order of the states at MRCI level of theory is $X^5\Delta$, $1^3\Pi$, $1^3\Delta$, $1^1\Sigma^+$, $1^1\Pi$, $1^3\Gamma$, $1^3\Phi$, $1^5\Sigma^+$, $1^3\Sigma^-$, $2^3\Pi$, $2^3\Sigma^-$, $1^3\Sigma^+$, $2^3\Delta$, and $1^1\Delta$. In 1985 Krauss and Stevens studied RuO and found $^5\Delta$, $^3\Pi$, $^3\Delta$, $^3\Sigma^-$, $^3\Phi$, $^7\Sigma^+$, $^5\Sigma^+$, $^3\Sigma^+$, $^5\Pi$, $^5\Phi$ pattern of states.[129] Our calculations located extra $^1\Sigma^+$, $^1\Pi$, $^3\Gamma$, $^3\Pi$, $^3\Sigma^-$, $^3\Delta$, $^1\Delta$ states within 0–11,500 cm^{-1}. The $^7\Sigma^+$, $^5\Pi$, $^5\Phi$ states rest beyond 11,500 cm^{-1}.

Dominant electronic configurations of the first four electronic states of RuO are given in the Table 5.2. Their proposed vbL diagrams are depicted in the Figure 5.14. The $X^5\Delta$ has a single bond and two electrons in antibonding orbitals. The CCSD(T) bond length of $X^5\Delta$ state is 1.707 Å. Since $1^3\Pi$ and $1^1\Sigma^+$ respectively have double and triple bonds, their bonds are expected to be shorter than $X^5\Delta$. As predicted, they are shorter with 1.650 ($1^3\Pi$) and 1.628 Å ($1^1\Sigma^+$) bonds at CCSD(T) level.

Table 5.2: Dominant electronic configurations for the first five electronic states of RuO.

State	Coef.	2σ	3σ	$1\pi_x$	$2\pi_x$	$1\pi_y$	$2\pi_y$	$1\delta_{x^2-y^2}$	$1\delta_{xy}$
$X^5\Delta$	0.95	2	α	2	α	2	α	2	α
$1^3\Pi$	0.80	2	α	2	α	2	0	2	2
$1^3\Delta$	0.79	2	β	2	α	2	α	2	α
	−0.41	2	α	2	β	2	α	2	α
	−0.41	2	α	2	α	2	β	2	α
$1^1\Sigma^+$	0.92	2	2	2	0	2	0	2	2

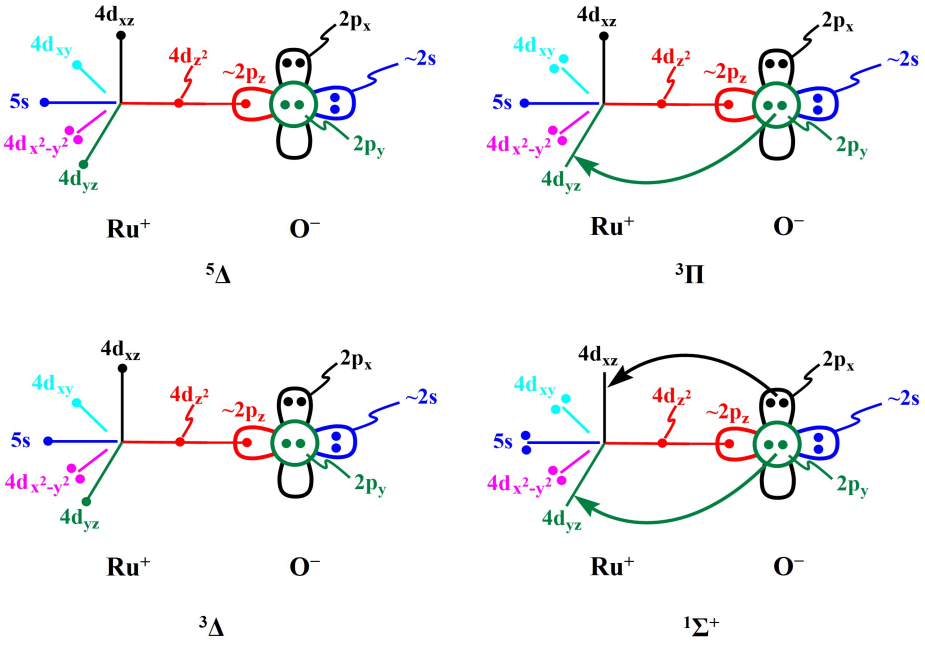

Figure 5.14: vbL diagrams for the four lowest energy electronic states of RuO. Only one component of $^5\Delta$, $^3\Pi$, $^3\Delta$ states are depicted.

5.3.3 RuO^-

To study ground and excited states of RuO^- three additional orbitals were used in the CASSCF active space similar to the MoO^- case. RuO^- has only two stable states with respect to RuO. They are $^4\Delta$ (ground state) and the $^2\Pi$ (excited state). These two states can be produced by placing an electron in the half filed $3\sigma_{RuO}$ ($\sim 5s_{Ru}$) orbital of $^5\Delta$ and $^3\Pi$ states of RuO. Compared to the $^5\Delta$ and $^3\Pi$ states of RuO, the bond lengths of $^4\Delta$ and $^2\Pi$ of RuO^- are 0.01–0.02 Å longer.

5.3.4 Water activation from $RuO^{2+,+,0,-}$

Water activation strengths of $MoO^{2+,+,-}$ increase in the order of MoO^{2+} < MoO^+ < MoO^-. A similar study was conducted to analyze and compare water activation strengths of ground and excited states of $RuO^{2+,+,0,-}$. $RuO^{2+,+,0}$ react with water similar to $MoO^{2+,+}$. IC, TS, and P of $RuO^{2+,+,0}$ + H_2O → $Ru(OH)_2{}^{2+,+,-}$ reaction have similar structures to those of $MoO^{2+,+}$ + H_2O → $Mo(OH)_2{}^{2+,+}$ reaction (see Figure 5.11). The IC of RuO^- +

H_2O reaction has a H−atom pointing towards the oxygen of RuO^- similar to the reaction of MoO^- with H_2O (see IC of MoO^- + H_2O reaction in Figure 5.11).

The $X^1\Sigma^+$ ground state of RuO^{2+} reacts with a water molecule to produce a singlet spin ground state for IC and P. Interestingly, the lowest energy TS that connects IC and P is a quintet. With respect to $RuO^{2+}(X^1\Sigma^+)$ + H_2O fragments the lowest energy IC, TS, and P are ~82/85, 11/24, 46/61 kcal/mol stable at MRCI+Q/CCSD(T) levels.[130] By dressing the RuO^{2+} with an ammonia ligand a triplet spin IC and a P can be stabilized over the singlet ones. The singlet and triplet IC are almost degenerate, but the triplet P is ~15 kcal/mol more stable than singlet P. The lowest energy IC, TS, P are ~69/71, 1/14, 37/49 kcal/mol stable with respect to $(NH_3)RuO^{2+}$ + H_2O ground state fragments. The IC, TS, P of $(NH_3)RuO^{2+}$ + H_2O reaction are destabilized compared to the reaction of naked RuO^{2+}. Overall, the IC destabilizes, TS barrier subsides, and P stabilizes in the RuO^{2+}, RuO^+, RuO, RuO^- order. Same pattern was observed for MoO^{2+}, MoO^+, MoO^-.

5.4 Conclusions

Selection of the correct CASSCF active space is crucial to obtain accurate results of ZrO^+. State average calculations with larger number of electronic states with *CAS(7,9)* active CASSCF active space can provide satisfactory results for ZrO^+ (active orbitals are $2p_{/O}$, $5s_{/Zr}$, $4d_{/Zr}$). But, state specific calculations put $3p_{x/O}$ and $3p_{y/O}$ orbitals instead $4d_{xz/Zr}$ and $4d_{yz/Zr}$ in the active space, hence application of bigger *CAS(7,12)* space is critically important for accurate results of ZrO^+. First three electronic states of ZrO^+ ($X^2\Delta$, $1^2\Sigma^+$, $1^2\Pi$) have $Zr^{3+}O^{2-}$ oxo nature. Its next ten electronic states ($1^2\Phi$, $2^2\Pi$, $1^4\Pi$, $1^4\Phi$, $3^2\Pi$, $2^4\Pi$, $4^2\Pi$, $1^4\Delta$, $2^2\Delta$, $2^4\Delta$) show $Zr^{2+}O^{\bullet-}$ oxyl character. These oxyl electronic states of ZrO^+ bear 0.2–0.3 Å longer bonds compared to its three more stable oxo states. Application of a bigger active space is not necessary for NbO^+. Its low−lying electronic states show $M^{3+}O^{2-}$ oxo character. The first five electronic states of NbO^+ are $X^3\Sigma^-$, $1^1\Gamma$, $1^1\Sigma^+$, $1^3\Delta$, and $1^1\Delta$ in the energy order with triple bonded character.

The first three electronic states of MoO^+ ($X^4\Sigma^-$, $a^2\Delta$, $A^4\Pi$) bear $Mo^{2+}O^-$ skeleton. The $X^4\Sigma^-$ and $a^2\Delta$ states of MoO^+ have triple bonds while $A^4\Pi$ has double bonds. First three states of MoO^{2+} ($X^3\Sigma^-$, $a^1\Gamma$, $a^1\Sigma^+$) bear triple bonds with $Mo^{2+}O$ electronic structures.

Unlike MoO^+ and MoO^{2+} three more additional orbitals are necessary to represent ground and excited states of MoO^- accurately. Specifically, the active space of MoO^- should consist of $2p_{/O}$, $5s_{/Mo}$, $4d_{/Mo}$, and $5p_{/Mo}$ orbitals. Calculated MRCI+Q EA of MoO^- at this active space is 1.07 eV which is closer to the CCSD(T) (= 1.20 eV) and experimental literature value (= 1.290 ± 0.006 eV). MoO^- has five stable electronic states ($X^4\Pi$, $1^2\Delta$, $1^6\Sigma^+$, $1^4\Sigma^-$, and $1^6\Pi$) with respect to MoO + e^- dissociation.

First five electronic states of RuO^+ are $X^2\Pi$, $1^4\Delta$, $1^6\Sigma^+$, $1^4\Phi$, $1^4\Pi$ with $Ru^{2+}O^-$ skeleton. The first five states of RuO are $X^5\Delta$, $1^3\Pi$, $1^3\Delta$, $1^1\Sigma^+$, $1^1\Pi$. The same number of active orbitals as MoO^- are necessary to represent RuO^-. RuO^- has only two bound states ($^4\Delta$ and $^2\Pi$) compared to the RuO + e^-. Two electronic states of RuO^- can be created by including an electron in the $5s_{Ru}$ orbital of $^5\Delta$ and $^3\Pi$ states of RuO.

H_2O and H_2S activation by a transition metal monoxide can be divided into three main processes: (1) Generate of the $[H_2X\cdots MO]$ intermediate, (2) Overcome the transition state energy hump that weaken a H−X bond of H_2X, (3) Produce [HX−M−OH]. Potential energy landscapes were created to test H_2O and H_2S activation barriers of several low−lying electronic states of ZrO^+ and NbO^+. The lowest energy reaction pathways from reactants to product are endothermic for $NbO^+ + H_2X$ (X = O, S) but exothermic for $ZrO^+ + H_2X$ (X = O, S). Products of the latter reactions are much more stabilized compared to the former ones. Interestingly, transition state barriers of $MO^+ + H_2X$ reactions are significantly smaller for high−spin oxyl $ZrO^+(^4\Pi)$ and $NbO^+(^5\Sigma^-)$. These high−spin oxyl states can be exploited to design molecular complexes for efficient H_2O or H_2S splitting. Specifically, by coupling two radical electrons for $ZrO^+(^4\Pi)$ by two Cl atoms or pairing three unpaired electrons of $NbO^+(^5\Sigma^-)$ by three Cl atoms we can produce doublet ground states for Cl_2ZrO^+ and Cl_3NbO^+ species. Ligation of these species with ammonia provides more realistic complexes for efficient H_2O or H_2S activation.

Multi−reference potential energy landscapes were also produced to compare water activation strengths of low−lying electronic states of $MoO^{2+,+,-}$ and $RuO^{0,+,-}$. The H_2O splitting mechanism of each $MoO^{2+,+}$ and $RuO^{0,+}$ is similar to ZrO^+ or NbO^+. Interestingly, the interacting complex of each MoO^- and RuO^- has $MO^-\cdots$H−OH form where others favor $H_2O\ldots MO$ mode. Transition state barriers are significantly smaller for anionic monoxides compared to others. Overall, the water activation strengths of MoO and RuO species vary

in the $MO^{2+} < MO^{+} < MO < MO^{-}$ order, suggesting that anionic metal oxides are better systems to facilitate the activation of chemical bonds.

Bibliography

(1) Lewars, E. G., *Computational Chemistry*, 3rd ed.; Springer International Publishing: Cham, 2016.

(2) Schrödinger, E *Phys. Rev.* **1926**, *28*, 1049–1070.

(3) Szalay, P. G.; Müller, T.; Gidofalvi, G.; Lischka, H.; Shepard, R. *Chem. Rev.* **2012**, *112*, 108–181.

(4) Lischka, H.; Nachtigallová, D.; Aquino, A. J. A.; Szalay, P. G.; Plasser, F.; Machado, F. B. C.; Barbatti, M. *Chem. Rev.* **2018**, *118*, 7293–7361.

(5) In *IUPAC Compend. Chem. Terminol.* IUPAC: Research Triagle Park, NC.

(6) Gupta, V. In *Princ. Appl. Quantum Chem.* Elsevier: 2016, pp 291–337.

(7) Linstrom, P.; Mallard, W. NIST Chemistry WebBook, NIST Standard Reference Database Number 69, National Institute of Standards and Technology, Gaithersburg MD, 20899.

(8) DeRosa, M *Coord. Chem. Rev.* **2002**, *233-234*, 351–371.

(9) Cheng, Y.-C.; Fleming, G. R. *Annu. Rev. Phys. Chem.* **2009**, *60*, 241–262.

(10) Wenderich, K.; Mul, G. *Chem. Rev.* **2016**, *116*, 14587–14619.

(11) Kalemos, A.; Ariyarathna, I. R.; Khan, S. N.; Miliordos, E.; Mavridis, A. *Comput. Theor. Chem.* **2019**, *1153*, 65–74.

(12) In *IUPAC Compend. Chem. Terminol.* Nič, M., Jirát, J., Košata, B., Jenkins, A., McNaught, A., Eds.; IUPAC: Research Triagle Park, NC, 2009.

(13) Kalemos, A. *J. Chem. Phys.* **2017**, *146*, 104307.

(14) Kramida, A.; Ralchenko, Y.; Reader, J.; NIST ASD Team. NIST Atomic Spectra Database (version 5.4), National Institute of Standards and Technology, Gaithersburg, MD 2016.

(15) Miessler, G. L.; Fischer, P. J.; Tarr, D. A., *Inorganic Chemistry*, 5th ed.; Pearson advanced chemistry series; Pearson: 2014.

(16) Cotton, F. A.; Wilkinson, G., *Advanced Inorganic Chemistry*, 4th ed.; John wiley and sons: New York, 1980.

(17) Lupinetti, A. J.; Frenking, G.; Strauss, S. H. *Angew. Chemie Int. Ed.* **1998**, *37*, 2113–2116.

(18) Scuseria, G. E.; Miller, M. D.; Jensen, F.; Geertsen, J. *J. Chem. Phys.* **1991**, *94*, 6660–6663.

(19) Ariyarathna, I. R.; Miliordos, E. *Int. J. Quantum Chem.* **2018**, *118*, e25673.

(20) Ariyarathna, I. R.; Miliordos, E. *J. Comput. Chem.* **2019**, *40*, 1740–1751.

(21) Gallagher, T. F., *Rydberg Atoms*; Cambridge University Press: 1994.

(22) Mulliken, R. S. *J. Am. Chem. Soc.* **1964**, *86*, 3183–3197.

(23) Herbert, J. M.; Coons, M. P. *Annu. Rev. Phys. Chem.* **2017**, *68*, 447–472.

(24) Zurek, E.; Edwards, P. P.; Hoffmann, R. *Angew. Chemie Int. Ed.* **2009**, *48*, 8198–8232.

(25) Thompson, H.; Wasse, J. C.; Skipper, N. T.; Hayama, S.; Bowron, D. T.; Soper, A. K. *J. Am. Chem. Soc.* **2003**, *125*, 2572–2581.

(26) Ariyarathna, I. R.; Pawłowski, F.; Ortiz, J. V.; Miliordos, E. *Phys. Chem. Chem. Phys.* **2018**, *20*, 24186–24191.

(27) Ariyarathna, I. R.; Khan, S. N.; Pawłowski, F.; Ortiz, J. V.; Miliordos, E. *J. Phys. Chem. Lett.* **2018**, *9*, 84–88.

(28) Ariyarathna, I. R.; Almeida, N. M. S.; Miliordos, E. *J. Phys. Chem. A* **2019**, *123*, 6744–6750.

(29) Ariyarathna, I. R.; Miliordos, E. *Phys. Chem. Chem. Phys.* **2019**, *21*, 15861–15870.

(30) Jena, P.; Sun, Q. *Chem. Rev.* **2018**, *118*, 5755–5870.

(31) Sun, W.-M.; Li, Y.; Wu, D.; Li, Z.-R. *Phys. Chem. Chem. Phys.* **2012**, *14*, 16467.

(32) Gutsev, G.; Boldyrev, A. *Chem. Phys. Lett.* **1982**, *92*, 262–266.

(33) Dutton, J. L.; Frenking, G. *Angew. Chemie Int. Ed.* **2016**, *55*, 13380–13382.

(34) Pan, S.; Jana, G.; Saha, R.; Zhao, L.; Chattaraj, P. K. *Phys. Chem. Chem. Phys.* **2020**, DOI: 10.1039/D0CP04912C.

(35) Ariyarathna, I. R.; Miliordos, E. *J. Phys. Chem. A* **2017**, *121*, 7051–7058.

(36) Buchner, M. R. *Chem. A Eur. J.* **2019**, *25*, 12018–12036.

(37) Ariyarathna, I. R.; Miliordos, E. *J. Phys. Chem. A* **2020**, *124*, 9783–9792.

(38) Strupp, C. *Ann. Occup. Hyg.* **2010**, *55*, 43–56.

(39) Zhao, L.; Pan, S.; Holzmann, N.; Schwerdtfeger, P.; Frenking, G. *Chem. Rev.* **2019**, *119*, 8781–8845.

(40) Nandi, A.; Kozuch, S. *Chem. A Eur. J.* **2020**, *26*, 759–772.

(41) Saha, R.; Pan, S.; Merino, G.; Chattaraj, P. K. *Angew. Chemie Int. Ed.* **2019**, *58*, 8372–8377.

(42) Wang, Q.; Pan, S.; Wu, Y.; Deng, G.; Bian, J.; Wang, G.; Zhao, L.; Zhou, M.; Frenking, G. *Angew. Chemie Int. Ed.* **2019**, *58*, 17365–17374.

(43) Wu, X.; Zhao, L.; Jin, J.; Pan, S.; Li, W.; Jin, X.; Wang, G.; Zhou, M.; Frenking, G. *Science (80-.).* **2018**, *361*, 912–916.

(44) Evers, J.; Gobel, M.; Krumm, B.; Martin, F.; Medvedyev, S.; Oehlinger, G.; Steemann, F. X.; Troyan, I.; Klapotke, T. M.; Eremets, M. I. *J. Am. Chem. Soc.* **2011**, *133*, 12100–12105.

(45) González, M.; Valero, R.; Anglada, J. M.; Sayós, R. *J. Chem. Phys.* **2001**, *115*, 7015–7031.

(46) Nguyen, K. A.; Gordon, M. S.; Montgomery, J. A. J.; Michels, H. H. *J. Phys. Chem.* **1994**, *98*, 10072–10078.

(47) Harcourt, R. D.; Schulz, A. *J. Phys. Chem. A* **2000**, *104*, 6510–6516.

(48) Khan, S. N.; Kalemos, A.; Miliordos, E. *J. Phys. Chem. C* **2019**, *123*, 21548–21553.

(49) Ariyarathna, I. R.; Miliordos, E. *J. Comput. Chem.* **2019**, *40*, 1344–1351.

(50) Kalemos, A.; Papakondylis, A.; Mavridis, A. *Chem. Phys. Lett.* **1996**, *259*, 185–192.

(51) Kertesz, M. *Chem. A Eur. J.* **2019**, *25*, 400–416.

(52) Møller, C.; Plesset, M. S. *Phys. Rev.* **1934**, *46*, 618–622.

(53) Andrews, L.; Tague, T. J.; Kushto, G. P.; Davy, R. D. *Inorg. Chem.* **1995**, *34*, 2952–2961.

(54) Ariyarathna, I. R.; Miliordos, E. *Phys. Chem. Chem. Phys.* **2019**, *21*, 24469–24477.

(55) Eliav, E.; Kaldor, U. In *Comput. Methods Lanthan. Actin. Chem.* John Wiley & Sons Ltd: Chichester, UK, 2015, pp 23–54.

(56) Zhou, M.; Andrews, L.; Li, J.; Bursten, B. E. *J. Am. Chem. Soc.* **1999**, *121*, 12188–12189.

(57) Merritt, J. M.; Bondybey, V. E.; Heaven, M. C. *Science (80-.).* **2009**, *324*, 1548–1551.

(58) Koput, J. *Phys. Chem. Chem. Phys.* **2011**, *13*, 20311.

(59) Thomas, S. J. M.; Edwards, P. P.; Kuznetsov, V. L. *ChemPhysChem* **2008**, *9*, 59–66.

(60) Gibson, G. E.; Argo, W. L. *Phys. Rev.* **1916**, *7*, 33–48.

(61) Seel, A. G.; Zurek, E.; Ramirez-Cuesta, A. J.; Ryan, K. R.; Lodge, M. T. J.; Edwards, P. P. *Chem. Commun.* **2014**, *50*, 10778–10781.

(62) Mammano, N.; Sienko, M. J. *J. Am. Chem. Soc.* **1968**, *90*, 6322–6324.

(63) Zurek, E.; Wen, X.-D.; Hoffmann, R. *J. Am. Chem. Soc.* **2011**, *133*, 3535–3547.

(64) Sommerfeld, T.; Dreux, K. M. *J. Chem. Phys.* **2012**, *137*, 244302–244309.

(65) Hashimoto, K.; Daigoku, K. *Chem. Phys. Lett.* **2009**, *469*, 62–67.

(66) Hashimoto, K.; Daigoku, K. *Phys. Chem. Chem. Phys.* **2009**, *11*, 9391.

(67) Takasu, R.; Hashimoto, K.; Fuke, K. *Chem. Phys. Lett.* **1996**, *258*, 94–100.

(68) Linderberg, J.; Öhrn, Y., *Propagators in Quantum Chemistry*; John Wiley & Sons: New Jersey, 2004.

(69) Corzo, H. H.; Ortiz, J. V. In *Adv. Quantum Chem.* Elsevier: 2017, pp 267–298.

(70) Ortiz, J. V. *Int. J. Quantum Chem.* **2005**, *105*, 803–808.

(71) Lide, D. R., *CRC Handbook of Chemistry and Physics*, 93rd ed.; CRC press: New York, 2012.

(72) Zimmerman, H. E. *Acc. Chem. Res.* **2012**, *45*, 164–170.

(73) Edwards, P. P. *J. Supercond.* **2000**, *13*, 933–946.

(74) Takasu, R.; Misaizu, F.; Hashimoto, K.; Fuke, K. *J. Phys. Chem. A* **1997**, *101*, 3078–3087.

(75) Takasu, R.; Ito, H.; Nishikawa, K.; Hashimoto, K.; Okuda, R.; Fuke, K. *J. Electron Spectros. Relat. Phenomena* **2000**, *106*, 127–139.

(76) Bauschlicher, C. W.; Langhoff, S. R. *Chem. Phys. Lett.* **1989**, *158*, 409–411.

(77) Prascher, B. P.; Woon, D. E.; Peterson, K. A.; Dunning, T. H.; Wilson, A. K. *Theor. Chem. Acc.* **2011**, *128*, 69–82.

(78) Kendall, R. A.; Dunning, T. H.; Harrison, R. J. *J. Chem. Phys.* **1992**, *96*, 6796–6806.

(79) Dunning, T. H. *J. Chem. Phys.* **1989**, *90*, 1007–1023.

(80) Yoshida, S.; Daigoku, K.; Okai, N.; Takahata, A.; Sabu, A.; Hashimoto, K.; Fuke, K. *J. Chem. Phys.* **2002**, *117*, 8657–8669.

(81) Albaqami, M. D.; Ellis, A. M. *Chem. Phys. Lett.* **2018**, *706*, 736–740.

(82) Khan, S. N.; Miliordos, E. *J. Phys. Chem. A* **2020**, *124*, 4400–4412.

(83) Almeida, N. M. S.; Pawłowski, F.; Ortiz, J. V.; Miliordos, E. *Phys. Chem. Chem. Phys.* **2019**, *21*, 7090–7097.

(84) Almeida, N. M. S.; Miliordos, E. *Phys. Chem. Chem. Phys.* **2019**, *21*, 7098–7104.

(85) Ariyarathna, I. R.; Pawłowski, F.; Ortiz, J. V.; Miliordos, E. *J. Phys. Chem. A* **2020**, *124*, 505–512.

(86) Yanai, T.; Tew, D. P.; Handy, N. C. *Chem. Phys. Lett.* **2004**, *393*, 51–57.

(87) Hart, E. J.; Boag, J. W. *J. Am. Chem. Soc.* **1962**, *84*, 4090–4095.

(88) Abel, B.; Buck, U.; Sobolewski, A. L.; Domcke, W. *Phys. Chem. Chem. Phys.* **2012**, *14*, 22–34.

(89) Walker, D. C. *Q. Rev. Chem. Soc.* **1967**, *21*, 79.

(90) Young, R. M.; Neumark, D. M. *Chem. Rev.* **2012**, *112*, 5553–5577.

(91) Turi, L.; Rossky, P. J. *Chem. Rev.* **2012**, *112*, 5641–5674.

(92) Sobolewski, A. L.; Domcke, W. *Phys. Chem. Chem. Phys.* **2007**, *9*, 3818.

(93) Misaizu, F.; Sanekata, M.; Fuke, K.; Iwata, S. *J. Chem. Phys.* **1994**, *100*, 1161–1170.

(94) Reinhard, B. M.; Niedner-Schatteburg, G. *Phys. Chem. Chem. Phys.* **2003**, *5*, 1970–1980.

(95) Tsurusawa, T.; Iwata, S. *J. Chem. Phys.* **2000**, *112*, 5705–5710.

(96) Gao, B.; Liu, Z.-F. *J. Chem. Phys.* **2007**, *126*, 084501.

(97) Steinbach, C.; Buck, U. *Phys. Chem. Chem. Phys.* **2005**, *7*, 986.

(98) Yang, T.; Li, A.; Chen, G. K.; Xie, C.; Suits, A. G.; Campbell, W. C.; Guo, H.; Hudson, E. R. *J. Phys. Chem. Lett.* **2018**, *9*, 3555–3560.

(99) Tsurusawa, T.; Iwata, S. *J. Phys. Chem. A* **1999**, *103*, 6134–6141.

(100) Reinhard, B. M.; Niedner-Schatteburg, G. *Phys. Chem. Chem. Phys.* **2002**, *4*, 1471–1477.

(101) Nooijen, M.; Bartlett, R. J. *J. Chem. Phys.* **1995**, *102*, 3629–3647.

(102) Ariyarathna, I. R.; Miliordos, E. *Phys. Chem. Chem. Phys.* **2020**, *22*, 22426–22435.

(103) Radoń, M.; Drabik, G. *J. Chem. Theory Comput.* **2018**, *14*, 4010–4027.

(104) Radoń, M.; Gąssowska, K.; Szklarzewicz, J.; Broclawik, E. *J. Chem. Theory Comput.* **2016**, *12*, 1592–1605.

(105) Kallies, B.; Meier, R. *Inorg. Chem.* **2001**, *40*, 3101–3112.

(106) Kumar, S.; Saralch, S.; Jabeen, U.; Pathak, D. In *Colloid. Met. Oxide Nanoparticles*; Elsevier: 2020, pp 471–504.

(107) Rodríguez, J. A.; Fernández-García, M., *Synthesis, Properties, and Applications of Oxide Nanomaterials*; Rodríguez, J. A., Fernández-García, M., Eds.; John Wiley & Sons, Inc.: Hoboken, NJ, USA, 2007.

(108) Védrine, J. C. *Catalysts* **2017**, *7*, 341.

(109) Védrine, J. C. *ChemSusChem* **2019**, *12*, 577–588.

(110) Vogiatzis, K. D.; Polynski, M. V.; Kirkland, J. K.; Townsend, J.; Hashemi, A.; Liu, C.; Pidko, E. A. *Chem. Rev.* **2019**, *119*, 2453–2523.

(111) Ess, D.; Gagliardi, L.; Hammes-Schiffer, S. *Chem. Rev.* **2019**, *119*, 6507–6508.

(112) Nørskov, J. K.; Bligaard, T.; Rossmeisl, J.; Christensen, C. H. *Nat. Chem.* **2009**, *1*, 37–46.

(113) Sakellaris, C. N.; Miliordos, E.; Mavridis, A. *J. Chem. Phys.* **2011**, *134*, 234308.

(114) Miliordos, E.; Mavridis, A. *J. Phys. Chem. A* **2010**, *114*, 8536–8572.

(115) Miliordos, E.; Mavridis, A. *J. Phys. Chem. A* **2007**, *111*, 1953–1965.

(116) Wang, J.; Yue, X.; Yang, Y.; Sirisomboonchai, S.; Wang, P.; Ma, X.; Abudula, A.; Guan, G. *J. Alloys Compd.* **2020**, *819*, 153346.

(117) Rajakaruna, R.; Ariyarathna, I. In *Handb. Funct. Nanomater. Ind. Appl.* Elsevier: 2020, pp 83–109.

(118) Portela, R.; Rubio-Marcos, F.; Leret, P.; Fernández, J. F.; Bañares, M. A.; Ávila, P. *J. Mater. Chem. A* **2015**, *3*, 1306–1316.

(119) Sadegh-Vaziri, R.; Babler, M. U. *Appl. Sci.* **2019**, *9*, 5316.

(120) Babich, I *Fuel* **2003**, *82*, 607–631.

(121) Ariyarathna, I. R.; Miliordos, E. *J. Quant. Spectrosc. Radiat. Transf.* **2020**, *255*, 107265.

(122) Ariyarathna, I. R.; Miliordos, E. *Phys. Chem. Chem. Phys.* **2021**, *23*, 1437–1442.

(123) Peterson, K. A.; Figgen, D.; Dolg, M.; Stoll, H. *J. Chem. Phys.* **2007**, *126*, 124101.

(124) Jackson, B. A.; Miliordos, E. *Phys. Chem. Chem. Phys.* **2020**, *22*, 6606–6618.

(125) Ariyarathna, I. R.; Miliordos, E. *Phys. Chem. Chem. Phys.* **2018**, *20*, 12278–12287.

(126) Gunion, R. F.; Dixon-Warren, S. J.; Lineberger, W. C.; Morse, M. D. *J. Chem. Phys.* **1996**, *104*, 1765–1773.

(127) Ariyarathna, I. R.; Almeida, N. M. S.; Miliordos, E. *Phys. Chem. Chem. Phys.* **2020**, *22*, 16072–16079.

(128) Carter, E. A.; Goddard, W. A. *J. Phys. Chem.* **1988**, *92*, 2109–2115.

(129) Krauss, M.; Stevens, W. J. *J. Chem. Phys.* **1985**, *82*, 5584–5596.

(130) Almeida, N. M. S.; Ariyarathna, I. R.; Miliordos, E. *J. Phys. Chem. A* **2019**, *123*, 9336–9344.

Appendix A

Supporting material for Chapter 2: *"Chemical bonding of main–group molecules"*

Appendix A contains the full copies of following articles. Reprints were made with permissions from the publisher.

- Ariyarathna, I. R.; Miliordos, E. *J. Comput. Chem.* **2019**, *40*, 1344–1351.
- Ariyarathna, I. R.; Miliordos, E. *J. Phys. Chem. A* **2017**, *121*, 7051–7058.
- Ariyarathna, I. R.; Miliordos, E. *Int. J. Quantum Chem.* **2018**, *118*, e25673.
- Ariyarathna, I. R.; Miliordos, E. *Phys. Chem. Chem. Phys.* **2019**, *21*, 24469–24477.
- Ariyarathna, I. R.; Miliordos, E. *J. Comput. Chem.* **2019**, *40*, 1740–1751.
- Ariyarathna, I. R.; Miliordos, E. *J. Phys. Chem. A* **2020**, *124*, 9783–9792.

Electronic and geometric structure analysis of neutral and anionic alkali metal complexes of the CX series (X = O, S, Se, Te, Po): The case of $M(CX)_{n=1-4}$ (M = Li, Na) and their dimers

Volume 40 | Issues 13–14 | 2019
Included in this print edition:
Issue 13 (May 15, 2019)
Issue 14 (May 30, 2019)

Journal of COMPUTATIONAL CHEMISTRY

Organic • Inorganic • Physical
Biological • Materials

www.c-chem.org

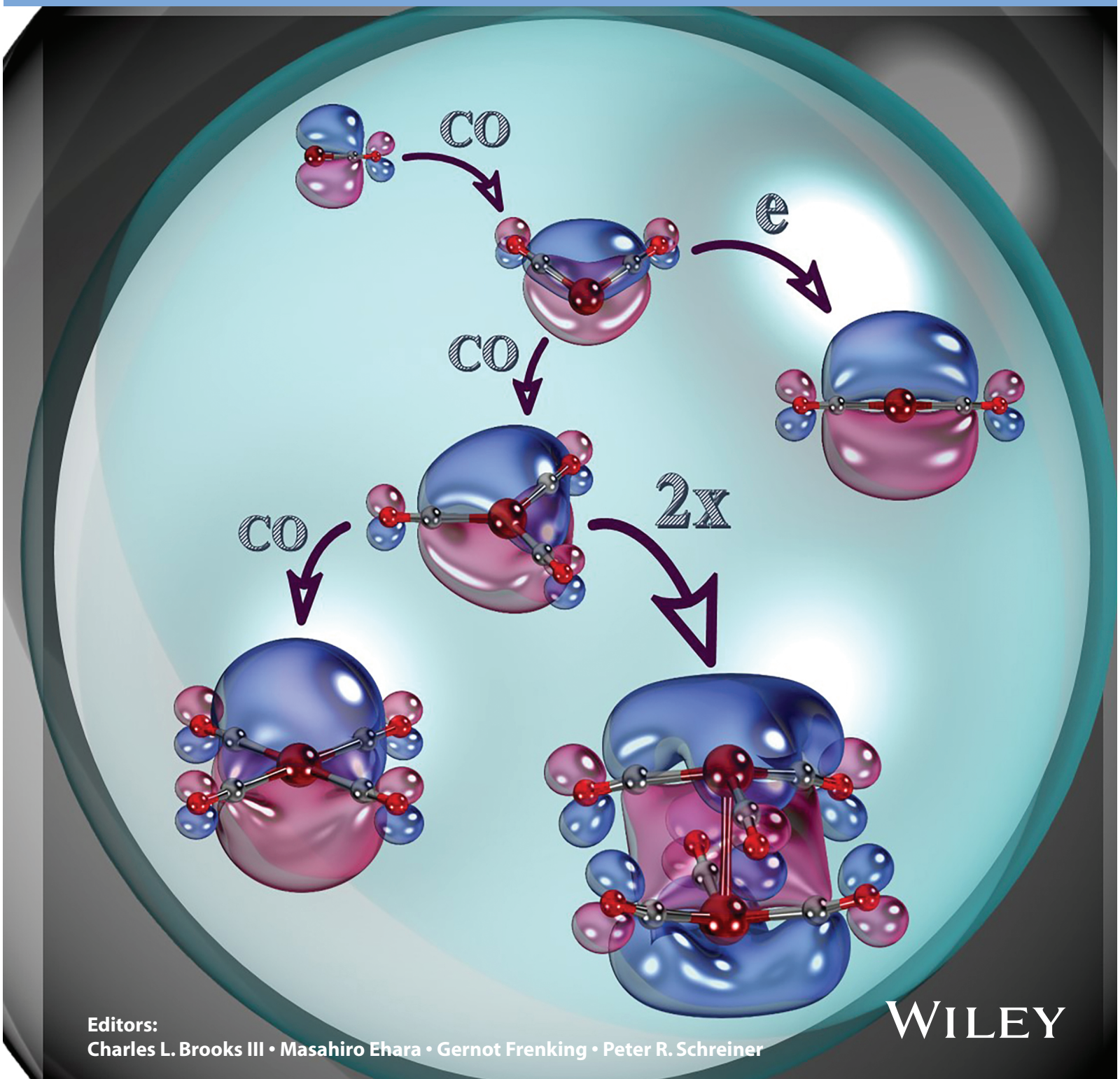

WILEY

Journal of COMPUTATIONAL CHEMISTRY

Electronic and geometric structure analysis of neutral and anionic alkali metal complexes of the CX series (X = O, S, Se, Te, Po): The case of $M(CX)_{n\ =\ 1-4}$ (M = Li, Na) and their dimers

Isuru R. Ariyarathna, and Evangelos Miliordos*

Bonding mechanisms, potential energy curves, accurate structures, energetics, and electron affinities are obtained for all $M(CX)_{1-3}$ species with M = Li, Na, and X = O, S, Se, Te, and Po, at the coupled-cluster level with triple-ζ quality basis sets. We discuss and rationalize the trends within different molecular groups. For example, we found larger binding energies for M = Li, for CX = CPo, and for the tri-coordinated (n = 3) complexes. All three facts are explained by the fact that the global minimum of the titled complexes originate from the first excited ^2P ($2p^1$ for Li or $3p^1$ for Na) state of the metal, with each ligand forming a dative bond with the metal. All of the complexes, except $Na(CO)_3$, have stable anions, and their electron affinity increases as $MCX < M(CX)_3 < M(CX)_2$. This sequence is attributed to the binding modes of these complexes. The $Li(CO)_3$ and $Li(CS)_3$ complexes are able to accommodate a fourth ligand, which is attached to the system electrostatically. Finally, two $Li(CO)_3$ molecules can bind together covalently to make the ethane analog. The staggered conformer was found lower in energy and unlike ethane the CO ligands bend toward the neighboring $Li(CO)_3$ moiety. © 2019 Wiley Periodicals, Inc.

DOI: 10.1002/jcc.25791

Introduction

Transition metal carbonyl chemistry is a well explored field because of the catalysis applications, especially in organometallic chemistry. Among them, $Mo(CO)_6$, $W(CO)_6$, $Cr(CO)_6$, $[FeCp(CO)_2]_2$, $Co_2(CO)_8$, and $Ni(CO)_4$ have been identified as efficient catalysts for liquefaction of coal,[1] while $M(CO)_3(NCCH_3)_3$ and $MI_2(CO)_3(NCCH_3)_2$ (M = Mo, W) are capable of facilitating acetylene polymerization.[2] Industrially, $Co_2(CO)_8$ and $Ni(CO)_4$ catalysts are utilized for the production of aldehydes from alkenes[3] and in the synthesis of propanoic acid,[4] respectively. Further, anions of metal carbonyls such as $Mn(CO)_5^-$ and $C_6H_6Fe(CO)_2^-$ have been used to synthesize various organometallic compounds.[5]

To understand and predict their chemical activity, the electronic structure of metal carbonyl bonds has been extensively studied.[6–11] Carbonyls can bind in two ways with a metal M: Carbon monoxide is a σ-donor (electron flow from CO to M along the M—C axis) and a π-acceptor (flow from M to CO through the π-frame). The π back donation strengthens the M—C bond but weakens C—O producing elongated C—O bonds and lower C—O stretching frequencies.[12] In anionic metal carbonyl complexes this C—O bond weakening is enhanced over neutral complexes.[12] On the other hand, the C—O bond of several late transition metal complexes such as $M(CO)_{1,2}^+$ (M = Cu, Ag, Au) is found to be stronger than free CO. These complexes are referred as nonclassical metal carbonyls.[6,13]

Considerable interest has been also shown for the s-block metal carbonyl systems in the literature. Several alkali metal carbonyl compounds, such as $Li(CO)_{n\ =\ 1-4}$, NaCO, KCO, $Li(CO)_2$, and $Li(CO)_3$, have been detected by means of matrix isolation,[14–16] and the vibrational spectra of $Li(CO)_{n\ =\ 1-4}$ in krypton have been experimentally recorded and analyzed by Ayed et al.[14] Electronic paramagnetic resonance spectrum of NaCO is reported by Joly and Howard who clearly identified an unpaired electron localized on Na.[17] From the theoretical stand point, in 1986 Silvi et al. has performed Hartree-Fock and configuration interaction (CI) calculations for Li—CO—Li and Li—CO species and suggested that the latter is ionic (Li^+CO^-).[18] Ten years later Kalemos et al. studied the chemical bonding of linear LiCO, LiCS, and LiSC including potential energy curves (PECs) with respect to the M-ligand distance.[19] According to their findings all three molecules are generated by the interaction of the first excited state of $Li(^2P;\ 2p^1)$ with the ground state, $^1\Sigma^+$, of CO/CS. The ground state of CO and CS has one electron pair at the carbon end which facilitates a dative bond with Li, $Li(2p_\sigma) \leftarrow CO/CS$. Additionally, $Li(2p_\pi) \rightarrow CO/CS(\pi^*)$ electron transfer is proposed by the same authors. Their population analysis demonstrated that almost half an electron is transferred from CO to Li in the σ-frame, and about 0.8 electrons flow toward the opposite direction in the π-frame. LiCO, LiOC, and LiSC were all found metastable with respect to $Li(^2S) + CO(^1\Sigma^+)$ or $Li(^2S) + CS(^1\Sigma^+)$, and only LiCS is bound by 25.7 kcal/mol at CI singles and doubles (CISD). Our calculations confirm fully the previous bonding patterns not only for LiCO

[a] I. R. Ariyarathna, E. Miliordos
Department of Chemistry and Biochemistry, Auburn University, Auburn, Alabama, 36849-5312
E-mail: emiliord@auburn.edu

but also extend them to all mono-, di-, and tri-carbonyl complexes.

Recently we have reported the BeCO, $Be(CO)_2$, and $Be(CO)_3$ molecules and found similar trends: BeCO is metastable with respect to $Be(^1S) + CO(^1\Sigma^+)$ but $Be(CO)_2$ and $Be(CO)_3$ are well bound.[20,21] The ground state of all three molecules originates from excited states of Be. BeCO, $Be(CO)_2$, and $Be(CO)_3$ result from $Be(^3P; 2s^12p^1)$, $Be(^3P; 2p^2)$, and $Be(^1D; 2p^2)$ interacting with $CO(^1\Sigma^+)$, respectively. In these cases, the valence electrons of beryllium tend to occupy π-orbitals exposing the *in situ* Be^{2+} charge more effectively to the attacking CO. We further noted that by replacing CO with the heavier isovalent CS, CSe, CTe, and CPo species the stability of $Be(CX)_3$ increases, and this higher stability was associated with their larger dipole moment. Can the same observations be made for alkali metals? Can the Li^+ and Na^+ cores, which have smaller charge than *in situ* Be^{2+} form the same type of complexes?

This article aims to address these questions and focusses on the chemical bonding of di-, tri- and tetra-CX (X = O, S, Se, Te, Po) coordination lithium and sodium complexes. Despite the smaller charge of the Li^+ core, we demonstrate that lithium and sodium carbonyl complexes are formed by the first excited state of lithium, $^2P(2p^1)$, which shares its unpaired electron with the coordinated CO molecules in the π-frame. Furthermore, we found that two such complexes, $Li(CO)_3$, can bind via a σ-type covalent bond making dimers. We also observed that a fourth CO or CS can bind to Li and we investigated its binding mode. Finally, we examined the ability of these systems to accommodate an additional electron pairing up with the existing one and make stable anions.

In the next section we describe our computational methodologies. After that, we first discuss the di- and tri-coordinated M-CX molecules, followed by $M(XC)1,2,3^-$ (M = Li, Na), $Li(CX)_4$, and $[Li(CO)_3]_2$. Finally, we summarize our findings.

Computational Details

Optimal geometries, binding energies, electron affinities, PECs for all species except $[Li(CO)_3]_2$ are obtained using coupled-cluster single, double, and perturbative triples [CCSD(T)] method building on the initial restricted Hartree-Fock wave function. Due to the prohibitive computational cost the second-order Møller–Plesset (MP2) method was employed for $[Li(CO)_3]_2$ instead. The augmented triple-ζ quality correlation consistent (aug-cc-pVTZ) basis set was employed for all calculations.[22–24] The aug-cc-pVTZ-PP basis set combined with the relevant relativistic pseudopotentials replacing 10, 28, and 60 inner electrons were used for Se, Te, and Po.[25] We optimized the structures at the CCSD(T) level. The vibrational harmonic frequencies obtained using B3LYP with the same basis set are included in Supporting Information. The PECs for $Li(CO)_2$ and $Li(CO)_3$ were constructed by varying the Li—C distance at the CCSD(T) level of theory, while CO length is fixed to its equilibrium bond distance 1.128 Å. The dipole moments μ of all CX diatomic molecules were calculated by the finite-field approach. We use an electric field intensity $f = 0.01$ a.u. toward two opposite directions along the C—X bond. The energies $E(f)$ and $E(-f)$ are introduced to the following equation: $\mu = [E(f) - E(-f)]/2f$. Coupled-cluster calculations were carried out invoking MOLPRO 2015.1,[26] while B3LYP and MP2 calculations were done with Gaussian16.[27]

$M(CX)_2$ Species

The first two states of Li and Na are of valence ns^1 and np^1 character (n = 2, 3 for Li, Na), followed by the lowest Rydberg $(n + 1)s^1$ state. The $ns^1 \rightarrow np^1/ns^1 \rightarrow (n + 1)s^1$ excitation energy for Li and Na are 14,904/21,206 cm^{-1} and 16,968/25,740 cm^{-1}, respectively.[28] Their Rydberg ^2S states are quite high and are not expected to create low energy structures, but rather higher energy states with a charge-bound electron diffused around the Li^+/Na^+ terminal.

The singly occupied hard (minimally polarizable) 2s/3s shell of Li/Na at the ground state is expected to have a repulsive interaction with closed-shell ligands such as CX. By promoting the valence s-electron to the neighboring p-orbital, the Li^+/Na^+ core opens up inviting the CX ligands to make dative bonds. This allows two CX ligands to approach the Li atom in linear or a bent fashion depending on which of the empty p-orbital will be preferred. The CCSD(T) PECs for the collinear and oblique attack are shown in Figure 1. For the latter PECs we used the angle of 95.5°, which is the optimal angle at the global minimum of $Li(CO)_2$ (see below). Indeed, the PECs of the collinear approach generates one repulsive PEC ($^2\Sigma_g^+$) from the $Li(^2S) + 2CO$ ($X^1\Sigma^+$) ground state fragments and a highly attractive PEC ($^2\Pi_u$) from the first excited state channel $Li(^2P) + 2CO$ ($X^1\Sigma^+$). Although the minimum of $^2\Pi_u$ is lower than the ground state fragments, it is not the global minimum of the ground state potential energy surface. The energy of the two $^2\Pi_u$ components splits into the $^2B_1$ and $^2A_1$ states upon bending the CLiC angle (Supporting Information Fig. S2). The former state creates the global minimum, which is 2.4 kcal/mol lower than $^2\Pi_u$. Based on the bending vibrational frequency of 49.5 cm^{-1} (see Supporting Information), the first vibrational level is just 0.07 kcal/mol ($\frac{1}{2}\omega_e$) above the global minimum and well below the barrier of 2.4 kcal/mol. According to Figure 1, $\tilde{X}^2B_1$

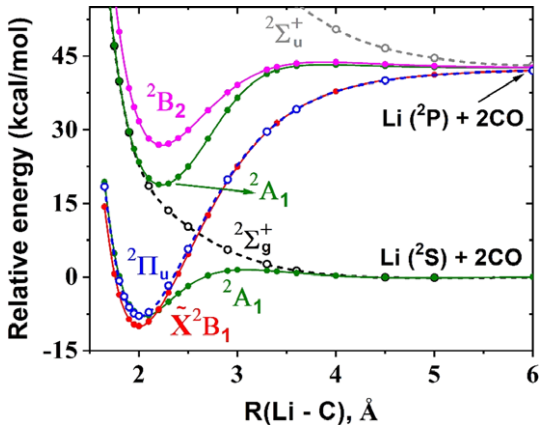

Figure 1. CCSD(T) PECs of $Li(CO)_2$ as a function of the Li—C distance. Dashed/continuous lines and open/solid symbols correspond to the collinear/oblique OC → Li ← CO attack. [Color figure can be viewed at wileyonlinelibrary.com]

correlates directly to Li(^{2}P) exactly like the parent $^2\Pi_u$ state. On the other hand, $^2A_1$ dissociates to Li(^{2}S) because of the avoided crossing between the two $^2A_1$ states coming from the first two channels (see Fig. 1).

Scheme 1 depicts the proposed bonding mechanism for $^2\Pi_u$ along with the frontier molecular orbitals supporting it. The two CO molecules use two vacant orbitals of Li (sp hybrids along the Li—C axis) to make dative bonds, while the $2p^1$ electron of Li is delocalized in the π-frame of the molecule. The same bonding is observed for the bent structures but the two π-orbitals of linear $Li(CO)_2$ take the shapes of orbitals $8a_1$ and $2b_1$ shown in Scheme 2. The lithium and sodium complexes with CO and CS are found to have a bent global minimum, which is 2.4 (LiCO), 0.4 Li(CS), 3.7 Na(CO), 1.1 (NaCS) kcal/mol lower than the linear structure. The larger ligands favor the linear conformation probably because of the larger repulsion between the terminal atoms. The same bonding was suggested by Kalemos et al. for the ground $^2\Pi$ state of LiCO and LiCS.[19]

Table 1 lists our numerical results on the optimal bond lengths and binding energies (D_e) of all $M(CO)_{n\ =\ 1-3}$ species. D_e values refer with respect to the ground state fragments. The tri-coordinated species are discussed later and for reasons of completeness we also report mono-carbonyl complexes, which compare favorably with the LiCO and LiCS results by Kalemos et al.[19] Focusing on $M(CX)_2$, we see that for a specific CX, the D_e for Li is always larger than Na by ~20 kcal/mol. Two reasons result in this trend: (1) The charge density of Li^+ is higher than Na^+ (because of its smaller size) attracting the ligands stronger and (2) The higher $^2S(2s^1) \rightarrow {}^2P(2p^1)$ excitation energy of Na shifts the Na(^{2}P) + 2CO adiabatic products higher yielding smaller binding energy with respect to the ground state Na(^{2}S) + 2CO fragments. The charge density of both cations and anions has also been used in the literature to explain the solubility trends among several salts.[29] Among the $M(CX)_2$ species, only $Na(CO)_2$ is metastable with respect to the M (^{2}S) + 2CO dissociation.

The binding energy increases in the $M(CO)_2 < M(CS)_2 < M(CSe)_2 < M(CTe)_2 < M(CPo)_2$ order and is proportional to the dipole moment (μ_{cx}) of CX. Our calculated μ values for CO, CS, CSe, CTe, and CPo are 0.102, 1.901, 2.163, 2.590, and 2.831 D, respectively, comparing very well with the available experimental values.[21] This nearly linear relationship between D_e versus μ_{CX} is shown in Figure 2. The plot suggests that the negative D_e of $Na(CO)_2$ can be connected to the relatively low μ_{CO}. It should be stressed that the linear relation between D_e and μ_{CX} does not imply plain electrostatic bonding between M and CX. Instead, μ_{CX} is rather used as a handy measure of the ability of CX to form a dative bond. Higher polarity of the CX species (C^-X^+) translates to an electron richer carbon,[30] which can attach stronger to the metal and strengthen the observed dative bond.

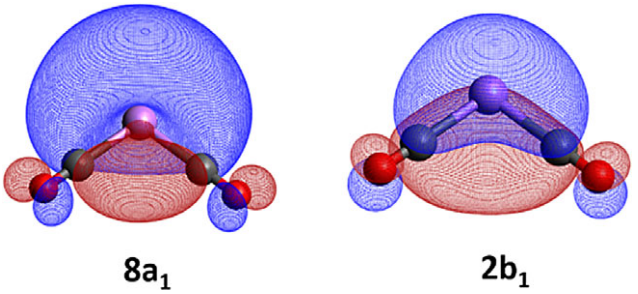

Scheme 2. The $8a_1$ and $2b_1$ MOs of bent $Li(CO)_2$ which transform to the two π MOs of linear $Li(CO)_2$. [Color figure can be viewed at wileyonlinelibrary.com]

$M(CX)_2$ species show higher D_e values compared to MCX. The reason is that in both cases we promote the same valence electron from 2s or 3s to 2p or 3p (for Li or Na) to enable the M ← CO donation, but there are two such bonds for $M(CX)_2$ versus one bond for MCX.[19] A similar linear dependence between D_e and μ_{CX} is observed for the di-coordinated metal carbonyls too (see Fig. 2).

The M—C equilibrium distances are shorter in mono-coordinated molecules than their bi-coordinated partners by ~0.1 Å. The size of the terminal atom X seems to play a minor role affecting the M—C lengths by less than 0.01 Å for all four $M(CX)_{1-2}$ groups. Note that $Na(CO)_2$ is an outlier in the $Na(CX)_2$ group and has considerably longer (~0.04 Å) M—C distance (see Table 1). On the other hand, the larger size of Na leads to longer M—C bonds. The difference between the Li—C and Na—C lengths of approximately 0.4 Å for all species is very close to the difference of the van der Waals atomic radii of the two metals: 1.82 Å (Li) versus 2.27 Å (Na).

Going from MCX to $M(CX)_2$ the C—X bond lengths contract and go closer to those of the free CX molecules, which are 1.136, 1.550, 1.691, 1.921, and 2.020 Å for X = O, S, Se, Te, and Po, respectively, at the same level of theory. This trend can be seen as consequence of two factors: (1) the longer M—C bonds for $M(CX)_2$ place the CX units further from the metal and closer to their free form and (2) that the π-electron is back donated to one carbonyl for MCX but to two carbonyls (half an electron per CX) for $M(CX)_2$. Table 1 shows a slight decrease of the CX bond length on average by 0.009 Å and 0.006 Å for MCX and $M(CX)_2$, respectively, when moving from Li to Na. Although this difference is within the error of our methodologies, it indicates a stronger π-back donation of Na relative to Li, which weakens the CX bonds.

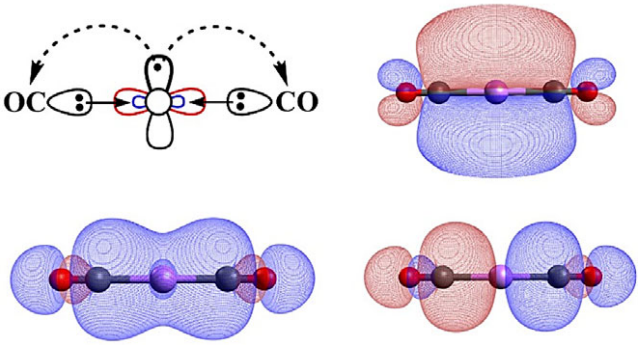

Scheme 1. Proposed bonding scheme for $\tilde{X}\,^2\Pi_u$ of $Li(CO)_2$. The singly occupied π-orbital (top-right) and two σ-orbitals represent the orthogonal combinations of the two M ← CO dative bonds (bottom orbitals) are also shown. [Color figure can be viewed at wileyonlinelibrary.com]

Table 1. CCSD(T) equilibrium bond lengths r_e (Å) and binding energies D_e (kcal/mol) for the formation of $M(CX)_{n=1-3}$ from $M(^2S)$ + $nCX(X^1\Sigma^+)$.

	r_e				r_e		
Molecule[a]	M—C	C—X	D_e	Molecule	M—C	C—X	D_e
LiCO	1.905	1.177	−3.6	NaCO	2.285	1.180	−20.2
LiCS	1.904	1.588	27.2	NaCS	2.265	1.596	11.7
LiCSe	1.907	1.729	31.6	NaCSe	2.269	1.739	16.6
LiCTe	1.913	1.947	39.3	NaCTe	2.276	1.957	24.8
LiCPo	1.914	2.051	39.0	NaCPo	2.277	2.063	24.6
$Li(CO)_2$	2.012	1.147	8.8	$Na(CO)_2$	2.447	1.149	−14.0
$Li(CO)_2$[a]	1.999	1.150	11.2	$Na(CO)_2$[a]	2.421	1.152	−10.3
$Li(CS)_2$	2.007	1.558	43.4	$Na(CS)_2$	2.390	1.570	20.9
$Li(CS)_2$[a]	1.990	1.561	43.9	$Na(CS)_2$[a]	2.385	1.569	22.0
$Li(CSe)_2$	2.012	1.698	48.4	$Na(CSe)_2$	2.403	1.705	26.4
$Li(CTe)_2$	2.019	1.919	57.9	$Na(CTe)_2$	2.407	1.927	36.5
$Li(CPo)_2$	2.021	2.019	58.0	$Na(CPo)_2$	2.409	2.027	36.7
$Li(CO)_3$	2.046	1.141	23.0	$Na(CO)_3$	2.555	1.154	−6.3
$Li(CS)_3$	2.047	1.552	58.2	$Na(CS)_3$	2.462	1.556	30.2
$Li(CSe)_3$	2.053	1.693	62.9	$Na(CSe)_3$	2.466	1.697	35.7
$Li(CTe)_3$	2.061	1.916	72.4	$Na(CTe)_3$	2.473	1.921	46.1
$Li(CPo)_3$	2.064	2.015	72.1	$Na(CPo)_3$	2.476	2.020	46.3

The electronic terms for the states studied presently are: $^2\Pi$ [MCX], $^2B_1$ [bent $M(CX)_2$], $^2\Pi_u$ [linear $M(CX)_2$], and $^2A_2'$ [$M(CX)_3$]. All $M(CX)_2$ systems are linear unless otherwise stated.
[a] Bent structures with XC—M—CX angles of 95.5° (M = Li, X = O), 99.7° (M = Li, X = S), 74.8° (M = Na, X = O), and 70.9° (M = Na, X = S).

$M(CX)_3$ Species

The transition from $Li(^2S;2s^1)$ to $Li(^2P;2p^1)$ renders all four valence orbitals of lithium available for bonding. Out of these four valence orbitals, only one is occupied. The question is can we use the rest three orbitals to facilitate the insertion of three CO ligands? Following the same strategy as for $M(CX)_2$ we constructed CCSD(T) PECs for the simultaneous approach of all three CO molecules toward lithium (see Fig. 3). Once again, the global minimum is made from the $Li(^2P)$ + 3CO fragments, whereas the ground state of $Li(^2S)$ interacts repulsively with the incoming carbon monoxides. Scheme 3 depicts the bonding action and the delocalized orbital of the π-electron for $Li(CO)_3$; identical schemes can be made for the rest species.

The exact same observations can be made as in section "M$(CX)_2$ Species" about the M—C and C—X bond lengths (see Table 1). The addition of the third ligand elongates M—C and shortens C—X rendering it practically the same as the ones of free CX. The terminal X atom still plays a minor role to the M—C bond length, while going from Li to Na the difference in the M—C length is again ~0.4 Å with $Na(CO)_3$ being an outlier. The C—X bonds increase also slightly transitioning from Li to Na.

The total binding energy D_e with respect to M + 3CO increases consistently by 15/10 kcal/mol for M = Li/Na, going from $M(CX)_2$ to $M(CX)_3$, and decreases by 25 kcal/mol going from $Li(CX)_3$ to $Na(CX)_3$. The additional stability of $M(CX)_3$ can be ascribed to the same reason causing the enhanced stability of $M(CX)_2$ over MCX (see section "$M(CX)_2$ Species"). The linear relation between μ_{CX} and D_e holds true as well and is plotted in Figure 2. The corresponding D_e values for $Be(CX)_3$ species, which were seen as *in situ* $Be^{2+}(CX)_3$ with two delocalized π-electrons, are 49.2, 115.3, 123.3, 139.7, and 139.1 kcal/mol,[21] which are almost twice and four times larger compared to the $Li(CX)_3$ and $Na(CX)_3$ ones, respectively. Overall, the smaller *in situ* charge of Li and Na allows the formation of tri-coordinated metal carbonyl complexes but affects appreciably their thermodynamic stability.

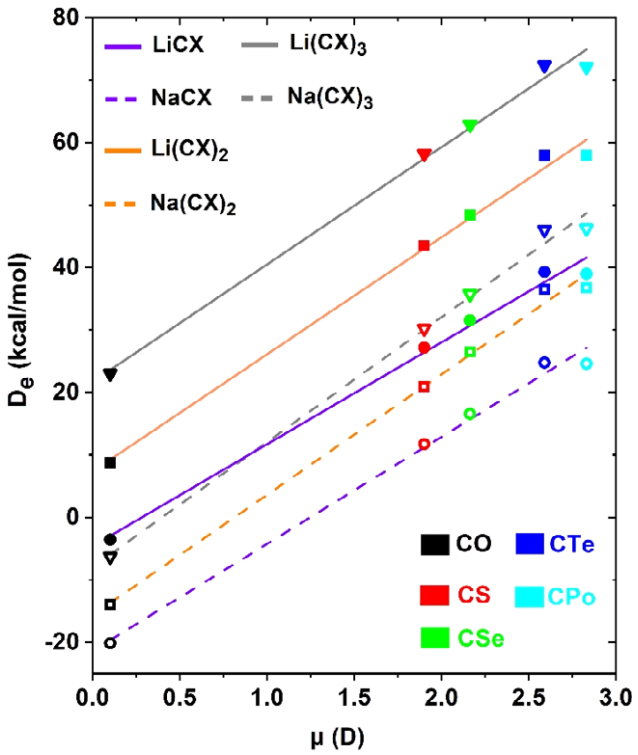

Figure 2. Binding energy (D_e) for the M + $nCX \rightarrow M(CX)_n$ [n = 1–3] reaction versus the dipole moment of CX (μ). Solid/open symbols and continuous/dashed lines correspond to Li/Na. Black, red, light green, dark blue, and light blue symbols pertain to CO, CS, CSe, CTe, and CPo, respectively. Finally, violet/orange/gray lines and circles/squares/triangles are used for the MCX/$M(CX)_2$/$M(CX)_3$ series. [Color figure can be viewed at wileyonlinelibrary.com]

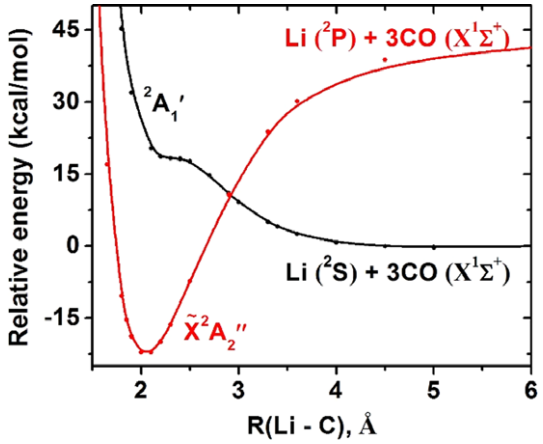

Figure 3. CCSD(T) PECs of $Li(CO)_3$ as a function of the Li—C distance. [Color figure can be viewed at wileyonlinelibrary.com]

$M(CX)_{1-3}^-$

The attachment of an electron to all of the neutral metal carbonyls examined in the previous sections leads to stable anionic systems. The additional electron couples to the existing unpaired electron of $M(CX)_3$ or occupy one of the vacant valence orbitals of $M(CX)_{1-2}$. MCX^- species have a $^3\Pi$ ground state, where the additional electron resides chiefly at the 2s orbital of lithium, which is polarized away from CO (see Fig. S1). The exact same electronic structure was observed for the isovalent BeCX species, which have a ground $^3\Pi$ state followed by a $^1\Pi$ and $^3\Sigma^-$.[20] The $M(CX)_2^-$ series are linear with two unpaired electrons in the two π-orbitals which assign the ground state as $^3\Sigma_g^-$. Finally, all $M(CX)_3^-$ are closed-shell systems with an electron pair in the π-frame. All three groups share identical electronic structure with the isoelectronic $Be(CO)_{1-3}$ molecules.[20,21] Table 2 summarizes the optimal structures and EAs for all three series of molecules.

The EA generally increases in the order: $M(CO)_n < M(CS)_n < M(CSe)_n < M(CTe)_n < M(CPo)_n$ for n = 1–3 (see Table 2). For n = 1 the EA values range within only 0.12 and 0.08 eV for M = Li and Na. The reason is that the additional electron goes at the "back" of the metal (see Supporting Information Fig. S1) and it is only minimally dependent on the ligand. Although the EA [$M(^2S; s^1) \rightarrow M^-(^1S; s^2)$] of naked Li (0.62 eV) is smaller than that of Na (0.55 eV),[31] the EA for all NaCX species (0.80 ± 0.04 eV) is larger than those of Li (0.63 ± 0.06 eV). Except for CO, the EAs for the di-coordinated complexes increase considerably being more than twice larger in some cases (see Table 2). The reason is that the additional electron is now going to the empty delocalized (over the metal and two carbon atoms; see Scheme 1) π-orbital, which is orthogonal to its singly occupied sister π-orbital. It is not clear to us why lithium and sodium di-carbonyls behave differently having smaller EAs. $Li(CO)_3$ has also relatively small EA and $Na(CO)_3$ anion is not even stable. The rest $M(CX)_3$ complexes have reduced EAs compared to the corresponding $M(CX)_2$. This reduction can be attributed to the fact that the extra electron is added to the already occupied off-plane π-orbital (see Scheme 3).

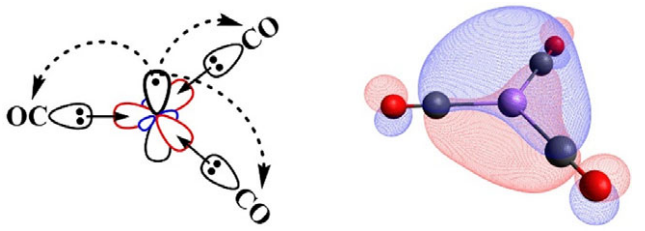

Scheme 3. Proposed bonding scheme for $\tilde{X}^2A_2''$ of $Li(CO)_3$. The delocalized $2p_\pi$-orbital is also shown. [Color figure can be viewed at wileyonlinelibrary.com]

Going from MCX to MCX^-, we see that both the M—C and C—X bonds elongate by ≥0.1 Å and ~0.02 Å, respectively. But going from $M(CX)_{2,3}$ to $M(CX)_{2,3}^-$, the M—C bonds either elongate less or even shorten; see for example the case of $Li(CX)_3$. On the other hand, the CX bonds elongate further by ~0.05 Å and 0.03–0.04 Å for $M(CX)_2$ and $M(CX)_3$. It seems that the additional π-electrons, which are mostly shared between the metal and carbon, strengthen the M—C bond weakening the C—X bond at the same time. Schemes 1 and 3 show that the orbitals of these π-electrons have bonding M—CX but anti-bonding MC—X character in agreement with the observed M—CX and MC—X bond length trends. The strengthening of the M—CX bond is quantified by the D_e(M—CX) values as well. These can be obtained as $D_e[M(CX)_n^-] = D_e[M(CX)_n] + EA[M(CX)_n] - EA[M]$. Since the EA of $M(CX)_{2-3}$ species are larger than MCX (see Table 2), their binding energies are larger.

$Li(CO)_4$ and $Li(CS)_4$

As described above, in $Li(CO)_3$ all valence orbitals of $Li(^2P)$ are "busy" with either hosting the unpaired electron or facilitating the three Li ← CO dative bonds. In principle, the addition of a fourth CO ligand to the saturated $Li(CO)_3$ complex should be unfavorable. However, there is experimental evidence for the existence of $Li(CO)_4$.[14] To verify the stability of $Li(CO)_4$ quantum mechanically, we obtained its optimal structure and calculated its harmonic vibrational frequencies. The CCSD(T) binding energy with respect to $Li(^2S)$ + 4CO is 29.9 kcal/mol and 6.8 kcal/mol with respect to $Li(CO)_3$ + CO. All frequencies (at B3LYP) are real with the smallest one being 7.4 cm^{-1} and corresponds to the off-plane deformation of the molecule (see Supporting Information). Correcting for the zero-point energy these values become 26.1 and 6.3 kcal/mol. A more "natural" binding energy of each Li—CO bond in $Li(CO)_3$ can be obtained by dividing by three the total binding energy with respect to $Li(^2P)$ + 3CO. This value is 22.2 kcal/mol, three times larger than the binding energy of the fourth CO unit.

The same small frequency for $Li(CS)_3$ is actually imaginary (14.7 cm^{-1}). Following the intrinsic coordinate of this frequency we found a nonplanar $Li(CS)_4$ structure with three very small imaginary frequencies of ≤5 cm^{-1} and 2.8 kcal/mol lower. More detailed calculations using a finer integration grid or stricter convergence criteria may be necessary to provide a final answer, but for both CO and CS this deformation is a soft

Table 2. CCSD(T) Equilibrium bond lengths r_e (Å) of $M(CX)_{1,2,3}^-$ and electron affinities EA (eV) of $M(CX)_{1,2,3}$.[a]

	r_e				r_e		
Molecule	M—C	C—X	EA	Molecule	M—C	C—X	EA
$LiCO^-$	2.008	1.179	0.57	$NaCO^-$	2.515	1.181	0.77
$LiCS^-$	2.002	1.603	0.62	$NaCS^-$	2.403	1.612	0.76
$LiCSe^-$	2.011	1.748	0.64	$NaCSe^-$	2.413	1.759	0.79
$LiCTe^-$	2.023	1.970	0.69	$NaCTe^-$	2.427	1.982	0.83
$LiCPo^-$	2.028	2.077	0.69	$NaCPo^-$	2.433	2.090	0.84
$Li(CO)_2^-$	1.983	1.171	0.23	$Na(CO)_2^-$	2.446	1.164	0.10
$Li(CS)_2^-$	2.005	1.606	1.31	$Na(CS)_2^-$	2.407	1.612	1.30
$Li(CSe)_2^-$	2.015	1.750	1.55	$Na(CSe)_2^-$	2.408	1.759	1.55
$Li(CTe)_2^-$	2.027	1.970	1.88	$Na(CTe)_2^-$	2.417	1.980	1.90
$Li(CPo)_2^-$	2.031	2.074	1.86	$Na(CPo)_2^-$	2.421	2.086	1.90
$Li(CO)_3^-$	2.014	1.159	0.21	$Na(CO)_3^-$	NA [b]	NA [b]	NA [b]
$Li(CS)_3^-$	2.026	1.585	1.05	$Na(CS)_3^-$	2.480	1.581	1.01
$Li(CSe)_3^-$	2.032	1.729	1.27	$Na(CSe)_3^-$	2.470	1.731	1.22
$Li(CTe)_3^-$	2.044	1.952	1.63	$Na(CTe)_3^-$	2.477	1.957	1.59
$Li(CPo)_3^-$	2.047	2.054	1.62	$Na(CPo)_3^-$	2.481	2.060	1.58

[a] The electronic terms for the states studied presently are: $^3\Pi$ [MCX^-], $^3\Sigma_g^-$ [$M(CX)_2^-$], $^1A_1'$ [$M(CX)_3^-$]; All $M(CX)_2^-$ systems are linear.
[b] $Na(CO)_3^-$ was found unstable dissociating to [Na + 3CO]$^-$.

normal mode. The binding energy of nonplanar $Li(CS)_4$ with respect to $Li(CS)_3$ + CS is 9.3 kcal/mol, and it is expected to be experimentally isolable. We further investigated the existence of other $M(CX)_4$ analogs with no success. Despite the larger dipole moment of CX (X = Se, Te, Po), which points to more stable $Li(CX)_4$ complexes, the steric congestion for these bulkier ligands wins. No bound $Na(CX)_4$ analog was identified, mainly due to the smaller charge density of the central Na^+ ion.

Similar to $Li(CO)_3$ a single electron is delocalized in the π-frame of $Li(CO)_4$ but the Li—C bond is as long as 2.161 Å, 0.115 Å longer than $Li(CO)_3$. Note that the elongation from $Li(CO)_2$ to $Li(CO)_3$ is just 0.034 Å. The combination of the adiabatic binding energy and Li—C elongation indicate a weak electrostatic interaction of the fourth CO unit with the *in situ* Li^+ center. Scheme 4 depicts the proposed bonding for this system, where three bonds are shown as dative and one as electrostatic. The four possible structures are in "equilibrium" (resonance) forming four equivalent bonds.

The $[Li(CO)_3]_2$ Dimer

The $Li(CO)_3$ radical can be visualized as the CH_3 radical. Just as two CH_3 radicals bind together, can two $Li(CO)_3$ make a stable ethane analog? We have probed the stability of $[Li(CO)_3]_2$ dimer under the MP2 level of theory. Its binding energy with respect to two $LiCO_3$ ($\tilde{X}^2A_2''$) monomers is calculated to be 27.2 kcal/mol. Indeed, the two electrons residing at the π-orbital of each $Li(CO)_3$ couple together to form HOMO of $[Li(CO)_3]_2$ shown in Scheme 5. This covalent type of chemical bond has been identified to occur between two π-conjugated radical systems and referred as "pancake chemical bonds" in the literature.[32]

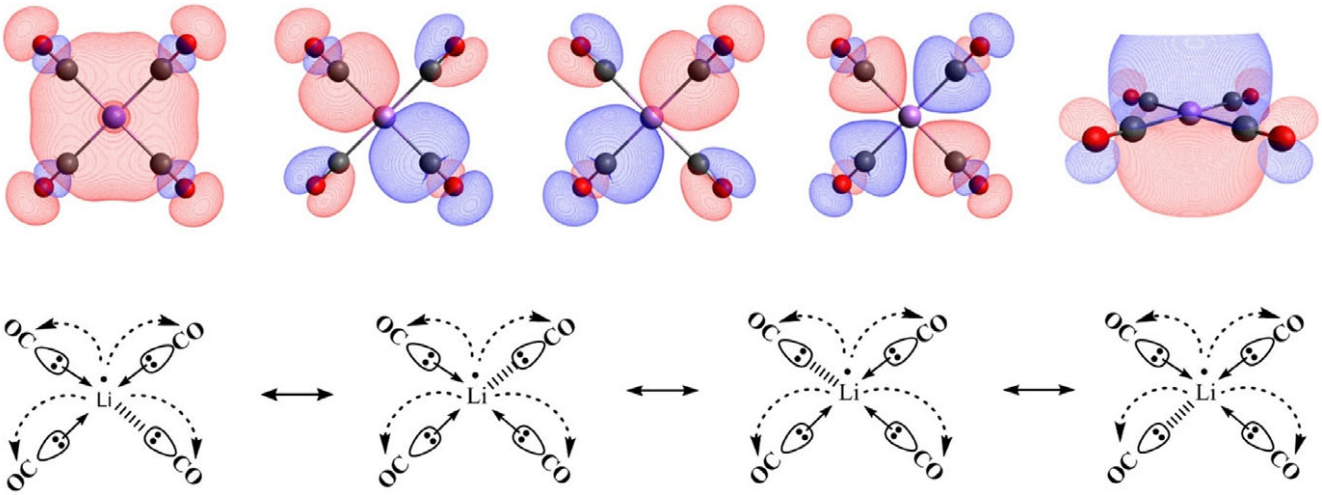

Scheme 4. The five highest energy occupies molecular orbitals (first row) and the proposed bonding scheme (second raw) for $Li(CO)_4$. [Color figure can be viewed at wileyonlinelibrary.com]

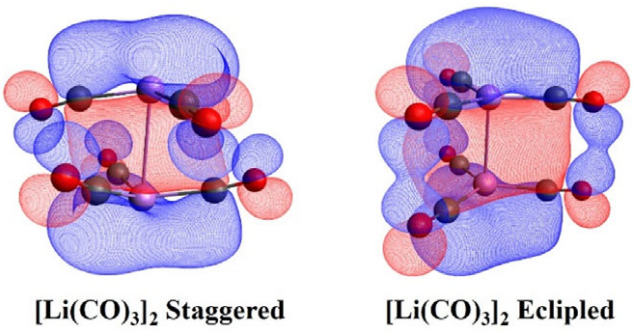

Scheme 5. $[Li(CO)_3]_2$ optimized geometries and their HOMOs. [Color figure can be viewed at wileyonlinelibrary.com]

We studied both staggered and eclipsed conformers for $[Li(CO)_3]_2$ depicted in Scheme 5. In the ground state of the dimer, carbonyls favor the staggered over the eclipsed arrangement. The metastable eclipsed structure lies 1.7 kcal/mol higher. By overriding a barrier of 2.7 kcal/mol the more stable staggered conformer can rotate into its eclipsed geometry. The variation of the energy with the rotation of one monomer is plotted in Figure 4. Here at each rotation angle, all the parameters other than the angle are optimized.

Interestingly, the higher energy eclipsed conformation possesses shorter Li—Li inter nuclear distance than the staggered one by as much as ~0.2 Å (see Table 3). It is also surprising that in both conformers O—C—Li angle is bent toward the other conformer. The O—C—Li bent of staggered conformer is 2.9° lower than that of eclipsed one. We cannot provide any simple explanation for these unusual structural patterns, but they are certainly because of the complex electrostatics of the systems.

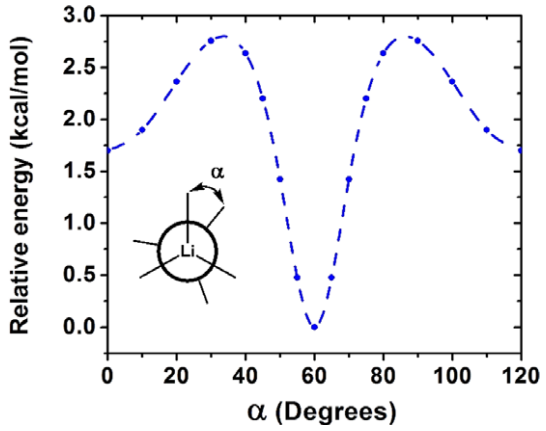

Figure 4. Energy variation for the internal rotation of $[Li(CO)_3]_2$ obtained at MP2 level of theory. [Color figure can be viewed at wileyonlinelibrary.com]

We have examined the existence of other $[M(CX)_{n\ =\ 1,2,3}]_2$ dimers, and found that only $Li(CO)_3$ makes a stable dimer.

Summary

Various alkali metal carbonyls, thiocarbonyls, and complexes with CSe, CTe, and CPo, were studied at a the CCSD(T) level of theory combined with triple-ζ basis sets equipped with a series of diffuse functions. We first calculated the optimal structures, binding energies, and electron affinities for all $M(CX)_{1-3}$ combinations with M = Li, Na, and X = O, S, Se, Te, Po.

After constructing the relevant potential energy profiles, we saw that all complexes are formed from the $M(^2P) + CX(X^1\Sigma^+)$ channel. The excitation of the valence s-electron to the valence p-shell of the metal enhances the exposure of the M^+ core to the incoming CX units. The higher dipole moment of the heavier CX members increases the interaction with the *in situ* metallic charge. Therefore, we found that within every group the binding energy correlates linearly with the dipole moment of CX. Another immediate consequence of the chemical bond formation from the first excited state of the metal is the counter-intuitive (due to the stronger steric effects) increase of the binding energy as we go from mono- to tri-coordinated complexes. The $M(^2S) \rightarrow M(^2P)$ energy penalty is the same among the same-metal species, but the number of M ← CX dative bonds is larger as we add more CX ligands. Finally, the smaller charge density of Na^+ explains the smaller binding energies of the sodium species.

We also commented on the structural properties of these systems. Generally, the addition of more ligands elongates M—C and shortens C—X. The size of terminal X atom plays a minor role to the M-C length as opposed to the size of the central metal.

The anions of these systems were all found stable except $Na(CO)_3$. The electron affinity of MCX is of the order of that of M since the additional electron attaches to the metal end; it increases for $M(CX)_2$ since the additional electron goes to the π-orbital delocalized over the metal and the carbon atom; and it decreases for $M(CX)_3$ since the additional electron is placed in the same orbital with the existing electron.

Finally, we were able to locate some unusual structures such as $Li(CO)_4$, $Li(CS)_4$, and $[Li(CO)_3]_2$. The former two complexes are the only stable $M(CX)_4$ species with respect to their tri-coordinated complexes. The binding of the fourth CO or CS ligand was assigned as electrostatic, while $[Li(CO)_3]_2$ can be seen as the ethane analog. The two $Li(CO)_3$ monomers share their single electrons to make a covalent bond. The staggered conformation is more stable than the eclipsed one, just like

Table 3. MP2 equilibrium bond lengths r_e (Å), equilibrium bond angles ϕ_e (degrees), and binding energies D_e (kcal/mol) for the formation of two conformers of $[Li(CO)_3]_2$ from $2Li(CO)_3$ ($\tilde{X}^2A_2''$).

	r_e			ϕ_e		
$[Li(CO)_3]_2$ Conformer	Li—C	C—O	Li—Li	O—C—Li	C—Li—Li	D_e
Staggered	2.031	1.150	3.052	171.5	78.9	27.2
Eclipsed	2.027	1.148	2.869	174.4	92.8	25.5

ethane. However, unlike ethane, the CO units bend toward the neighboring $Li(CO)_3$ moiety.

Acknowledgment

The authors are indebted to Auburn University for financial support. The computational work was completed in part by the Auburn University Hopper Cluster and in part by the Alabama Supercomputer Center.

Keywords: potential energy curves · stable anions · lithium carbonyl complexes · $[Li(CO)_3]_2$ dimer

How to cite this article: I. R. Ariyarathna, E. Miliordos. *J. Comput. Chem.* **2019**, *40*, 1344–1351. DOI: 10.1002/jcc.25791

Additional Supporting Information may be found in the online version of this article.

[1] O. Yamada, T. Suzuki, J. H. Then, T. Ando, Y. Watanabe, *Fuel Process. Technol.* **1985**, *11*, 297.
[2] K. Xu, H. Peng, J. W. Y. Lam, T. W. H. Poon, Y. Dong, H. Xu, Q. Sun, K. K. L. Cheuk, F. Salhi, P. P. S. Lee, B. Z. Tang, *Macromolecules* **2000**, *33*, 6918.
[3] I. Ojima, C.-Y. Tsai, M. Tzamarioudaki, D. Bonafoux, Organic Reactions, Wiley, Hoboken, NJ, **2000**.
[4] W. Bertleff, Ullmann's Encyclopedia of In/dustrial Chemistry, Wiley-VCH Verlag GmbH & Co. KGaA, Weinheim, Germany, **2000**, p. 1.
[5] P. K. Sazonov, V. A. Ivushkin, V. N. Khrustalev, N. G. Kolotyrkina, I. P. Beletskaya, *Dalt. Trans.* **2014**, *43*, 13392.
[6] C. Poggel, G. Frenking, *Chem. A Eur. J.* **2018**, *24*, 11675.
[7] X. Wu, L. Zhao, J. Jin, S. Pan, W. Li, X. Jin, G. Wang, M. Zhou, G. Frenking, *Science* **2018**, *361*, 912.
[8] A. M. Ricks, Z. E. Reed, M. A. Duncan, *J. Mol. Spectrosc.* **2011**, *266*, 63.
[9] X. Wu, L. Zhao, D. Jiang, I. Fernández, R. Berger, M. Zhou, G. Frenking, *Angew. Chemie Int. Ed.* **2018**, *57*, 3974.
[10] J. Jin, T. Yang, K. Xin, G. Wang, X. Jin, M. Zhou, G. Frenking, *Angew. Chemie Int. Ed.* **2018**, *57*, 6236.
[11] G. Wang, M. Zhou, *Chinese J. Chem. Phys.* **2018**, *31*, 1.
[12] F. A. Cotton, G. Wilkinson, Advanced Inorganic Chemistry, 4th ed., Wiley, New York, **1980**.
[13] A. J. Lupinetti, G. Frenking, S. H. Strauss, *Angew. Chemie Int. Ed.* **1998**, *37*, 2113.
[14] O. Ayed, A. Loutellier, L. Manceron, J. P. Perchard, *J. Am. Chem. Soc.* **1986**, *108*, 8138.
[15] O. Ayed, L. Manceron, B. Silvi, *J. Phys. Chem.* **1988**, *92*, 37.
[16] P. Pullumbi, Y. Bouteiller, J. P. Perchard, *J. Chem. Phys.* **1995**, *102*, 5719.
[17] H. A. Joly, J. A. Howard, *J. Phys. Chem. A* **1997**, *101*, 2817.
[18] B. Silvi, O. Ayed, W. B. Person, *J. Am. Chem. Soc.* **1986**, *108*, 8148.
[19] A. Kalemos, A. Papakondylis, A. Mavridis, *Chem. Phys. Lett.* **1996**, *259*, 185.
[20] I. R. Ariyarathna, E. Miliordos, *J. Phys. Chem. A* **2017**, *121*, 7051.
[21] I. R. Ariyarathna, E. Miliordos, *Int. J. Quantum Chem.* **2018**, *118*, e25673.
[22] T. H. Dunning, *J. Chem. Phys.* **1989**, *90*, 1007.
[23] R. A. Kendall, T. H. Dunning, R. J. Harrison, *J. Chem. Phys.* **1992**, *96*, 6796.
[24] D. E. Woon, T. H. Dunning, *J. Chem. Phys.* **1994**, *100*, 2975.
[25] K. A. Peterson, D. Figgen, E. Goll, H. Stoll, M. Dolg, *J. Chem. Phys.* **2003**, *119*, 11113.
[26] H.-J. Werner, P. J. Knowles, G. Knizia, F. R. Manby, M. Schütz, P. Celani, W. Györffy, D. Kats, T. Korona, R. Lindh, A. Mitrushenkov, G. Rauhut, K. R. Shamasundar, T. B. Adler, R. D. Amos, A. Bernhardsson, A. Berning, D. L. Cooper, M. J. O. Deegan, A. J. Dobbyn, F. Eckert, E. Goll, C. Hampel, A. Hesselmann, G. Hetzer, T. Hrenar, G. Jansen, C. Köppl, Y. Liu, A. W. Lloyd, R. A. Mata, A. J. May, S. J. McNicholas, W. Meyer, M. E. Mura, A. Nicklass, D. P. O'Neill, P. Palmieri, D. Peng, K. Pflüger, R. Pitzer, M. Reiher, T. Shiozaki, H. Stoll, A. J. Stone, R. Tarroni, T. Thorsteinsson, M. Wang, MOLPRO, version **2015**.1, a package of ab initio programs, see http://www.molpro.net (accessed January 17, 2019).
[27] M. J. Frisch, G. W. Trucks, H. B. Schlegel, G. E. Scuseria, M. A. Robb, J. R. Cheeseman, G. Scalmani, V. Barone, G. A. Petersson, H. Nakatsuji, X. Li, M. Caricato, A. V Marenich, J. Bloino, B. G. Janesko, R. Gomperts, B. Mennucci, H. P. Hratchian, J. V Ortiz, A. F. Izmaylov, J. L. Sonnenberg, D. Williams-Young, F. Ding, F. Lipparini, F. Egidi, J. Goings, B. Peng, A. Petrone, T. Henderson, D. Ranasinghe, V. G. Zakrzewski, J. Gao, N. Rega, G. Zheng, W. Liang, M. Hada, M. Ehara, K. Toyota, R. Fukuda, J. Hasegawa, M. Ishida, T. Nakajima, Y. Honda, O. Kitao, H. Nakai, T. Vreven, K. Throssell, J. A. Montgomery Jr., J. E. Peralta, F. Ogliaro, M. J. Bearpark, J. J. Heyd, E. N. Brothers, K. N. Kudin, V. N. Staroverov, T. A. Keith, R. Kobayashi, J. Normand, K. Raghavachari, A. P. Rendell, J. C. Burant, S. S. Iyengar, J. Tomasi, M. Cossi, J. M. Millam, M. Klene, C. Adamo, R. Cammi, J. W. Ochterski, R. L. Martin, K. Morokuma, O. Farkas, J. B. Foresman, D. J. Fox, Gaussian 16, Revision A.03, Gaussian Inc., Wallingford CT, **2016**.
[28] A. Kramida, Y. Ralchenko, J. Reader, N. I. S. T. A. S. D. Team, NIST Atomic Spectra Database (version 5.4), Vol. *2016*, National Institute of Standards and Technology, Gaithersburg, MD, **2016**. http://physics.nist.gov/asd (accessed October 8, 2017).
[29] M. O. Hurst, R. C. Fortenberry, *Comput. Theor. chem.* **2015**, *1069*, 132.
[30] A. Burritt, R. G. A. R. Maclagan, M. R. Morrison, *J. Mol. Struct.* **1992**, *261*, 63.
[31] D. R. Lide, CRC Handbook of Chemistry and Physics, 93rd ed., CRC Press, New York, **2012**.
[32] M. Kertesz, *Chem. - A Eur. J* **2018**, *25*, 400–416. Accepted Article. https://doi.org/10.1002/chem.201802385.

Received: 8 October 2018
Revised: 21 November 2018
Accepted: 6 January 2019
Published online on 12 February 2019

The Versatile Personality of Beryllium: $Be(O_2)_{1-2}$ vs $Be(CO)_{1-2}$

THE JOURNAL OF PHYSICAL CHEMISTRY A

Article

pubs.acs.org/JPCA

The Versatile Personality of Beryllium: $Be(O_2)_{1-2}$ vs $Be(CO)_{1-2}$

Isuru R. Ariyarathna and Evangelos Miliordos*

Department of Chemistry and Biochemistry, Auburn University, Auburn, Alabama 36849, United States

ABSTRACT: To reveal the diverse chemistry of beryllium, we employ multireference methodologies to study the ground and several excited electronic states of the titled beryllium oxides and carbonyls. The two types of complexes serve as model systems to describe the various ways that beryllium can form chemical bonds. $Be(O_2)$, its isomer OBeO, and $Be(O_2)_2$ are ionic compounds where beryllium is best represented in its Be(II) oxidation state. On the other hand, CO induces the excitation of one or two 2s electrons of beryllium to its 2p shell. In this manner, the beryllium core (Be^{2+}) is exposed and enables the formation of dative bonds from the lone pair of carbonyls to Be. For all of the considered electronic states, we provide accurate optimal geometries and excitation energies.

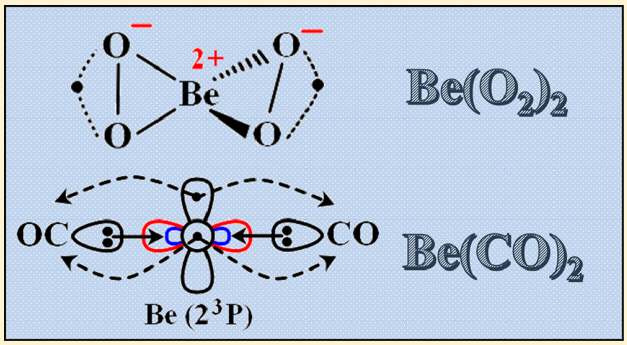

I. INTRODUCTION

Experimental work on beryllium chemistry has been hindered by its high toxicity. Our knowledge on beryllium compounds is gained mostly by theoretical studies.[1] Beryllium bears a ground ^1S state with a $1s^22s^2$ electronic configuration. Its first two excited states, ^3P (at 21 980 cm^{-1}) and ^1P (at 42 565 cm^{-1}), are produced by promoting one 2s electron to the empty 2p shell. We can further promote the second 2s electron generating the three $2p^2$ electronic states ^3P, ^1D, and ^1S. Interestingly, unlike the $1s^22s^22p^2$ configuration of carbon, the lowest among them is ^1D at 56 882 cm^{-1} followed by ^3P at 59 696 cm^{-1}, while ^1S is above the ionization limit.[2] To distinguish the two ^3P states, we call them here 1^3P ($2s^12p^1$) and 2^3P ($2p^2$).

Despite the closed shell nature of its ground state, beryllium has rich chemistry[3] forming tri- and tetra-coordinated complexes.[4−7] Interestingly, under standard conditions of temperature and pressure beryllium is metallic unlike the closed-shell noble gases. The stabilization of the smallest Be_2 and Be_3 clusters has recently been attributed to the involvement of its first excited state 1^3P, which opens the possibility of covalent bonds between the beryllium atoms.[8]

The ionic or covalent nature of beryllium bonds has been the subject of an open debate.[9] Beryllium compounds are described by either invoking a Be^{2+} core[6] or assigning two covalent and one or two dative bonds between Be and its ligands.[4,5] Here we examine the bonding in the recently synthesized and characterized titled beryllium oxides[6,10] and carbonyls (see Figure 1), which have been observed experimentally (infrared spectroscopy) in the past[11] and have redrawn attention very recently.[12] We show that the OBeO isomer is more stable than $Be(O_2)$ and the relative stability of its lowest lying electronic states can be predicted by assuming a $O^-Be^{2+}O^-$ model. The addition of a second O_2 stabilizes the triagonal isomer and generates $Be(O_2)_2$ which is the global BeO_4 minimum and can be described as $Be^{2+}(O_2^-)_2$.[6] On the other hand, BeCO and $Be(CO)_2$ are shown to form via dative bonds from CO to the excited states of Be. $Be(CO)_2$ is found to be linear stemming from the 2^3P state of beryllium. This is a unique paradigm, where a highly lying state of Be with two electrons being promoted from 2s to 2p generates the ground state of a beryllium complex. These two systems reveal the flexibility of beryllium to form both ionic and nonionic (dative) bonds.

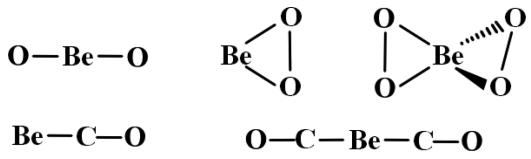

Figure 1. Geometrical structures of OBeO, $Be(O_2)_{1-2}$, and $Be(CO)_{1-2}$.

In section II we provide the computational details of our calculations. sections III and IV pertain to the beryllium oxides and carbonyls, respectively. Our results are summarized in section V.

II. COMPUTATIONAL DETAILS

The multireference character of beryllium complexes, such as beryllium−benzene and beryllium−graphene, has already been mentioned in the literature.[13] Therefore, the construction of the reported full potential energy profiles (PEPs) was achieved by employing the multireference configuration interaction (MRCI) approach which includes all single and double excitations from the reference wave function. In the case of the BeO_2 isomers, the reference multiconfiguration self-consistent field (MCSCF) wave function was produced by allocating 10 valence electrons to 10 valence orbitals. This space includes all valence electrons

Received: July 3, 2017
Revised: August 11, 2017
Published: August 14, 2017

DOI: 10.1021/acs.jpca.7b06519
J. Phys. Chem. A 2017, 121, 7051−7058

and orbitals except the 2s ones of the two oxygen atoms, which are correlated though at the MRCI level. The use of the full valence space for BeO_4 was not possible. Specifically, for the construction of the $O_2 \rightarrow BeO_2$ PEPs, we had to decrease the active space of the reference wave function to only those orbitals that guarantee the correct dissociation. The choice of the appropriate space is rationalized in section III. In the BeCO case, all but $2s_O$ are included in the reference active space. The CO moiety was found to remain intact for all of the examined electronic states along the Be ← CO pathway. Therefore, in the case of $Be(CO)_2$ we included only the valence atomic orbitals of Be in the active space to study the OC → Be ← CO reaction. In all cases, all valence electrons are correlated at the MRCI level. Finally, the Davidson correction (MRCI+Q) was invoked to estimate the missing electron correlation.

For the electronic states with significant single-reference character, we also carried out coupled-cluster calculations in the singles, doubles plus perturbative triples, or CCSD(T), approxiamation. The correlation consistent aug-cc-pVTZ basis set was used for all atoms.[14,15] All calculations were performed with the MOLPRO suite of programs.[16]

Atomic charges were calculated with the iterative Hirshfeld technique which has been shown to be insensitive to the basis set size.[17] The final charges were found to be independent of the chosen promolecular density. The promolecules used for the reported results were built using the electronic densities of $Be(^1S)$, $Be^{2+}(^1S)$, $O(^3P)$, and $O^-(^2P)$.

III. BERYLLIUM OXIDES

This section is divided into four parts which include our results on the OBeO and $Be(O_2)$ isomers, and their interconversion. We finally refer to $Be(O_2)_2$.

III.A. OBeO. Linear OBeO is the most stable structure of BeO_2 composition with a $^3\Sigma_g^-$ ground state.[18] The simpler diatomic beryllium oxide, BeO, has been investigated extensively.[19−22] The bonding in its ground $\tilde{X}^1\Sigma^+$ state has been studied in detail and assigned as ionic with a single σ-bond between $Be^+(^2S)$ and $O^-(^2P)$ in harmony with its large dipole moment (5.9 D).[22] Its large dipole moment is responsible for the three dipole bound electronic states of BeO^-.[23] Considering the ionic character of the Be−O bonds (Be^+O^-)[8] proposed in the literature, where Be is represented as either Be^{2+} or Be^+,[6,8,23] it is natural to consider a $O^-Be^{2+}O^-$ model when two oxygen atoms are present.[6] It is shown that this picture can predict the low-lying electronic states and their relative stability. The central Be^{2+} core $(1s^2)$ is closed shell (^1S), while O^- has a ^2P ground state with a $1s^22s^22p^5$ configuration. If we combine the three $M_L = 0, \pm 1$ components of the two O^- terminals, we produce the following set of singlet and triplet states (Wigner−Witmer rules)

$$^1\{\Sigma_g^+, \Sigma_g^+, \Sigma_u^-, \Pi_g, \Pi_u, \Delta_g\}$$

$$^3\{\Sigma_u^+, \Sigma_u^+, \Sigma_g^-, \Pi_g, \Pi_u, \Delta_u\}$$

These sets of states are indeed the lowest states of OBeO. The $O(^3P) + Be(^1S;1s^22s^2) + O(^3P)$ fragments will produce the exact same states with a set of additional quintet ones, $^5\{\Sigma_g^+,\Sigma_g^+,\Sigma_u^-,\Pi_g,\Pi_u,\Delta_g\}$. Our chemical intuition suggests that the closed shell 2s orbital of the beryllium atom would prevent any covalent bonding. The full PEPs for the simultaneous approach of the two oxygen centers to beryllium are shown in Figure 2. Our numerical results for all of them are listed in Table 1. Observe that these states are grouped in three different clusters.

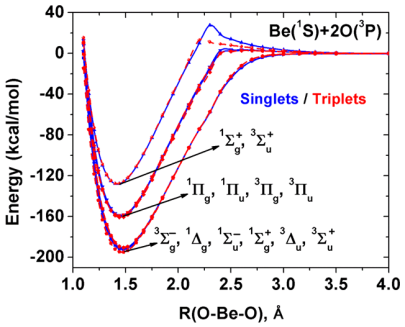

Figure 2. MRCI PEPs as a function of the Be−O distance. The two oxygen atoms are approaching with the same Be−O distance.

Table 1. Optimal Be−O Distances r_e (Å), Equilibrium Energy E_e (au) and Excitation Energies T_e (cm^{-1}) for the Lowest Electronic States of OBeO

state	method	r_e	$-E_e$	T_e
$^3\Sigma_g^-$	MRCI	1.466	164.860362	0.0
	MRCI+Q	1.469	164.888502	0.0
$^1\Delta_g$	MRCI	1.474	164.855505	1066
	MRCI+Q	1.477	164.883826	1026
$^1\Sigma_u^-$	MRCI	1.480	164.854163	1361
	MRCI+Q	1.483	164.882493	1318
$^1\Sigma_g^+$	MRCI	1.478	164.853088	1597
	MRCI+Q	1.481	164.881652	1503
$^3\Delta_u$	MRCI	1.482	164.852625	1698
	MRCI+Q	1.484	164.881005	1645
$^3\Sigma_u^+$	MRCI	1.483	164.851855	1867
	MRCI+Q	1.485	164.880257	1809
$^3\Pi_u$	MRCI	1.452	164.805335	12077
	MRCI+Q	1.457	164.836825	11341
$^1\Pi_g$	MRCI	1.449	164.804049	12359
	MRCI+Q	1.453	164.835483	11636
$^3\Pi_g$	MRCI	1.446	164.802590	12680
	MRCI+Q	1.450	164.833927	11978
$^1\Pi_u$	MRCI	1.452	164.801999	12809
	MRCI+Q	1.457	164.833447	12083
$2^1\Sigma_g^+$	MRCI	1.421	164.752283	23720
	MRCI+Q	1.427	164.786439	22400
$2^3\Sigma_u^+$	MRCI	1.422	164.752246	23729
	MRCI+Q	1.428	164.786315	22427

The first six states lie within 2000 cm^{-1}, the next four are in the range 12000−13000 cm^{-1}, and the last two are almost degenerate at 23725 cm^{-1}. In addition, the equilibrium bond lengths are almost equal within each group: 1.466−1.483, 1.446−1.452, and 1.421−1.422 Å. The PEPs of Figure 2 indicate that the electronic states of the lowest group dissociate rather smoothly to the ground state neutral products, but the rest of the PEPs reveal clearly some avoided crossings related to the ionic nature of the molecule.

Looking at the CI vectors, we notice that the common feature in each group is the number of electrons residing in the σ-frame (see Figure 3). For example, in the lowest energy group the two p_σ orbitals of the two oxygen anions are doubly occupied. This fact enhances the Coulombic attraction between Be^{2+} and the incoming oxygen anions which stabilizes these states further. On the other hand the interelectronic repulsion within the σ-frame seems to push the two terminal oxygen anions further away increasing the Be−O bond length (see Table 1). The bonding in

DOI: 10.1021/acs.jpca.7b06519
J. Phys. Chem. A 2017, 121, 7051−7058

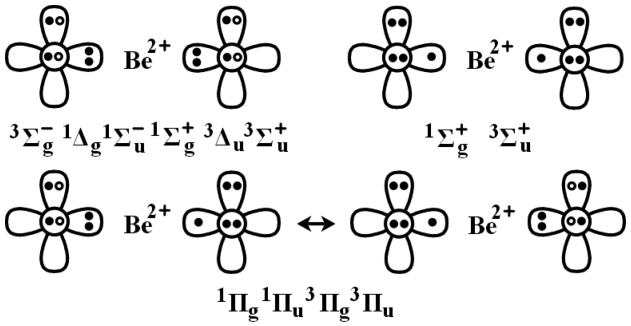

Figure 3. Electronic configurations for the low lying electronic states of OBeO. Open circles define one electron residing in either of the p_π orbitals of the same oxygen atom.

the ground $\tilde{X}^3\Sigma_g^-$ state can be represented by the valence-bond–Lewis (vbL) diagram of Scheme 1.

Scheme 1. vbL Diagram for the $\tilde{X}^3\Sigma_g^-$ of OBeO

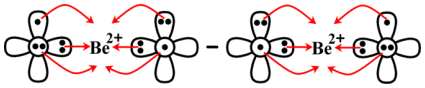

The two pictures of Scheme 1 indicate that the p_π orbitals of each oxygen share 1.5*e*. We represent the electrons participating in such resonances with open circles in Figure 3. The electrons in the π-frame define the overall symmetry of the wave function for all states. The Hirshfeld analysis for the ground state shows that there is an electron transfer of 0.33*e* from each O^- to the various valence orbitals of Be^{2+} reducing its charge to +1.34. The 0.33*e* from each oxygen are transferred almost equally via the σ, π_x, and π_y routes (shown with red arrows in Scheme 1). These small 0.1*e* transfers (six in total) reduce the formal Be^{2+} charge to a value closer to Be^+, but we believe that the Be(II) oxidation state provides a better description and chemically intuitive picture.[6]

III.B. Be(O_2). Two different ionic assignments can be made for the triangular Be(O_2) isomer: $Be^{2+}O_2^{2-}$ or $Be^+O_2^-$. The first one combines two closed-shell moieties and is expected to give a $^1A_1$ state (under C_{2v}). The combination of the ground state of Be^+ (^2S; $1s^22s^1$) with the doubly degenerate O_2^- ($^2\Pi_g$) state provides four states, $^{1,3}A_2$ and $^{1,3}B_2$ (see Figure 4). In all cases we have two

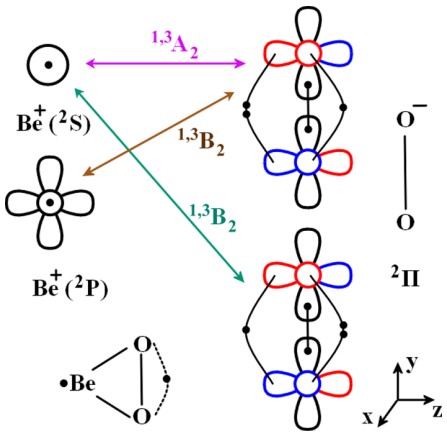

Figure 4. Electronic configurations for the low lying electronic states of Be(O_2) coming from $Be^+O_2^-$. For clarity reasons only the $1\pi_g$ and $3\sigma_g$ orbitals of O_2^- are shown omitting the $1\pi_u^4$ electrons.

unpaired electrons, one localized on Be and one on O_2, coupled to a singlet or a triplet. It should be emphasized that free O_2^{2-} is unstable with respect to O_2^- and O_2 by 6.6 and 6.2 eV at the CCSD(T)/aug-cc-pVTZ level of theory. These values imitate the O^{2-} vs O^- and O values of 6.4 and 5.0 eV, respectively. However, the electrostatic stabilization of *in situ* O^{2-} or O_2^{2-} by some metal cation should not be considered unusual; see for example the iron-oxo complexes of ref 24.

The optimal geometries and excitation energies for the first seven electronic states are given in Table 2. According to the dominant configuration of Table 3 and the molecular orbitals (MO) of Figure 5, the ground state can be fairly ascribed as $Be^{2+}O_2^{2-}$. The $5a_1$, $1b_1$, and $1a_2$ MOs are purely localized on O_2. The remaining occupied $4a_1$ and $3b_2$ orbitals are also highly localized on O_2 but slightly polarized toward beryllium indicating partial electron transfer from O_2^{2-} to Be^{2+}. Similarly, the CI vectors (Table 3) combined with the MOs of the next four states ($^{1,3}A_2$ and $^{1,3}B_2$) point to the bonding schemes of Figure 4 which relate to the $Be^+(^2S;1s^22s^1)$ + $O_2^-(^2\Pi_g)$ fragments. The last two electronic states stem from the first excited state of $Be^+(^2P;1s^22p^1)$, 32000 cm^{-1} above,[2] as shown in Figure 4. Observe that the geometry of the ground state is very different bearing a much shorter Be–O_2 distance and a much longer O–O distance. This trend is in agreement with a $Be^{2+}O_2^{2-}$ vs $Be^+O_2^-$ model. At the CCSD(T) level the O–O bond of free O_2^{2-} is 0.22 Å longer than free O_2^- (1.36 vs 1.58 Å) and the stronger attraction for $Be^{2+}O_2^{2-}$ brings Be and O_2 closer together.

The dipole moment of the ground state is dramatically larger than that of the rest states: 5.7 D vs an average value of 0.5 D (see Table 2). Accordingly, the atomic charge on beryllium is +1.36 for the ground state and +0.2 to +0.4 for the rest six states. The former value is identical to that of the ground state of OBeO which also has a Be^{2+} origin. Although the $Be^+O_2^-$ model provides a reasonable prediction for the nature of the considered excited states, there is certainly a large covalent component judging by the small atomic charges and dipole moments.

To further understand the formation of Be(O_2), we created the PEPs as a function of the Be–O_2 distance (see Figure 6). The O–O distance is kept fixed to that of free O_2. Because of this constraint, the $\tilde{X}^1A_1$ minimum is not the lowest one. The relaxed PEPs around equilibrium for the first three states are given in Figure 7. PEPs for all states (except $\tilde{X}^1A_1$) dissociate smoothly to the neutral products, whereas the PEP of $\tilde{X}^1A_1$ is steeper and undergoes several avoided crossings. All asymptotes pertaining to the inert closed-shell Be(^1S) state produce repulsive PEPs as expected.

The $^{1,3}A_2$ states dissociate to Be(1^3P) + $O_2(X^3\Sigma_g^-)$. Beryllium reacts with the $2s^12p_y^1$ component of 1^3P. The $2s_{Be}$ polarizes away from O_2 ($6a_1$ orbital of Figure 5) to facilitate the donation of electronic density from π_z orbital of O_2 to the empty $2p_z$ of Be ($4a_1$ orbital). The $2p_y$ orbital bears the same symmetry as π_z^* of O_2 allowing the two corresponding unpaired electrons to couple ($3b_2$ orbital). The two bonding interactions are illustrated in Scheme 2. To avoid confusion, the two diagrams of Scheme 2 show only those specific electrons and orbitals (shown in color) involved in the formation of $4a_1$ and $3b_2$. The $4a_1$ and $3b_2$ diagrams of Scheme 2 do not imply Be^{2+} and Be^+ moieties. This covalent-dative interaction produces a small dipole moment for both states of about 0.3 D (see Table 2). The observer electrons, $\sim 2s_{Be}$ ($6a_1$) and π_x^* ($1a_2$), can couple to an open singlet or a triplet state.

DOI: 10.1021/acs.jpca.7b06519
J. Phys. Chem. A 2017, 121, 7051–7058

Table 2. Optimal Be−O_2 and O−O Distances (Å), Equilibrium Energies E_e (au), Excitation Energies T_e (cm^{-1}), and Dipole Moments μ_e (D) for the Seven Lowest Electronic States of $Be(O_2)$

state	method	R(Be−O_2)	R(O−O)	$-E_e$	T_e	μ_e
$\tilde{X}\ ^1A_1$	MRCI	1.135	1.743	164.833637	0.0	5.66
	MRCI+Q	1.136	1.747	164.861369	0.0	
	CCSD(T)	1.144	1.724	164.861673	0.0	
$\tilde{a}\ ^3A_2$	MRCI	1.421	1.373	164.803070	6709	0.29
	MRCI+Q	1.423	1.378	164.827799	7368	
	CCSD(T)	1.424	1.370	164.828214	7343	
$\tilde{A}\ ^1A_2$	MRCI	1.421	1.373	164.802708	6788	0.32
	MRCI+Q	1.423	1.378	164.827406	7454	
$\tilde{b}\ ^3B_2$	MRCI	1.491	1.387	164.752433	17822	0.86
	MRCI+Q	1.494	1.390	164.779428	17984	
	CCSD(T)	1.496	1.384	164.779858	17956	
$\tilde{B}\ ^1B_2$	MRCI	1.489	1.388	164.744206	19628	0.84
	MRCI+Q	1.491	1.391	164.771024	19828	
$\tilde{c}\ ^3B_2$	MRCI	1.428	1.370	164.666523	36677	0.45
	MRCI+Q	1.430	1.374	164.698058	35843	
	CCSD(T)	1.431	1.368	164.700154	35449	
$\tilde{C}\ ^1B_2$	MRCI	1.441	1.367	164.657996	38548	0.23
	MRCI+Q	1.443	1.371	164.689570	37706	

Table 3. Dominant Electronic Configurations for the Seven Lowest Electronic States of $Be(O_2)$

state	$4a_1$	$5a_1$	$6a_1$	$7a_1$	$1b_1$	$2b_1$	$3b_2$	$4b_2$	$5b_2$	$1a_2$
$\tilde{X}\ ^1A_1$	2	2	0	0	2	0	2	0	0	2
$\tilde{a}\ ^3A_2$	2	2	1	0	2	0	2	0	0	1
$\tilde{A}\ ^1A_2$	2	2	1	0	2	0	2	0	0	1
$\tilde{b}\ ^3B_2$	2	2	1	0	2	0	1	0	0	2
$\tilde{B}\ ^1B_2$	2	2	1	0	2	0	1	0	0	2
$\tilde{c}\ ^3B_2$	2	2	0	0	2	1	2	0	0	1
$\tilde{C}\ ^1B_2$	2	2	0	0	2	1	2	0	0	1

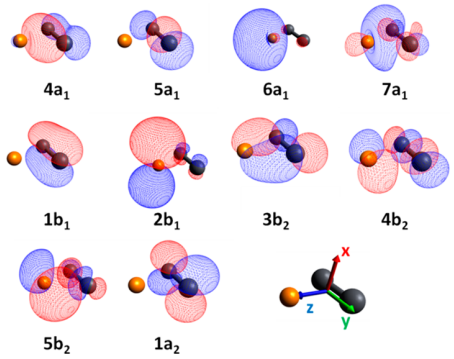

Figure 5. Valence MOs of $Be(O_2)$. Beryllium is shown in orange and oxygen in gray.

Similar observations can be made for the rest of the excited states. For example, the last two states, $\tilde{c}\ ^3B_2$ and $\tilde{C}\ ^1B_2$, differ from $^{1,3}A_2$ only in that $4a_1 \sim 2s_{Be}$ is replaced by $2b_1 \sim 2p_{x,Be}$.

III.C. OBeO ↔ $Be(O_2)$. Figure 8 illustrates the energy variation as a function of the O−Be−O angle θ for selected states. Linear OBeO corresponds to $\theta = 180°$, whereas angles smaller than 80° relate to the triangular $Be(O_2)$ isomer. The linear structures are always more stable than the triangular ones. Note that the ground state of $Be(O_2)$ is a shallow minimum and decays to OBeO after a minor barrier of less than 1 kcal/mol. On the other hand, the first two excited states ($^{1,3}A_2$) of $Be(O_2)$ are quite stable and need to overcome an energy barrier of about 45 kcal/mol to convert to the clearly more stable linear OBeO minima ($^1\Sigma_u^-$, $^3\Delta_u$). Finally the ground state $^3\Sigma_g^-$ of OBeO is not connected to any stationary $Be(O_2)$ structure.

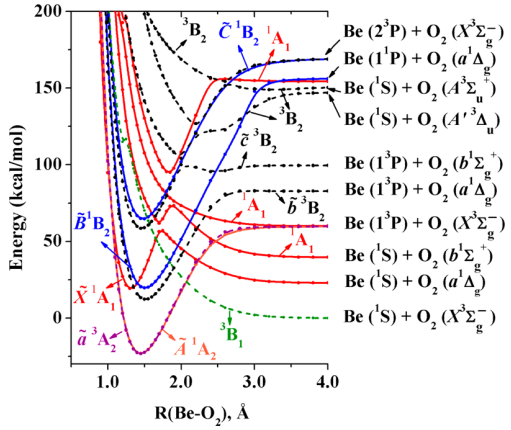

Figure 6. Bound and selected repulsive MRCI PEPs of $Be(O_2)$ as a function of the Be−O_2 distance. The O−O distance is kept fixed at 1.21 Å.

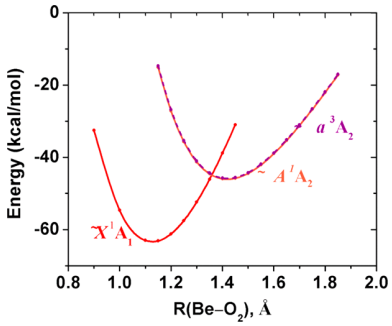

Figure 7. MRCI PEPs of the first three states of $Be(O_2)$ as a function of the Be−O_2 distance around their equilibrium structures. The O−O distance is optimized as each Be−O_2 distance.

III.D. $Be(O_2)_2$. The global minimum of the BeO_4 species has been shown recently to be $Be(O_2)_2$,[6] the structure of which is D_{2d}

DOI: 10.1021/acs.jpca.7b06519
J. Phys. Chem. A 2017, 121, 7051−7058

Scheme 2. vbL Diagrams for the Two Bonding MOs of $Be(O_2)$

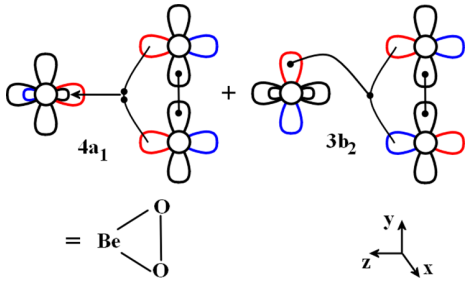

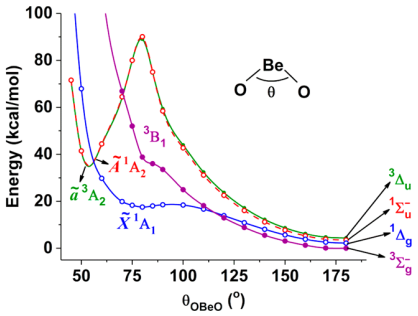

Figure 8. Fully relaxed MRCI PEPs of selected states as a function of the O−Be−O angle connecting the linear OBeO ($\theta = 180^o$) with triangular $Be(O_2)$ ($\theta < 80°$).

(see Figure 1). On the basis of the Hirshfeld beryllium charge of +1.22, which resembles that of $O^-Be^{2+}O^-$ and $Be^{2+}O_2^{2-}$, we consider a $O_2^-(^2\Pi_g)$ Be^{2+} $O_2^-(^2\Pi_g)$ bonding scheme. The CI expansion along with the corresponding natural orbitals suggest the bonding of Scheme 3 for the lowest two electronic states, $^{1,3}B_2$.

Scheme 3. Bonding Scheme for $^{1,3}B_2$ States of $Be(O_2)_2$[a]

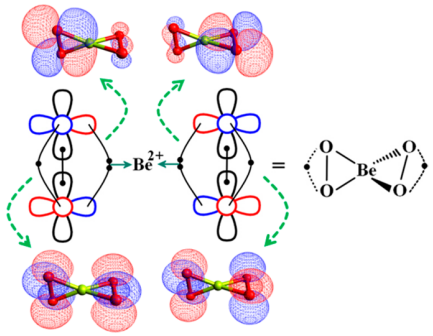

[a]The π^* Orbitals of O_2^- are highlighted.

Similar to OBeO, the electronic configuration with the electron pairs along the intermolecular axis is favored. The calculated geometries for the lowest two states and their energy difference are given in Table 4. Our multireference calculations predict the open-shell singlet lower by 122 cm^{-1}. CCSD calculations predicted the triplet state to be the ground state.[6] CCSD is unable to capture the open-shell singlet without any special treatment, such as equation-of-motion spin-flip CCSD.[25] It is unclear to us if these authors applied such an approach.

The MRCI PEPs for the dissociation of the two lowest states to $Be(O_2)$ + O_2 are shown in Figure 9. The active space of the reference MCSCF wave function was limited to the $6a_1$, $2b_1$, $3b_2$,

Table 4. Optimal Be−O_2 and O−O Distances (Å), Equilibrium Energies E_e (au), and Excitation Energies T_e (cm^{-1}) for the Two Lowest Electronic States of $Be(O_2)_2$[a]

state	method	R(Be−O_2)	R(O−O)	$-E_e$	T_e
$\tilde{X}\ ^1B_2$	MRCI	1.416	1.317	314.903274	0.0
	MRCI+Q	1.420	1.346	315.044839	0.0
$\tilde{a}\ ^3B_2$	MRCI	1.417	1.317	314.902867	92
	MRCI+Q	1.421	1.346	315.044283	122
	CCSD(T)	1.427	1.372	315.102265	

[a]Minimal active space was used for MCSCF including only the two unpaired electrons. All valence electrons were correlated at the MRCI level.

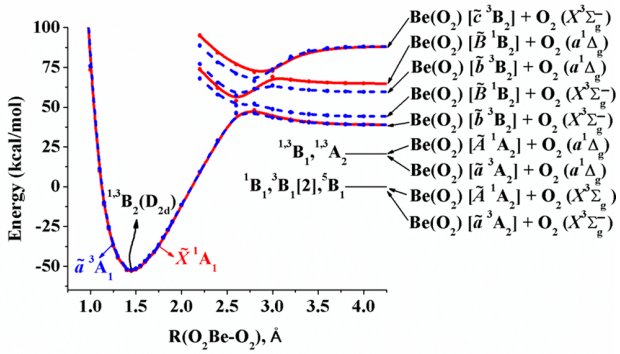

Figure 9. PEPs for the $^1A_1$ (red lines) and $^3A_1$ (blue lines) states of $Be(O_2)_2$ as a function of the O_2Be-O_2 distance.

and $1a_2$ MOs of $Be(O_2)$ and the 2p orbitals of the two oxygen atoms of the attacking O_2. These orbitals are the "active" ones (not always doubly occupied) for the lowest seven studied $Be(O_2)$ states and are prone to making covalent bonds (see Table 3). Therefore, they were deemed necessary for the correct dissociation of the O_2−$Be(O_2)$ PEPs to these states. All valence electrons are correlated at the CI level. The symmetry along this reaction pathway is C_{2v} and therefore the irreducible representation of the two states becomes $^{1,3}A_1$ away from the equilibrium. Both states dissociate to $Be(O_2)$ $[\tilde{b}^3B_2]$ + $O_2(X^3\Sigma_g^-)$ but coming naturally from $Be(O_2)$ $[\tilde{c}^3B_2]$ + $O_2(X^3\Sigma_g^-)$ via several avoided crossings. The underlying electronic transformations during the approach of the latter fragments can be captured by the binding interactions of Scheme 4. Similarly to Scheme 2, for clarity of the picture we only show those electrons and orbitals (shown in color) involved in the formation of the two bonds. The rest of the oxygen electrons ($1\sigma_g2\sigma_g1\sigma_u2\sigma_u$) are implied and the electrons shown as open circles indicate an electron shared between the p_π atomic orbitals of the two oxygen atoms. At

Scheme 4. Binding Interactions between $Be(O_2)$ $[\tilde{c}\ ^3B_2]$ + $O_2(X\ ^3\Sigma_g^-)$ Leading to $^{1,3}B_2$ States of $Be(O_2)_2$

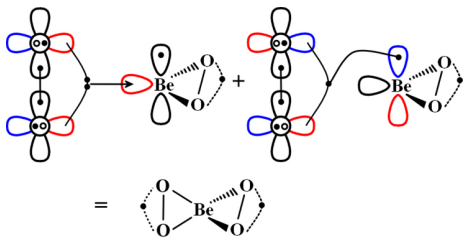

DOI: 10.1021/acs.jpca.7b06519
J. Phys. Chem. A 2017, 121, 7051−7058

equilibrium both bonding interactions are polarized toward O_2 leading to the aforementioned ionic picture.

An interesting observation is that the Be−O_2 and O−O bond lengths of $Be(O_2)_2$ and the parent $\tilde{c}\ ^3B_2$ $Be(O_2)$ are practically identical [see the CCSD(T) values in Tables 2 and 4]. This can be explained by the fact that the $Be(O_2)$ ring of the parent state has the same bonding pattern as the two $Be(O_2)$ rings of $Be(O_2)_2$; compare Schemes 2 and 4.

IV. BERYLLIUM CARBONYLS

Stable beryllium−carbonyl bonds had been predicted theoretically[26,27] before they were detected experimentally in 1995.[11] Only recently complexes have such been revisited.[12] The goal of the present work is to furnish a first in-depth study of the ground and excited states of the simplest possible beryllium carbonyls, BeCO and $Be(CO)_2$. Potential energy curves are constructed to provide the *in situ* electronic state of beryllium. It is shown that the promotion of one or two 2s electrons to the 2p orbitals allows the more effective donation of electronic density from CO to Be. In fact, the ground state of $Be(CO)_2$ originates from 2^3P and the first two excited states from ^1D, both of which have $1s^22p^2$ configuration.

IV.A. BeCO. Figure 10 shows the PEPs as a function of the Be−CO distance. The ground state fragments, Be(^1S) + CO($^1\Sigma^+$), are both closed-shell and they reveal only a weak attraction at 4.5 Å. The first two excited states of Be ($1^{1,3}P$) with a $1s^22s^12p^1$ configuration have an empty p_σ orbital which can accommodate electronic density from the incoming carbonyl. The 2s electron polarizes away from CO to facilitate this donation. A π-back-donation from Be to CO has been proposed recently for similar beryllium−carbonyl complexes.[12] The result is the formation of the $^{1,3}\Pi$ states of BeCO. We also drew the curve originating from Be (2^3P) with a $1s^22p^2$ configuration. We see that this also generates a strongly bound $^3\Sigma^-$ state, the bonding of which can be described as in Scheme 5. For clarity reasons the bonding $1\pi_x^2 1\pi_y^2$ electrons of CO are omitted.

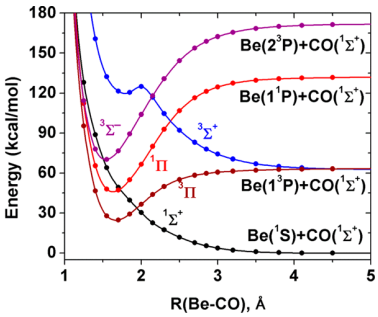

Figure 10. MRCI PEPs of BeCO as a function of the Be−CO distance.

The optimal structures of the three states are listed in Table 5. In all cases, the CO bond has been elongated significantly from the free CO bond length of 1.136 Å at CCSD(T). This can be explained by the back-donation of electrons from Be ($2p_\pi$) to CO ($1\pi_g$) in the π-frame which weakens the triple bond of free CO. Most importantly, carbonyl more closely approaches Be ($2^3P;2p^2$) [$^3\Sigma^-$ state, R(Be−CO) = 1.529 Å] than Be ($1^{1,3}P;2s^12p^1$) [$^{1,3}\Pi$ states, R(Be−O) = 1.668 Å]. It seems that the $2s^1$ electron, although polarized away, exerts some Coulombic repulsion along the σ-frame which is not present in the 2^3P state. The equilibrium energy of all of these states is above the ground state fragments which may explain that BeCO has not been detected experimentally.[11]

Scheme 5. Bonding Scheme for the $^3\Sigma^-$ State of BeCO

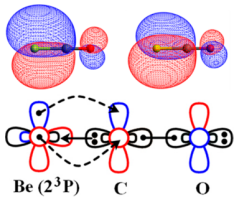

Table 5. Optimal Be−CO and C−O distances (Å), equilibrium energies E_e (a.u.), and excitation energies T_e (cm^{-1}) for the three lowest electronic states of BeCO and OCBeCO

state	method	R(Be−CO)	R(C−O)	$-E_e$	T_e
		BeCO			
$^3\Pi$	MRCI	1.660	1.148	127.701727	0.0
	CCSD(T)	1.668	1.163	127.751360	0.0
$^1\Pi$	MRCI	1.648	1.163	127.681990	4332
$^3\Sigma^-$	MRCI	1.531	1.164	127.639239	13714
	CCSD(T)	1.539	1.181	127.693847	12623
		OCBeCO			
$^3\Sigma_g^-$	MRCI	1.608	1.133	240.805501	0.0
	CCSD(T)	1.612	1.157	240.966285	0.0
$^1\Delta_g$	MRCI	1.610	1.135	240.789977	4332
$^1\Sigma_g^+$	MRCI	1.620	1.135	240.778924	13714

IV.B. $Be(CO)_2$. As opposed to BeCO, $Be(CO)_2$ has been identified by means of infrared spectroscopy.[11] The first theoretical calculation, at the Hartree−Fock (HF) level, showed that the ground state is triplet and is bent with an OC−Be−CO angle of 110°.[11] Although at the HF level we were able to reproduce their optimal structure, our CCSD(T) calculations could not locate a bent minimum. Our CCSD(T) energy at the HF optimized geometry was 0.01 au higher than our linear CCSD(T) global minimum.

Figure 11 includes the energy curves of selected states for the concerted approach of the two carbonyls toward beryllium in a linear fashion. The Be (^1S) + 2CO ($^1\Sigma^+$) interaction is repulsive but turns attractive at shorter distances due to the avoided crossing with a $^1\Sigma^+$ state coming from Be ($^1D;2p^2$) + 2CO ($^1\Sigma^+$). The curves from Be (1^3P) are repulsive due to the presence of the 2s electron which hinders the approach of the incoming carbonyls. The ground state $^3\Sigma_g^-$ hails from Be (2^3P), and its bonding can be depicted by Scheme 6.

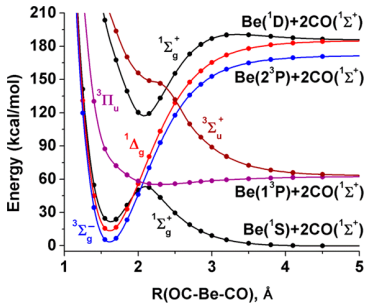

Figure 11. MRCI PEPs for the simultaneous linear approach of the two carbonyls to beryllium.

DOI: 10.1021/acs.jpca.7b06519
J. Phys. Chem. A 2017, 121, 7051−7058

Scheme 6. Bonding Scheme for the Ground State $^3\Sigma_g^-$ of $Be(CO)_2$

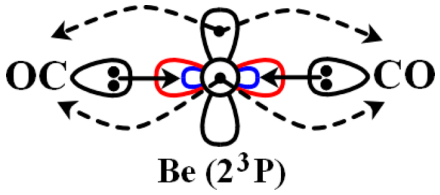

Two dative bonds combined with π-back bonding is observed similarly to the $^3\Sigma^-$ state of BeCO. In the $^1\Delta_g$ and $^1\Sigma_g^+$ states, the two electrons also reside at the $2p_x$ or $2p_y$ orbitals of Be but are coupled into a singlet (both $^1\Delta_g$ components are listed):

$$|^1\Sigma_g^+\rangle \sim |2p_x^{\,2}\rangle + |2p_y^{\,2}\rangle$$

$$|^1\Delta_g\rangle \sim |2p_x^{\,2}\rangle - |2p_y^{\,2}\rangle$$

$$|^1\Delta_g\rangle \sim |2p_x\overline{2p_y}\rangle - |\overline{2p_x}2p_y\rangle$$

All three states of BeCO are of multireference character. The MRCI Be−CO and BeC−O equilibrium distances are 1.61 and 1.13 Å for all of them (see Table 5). The $^1\Delta_g$ and $^1\Sigma_g^+$ states lie at 3407 and 5833 cm^{-1}, respectively. The MCSCF active space used was just the 2s and 2p of Be but all valence electrons were correlated in MRCI.

An interesting observation relative to the CO bond length is in order (see Table 5). Free CO has a bond distance of 1.136 Å, which increases to 1.181 Å in the $^3\Sigma^-$ state of BeCO. In the sister $^3\Sigma_g^-$ state of $Be(CO)_2$ the CO length becomes 1.157 Å, which is right in the middle of the other two. The reason becomes obvious after comparing Schemes 5 and 6. Two electrons of Be are reserved for π-back-donation in both molecules. Therefore, half of the electrons transferred in BeCO are transferred to each CO of $Be(CO)_2$. Therefore, the weakening effect of the CO bond has to be twice as strong in the BeCO case resulting in a twice larger elongation of the CO bond.

The Be(^{1}S) → Be(2^3P) CCSD(T) excitation energy is 172 kcal/mol. The CCSD(T) binding energy of the first CO to Be(2^3P) is 117 kcal/mol (see Figure 10). The second CO binds more weakly, but the overall stabilization because of both carbonyls is 186 kcal/mol. This brings $Be(CO)_2$ 14 kcal/mol lower than the lowest Be + 2CO asymptote, which explains why $Be(CO)_2$ was experimentally observed while BeCO was not.[11]

V. CONCLUSIONS

We selected O_2 and CO to disclose the diverse chemical activity of Be. O_2 expresses its ionic nature causing the *in situ* formation of Be^{2+}. Specifically, the most stable structure of BeO_2 is linear OBeO which can be viewed as $O^-Be^{2+}O^-$. The ground state of $Be(O_2)$ was found to be metastable with a $Be^{2+}O_2^{2-}$ character. The excited states have a rather covalent character and are stably separated from OBeO by high energy barriers. The introduction of a second O_2 stabilizes considerably the sixth excited state of $Be(O_2)$ producing the highly ionic $Be^{2+}(O_2^-)_2$ complex.

On the other hand, CO induces the excitation of one or two 2s electrons of Be to its 2p shell. In this way, beryllium can accommodate dative bonds from the lone electron pair localized on carbon. The formation of a single Be←CO bond, accompanied by a π-back-donation, is not enough to compensate for the beryllium excitation cost. On the contrary two dative bonds may enable an excitation as expensive as the two-electron promotion from 2s to 2p of Be.

Numerical results and full PEPs have been produced for the ground and several excited electronic states at the MRCI and CCSD(T) level of all systems examined. Our study provides the basis for the comprehension of more exotic beryllium complexes and the reference for future experimental characterization of the present model systems.

AUTHOR INFORMATION

Corresponding Author

*(E.M.) E-mail: emiliord@auburn.edu.

ORCID

Evangelos Miliordos: 0000-0003-3471-7133

Notes

The authors declare no competing financial interest.

ACKNOWLEDGMENTS

The authors are indebted to Auburn University for financial support.

REFERENCES

(1) Puchta, R. A brighter beryllium. *Nat. Chem.* **2011**, *3*, 416.
(2) Kramida, A.; Ralchenko, Yu.; Reader, J. NIST ASD Team 2016. *NIST Atomic Spectra Database* (version 5.4). Available: http://physics.nist.gov/asd (Tue May 23 2017). National Institute of Standards and Technology: Gaithersburg, MD.
(3) Arrowsmith, M.; Braunschweig, H.; Celik, M. A.; Dellermann, T.; Dewhurst, R. D.; Ewing, W. C.; Hammond, K.; Kramer, T.; Krummenacher, I.; Mies, J.; Radacki, K.; Schuster, J. K. Neutral Zero-Valent s-Block Complexes with Strong Multiple Bonding. *Nat. Chem.* **2016**, *8*, 890−894.
(4) Braunschweig, H.; Gruss, K.; Radacki, K. Complexes with Dative Bonds Between d- and s-Block Metals: Synthesis and Structure of $[(Cy_3P)_2Pt\text{-}Be(Cl)X]$ (X = Cl,Me). *Angew. Chem., Int. Ed.* **2009**, *48*, 4239−4241.
(5) Iversen, K. J.; Couchman, S. A.; Wilson, D. J. D.; Dutton, J. L. Modern Organometallic and Coordination Chemistry of Beryllium. *Coord. Chem. Rev.* **2015**, *297−298*, 40−48.
(6) Zhang, Q.; Jerabek, P.; Chen, M.; Zhou, M.; Frenking, G. The Oxygen-Rich Beryllium Oxides BeO_4 and BeO_6. *Angew. Chem., Int. Ed.* **2016**, *55*, 10863−10867.
(7) Buchner, M. R.; Müller, M.; Rudel, S. R. Beryllium Phosphine Complexes: Synthesis, Properties, and Reactivity of $(PMe_3)_2BeCl_2$ and $(Ph_2PC_3H_6PPh_2)BeCl_2$. *Angew. Chem., Int. Ed.* **2017**, *56*, 1130−1134.
(8) Kalemos, A. The nature of the Chemical Bond Be_2^+, Be_2, Be_2^-, and Be_3. *J. Chem. Phys.* **2016**, *145*, 214302.
(9) Yáñez, M.; Sanz, P.; Mó, O.; Alkorta, I.; Elguero, J. Beryllium Bonds, Do They Exist? *J. Chem. Theory Comput.* **2009**, *5*, 2763−2771.
(10) Zhou, Z.; Li, Y.; Zhuang, J.; Chen, M.; Zhao, Y.; Zheng, X.; Zhou, M.; et al. Formation and Characterization of Two Interconvertible Side-On and End-On Bonded Beryllium Ozonide Complexes. *J. Phys. Chem. A* **2011**, *115*, 9947−9953.
(11) Andrews, L.; Tague, T. J.; Kushto, G. P.; Davy, R. D. Infrared Spectra of Beryllium Carbonyls from Reactions of Beryllium Atoms with Carbon Monoxide in Solid Argon. *Inorg. Chem.* **1995**, *34*, 2952−2961.
(12) Saha, R.; Pan, S.; Frenking, G.; Chattaraj, P. K.; Merino, G. The Strongest CO binding and the Highest C-O Stretching Frequency. *Phys. Chem. Chem. Phys.* **2017**, *19*, 2286−2293.
(13) Fernandez, N.; Ferro, Y.; Carissan, Y.; Marchois, J.; Allouche, A. The Interaction of Beryllium with Benzene and Graphene: A Comparative Investigation Based on DFT, MP2, CCSD(T), CAS-SCF and CAS-PT2. *Phys. Chem. Chem. Phys.* **2014**, *16*, 1957−1966.
(14) Dunning, T. H., Jr. Gaussian Basis Sets for Use in Correlated Molecular Calculations. I. The Atoms Boron Through Neon and Hydrogen. *J. Chem. Phys.* **1989**, *90*, 1007−1023.

DOI: 10.1021/acs.jpca.7b06519
J. Phys. Chem. A 2017, 121, 7051−7058

(15) Kendall, R. A.; Dunning, T. H., Jr.; Harrison, R. J. Electron Affinities of the First-Row Atoms Revisited. Systematic Basis Sets and Wave Functions. *J. Chem. Phys.* **1992**, *96*, 6796−6806.
(16) Werner, H.-J.; Knowles, P. J.; Knizia, G.; Manby, F. R.; Schütz, M.; et al. *MOLPRO*, version 2015.1, a package of ab initio programs; see http://www.molpro.net.
(17) Miliordos, E.; Harrison, J. F. Hirshfeld Density Partitioning Technique: A First Application to the Transition Metal Compounds, HScO, TiO, VO. *J. Chem. Phys.* **2013**, *138*, 184305.
(18) Bauschlicher, C. W., Jr.; Partridge, H.; Sodupe, M.; Langhoff, S. R. Theoretical Study of the Alkaline-Earth Metal Superoxides BeO_2 through SrO_2. *J. Phys. Chem.* **1992**, *96*, 9259−9264.
(19) Boldyrev, A. I.; Simons, J. Ab Initio Study of the Strong Binding of BeO to Li, Be, and B Atoms in the Hyperstoichiometric LiOBe, BeOBe, and BeOB Molecules. *J. Phys. Chem.* **1995**, *99*, 15041−15045.
(20) Buenker, R. J.; Liebermann, H.-P.; Pichl, L.; Tachikawa, M.; Kimura, M. Role of the Electric Dipole Moment in Positron Binding to the Ground and Excited States of the BeO Molecule. *J. Chem. Phys.* **2007**, *126*, 104305.
(21) Yu, H.; Truhlar, D. G. Components of the Bond Energy in Polar Diatomic Molecules, Radicals, and Ions Formed by Group-1 and Group-2 Metal Atoms. *J. Chem. Theory Comput.* **2015**, *11*, 2968−2983.
(22) Kalemos, A. The Nature of the Chemical Bond in $BeO^{0,-}$, $BeOBe^{+,0,-}$, and in Their Hydrogenated Products $HBeO^{0,-}$, BeOH, HBeOH, $BeOBeH^{+,0,-}$, and HBeOBeH. *J. Chem. Phys.* **2017**, *146*, 104307.
(23) Gutsev, G. L.; Nooijen, M.; Bartlett, R. J. Valence and Excited Dipole-bound States of Polar Diatomic Anions: LiH^-, LiF^-, $LiCl^-$, NaH^-, NaF^-, $NaCl^-$, BeO^-, and MgO^-. *Chem. Phys. Lett.* **1997**, *276*, 13.
(24) Kazaryan, A.; Baerends, E. J. Ligand Field Effects and the High Spin-High Reactivity Correlation in the H Abstraction by Non-Heme Iron(IV)-Oxo Complexes: A DFT Frontier Orbital Perspective. *ACS Catal.* **2015**, *5*, 1475.
(25) Levchenko, S. V.; Krylov, A. I. Equation-of-Motion Spin-Flip Coupled-Cluster Model with Single and Double Substitutions: Theory and Application to Cyclobutadiene. *J. Chem. Phys.* **2004**, *120*, 175.
(26) Frenking, G.; Koch, W.; Collins, J. R. Fixation of Nitrogen and Carbon Monoxide by Beryllium Oxide: Theoretical Investigation of the Structures and Stabilities of NNBeO, OCBeO, and COBeO. *J. Chem. Soc., Chem. Commun.* **1988**, 1147.
(27) Sunil, K. K. The Nature of Bonding and Stability of $(CO)_2Be$-$Be(CO)_2$: A Molecule with a Be-Be Double Bond. *J. Am. Chem. Soc.* **1992**, *114*, 3985−3986.

DOI: 10.1021/acs.jpca.7b06519
J. Phys. Chem. A 2017, 121, 7051−7058

Dative bonds versus electron solvation in tri–coordinated beryllium complexes: $Be(CX)_3$ [X = O, S, Se, Te, Po] and $Be(PH_3)_3$ versus $Be(NH_3)_3$

Volume 118 | Issue 18 | September 15, 2018

International Journal of QUANTUM CHEMISTRY

www.q-chem.org

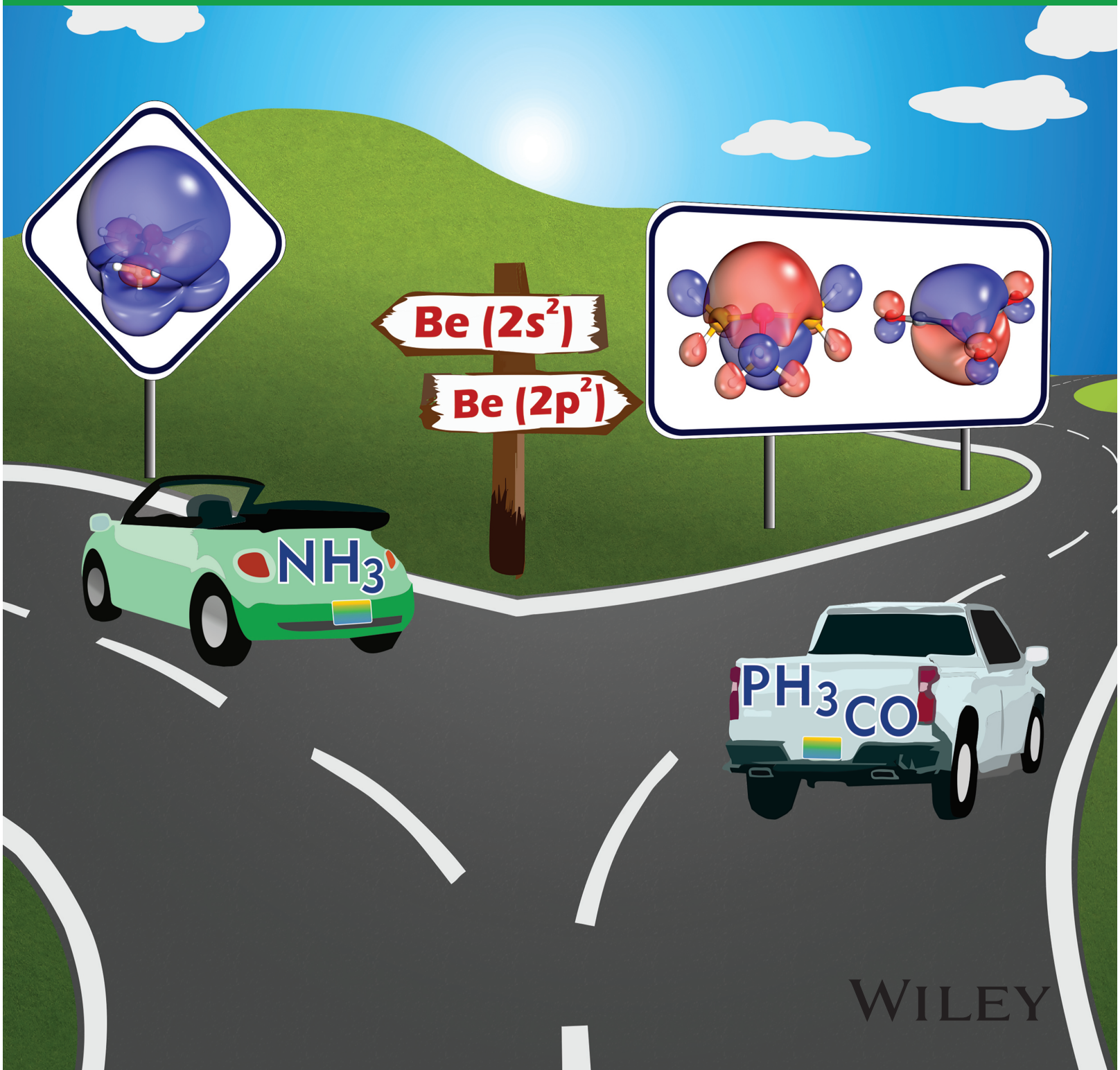

WILEY

Received: 15 February 2018 | Revised: 9 April 2018 | Accepted: 7 May 2018

DOI: 10.1002/qua.25673

WILEY International Journal of QUANTUM CHEMISTRY

FULL PAPER

Dative bonds versus electron solvation in tri-coordinated beryllium complexes: $Be(CX)_3$ [X = O, S, Se, Te, Po] and $Be(PH_3)_3$ versus $Be(NH_3)_3$

Isuru R. Ariyarathna | Evangelos Miliordos

Department of Chemistry and Biochemistry, Auburn University, Auburn, Alabama

Correspondence
Evangelos Miliordos, Department of Chemistry and Biochemistry, Auburn University, Auburn, AL 36849.
Email: emiliord@auburn.edu

Funding information
Auburn University

Abstact

The formation mechanism and bonding scheme for the titled molecules is proposed based on high-level theoretical calculations. All species are formed via three dative bonds from the ligands to Be. For $Be(CX)_3$ [X = O, S, Se, Te, Po] species and $Be(PH_3)_3$ the two electrons of beryllium are promoted from 2s to 2p facilitating these bonds. At the same time, electronic density is donated toward the ligands via the π-frame. In contrast, ammonia partly solvates the valence 2s electrons of Be, which are delocalized in the periphery of the molecule. Based on the proton affinity of all of these complexes and their derivatives, we found that they are strong Lewis bases. For example, $Be(PMe_3)_3$ is stronger than ammonia and its ethyl substituted analogue and could serve as the basis of more efficient frustrated Lewis pairs.

KEYWORDS

beryllium, electron solvation, excited states, frustrated Lewis pairs, tri-coordinated complexes

1 | INTRODUCTION

Beryllium is one of the less studied elements of the periodic table. In spite of its rich and diverse chemical activity,[1,2] the experimental interest is limited compared to its alkaline earth counterparts and other elements due to its high toxicity.[3] Theory provides a safer alternative toward the comprehension of its bonding patterns.[4] It has been found that despite the closed-shell nature of its ground state ($1s^2 2s^2$), beryllium forms all kinds of chemical bonds: beryllium complexes are stabilized by dative, covalent, or ionic binding schemes.[5–8]

Our recent theoretical work on $Be(O_2)_{1\text{-}2}$ and $Be(CO)_{1\text{-}2}$ showed that beryllium oxides are highly ionic systems bearing a Be^{2+} character, while carbonyls form Be←CO dative bonds and receive electronic density via π back-bonding.[5] These bidirectional dative bonding is facilitated by the $^{1,3}P$ ($1s^2 2s^1 2p^1$) and ^1D, ^3P ($1s^2 2p^2$) excited states of beryllium lying between 20 000 and 60 000 cm^{-1} above its ground ^1S ($1s^2 2s^2$) state.[9] The promotion of one or two electrons from 2s to 2p unveils the nuclear charge of beryllium and enables the donation of electrons to the empty 2p orbitals. $Be(CO)_2$ is linear, OCBeCO, and both valence beryllium electrons occupy two 2p orbitals (p_x, p_y). The electron σ-pairs localized on the carbons of the two carbonyls invade the two sp_z hybrids made by the vacant 2s and remaining $2p_z$ orbitals. In the first three electronic states the two electrons of beryllium occupy both $2p_x$ and $2p_y$: $^3\Sigma_g^-(2p_x^1 2p_y^1)$, $^1\Delta_g(2p_x^2 - 2p_y^2)$, $^1\Sigma_g^+(2p_x^2 + 2p_y^2)$. Can these two electrons reside in one of the $2p_x$, $2p_y$ releasing an additional 2p and opening the possibility of a third Be←CO bond? The answer is yes and indeed $Be(CO)_3$ has been shown theoretically to be stable revealing Lewis base features.[10] Experimentally, some infrared absorption bands of beryllium carbonyl compounds in solid argon were assigned to $Be(CO)_3$ more than 20 years ago.[11]

A couple of naturally forthcoming questions are: Can other σ-donors produce similar complexes? How important is π back-bonding in stabilizing such complexes? To provide useful insights we studied several other tri-coordinated complexes. We first employed carbonyl and its isovalent species, CX where X = O, S, Se, Te, Po. We then used ammonia, which is a pure σ-donor, and phosphine, which is also a strong σ-donor but has some π-acidity too.[12] The structures of the examined species are shown in Scheme 1. We show that $Be(CO)_3$ is the least stable among the $Be(CX)_3$ species and that their binding energies with respect to Be + 3CX correlate linearly with the CX dipole moments. Based on the Lewis base features of $Be(CO)_3$,[10] the $Be(CX)_3$ species should be considered of high interest since they may be employed in frustrated Lewis pairs (FLP) facilitating bonds activation.[13]

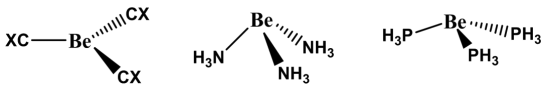

SCHEME 1 Geometries of $Be(CX)_3$ [X = O, S, Se, Te, Po], $Be(NH_3)_3$, and $Be(PH_3)_3$

Phosphine creates similar complexes, but ammonia has strikingly different behavior. We recently observed that beryllium can make a novel type of chemical bonds when it reacts with four ammonia molecules creating a solvated electron precursor (SEP).[14] The 2s electron pair of Be is shifted from the metal to the periphery of the tetrahedral $Be(NH_3)_4$ complex. The final product is described better as a $Be(NH_3)_4^{2+}$ core with two electrons orbiting around it within an s-type diffuse orbital. We found that the ground state of $Be(NH_3)_3$ imitates SEPs but it has an excited electronic state with three Be←NH_3 dative bonds and one electron pair in a $2p_{Be}$ similar to the ground state of $Be(PH_3)_3$.

In section 2, we describe our computational approach. In sections 3 and 4, we discuss our findings on $Be(CX)_3$ [X = O, S, Se, Te, Po] and $Be(AH_3)_3$ [A = N, P] species, respectively. In section 5, we assess the Lewis basicity of these molecules and their derivatives. We found that the protonation of $Be(NH_3)_3$ is as exothermic as the protonation of single ammonia, while $Be(PMe_3)_3$ (Me = CH_3) binds about 50% stronger to H^+ than ammonia. Section 6 summarizes our findings.

2 | COMPUTATIONAL DETAILS

Optimal geometries were obtained for all $Be(CX)_3$ and $Be(AH_3)_3$ species at the coupled cluster level including single, double, and perturbative triple excitations, CCSD(T).[15] The correlation consistent basis set of triple quality-ζ equipped with a series of diffuse functions, aug-cc-pVTZ, was used for all atoms.[16–18] For Se, Te, and Po relativistic effective core potentials that replace 10, 28, and 60 core electrons, respectively, are combined with the relative aug-cc-pVTZ-PP basis functions.[19] The CCSD(T) structures were re-optimized at the density functional theory (DFT) using the B3LYP functional[20,21] and the harmonic vibrational frequencies are calculated to ensure that the structures are real minima. Our optimal geometries and harmonic frequencies are given in the Supporting Information. All derivative molecules examined in section 5 are optimized at the B3LYP level.

Potential energy curves (PEC) are constructed at the multireference configuration interaction (MRCI) level. The active space at the reference multiconfigurational self-consistent field (MCSCF) level consists of 2s and 2p orbitals of beryllium, but all valence electrons are correlated at MRCI. The PECs for all beryllium complexes are constructed starting at the optimal geometry and varying only the beryllium-ligand distance, that is, all other parameters are kept fixed to those of the equilibrium structure.

The reported dipole moments for all CX molecules are obtained by the finite-field approach. A field intensity f = 0.01 a.u. is applied toward both the positive and negative direction of the C-X axis. The two energies, $E(f)$ and $E(-f)$, are then used to provide the dipole moment value μ:

$$\mu = \frac{E(f) - E(-f)}{2f}$$

The reported molecular orbitals are natural orbitals obtained at MRCI. Natural bond orbitals (NBOs) [22] are also provided at Supporting Information for $Be(CO)_3$ and $Be(NH_3)_3$. Multireference and coupled-cluster calculations were carried out with MOLPRO[23] and DFT results were obtained using Gaussian.[24]

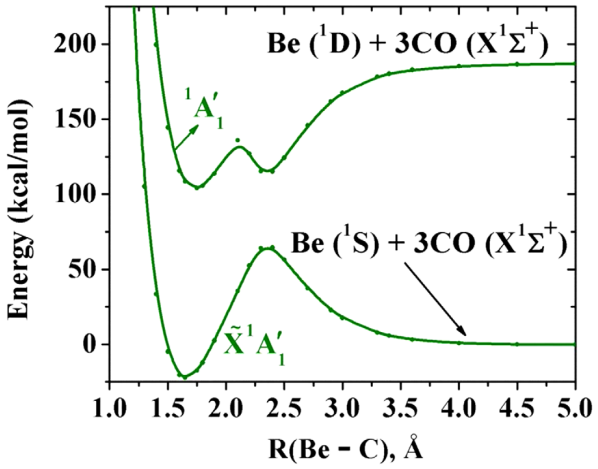

FIGURE 1 MRCI PECs of the first two $^1A_1'$ states of $Be(CO)_3$ as a function of the Be—C distance

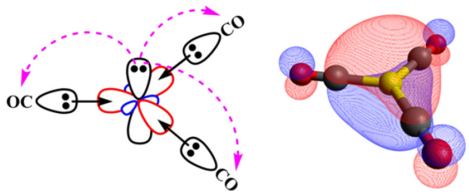

SCHEME 2 Proposed bonding scheme for $\tilde{X}^1A_1'$ of $Be(CO)_3$. The delocalized $2p_\pi$-orbital is also shown

3 | $Be(CX)_3$

We first discuss the chemical bonding for $Be(CO)_3$. The PECs for the simultaneous dissociation of the three carbonyls to beryllium are shown in Figure 1. Only those states which have same symmetry as the ground state ($^1A_1'$) are included. The complete set of PECs up to Be(^{1}D), including the ^{1}S ($1s^12s^2$), 1^3P ($1s^12s^12p^1$), ^{1}P ($1s^12s^12p^1$), 2^3P ($1s^12p^2$), and ^{1}D ($1s^12p^2$) channels, are shown in the Supporting Information (Figure S1). For the PECs, the C—O length is fixed at the experimental equilibrium value of 1.128 Å.[25] The ground state fragments, Be(^{1}S) and CO($X^1\Sigma^+$), are closed shell species, and in principle they are expected to produce a repulsive PEC. Indeed, our calculated lowest PEC is strongly repulsive for distances longer than 2.5 Å. At shorter distances, it becomes attractive and forms the global minimum of the molecule. The inflection point results from an avoided crossing with a $^1A_1'$ state which arises from Be(^{1}D) + 3CO($X^1\Sigma^+$). The CCSD(T) structure of the transition state is given at the Supporting Information. As the molecule forms, the original $2s^2$ electrons of beryllium are forced to polarize away from the plane of the molecule and populate the out-of-plane beryllium $2p_\pi$ orbital, which delocalizes toward CO. In this manner, the in-plane effective Be^{2+} core triggers the formation of three in-plane dative bonds from the three carbonyls to the three empty sp^2 hybrids (see Scheme 2).

The CCSD(T) optimal C—O distances of BeCO, $Be(CO)_2$, and $Be(CO)_3$ are 0.045, 0.021, and 0.013 Å longer than the bond distance of free CO, 1.136 Å.[5] In all BeCO, $Be(CO)_2$, and $Be(CO)_3$ systems there are two π electrons donated to one, two, and three carbonyls, respectively. As a result, 2, 1, and 2/3 of electrons are back donated per carbonyl ligand. These numbers indicate that for every available π-electron given to CO, the CO bond elongates consistently for all species by 0.021 ± 0.002 Å. This implies that the σ-donation has little effect on the bond elongation of CO which can be explained by the fact the electron pair of CO donated to Be is mostly localized on carbon and has little density in the C—O bonding region (see NBOs of Figure S5 at Supporting Information).

The PECs for $Be(CS)_3$ relative to the simultaneous approach of three CS molecules to Be are shown in the Supporting Information (Figure S2). This figure confirms the origin of $Be(CS)_3$ from Be(^{1}D) + 3CS($X^1\Sigma^+$). The overall binding energy D_e of $Be(CS)_3$ with respect to the ground state fragments is more than twice larger compared to $Be(CO)_3$: 49.2 versus 115.3 kcal/mol. Table 1 lists our calculated binding energies for all $Be(CX)_3$ species, X = O, S, Se, Te, and Po. D_e is an increasing function going from O to Te; Po is very similar to Te. Observe that the CCSD(T) binding energy for $Be(CO)_3$ of 49.2 kcal/mol is twice larger than that the MRCI one (∼25 kcal/mol; see Figure 1). This is attributed to the large number of correlated electrons (32 electrons) which introduces large size extensivity errors at the MRCI level.

In Table 1, we also tabulate the height of the energy barrier from the ground state fragments to equilibrium. This is a decreasing function going from O to Te; Po is again resembling Te. Larger binding energy (D_e) means that the PEC from Be (^{1}D) should be steeper. This in turn shifts its avoided crossing with the repulsive PEC coming from Be (^{1}S) to longer distances, which implies that the energy barrier E_A of the latter PEC will decrease. Indeed, there is a nearly linear correlation between D_e and E_A (see Figure 2).

A larger negative charge on carbon, which can be expressed by the CX dipole moment μ, is expected to increase its σ-donation ability. Therefore, we expect that D_e should correlate with μ. The delocalization of beryllium $2p_\pi$ is always from Be to mainly C and is not expected to make a substantial difference among the CX species. Figure 3 confirms the nearly linear correlation between D_e and μ.

The calculated dipole moment of CO is 0.102 D which is in excellent agreement with the experimental value of 0.10980 D.[26] The reported experimental dipole moments of CS and CSe are 1.958 and 1.99 D[26] which agree with our values of 1.90 and 2.16 D, respectively.

TABLE 1 CCSD(T) equilibrium bond lengths r_e (Å) of $Be(CX)_3$, dipole moment μ (D) of CX, binding energy D_e (kcal/mol), and activation energy barrier E_A (kcal/mol) for the formation of $Be(CX)_3$ from Be + 3CX

Molecule	r_e (Be—C)	r_e (C—X)	μ	D_e	E_A
$Be(CO)_3$	1.658	1.149	0.10	49.2	53.9
$Be(CS)_3$	1.663	1.551	1.90	115.3	43.8
$Be(CSe)_3$	1.666	1.690	2.16	123.3	42.9
$Be(CTe)_3$	1.671	1.907	2.59	139.7	41.9
$Be(CPo)_3$	1.674	2.007	2.83	139.1	41.8

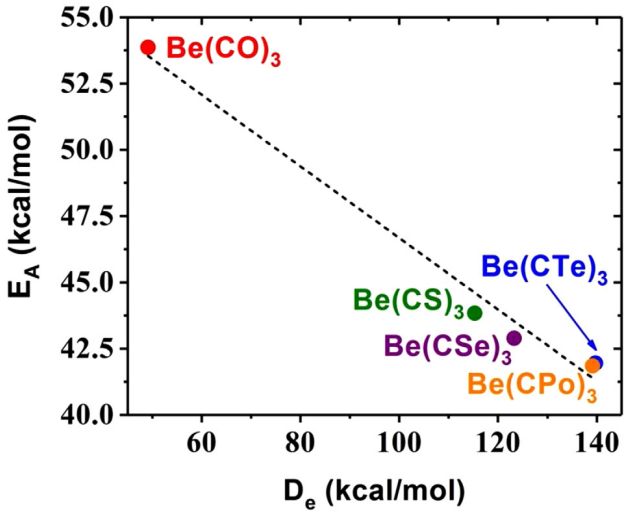

FIGURE 2 Activation energy (E_A) for the Be + 3CX [X = O, S, Se, Te, Po] reaction versus the $Be(CX)_3$ binding energy (D_e) with respect to the same fragments

4 | $Be(AH_3)_3$

We first turn our attention to $Be(PH_3)_3$. Phosphine is a moderate σ-donor but also can accept some electronic density via the π-frame. The PECs as a function of the Be-P distance are shown in Figure 4 and they bear the exact same features as $Be(CO)_3$ (see Figure 1). The $2p_\pi^2$ component of $Be(^1D)$ is also responsible for the formation of this molecule by allowing the three nearly planar dative bonds. Scheme 3 shows the $2p_\pi$ of beryllium along with the proposed bonding scheme.

Ammonia, albeit isovalent to phosphine, exhibits a thoroughly different behavior. The PECs of $^1A_1$ symmetry as a function of the Be—N distance are shown in Figure 5. The full set of PECs is given in the Supporting Information (Figure S3). The barrier from the ground state fragments $Be(^1S) + 3NH_3$ is considerably smaller (11.6 kcal/mol) while no evidence for avoided crossing is noticed. In the ground state, the two valence electrons of beryllium at the equilibrium of the ground state do not occupy a delocalized $2p_\pi$ orbital any more. Instead these two electrons reside a rather spherical orbital delocalized in the periphery of the molecule. The transition of $2s_{Be}$ to this outer orbital is depicted by the snapshots of Figure 6. The sequential $Be(NH_3)_{x-1} + NH_3 \rightarrow Be(NH_3)_x$ binding energies at the CCSD(T)/aug-cc-pVTZ level are 5.2, 11.4, and 21.7 kcal/mol for x = 1, 2, 3, respectively.

This observation is in harmony with the unique property of ammonia to solvate electrons.[27] The addition of a fourth ammonia molecule leads to the pseudo-spherical $Be(NH_3)_4$ complex which is clearly composed of a $Be(NH_3)_4^{2+}$ core and two "solvated" electrons orbiting around it in hydrogenic-type (s, p, d, f, …) orbitals.[14] This is largely due to its high N—H bond dipole: The NH_3 dipole moment is 2.5 times larger than that of PH_3 (1.518 vs. 0.606 D).

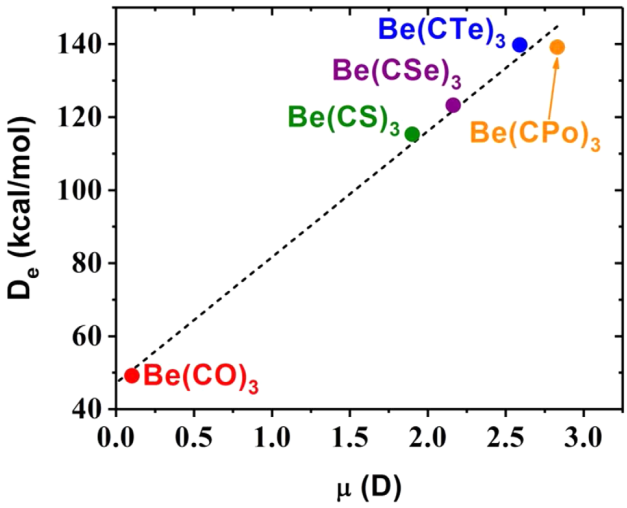

FIGURE 3 Binding energy (D_e) for the Be + 3CX [X = O, S, Se, Te, Po] reaction versus the CX dipole moment (μ)

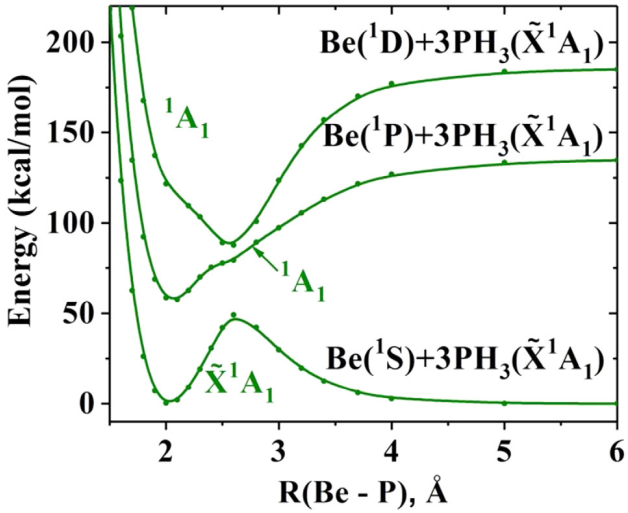

FIGURE 4 MRCI PECs of $Be(PH_3)_3$ as a function of Be—P distance

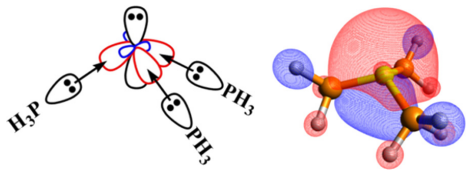

SCHEME 3 Proposed bonding scheme for $\tilde{X}^1A_1$ of $Be(PH_3)_3$. The $2p_\pi$ orbital is also shown

The electronic state, similar to the ground state of the previous species originating from Be (^1D) where two electrons occupy a $2p_\pi$ orbital, is now an excited state corresponding to the higher PEC of Figure 5. The optimal structure for this state is quasi-planar and the bonding resembles that of Scheme 3, but of course with no π-back bonding present as expected for ammonia (see Scheme 4).

The CCSD(T) excitation energy from the first to third $^1A_1$ is 59.4 kcal/mol. The reference Hartree–Fock determinant for the first and third $^1A_1$ states have both 11 closed a′ and 5 closed a″ orbitals under the C_s symmetry used for the calculations. To obtain the correct electronic configuration for the third $^1A_1$, we used the ground state orbitals as an initial guess but 11a′ (last orbital of Figure 6) was switched with 15a′ (Scheme 4) and launched the self-consistent field iterations, which converged to the excited state determinant. Conclusively, the quasi-planar structure is observed for both pure σ-donors, such as NH_3, and σ-donors/π-acceptors, such as CX species and PH_3. The π-back bonding increases the stability of these systems but it's not necessary for their existence.

It should be noted that the $Be(AH_3)_3$ complexes are metastable with respect to the $(AH_3)Be(AH_2)_2 + H_2$ dissociation, with a barrier of 18.4 and 16.2 kcal/mol for A = N and P, respectively (see Figure S4 of Supporting Information).

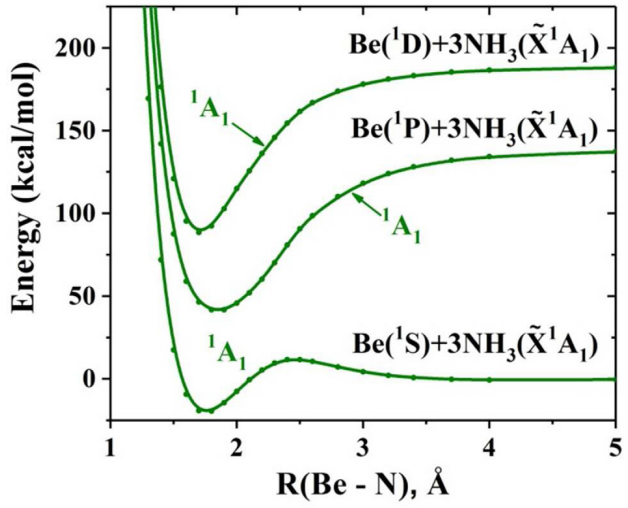

FIGURE 5 MRCI PECs of $Be(NH_3)_3$ as a function of the Be—N distance

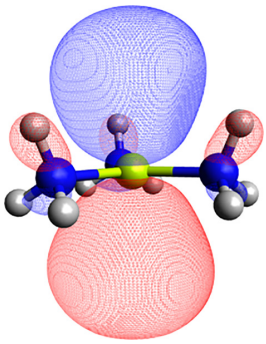

SCHEME 4 Highest occupied molecular orbital of the third $^1A_1$ state of $Be(NH_3)_3$

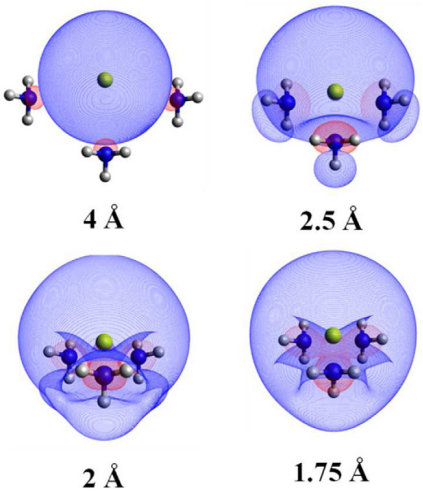

FIGURE 6 The highest occupied molecular orbital of $Be(NH_3)_3$ (ground state) for different Be—N distances

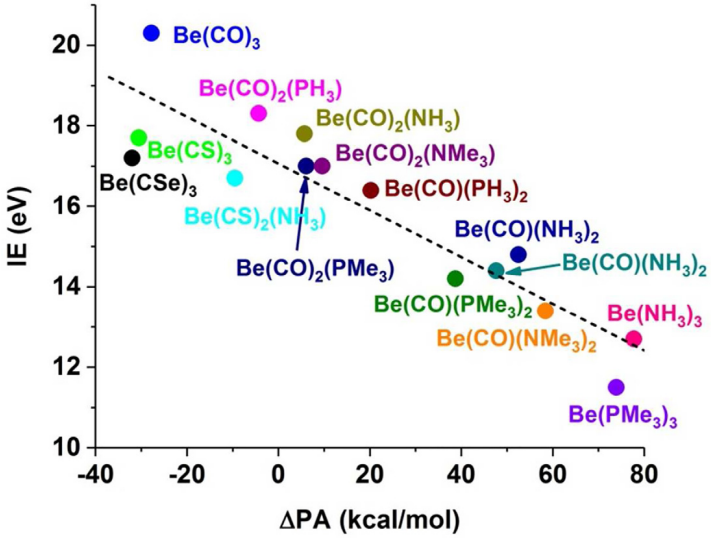

FIGURE 7 Ionization energy IE versus relative proton affinity ΔPA for several beryllium tri-coordinated complexes

TABLE 2 Total binding energy D_e (kcal/mol) with respect to Be + ligands, absolute proton affinity PA (kcal/mol), relative proton affinity ΔPA (kcal/mol) with respect to Et_3N, and ionization energy IE (eV) to dicationic species of different tri-coordinated beryllium complexes

Complex	PA	ΔPA	IE
$Be(CO)_3$	215.1	-27.8	20.3
$Be(CS)_3$	212.4	-30.5	17.7
$Be(CSe)_3$	210.9	-32.0	17.2
$Be(PH_3)_3$	290.5	47.6	14.4
$Be(CO)(PH_3)_2$	263.1	20.2	16.4
$Be(CO)_2(PH_3)$	238.6	-4.3	18.3
$Be(NH_3)_3$	320.6	77.7	12.7
$Be(CO)(NH_3)_2$	295.4	52.5	14.8
$Be(CO)_2(NH_3)$	248.6	5.7	17.8
$Be(CS)_2(NH_3)$	233.4	-9.5	16.7
Be $(PMe_3)_3$	316.8	73.9	11.5
$Be(CO)(PMe_3)_2$	281.7	38.7	14.2
$Be(CO)_2(PMe_3)$	249.0	6.1	17.0
$Be(CO)(NMe_3)_2$	301.4	58.4	13.4
$Be(CO)_2(NMe_3)$	252.6	9.6	17.0
NH_3	211.1	-31.8	33.8
Et_3N	242.9	0.0	21.4

5 | LEWIS BASICITY OF TRI-COORDINATED BERYLLIUM COMPLEXES

Independently of the bonding pattern, all of the titled beryllium complexes possess a diffuse electron pair which makes them potential Lewis bases. To provide a quantitative measure of their basicity strength, we calculated the proton affinity (PA) of these systems, which is defined as the binding energy of a proton to them. We then compare these PAs to the PA of one of the strongest conventional Lewis base, Et_3N (Et = CH_3CH_2) defining the quantity ΔPA = PA — PA(Et_3N). Table 2 lists our numerical results for several complexes including combinations of the ligands used so far but also NMe_3 and PMe_3.

Our calculated PA of Et_3N is 242.9 kcal/mol being about 30 kcal/mol larger than that of ammonia (PA = 211.1 kcal/mol). $Be(CO)_3$, $Be(CS)_3$, and $Be(CSe)_3$ have very similar PAs with ammonia. The $Be(NH_3)_3$ and $Be(PH_3)_3$ molecules have appreciably larger PAs (see Table 2): $Be(NH_3)_3$ is almost 50% stronger base than Et_3N. Replacing one and two AH_3 ligands with CO the PAs drop gradually toward that of $Be(CO)_3$, as expected. This effect makes the beryllium complexes highly tunable and potential candidates for different FLP applications. We also examined methyl substituted ammonia and phosphine as ligands. $Be(PMe_3)_3$ is the second strongest Lewis base of our pool. Although $Be(NMe_3)_3$ is unstable, probably because of the large steric repulsion among the methyl groups, the monosubstituted or disubstituted by CO complexes, $Be(CO)(NMe_3)_2$ and $Be(CO)_2(NMe_3)$, are stable and stronger bases than Et_3N.

Additionally, we considered the energy needed to remove the diffuse electron pair from our complexes as another measure of Lewis basicity. This "double ionization" energy (IE) should correlate with PA in an inverse manner: The higher IE means that the complex is reluctant to donate its electrons leading to lower PA values. Our IEs are listed in Table 2 and they are plotted against ΔPA in Figure 7. Observe that the two quantities correlate almost linearly and the majority of the complexes have positive ΔPA meaning they are stronger Lewis bases than Et_3N. If we focus on the $Be(CO)_x(PMe_3)_{3-x}$ (x = 1 − 3) series, we see that they span the whole range of our PA and IE values: $Be(CO)_3$ and $Be(PMe_3)_3$ are among the weakest and strongest bases, respectively.

As in $Be(NH_3)_3$ and $Be(PH_3)_3$, the $Be(CO)(NH_3)_2$ and $Be(CO)(PH_3)_2$ species are also metastable with respect to the fragments producing H_2. These reactions are exothermic by 43.2 and 20.7 kcal/mol and have a barrier of 26.9, and 27.4 kcal/mol for $Be(CO)(NH_3)_2$ and $Be(CO)(PH_3)_2$, respectively. Our strongest Lewis base with considerable thermodynamic stability is $Be(PMe_3)_3$.

6 | SUMMARY AND CONCLUSIONS

Presently, we examined the tri-coordinated neutral beryllium complexes with various ligands such as: the CX [X = O, S, Se, Te, Po] species, which are both σ-donors and π-acceptors, phosphine (σ-donor, weak π-acceptor) and ammonia, which is pure σ-donor. In the CX and PH_3 cases the bond is formed from Be(^{1}D; $1s^2 2p^2$). The two 2p electrons are coupled into a single 2p orbital and the remaining vacant valence sp^2 hybrid orbitals facilitate three dative bonds from the ligands to beryllium. The Be-CX binding energy was found to be linearly correlated with both the CX dipole moment and the activation energy of the Be + 3CO reaction. On the contrary, ammonia is found to prefer to "solvate" the 2s electron pair of Be(^{1}S; $1s^2 2s^2$), but it bears an excited state which also comes from Be(^{1}D) and forms the same planar structure as $Be(CX)_3$ series. For these systems and their derivatives we calculated the proton affinities as a measure of their Lewis basicity and we found that many of them are stronger

Lewis bases than the conventional Et_3N one. This means that beryllium complexes can potentially be used in FLPs. Other alkaline earth metals, such Mg and Ca, will be considered in the near future.

ACKNOWLEDGMENTS

The authors are indebted to Auburn University for financial support. The computational work was completed in part by the Auburn University Hopper Cluster and in part by the Alabama Supercomputer Center.

ORCID

Evangelos Miliordos http://orcid.org/0000-0003-3471-7133

REFERENCES

[1] K. J. Iversen, S. A. Couchman, D. J. D. Wilson, J. L. Dutton, *Coord. Chem. Rev*. **2015**, *297–298*, 40.
[2] M. Arrowsmith, H. Braunschweig, M. A. Celik, T. Dellermann, R. D. Dewhurst, W. C. Ewing, K. Hammond, T. Kramer, I. Krummenacher, J. Mies, K. Radacki, J. K. Schuster, *Nat. Chem.* **2016**, *8*, 890.
[3] A. Puchta, *Nat. Chem.* **2011**, *3*, 416.
[4] S. A. Couchman, N. Holzmann, G. Frenking, D. J. D. Wilson, J. L. Dutton, *Dalton Trans.* **2013**, *42*, 11375.
[5] I. R. Ariyarathna, E. Miliordos, *J. Phys. Chem. A* **2017**, *121*, 7051.
[6] M. R. Buchner, M. Müller, S. S. Rudel, *Angew. Chem. Int. Ed.* **2017**, *56*, 1130.
[7] A. Kalemos, *J. Chem. Phys.* **2017**, *146*, 104307.
[8] O. Brea, I. Corral, *J. Phys. Chem. A* **2018**, *122*, 2258.
[9] A. Kramida, Y. Ralchenko, J. Reader, *NIST ASD Team 2016, NIST Atomic Spectra Database (version 5.4)*, National Institute of Standards and Technology, Gaithersburg, MD **2016**, http://physics.nist.gov/asd (accessed on May 23, 2017).
[10] S. De P. Parameswaran, *Dalton Trans.* **2013**, *42*, 4650.
[11] L. Andrews, T. J. Tague, G. P. Kushto, R. D. Davy, *Inorg. Chem.* **1995**, *34*, 2952.
[12] M. P. Mitoraj, A. Michalak, *Inorg. Chem.* **2010**, *49*, 578.
[13] F. G. Fontaine, D. W. Stephan, *Philos. Trans. R. Soc. A* **2017**, *375*, 20170004.
[14] I. R. Ariyarathna, S. N. Khan, F. Pawłowski, J. V. Ortiz, E. Miliordos, *J. Phys. Chem. Lett.* **2018**, *9*, 84.
[15] K. Raghavachari, G. W. Trucks, J. A. Pople, M. A. Head-Gordon, *Chem. Phys. Lett.* **1989**, *157*, 479.
[16] T. H. Dunning, Jr, *J. Chem. Phys.* **1989**, *90*, 1007.
[17] R. A. Kendall, T. H. Dunning, Jr, R. J. Harrison, *J. Chem. Phys.* **1992**, *96*, 6796.
[18] T. H. Dunning, Jr, D. E. Woon, *J. Chem. Phys.* **1994**, *100*, 2975.
[19] K. A. Peterson, D. Figgen, E. Goll, H. Stoll, M. Dolg, *J. Chem. Phys.* **2003**, *119*, 11113.
[20] A. D. Becke, *J. Chem. Phys.* **1993**, *98*, 5648.
[21] C. Lee, W. Yang, R. G. Parr, *Phys. Rev. B Condens. Matter.* **1988**, *37*, 785.
[22] F. Weinhold, *Int. J. Quantum Chem.* **2012**, *33*, 2363.
[23] H. J. Werner, P. J. Knowles, G. Knizia, F. R. Manby, M. Schütz, P. Celani, W. Györffy, D. Kats, T. Korona, R. Lindh, A. Mitrushenkov, G. Rauhut, K. R. Shamasundar, T. B. Adler, R. D. Amos, A. Bernhardsson, A. Berning, D. L. Cooper, M. J. O. Deegan, A. J. Dobbyn, F. Eckert, E. Goll, C. Hampel, A. Hesselmann, G. Hetzer, T. Hrenar, G. Jansen, C. Köppl, Y. Liu, A. W. Lloyd, R. A. Mata, A. J. May, S. J. McNicholas, W. Meyer, M. E. Mura, A. Nicklass, D. P. O'Neill, P. Palmieri, D. Peng, K. Pflüger, R. Pitzer, M. Reiher, T. Shiozaki, H. Stoll, A. J. Stone, R. Tarroni, T. Thorsteinsson, and M. Wang, MOLPRO, Version 2015.1, A Package of Ab Initio Programs, see http://www.molpro.net (accessed on 1/4/2018)
[24] M. J. Frisch, G. W. Trucks, H. B. Schlegel, G. E. Scuseria, M. A. Robb, J. R. Cheeseman, G. Scalmani, V. Barone, G. A. Petersson, H. Nakatsuji, X. Li, M. Caricato, A. V. Marenich, J. Bloino, B. G. Janesko, R. Gomperts, B. Mennucci, H. P. Hratchian, J. V. Ortiz, A. F. Izmaylov, J. L. Sonnenberg, D. Williams-Young, F. Ding, F. Lipparini, F. Egidi, J. Goings, B. Peng, A. Petrone, T. Henderson, D. Ranasinghe, V. G. Zakrzewski, J. Gao, N. Rega, G. Zheng, W. Liang, M. Hada, M. Ehara, K. Toyota, R. Fukuda, J. Hasegawa, M. Ishida, T. Nakajima, Y. Honda, O. Kitao, H. Nakai, T. Vreven, K. Throssell, J. A. Montgomery, Jr, J. E. Peralta, F. Ogliaro, M. J. Bearpark, J. J. Heyd, E. N. Brothers, K. N. Kudin, V. N. Staroverov, T. A. Keith, R. Kobayashi, J. Normand, K. Raghavachari, A. P. Rendell, J. C. Burant, S. S. Iyengar, J. Tomasi, M. Cossi, J. M. Millam, M. Klene, C. Adamo, R. Cammi, J. W. Ochterski, R. L. Martin, K. Morokuma, O. Farkas, J. B. Foresman, D. J. Fox, *Gaussian 16, Revision A.03*, Gaussian, Inc., Wallingford, CT **2016**.
[25] K. P. Huber, G. H. Herzberg, in *Constants of Diatomic Molecules*, Vol. IV, Van Nostrand Reinhold, New York **1979**.
[26] D. R. Lide, *CRC Handbook of Chemistry and Physics*, 93rd ed., CRC Press, New York, **2012**.
[27] E. Zurek, P. P. Edwards, R. Hoffmann, *Angew. Chem. Int. Ed.* **2009**, *48*, 8198.

SUPPORTING INFORMATION

Additional supporting information may be found online in the Supporting Information section at the end of the article.

How to cite this article: Ariyarathna IR, Miliordos E. Dative bonds versus electron solvation in tri-coordinated beryllium complexes: Be$(CX)_3$ [X = O, S, Se, Te, Po] and Be$(PH_3)_3$ versus Be$(NH_3)_3$. *Int J Quantum Chem*. 2018;118:e25673. https://doi.org/10.1002/qua.25673

Carbon monoxide activation by atomic thorium: ground and excited state reaction pathways

PCCP

PAPER

View Article Online
View Journal

Cite this: DOI: 10.1039/c9cp04946k

Carbon monoxide activation by atomic thorium: ground and excited state reaction pathways†

Isuru R. Ariyarathna and Evangelos Miliordos *

Received 5th September 2019,
Accepted 25th October 2019

DOI: 10.1039/c9cp04946k

rsc.li/pccp

Multi-reference configuration interaction (MRCI) and single reference coupled cluster calculations are performed for the ThCO and OThC isomers. Scalar and spin–orbit relativistic effects are considered through a relativistic pseudopotential and the coupling of MRCI wavefunctions *via* the Breit–Pauli spin–orbit Hamiltonian. Optimized geometries, excitation energies, and vibrational frequencies are reported for both isomers. Full potential energy profiles are constructed for the Th+CO reaction and the conversion of the produced ThCO to OThC. Linear ThCO was found to be more stable than the highly ionic bent OThC system by about 4 kcal mol^{-1}. The interconversion barrier is estimated to be around 30 kcal mol^{-1}. Our results are in agreement with earlier experimental data for the two isomers. The lowest lying states of Th do not populate f-orbitals and resemble the electronic structure of Ti. Therefore, the ability of the two atoms to activate the C≡O bond is compared. OTiC is found to be about 40 kcal mol^{-1} less stable than TiCO revealing the efficiency of Th and possibly other f-block elements to activate multiple chemical bonds as opposed to d-block metals.

1. Introduction

Over the past two decades the chemistry of actinides has received special attention in our attempt to improve their applicability as nuclear fuels and find ways to minimize their hazardous impact on the environment.[1] The unusual chemistry of actinides has attracted the interest of both chemists and physicists. More and more studies are dedicated to disclose their distinctive chemistry and atypical properties. Among actinides, uranium and plutonium materials are heavily used as nuclear fuels, while thorium is examined as a potential nuclear fuel[2,3] because of its easier treatment.[3,4]

The growth of actinide chemistry is checked by the multiple challenges and necessary caution of the used experimental processes. Due to the experimental limitations, computational studies have enhanced considerably our knowledge of actinide chemistry.[5–11] But even the theoretical exploration of the chemistry of actinides often presents insurmountable difficulties due to their many valence electrons and orbitals combined with the strong scalar and spin–orbit relativistic effects.[12,13] Both density functional and multireference calculations have been used to predict and explain the chemistry of actinide containing molecules,[5–11,14–19] with the latter ones being more appropriate to describe the complex electronic structure of these heavy metals.[6–10,17]

Among actinides, Ac and Th are unique in the sense that they lack f-electrons in their lowest-lying electronic states simplifying the quantum calculations. The first state with a populated f-shell is the tenth excited state of Th, whereas there is no f-electron up to the first forty states of Ac.[20] Multireference calculations have been used in several studies to explore the chemical bonding of thorium molecules. Triply bonded ThC is one example,[21] while many reports focus on the ground and excited states of neutral and charged thorium carbides and oxides.[14,15,17–19,22–28] The thorium dimer (Th_2) with a quadruple bond is another interesting system, where despite the minor contribution of 5f orbitals to the bonding,[29] strong spin–orbit coupling increases the complexity of the system.

Actinide carbonyl complexes are less studied compared to their s and d-block metal counterparts used in organometallic and coordination chemistry. Referring to thorium carbonyls, the first study was done by Zhou and Andrews in 1999,[4] who studied the reaction of thorium with carbonyl by means of laser ablation in the presence of excess neon and characterized the products with matrix isolation spectroscopy. The recorded infrared (IR) spectrum exhibited the presence of two major products designated as ThCO and OThC. For these two molecules, the authors performed relativistic density functional theory (DFT) calculations. The measured experimental C–O stretching frequency of ThCO is 1817.5 cm^{-1} with its DFT value being 1790 cm^{-1}. The observed peaks around 617.7 and 812.2 cm^{-1} were assigned to the Th–C and Th–O stretches based on the predicted DFT values of 621 and 811 cm^{-1} respectively. They proposed $^3A'$ and $^3\Sigma^-$ ground states for bent OThC and

Department of Chemistry and Biochemistry, Auburn University, Auburn, AL 36849-5312, USA. E-mail: emiliord@auburn.edu

† Electronic supplementary information (ESI) available. See DOI: 10.1039/c9cp04946k

linear ThCO, respectively. Furthermore, Th is found to have a $6d^27s^2$ electron configuration within ThCO($^3\Sigma^-$). The $6d^2$ electrons were found to actively participate in Th → CO π-back-donation. A year later, the same authors revisited thorium carbonyls reporting the presence of the OThC$^{0/-}$, OThCCO, and Th(CO)$_{n=1-6}$ species.[30] Their DFT calculations predicted the ground and excited states of OThC as ^{3}A′, a^{3}A′, ^{1}A′, ^{5}A′, and b^{3}A′ in increasing energy order.[30]

ThCO and OThC are expected to have multiple low-lying electronic states of multi-configurational nature, which can be described accurately only with multi-reference approaches. Herein we examine the reaction between Th and CO employing multireference calculations. In an attempt to gain deeper understanding on the electronic structure of this system, we produced full potential energy profiles for the Th–CO approach by varying the Th–C distance. The ground and several excited states of ThCO, its OThC isomer, and the intermediates or transition states connecting them were investigated. We further propose chemical bonding patterns for all of them and supply a detailed mechanism for the activation of carbon monoxide by atomic thorium.

2. Computational details

The lowest lying states of thorium up to about 8000 cm^{-1} (^{3}F, ^{3}P, and ^{5}F) are all of $6d^{4-x}7s^x$ character followed by states populating the 5f and 7p orbitals.[20] We performed three series of single and double multi-reference configuration interaction (MRCISD ≡ MRCI) calculations to reproduce the experimental electronic energies for the thorium atom. The reference complete active space self-consistent field (CASSCF) in these three cases is constructed by allocating the four valence electrons of thorium to the (1) 7s, 6d, 7p, and 5f, (2) 7s, 6d, and 7p, (3) 7s and 6d orbitals of thorium. In all cases, the four valence electrons and the subvalence 6s and 6p electrons are correlated at MRCI. The 5s, 5p, and 5d orbitals were kept closed, while the rest of the sixty inner electrons ($1s^22s^22p^63s^23p^63d^{10}4s^24p^64d^{10}4f^{14}$) are replaced by the Stuttgart relativistic pseudopotential.[31] The cc-pVQZ-PP basis set is used to build the atomic orbitals.[32,33] Finally, the Davidson correction (MRCI+Q) was invoked to estimate part of the missing electron correlation energy.[34] Spin–orbit coupling was considered by mixing the ^{3}F, ^{3}P, ^{5}F, and ^{1}D states. The spin–orbit wavefunctions were expanded in terms of all of the involved atomic states, and the corresponding coefficients were obtained by diagonalizing the perturbed Hamiltonian (electronic Hamiltonian plus the full Breit–Pauli spin–orbit operator) as implemented in MOLPRO.[35–37] In the case of MRCI+Q, the MRCI electronic energies are replaced by the MRCI+Q ones but the MRCI matrix elements are still used for the spin–orbit terms.

The calculations for ThCO and OThC were performed using the cc-pVTZ-PP[32,33] basis set for Th with the same Stuttgart pseudopotential,[31] and the cc-pVTZ set for carbon and oxygen.[38] Full potential energy profiles (PEPs) were constructed at MRCI to study the ground and excited energy channels of the Th ← CO reaction. Based on the results on the atomic calculations, we decided to include four electrons in nine orbitals in the CASSCF active space, which correspond to the 7s, 6d, and 7p orbitals of Th at long Th–CO distances (case 2 of the previous paragraph). Our calculations show that the 5f orbitals are not occupied in the lowest energy equilibrium structures, and their presence in the active space is not necessary. This is in line with the observations on Th_2[29] and the work of Wilson and co-workers, who found that f-orbitals are important for Pa and later actinides.[39] The thorium active orbitals mix with CO orbitals in a dative manner: σ-donation of the carbon lone pair to the metal and the π-back donation of metallic orbitals to the anti-bonding π orbitals of CO.[40–42] Therefore, no additional orbitals were found necessary, as would happen in the case of homolytic dissociation. All valence electrons of C, O, and Th plus the 6s and 6p ones of Th were promoted to virtual orbitals at the MRCI level. Restricted open-shell coupled clusters with single, double and perturbative triple replacements, CCSD(T), were also done in single reference cases. As in MRCI, all valence electrons plus the 6s and 6p electrons of Th are correlated at CCSD(T). The symmetry operations of the C_{2v} point group were exploited.

The calculations for bent OThC were proven to be more demanding because of the lower symmetry (C_s). To keep the calculations manageable, we had to lower the CASSCF active space to seven a′ and four a″ orbitals (15a′ through 21a′ and 5a″ through 8a″; eight electrons to eleven orbitals). All valence electrons plus the sub-valence 6s and 6p ones are still correlated at MRCI. Based on extensive tentative calculations, the active space is chosen to describe properly the first five electronic states of OThC. CCSD(T) calculations were done for the first four states of single determinantal nature. In all cases, the T1 diagnostic is lower than 0.036, which is lower than the limit of 0.05 suggested for multi-reference character in transition metal compounds.[43]

The same active space and basis set of OThC were used to study the pathways from ThCO to OThC. The MRCI+Q potential energy profiles (PEPs) of the ThCO to OThC transformation for their low-lying states were constructed using the optimized geometries of the ^{3}A″ state at every O–X–C angle, where X is the center of the Th–C bond. The geometry optimizations were done at the complete active space second order perturbation theory (CASPT2) level as implemented in MOLPRO[44] with the same CASSCF active space as OThC but with a smaller basis set: cc-pVDZ-PP for Th and cc-pVDZ for C and O. For the OThC region, we performed additional calculations for the first three states, where the geometry of each state is optimized at the MRCI level. We faced insurmountable technical issues with CASPT2 geometry optimizations for ^{3}A′ (intruder state issues). All valence plus 6s and 6p (Th) electrons are correlated at the CASPT2 and MRCI level. All optimized structures are given in the ESI.† Finally, zero-point vibrational energy (ZPVE) values are obtained as half of the sum of all harmonic vibrational frequencies.

3. Results and discussion

Th

We first assess our methodologies comparing the calculated excitation energies T_e of Th to the available experimental ones.[20]

Pure relativistic calculations have been performed by Eliav and Kaldor.[13] The spin–orbit corrected values at MRCI and MRCI+Q along with the experimental values for three different active spaces (7s,6d,7p,5f; 7s,6d,7p; and 7s,6d) of the reference CASSCF wavefunctions are listed in Table 1. MRCI with the largest active space (7s,6d,7p,5f) predicts almost always larger excitation energies than experiment by at least 144 cm^{-1} ($^5F_1$) and up to 907 cm^{-1} ($^5F_4$). The only case where MRCI underestimates T_e is for $^3P_0$ by 214 cm^{-1}. MRCI+Q brings experiment and theory closer together by an average of 100 cm^{-1}. The removal of 5f orbitals from the CASSCF active space actually improves the theoretical values. Roughly, half of the values are underestimated and half of them overestimated by at most 516 cm^{-1}. The average difference between theory and experiment is accidentally 0 cm^{-1} at MRCI and 14 cm^{-1} at MRCI+Q. Further reduction of the active space worsens the agreement between theory and experiment with some differences being larger than 1000 cm^{-1}. Therefore, the calculations for ThCO are performed using the medium active space (7s, 6d, 7p). Finally, MRCI+Q directs almost always the theoretical results towards the experimental ones. Overall, the applied methodology is considered quite accurate and is capable of describing spin–orbit effects properly.

ThCO

To get a better understanding of the bonding between Th and CO, we constructed the potential energy curves with respect to the Th–C distance (ThCO is kept linear). We considered the first four electronic states of Th spanning an energy range of about 10 000 cm^{-1} (see Table 1). In energy order (not considering spin–orbit effects) these are ^3F, ^3P, ^1D, and ^5F spanning an energy range of only 15 kcal mol^{-1} or 5250 cm^{-1}. The first three are of $7s^26d^2$ and the last one of $7s^13d^3$ character. For this system we considered spin–orbit coupling only at the equilibrium region (see below). The Th ← CO PEPs are shown in Fig. 1, the equilibrium configurations for seven states are given in Table 2,

Table 1 Excitation energies (cm^{-1}) for the lowest electronic states of Th at the MRCI and MRCI+Q levels using the cc-pVQZ-PP basis set with different CASSCF active spaces

	MRCI	MRCI+Q	MRCI	MRCI+Q	MRCI	MRCI+Q	
State[a]	(7s,6d,7p,5f)[b]		(7s,6d,7p)[b]		(7s,6d)[b]		Expt.[c]
$^3F_2$	0	0	0	0	0	0	0.0
$^3P_0$	2772	2838	3074	3078	2114	2575	2558.1
$^3F_3$	2427	2429	2470	2496	2299	2310	2869.3
$^3P_2$	3360	3413	3650	3611	3012	3213	3688.0
$^3P_1$	3390	3428	3661	3657	2724	3297	3865.5
$^3F_4$	4741	4743	4864	4891	4455	4582	4961.7
$^5F_1$	5418	5624	5988	5971	4591	5208	5563.1
$^5F_2$	5968	6174	6562	6545	4812	5776	6362.4
$^1D_2$	6602	6618	6979	6884	6461	6525	7280.1
$^5F_3$	6794	7000	7426	7409	5666	6629	7502.3
$^5F_4$	7894	8100	8575	8558	6802	7764	8800.2
$^5F_5$	9265	9471	10 006	9989	8212	9177	9804.8

[a] The electronic configurations for the listed states are $7s^26d^2$ (^3F, ^3P, ^1D) and $7s^16d^3$ (^5F). [b] Active space used for the reference CASSCF wavefunction. [c] Obtained from ref. 20.

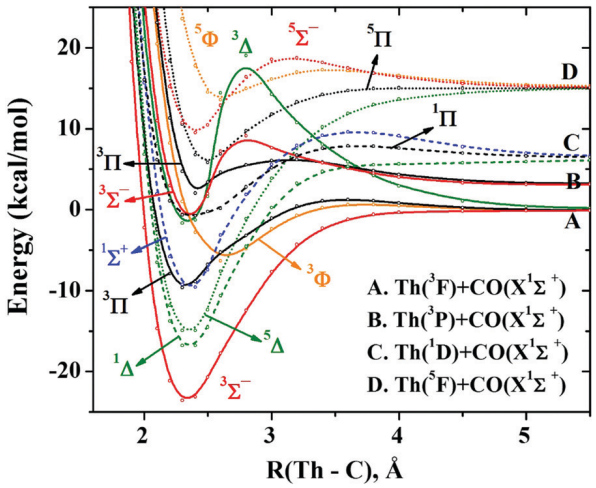

Fig. 1 MRCI PEPs for the approach of Th and CO in a linear fashion. The CO distance is kept fixed to the experimental CO distance of 1.128 Å.

Table 2 Dominant electronic configurations and coefficients of several low-lying electronic states of linear ThCO

State[a]	Coeff.	16σ	$10\pi_x$	$10\pi_y$	$6\delta_{xy}$	$6\delta_{x^2-y^2}$
$^3\Sigma^-$ (A_2)	0.88	2	α	α	0	0
$^1\Delta$ (A_1)	−0.59	2	0	2	0	0
	0.59	2	2	0	0	0
$^5\Delta$ (A_1)	0.97	α	α	α	α	0
$^1\Sigma^+$ (A_1)	0.58	2	0	2	0	0
	0.58	2	2	0	0	0
$^3\Pi$ (B_1)	0.80	α	α	2	0	0
	0.23	2	α	0	0	α
	−0.23	2	0	α	α	0
$^3\Phi$ (B_1)	0.62	2	0	α	α	0
	0.62	2	α	0	0	α
$^1\Pi$ (B_1)	0.41	2	0	β	α	0
	−0.41	2	0	α	β	0
	0.41	2	α	0	0	β
	−0.41	2	β	0	0	α
$^3\Delta$ (A_1)	0.46	β	α	α	α	0
	−0.43	α	β	α	α	0
	−0.43	α	α	β	α	0
	0.41	α	α	α	β	0
$2^3\Sigma^-$ (A_2)	−0.48	α	α	β	0	α
	0.48	α	β	α	0	α
	0.48	α	0	2	α	0
	−0.48	α	2	0	α	0

[a] The electronic term of the C_{2v} component is given in parentheses.

and selected frontier molecular orbitals are depicted in Fig. 2. The first excited state of CO, $^3\Pi$, resides well above (48 686.7 cm^{-1})[45] its $^1\Sigma^+$ ground state, and therefore no excited states of CO are considered here.

The symmetry defining orbitals are 16σ, 10π, and $6d_{xy}$/$6d_{x^2-y^2}$, which are largely the 7s orbital of Th polarized away from CO, π-bonding orbitals between the d_π orbitals of Th and the p_π orbitals of C (or π* of CO), and pure $6d_\delta$ ($6d_{xy}$/$6d_{x^2-y^2}$) orbitals of Th, respectively. The ground state $^3\Sigma^-$ is dominated by the $16\sigma^2\ 10\pi_x^1\ 10\pi_y^1$ configuration, and it is followed by the sibling $16\sigma^2\ 10\pi^2$ states of $^1\Delta$ and $^1\Sigma^+$ symmetry. The $^5\Delta$ state intervenes between them, where one 16σ electron is promoted to one of the $6d_\delta$ orbitals. The next state is of $^3\Pi$ symmetry with

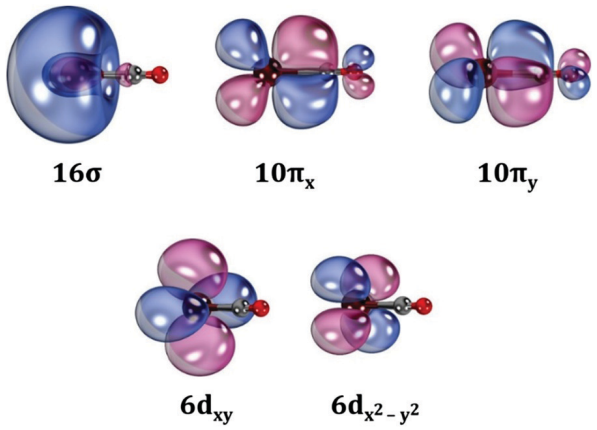

Fig. 2 Selected molecular orbitals of ThCO. Th, C, and O are represented by a maroon, grey, and red sphere, respectively.

a dominant $16\sigma^1\ 10\pi^3$ configuration, but also has smaller contributions similar to the following $^1\Pi$ and $^3\Phi$ states. These states are of $16\sigma^2\ 10\pi^1\ 6d^1_\delta$ nature. The bonding schemes for these states can be succinctly captured by the valence-bond-Lewis (vbL) diagrams of Fig. 3. In all cases, there is σ-donation from the :CO lone pair to a 7s–6d$_{z^2}$ hybrid orbital combined with some metal-to-ligand π-back donation. All states bear an *in situ* $7s^23d^2$ nature (16σ–7s) except for $^5\Delta$ and $^3\Pi$, which come from the $^5F(7s^16d^3)$ state of Th. Indeed, $^5\Delta$ dissociates smoothly to ^5F, $^3\Pi$ dissociates to ^3F and not to ^5F of the thorium atom due to an avoided crossing at around 2.6 Å (see Fig. 1), while all others dissociate to the first three channels pertaining to $7s^26d^2$.

Fig. 1 includes all PEPs dissociating to the first four channels, and some additional higher energy minima in the 2.2–2.7 Å region. In some cases, these minima originate from higher energy fragments, and therefore the PEPs for these minima undergo avoided crossings. For example, see the PEPs for the $^3\Delta$ and the second $^3\Sigma^-$ states. The dominant electronic configurations for these states are also included in Table 2, but currently, we focus on the previous seven electronic states.

Optimized MRCI geometries and MRCI/MRCI+Q excitation energies are listed in Table 3. For the single reference $^3\Sigma^-$ and $^5\Delta$ states, we also list CCSD(T) results. In both cases, CCSD(T) predicts shorter Th–C and longer C–O bond lengths by ∼0.01 and ∼0.02 Å compared to MRCI, respectively. The C–O bond elongates by ∼0.02 Å in the first five states, less than 0.01 Å for $^1\Pi$, and remains unaffected for $^3\Phi$ with respect to free CO. For the first five states the reason is the Th-to-CO π-back donation, which is weaker for the last two states (only one electron in the 10π orbitals).

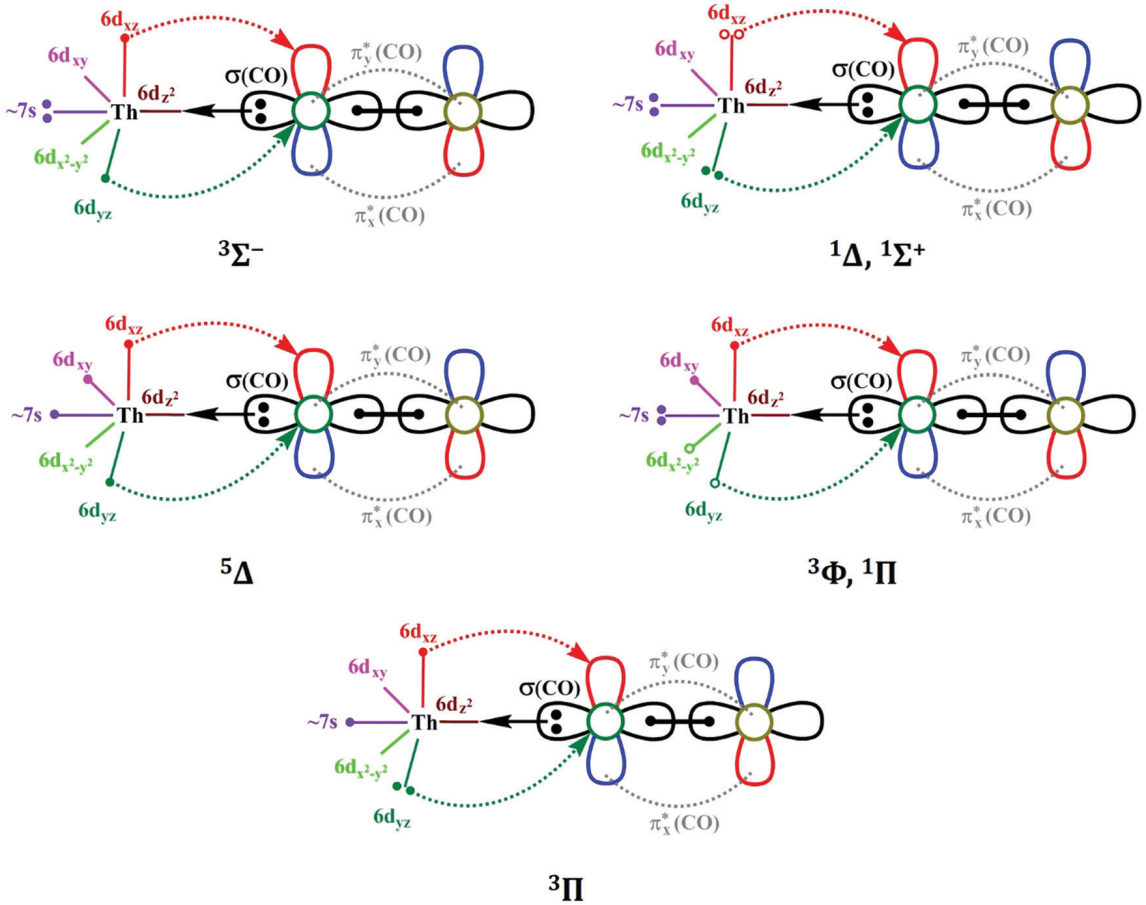

Fig. 3 Proposed vbL diagrams for the lowest seven states of ThCO depicting the bonding interactions between Th and CO. The $(10\pi_x)^2 \pm (10\pi_y)^2$ combinations of $^1\Delta$ and $^1\Sigma^+$ states (see Table 2) are represented by electron pairs with solid ($10\pi_y$) and open circles ($10\pi_x$). Similarly, for the $10\pi^16\delta^1$ states $^1\Pi$ and $^3\Phi$, only the major component of $^3\Pi$ is shown.

Table 3 Excitation energies T_e (cm^{-1}), equilibrium Th–C and C–O bond distances r_e (Å), and harmonic vibrational frequencies ω_e (cm^{-1}) of several low-lying states of ThCO at the MRCI(+Q) and CCSD(T) levels of theory

			r_e		
State	Method	T_e	Th–C	C–O	ω_e[c]
$^3\Sigma^-$	MRCI	0	2.308	1.147	
	MRCI+Q[a]	0			
	CCSD(T)	0	2.289	1.170	312, 312, 354, 1853
	CCSD(T)[b]	0	2.287	1.171	310, 310, 358, 1842
$^1\Delta$	MRCI	2341	2.334	1.151	
	MRCI+Q[a]	1976			
$^5\Delta$	MRCI	2825	2.341	1.151	
	MRCI+Q[a]	2814			
	CCSD(T)	3071	2.325	1.170	303, 303, 342, 1855
	CCSD(T)[b]	3055	2.323	1.172	303, 303, 346, 1842
$^1\Sigma^+$	MRCI	4967	2.351	1.151	
	MRCI+Q[a]	4396			
$^3\Pi$	MRCI	5286	2.279	1.161	
	MRCI+Q[a]	4760			
$^3\Phi$	MRCI	6219	2.521	1.128	
	MRCI+Q[a]	6661			
$^1\Pi$	MRCI	7688	2.476	1.137	
	MRCI+Q[a]	8103			

[a] Calculated with MRCI+Q energies at the MRCI optimized geometries. [b] CCSD(T)/cc-pVTZ-PP(Th), aug-cc-pVTZ(C,O). [c] The only stable ^{232}Th isotope is used with atomic mass 232.03810.

This also results in much longer Th–C bonds for $^1\Pi$ and $^3\Phi$ (see Table 3). For the $^3\Sigma^-$ and $^5\Delta$ states, we also calculated harmonic vibrational frequencies at the CCSD(T) level (see Table 3). The lowest frequency corresponds to the doubly degenerate bending mode of ThCO, and the other two to the Th–C and C–O stretches. The frequencies of the same mode are within 10 cm^{-1} for the two states. Our CCSD(T) Th–C and C–O bond lengths for the ground state differ by 0.03 and 0.01 Å from the DFT/PW91 values of Zhou and Andrews.[4] Their CO stretching harmonic vibrational frequency of 1790 cm^{-1} is smaller than our CCSD(T) value by 60 cm^{-1}. If we subtract the experimental anharmonicity for free CO ($2\omega_e x_e$ = 26.6 cm^{-1})[20] our 1853 cm^{-1} harmonic frequency becomes 1826 cm^{-1}. This estimated anharmonic frequency ($\Delta G_{1/2} \approx \omega_e - 2\omega_e x_e$) is in very good agreement with the experimental vibrational C–O frequency of 1817.5 cm^{-1}.[4]

Finally, we performed spin–orbit calculations at the MRCI level. After the inclusion of spin–orbit effects (by diagonalizing the spin–orbit Hamiltonian on the basis of the $^3\Sigma^-$, $^1\Delta$, $^5\Delta$, $^3\Pi$, and $^1\Sigma^+$ MRCI wavefunctions) at an equilibrium distance of 2.30 Å we obtained the following state series in increasing energy order (energies in cm^{-1}): $^3\Sigma^-_{0^+}$ (0.0), $^3\Sigma^-_1$(133), $^5\Delta_{0^-}$ (1810), $^5\Delta_{0^+}$ (1819), $^1\Delta_2$ (2269), $^5\Delta_1$ (2336), $^5\Delta_2$ (2976), $^5\Delta_3$ (3660), $^5\Delta_4$ (4355), $^3\Pi_2$ (4992), $^3\Pi_1$ (4995), $^1\Sigma^+_{0^+}$ (5008), $^3\Pi_{0^-}$ (5316), and $^3\Pi_{0^+}$ (5369). Note that there is a second order spin–orbit splitting in the ground Σ-state of 133 cm^{-1}. The $^5\Delta$ Ω-components span a range of 2545 cm^{-1} and they follow a normal order (smaller Ω values have smaller energies), while the $^3\Pi$ Ω-components cover a range of only 377 cm^{-1} and follow a reverse order (smaller Ω values have higher energies). The $^1\Delta_2$ state was the first excited state before the inclusion of spin–orbit, and it is replaced by $^5\Delta_{0^-}$. Similarly, the $^1\Sigma^+$ state was below $^3\Pi$, but now lies in between the $^3\Pi_\Omega$ states.

Surprisingly, the electronic structures of the lowest lying states of Th resemble those of Ti and are of s^2d^2 or s^1d^3 character. For example, the ground state in both cases is $^3F(s^2d^2)$, while $^5F(s^1d^3)$ is ~6000 cm^{-1} above for Ti and 5500–10 000 cm^{-1} for Th due to the stronger spin–orbit splitting. TiCO has been studied theoretically at a high level of theory by Mavridis and co-workers.[46] The existing experimental results are summarized by the same authors. Despite the similarity of Ti and Th, their carbonyls present completely different electronic structures. Specifically, the ground state of TiCO is $^5\Delta$ and not $^3\Sigma^-$ as happens in ThCO, and all low-lying states (including $^5\Delta$) of TiCO have an *in situ* s^1d^3 titanium center. The potential energy curves of Mavridis and co-workers show clearly that states originating from the $^3F(4s^23d^2)$ state are repulsive. In contrast, ThCO prefers the $7s^26d^2$ configuration (see Fig. 3), and only the $^5\Delta$ state (among the first seven states) is of $7s^16d^3$ character. This observation is a very good example of the distinct chemistry of f-block elements.

OThC

This isomer has been observed experimentally,[4] and in this case the CO molecule appears to be cleaved with the triple CO bond being replaced by ThO and ThC bonds. The reaction of excited Th with CO and the photo-induced isomerization of ThCO have been suggested as generation mechanisms for OThC.[4,30] Our preliminary calculations for the lowest lying electronic states indicated a highly ionic compound with zero or one electron residing at local thorium orbitals. After extensive attempts, we finally included the orbitals described in Section 2 in the active space (see Fig. 4), which were found to be adequate for the description of the wavefunction for the first five states.

Table 5 lists the main configurations of these states labeled as $^3A'$, $^5A''$, $1^3A''$, $2^3A''$, and $^1A'$. In all cases the 13a′, 14a′, 15a′, and 5a″ orbitals are doubly occupied. The first one is primarily the 2s(C) atomic orbital, while the last three are predominantly the 2p(O) ones. The latter signifies a nearly O^{2-} terminal. Similarly, the 16a′, 17a′, and 6a″ orbitals resemble closely the 2p(C) orbitals, and only 18a′ could be considered as a thorium ~7s orbital. Consequently, the $^3A'$, $2^3A''$, and $^1A'$ states have four electrons to carbon p-orbitals amounting totally to six electrons on carbon suggesting C^{2-} for these states and a Th^{4+} center. The $^5A''$ state has a rather C^- terminal (three electrons

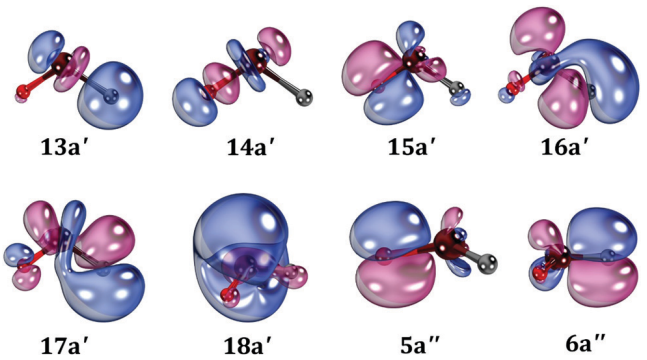

Fig. 4 Selected valence molecular orbitals (see Table 5) of bent OThC. Th, C, and O are represented by a maroon, grey, and red sphere, respectively.

Table 4 Excitation energies T_e (cm^{-1}), equilibrium Th–C and Th–O bond distances r_e (Å), equilibrium O–Th–C bond angles (degrees), and harmonic vibrational frequencies ω_e (cm^{-1}) for low-lying states of OThC

			r_e			
State	Method	T_e	Th–C	Th–O	O–Th–C	ω_e[c]
$^3A'$	MRCI	2561	2.149	1.877	115.5	
	MRCI+Q[a]	0.0				
	CCSD(T)	0.0	2.160	1.886	111.2	171, 630, 825
	CCSD(T)[b]	0.0	2.164	1.888	111.2	171, 624, 820
$^5A''$	MRCI	0.0	2.409	1.856	113.1	
	MRCI+Q[a]	2194				
	CCSD(T)	1466	2.394	1.869	112.4	133, 500, 858
	CCSD(T)[b]	1600	2.401	1.869	112.1	128, 495, 856
$1^3A''$	MRCI	1973	2.438	1.851	112.3	
	MRCI+Q[a]	3327				
$2^3A''$	MRCI	2057	2.243	1.871	120.4	
	MRCI+Q[a]	3620				
	CCSD(T)	2713	2.198	1.890	119.4	160, 553, 818
	CCSD(T)[b]	2702	2.202	1.891	119.4	158, 548, 813
$^1A'$	MRCI	1755	2.030	1.889	148.6	
	MRCI+Q[a]	3741				
	CCSD(T)	3538	2.040	1.897	138.5	101, 690, 797
	CCSD(T)[b]	3516	2.041	1.899	140.1	97, 685, 792

[a] Calculated with MRCI+Q energies at the MRCI optimized geometries. [b] CCSD(T)/cc-pVTZ-PP(Th), aug-cc-pVTZ(C,O). [c] The only stable ^{232}Th isotope is used with atomic mass 232.03810.

Table 5 Dominant electronic configurations and coefficients for low-lying states of bent OThC. The 19a′, 20a′, 21a′, 7a″, and 8a″ active orbitals are unoccupied in the dominant configurations

State	Coef.	13a′	14a′	15a′	16a′	17a′	18a′	5a″	6a″
$^3A'$	0.96	2	2	2	α	α	0	2	2
$^5A''$	0.98	2	2	2	α	α	α	2	α
$1^3A''$	0.67	2	2	2	2	α	0	2	α
	−0.47	2	2	2	0	α	2	2	α
$2^3A''$	0.86	2	2	2	2	α	0	2	α
$^1A'$	0.95	2	2	2	2	0	0	2	2

in 16a′, 17a′, and 6a″) and one electron in 18a′ resulting in a Th^{3+} center. The $1^3A''$ state has two major components involving Th^{4+} ($18a'^0$) and Th^{2+} ($18a'^2$). The orbital occupation for all active orbitals in the various states is given in the ESI.†

The optimized bond lengths and bond angles for these states are listed in Table 4. The ThO bonds range between 1.85 and 1.90 Å, but the ThC bond lengths span a larger range. Specifically, at the MRCI level, the shortest ThC distance of 2.030 Å belongs to $^1A'$, while the longest one to $1^3A''$ (2.438 Å). The bond length of the diatomic ThO species is in the same range, but the ThC ground state has a quite shorter bond (∼1.96 Å) attributed to the triple bond character of diatomic ThC.[18] The CCSD(T) geometries are in good agreement with the MRCI ones. However, the excitation energies of MRCI and CCSD(T) are quantitatively different. For example, MRCI predicts $^5A''$ as the ground state, while MRCI+Q and CCSD(T) prefer the $^3A'$ one. More than double excitations are necessary to get the correct energetics. All of these five states lie within ∼3500 cm^{-1}. For four of these states we calculated CCSD(T) harmonic vibrational frequencies (see Table 4). Frequencies of the same modes are now significantly different (as opposed to ThCO) among the four states. The spin–orbit effects for the non-linear OThC species are small. The spin–orbit components of the two lowest states lie within 60 ($^3A'$) and 80 ($^5A''$) cm^{-1}.

Given the ionic nature of OThC, we performed an additional set of CCSD(T) calculations, where diffuse basis functions are added on carbon and oxygen centers. The optimized geometries and frequencies for these calculations are included in Table 4. The bond lengths and frequencies change by no more than 0.005 Å and 7 cm^{-1}, respectively. Similar trends are observed for ThCO when the diffuse functions are added (see Table 3).

ThCO → OThC

The experimental observation of both isomers raises the question about the relative energies of the two structures and the transition states connecting them.[4,30] To get a clear picture of this isomerization reaction, we constructed the PEPs as a function of the OXC angle (see Fig. 5), where X is the middle point between Th and C (see the inset of Fig. 5). All other parameters are optimized for every angle. Zero angles correspond to linear ThCO and ∼140° angles to bent OThC. The $^3\Sigma^-$ state converts to $1^3A''$, $^1\Delta$ to $^1A'$ and $^1A''$, $^5\Delta$ to $^5A'$ and $^5A''$, and $^3\Pi$ to $^3A'$ and $2^3A''$. Recall that the optimized geometries of the $^3\Sigma^-$–$^3A''$ couple are used for all states, and therefore $1^3A''$ seems erroneously to be the overall minimum in the OThC region. The order of all states in the OThC region is not the same as in Table 4. Therefore, we re-constructed the PEPs in the 100–140° region by optimizing the geometry of the first three states (see Fig. 6). It is now apparent that the reaction will proceed *via* the crossing at 105° between $^3A'$ and $1^3A''$ connecting the ground states of the two isomers.

All of the PEPs undergo several avoided crossings at different angles, and the lower energy pathway from ThCO ($X^3\Sigma^-$) to OThC (X^3A') involves multiple crossings at around 45°, 70°, 80°, and 105° with the PEP of $^1A'$. These crossings will be certainly facilitated by spin–orbit coupling. According to our calculations, a barrier of ∼30 kcal mol^{-1} has to be overcome for the transition from ThCO to OThC.

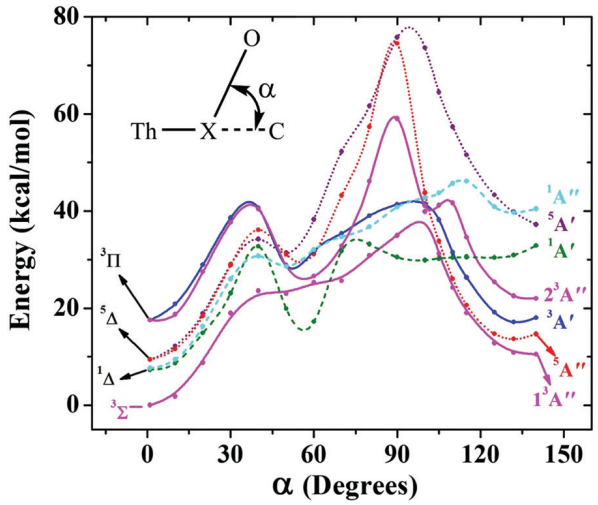

Fig. 5 MRCI+Q energy landscape pertaining to the ThCO → OThC transformation for ground and several excited states. The optimized geometry of the lowest $^3A''$ state is used (see ESI†).

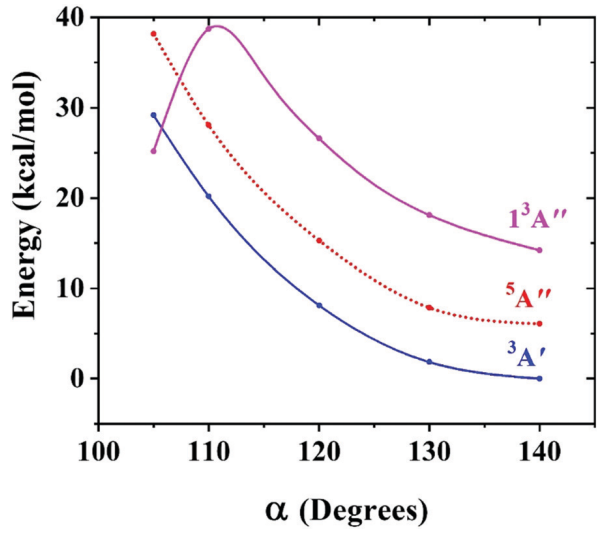

Fig. 6 MRCI+Q energy landscape pertaining to the ThCO → OThC transformation for the ground and two excited states in the OThC region. The MRCI optimized geometry for each state is used (see ESI†).

The optimized CCSD(T) structures of the ground states of ThCO and OThC differ by 6.9 kcal mol^{-1}, ThCO being more stable. Their energy difference becomes 5.4 kcal mol^{-1} after the inclusion of diffuse functions on carbon and oxygen, while using the CCSD(T) energies of a larger basis set (cc-pVQZ-PP(Th), aug-cc-pVQZ(C,O)) at the CCSD(T)/cc-pVTZ-PP(Th) aug-cc-pVTZ(C,O) optimized structure we get 4.4 kcal mol^{-1}. The bent structure was found to be lower by 2.4 kcal mol^{-1} at the DFT/PW91 level.[4] If we include the spin–orbit stabilization ΔE of the two isomers and their ZPVE, our energy difference becomes: 4.4 kcal mol^{-1} + 0.63 kcal mol^{-1} (ΔE_{ThCO}) − 0.57 kcal mol^{-1} (ΔE_{OThC}) + 2.31 kcal mol^{-1} ($\mathrm{ZPVE}_{\mathrm{OThC}}$) − 4.03 kcal mol^{-1} ($\mathrm{ZPVE}_{\mathrm{ThCO}}$) = 3.5 kcal mol^{-1}. The two isomers are quasi-isoenergetic. Our CCSD(T) electronic energy difference for titanium, which is "isoelectronic" to Th (see above), between TiCO ($X^5\Delta$) and OTiC (X^3A') is 40 kcal mol^{-1}. This comparison demonstrates the better ability of Th and possibly all f-block elements to activate chemical bonds (as strong as the triple bond of CO) compared to transition metals.

4. Summary

In this work we perform high level electronic structure calculations, including multi-reference and coupled-cluster methodologies for the ground and excited states of ThCO, OThC, and the path connecting them. Both scalar and spin–orbit effects are important for f-block elements and are also considered here by means of a relativistic pseudo-potential and the Breit–Pauli Hamiltonian. The chemical bonding of the two isomers is analyzed in terms of configuration interaction expansions and molecular orbitals. ThCO is formed as usual metal carbonyls: a σ dative bond from CO to Th is accompanied by two π back-bonding donations in the opposite direction. On the other hand, OThC is strongly ionic represented by a Th^{3+} or Th^{4+} center depending on the electronic state. The OThC isomer is found just 3.5 kcal mol^{-1} above ThCO and has been observed experimentally. The energy barrier separating ThCO from OThC is calculated to be of the 30 kcal mol^{-1} order. The ThCO–OThC couple is compared with the TiCO–OTiC one based on the similarity of the ground state electronic structure between Ti and Th. The OTiC molecule is much (5.5 times compared to thorium compounds) higher than TiCO demonstrating the ability of thorium and possibly other f-block metals to activate strong triple bonds such as the CO bond. In the future the ability of more lanthanides and actinides to activate molecules with multiple bonds will be probed.

Conflicts of interest

There are no conflicts to declare.

Acknowledgements

The authors are indebted to Auburn University (AU) for financial support. This work was completed with resources provided by the Auburn University Hopper Cluster.

References

1 L. R. Morss, N. M. Edelstein and J. Fuger, *The Chemistry of the Actinide and Transactinide Elements*, Springer, Netherlands, Dordrecht, 2006.
2 K.-M. Bae and M.-H. Kim, Core design for heterogeneous Thorium fuel assemblies for PWR(I)-Nuclear Design and Fuel Cycle Economy, *Nucl. Eng. Technol.*, 2005, **37**, 91–100.
3 M. B. Schaffer, Abundant thorium as an alternative nuclear fuel, *Energy Policy*, 2013, **60**, 4–12.
4 M. Zhou, L. Andrews, J. Li and B. E. Bursten, Reactions of Th Atoms with CO: The First Thorium Carbonyl Complex and an Unprecedented Bent Triplet Insertion Product, *J. Am. Chem. Soc.*, 1999, **121**, 12188–12189.
5 C. C. L. Pereira, R. Maurice, A. F. Lucena, S. Hu, A. P. Gonçalves, J. Marçalo, J. K. Gibson, L. Andrews and L. Gagliardi, Thorium and Uranium Carbide Cluster Cations in the Gas Phase: Similarities and Differences between Thorium and Uranium, *Inorg. Chem.*, 2013, **52**, 10968–10975.
6 G. La Macchia, I. Infante, J. Raab, J. K. Gibson and L. Gagliardi, A theoretical study of the ground state and lowest excited states of $PuO^{0/+/+2}$ and $PuO_2^{0/+/+2}$, *Phys. Chem. Chem. Phys.*, 2008, **10**, 7278.
7 L. Gagliardi and B. O. Roos, Quantum chemical calculations show that the uranium molecule U_2 has a quintuple bond, *Nature*, 2005, **433**, 848–851.
8 S. Knecht, H. J. A. Jensen and T. Saue, Relativistic quantum chemical calculations show that the uranium molecule U_2 has a quadruple bond, *Nat. Chem.*, 2019, **11**, 40–44.
9 L. Gagliardi, P. Pyykkö and B. O. Roos, A very short uranium–uranium bond: the predicted metastable U_2^{2+}, *Phys. Chem. Chem. Phys.*, 2005, **7**, 2415.
10 J. Su, P. D. Dau, H.-T. Liu, D.-L. Huang, F. Wei, W. H. E. Schwarz, J. Li and L.-S. Wang, Photoelectron spectroscopy

and theoretical studies of gaseous uranium hexachlorides in different oxidation states: UCl_6^{q-} (q = 0–2), *J. Chem. Phys.*, 2015, **142**, 134308.
11 W. Su, S. Pan, X. Sun, S. Wang, L. Zhao, G. Frenking and C. Zhu, Double dative bond between divalent carbon(0) and uranium, *Nat. Commun.*, 2018, **9**, 4997.
12 C. Celis-Barros, D. Páez-Hernández, M. J. Beltrán-Leiva and R. Arratia-Perez, Ab initio calculations of heavy-actinide hexahalide compounds: do these heavy actinides behave like their isoelectronic lanthanide analogues?, *Phys. Chem. Chem. Phys.*, 2018, **20**, 4038–4049.
13 E. Eliav and U. Kaldor, *Computational Methods in Lanthanide and Actinide Chemistry*, John Wiley & Sons Ltd, Chichester, UK, 2015, pp. 23–54.
14 V. Goncharov, J. Han, L. A. Kaledin and M. C. Heaven, Ionization energy measurements and electronic spectra for ThO, *J. Chem. Phys.*, 2005, **122**, 204311.
15 Y. Li, J. Zou, X.-G. Xiong, H. Xie, Z. Tang, M. Ge, Y. Zhao and H. Liu, Anion photoelectron spectroscopy and chemical bonding of ThO_2^- and ThO_3^-, *J. Chem. Phys.*, 2018, **148**, 244304.
16 M. Straka and P. Pyykkö, Linear HThThH: a candidate for a Th–Th triple bond, *J. Am. Chem. Soc.*, 2005, **127**, 13090–13091.
17 Y. Li, J. Zou, X.-G. Xiong, J. Su, H. Xie, Z. Fei, Z. Tang and H. Liu, Probing Chemical Bonding and Electronic Structures in ThO^- by Anion Photoelectron Imaging and Theoretical Calculations, *J. Phys. Chem. A*, 2017, **121**, 2108–2113.
18 J. Paulovič, T. Nakajima, K. Hirao, R. Lindh and P. Å. Malmqvist, Relativistic and correlated calculations on the ground and excited states of ThO, *J. Chem. Phys.*, 2003, **119**, 798–805.
19 V. Goncharov and M. C. Heaven, Spectroscopy of the ground and low-lying excited states of ThO^+, *J. Chem. Phys.*, 2006, **124**, 064312.
20 A. Kramida, Y. Ralchenko, J. Reader and NIST ASD Team, *NIST Atomic Spectra Database (version 5.4)*, National Institute of Standards and Technology, Gaithersburg, MD, 2016, http://physics.nist.gov/asd, accessed 13 December 2018.
21 P. Pogány, A. Kovács, L. Visscher and R. J. M. Konings, Theoretical study of actinide monocarbides (ThC, UC, PuC, and AmC), *J. Chem. Phys.*, 2016, **145**, 244310.
22 L. V. Skripnikov, Combined 4-component and relativistic pseudopotential study of ThO for the electron electric dipole moment search, *J. Chem. Phys.*, 2016, **145**, 214301.
23 P. Tecmer and C. E. González-Espinoza, Electron correlation effects of the ThO and ThS molecules in the spinor basis. A relativistic coupled cluster study of ground and excited states properties, *Phys. Chem. Chem. Phys.*, 2018, **20**, 23424–23432.
24 A. Kovács and R. J. M. Konings, Molecular structure and thermodynamic properties of the gaseous ThC_2 and ThC_4 species, *J. Nucl. Mater.*, 2008, **372**, 391–393.
25 P. Pogány, A. Kovács, Z. Varga, F. M. Bickelhaupt and R. J. M. Konings, Theoretical Study of the Structure and Bonding in ThC_2 and UC_2, *J. Phys. Chem. A*, 2012, **116**, 747–755.
26 P. Tecmer, K. Boguslawski and P. W. Ayers, Singlet ground state actinide chemistry with geminals, *Phys. Chem. Chem. Phys.*, 2015, **17**, 14427–14436.
27 A. Kovács and R. J. M. Konings, Computed Vibrational Frequencies of Actinide Oxides $AnO^{0/+/2+}$ and $AnO_2^{0/+/2+}$ (An = Th, Pa, U, Np, Pu, Am, Cm), *J. Phys. Chem. A*, 2011, **115**, 6646–6656.
28 L. V. Skripnikov and A. V. Titov, Theoretical study of thorium monoxide for the electron electric dipole moment search: Electronic properties of $H^3\Delta_1$ in ThO, *J. Chem. Phys.*, 2015, **142**, 024301.
29 B. O. Roos, P.-Å. Malmqvist and L. Gagliardi, Exploring the Actinide–Actinide Bond: Theoretical Studies of the Chemical Bond in Ac_2, Th_2, Pa_2, and U_2, *J. Am. Chem. Soc.*, 2006, **128**, 17000–17006.
30 J. Li, B. E. Bursten, M. Zhou and L. Andrews, A Combined Theoretical and Experimental Study of the Reaction Products of Laser-Ablated Thorium Atoms with CO: First Identification of the CThO, $CThO^-$, OThCCO, $OTh(\eta^3\text{-CCO})$, and $Th(CO)_n$ (n = 1–6) Molecules, *Inorg. Chem.*, 2001, **40**, 5448–5460.
31 A. Weigand, X. Cao, T. Hangele and M. Dolg, Relativistic Small-Core Pseudopotentials for Actinium, Thorium, and Protactinium, *J. Phys. Chem. A*, 2014, **118**, 2519–2530.
32 K. A. Peterson, Correlation consistent basis sets for actinides. I. The Th and U atoms, *J. Chem. Phys.*, 2015, **142**, 074105.
33 M. Vasiliu, K. A. Peterson, J. K. Gibson and D. A. Dixon, Reliable Potential Energy Surfaces for the Reactions of H_2O with ThO_2, PaO_2^+, UO_2^{2+}, and UO_2^+, *J. Phys. Chem. A*, 2015, **119**, 11422–11431.
34 S. R. Langhoff and E. R. Davidson, Configuration interaction calculations on the nitrogen molecule, *Int. J. Quantum Chem.*, 1974, **8**, 61–72.
35 H.-J. Werner, P. J. Knowles, G. Knizia, F. R. Manby, M. Schütz and M. W. P. Celani, W. Györffy, D. Kats, T. Korona, R. Lindh, A. Mitrushenkov, G. Rauhut, K. R. Shamasundar, T. B. Adler, R. D. Amos, A. Bernhardsson, A. Berning, D. L. Cooper, M. J. O. Deegan, A. J. Dobbyn, F. Eckert, E. Goll, C. Hampel, A. Hesselmann and G. Hetzer, *MOLPRO, version 2015.1, a package of ab initio programs*, see http//www.molpro.net.
36 H.-J. Werner, P. J. Knowles, G. Knizia, F. R. Manby and M. Schütz, Molpro: a general-purpose quantum chemistry program package, *Wiley Interdiscip. Rev.: Comput. Mol. Sci.*, 2012, **2**, 242–253.
37 A. Berning, M. Schweizer, H.-J. Werner, P. J. Knowles and P. Palmieri, Spin-orbit matrix elements for internally contracted multireference configuration interaction wavefunctions, *Mol. Phys.*, 2000, **98**, 1823–1833.
38 T. H. Dunning, Gaussian basis sets for use in correlated molecular calculations. I. The atoms boron through neon and hydrogen, *J. Chem. Phys.*, 1989, **90**, 1007–1023.
39 R. E. Wilson, S. D. Sio and V. Vallet, Protactinium and the intersection of actinide and transition metal chemistry, *Nat. Commun.*, 2018, **9**, 622.
40 I. R. Ariyarathna and E. Miliordos, Dative bonds versus electron solvation in tri-coordinated beryllium complexes: $Be(CX)_3$ [X = O, S, Se, Te, Po] and $Be(PH_3)_3$ versus $Be(NH_3)_3$, *Int. J. Quantum Chem.*, 2018, **118**, e25673.
41 I. R. Ariyarathna and E. Miliordos, Electronic and geometric structure analysis of neutral and anionic alkali metal

complexes of the CX series (X = O, S, Se, Te, Po): The case of $M(CX)_{n=1-4}$ (M = Li, Na) and their dimers, *J. Comput. Chem.*, 2019, **40**, 1344–1351.

42 A. Kalemos, I. R. Ariyarathna, S. N. Khan, E. Miliordos and A. Mavridis, "Hypervalency" and the chemical bond, *Comput. Theor. Chem.*, 2019, **1153**, 65–74.

43 W. Jiang, N. J. DeYonker and A. K. Wilson, Multireference Character for 3d Transition-Metal-Containing Molecules, *J. Chem. Theory Comput.*, 2012, **8**, 460–468.

44 H. J. Werner, Third-order multireference perturbation theory The CASPT3 method, *Mol. Phys.*, 1996, **89**, 645–661.

45 K. P. Huber and G. H. Herzberg, *(data prepared by J. W. Gallagher and R. D. Johnson, III), Constants of Diatomic Molecules in NIST Chemistry WebBook, NIST Standard Reference Database Number 69*, ed. P. J. Linstrom and W. G. Mallard, National Institute of Standards and Technology, Gaithersburg MD, 20899, https://doi.org/10.18434/T4D303, retrieved October 17, 2019.

46 C. Koukounas, S. Kardahakis and A. Mavridis, Electronic and geometric structure of the 3d-transition metal monocarbonyls MCO, M = Sc, Ti, V, and Cr, *J. Chem. Phys.*, 2005, **123**, 074327.

Electronic and Geometric Structure Analysis of Neutral and Anionic Metal Nitric Chalcogens: The Case of MNX Series (M=Li, Na, Be and X=O, S, Se, Te)

Volume 40 | Issues 19–20 | 2019
Included in this print edition:
Issue 19 (July 15, 2019)
Issue 20 (July 30, 2019)

Journal of COMPUTATIONAL CHEMISTRY

Organic • Inorganic • Physical
Biological • Materials

www.c-chem.org

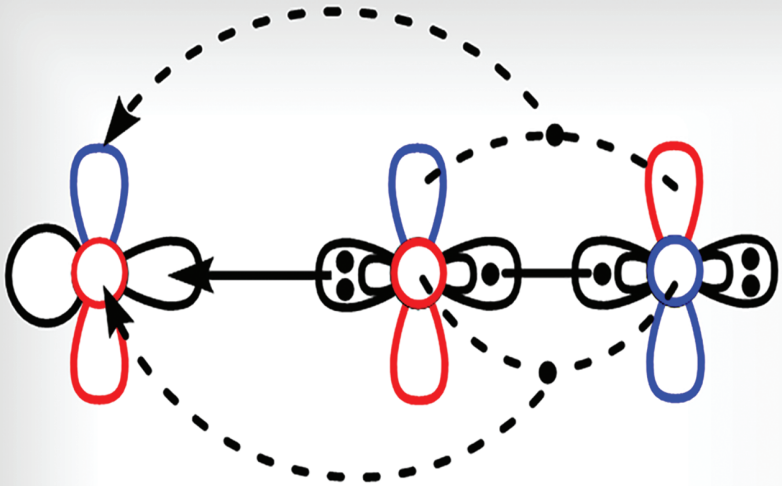

LiNO

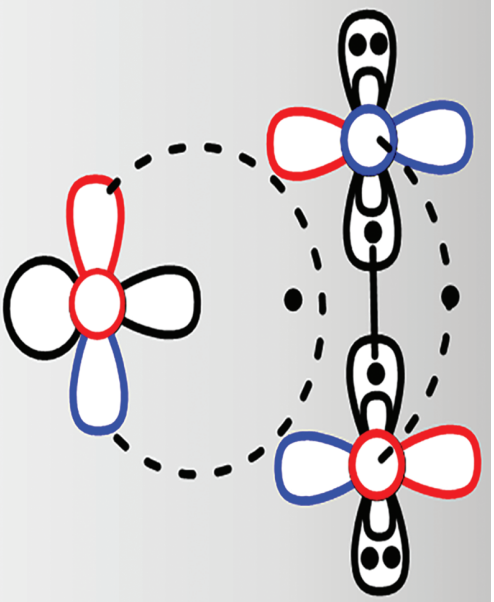

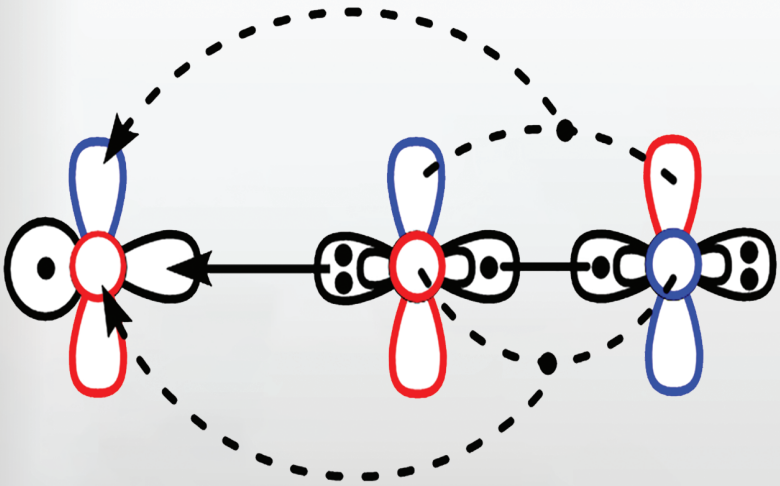

BeNO

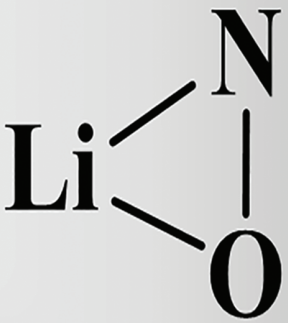

Editors:
Charles L. Brooks III • Masahiro Ehara • Gernot Frenking • Peter R. Schreiner

WILEY

Journal of COMPUTATIONAL CHEMISTRY

Electronic and Geometric Structure Analysis of Neutral and Anionic Metal Nitric Chalcogens: The Case of MNX Series (M=Li, Na, Be and X=O, S, Se, Te)

Isuru R. Ariyarathna and Evangelos Miliordos*

Coupled cluster and multireference configuration approaches are employed to study the electronic and geometric structures of mono-coordinated complexes of lithium, sodium, and beryllium with nitric oxide and its isovalent NS, NSe, and NTe species. Ground and low-lying excited states were examined for both linear-bonded and side-bonded isomers. We show that the ionic M^+NX^- (M=Li, Na, Be and X=O, S, Se, Te) picture is a more natural representation and can account for the symmetry of the low–lying electronic states as Σ^-, Δ, and Σ^+, the smaller excitation energies and the larger binding energies for heavier X. An additional electron binds to the positively charged Li and Na terminal creating stable anions. The electron affinity (EA) of LiNX and NaNX species is in the 0.5–0.8 eV range. Despite the negative EA of beryllium and the very small EA of NO, the BeNO molecule has an EA of ~1.0 eV, which is increased to ~1.5 eV for the heavier BeNX species. This is attributed to the fact that the additional electron goes to the beryllium end for BeNO but to a π(MN)—π^*(NX) orbital of the rest species. Our accurate results contradict previous findings and serve as a guide for future experimental studies. © 2019 Wiley Periodicals, Inc.

DOI: 10.1002/jcc.25829

Introduction

In 1992, nitric oxide (NO) was named the "Molecule of the year" [1], soon after the discovery of its biological importance as a cardiovascular signaling agent in physiological processes in mammals.[2] For this discovery, Robert Furchgott, Louis Ignarro, and Ferid Murad received the 1998 Nobel Prize in Physiology or Medicine.[3] On the other hand, overexposure of NO can be life threatening.[4] The Occupational Safety Health Administration has set the exposure limit of NO to 25 ppm over an 8-hour workday.[5]

In the atmosphere, NO is produced naturally by lightning, which triggers the $N_2 + O_2 \rightarrow 2NO$ reaction. In the stratosphere, NO is generated by oxidation of N_2O and depletes the ozone layer producing N_2O and O_2.[6] NO reacts with atmospheric O_2 and H_2O to produce HNO_2 and HNO_3 creating acid rains, while it can also generate ozone via smog reactions.[6] Commercially NO is produced by oxidizing NH_3 or by reacting O_2 with N_2 at 3000°C in the presence of an electric arc.[7,8] NO is a key precursor in the industrial production of nitric acid and nitrogen-based fertilizers.[9]

Transition metal NO complexes have found numerous application in organometallic chemistry.[10] For example, $MH(NO)(PPh_3)_3$ (M=Ru, Os) [11] and ReBrH(NO)(L) [12] are competent catalysts for hydrogenation. Further $Rh(NO)(PPh_3)_3$ and $Fe(NO)_2(CO)_2$ can catalyze isomerization and dimerization reactions.[13] A comprehensive overview of catalytic potency of metal —NO complexes can be found in "Coordination and Organometallic Chemistry of Metal —NO Complexes" review by Sharp et al.[14]

Cotton and Wilkinson classify the M—NO species as linear or bent based on the binding mode. In the case, when the N terminal donates an electron pair to the metal, the M—N—O angle vary in between 161° and 180°.[15] The angle is determined by the backdonation strength of the metal to π^*(NO).[13,14] Smaller M—NO angles (~120 – 140°) are usually assigned to the covalent bond between the unpaired electron of NO and the metal.[13,14] About 120° angles have been observed for M—N—O angles in $[IrCl(CO)(PPh_3)_2NO]^+$, $IrCl_2(NO)(PPh_3)_2$, $[Co\ en_2Cl(NO)]^+$, and $IrI(CH_3)(NO)(PPh_3)_2$ complexes.[15]

Chemical bonding of a linear M—NO is often collated with the M—CO bond. In both cases, each ligand acts as a dative σ-donor and π-acceptor [15], but smaller π-acceptance from metal to ligand should be expected for M—NO due to the presence of one electron in a π^*(NO); π^*(CO) orbitals are vacant. NO is also referred as a three-electron donor in the literature, in contrast with CO, which is clearly a two-electron donor.[15]

The geometric and electronic features of the main group metal-NO species are less studied in the literature. However, recently main group metal-ligand systems have become more and more popular because of their versatile chemical bonding patterns.[16–21] Specifically, Andrews et al. studied linear Li—NO, linear Li—ON, and side-bonded Li[NO] species under density functional theory (DFT).[22] They have found that the ground state $^3A''$ of Li[NO] is 1.4 kcal/mol higher than the ground state $^3\Sigma^-$ of Li—NO. This study further reports the ground state of Li—ON (also $^3\Sigma^-$), which is found 5.4 kcal/mol higher in energy than Li—NO. On the contrary, seven years later Henry Schaefer et al. revealed that the global minimum of lithium nitroxide is Li[NO] according to the coupled cluster (CCSD(T)) theory.[23]

The only study related to the Be interaction with NO belongs to Andrews et al.[24] They have studied the Be + NO reaction at 10 K

[a] I. R. Ariyarathna, E. Miliordos
Department of Chemistry and Biochemistry, Auburn University, Auburn, Alabama 36849-5312
E-mail: emiliord@auburn.edu
Contract Grant sponsor: Auburn University

in argon matrix by laser-ablation and analyzed the recorded infrared spectra.[24] Their results suggest that the major adducts are BeNO and BeOBeNO. They supported their experimental work by obtaining structures and frequencies at the DFT and predicted a linear Be—NO structure at a $^2\Sigma^-$ state as the global minimum. Although, not stated by the authors, $^2\Sigma^-$ implies an "open-shell" doublet with three unpaired electrons. Both linear and bent interactions of Be or Li with NO can generate "open-shell" states, the wave function of which cannot be represented accurately by either DFT or single-reference coupled cluster theory. These open shell electronic configurations can only be described properly by multireference calculations. The present study aims at the performance of multireference calculations to elucidate the electronic structure of the titled systems and their energetics.

Recently, we have studied the chemical bonding of the LiCO and BeCO molecules using high-level MRCI and CCSD(T) methods.[25,26] Both LiCO and BeCO are meta stable with respect to their ground state fragments Li(^{2}S) + CO($^1\Sigma^+$) and Be(^{1}S) + CO ($^1\Sigma^+$). LiCO and BeCO generate from the excited Li(^{2}P; $2p^1$) + CO ($^1\Sigma^+$) and Be(^{3}P; $2s^12p^1$) + CO($^1\Sigma^+$) channels, respectively. By promoting electrons into 2p-orbitals, these metals expose their charged nucleus to facilitate the attack by CO. Is the chemical bonding present in LiNO and BeNO similar to the LiCO and BeCO? If BeNO results from Be(^{3}P; $2s^12p^1$), then several low energy multireference doublet and quartet states should be expected. Actually, our advanced electronic structure calculations suggest a $^4\Sigma^-$ ground state for BeNO contradicting the $^2\Sigma^-$ state assignment by Andrews et al.[24] Additionally, NO complexes as opposed to the CO ones have low-energy linear and side-bonded structures, also adding some complexity to the metal-NO species. How do their relative stabilities change with NX (X=O, S, Se, Te) series or with different main group metals?

In this article, we address these questions by performing high-level multireference configuration interaction and single-reference coupled cluster calculations, when appropriate, on MNX (M=Li, Na, Be and X=O, S, Se, Te) series. We obtained potential energy profiles and studied the excited states of each species. Finally, we investigated all stable anions of the titled molecules.

Computational Details

Full potential energy curves (PECs), optimal geometries, excitation energies, and electron affinities for all of the species are obtained using multireference configuration interaction (MRCI) method building on the initial complete active space self-consistent field (CASSCF) wave function. The active space consists of all the valence electrons of all atoms at CASSCF. All valence electrons are promoted to the virtual orbital space at MRCI. As a correction to the size extensivity errors of MRCI, the Davidson correction (MRCI+Q) was applied. Coupled cluster single, double, and perturbative triples [CCSD(T)] method based on a restricted Hartree–Fock reference wavefunction was employed for the cases with minimal multireference character. All calculations were carried out using augmented correlation consistent triple–ζ quality (aug-cc-pVTZ) basis sets for all atoms.[27–29] For Se and Te, we replaced their inner 10 and 28 electrons with relativistic pseudopotentials.[30] The rest of the electrons were treated explicitly using the aug-cc-pVTZ basis set. CCSD(T) harmonic vibrational frequencies were calculated for the ground states of all molecules (see Supporting Information). Binding energies (D_e) were extrapolated to the complete basis set (CBS) limit using the aug-cc-pVXZ (X=T, Q, 5) series. All D_e values are given in the Supporting Information and were fitted in a simple exponential form. As shown below, the aug-cc-pVTZ values differ less than 2 kcal/mol from the aug-cc-pV5Z ones, and that the last values are nearly identical to the CBS limit. Therefore, the extrapolation expression is expected to affect the CBS limit only minimally. The PECs were constructed by varying the M—N distances, but the NO length was fixed to the experimental equilibrium bond distance of free NO (1.151 Å). All calculations were done invoking MOLPRO 2015.1.[31]

MNX (M=Li, Na and X=O, S, Se, Te)

Li can bind to NO to generate the linear Li—ON, linear Li—NO, or side-bonded Li[NO] isomers. The Li—ON isomer has been found to lie energetically higher than both Li—NO and Li[NO] by 4.1 and 6.5 kcal/mol.[23] In this article, we focus on the lower energy linear Li—NO and bent Li[NO] isomers. We provide accurate optimal geometries, binding energies, excitation energies, and vibrational frequencies. We also examine the chemical bonding by constructing potential energy profiles (PEPs) with respect to the linear and oblique Li ← NO attack including the first two asymptotes Li(^{2}S; $1s^22s^1$) + NO($X^2\Pi$) and Li(^{2}P; $1s^22p^1$) + NO($X^2\Pi$), which are 14,904 cm^{-1} apart.

In the linear approach of Li(^{2}S; $1s^22s^1$) + NO($X^2\Pi$), an electron pair localized at the "back" of the nitrogen terminal of NO points toward Li. We expect this interaction to be strongly repulsive because of the coulombic repulsion between the $2s^1$(Li) electron and the aforementioned electron pair. The two unpaired electrons, 2 s(Li) and π*(NO), form a $^3\Pi$ and an open-shell $^1\Pi$ state. This dissociative interaction is confirmed by the repulsive nature of the corresponding PEPs (see Fig. 1). Moving to the next channel, according to the Wigner–Witmer rules, the linear Li(^{2}P; $1s^22p^1$) + NO($X^2\Pi$) combination produces the $^{1,3}\{\Sigma^+, \Sigma^-, \Pi, \Delta\}$ manifold of states. Among those, $^3\Sigma^-$, $^1\Delta$, and $^1\Sigma^+$ are strongly attractive, whereas $^1\Pi$ and $^3\Pi$ are repulsive (see Fig. 1). The remaining $^3\Delta$, $^3\Sigma^+$, and $^1\Sigma^-$ make shallow minima of ~2 kcal/mol at ~2 Å. Our PEPs suggest that the ground state is $^3\Sigma^-$, followed by the $^1\Delta$ and $^1\Sigma^+$ excited states. Remarkably, the two of them, $^3\Sigma^-$ and $^1\Delta$, become stable with respect to the lowest energy channel Li(^{2}S; $1s^22s^1$) + NO($X^2\Pi$).

In the ground state, $^3\Sigma^-$ of LiNO, each of $2\pi_x$ and $2\pi_y$ orbitals possesses a single electron. The $2\pi_x$ and $2\pi_y$ orbitals correspond largely to the two π* orbitals of NO (see Fig. 2) suggesting the Li^+NO^- picture. Similarly, $^1\Delta$ and $^1\Sigma^+$ bear two-coupled electrons in the two $2\pi_{x,y}$ orbitals pointing also to an ionic structure. The $2\pi_x^2$ and $2\pi_y^2$ configurations are combined with ± signs to create the $^1\Sigma^+$ state and one component of $^1\Delta$. The first three states of LiNO, $^3\Sigma^-$, $^1\Delta$, and $^1\Sigma^+$ can be corelated to the first three states of NO^-, $^3\Sigma^-$, $^1\Delta$, and $^1\Sigma^+$. Our MRCI+Q calculations predicted that $^1\Delta$ and $^1\Sigma^+$ of NO^- are located 6944 and 11,078 cm^{-1} above the ground $^3\Sigma^-$ state. The experimental first and second excitation energies of NO^- is 6050 and 9300 cm^{-1}

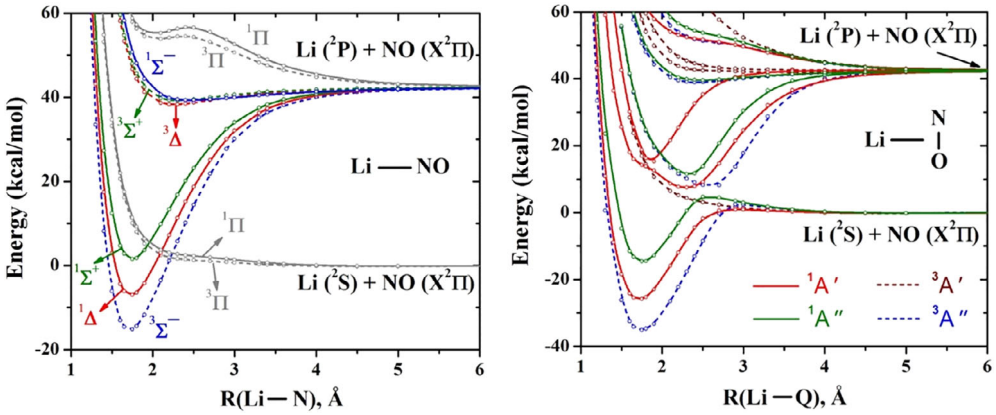

Figure 1. MRCI PEPs for the approach of Li and NO in a linear (left plot) and an oblique (right plot) fashion. In the first case, the energy is plotted against the Li – N distance and in the second case with respect to the Li – Q distance, where Q is the center of NO. In each case, the NO distance is kept fixed to the experimental NO distance 1.151 Å.[32] [Color figure can be viewed at wileyonlinelibrary.com]

are in fair agreement with our values.[32] The calculated first and second excitation energies of linear LiNO at MRCI+Q are 5549 and 8836 cm^{-1}, respectively. The identical energy pattern in the first three electronic states of LiNO and NO^- further supports the ionic bonding of Li^+NO^-.

The proposed valance-bond-Lewis (vbL) diagrams based on the occupied molecular orbitals of Figure 2 and the CI vectors collected in Table 1 are drawn in Scheme 1. The bonding for all three states can be seen with two aspects. They can be formed from the neutral fragments Li(^{2}P) + NO($^2\Pi$) (left vbL diagrams of Scheme 1) or the ionic species Li^+(^{1}S) + NO^-($^3\Sigma^-$,$^1\Sigma^+$,$^1\Delta$) (right vbL diagrams of Scheme 1). The Mulliken charges for the three states on lithium are +0.36, +0.44, and + 0.51. In all three cases, the population in the σ-frame of Li is about ~2.35 electrons ($1s^2$ + 0.35 donated electrons from NO or NO^-), while the π-frame is occupied by 0.1–0.25 electrons (donated electrons from the π* orbitals of NO^- or π-backdonation of 0.75–0.9 electrons from Li to NO). Although the PEPs of all three electronic states are stemming from the Li(^{2}P) + NO($^2\Pi$) adiabatic channel, for three reasons we suggest the ionic picture as a more natural way to describe the binding mode. First, the excitation energies of LiNO and the parent Li^+NO^- asymptotes match very well (see above). Second, it is more natural to accept that 0.1–0.25 π-electrons go from NO to Li rather than 0.75–0.9 electrons to the opposite direction. Third, The MOs $2\pi_x$ and $2\pi_y$ of Figure 2 are clearly polarized toward NO supporting this icon. Therefore, we propose that the "equilibrium" (or resonance) between the neutral and ionic pictures of Scheme 1 is shifted to the right.

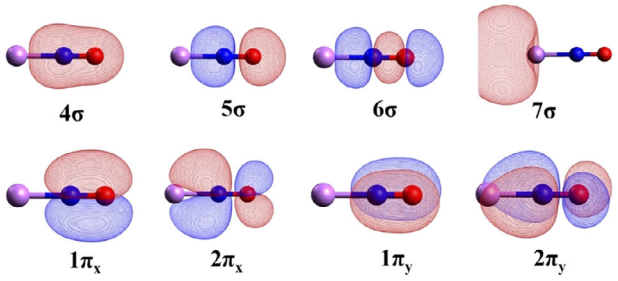

Figure 2. Selected molecular orbitals of linear LiNO. Purple, blue, and red spheres represent Li, N, and O, respectively. [Color figure can be viewed at wileyonlinelibrary.com]

The $^3\Sigma^-$, $^1\Delta$, and $^1\Sigma^+$ states of linear Li—NO result in four states, ^{1}A″, ^{3}A″, two ^{1}A′ under C_s symmetry for bent Li[NO]. The PEPs of the oblique Li + NO approach reveal avoided crossings not present in the linear case (see Fig. 1) due to the lower symmetry (C_s vs. $C_{\infty v}$). Under C_s, the lowest energy Li(^{2}S; $1s^22s^1$) + NO($X^2\Pi$) fragments produce two triplets (^{3}A′, ^{3}A″) and two singlets (^{1}A′, ^{1}A″), which are the counterparts of $^{1,3}\Pi$ ($C_{\infty v}$). The PEP of ^{3}A′ remains repulsive, imitating $^3\Pi$ (see Fig. 1), but ^{3}A″, ^{1}A′, and ^{1}A″ although repulsive for distances larger than 2.75 Å, they become attractive forming the minima at ~1.75 Å of the lowest three PEPs. The turning point arises because of the avoided crossings they undergo with the ^{3}A″, ^{1}A′, and ^{1}A″ PECs coming from Li(^{2}P) + NO($X^2\Pi$). All three equilibrium structures are lower than the Li(^{2}S) + NO($X^2\Pi$) dissociation limit and are more stable than the linear ones.

The dominant electronic configurations for Li[NO] are given in Table 2, which highly resemble the ones for linear LiNO. Specifically, the ^{3}A″ has two electrons in 8a′ and 2a″, which are chiefly of $\pi_{x,y}$*(NO) character and look very much like $2\pi_{x,y}$ of linear LiNO (compare Figs. 2 and 3). One difference is that 2a″~π_x*(NO) does not overlap with any of the lithium valence orbital because of symmetry. Therefore ^{3}A″ resembles $^3\Sigma^-$, and likewise ^{1}A″ is similar to the $^1A_2$ component of $^1\Delta$ (see Tables 1 and 2). Finally, the $^1A_1$ component of $^1\Delta$ and $^1\Sigma^+$ adopt the ^{1}A′ irreducible representation under C_s, and their two $2\pi_x^2 \pm 2\pi_y^2$ components separate to make the 1^1A′ and 2^1A′ states. The in-plane $2\pi_y^2$ component (1^1A′) is stabilized appreciably over the off-plane $2\pi_x^2$ one (2^1A′). The former makes the minimum at −25 kcal/mol of Figure 1, and the latter makes a minimum at ~18 kcal/mol. Observe that the PEP of 2^1A′ undergoes a crossing right at its minimum with the repulsive curves coming from the ground state fragments (see Fig. 1). In Table 2, we list the electronic configuration at the minimum of the third ^{1}A′ state, which is the result of this rare crossing. As in the case of linear LiNO, we also suggest an ionic picture for Li[NO]. The corresponding vbL diagrams are shown in Scheme 2.

Our MRCI and CCSD(T) geometry optimizations placed the side-bonded Li[NO] as the global minimum with the linear LiNO being 7.7, 2.5, and 1.8 kcal/mol higher at MRCI, MRCI+Q, and CCSD(T), respectively. Both isomers are stationary points on the ground state potential energy surface with real harmonic vibrational frequencies (see Supporting Information). The PEPs of

Table 1. Dominant electronic configurations for the lowest electronic states of linear LiNO.

State	Coefficient	4σ	5σ	6σ	7σ	$1\pi_x$	$2\pi_x$	$1\pi_y$	$2\pi_y$
$^3\Sigma^-$	0.97	2	2	2	0	2	α	2	α
$^1\Delta$ ($^1A_2$)[a]	0.68	2	2	2	0	2	α	2	β
	−0.68	2	2	2	0	2	β	2	α
$^1\Delta$ ($^1A_1$)[a]	0.68	2	2	2	0	2	2	2	0
	−0.68	2	2	2	0	2	0	2	2
$^1\Sigma^+$	0.68	2	2	2	0	2	2	2	0
	0.68	2	2	2	0	2	0	2	2

[a] The C_{2v} irreducible representation is written in parenthesis.

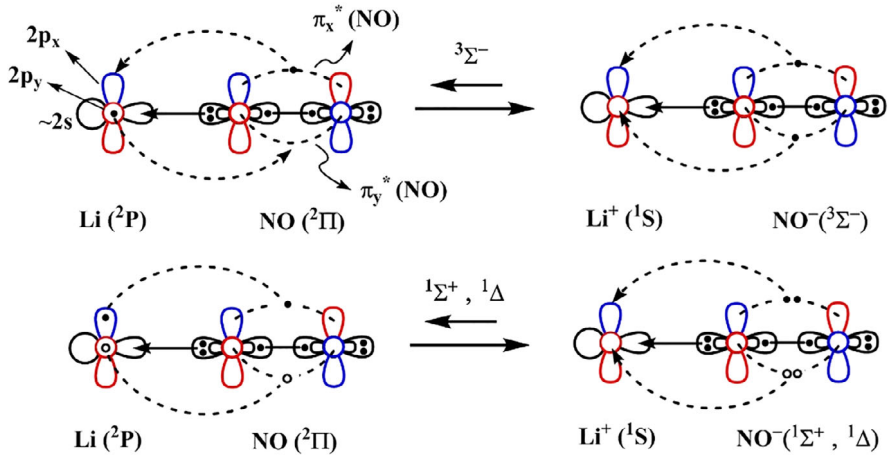

Scheme 1. Proposed vbL diagram for the lowest three states of LiNO. In $^3\Sigma^-$ state, each π*(NO) is occupied by one electron, and the two electrons have the same spin. The $2\pi^2_x \pm 2\pi^2_y$ combinations of $^1\Delta$ and $^1\Sigma^+$ (see Table 1) are represented with electron pairs shown with solid ($2\pi_x^2$) and open circles ($2\pi_y^2$). The π(NO)~1π orbitals are not included for clarity. [Color figure can be viewed at wileyonlinelibrary.com]

Table 2. Dominant electronic configurations for the lowest electronic states of side-bonded Li[NO].

State	Coefficient	4a′	5a′	6a′	7a′	8a′	9a′	1a″	2a″
^{3}A″	0.97	2	2	2	2	α	0	2	α
1^1A′	0.95	2	2	2	2	2	0	2	0
^{1}A″	0.68	2	2	2	2	α	0	2	β
	−0.68	2	2	2	2	β	0	2	α
2^1A′ [a]	0.76	2	2	2	2	0	0	2	2

[a] The electronic configuration for 2^1A′ state is obtained at the minimum of the third ^{1}A′ PEP; see text.

Figure 4 confirm that both isomers are real minima and shows that they are bridged with a small (~10 kcal/mol) energy barrier. Figure 4 also shows that 2^1A′ is not a local minimum but it slides directly to the $^1\Sigma^+$ state of linear LiNO.

For the single-reference ground state, the variation between MRCI and CCSD(T) optimal geometries for LiNO or Li[NO] is minimal. The small differences for bond lengths and angles of at most 0.004 Å and 0.5° indicate that our structures are converged with respect to the correlation energy included. On the other hand, the excitation energies are rather underestimated at MRCI, especially for LiNO, where MRCI + Q increases them considerably (see Table 3). For the lowest excited state, 1^1A′ of Li[NO], the MRCI excitation energy is 3364 cm^{-1} increased to 3739 cm^{-1} at MRCI + Q going closer to the CCSD(T) value of 3831 cm^{-1} (see Table 3).

Comparing the LiNO and Li[NO] structures, we see that the N—X bond elongates by ~0.06 Å going from linear to side-bonded species since oxygen binds also to Li. An equivalent expression is that the π and π* orbitals of NO have a larger overlap with lithium valence orbitals. For example the $1\pi_{x,y}$ orbitals of Figure 2 are mostly localized on NO, but the 7a′ of Figure 3 is delocalized in the inter-nuclear region of the three atoms. Similar observation can be made for $2\pi_{x,y}$ and 8a′ orbitals.

As an extension to the LiNO and Li[NO] study, we further investigated the ground and excited states of the isovalent

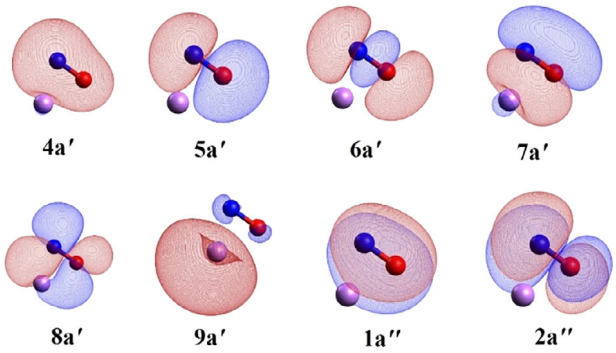

Figure 3. Selected MOs of the side-bonded Li[NO]. Li, N, and O are represented by purple, blue, and red spheres respectively. [Color figure can be viewed at wileyonlinelibrary.com]

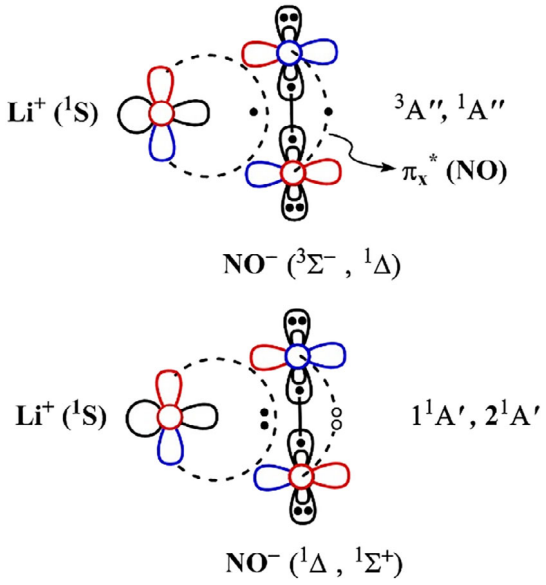

Scheme 2. Proposed vbL diagram for the lowest three states of side-bonded Li[NO]. In ^{1,3}A″, the two electrons occupy different orbitals, while in the ^{1}A′ states the two electrons are coupled into the same orbital. The electron configuration of 1^{1}A′ and 2^{1}A′ is depicted with closed and open circles, respectively. [Color figure can be viewed at wileyonlinelibrary.com]

LiNS, Li[NS], LiNSe, Li[NSe], LiNTe, and Li[NTe] species. The energetics, excitation energies, and optimal geometric parameters are given in the Table 3. Some observations are in order. For all Li—NX (X=S, Se, Te) species, the linear isomers are favored over the side-bonded structures in contrast to Li—NO. The stabilization of linear structures for Li—NX over the bent ones are 2.3 (X=S), 1.7 (X=Se), and 1.8 (X=Te) kcal/mol.

Within each LiNX and Li[NX] species the order of the lowest-lying electronic states is identical to LiNO and Li[NO], respectively: $^{3}\Sigma^{-} < {}^{1}\Delta < {}^{1}\Sigma^{+}$ and ^{3}A″ < ^{1}A′ < ^{1}A″. However, the energy gaps between the excited and ground states shrinks as we go from O to Te, as exactly happens for the excited states of NX^{-}. Specifically, the MRCI+Q $^{3}\Sigma^{-} \rightarrow {}^{1}\Delta$ excitations for the NX^{-} species are 6944, 6079 (865 cm^{-1} decrease), 5993 (86 cm^{-1} decrease), and 5624 cm^{-1} (369 cm^{-1} decrease) for X=O, S, Se, Te. The MRCI+Q $^{3}\Sigma^{-} \rightarrow {}^{1}\Delta$ excitation for LiNX follows the exact same trend: It drops considerably going from O to S (711 cm^{-1}), drops by only 234 cm^{-1} from S to Se, and by 404 cm^{-1} from Se to Te. In any case, the first and second excitation energies of Li[NS], Li[NSe], and Li[NTe] are lower than their corresponding linear isomers, suggesting that electronic spectroscopy of the two isomers is very distinct.

The CCSD(T) binding energies of the Li—NX series increase as NO is replaced by its heavier NS, NSe, and NTe analogues. This is in agreement with their carbonyl-like MCX counterparts.[25,26] In the case of carbonyls, this trend was rationalized in terms of the higher dipole moment of heavier CX species. Presently, the higher binding energies are attributed to the larger NX electron affinities (EA) as we go from O to Te. These are 0.00, 1.17, 1.46, and 1.80 eV at the CCSD(T)/aug-cc-pVTZ level of theory and correcting for ZPE. The accurate theoretical prediction of EA(NO), which experimentally is 0.028 eV, has been proven as an arduous task.[33] Larger EAs stabilize the $Li^{+}NX^{-}$ asymptotes over the Li + NX ones, which in turn stabilize the mainly ionic equilibrium structures. Indeed, the correlation between the D_e and EA values is linear (see Supporting Information Fig. S4). It should be mentioned that the aug-cc-pVTZ binding energies are less than 2 kcal/mol away from the CBS limit (see Table 3 and Supporting Information Table S16). The same is true for all of the considered molecules.

A similar analysis was carried out for the Na—NX series. This time, the side-bonded Na[NX] isomers are favored in all cases by 3.2, 0.6, 1.3, and 1.0 kcal/mol. The order of the ground and excited states of NaNX and Na[NX] is the same as LiNX and Li[NX]. As happens for lithium, the first and second excitation energies are higher in linear structures compared to the side-bonded ones. Additionally, the excitation energies are always larger in the case of Na over Li. The binding energies of NaNX or Na[NX] are smaller than LiNX or Li[NX], which can be attributed to the smaller charge density of Na^{+} over Li^{+}.[26] The heavier NX groups increased the binding energies similarly to the lithium case and are still linearly correlated with the NX EAs (see Supporting Information Fig. S4). The MRCI and CCSD(T)-predicted geometries of NaNX and Na[NX] are in harmony (see the Table 4). Within the NaNX series, the Na—N distances are approximately about 2.1 Å but for the Na[NX] this length varies within 2.2–2.3 Å. The same values for LiNX and Li[NX] are shorter by about 0.3–0.4 Å (1.75 Å and 1.8–1.9 Å, respectively), which matches with the difference of the atomic radii of Li and Na.[34]

MNX^{-} (M=Li, Na and X=O, S, Se, Te)

The ground states of Li[NO] and LiNO contain two unpaired electrons occupying primarily a π*(NO) orbital. Will an additional electron couple with an existing electron or will it populate orbitals localized on Li as happens for LiCO? [26] The latter seems a more plausible scenario since the lithium terminal is positively charged. To answer these questions, we first probed the stability of linear and bent isomers of lithium nitroxide anion. We found

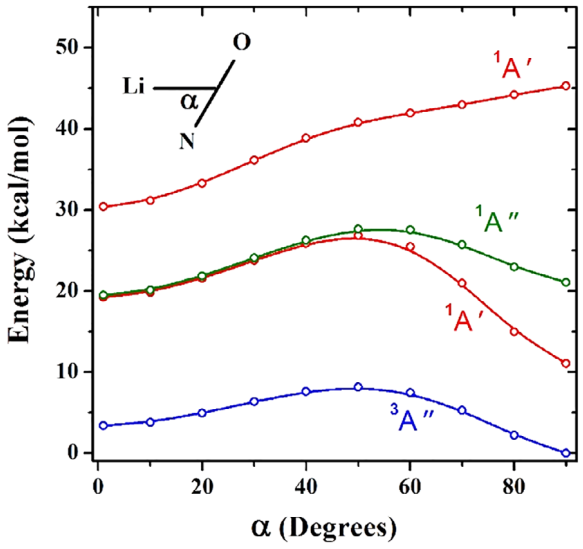

Figure 4. The energy variation with respect to angle α (see inset) connecting LiNO and Li[NO]. [Color figure can be viewed at wileyonlinelibrary.com]

Table 3. Binding energy D_e (kcal/mol) with respect to Li(^{2}S)+NX($X^2\Pi$), excitation energy T_e (cm^{-1}), optimal bond lengths r_e (Å), and Li-N-X angles (degrees) for the lowest electronic states of LiNX (X = O, S, Se, Te).

					r_e			
Molecule [a]	State	Method	D_e [b]	T_e	Li–N	N–X	Li–X	Li–N–X
Li[NO]	$^3A''$	MRCI		0	1.905	1.282	1.812	66.0
		MRCI+Q		0				
		CCSD(T)	34.5 (35.5)	0	1.903	1.278	1.821	66.5
	$1^1A'$	MRCI		3364	1.856	1.266	1.783	66.6
		MRCI+Q		3739				
		CCSD(T)		3831	1.857	1.264	1.786	66.7
	$^1A''$	MRCI		7625	1.901	1.274	1.831	67.1
		MRCI+Q		7441				
LiNO	$^3\Sigma^-$	MRCI		0	1.728	1.224		
		MRCI+Q		0				
		CCSD(T)	32.8 (33.6)	0	1.732	1.223		
	$^1\Delta$	MRCI		4228	1.726	1.218		
		MRCI+Q		5549				
	$^1\Sigma^+$	MRCI		7478	1.740	1.214		
		MRCI+Q		8836				
LiNS	$^3\Sigma^-$	MRCI		0	1.751	1.563		
		MRCI+Q		0				
		CCSD(T)	54.5 (55.7)	0	1.752	1.560		
	$^1\Delta$	MRCI		5115	1.746	1.565		
		MRCI+Q		4838				
	$^1\Sigma^+$	MRCI		8489	1.745	1.571		
		MRCI+Q		8287				
Li[NS]	$^3A''$	MRCI		0	1.849	1.600	2.389	87.4
		MRCI+Q		0				
		CCSD(T)	52.2 (53.2)	0	1.852	1.597	2.393	87.5
	$1^1A'$	MRCI		2614	1.893	1.595	2.204	77.9
		MRCI+Q		2957				
		CCSD(T)		2824	1.895	1.596	2.212	78.1
	$^1A''$	MRCI		5925	1.842	1.594	2.403	88.4
		MRCI+Q		5903				
LiNSe	$^3\Sigma^-$	MRCI		0	1.754	1.709		
		MRCI+Q		0				
		CCSD(T)	58.9 (60.5)	0	1.753	1.701		
	$^1\Delta$	MRCI		4817	1.748	1.712		
		MRCI+Q		4604				
	$^1\Sigma^+$	MRCI		7916	1.747	1.720		
		MRCI+Q		7758				
Li[NSe]	$^3A''$	MRCI		0	1.844	1.752	2.561	90.8
		MRCI+Q		0				
		CCSD(T)	57.2 (58.6)	0	1.846	1.745	2.561	90.9
	$1^1A'$	MRCI		2717	1.896	1.750	2.345	79.9
		MRCI+Q		2959				
		CCSD(T)		2750	1.899	1.751	2.355	80.2
	$^1A''$	MRCI		5511	1.828	1.744	2.628	94.7
		MRCI+Q		5514				
LiNTe	$^3\Sigma^-$	MRCI		0	1.758	1.906		
		MRCI+Q		0				
		CCSD(T)	64.4 (66.1)	0	1.755	1.895		
	$^1\Delta$	MRCI		4408	1.751	1.911		
		MRCI+Q		4200				
	$^1\Sigma^+$	MRCI		7161	1.750	1.922		
		MRCI+Q		6994				
Li[NTe][c]	$^3A''$	MRCI		0	1.815	1.943	2.946	103.2
		MRCI+Q		0				
		CCSD(T)	62.6 (66.3)	0	1.818	1.936	2.943	103.2
	$1^1A'$	MRCI		2767	1.896	1.958	2.587	84.3
		MRCI+Q		2918				
		CCSD(T)		2593	1.897	1.962	2.588	84.2

[a] LiNX and Li[NX] correspond to the linear-bonded and side-bonded species, respectively.
[b] CBS D_e values are given in parentheses.
[c] The $^1A''$ state converges to $^1\Delta$ of linear LiNTe.

Table 4. Binding energy D_e (kcal/mol) with respect to Na(^{2}S)+NX($X^2\Pi$), excitation energies T_e (cm^{-1}), optimal bond lengths r_e (Å), and Na-N-X angles (degrees) for the lowest electronic states of NaNX (X=O, S, Se, Te).

					r_e			
Molecule [a]	State	Method	D_e [b]	T_e	Na–N	N–X	Na–X	Na–N–X
Na[NO]	$^3A''$	MRCI		0	2.260	1.282	2.195	70.5
		MRCI+Q		0				
		CCSD(T)	18.0 (19.2)	0	2.271	1.279	2.225	71.5
	$^1A'$	MRCI		5686	2.264	1.268	2.219	71.6
		MRCI+Q		6027				
		CCSD(T)		6219	2.285	1.268	2.255	72.5
	$^1A''$	MRCI		7727	2.263	1.273	2.221	71.7
		MRCI+Q		7508				
NaNO	$^3\Sigma^-$	MRCI		0	2.101	1.239		
		MRCI+Q		0				
		CCSD(T)	14.8 (16.6)	0	2.112	1.235		
	$^1\Delta$	MRCI		6245	2.104	1.232		
		MRCI+Q		5952				
	$^1\Sigma^+$	MRCI		10,241	2.111	1.228		
		MRCI+Q		9871				
Na[NS]	$^3A''$	MRCI		0	2.236	1.604	2.717	88.5
		MRCI+Q		0				
		CCSD(T)	37.9 (39.2)	0	2.246	1.602	2.724	88.5
	$^1A'$	MRCI		4628	2.293	1.597	2.619	82.5
		MRCI+Q		4953				
		CCSD(T)		4809	2.304	1.599	2.623	82.3
	$^1A''$	MRCI		6125	2.225	1.596	2.760	91.0
		MRCI+Q		6104				
NaNS	$^3\Sigma^-$	MRCI		0	2.125	1.572		
		MRCI+Q		0				
		CCSD(T)	37.3 (39.0)	0	2.129	1.567		
	$^1\Delta$	MRCI		5439	2.121	1.572		
		MRCI+Q		5173				
	$^1\Sigma^+$	MRCI		8851	2.121	1.577		
		MRCI+Q		8613				
Na[NSe]	$^3A''$	MRCI		0	2.241	1.758	2.862	90.6
		MRCI+Q		0				
		CCSD(T)	43.1 (44.9)	0	2.252	1.754	2.855	90.0
	$^1A'$	MRCI		4549	2.298	1.752	2.753	84.5
		MRCI+Q		4762				
		CCSD(T)		4533	2.303	1.754	2.759	84.5
	$^1A''$	MRCI		6733	2.229	1.755	2.857	90.8
		MRCI+Q		5941				
NaNSe	$^3\Sigma^-$	MRCI		0	2.131	1.719		
		MRCI+Q		0				
		CCSD(T)	41.8 (43.9)	0	2.133	1.711		
	$^1\Delta$	MRCI		5158	2.123	1.719		
		MRCI+Q		4955				
	$^1\Sigma^+$	MRCI		8380	2.123	1.727		
		MRCI+Q		8236				
Na[NTe]	$^3A''$	MRCI		0	2.232	1.962	3.104	95.3
		MRCI+Q		0				
		CCSD(T)	48.4 (50.2)	0	2.243	1.957	3.099	94.8
	$^1A'$	MRCI		4316	2.297	1.960	2.982	88.6
		MRCI+Q		4389				
		CCSD(T)		3931	2.307	1.965	2.984	88.2
	$^1A''$	MRCI		5303	2.220	1.958	3.097	95.5
		MRCI+Q		5261				
NaNTe	$^3\Sigma^-$	MRCI		0	2.138	1.917		
		MRCI+Q		0				
		CCSD(T)	47.4 (49.5)	0	2.140	1.911		
	$^1\Delta$	MRCI		4728	2.128	1.919		
		MRCI+Q		4535				
	$^1\Sigma^+$	MRCI		7581	2.127	1.929		
		MRCI+Q		7432				

[a] NaNX and Na[NX] correspond to the linear-bonded and side-bonded species, respectively.
[b] CBS D_e values are given in parentheses.

Table 5. Ionization energy IE (eV) with respect to the global minimum of the neutral species, excitation energies T_e (cm^{-1}), and optimal bond lengths r_e (Å) for the lowest two electronic states of MNX^- (M=Li, Na and X=O, S, Se, Te).

					r_e	
Molecule	State	Method	IE [a]	T_e	Li-N	N-X
$LiNO^-$	$^4\Sigma^-$	CCSD(T)	0.51	0	1.813	1.235
		MRCI	0.34	0	1.805	1.240
		MRCI+Q	0.43	0		
	$^2\Sigma^-$	MRCI		439	1.807	1.243
		MRCI+Q		476		
$LiNS^-$	$^4\Sigma^-$	CCSD(T)	0.64	0	1.845	1.568
		MRCI	0.54	0	1.847	1.572
		MRCI+Q	0.61	0		
	$^2\Sigma^-$	MRCI		247	1.848	1.572
		MRCI+Q		261		
$LiNSe^-$	$^4\Sigma^-$	CCSD(T)	0.64	0	1.854	1.715
		MRCI	0.57	0	1.856	1.720
		MRCI+Q	0.63	0		
	$^2\Sigma^-$	MRCI		238	1.857	1.720
		MRCI+Q		248		
$LiNTe^-$	$^4\Sigma^-$	CCSD(T)	0.66	0	1.866	1.918
		MRCI	0.57	0	1.866	1.920
		MRCI+Q	0.64	0		
	$^2\Sigma^-$	MRCI		217	1.867	1.920
		MRCI+Q		225		
$NaNO^-$	$^4\Sigma^-$	CCSD(T)	0.62	0	2.225	1.246
		MRCI	0.45	0	2.210	1.252
		MRCI+Q	0.53	0		
	$^2\Sigma^-$	MRCI		301	2.211	1.253
		MRCI+Q		334		
$NaNS^-$	$^4\Sigma^-$	CCSD(T)	0.78	0	2.254	1.577
		MRCI	0.66	0	2.253	1.581
		MRCI+Q	0.73	0		
	$^2\Sigma^-$	MRCI		214	2.253	1.581
		MRCI+Q		223		
$NaNSe^-$	$^4\Sigma^-$	CCSD(T)	0.78	0	2.267	1.728
		MRCI	0.69	0	2.265	1.732
		MRCI+Q	0.74	0		
	$^2\Sigma^-$	MRCI		214	2.265	1.732
		MRCI+Q		220		
$NaNTe^-$	$^4\Sigma^-$	CCSD(T)	0.82	0	2.283	1.933
		MRCI	0.73	0	2.278	1.934
		MRCI+Q	0.79	0		
	$^2\Sigma^-$	MRCI		205	2.282	1.933
		MRCI+Q		209		

[a] This is also the EA of MNX.

that both the linear- and side-bonded Li—NO form stable anions, the ground states of which are $^4\Sigma^-$ and $^4A''$, respectively. The Li[NO]$^-$ ($^4A''$) isomer lies 1.4 kcal/mol above the $LiNO^-$ ($^4\Sigma^-$) at the CCSD(T) level, and in both cases the additional electron is placed in 7σ and 9a′ orbitals of Figures 2 and 3, which are chiefly the 2s of lithium polarized away from NO. An additional indication supporting the attachment of the electron to the positive lithium terminal is the higher electron affinity of bare Li over NO (experimental values are 0.618 vs. 0.026 eV).[34]

In the $^4\Sigma^-$ state, all unpaired electrons bear the same spin, but the sister $^2\Sigma^-$ state is found to shadow in close proximity (less than 500 cm^{-1}; see Table 5). The $^2\Sigma^-$ state is actually stable with respect to neutral Li[NO] ($^3A''$). The EA of LiNO is 0.51 eV under CCSD(T). The MRCI+Q prediction (0.43 eV) is closer to the CCSD(T) than the MRCI value (0.34 eV).

We further examined the anions of all linear LiNX and NaNX species. Similarly to LiNO, all these species form stable linear $^4\Sigma^-$ and $^2\Sigma^-$ anions, with the former being always the ground state. The CCSD(T) EAs are 0.51 and 0.62 for LiNO and NaNO, respectively. The difference of 0.09 eV falls close to the difference of the EAs of the bear metals: EA(Li) = 0.618 eV and EA(Na) = 0.548 eV.[34] Going to S, Se, and Te, the corresponding EA of MNX for M=Li and Na, remains practically the same: EA(LiNX) = 0.65 ± 0.01 eV and EA(NaNX) = 0.80 ± 0.02 eV. Increasing the basis set to aug-cc-pVQZ and aug-cc-pV5Z, the EAs change only by less than 0.06 eV (see Supporting Information Table S17). The energy gap from $^4\Sigma^-$ to $^2\Sigma^-$ exhibits the same trend but in the opposite direction: It is 476 and 334 cm^{-1} for LiNO and NaNO (MRCI+Q values; see Table 5) and drops to 245 ± 20 cm^{-1} and 220 ± 15 cm^{-1} for LiNX and NaNX (X=S, Se, Te). The Li—N and N—X distances between $^4\Sigma^-$ and $^2\Sigma^-$ vary within less than 0.01 Å for all the species. An interesting observation is that the N—X distance remains almost intact going from MNX to MNX^- (compare Tables 3–4, and 5), a result of the attachment of the electron to the metal side.

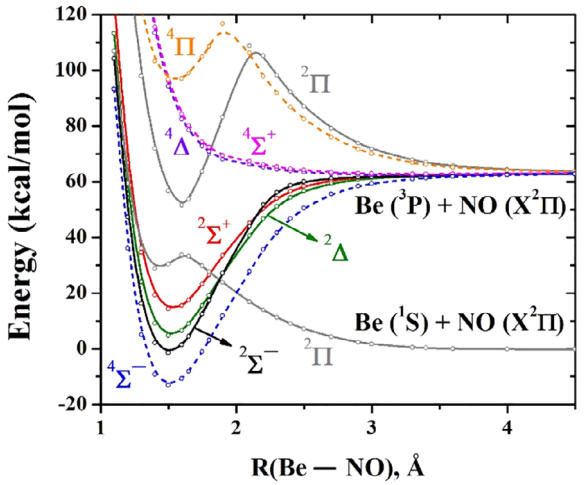

Figure 5. MRCI PECs of BeNO as a function of Be–NO distance. The dashed and solid lines represent quartets and doublets, respectively. [Color figure can be viewed at wileyonlinelibrary.com]

BeNX (X=O, S, Se, Te) Series

The ground state of Be(^{1}S) bears a $1s^2 2s^2$ electronic configuration. Its first excited state $^3P(1s^2 2s^1 2p^1)$ is generated by promoting one electron from 2s to the neighboring 2p shell. This excitation requires 21,980 cm^{-1} amount of energy. The second excited state of Be, $^1P(1s^2 2s^1 2p^1)$, is well separated from its sister ^{3}P state, located as high as 42,565 cm^{-1}. We have seen in the past that monocoordinated beryllium complexes originate from these excited states.[19,25]

The interaction of closed shell $2s^2$ of Be(^{1}S) with NO($X^2\Pi$) should be repulsive and actually more repulsive than the Li(^{2}S) + NO($^2\Pi$) interaction, since the incoming NO unit faces two electrons. By exciting one electron from 2s to 2p, Be increases the availability of its valence space and enables the formation of covalent or dative bonds with NO. A covalent bond between Be(^{3}P) and NO($X^2\Pi$) can be formed if the two fragments approach in a bent manner coupling the unpaired π*(NO) electron with a 2p(Be) electron. On the other hand, the Be←:NO binding will dominate the linear Be + NO attack. Our calculations show that the ground state of side bonded Be[NO] is ^{2}A′ located 7.5 kcal/mol higher than $^4\Sigma^-$ of linear BeNO. Additionally, the ground state of linear BeON ($^4\Sigma^-$) is 7.1 kcal/mol above the linear BeNO global minimum.

The constructed PEPs for the linear approach of Be + NO is shown in Figure 5. As we predicted earlier, the Be(^{1}S) + NO ($X^2\Pi$) combination creates a strongly repulsive $^2\Pi$ PEP. This $^2\Pi$ PEP undergoes an avoided crossing with a $^2\Pi$ curve stemming from higher energy fragments and finally creates a shallow minimum at around 1.4 Å. This minimum is higher than the minima of states stemming from the second lowest energy asymptote Be(^{3}P) + NO($X^2\Pi$), which lies about 60 kcal/mol above Be(^{1}S) + NO($X^2\Pi$). According to the Wigner–Witmer rules, the Be(^{3}P) + NO($X^2\Pi$) channel produces the $^{2,4}\{\Sigma^-, \Sigma^+, \Pi, \Delta\}$ manifold of states. The lowest four electronic states ($^4\Sigma^-$, $^2\Sigma^-$, $^2\Delta$, and $^2\Sigma^+$) indeed dissociate to this channel.

The ground state wavefunction is single reference, but that of the first, second, and third excited states express multireference character. Their dominant electronic configurations along with their coefficients and the relative molecular orbitals are very similar to those of LiNO and are given in the Supporting Information (see Supporting Information Table S1 and Supporting Information Fig. S1). The BeNO states can be produced from LiNO by adding one electron to the 2s of Be, which is polarized away from NO. Specifically, the $^{2,4}\Sigma^-$ states can come from $^3\Sigma^-$ of LiNO with the additional electron to couple ferromagnetically or antiferromagnetically with the triplet state of the existing two electrons. Likewise, $^2\Sigma^+$, $^2\Delta$ states are produced from $^1\Sigma^+$, $^1\Delta$ of LiNO. In all four states, the lone electron pair of nitrogen makes a sigma bond with the empty sp_z hybrid of Be, and three electrons occupy 2s of Be and the two delocalized toward Be π*(NO) orbitals. As in LiNO, a more natural representation of the bonding is $Be^+(^2S)\ NO^-(^3\Sigma^-, {}^1\Delta, {}^1\Sigma^+)$, which results to the lowest four electronic states. The proposed valence–bond–Lewis (vbL) diagrams are drawn in Scheme 3.

All our numerical results are tabulated in Table 6. The CCSD(T) and MRCI methods agree within just 0.002 Å for both bond Be—N and N—O lengths. The first three excited states of BeNO are of multireference nature and therefore no CCSD(T) values are reported in Table 6. Both Be—NO and BeN—O bond lengths vary only within a few mili–Å for all states: r_{Be-NO} = 1.513 ± 0.0006 Å and r_{BeN-O} = 1.202 ± 0.006 Å. The optimal Be—NO length of $^2\Sigma^-$ is identical to its quartet counterpart $^4\Sigma^-$ but BeN—O of $^2\Sigma^-$ is longer by 0.011 Å. The previously reported Be—N and N—O bond distances of BeNO($^2\Sigma^-$) under B3LYP/6–311 + G* are 1.500, 1.199 Å, respectively, [24] in excellent agreement with our values.

The calculated CCSD(T) optimal internuclear distance of free NO is 1.157 Å, while for NO^- is 1.273 Å. The BeN—O length of the ground $^4\Sigma^-$ state is 1.198 Å closer to the neutral NO. On the other hand, the LiN—O and NaN—O lengths are 1.224 and 1.239 Å closer to NO^-. Sticking to the ionic picture, *in situ* beryllium within BeNO interacts with NO^- more as Be^{2+} with a 2s electron polarized away

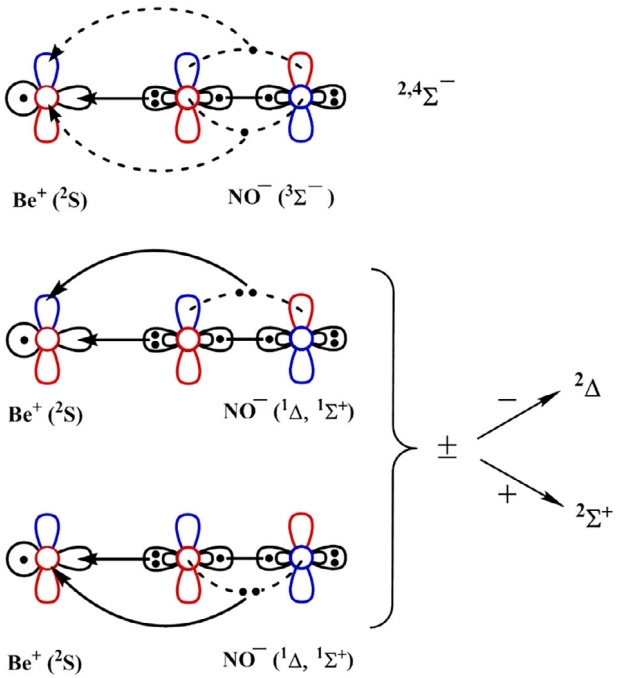

Scheme 3. Electronic configurations for the first four electronic states of BeNO. [Color figure can be viewed at wileyonlinelibrary.com]

Table 6. Binding energy D_e (kcal/mol) with respect to Be(^{1}S)+NO($^2\Pi$), excitation energy T_e (cm^{-1}), and optimal bond lengths r_e (Å) for the lowest electronic states of BeNX (X = O, S, Se, Te).

					r_e	
Species	State	Method	D_e [a]	T_e	Be–N	N–X
BeNO	$^4\Sigma^-$	MRCI		0	1.507	1.196
		MRCI+Q		0		
		CCSD(T)	18.3 (19.5)	0	1.509	1.198
	$^2\Sigma^-$	MRCI		3076	1.507	1.207
		MRCI+Q		3007		
	$^2\Delta$	MRCI		6311	1.512	1.198
		MRCI+Q		6284		
	$^2\Sigma^+$	MRCI		9579	1.519	1.199
		MRCI+Q		9727		
BeNS	$^4\Sigma^-$	MRCI		0	1.506	1.542
		MRCI+Q		0		
		CCSD(T)	44.1 (45.7)	0	1.507	1.541
	$^2\Sigma^-$	MRCI		1554	1.507	1.544
		MRCI+Q		1635		
	$^2\Delta$	MRCI		5383	1.507	1.549
		MRCI+Q		5138		
	$^2\Sigma^+$	MRCI		8581	1.510	1.556
		MRCI+Q		8456		
BeNSe	$^4\Sigma^-$	MRCI		0	1.505	1.684
		MRCI+Q		0		
		CCSD(T)	50.0 (52.0)	0	1.505	1.684
	$^2\Sigma^-$	MRCI		1427	1.506	1.686
		MRCI+Q		1487		
	$^2\Delta$	MRCI		4983	1.506	1.693
		MRCI+Q		4782		
	$^2\Sigma^+$	MRCI		7957	1.509	1.703
		MRCI+Q		7838		
BeNTe	$^4\Sigma^-$	MRCI		0	1.503	1.878
		MRCI+Q		0		
		CCSD(T)	59.1 (61.2)	0	1.503	1.880
	$^2\Sigma^-$	MRCI		1187	1.503	1.878
		MRCI+Q		1240		
	$^2\Delta$	MRCI		4542	1.505	1.889
		MRCI+Q		4327		
	$^2\Sigma^+$	MRCI		7237	1.508	1.904
		MRCI+Q		7075		

[a] CBS D_e values are given in parentheses.

from NO. Therefore, the donation of electron from NO^- to beryllium (Scheme 3) is stronger giving a less ionic equilibrium character. Of course, this elongation of the N—O distance after it binds to Be(^{3}P; $2s^12p^1$) may also be seen as the result of the partial donation of the $2p^1$ electron to the empty π^*(NO). However, the ionic model still can explain in a simple direct way the splitting among the lowest-lying electronic states of BeNO.

The isovalent BeNS, BeNSe, and BeNTe species were also found to favor the linear structures over the bent ones. The ground and first three excited states of BeNS, BeNSe, and BeNTe followed the same order as BeNO. The excitation energies of BeNX series drop as we move to heavier X (X=O, S, Se, Te), as happens for the LiNX series. The CCSD(T) optimal distances of NS and NSe diatomics are 1.511 and 1.661 Å, respectively, and they are shorter by ~0.03 and ~0.02 Å than their corresponding BeN—X lengths. The internuclear distance of free NTe is identical to the BeN—Te distance. On the other hand, the Be—N distances are nearly unaffected by the nature of X (see Table 6). Finally, the binding energy of the BeNO is 18.25 kcal/mol at CCSD(T). By replacing NO with NS, the binding energy increased by as much as 25.8 kcal/mol (141%). Overall, the binding energies increased in the BeNO < BeNS < BeNSe < BeNTe order as a consequence of the larger EA for the heavier NX systems (see Section 3).

$BeNX^-$ Series

Beryllium anion is unstable with respect to neutral beryllium [34], while the EA of NO is as small as 0.028 eV at CCSD(T).[33] Interestingly, BeNO has a quite large EA of 0.99 eV under the same level of theory. MRCI gives an EA about half of this values (0.48 eV), and MRCI + Q somewhere in the middle (0.73 eV) trying to compensate for the missing electron correlation. The size-extensive CCSD(T) approach should be considered more accurate. We observed the same trend for MoO and PdO in the past.[35,36]

The additional electron pairs with the ~2s(Be) electron of BeNO ($^4\Sigma^-$) to generate the ground state of $BeNO^-$. CCSD(T) predicted a non-linear ^{3}A″ ground state for $BeNO^-$ with a Be—N—O angle of 159.5°. This slightly bent ^{3}A″ ground state is stabilized by 0.07 kcal/mol over its linear $^3\Sigma^-$ counterpart (see the Table 7), which has a doubly degenerate imaginary frequency of 78.18 cm^{-1} corresponding to the bending mode. As a rough estimate, we notice that the first vibrational level of this mode is ½(78.18) cm^{-1} or

Table 7. Ionization energy IE (eV), excitation energy T_e (cm^{-1}), and optimal bond lengths r_e (Å) for the lowest electronic states of $BeNX^-$ (X = O, S, Se, Te).

					r_e	
Molecule	State [a]	Method	IE [b]	T_e	Be-N	N-X
$BeNO^-$	$^3A''$	CCSD(T)	0.99	0	1.619	1.225
	$^3\Sigma^-$	CCSD(T)	0.99	24	1.606	1.221
		MRCI	0.48	659	1.582	1.225
		MRCI+Q	0.73	689		
	$^3\Pi$	CCSD(T)		884	1.457	1.257
		MRCI		0	1.455	1.253
		MRCI+Q		0		
	$^1\Pi$	MRCI		2271	1.454	1.262
		MRCI+Q		2401		
$BeNS^-$	$^3\Pi$	CCSD(T)	1.29	0	1.451	1.617
		MRCI	1.00	0	1.448	1.623
		MRCI+Q	1.19	0		
	$^1\Pi$	MRCI		1556	1.445	1.628
		MRCI+Q		1411		
	$^3A''$	CCSD(T)		2466	1.612	1.558
	$^3\Sigma^-$	CCSD(T)		2497	1.606	1.554
		MRCI		3979	1.592	1.557
		MRCI+Q		3163		
$BeNSe^-$	$^3\Pi$	CCSD(T)	1.47	0	1.448	1.750
		MRCI	1.19	0	1.450	1.764
		MRCI+Q	1.37	0		
	$^1\Pi$	MRCI		1017	1.450	1.766
		MRCI+Q		1034		
	$^3A''$	CCSD(T)		4114	1.629	1.713
	$^3\Sigma^-$	CCSD(T)		4251	1.608	1.696
		MRCI		5707	1.597	1.704
		MRCI+Q		4666		
$BeNTe^-$	$^3\Pi$	CCSD(T)	1.59	0	1.456	1.958
		MRCI	1.37	0	1.454	1.954
		MRCI+Q	1.52	0		
	$^1\Pi$	MRCI		838	1.454	1.954
		MRCI+Q		867		
	$^3A''$	CCSD(T)		5233	1.536	1.899
	$^3\Sigma^-$	CCSD(T)		5691	1.604	1.891
		MRCI		6833	1.610	1.909
		MRCI+Q		5892		

[a] The $^3A''$ of $BeNX^-$ corresponds to a bent structure. The Be–N–X^- angle of $^3A''$ of BeNO, BeNS, BeNSe, and BeNTe are 159.5, 160.3, 156.6, and 164.2, respectively.
[b] This is also the EA of BeNX.

0.11 kcal/mol, which is above the 0.07 kcal/mol bent→linear→bent barrier. Consequently, $BeNO^-$ is a floppy pseudo-linear molecule.

Under CCSD(T), the first excited state is a linear $^3\Pi$ with four real frequencies (see Supporting Information Table S15), which however is predicted as the MRCI and MRCI + Q ground state. The first and the second excited states of $BeNO^-$ under the MRCI and MRCI + Q are $^3\Sigma^-$ and $^1\Pi$, respectively. Interestingly, the first ($^3\Pi$)- and the second ($^1\Pi$)-excited states of $BeNO^-$ are also stable with respect to the BeNO($^4\Sigma^-$). The $^3\Pi$ and the $^1\Pi$ states of $BeNO^-$ are formed by coupling the additional electron with the $2\pi_y$ electron of BeNO ($^4\Sigma^-$). The dominant electronic configurations of each state and the orbitals are given in Supporting Information Table S2 and Supporting Information Figure S2.

As a continuation to the $BeNO^-$ work, we further investigated the ground and excited states of $BeNS^-$, $BeNSe^-$, and $BeNTe^-$ species (see the Table 7). All these anions possess three stable states with respective to their corresponding neutral molecule. Our CCSD(T), MRCI, and MRCI+Q calculations demonstrate that the $^3\Pi$ ground state is followed by $^1\Pi$ and $^3A''$ excited states in all cases. The linear $^3\Sigma^-$ $BeNX^-$ lies always above its $^3A''$ partner. The electron affinities of BeNX series varies in the BeNO (=0.99 eV) < BeNS (=1.29 eV) < BeNSe (=1.47 eV) < BeNTe (=1.59 eV) order. For all the studied BeNX, CCSD(T) predicted higher EAs than MRCI+Q.

The Be—N distances of $^3A''$ and $^3\Sigma^-$ for every BeNX species are about 1.6 Å, while in both $^3\Pi$ and $^1\Pi$ states Be—N is shorter by ~0.15 Å. The Be—N distances of the neutral species is always ~1.5 Å, which means that the attachment of an electron shortens the Be—N bond for $^{1,3}\Pi$ but elongates it for $^3A''$ and $^3\Sigma^-$. This is in agreement with the fact that the additional electron attaches to the mainly bonding Be—N $2\pi_x$ orbital of Supporting Information Figure S2 (~$2\pi_x$ of Fig. 2) in the case of $^{1,3}\Pi$, but it goes to the nearly non-bonding 7σ orbital of Supporting Information Figure S2 (~7σ of Fig. 2) at the back of Be.

Summary

High-level quantum chemical calculations are performed for a series of monocoordinated metal-nitrosyl compounds aiming at the elucidation of the electronic structure of their ground and low-lying states. Our results on lithium, sodium, and beryllium complexes suggest that the M—NO bond is fairly ionic and such an interpretation justifies the observed trends. For example, the

low-lying electronic states follow the pattern of the NO^- ones with its ground $^3\Sigma^-$ and first two excited states ($^1\Delta$, $^1\Sigma^+$) generating the ground and first two excited states of the complexes. We also constructed the potential energy profiles with respect to the M—NO distance, and we showed that all three states dissociate adiabatically to the first excited state of the metal in every case. The energy difference between the linear and bent structures is rather small, with the former being preferred for beryllium and the latter for both lithium and sodium.

The ionic character was confirmed for the isovalent MNX species, where X=S, Se, Te. We were able to attribute the larger binding energies for the heavier systems to the higher electron affinities of NX. For all these species, we report accurate geometries, binding energies, and excitation energies for their low-lying electronic states, which are identical to the MNO ones. We found that the excitation energies decrease for the heavier systems, which is a consequence of the lower excitation energies of the NX^- *in situ* moiety. We also found that the metal-nitrogen bond lengths are practically independent of X. LiNX prefers the linear conformation, whereas NaNX prefers the bent one. For binding energies and electron affinities, CBS limits are reported.

Finally, we studied the anions of all MNX species with M=Li, Na, Be and X=O, S, Se, Te, and we revealed that they are all stable and have EAs of 0.5–0.8 eV order. We also examined excited states of them, which are still stable with respect to the neutral species. The electron affinities are practically uncorrelated with the nature of X within the LiNX and NaNX series, since the additional electron attaches to the metal side, which is largely in its cationic form in MNX (M^+NX^-). The same is true for BeNO and this explains why $BeNO^-$ exists despite the small electron affinity of NO and the negative electron affinity of Be. However, the electron attaches to a π(MN) − π^*(NX) orbital for all other BeNX species, increasing the EA from 0.99 eV (O) to ~1.45 ± 0.15 eV (S, Se, Te). Our results will be of high importance and can serve as a guide for future experimental work, especially for photoelectron spectroscopy experiments.

Acknowledgments

We are indebted to Auburn University for financial support. The computational work was completed in part by the Auburn University Hopper Supercomputer Center. We also would like to thank the reviewer for his/her suggestion to extrapolate our binding energies to the CBS limit.

Keywords: metal nitric chalcogens · multireference calculations · potential energy curves · stable anions

How to cite this article: I. R. Ariyarathna, E. Miliordos. *J. Comput. Chem.* **2019**, *40*, 1740–1751. DOI: 10.1002/jcc.25829

Additional Supporting Information may be found in the online version of this article.

[1] E. Culotta, D. Koshland, *Science (80-.).* **1992**, *258*, 1862.
[2] Y. C. Hou, A. Janczuk, P. G. Wang, *Curr. Pharm. Des.* **1999**, *5*, 417.
[3] T. N. Raju, *Lancet* **2000**, *356*, 346.
[4] J. R. Lancaster, *Futur. Sci. OA* **2015**, *1*, fso.15.59.
[5] J. Ku, *Nitric oxide in workplace atmospheres*, United States Department of Labor, **1991**, see https://www.osha.gov/dts/sltc/methods/inorganic/id190/id190.html (retrieved March 24, 2019).
[6] P. J. Crutzen, *Annu. Rev. Earth Planet. Sci.* **1979**, *7*, 443.
[7] G. B. Taylor, J. H. Capps, A. S. Coolidge, *J. Ind. Eng. Chem.* **1918**, *10*, 270.
[8] G. J. Leigh, Nitrogen Fixation at the Millennium, Elsevier, Amsterdam, **2002**.
[9] R. T. Venterea, D. E. Rolston, *J. Geophys. Res. Atmos.* **2000**, *105*, 15117.
[10] J. A. McCleverty, *Chem. Rev.* **1979**, *79*, 53.
[11] J. A. Osborn, S. T. Wilson, *J. Am. Chem. Soc.* **1971**, *93*, 3068.
[12] B. Dudle, K. Rajesh, O. Blacque, H. Berke, *J. Am. Chem. Soc.* **2011**, *133*, 8168.
[13] R. Eisenberg, C. D. Meyer, *Acc. Chem. Res.* **1975**, *8*, 26.
[14] T. W. Hayton, P. Legzdins, W. B. Sharp, *Chem. Rev.* **2002**, *102*, 935.
[15] F. A. Cotton, G. Wilkinson, Advanced Inorganic Chemistry, 4th ed., John wiley and sons, New York, **1980**.
[16] X. Wu, L. Zhao, J. Jin, S. Pan, W. Li, X. Jin, G. Wang, M. Zhou, G. Frenking, *Science (80-.).* **2018**, *361*, 912.
[17] X. Wu, L. Zhao, D. Jiang, I. Fernández, R. Berger, M. Zhou, G. Frenking, *Angew. Chemie Int. Ed.* **2018**, *57*, 3974.
[18] I. R. Ariyarathna, S. N. Khan, F. Pawłowski, J. V. Ortiz, E. Miliordos, *J. Phys. Chem. Lett.* **2018**, *9*, 84.
[19] I. R. Ariyarathna, E. Miliordos, *Int. J. Quantum Chem.* **2018**, *118*, e25673.
[20] I. R. Ariyarathna, F. Pawłowski, J. V. Ortiz, E. Miliordos, *Phys. Chem. Chem. Phys.* **2018**, *20*, 24186.
[21] T. Yang, A. Li, G. K. Chen, C. Xie, A. G. Suits, W. C. Campbell, H. Guo, E. R. Hudson, *J. Phys. Chem. Lett.* **2018**, *9*, 3555.
[22] L. Andrews, M. Zhou, X. Wang, *J. Phys. Chem. A* **2000**, *104*, 8475.
[23] J. M. Turney, H. F. Schaefer, *Collect. Czechoslov. Chem. Commun.* **2007**, *72*, 129.
[24] G. P. Kushto, F. Ding, B. Liang, X. Wang, A. Citra, L. Andrews, *Chem. Phys.* **2000**, *257*, 223.
[25] I. R. Ariyarathna, E. Miliordos, *J. Phys. Chem. A* **2017**, *121*, 7051.
[26] I. R. Ariyarathna, E. Miliordos, *J. Comput. Chem.* **2018**. https://doi.org/10.1002/jcc.25791.
[27] T. H. Dunning, *J. Chem. Phys.* **1989**, *90*, 1007.
[28] R. A. Kendall, T. H. Dunning, R. J. Harrison, *J. Chem. Phys.* **1992**, *96*, 6796.
[29] D. E. Woon, T. H. Dunning, *J. Chem. Phys.* **1994**, *100*, 2975.
[30] K. A. Peterson, D. Figgen, E. Goll, H. Stoll, M. Dolg, *J. Chem. Phys.* **2003**, *119*, 11113.
[31] H.-J. Werner, P. J. Knowles, G. Knizia, F. R. Manby, M. Schütz and M. W. P. Celani, W. Györffy, D. Kats, T. Korona, R. Lindh, A. Mitrushenkov, G. Rauhut, K. R. Shamasundar, T. B. Adler, R. D. Amos, A. Bernhardsson, A. Berning, D. L. Cooper, M. J. O. Deegan, A. J. Dobbyn, F. Eckert, E. Goll, C. Hampel, A. Hesselmann, G. Hetzer, *MOLPRO, version 2015.1, a Packag. ab initio programs; see* http//www.molpro.net.
[32] K. P. Huber, G. H. Herzberg, Constants of Diatomic Molecules, in NIST Chemistry WebBook, NIST Standard Reference Database Number 69, P. J. Linstrom, and W. G. Mallard, Eds. National Institute of Standards and Technology: Gaithersburg MD, 20899, https://doi.org/10.18434/T4D303, (retrieved March 24, 2019)
[33] C. A. Arrington, T. H. Dunning, D. E. Woon, *J. Phys. Chem. A* **2007**, *111*, 11185.
[34] D. R. Lide, CRC Handbook of Chemistry and Physics, 93rd ed., CRC press, New York, **2012**.
[35] I. R. Ariyarathna, E. Miliordos, *Phys. Chem. Chem. Phys.* **2018**, *20*, 12278.
[36] N. M. S. Almeida, I. R. Ariyarathna, E. Miliordos, *Phys. Chem. Chem. Phys.* **2018**, *20*, 14578.

Received: 18 December 2018
Revised: 15 February 2019
Accepted: 12 March 2019
Published online on 28 March 2019

Be–Be Bond in Action: Lessons from the Beryllium–Ammonia Complexes $[Be(NH_3)_{0-4}]_2^{0,2+}$

JPCAFH

NOVEMBER 26, 2020
VOLUME 124
NUMBER 47

pubs.acs.org/JPCA

THE JOURNAL OF PHYSICAL CHEMISTRY A

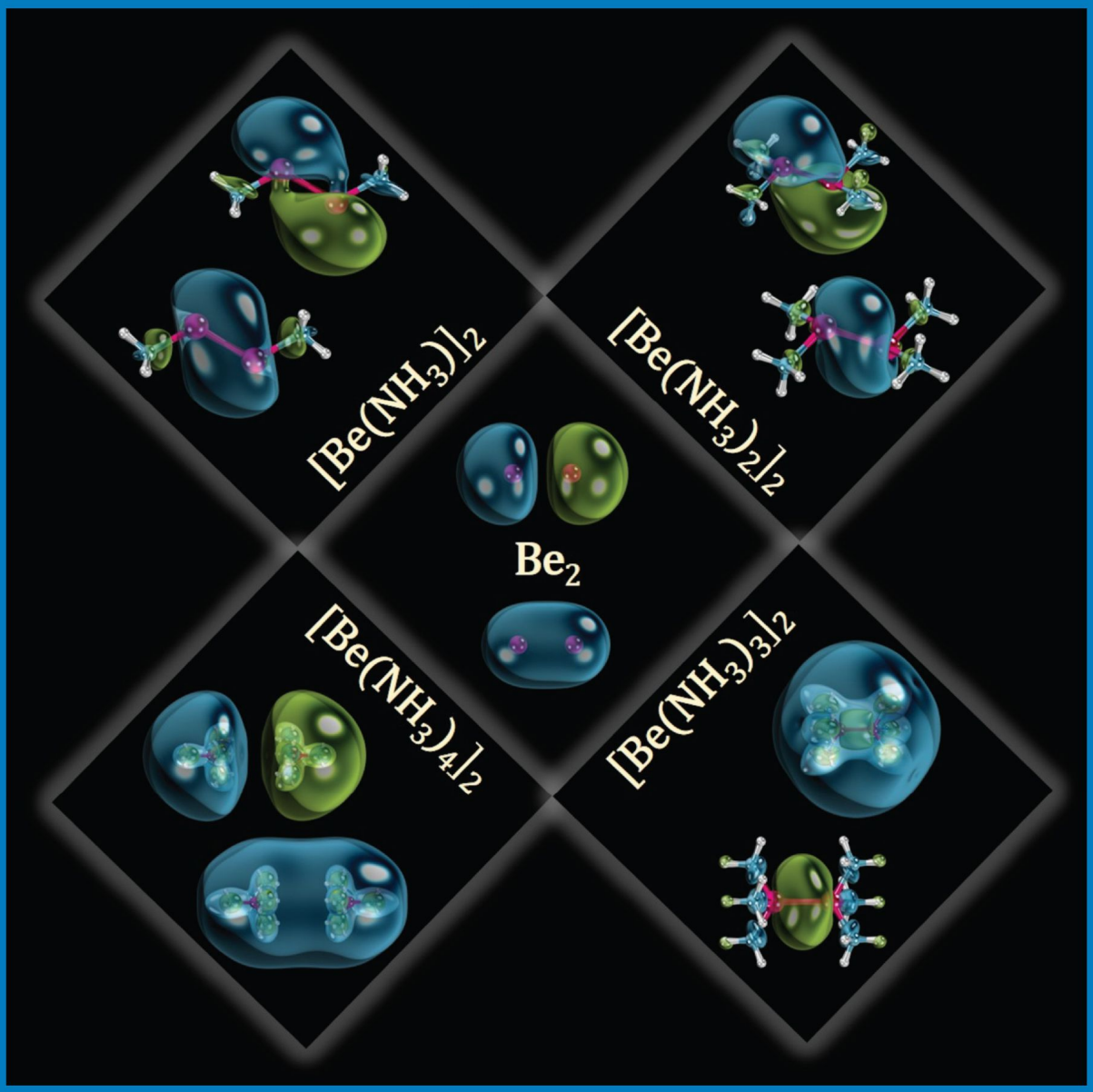

Molecular Orbitals of Be_2 and Be_2–Ammonia Complexes Reveal the Be–Be Bonding Character

ISOLATED MOLECULES, CLUSTERS, RADICALS, AND IONS; ENVIRONMENTAL CHEMISTRY, GEOCHEMISTRY, AND ASTROCHEMISTRY; NEW TOOLS AND METHODS

ACS Publications
Most Trusted. Most Cited. Most Read.

www.acs.org

THE JOURNAL OF PHYSICAL CHEMISTRY A

pubs.acs.org/JPCA Article

Be−Be Bond in Action: Lessons from the Beryllium−Ammonia Complexes $[Be(NH_3)_{0-4}]_2^{0,2+}$

Published as part of The Journal of Physical Chemistry virtual special issue "Alexander Boldyrev Festschrift".

Isuru R. Ariyarathna and Evangelos Miliordos*

Cite This: *J. Phys. Chem. A* 2020, 124, 9783−9792 Read Online

ACCESS | Metrics & More | Article Recommendations | Supporting Information

ABSTRACT: High-level electronic structure calculations are performed to elucidate the Be−Be chemical bond in the $(NH_3)_nBe-Be(NH_3)_n$ species for $n = 0-4$. We show that the Be_2 bond is explained as a resonance between two Lewis structures, where one beryllium atom donates an electron pair to the second one, and vice versa. The presence of ammonia ligands enhances the stability of this bond considerably. The ∼2.5 kcal/mol binding energy of Be_2 becomes ∼30 kcal/mol for $[Be(NH_3)_{1-3}]_2$ because of their more polarizable electron pairs. The larger $Be(NH_3)_4$ complex has been classified as a solvated electron precursor in the past and has an electron pair in the periphery of a $Be(NH_3)_4^{2+}$ core occupying a diffuse s-type orbital. The analogy of $Be(NH_3)_4$ to Be reflects into the electronic structure of their dimers. The two systems have identical bonding patterns and low-lying electronic states. The ground state binding energy of $[Be(NH_3)_4]_2$ is 3 times larger than Be_2, and its excitation energies are considerably lower by a factor of 3. We also studied the dimers of the cationic $Be(NH_3)_n^+$ species, and we found that the Coulombic repulsion is counterbalanced by the formation of a single covalent bond in the cases of $n = 1, 2$ forming stable dicationic $[(NH_3)_nBe-Be(NH_3)_n]^{2+}$ systems, unlike Be_2^{2+}. We believe that our numerical results will allow the identification and characterization of these exotic species and their solid state (beryllium liquid metals) analogues in future experiments.

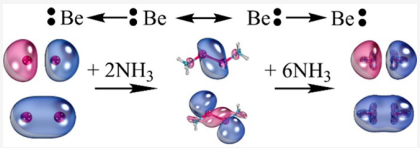

I. INTRODUCTION

The interaction energy between two identical noble gas atoms is as small as 7.26 cm^{-1} (He−He interaction).[1] This weak electrostatic attraction increases with the size (or more accurately the polarizability) of the atom to 29.40 and 99.2 cm^{-1} for the Ne and Ar dimers.[2,3] Chemical bonding is observed only between their excited states, where unpaired electrons are present. See for example the potential energy curves of ref 4 and the spectroscopic study of ref 5 regarding He_2. The ground state of Be is a $1s^22s^2$ closed-shell singlet state, and its dimer is expected to form a weakly bound system. However, the experimental Be_2 interaction energy of 929.7 cm^{-1} (30 times larger than its second-row noble gas analogue, Ne_2) and its 2.45 Å equilibrium distance[6] (as opposed to the 2.98 Å equilibrium distance of the smaller He_2)[1,7] pose questions about the nature of the Be−Be bond.

The bonding in Be_2 has attracted the interest of several quantum chemical studies (see refs 6 and 8−10 and references therein). The recent high-level electronic structure calculations by Kalemos point to a complex wave function of rather multireference nature with a 79% weight for the most dominant configuration.[8] Kalemos further claimed that the global minimum of Be_2 actually originates from the double bond of two $^3P(1s^22s^12p^1)$ excited beryllium atoms. The complex nature of the Be_2 bond reflects to the difficulty of calculating its dissociation energy accurately. For example, Patkowski et al. found that the "golden standard" all-electron CCSD(T) level of theory gives a value of 715 ± 6 cm^{-1} at the complete basis set limit (only 77% of the experimental value).[10] These authors found that the $1s^2$ electron correlation for Be is important and contributes to this number by 85 cm^{-1}. The addition of higher electron "excitations" through full configuration interaction (FCI) calculations were found indispensable to obtain a more accurate value of 942 cm^{-1}.[10] Kalemos, on the other hand, demonstrated that the problem is the "pathologically inappropriate" description of the zero order level wave function (Hartree−Fock−Slater determinant in the case of CCSD(T)) and emphasized the necessity of high-angular momentum basis functions.[8]

The addition of ligands to Be_2 induces the promotion of the beryllium centers to *in situ* excited electronic states facilitating the formation of stronger Be−Be bonds. See, for example, the double bond of around 10 kcal/mol in $(CO)_2BeBe(CO)_2$,[11] the HBeBeH,[12,13] and FBeBeF[14] molecules with 85 and 77 kcal/mol dissociation energies or the exotic Be−Li clusters.[15] In the HBeBeH case, the Be−H bond formation places Be to its first excited state ^3P $(1s^22s^12p^1)$, 21980 cm^{-1} above its $^1S(1s^2s^2)$ ground state,[16] creating a ground ·BeH $(^2\Sigma^+)$ state.[8]

Received: August 31, 2020
Revised: October 9, 2020
Published: October 15, 2020

https://dx.doi.org/10.1021/acs.jpca.0c07939
J. Phys. Chem. A 2020, 124, 9783−9792

The two electrons localized at the two beryllium ends form a covalent Be−Be bond. A similar scheme can be inferred for FBeBeF based on its molecular orbitals.[14] Beryllium is in its ^{3}P state as well in BeCO, which is however metastable dissociating to Be(^{1}S; $1s^2 2s^2$) + CO. On the other hand, $Be(CO)_2$ is stable with respect to Be + 2CO, and the beryllium center is in an even higher *in situ* electronic state, 2^3P ($1s^2 2p^2$) at 59696 cm^{-1}.[17] The stabilization of 2^3P is due to the "simultaneous" OC → Be ← CO dative bonds formation and π-back-donation of the two $2p_\pi$ electrons of Be to π^*-(CO).[17,18] Finally, high electron affinity ligands, such as O_2 or NO, oxidize beryllium to Be^+ or Be^{2+}; see for example $Be(O_2)_{1-2}$ and Be(NO) compounds.[17,19]

Ammonia is found to interact in a completely different manner with Be. Ammonia is a strong σ-donor, but unlike CO it cannot ease π-back-donation. For $Be(NH_3)_3$, we recently found that ammonia instead of inducing electronic excitation of the beryllium center, its lone electrons "displace" partly the beryllium valence electrons to the periphery of the molecular skeleton.[20] The attachment of a fourth ammonia creates a pure $Be^{2+}(NH_3)_4$ center with two peripheral electrons occupying hydrogen-like orbitals.[21] Such systems are referred to as solvated electron precursors, or SEPs.[21−26] The unusual chemistry of ammonia has been attributed to the strong metal−ammonia bonds and the ability of ammonia to solvate electrons.[22] In the case of water, such complexes (called SEPs) are less stable, and the diffuse electrons reduce the water hydrogens ("protons"), releasing easily H_2.[22] The second-row analogue of ammonia, PH_3, acts like CO promoting beryllium to its 2^3P state.[20]

A natural question is how the Be−Be bonding changes with the number of ammonia "ligands" present in the $(NH_3)_n$BeBe-$(NH_3)_n$ (n = 1−3) systems. In addition to the dimers of the neutral beryllium−ammonia complexes, we studied the dimers of the cationic $Be(NH_3)_{n=1-3}^+$ systems, which formed stable dicationic systems, unlike the metastable (by 54.1 kcal/mol) Be_2^{2+}.[14]

Lithium and sodium form the stable (experimentally observed) $Li(NH_3)_4$ and $Na(NH_3)_4$ SEPs, where one electron orbits around $Li(NH_3)_4^+$ and $Na(NH_3)_4^+$.[25] We showed that these H-mimicking molecules can bind together with a single covalent bond of highly diffuse nature exactly like Li_2 or Na_2 is formed by two Li or Na atoms.[25] Furthermore, saturation of ammonia solutions with metal atoms, such as Li, creates polymers of SEPs, known as liquid metals.[27,28] Our present goal is to extend our studies to the Be_2 analogue and investigate the formation of $[Be(NH_3)_4]_2$ and by extension the existence of beryllium liquid metals. Will it act as Be_2 or as He_2? What is the effect of the diffuse nature of the outer electrons and the electronic structure of the $Be(NH_3)_4$ monomer?

In section II we describe the computational details, section III.1 is devoted to $Be(NH_3)$, the $Be(NH_3)_{2-4}$ are discussed in section III.2, their dimers are studied in section III.3, and section III.4 deals with both the monomeric and dimeric cationic systems.

II. METHODS

Optimal structures for all of the $Be(NH_3)_{n=1-3}^{0/+}$ species are obtained at the coupled cluster CCSD(T) level of theory[29] using the triple-ζ quality correlation-consistent aug-cc-pVTZ basis set.[30,31] Harmonic vibrational frequencies were also calculated to confirm the stability of the located minima. For the construction of the potential energy profiles (PEPs) as a function of the Be−N distance for the ground and excited electronic states, we employed the internally contracted multireference configuration interaction (MRCI).[32−34] The N−H bond lengths and Be−N−H bond angles were kept constant and equal to their ground state equilibrium values at all Be−N distances. The cc-pVTZ set is used for the MRCI calculations. Considering that excitations out of the NH_3 electrons are high in energy, the starting CASSCF active space consists of the one/two "beryllium" valence electrons and four active orbitals. These correspond to the 2s and 2p orbitals of Be at long Be−N interatomic distances. All valence electrons are correlated at the MRCI level. For $Be(NH_3)$ and $Be(NH_3)_2$ we optimized the geometries of the excited electronic states at MRCI, but we kept the C_{3v} and C_{2v} symmetry of the ground state. The single-point energy calculations considering the Davidson correction (MRCI +Q)[35] were also performed to account for higher order electron correlation effects using the MRCI geometries.

A similar methodology was used for the $Be(NH_3)_n^{0/+}$ dimers. Because of technical limitations, the optimizations and frequency calculations were performed at CCSD(T)/cc-pVTZ for $[Be(NH_3)_{1,2}]_2^{0/2+}$, at MP2/aug-cc-pVTZ for $[Be(NH_3)_3]_2^{0/2+}$, and at MP2/cc-pVTZ(Be,N) aug-cc-pVTZ(H) for $[Be(NH_3)_4]_2$. For $[Be(NH_3)]_2^{0/2+}$ and $[Be(NH_3)_2]_2^{2+}$, PEPs are constructed with respect to the Be−Be distance at the MRCI level of theory. The equilibrium geometries are used for the construction of the PEPs varying only the Be−Be distance. The active space of $[Be(NH_3)_{1-2}]_2^{0/2+}$ consists of two or four electrons in eight orbitals. For $[Be(NH_3)_4]_2$, the geometry is optimized at every Be−Be distance at the density functional theory DFT/B3LYP level of theory, and CASPT2 calculations followed for the ground excited electronic states. The active space was four electrons into 18 orbitals. These 18 orbitals correspond to the outer 1s, 1p, and 1d superatomic orbitals of the monomers.[21] For the dimers we used the cc-pVDZ basis set for Be and N and the d-aug-cc-pVDZ set for H centers. In every case all valence electrons are correlated at the post-CASSCF level of theory except for the $[Be(NH_3)_4]_2$, where excitations from the CASSCF active orbitals to the virtual space are allowed.

Providing very accurate interaction/binding energies is beyond the scope of this work since FCI calculations may be necessary. We rather aim at the disclosure of the interesting electronic structure features of these systems. Therefore, we compare binding energies of all (small and large) systems at the CCSD(T)/aug-cc-pVTZ and MP2/aug-cc-pVTZ levels (see below for more details about each system).

Finally, we calculated dipole polarizabilities α_{zz} for the $Be(NH_3)_{n=0-4}$ systems, where z is their principal axis of symmetry. To this end, electric fields of f = 0.001 au intensity are applied along the z-axis with both positive and negative polarity. The α_{zz} value is estimated as the second derivative of the energy with respect to the applied field intensity $\partial^2 E/\partial f^2 \approx [E[+f] + E[-f] - 2E[0]]/f^2$, where $E[\pm f]$ and $E[0]$ are the CCSD(T)/aug-cc-pVTZ or MP2/aug-cc-pVTZ energies with the two opposite polarities and zero electric field.

All DFT and MP2 calculations are performed with Gaussian16,[36] and all MRCI, CASPT2, and CCSD(T) calculations are performed with MOLPRO.[37]

https://dx.doi.org/10.1021/acs.jpca.0c07939
J. Phys. Chem. A 2020, 124, 9783−9792

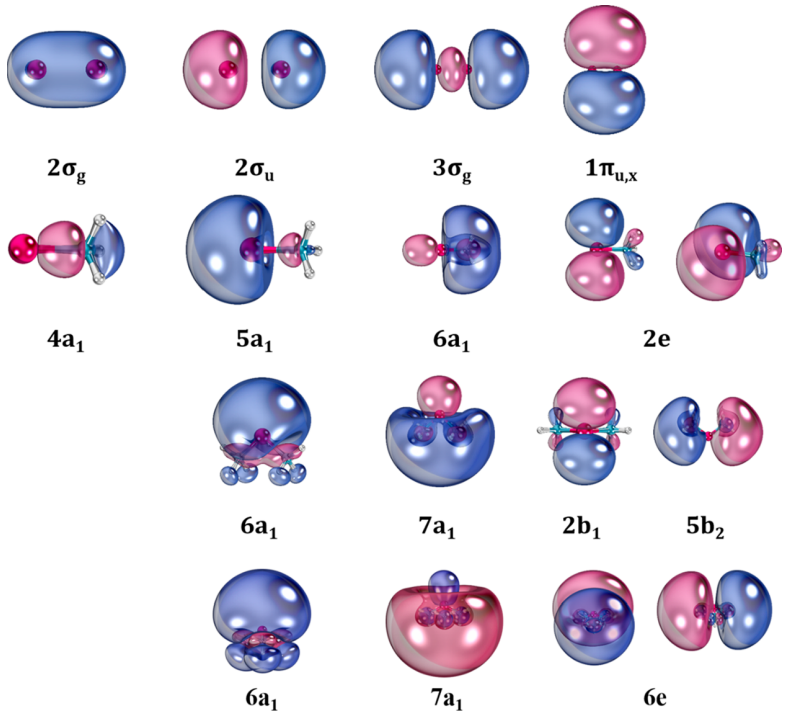

Figure 1. Selected molecular orbitals of Be_2 (first row), $Be(NH_3)$ (second row), $Be(NH_3)_2$ (third row), and $Be(NH_3)_3$ (fourth row).

III. RESULTS AND DISCUSSION

III.1. $Be(NH_3)$ and Be_2. The interaction between the ground closed-shell Be and NH_3 moieties is expected rather repulsive with a shallow potential well at long Be−N distances, as happens for $Be(^1S)$ + $CO(X^1\Sigma^+)$.[17] Indeed, the lowest energy Be−NH_3 CCSD(T)/aug-cc-pVTZ potential energy curve reveals a plateau in the 3 Å region as a result of this interaction. However, the PEC at ∼2.8 Å plunges into a potential well of 1802 cm^{-1} or 5.15 kcal/mol depth with respect to the Be + NH_3 fragments at a Be−N distance of 1.79 Å (see Figure S1 of the Supporting Information). This distance is substantially shorter than that of Be_2 (2.45 Å), and the binding energy is about 4 times larger than that of Be_2 at the same level of theory (472 cm^{-1}), suggesting a weak but present chemical bond. The Be−N harmonic vibrational frequency is ω_e = 456 cm^{-1}, giving an estimate of the zero point vibrational energy of around 228 cm^{-1} and placing the ground vibrational level well below the dissociation limit.

The molecular orbitals of Figure 1 indicate clearly that the electron pair of ammonia "pushes" the electron pair of Be at the "back" of it, making way for the formation of a dative bond from H_3N: to an effective Be^{2+} center. The shielding of the displaced beryllium electrons is still quite efficient to prevent a strong Be−NH_3 bond.

This observation raises the question of whether the bond formation in Be_2 is of similar nature: the electrons of the first beryllium atom "push" the electron pair of the second, and vice versa. The two resonance structures are indistinguishable. In the higher symmetry case of Be_2, the analogous $4a_1$ and $5a_1$ orbitals ($4a_1 \sim 2s_{Be,right}$, $5a_1 \sim 2s_{Be,left}$; see Figure 1) are combined to make orbitals $2\sigma_g$ and $2\sigma_u$ of Be_2 (see Figure 1), which are doubly occupied in the main ($2\sigma_g^2 2\sigma_u^2$; 79%) electronic configuration of Be_2 as happens for $Be(NH_3)$. The second most important electronic configuration ($2\sigma_g^2 3\sigma_g^2$; 7%) of Be_2 involves orbital $3\sigma_g$ (see Figure 1), which is better assigned to a $2p_z-2p_z$ covalent bond, in addition to the 2s−2s σ-bonding orbital ($2\sigma_g$ orbital of Figure 1). The latter configuration points to a contribution of a double bond between two $Be(^3P; 1s^2 2s^1 2p_z^1)$ atoms and has been suggested as the main binding mechanism by Kalemos in the past.[8] Presently, we provide an alternative view of the Be_2 bond depicted in terms of Lewis structures in Scheme 1, which combines these two contributions. The coefficient of the second configuration is even smaller (−0.11 or 1.2%) for $Be(NH_3)$.

Scheme 1. Lewis Structures for the Be−Be Bonding in Be_2

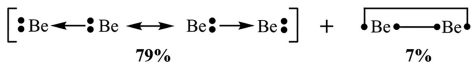

A natural question is why beryllium is special. We believe that beryllium can act as a base and acid at the same time, as opposed to noble gases. Its metallic nature renders it a relatively good base,[20] and its lower excitation energies make it more polarizable and thus eager to displace its electrons in favor of an electron pair of an "attacking" base. Specifically, the polarizability of Be (5.60 $Å^3$) is at least 3 times larger than that of He (0.205 $Å^3$), Ne (0.394 $Å^3$), and Ar (1.64 $Å^3$).[38] Because excitation energies and polarizability are connected (via perturbation theory), an equivalent statement is that given by the authors of ref 9, who assign the difference between Be and He or Ne to the low 2s−2p gap of Be. The proposed chemical bond of Scheme 1 falls under the general category of charge-shift bonds reported recently in the literature.[39]

We turn our discussion to the excited states of $Be(NH_3)$. Complete PEPs for the first five adiabatic channels are plotted in Figure 2, and optimal Be−N distances and excitation energies are listed in Table 1 along with their dominant electronic configurations; the molecular orbitals associated with them are shown in Figure 1. It should be noted that

https://dx.doi.org/10.1021/acs.jpca.0c07939
J. Phys. Chem. A 2020, 124, 9783−9792

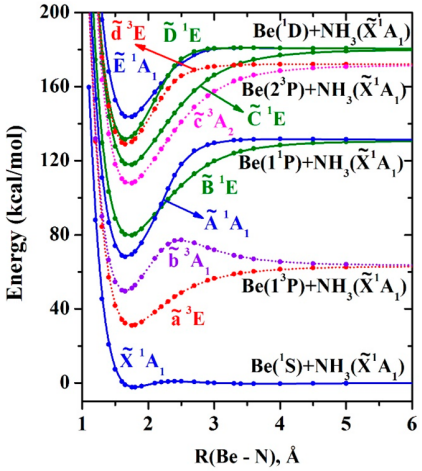

Figure 2. MRCI PEPs of $Be(NH_3)$ as a function of the Be−N distance. All other bond lengths and angles are kept fixed to their optimal values of the ground state global minimum.

Table 1. Excitation Energy ΔE (cm^{-1}), Be−N Bond Length r_{BeN} (Å), and Dominant Electronic Configurations for the Lowest Electronic States of $BeNH_3$

				electronic configuration[a]				
state	method	ΔE	r_{BeN}	coeff	$5a_1$	$6a_1$	$2e_x$	$2e_y$
$\tilde{X}^1A_1$	MRCI	0	1.786	0.95	2	0	0	0
	MRCI+Q	0						
	CCSD(T)	0	1.798					
$\tilde{a}^3E$	MRCI	11571	1.750	1.00	α	0	0	α
	MRCI+Q	12140						
	CCSD(T)	12223	1.755					
$\tilde{b}^3A_1$	MRCI	21781	1.634	1.00	α	α	0	0
	MRCI+Q	21578						
	CCSD(T)	21284	1.641					
$\tilde{A}^1A_1$	MRCI	29145	1.721	0.71	α	β	0	0
	MRCI+Q	27697		−0.71	β	α	0	0
$\tilde{B}^1E$	MRCI	29361	1.720	0.71	α	0	0	β
	MRCI+Q	27790		−0.71	β	0	0	α
$\tilde{c}^3A_2$	MRCI	38595	1.718	1.00	0	0	α	α
	MRCI+Q	38748						
	CCSD(T)	38788	1.722					
$\tilde{C}^1E$	MRCI	42665	1.716	0.71	0	0	α	β
	MRCI+Q	41707		−0.71	0	0	β	α
$\tilde{d}^3E$	MRCI	50026	1.654	1.00	0	α	0	α
	MRCI+Q	49350						
$\tilde{D}^1E$	MRCI	51803	1.643	0.71	0	α	0	β
	MRCI+Q	50160		−0.71	0	β	0	α
$\tilde{E}^1A_1$	MRCI	52103	1.708	0.66	0	0	2	0
	MRCI+Q	56917		0.67	0	0	0	2

[a]Coeff is the coefficient of each determinant, and α, β occupations correspond to spin-up or spin-down electrons. Contours of the relative orbitals are plotted in Figure 1.

harmonic vibrational frequencies were calculated only for the ground state ensuring that the structure is a stable minimum. For the excited states, geometry distortions from the imposed C_{3v} geometry may apply. In addition, the MRCI PEP of the ground state differs from that of CCSD(T) (compare Figure 1 and Figure S1). MRCI predicts a small barrier between the long-range interaction and the binding minimum.

The $2s_{Be}$ orbital composes practically the $5a_1$ orbital, while the 2p orbitals of Be split to the $6a_1$ and 2e orbitals. The latter ones are nearly the $2p_x$ and $2p_y$ orbitals (z being the Be−N axis), while $6a_1$ is a $2p_z$-like orbital diffused toward the N−H terminal bonds. The two valence electrons in the ground $\tilde{X}^1A_1$ state remain in the $\sim 2s_{Be}$ ($5a_1$) orbital. The first four excited states include excitation of one $5a_1$ electron to either $6a_1$ ($\tilde{b}^3A_1$ and $\tilde{A}^1A_1$) or 2e ($\tilde{a}^3E$ and $\tilde{B}^1E$). These states lie between 12000 and 28000 cm^{-1} at MRCI+Q. The same pattern is observed for the lowest lying states of BeCO, except for the ground state PEC, which is purely repulsive.[17] The next batch of states between 38000 and 57000 cm^{-1} involve the promotion of both $5a_1$ electrons to a $6a_1^12e^1$ ($\tilde{d}^3E$ and $\tilde{D}^1E$) or $2e^2$ ($\tilde{c}^3A_2$, $\tilde{C}^1E$, and $\tilde{E}^1A_1$) configuration. The bond length in all excited states is shorter than this of the ground state (1.79 Å at MRCI) with the smallest one belonging to $\tilde{b}^3A_1$ (1.63 Å at MRCI), and they are well bound with respect to their adiabatic fragments.

III.2. $Be(NH_3)_2$, $Be(NH_3)_3$, and $Be(NH_3)_4$. The PECs, selected molecular orbitals, and numerical data for the ground and excited states of $Be(NH_3)_2$ and $Be(NH_3)_3$ are provided in Figures 1 and 3 as well as Tables 2 and 3. PEPs for $Be(NH_3)_3$

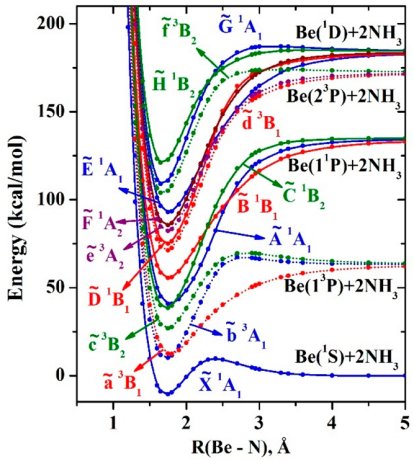

Figure 3. MRCI PEPs of $Be(NH_3)_2$ as a function of the two equal Be−N distances. All other bond lengths and angles are kept fixed to their optimal values of the ground state global minimum.

are given in the Supporting Information (Figure S3) of our previous work.[20] The ground state for both systems retains the $\sim 2s_{Be}^2$ configuration, and their PECs are characterized by an "activation barrier" when ammonias approach Be. Interestingly enough, the Be−NH_3 bonds become stronger as more ammonia molecules attach to beryllium. Specifically, the CCSD(T)/aug-cc-pVTZ binding energy per Be−NH_3 bond is 5.2, 8.3, and 12.8 kcal/mol calculated as $[E[Be] + nE[NH_3] - E[Be(NH_3)_n]]/n$, where $E[X]$ is the equilibrium energy of molecule X. It seems that the concerted displacement of the beryllium valence electrons by more ammonias exposes further the Be nuclear charge. The larger effective charge on the beryllium center enhances the stability of the Be−NH_3 bonds.

The excited states of $Be(NH_3)_{2,3}$ follow the same pattern as in $Be(NH_3)$. The promotion of a $6a_1$ ($\sim 2s_{Be}$) electron to one of the $\sim 2p_{Be}$ orbitals provide the lowest energy states. The $7a_1$ orbital is along the principal axis of symmetry in each case ($\sim 2p_{z,Be}$). The remaining two 2p orbitals are degenerate only for $Be(NH_3)_3$ since the C_{2v} symmetry of $Be(NH_3)_2$ lifts their degeneracy ($2b_1$ and $5b_2$ orbitals). The two unpaired electrons

https://dx.doi.org/10.1021/acs.jpca.0c07939
J. Phys. Chem. A 2020, 124, 9783−9792

Table 2. Excitation Energy ΔE (cm^{-1}), Be−N Bond Length r_{BeN} (Å), N−Be−N Angles θ_{NBeN} (deg), and Dominant Electronic Configurations for the Lowest Electronic States of $Be(NH_3)_2$

					electronic configuration[a]				
state	method	ΔE	r_{BeN}	θ_{NBeN}	coeff	$6a_1$	$7a_1$	$2b_1$	$5b_2$
$\tilde{X}^1A_1$	MRCI	0	1.730	101.7	0.95	2	0	0	0
	MRCI+Q	0							
	CCSD(T)	0	1.747	100.3					
$\tilde{a}^3B_1$	MRCI	5933	1.774	110.8	1.00	α	0	α	0
	MRCI+Q	6502							
$\tilde{b}^3A_1$	MRCI	10270	1.694	115.2	1.00	α	α	0	0
	MRCI+Q	10791							
	CCSD(T)	10858	1.703	111.6					
$\tilde{c}^3B_2$	MRCI	16396	1.724	109.2	1.00	α	0	0	α
	MRCI+Q	16661							
$\tilde{A}^1A_1$	MRCI	20281	1.754	112.1	0.65	α	β	0	0
	MRCI+Q	19804			−0.65	β	α	0	0
$\tilde{B}^1B_1$	MRCI	21323	1.757	118.8	0.71	α	0	β	0
	MRCI+Q	20169			−0.71	β	0	α	0
$\tilde{d}^3B_1$	MRCI	21416	1.732	180.0	1.00	0	α	α	0
	MRCI+Q	21579							
$\tilde{C}^1B_2$	MRCI	24796	1.692	116.9	0.71	α	0	0	β
	MRCI+Q	23610			−0.71	β	0	0	α
$\tilde{D}^1B_1$	MRCI	25807	1.687	172.6	0.71	0	α	β	0
	MRCI+Q	24098			−0.71	0	β	α	0
$\tilde{E}^1A_1$	MRCI	27904	1.652	177.9	0.93	0	0	2	0
	MRCI+Q	26479							
$\tilde{e}^3A_2$	MRCI	31746	1.664	177.9	1.00	0	0	α	α
	MRCI+Q	31593							
$\tilde{f}^3B_2$	MRCI	31755	1.664	180.0	1.00	0	α	0	α
	MRCI+Q	31596							
$\tilde{F}^1A_2$	MRCI	32951	1.661	180.0	0.71	0	0	α	β
	MRCI+Q	32371			−0.71	0	0	β	α
$\tilde{G}^1A_1$	MRCI	35415	1.692	180.0	0.60	0	0	0	2
	MRCI+Q	33384			−0.77	0	2	0	0
$\tilde{H}^1B_2$	MRCI	35264	1.664	180.0	0.71	0	α	0	b
	MRCI+Q	33588			−0.71	0	β	0	α

[a]Coeff is the coefficient of each determinant, and α, β occupations correspond to spin-up or spin-down electrons. Contours of the relative orbitals are plotted in Figure 1.

can couple into a singlet or triplet spin multiplicity, making the lowest lying electronic states (see Tables 2 and 3). The promotion of the second $6a_1$ electron to either $7a_1$ or one of the two (quasi-)degenerate $2p_{Be}$ orbitals generates the rest of the studied states.

The range of MRCI+Q excitation energies for the same 15 (counting degenerate states twice) states is 0−56917, 0−33588, and 0−40000 cm^{-1} for one, two, and three ammonia ligands. It is noteworthy that the triplet state with one electron in $\sim 2s_{Be}$ and one in $\sim 2p_{z,Be}$ orbitals is stabilized with the number of ammonias. It is the third excited state at 21578 cm^{-1} for $Be(NH_3)$, it becomes the second excited state at 10791 cm^{-1} for $Be(NH_3)_2$, and ends up the first excited state at 7830 cm^{-1} for $Be(NH_3)_3$. A possible reason is that the $\sim 2p_{z,Be}$ orbital actually diffuses more and more toward the ammonias' terminal, enabling a stronger "solvation" of the occupying electron by more N−H bonds. It should also be mentioned that the *in situ* electronic structure of beryllium within the $Be(NH_3)_{1-3}$ molecule retains the energy order of the isolated beryllium atom. Specifically, Be(^1S; $1s^22s^2$) corresponds to the ground $6a_1^2$ state, Be(1^3P and ^1P; $1s^22s^12p^1$) relate to the lowest lying states of the complexes, and Be(2^3P and ^1D; $1s^22p^2$) pertain to their higher energy states (see Figures 2 and 3 as well as Figure S3 of ref 20).

The addition of a fourth ammonia leads to $Be(NH_3)_4$, where four ammonia ligands are attached to a Be^{2+} center and the two valence electrons orbit in the periphery of this complex. This last addition turns out to be more exothermic than the other three with a $Be(NH_3)_3 + NH_3$ binding energy of 28 kcal/mol,[21] which gives an average Be−NH_3 bond of 16.6 kcal/mol. Again, the bond energy increases compared to the smaller complexes. The beryllium valence electrons become now electrons of the molecule occupying one of the "super-atomic" orbitals that arise (1s, 1p, 1d, 2s). The type of the three lower electronic states mimic those of Be: $1s^2$ vs $2s_{Be}^2$ (ground state), triplet $1s^11p^1$ vs triplet $2s_{Be}^12p_{Be}^1$ (first excited state), and singlet $1s^11p^1$ vs singlet $2s_{Be}^12p_{Be}^1$ (second excited state). The excitation energies of $Be(NH_3)_4$ are much smaller though: 0.81 vs 2.725 eV and 1.62 vs 5.28 eV.[16,21] How this energy lowering affects the binding of two $Be(NH_3)_4$ moieties compared to Be_2? Do the "intermediates" $Be(NH_3)_{n=1-3}$ moieties bind and how strongly?

III.3. $Be(NH_3)_{n=1-4}$ Dimers. The discussion of section III.4 shows that the addition of ammonia ligands to beryllium retains its $1s^22s^2$ *in situ* electronic state as opposed to other

https://dx.doi.org/10.1021/acs.jpca.0c07939
J. Phys. Chem. A 2020, 124, 9783−9792

Table 3. Vertical Excitation Energy ΔE (cm^{-1}) and Dominant Electronic Configurations for the Lowest Electronic States of $Be(NH_3)_3$

			electronic configuration[a]				
state	method	ΔE	coeff	$6a_1$	$7a_1$	$6e_x$	$6e_y$
$\tilde{X}^1A_1$	MRCI	0	0.95	2	0	0	0
	MRCI+Q	0					
$\tilde{a}^3A_1$	MRCI	7441	1.00	α	α	0	0
	MRCI+Q	7830					
$\tilde{b}^3E$	MRCI	12338	0.96	α	0	α	0
	MRCI+Q	12704					
$\tilde{A}^1A_1$	MRCI	21638	0.71	α	β	0	0
	MRCI+Q	20541	−0.71	β	α	0	0
$\tilde{B}^1E$	MRCI	21729	0.71	α	0	0	β
	MRCI+Q	19764	−0.71	β	0	0	α
$\tilde{c}^3E$	MRCI	33193	0.96	0	α	α	0
	MRCI+Q	32928					
$\tilde{C}^1A_1$	MRCI	37457	0.77	0	2	0	0
	MRCI+Q	35477	−0.42	0	0	2	0
			−0.42	0	0	0	2
$\tilde{d}^3A_2$	MRCI	37351	1.00	0	0	α	α
	MRCI+Q	37476					
$\tilde{D}^1E$	MRCI	38721	−0.45	0	0	α	β
	MRCI+Q	37492	0.45	0	0	β	α
			−0.54	0	α	0	β
			0.54	0	β	0	α
$\tilde{E}^1E$	MRCI	41279	0.54	0	0	2	0
			−0.54	0	0	0	2
			−0.45	0	α	β	0
	MRCI+Q	40000	0.45	0	β	α	0

[a]Coeff is the coefficient of each determinant, and α, β occupations correspond to spin-up or spin-down electrons. Contours of the relative orbitals are plotted in Figure 1.

ligands (see section III.1), and they polarize the 2s orbital at the "back" of beryllium. The approach of two $Be(NH_3)$ molecules results in a stronger Be−Be bond compared to Be_2. Specifically, the binding energy becomes 22.4, 25.2, and 25.8 kcal/mol at MRCI, MRCI+Q, and CCSD(T), an order of magnitude larger than plain Be_2 values of 1.96, 2.15, and 1.35 kcal/mol. The optimal geometry of $[Be(NH_3)]_2$ has a N−Be−Be−N zigzag skeleton to provide the necessary space for the two beryllium electron pairs and accommodate the same bonding observed for Be_2. The main configuration of the ground state points to the first two resonance structures of Scheme 1 and the next dominant configuration to the last configuration of the same scheme (see Table 4 as well as Figures 4 and 5). The relative contribution of the two configurations does not change significantly going from Be_2 to $[Be(NH_3)]_2$ (coefficients = 0.89 vs 0.89 and −0.26 vs −0.36). This traces back to the small difference between the excitation energy of the $2s^12p^1$-like states of the two systems (^3P and $\tilde{b}^3A_1$), which generate the second configuration: 21978−21981 cm^{-1} ($^3P_{0-2}$)[38] and 21284 cm^{-1} (Table 1). The enhanced binding is rather attributed to the more diffuse nature of the polarized $2s_{Be}$ orbitals in the case of $Be(NH_3)$. Our CCSD(T)/aug-cc-pVTZ polarizabilities for Be and $Be(NH_3)$ are 5.63 and 14.3 $Å^3$. The former compares favorably with the experimental value of 5.60 $Å^3$.[38]

The first three excited electronic states of $[Be(NH_3)]_2$ resemble those of Be_2. The first one ($\tilde{a}^3B_g$) has a $6a_g^2 6b_u^1 2a_u^1$ configuration which is the analogue of one of the $2^3\Pi_g$ ($1\sigma_g^2 1\sigma_u^1 1\pi_u^1$) components of Be_2 ($6a_g \sim 1\sigma_g$; $6b_u \sim 1\sigma_u$; $2a_u \sim 1\pi_u$).[8] The symmetry lowering of $[Be(NH_3)]_2$ results to

Table 4. Vertical Excitation Energy ΔE (cm^{-1}) and Dominant Electronic Configurations for the Lowest Electronic States of $[Be(NH_3)]_2$

			electronic configuration[a]					
state	method	ΔE	coeff	$6a_g$	$7a_g$	$2a_u$	$6b_u$	$2b_g$
$\tilde{X}^1A_g$	MRCI	0	0.89	2	0	0	2	0
	MRCI+Q	0	−0.36	2	2	0	0	0
$\tilde{a}^3B_g$	MRCI	1584	0.94	2	0	α	α	0
	MRCI+Q	1770						
$\tilde{b}^3B_u$	MRCI	4670	0.96	2	α	0	α	0
	MRCI+Q	4665						
$\tilde{A}^1B_g$	MRCI	6381	0.65	2	0	β	α	0
	MRCI+Q	5955	−0.65	2	0	α	β	0
$\tilde{c}^3A_u$	MRCI	12785	0.96	2	α	α	0	0
	MRCI+Q	12838						
$\tilde{B}^1A_u$	MRCI	12861	0.56	2	α	β	0	0
	MRCI+Q	12950	−0.56	2	β	α	0	0
$\tilde{C}^1A_g$	MRCI	13513	0.89	2	0	2	0	0
	MRCI+Q	13180						
$\tilde{d}^3A_g$	MRCI	15647	0.95	2	α	α	0	0
	MRCI+Q	14643						

[a]Coeff is the coefficient of each determinant, and α, β occupations correspond to spin-up or spin-down electrons. Contours of the relative orbitals are plotted in Figure 5.

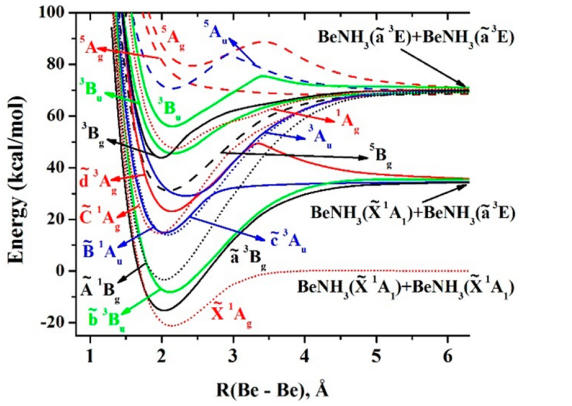

Figure 4. MRCI PEPs of $[Be(NH_3)]_2$ as a function of the Be−Be distance. All other bond lengths and angles are kept fixed to their optimal values of the ground state global minimum.

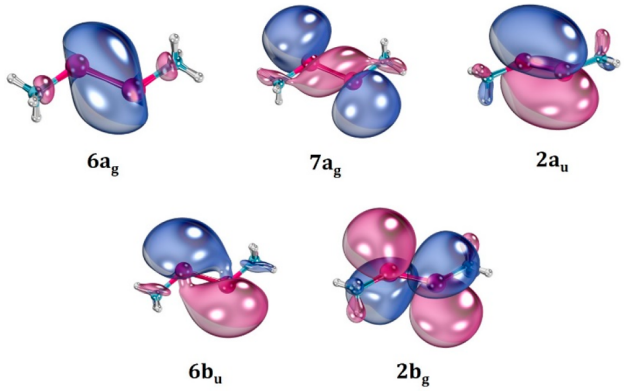

Figure 5. Selected active molecular orbitals of $[Be(NH_3)]_2$.

https://dx.doi.org/10.1021/acs.jpca.0c07939
J. Phys. Chem. A 2020, 124, 9783−9792

the destabilization of one $1\pi_u$ orbital and the shift of the other $2^3\Pi_g$ component to higher energies. The $\tilde{A}^1B_g$ and $3^1\Pi_g$ are the singlet spin counterparts of the two systems, and the $\tilde{b}^3B_u$ corresponds to $1^3\Sigma_u^+$ of Be_2: $6a_g^2 7a_g^1 6b_u^1$ vs $1\sigma_g^2 2\sigma_g^1 1\sigma_u^1$ ($7a_g \sim 2\sigma_g$).[8] The excitation energies ΔE are about half or smaller in the $[Be(NH_3)]_2$ case at the MRCI level of theory: $\Delta E(\tilde{a}^3B_g/2^3\Pi_g)$ = 1584/8604 cm^{-1}, $\Delta E(\tilde{A}^1B_g/3^1\Pi_g)$ = 4670/14007 cm^{-1}, and $\Delta E(\tilde{b}^3B_u/1^3\Sigma_u^+)$ = 6381/7508 cm^{-1}.[8]

The addition of a second ammonia ligand to the system polarizes further $2s_{Be}$. The CCSD(T)/aug-cc-pVTZ polarizability becomes 39.7 $Å^3$. As a result, the Be−Be binding energy for two $Be(NH_3)_2$ systems is larger by about 4 kcal/mol at all three levels of theory: 26.6 [MRCI], 29.4 [MRCI+Q], and 29.4 kcal/mol [CCSD(T)]. The coefficients for the two electronic configurations are 0.91 and −0.34, and the x−Be−Be−x line keeps the zigzag character (x = middle point between two N atoms of the same Be center) to accommodate the same binding scheme. Note also that although CCSD(T) fails considerably for Be_2 (see section III.1), it performs very well when ammonia ligands are present; compare the MRCI +Q and CCSD(T) values of this section. This observation confirms the difficulty to obtain accurate energetics for small quantities such as the binding energy of purely weak molecular interactions.

The case of $[Be(NH_3)_3]_2$ differs significantly. The two additional ammonias in the system force the displacement of a $2s_{Be}$ electron pair to the periphery of a $[Be(NH_3)_3]_2^{2+}$ core, as happens going from $Be(NH_3)_3$ to $Be(NH_3)_4$. A covalent bond forms between two $(NH_3)_3Be^{\bullet+}$ radicals, and the excessive repulsion due to two positively charged molecules is balanced out by the attraction of the $[Be(NH_3)_3]_2^{2+}$ core and the two outer electrons. The absence of the two outer electrons causes the destabilization of the system reducing the dissociation energy to two $(NH_3)_3Be^+$ fragments (see also section III.4). The Be−Be binding energy at MP2 is 35.0 kcal/mol. Because MRCI or CCSD(T) calculations were impractical, we resorted to MP2 calculations. For a fair comparison, the MP2 binding energies for the smaller systems Be_2, $[Be(NH_3)]_2$ and $[Be(NH_3)_2]_2$ are 1.05, 28.3, and 37.2 kcal/mol, meaning that the Be−Be bond for $[Be(NH_3)_3]_2$ drops slightly compared to $[Be(NH_3)_2]_2$.

The trends for the Be−Be bond lengths agree with these of the binding/interaction energies. The bonds for Be_2, $[Be(NH_3)]_2$, $[Be(NH_3)_2]_2$, and $[Be(NH_3)_3]_2$ are 2.477, 2.125, 2.071, and 2.178 Å long. The Be−Be bond contracts considerably in the presence of ammonia ligands despite the increased steric repulsions. The bond shortening is larger for $[Be(NH_3)_2]_2$ which also has the larger binding energy.

A completely different picture from any of the previous systems is found when two more ammonia ligands are included in the system. There is no direct Be−Be bond anymore, but instead two $Be(NH_3)_4$ moieties attach to each other as in Be_2. Be and $Be(NH_3)_4$ have similar electronic structures in the sense that their ground and first excited states have s^2 and s^1p^1 character. In the former case s and p correspond to the $2s_{Be}$ and $2p_{Be}$ atomic orbitals but in the latter to diffuse "superatomic" orbitals of the $Be(NH_3)_4^{2+}$ complex.[21] The excitation energy in the two systems is 2.725 and 0.81 eV,[16,21] suggesting that the contribution of the second Lewis structure of Scheme 1 will contribute more to the wave function of the ground state $[Be(NH_3)_4]_2$ molecule. The coefficients for the relative two configurations are in agreement showing a smaller ratio between the first two coefficients of the CI vector: c_1 = 0.82 and c_2 = −0.34 (c_1/c_2 = 2.4 or c_1^2/c_2^2 = 5.8) vs c_1 = 0.89 and c_2 = −0.26 (c_1/c_2 = 3.4 or c_1^2/c_2^2 = 11.7) for Be_2.

The MP2 $(NH_3)_4Be-Be(NH_3)_4$ binding energy is 3 times larger (7.26 kcal/mol or 2539 cm^{-1}) than plain Be−Be. The larger binding energy can be ascribed to two factors: the larger contribution of its first excited state in the bonding and the higher polarizability of $Be(NH_3)_4$. At the MP2/aug-cc-pVTZ level of theory, the two polarizabilities are 6.31 and 71.7 $Å^3$. The CASPT2 binding energy in the case of the clear covalent $(NH_3)_4Li-Li(NH_3)_4$ and $(NH_3)_4Na-Na(NH_3)_4$ bonds is 14.7 and 5.6 kcal/mol, respectively.[25] Both saturated sodium and lithium ammonia solutions form bronze liquid metal materials.[40,41] Based on the comparable $(NH_3)_4Be-Be(NH_3)_4$ binding energy, the formation of beryllium ammonia liquid metals is possible.

The PEPs for the five lowest energy states of $[Be(NH_3)_4]_2$ as a function of the Be−Be distance are plotted in Figure 6;

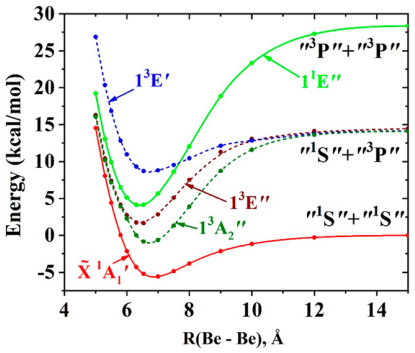

Figure 6. CASPT2 PEPs of $[Be(NH_3)_4]_2$ as a function of the Be−Be distance. All other bond lengths and angles are kept fixed to their DFT/B3LYP optimal values of the ground state at each Be−Be distance. The states of the $Be(NH_3)_4$ fragments are denoted by using the corresponding atomic terms of atomic Be: $^1S(1s^2 2s^1)$ and $^{1,3}P(1s^2 2p^1)$.

vertical excitation energies at the CASSCF and CASPT2 levels are tabulated in Table 5 along with the dominant electronic configurations (see Figure 7 for the involved molecular orbitals). The PEPs and electronic configurations echo those of Be_2 reflecting the similarity between Be and $Be(NH_3)_4$. Specifically, the first four states of $[Be(NH_3)_4]_2$ are $\tilde{X}\ ^1A_1'$,

Table 5. CASSCF and CASPT2 Vertical Excitation Energy ΔE (cm^{-1}) and Dominant Electronic Configurations for the Lowest Electronic States of $[Be(NH_4)]_2$

	ΔE			configuration[a]				
state	CASSCF	CASPT2	coeff	$1a_1'$	$2a_1'$	$1a_2''$	$1e_x'$	$1e_y'$
$\tilde{X}^1A_1'$	0	0	0.82	2	0	2	0	0
			−0.34	2	2	0	0	0
$1^3A_2''$	1564	1557	0.92	2	α	α	0	0
$1^3E''$[b]	2567	2579	0.85	2	0	α	α	0
$1^1E''$[b]	3679	3537	0.59	2	0	α	0	β
			−0.59	2	0	β	0	α
$1^3E'$[b]	4693	4772	0.68	α	0	2	α	0
			0.43	2	α	0	α	0

[a]Coeff is the coefficient of each Slater determinant, and α, β occupations correspond to spin-up or spin-down electrons. Contours of the relative orbitals are plotted in Figure 7. [b]The electronic configuration of one out of the two degenerate components is listed.

https://dx.doi.org/10.1021/acs.jpca.0c07939
J. Phys. Chem. A 2020, 124, 9783−9792

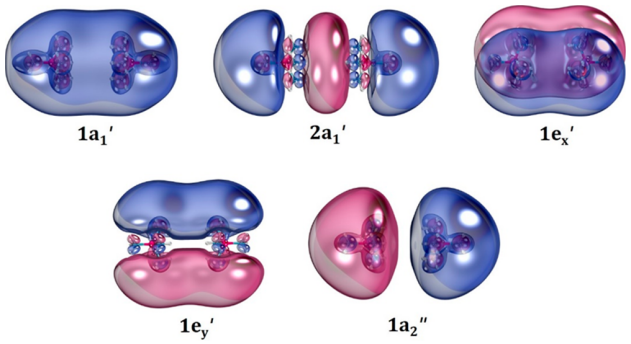

Figure 7. Selected active molecular orbitals of $[Be(NH_3)_4]_2$. Only outer orbitals are counted.

$1^3A_2''$, $1^3E''$, and $1^1E''$, which have identical energy order and electronic structure to the first four states ($X^1\Sigma_g^+$, $1^3\Sigma_u^+$, $2^3\Pi_g$, and $3^1\Pi_g$) of Be_2; compare configurations of Table 5 and those of Be_2 in ref 8. The excitation energies of $[Be(NH_3)_4]_2$ are at least 3 times smaller because of the diffuse nature of its molecular orbitals (see Table 5 and Table 2 of ref 8). The $[Be(NH_3)_4]_2$ and Be_2 PEPs for these states have similar morphology and dissociate to the same states of the fragments (compare present Figure 6 and Figure 6 of ref 8). A noticeable difference is that the ground state PEP is steeper and more bound for $[Be(NH_3)_4]_2$. The fifth state of $[Be(NH_3)_4]_2$ ($1^3E'$) is also bound and dissociates to the "^1S" and "^3P" fragments (analogue ^1S and ^3P states of Be). On the other hand, the corresponding $5^3\Pi_u$ of Be_2 is purely repulsive. Finally, we observe that excitation energies at the CASSCF and CASPT2 levels differ by less than 200 cm^{-1} (see Table 5) due to the partial inclusion of the dynamic electron correlation (see section III.2).

III.4. Cationic Species $Be(NH_3)_{0-4}^+$ and Their Dimers.

The removal of one electron from Be creates the radical $Be^+(^2S; 1s^22s^1)$ species. Ammonia molecules bind easier now to Be^+ guided by the positive charge and the presence of only one electron in 2s, which screens less efficiently the Be^{2+} nuclear charge. As a result, the PECs with respect to the addition of one ammonia are all highly attractive (see Figure S2) leading to $(NH_3)_{n-1}Be^+-NH_3$ CCSD(T) binding energies of 78.3, 51.1, and 38.3 kcal/mol for n = 1, 2, and 3, respectively. The corresponding Be−N bond lengths are 1.681, 1.724, and 1.765 Å. Both the decreasing trend of binding energies and increasing trend of bond lengths are due to the steric repulsion among the ammonia molecules.

Two Be^+ cations repel each other, but they can also bind via a covalent bond. Similar electronic structure and identical interactions occur for two $Be(NH_3)_{n=1-4}^+$ species. Interestingly, the first and last members of the series (Be^+ and $Be(NH_3)_4^+$) create metastable or unstable dimers. There is a Be_2^{2+} minimum, but it is nearly 50 kcal/mol higher than the Be^+ + Be^+ fragments at MRCI, in agreement with the CCSD(T) value of ref 14. In addition, we were not able to capture a stable $[Be(NH_3)_4]_2^{2+}$ minimum. However, the covalent bond counterbalances the Coulombic repulsion for the $Be(NH_3)_{1,2,3}^+$ dimers, which have lower energy than the corresponding fragments by 16.2/11.2, 22.9/18.3, and NA/7.13 kcal/mol (NA = not available) at the CCSD(T)/MP2 levels (using the aug-cc-pVTZ basis set), respectively. For comparison, the binding energy of the dimer of the isovalent neutral $(CO)_3Li^\bullet$ radical is 4 times larger (27.2 kcal/mol).[42]

Notice that the MP2 binding energies are smaller by 4−5 kcal/mol for $[Be(NH_3)_{1,2}]_2^{2+}$, and thus the CCSD(T) binding energy for $[Be(NH_3)_3]_2^{2+}$ is expected to be around 12 kcal/mol. In any case, it is the less stable among these species, maybe because of the enhanced repulsion between ammonia ligands of different beryllium centers. Interestingly, the $(NH_3)_3Be-Be(NH_3)_3$ bond gets significantly stronger when two electrons are added to the system (see section III.3). Similar dicationic (RuO^{2+}, MoO^{2+}, and TM_2^{2+}, TM = transition metal)[43−45] or dianionic ($(B_{12}I_9)_2^{2-}$)[46] systems have been observed in the past.

The optimal structures for the stable cationic dimers differ from the corresponding neutral dimers. The N−Be−Be−N and x−Be−Be−x (see section III.3 for definition of x) lines are now collinear because of the absence of electrons in the $2s_{Be}-2s_{Be}$ antibonding orbital. The $[Be(NH_3)_{1,2,3}]_2^{2+}$ structures resemble those of ethyne, ethene, and ethane molecules. The Be−Be bond length increases respectively with the number of ammonia ligands as 2.086, 2.170, and 2.326 Å, while the Be−N bond lengths change within 0.05 Å during the dimerization. Finally, it should be stated that the wave function for all cationic or dicationic systems is pure single-reference with the main coefficient of the CI expansion being 0.95 or higher.

The PEPs for the ground state of $Be(NH_3)_{1,2}^+$ dimers are shown in Figure 7. As expected, they are repulsive for long Be−

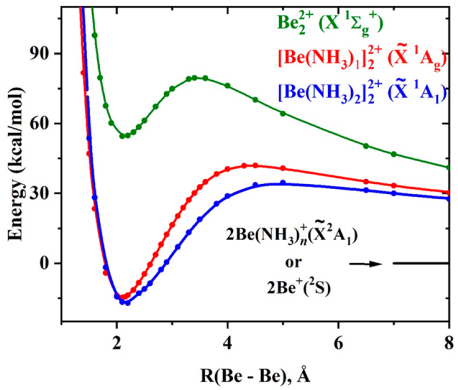

Figure 8. MRCI PEPs of $[Be(NH_3)_{0,1,2}]_2^{2+}$ as a function of the Be−Be distance. All other bond lengths and angles are kept fixed to their optimal values of the ground state global minimum.

Be distances. After an energy barrier at 4.5 and 5.0 Å of 42 and 35 kcal/mol, they turn attractive, forming the equilibrium dimer structures. We were not able to make the PECs for $Be(NH_3)_3^+$, but based on the trends for $Be(NH_3)_{1,2}^+$, we expect a smaller activation barrier occurring at longer distances: The more and more diffuse nature of the unpaired electron going from $Be(NH_3)^+$ to $Be(NH_3)_3^+$ enables the formation of the chemical bond "faster".

IV. CONCLUSIONS

High-level electronic structure methodologies are applied to study the Be−Be bond in the naked Be_2 and when it is coordinated with ammonia ligands. To this end, the electronic structure of the $Be(NH_3)_{n=0-4}$ units was investigated first. We found that ammonia, as opposed to other ligands, retains the ground state $1s^22s^2$ character of Be by polarizing the 2s orbital away from ammonia molecules. We propose for the first time that the bonding between two such closed-shell units can be

https://dx.doi.org/10.1021/acs.jpca.0c07939
J. Phys. Chem. A 2020, 124, 9783−9792

described as a give-and-take mechanism of an electron pair of each $Be(NH_3)_{n=0-4}$ monomer. This picture is rationalized in terms of the Lewis acidity and basicity of beryllium: closed-shell beryllium centers as opposed to rage gas atoms can equally donate an electron pair and polarize to accept an electron pair. This bonding scheme explains the weak, but not so weak, bond in Be_2. The higher polarizability of the ligated units can explain the significantly larger binding energy of their dimers. The previously proposed double bond between two excited ^3P Be atoms is presently found to have small contribution to the formation of the ground state of Be_2 and $(NH_3)_{n=1-3}Be-Be(NH_3)_{n=1-3}$ bonds.

Our larger beryllium ammonia coordination complex, $Be(NH_3)_4$, has two diffuse electrons around a $Be(NH_3)_4^{2+}$ core and imitates the electronic structure of Be. Two such units also bond together as happens for Be_2, and their binding energy is also (3−4 times) larger than that of Be_2. The low-lying excited states for the two dimers have identical electronic configurations and PEPs with similar morphology. However, the excitation energies of both the monomers and dimers are significantly lower in the case of beryllium−ammonia complexes.

The present work and previous literature indicate that there are two ways to enhance the Be−Be bond. The first way is by promoting the Be center to an excited state as happens for H, F, and CO and has been described in the literature (see the Introduction). The second way is by rendering the $2s^2$ electrons of beryllium more polarizable by adding NH_3 ligands or probably other ligands with lone electron pairs such as water or alcohols.

The cationic $Be(NH_3)_{0-4}^+$ species and their dimers were also investigated. In these systems, the repulsion between two positively charged units deters the formation of a single covalent bond. It turns out that Be^+ creates a metastable dimer, $Be(NH_3)_4^+$ does not form a stable dimer, but the intermediate complexes $Be(NH_3)_{1,2,3}^+$ do form dimers with energies lowest than the dissociation limit and protected by large dissociation barriers.

Potential energy profiles for the ground and excited electronic states have been plotted for the monomers and dimers. We believe that our calculated optimized geometries, harmonic vibrational frequencies, binding energies for the ground states, and excitation energies for several low-lying excited electronic states for these exotic molecular systems will allow the experimental identification and characterization of these species in the future. Beryllium−ammonia liquid metals are finally predicted as novel materials by our calculations.

■ ASSOCIATED CONTENT

Supporting Information

The Supporting Information is available free of charge at https://pubs.acs.org/doi/10.1021/acs.jpca.0c07939.

Additional plots of potential energy profiles; tables with optimized geometries and harmonic vibrational frequencies (PDF)

■ AUTHOR INFORMATION

Corresponding Author

Evangelos Miliordos − *Department of Chemistry and Biochemistry, Auburn University, Auburn, Alabama 36849, United States;* orcid.org/0000-0003-3471-7133; Email: emiliord@auburn.edu

Author

Isuru R. Ariyarathna − *Department of Chemistry and Biochemistry, Auburn University, Auburn, Alabama 36849, United States;* orcid.org/0000-0002-5259-4248

Complete contact information is available at: https://pubs.acs.org/10.1021/acs.jpca.0c07939

Notes

The authors declare no competing financial interest.

■ ACKNOWLEDGMENTS

The authors are indebted to Auburn University (AU) for financial support. This work was completed with resources provided by the Auburn University Hopper Cluster and Alabama Supercomputer Center. This material is based upon work supported by the National Science Foundation under Grant CHE-1940456. Any opinions, findings, and conclusions or recommendations expressed in this material are those of the author(s) and do not necessarily reflect the views of the National Science Foundation.

■ REFERENCES

(1) Huber, K. P.; Herzberg, G. *Molecular Spectra and Molecular Structure*; Springer: Boston, MA, 1979.

(2) Wüest, A.; Merkt, F. Determination of the Interaction Potential of the Ground Electronic State of Ne_2 by High-Resolution Vacuum Ultraviolet Laser Spectroscopy. *J. Chem. Phys.* **2003**, *118* (19), 8807−8812.

(3) Herman, P. R.; LaRocque, P. E.; Stoicheff, B. P. Vacuum Ultraviolet Laser Spectroscopy. V. Rovibronic Spectra of Ar_2 and Constants of the Ground and Excited States. *J. Chem. Phys.* **1988**, *89* (8), 4535−4549.

(4) Ginter, M. L.; Battino, R. Potential-Energy Curves for the He_2 Molecule. *J. Chem. Phys.* **1970**, *52* (9), 4469−4474.

(5) Focsa, C.; Bernath, P. F.; Colin, R. The Low-Lying States of He_2. *J. Mol. Spectrosc.* **1998**, *191* (1), 209−214.

(6) Merritt, J. M.; Bondybey, V. E.; Heaven, M. C. Beryllium Dimer–Caught in the Act of Bonding. *Science* **2009**, *324* (5934), 1548−1551.

(7) Tong, X.-F.; Yang, C.-L.; Xiao, J.; Wang, M.-S.; Ma, X.-G. Theoretical Study on the Complexes of He, Ne and Ar. *Chin. Phys. B* **2010**, *19* (12), 123102.

(8) Kalemos, A. The Nature of the Chemical Bond in Be_2^+, Be_2, Be_2^-, and Be3. *J. Chem. Phys.* **2016**, *145* (21), 214302.

(9) Montero-Campillo, M. M.; Mó, O.; Yáñez, M.; Alkorta, I.; Elguero, J. The Beryllium Bond. *Adv. Inorg. Chem.* **2019**, *73*, 73−121.

(10) Patkowski, K.; Podeszwa, R.; Szalewicz, K. Interactions in Diatomic Dimers Involving Closed-Shell Metals. *J. Phys. Chem. A* **2007**, *111* (49), 12822−12838.

(11) Sunil, K. K. The Nature of Bonding and Stability of Beryllium Carbonyl $(CO)_2Be-Be(CO)_2$: A Molecule with a Beryllium-Beryllium Double Bond. *J. Am. Chem. Soc.* **1992**, *114* (10), 3985−3986.

(12) Tague, T. J.; Andrews, L. Reactions of Beryllium Atoms with Hydrogen. Matrix Infrared Spectra of Novel Product Molecules. *J. Am. Chem. Soc.* **1993**, *115* (25), 12111−12116.

(13) Narendrapurapu, B. S.; Bowman, M. C.; Xie, Y.; Schaefer, H. F.; Tkachenko, N. V.; Boldyrev, A. I.; Li, G. Dibridged, Monobridged, Vinylidene-Like, and Linear Structures for the Alkaline Earth Dihydrides Be_2H_2, Mg_2H_2, Ca_2H_2, Sr_2H_2, and Ba_2H_2. Proposals for Observations. *Inorg. Chem.* **2020**, *59* (15), 10404−10408.

(14) Cui, Z.; Yang, W.; Zhao, L.; Ding, Y.; Frenking, G. Unusually Short Be-Be Distances with and without a Bond in Be 2 F 2 and in the Molecular Discuses Be_2B_8 and $Be_2B_7^-$. *Angew. Chem., Int. Ed.* **2016**, *55* (27), 7841−7846.

(15) Lundell, K. A.; Olson, J. K.; Boldyrev, A. I. Exploring the Limits of Electronic Transmutation: Ab Initio Study of Li_nBe_n (n = 3−5). *Chem. Phys. Lett.* **2020**, *739*, 136994.
(16) Kramida, A.; Ralchenko, Y.; Reader, J.; NIST ASD Team. *NIST Atomic Spectra Database* (version 5.4); National Institute of Standards and Technology: Gaithersburg, MD, 2016; http://physics.nist.gov/asd (accessed Dec 13, 2019).
(17) Ariyarathna, I. R.; Miliordos, E. The Versatile Personality of Beryllium: $Be(O_2)_{1-2}$ vs $Be(CO)_{1-2}$. *J. Phys. Chem. A* **2017**, *121* (37), 7051−7058.
(18) Kalemos, A.; Ariyarathna, I. R.; Khan, S. N.; Miliordos, E.; Mavridis, A. "Hypervalency" and the Chemical Bond. *Comput. Theor. Chem.* **2019**, *1153*, 65−74.
(19) Ariyarathna, I. R.; Miliordos, E. Electronic and Geometric Structure Analysis of Neutral and Anionic Metal Nitric Chalcogens: The Case of MNX Series (M = Li, Na, Be and X = O, S, Se, Te). *J. Comput. Chem.* **2019**, *40* (19), 1740−1751.
(20) Ariyarathna, I. R.; Miliordos, E. Dative Bonds versus Electron Solvation in Tri-Coordinated Beryllium Complexes: $Be(CX)_3$ [X = O, S, Se, Te, Po] and $Be(PH_3)_3$ versus $Be(NH_3)_3$. *Int. J. Quantum Chem.* **2018**, *118* (18), No. e25673.
(21) Ariyarathna, I. R.; Khan, S. N.; Pawłowski, F.; Ortiz, J. V.; Miliordos, E. Aufbau Rules for Solvated Electron Precursors: $Be(NH_3)_4^{0,\pm}$ Complexes and Beyond. *J. Phys. Chem. Lett.* **2018**, *9* (1), 84−88.
(22) Ariyarathna, I. R.; Miliordos, E. Superatomic Nature of Alkaline Earth Metal−Water Complexes: The Cases of $Be(H_2O)_4^{0,+}$ and $Mg(H_2O)_6^{0,+}$. *Phys. Chem. Chem. Phys.* **2019**, *21* (28), 15861−15870.
(23) Ariyarathna, I. R.; Almeida, N. M. S.; Miliordos, E. Stability and Electronic Features of Calcium Hexa-, Hepta-, and Octa-Coordinated Ammonia Complexes: A First-Principles Study. *J. Phys. Chem. A* **2019**, *123* (31), 6744−6750.
(24) Ariyarathna, I. R.; Pawłowski, F.; Ortiz, J. V.; Miliordos, E. Aufbau Principle for Diffuse Electrons of Double-Shell Metal Ammonia Complexes: The Case of $M(NH_3)_4@12NH_3$, M = Li, Be^+, B^{2+}. *J. Phys. Chem. A* **2020**, *124* (3), 505−512.
(25) Ariyarathna, I. R.; Pawłowski, F.; Ortiz, J. V.; Miliordos, E. Molecules Mimicking Atoms: Monomers and Dimers of Alkali Metal Solvated Electron Precursors. *Phys. Chem. Chem. Phys.* **2018**, *20* (37), 24186−24191.
(26) Ariyarathna, I. R.; Miliordos, E. Geometric and Electronic Structure Analysis of Calcium Water Complexes with One and Two Solvation Shells. *Phys. Chem. Chem. Phys.* **2020**, DOI: 10.1039/D0CP04309E.
(27) Zurek, E.; Edwards, P. P.; Hoffmann, R. A Molecular Perspective on Lithium-Ammonia Solutions. *Angew. Chem., Int. Ed.* **2009**, *48* (44), 8198−8232.
(28) Seel, A. G.; Zurek, E.; Ramirez-Cuesta, A. J.; Ryan, K. R.; Lodge, M. T. J.; Edwards, P. P. Low Energy Structural Dynamics and Constrained Libration of $Li(NH_3)_4$, the Lowest Melting Point Metal. *Chem. Commun.* **2014**, *50* (74), 10778−10781.
(29) Raghavachari, K.; Trucks, G. W.; Pople, J. A.; Head-Gordon, M. A Fifth-Order Perturbation Comparison of Electron Correlation Theories. *Chem. Phys. Lett.* **1989**, *157* (6), 479−483.
(30) Kendall, R. A.; Dunning, T. H.; Harrison, R. J. Electron Affinities of the First-row Atoms Revisited. Systematic Basis Sets and Wave Functions. *J. Chem. Phys.* **1992**, *96* (9), 6796−6806.
(31) Prascher, B. P.; Woon, D. E.; Peterson, K. A.; Dunning, T. H.; Wilson, A. K. Gaussian Basis Sets for Use in Correlated Molecular Calculations. VII. Valence, Core-Valence, and Scalar Relativistic Basis Sets for Li, Be, Na, and Mg. *Theor. Chem. Acc.* **2011**, *128* (1), 69−82.
(32) Shamasundar, K. R.; Knizia, G.; Werner, H.-J. A New Internally Contracted Multi-Reference Configuration Interaction Method. *J. Chem. Phys.* **2011**, *135* (5), 054101.
(33) Knowles, P. J.; Werner, H.-J. An Efficient Method for the Evaluation of Coupling Coefficients in Configuration Interaction Calculations. *Chem. Phys. Lett.* **1988**, *145* (6), 514−522.
(34) Werner, H.; Knowles, P. J. An Efficient Internally Contracted Multiconfiguration−Reference Configuration Interaction Method. *J. Chem. Phys.* **1988**, *89* (9), 5803−5814.
(35) Langhoff, S. R.; Davidson, E. R. Configuration Interaction Calculations on the Nitrogen Molecule. *Int. J. Quantum Chem.* **1974**, *8* (1), 61−72.
(36) Frisch, M. J.; Trucks, G. W.; Schlegel, H. B.; Scuseria, G. E.; Robb, M. A.; Cheeseman, J. R.; Scalmani, G.; Barone, V.; Petersson, G. A.; Nakatsuji, H.; et al. *Gaussian 16*; Gaussian, Inc.: Wallingford, CT, 2016.
(37) Werner, H.-J.; Knowles, P. J.; Knizia, G.; Manby, F. R.; Schütz, M.; Celani, P.; Györffy, W.; Kats, D.; Korona, T.; Lindh, R.; et al. *Molpro: A General-Purpose Quantum Chemistry Program Package*; MOLPRO: version 2015.1; http://www.molpro.net.
(38) Lide, D. R. *CRC Handbook of Chemistry and Physics*, 93rd ed.; CRC Press: New York, 2012.
(39) Shaik, S.; Danovich, D.; Galbraith, J. M.; Braïda, B.; Wu, W.; Hiberty, P. C. Charge-Shift Bonding: A New and Unique Form of Bonding. *Angew. Chem., Int. Ed.* **2020**, *59* (3), 984−1001.
(40) Zurek, E.; Wen, X.-D.; Hoffmann, R. (Barely) Solid $Li(NH_3)_4$: The Electronics of an Expanded Metal. *J. Am. Chem. Soc.* **2011**, *133* (10), 3535−3547.
(41) Buttersack, T.; Mason, P. E.; McMullen, R. S.; Schewe, H. C.; Martinek, T.; Brezina, K.; Crhan, M.; Gomez, A.; Hein, D.; Wartner, G.; et al. Photoelectron Spectra of Alkali Metal−Ammonia Microjets: From Blue Electrolyte to Bronze Metal. *Science* **2020**, *368* (6495), 1086−1091.
(42) Ariyarathna, I. R.; Miliordos, E. Electronic and Geometric Structure Analysis of Neutral and Anionic Alkali Metal Complexes of the CX Series (X = O, S, Se, Te, Po): The Case of $M(CX)_{n=1-4}$ (M = Li, Na) and Their Dimers. *J. Comput. Chem.* **2019**, *40* (13), 1344−1351.
(43) Almeida, N. M. S.; Ariyarathna, I. R.; Miliordos, E. O−H and C−H Bond Activations of Water and Methane by RuO^{2+} and $(NH_3)RuO^{2+}$: Ground and Excited States. *J. Phys. Chem. A* **2019**, *123* (43), 9336−9344.
(44) Zhao, T.; Zhou, J.; Wang, Q.; Jena, P. Like Charges Attract? *J. Phys. Chem. Lett.* **2016**, *7* (14), 2689−2695.
(45) Ariyarathna, I. R.; Miliordos, E. Ab Initio Investigation of the Ground and Excited States of $MoO^{+,2+,-}$ and Their Catalytic Strength on Water Activation. *Phys. Chem. Chem. Phys.* **2018**, *20* (17), 12278−12287.
(46) Liu, F.; Press, M. R.; Khanna, S. N.; Jena, P. Stability of Doubly Charged Transition-Metal Dimers. *Phys. Rev. Lett.* **1987**, *59* (22), 2562−2565.

https://dx.doi.org/10.1021/acs.jpca.0c07939
J. Phys. Chem. A 2020, 124, 9783−9792

Appendix B

Supporting material for Chapter 3: *"Superatomic nature of ground and excited states of neutral and partially oxidized metal–ammine complexes"*

Appendix B contains the full copies of following articles. Reprints were made with permissions from the publisher.

• Ariyarathna, I. R.; Pawłowski, F.; Ortiz, J. V.; Miliordos, E. *Phys. Chem. Chem. Phys.* **2018**, *20*, 24186–24191.

• Ariyarathna, I. R.; Khan, S. N.; Pawłowski, F.; Ortiz, J. V.; Miliordos, E. *J. Phys.Chem. Lett.* **2018**, *9*, 84–88.

• Ariyarathna, I. R.; Almeida, N. M. S.; Miliordos, E. *J. Phys. Chem. A* **2019**, *123*, 6744–6750.

• Ariyarathna, I. R.; Pawłowski, F.; Ortiz, J. V.; Miliordos, E. *J. Phys. Chem. A* **2020**, *124*, 505–512.

Molecules mimicking atoms: monomers and dimers of alkali metal solvated electron precursors

PCCP

PAPER

Cite this: *Phys. Chem. Chem. Phys.*, 2018, **20**, 24186

Molecules mimicking atoms: monomers and dimers of alkali metal solvated electron precursors†

Isuru R. Ariyarathna, Filip Pawłowski, Joseph Vincent Ortiz and Evangelos Miliordos *

Received 29th August 2018,
Accepted 7th September 2018

DOI: 10.1039/c8cp05497e

rsc.li/pccp

Tetra-amino lithium and sodium complexes $M(NH_3)_4^{0,-}$ (M = Li, Na) have one or two electrons that occupy diffuse orbitals distributed chiefly outside the $M(NH_3)_4^+$ core. The lowest-energy 1s, 1p, and 1d orbitals follow Aufbau principles found earlier for beryllium tetra-ammonia complexes. Two ground state $M(NH_3)_4$ complexes can bind covalently by coupling their $1s^1$ electrons into a σ-type molecular orbital. The lowest excited states of the $[M(NH_3)_4]_2$ species are obtained by promoting one or two electrons from this σ to other bonding or anti-bonding σ and π-type molecular orbitals. The electronic structure of solvated electron precursors provides insights into chemical bonding between super-atomic species that are present in concentrated alkali-metal–ammonia solutions.

I. Introduction

The addition of alkali metals into liquid ammonia is known to produce solvated electrons (e^-_{solv}) and positively charged metal–ammonia coordination complexes (M^+_{solv}).[1] Increase of the metal concentration causes the formation of $M^+_{solv}e^-_{solv}$ ion pairs, also called solvated electron precursors (SEP).[2] A SEP is a complex that displaces one or more electrons from its coordinated metal atom to the periphery of its ligands. At higher concentrations, M^+_{solv} binds an electron pair making M^-_{solv} or SEPs form dimers ($M^+_{solv}e^-_{solv}$–$M^+_{solv}e^-_{solv}$). Finally, very dense solutions conduct like a metal rather than an electrolyte, signaling the formation of crystal-like, liquid–metal structures.[1,3–6] Recently, similar electric and structural properties were observed for lithium–ammonia–methyl ammonia mixtures.[7]

In an effort to better comprehend the electronic structure of the species present in intermediate concentrations, we perform high-level quantum chemical calculations on isolated SEPs, their anions, and their dimers. We elucidate the electronic spectrum of all of these species and provide accurate excitation energies and structural information. The presently reported data are expected to facilitate additional ways, such as spectroscopic methodologies, to identify these species in the gas or condensed phases. Presently, we examine the two smallest alkali-metal atoms in an attempt to identify possible differences between them and clarify the role of the central metal. Does the metal change the electronic spectrum of its SEP? Do the binding energies of the two Li-SEP and Na-SEP monomers differ? Would different binding energies for the two SEP dimers mean that the formation of one of them is less likely in solution?

Recently, we worked on beryllium ammonia complexes such as $Be(NH_3)_3$,[8] and $Be(NH_3)_4$.[2] We found that $Be(NH_3)_3$ demonstrates different bonding patterns than other tri-coordinated beryllium complexes. Specifically, $Be(CX)_3$ [X = O, S, Se, Te, Po] and $Be(PH_3)_3$ induce the excitation of the ground state $Be(^1S;2s^2)$ to its sixth excited state $Be(^1D;2p^2)$, while $Be(NH_3)_3$ prefers to "solvate" the $2s^2$ electron pair in its periphery. This solvation process is more profound for the beryllium SEP and its ions, $Be(NH_3)_4^{0,\pm}$, for which we calculated the ground and a series of excited electronic states.[2] We discovered that for all three species there is a $Be(NH_3)_4^{2+}$ core which hosts up to three electrons on its periphery. These outer electrons occupy diffuse atomic-like orbitals which do not follow the hydrogenic Aufbau principle. The lowest energy orbitals are 1s, 1p, 1d, 2s, 1f, and 2p (see Fig. 1). We proved that this sequence of orbitals is caused by the electrostatic potential experienced by the outer electrons. Here we examine the $Li(NH_3)_4$ and $Na(NH_3)_4$ SEPs, which have an $M(NH_3)_4^+$ (M = Li, Na) core and one outer electron, as well as their anions and dimers.

Both experimental[9–12] and theoretical[13–19] work has been devoted to lithium and sodium ammonia clusters in the literature. Previous studies focus on the micro-solvation process and how valence electrons migrate from the metal to remote solvent molecules. We are aware of only three theoretical studies that report two low-lying excited states of $Li(NH_3)_4$ and $Na(NH_3)_4$.[1,16,17]

Department of Chemistry and Biochemistry, Auburn University, Auburn, AL 36849, USA. E-mail: emiliord@auburn.edu

† Electronic supplementary information (ESI) available. See DOI: 10.1039/c8cp05497e

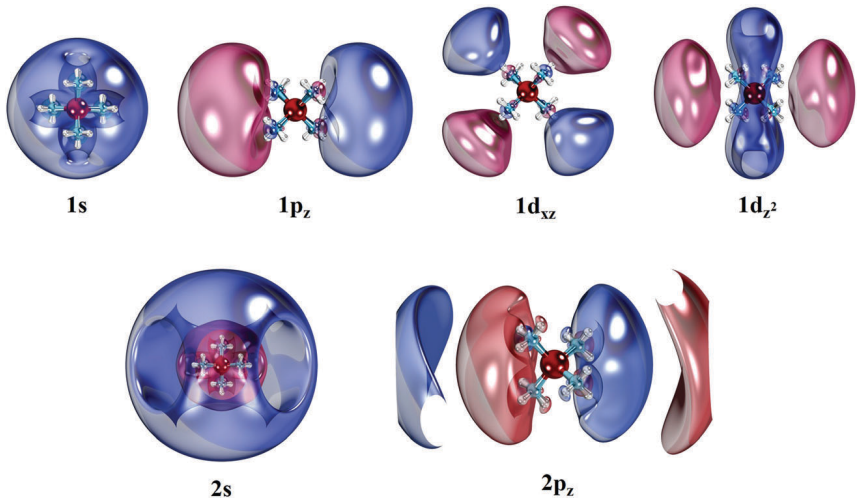

Fig. 1 Contours of selected outer orbitals of $Li(NH_3)_4$.

Here we report a larger number of excited states and we investigate the bonding between two SEPs. We see that two SEPs bind similarly to diatomic molecules and form molecular orbitals of σ- and π-type symmetry.

In Section II we describe our computational approach, in Sections III and IV we discuss our results on the SEP monomers and dimers, respectively, and in Section V we summarize our findings.

II. Computation details

A variety of *ab initio* methods have been applied to the ground and excited states of $M(NH_3)_4$. Ground state structures were optimized with coupled-cluster singles, doubles and perturbative triples [CCSD(T)][20] total energies. With density functional theory (B3LYP),[21,22] these structures were re-optimized and all real harmonic vibrational frequencies were calculated [see ESI†].

Complete-active-space, second-order perturbation theory (CASPT2) produced accurate vertical excitation energies. All valence electrons are correlated to describe dynamic correlation. The reference wavefunction was built at the complete active space self-consistent field (CASSCF) level. The active space consists only of outer orbitals and electrons, and the exact kind of orbitals included for each system is discussed in Sections III and IV. Electron affinities of cations were calculated with the renormalized partial third-order quasiparticle (P3+) electron propagator method[23] (see ESI†), and vertical excitation energies of doublet molecules were inferred from differences of these electron binding energies.

Our earlier work on beryllium[2] revealed that double diffuse functions on the terminal hydrogen atoms are important and that the contribution of diffuse functions on the metal or nitrogen is minimal. Very similar conclusions were drawn recently by Palmer *et al.* who studied Rydberg states of difluoromethane. The optimum position for the diffuse functions was found to be the terminal hydrogen atoms.[24] Excitation energies for low-lying states of $Be(NH_3)_4$ were practically converged with the following correlation-consistent basis set[25,26] combination: cc-pVTZ for the metal and nitrogen, and d-aug-cc-pVTZ for all hydrogen centers. We employ this combination for the calculations of the vertical excitation energies, but aug-cc-pVTZ on all atoms for the geometry optimization of the ground states. The diffuse functions were found to be necessary for accurate excitation energies and the prediction of stable anionic species (see ESI†).

All calculations were done under C_{2v} symmetry. The MOLPRO[27] and Gaussian[28] electronic structure codes were invoked. The computational details for the dimers will be given below.

III. The lithium and sodium SEP monomers

CCSD(T) optimizations produce tetrahedral minima for all molecular species $M(NH_3)_4^{0,\pm}$, the ground states of which have zero, one or two outer electrons in the pseudo-spherical 1s orbital (see Fig. 1). The optimal geometries are given in Table 1. Observe that the metal–nitrogen distance contracts appreciably when at least one outer electron is present. For both metals, the distance in $M(NH_3)_4^{0,-}$ is about 0.03 Å shorter than in the naked $M(NH_3)_4^+$ complexes, but the N–H bonds elongate by only 0.003 Å. A strong attraction between the central metal and the first outer electron pulls the ammonia ligands closer to the metal. Addition of another electron in the anion produces more diffuse outer orbitals and therefore the M–N distances are almost unchanged.

Table 1 CCSD(T) optimized M–N and N–H bond distances (Å), M–N–H angles (degrees), and relative energies ΔE (eV) for M = Li and Na

Species	M–N	N–H	M–N–H	ΔE
$Li(NH_3)_4^+$	2.109	1.017	113.6	2.92
$Li(NH_3)_4$	2.078	1.020	112.8	0.0
$Li(NH_3)_4^-$	2.079	1.020	112.8	−0.45
$Na(NH_3)_4^+$	2.504	1.017	113.6	2.79
$Na(NH_3)_4$	2.477	1.019	112.9	0.0
$Na(NH_3)_4^-$	2.473	1.020	112.8	−0.45

The ionization energies of the Li and Na tetra-ammonia complexes (2.92 and 2.79 eV) are about half of those of the corresponding metal atoms (5.39 and 5.14 eV)[29] and approximately twice as large as those of solvated atoms (1.47 and 1.66 eV).[10,12] The electron affinities of plain Li and Na are 0.62 and 0.55 eV,[29] whereas those of the ammonia complexes are smaller (0.45 eV for both). In the case of Be, we noticed the opposite effect. The electron affinity for the $Be(NH_3)_4$ complex is 0.26 eV, but Be^- is not stable.[2]

Lithium makes stronger ammonia complexes than sodium. The binding energies of all four ammonia ligands to the metal are 56.8 and 31.8 kcal mol^{-1} for Li and Na, which become 50.6 and 26.7 kcal mol^{-1} after zero-point-energy (ZPE) corrections. We plotted the potential energy curve (PEC) with respect to the metal–nitrogen distance pertaining to the simultaneous approach of the four ligands. The PECs shown in Fig. 2 decrease monotonically from infinity to equilibrium without the barrier that occurred in the Be case, where there are two valence electrons instead of one.[2] We next studied the abstraction of one ammonia molecule from the complex leading to the lower energy $M(NH_3)_3 + NH_3$ asymptote. These PECs are also monotonic for alkali-metals, but their beryllium counterparts also had a small energy barrier. The ZPE-corrected binding energies are 9.4 and 7.4 kcal mol^{-1} for Li and Na.

Table 2 lists the vertical excitation energies for ten electronic states for both systems at the CASSCF, CASPT2 and P3+ levels. In all cases, CASSCF underestimates them by 0.2–0.3 eV. Our CASSCF active space consists of 1 electron in 24 orbitals ($9a_1$, $6a_2$, $6b_1$, $3b_2$ under C_{2v}). All 24 orbitals are outer orbitals, but all valence electrons (including those of the $M(NH_3)_4^+$ core) are correlated at the CASPT2 level. The ground state (1^2A_1) for both complexes has a $1s^1$ configuration. The first excited state corresponds to a sextuply degenerate state 1^2T_2 ($1p^1$) that is 0.72 (Li) or 0.65 (Na) eV higher. The $1d^1$ configuration splits to the 2^2T_2 and 1^2E states, which are practically degenerate. All $1d^1$ components lie within 0.03 eV of each other for both species. In the next state (2^2A_1), the electron occupies the 2s orbital, while the 3^2T_2 state follows with a $2p^1$ configuration. In the outer orbitals of the remaining four states (1^2T_1, 4^2T_2, 2^2E, and 5^2T_2), functions of different angular momenta mix considerably.

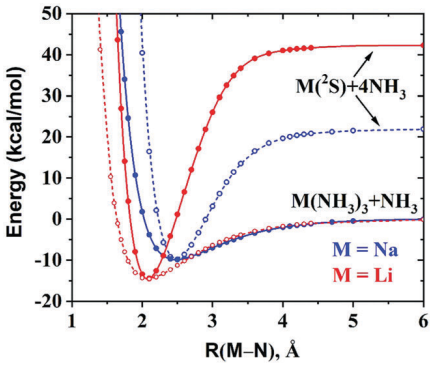

Fig. 2 CCSD(T) PECs for the dissociation of one or four ammonia ligands from $M(NH_3)_4$, M = Li, Na.

Table 2 CASSCF, CASPT2, and P3+ excitation energies (eV) of $Li(NH_3)_4$ and $Na(NH_3)_4$

		$Li(NH_3)_4$			$Na(NH_3)_4$		
State	E.C.[a]	CASSCF	CASPT2	P3+	CASSCF	CASPT2	P3+
1^2A_1	$1s^1$	0.00	0.00	0.00	0.00	0.00	0.00
1^2T_2	$1p^1$	0.55	0.72	0.72	0.51	0.65	0.66
2^2T_2	$1d^1$	1.12	1.40	1.40	1.06	1.31	1.32
1^2E	$1d^1$	1.13	1.43	1.43	1.06	1.33	1.34
2^2A_1	$2s^1$	1.28	1.52	1.56	1.22	1.43	1.48
3^2T_2	$2p^1$	1.53	1.79	1.88	1.43	1.67	1.73
1^2T_1		1.61	1.96	1.99	1.52	1.83	1.87
4^2T_2		1.88	2.14	2.26	1.82	2.05	2.18
2^2E		1.94	2.22	2.32	1.87	2.12	2.23
5^2T_2		2.12	2.40	2.56	2.03	2.27	2.50

[a] Electronic configuration.

CASPT2 and P3+ excitation energies are in excellent agreement for lower lying states and produce the same Aufbau principle for diffuse electrons. Hashimoto and Daigoku's MP2 calculations on $Li(NH_3)_4$ located two doublet excited states, at 0.62 and 1.54 eV,[16,17] which match well with our 1^2T_2 and 2^2A_1 predictions. Numerical discrepancies between CASPT2 and P3+ excitation energies may be larger for certain higher states and could be consequences of incomplete basis sets in those cases.

The transition dipole moments (μ_T) between the ground state $^2A_1$ ($1s^1$) and all excited states, except the $^2T_2$ ones, are zero by symmetry. The μ_T^2 values for 1^2T_2 ($1p^1$) and 2^2T_2 ($1d^1$) are 177/189 and 0.01/0.05 D^2 (Li/Na), respectively. These data approach atomic selection rules where the 1s → 1p transition is allowed, unlike 1s → 1d. Similarly, among the states of Table 2 only 1s → 2p (3^2T_2) has a small non-zero μ_T^2 value (0.2/0.5 D^2).

The largest amplitudes of the orbitals of Fig. 1 occur outside the covalent radii of the atoms, especially on the periphery of the complex, and differ significantly from those of valence or Rydberg orbitals of the metal atoms. Regions outside the covalent radii include interstices between ammonia ligands. Orthogonality to lower, occupied orbitals produces minor amplitudes within the covalent radii. Similar conclusions on the 1s orbital have followed from analysis in terms of metal and ligand fragment orbitals[1] or spatial distributions of natural orbitals.[30] Although the two parent metals have different energy level patterns ($2s^1$, $2p^1$, $3s^1$, $3p^1$, $3d^1$ for Li *versus* $3s^1$, $3p^1$, $3d^1$, $4s^1$, $4p^1$, $4d^1$, $4f^1$ for Na), they adopt the same shell model after coordination. This complex pattern of interference arises from an electrostatic potential that is not hydrogenic and which generates the relatively simple Aufbau rules summarized in Fig. 1 and Table 2.

IV. The lithium and sodium SEP dimers

The $M(NH_3)_4$ systems have an unpaired electron orbiting around the $M(NH_3)_4^+$ core as in the hydrogen atom. Pushing two such complexes together, we expect to see the formation of a covalent bond. Indeed, the binding energies of $[M(NH_3)_4]_2$ were found to be practically the same for the two metals with B3LYP: 9.1 (M = Li) and 9.5 (M = Na) kcal mol^{-1}. For M = Li, we also obtained the CASPT2 optimal geometry which is shown in Fig. 3.

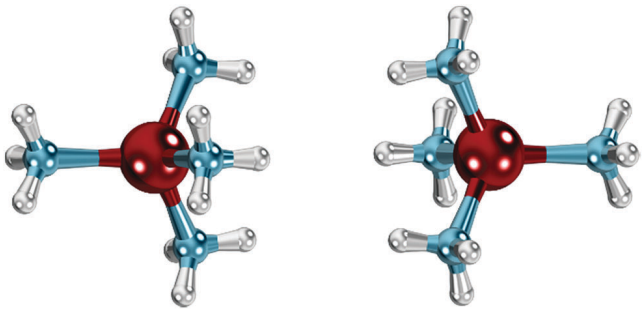

Fig. 3 Optimal geometry of $[Li(NH_3)_4]_2$.

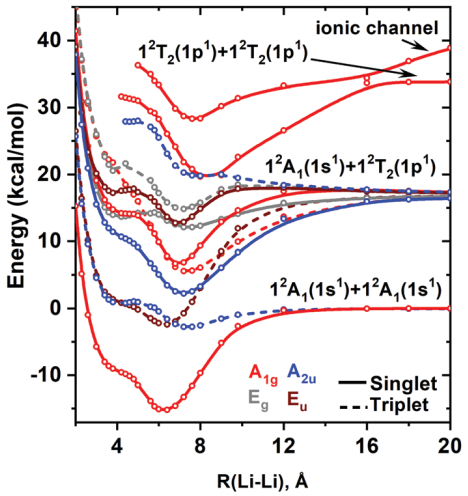

Fig. 5 CASPT2 PECs of $[Li(NH_3)_4]_2$ for its dissociation to two $Li(NH_3)_4$ monomers.

The CASPT2 binding energy for lithium is 14.7 kcal mol^{-1}, 5.6 kcal mol^{-1} larger than B3LYP. The optimal structures for both dimers are given in the ESI.† The basis set used for the dimers is cc-pVTZ for the metal and nitrogen, and aug-cc-pVTZ for hydrogen.

Three ammonia ligands of each monomer stay in the middle in a staggered conformation and hydrogen atoms from different monomers approach each other in a D_{3d} structure. The reason for these contacts is the electronic density in the middle of the two monomers resulting from the formation of a σ-covalent bond. Zurek *et al.* considered more relative orientations of the two monomers, which were found to be nearly degenerate.[1] Our structure is not reported by these authors and it is lower in energy than all of theirs at the B3LYP level. Our geometry optimizations using their geometries as initial guesses converged to our structure, which has only real frequencies (see ESI†). To rule out any artifacts due to the basis set incompleteness, we employed also quadruple-ζ quality basis sets, which showed the exact same trends. Tight convergence criteria needed to be applied to obtain optimal structures without imaginary frequencies.

In all of the structures, the density of the diffuse electron pair is concentrated in the middle of the two $M(NH_3)_4^+$ cores (see Fig. 23 of ref. 1 and present Fig. 4). Among all of the structures, the D_{3d} one contains the larger number of O–H bonds interacting with the diffuse electron pair and this electrostatic attraction seems to be the reason for its additional stability.

Selected molecular orbitals of the structure of Fig. 3 are depicted in Fig. 4. These functions have shapes that are similar to those of typical diatomic molecules: $1a_{1g} \sim 1s_A + 1s_B$, $1a_{2u} \sim 1s_A - 1s_B$, $2a_{1g} \sim 1p_{z,A} - 1p_{z,B}$, $2a_{2u} \sim 1p_{z,A} + 1p_{z,B}$, $1e_u \sim (1p_{x,A} + 1p_{x,B}$ or $1p_{y,A} + 1p_{y,B})$, and $1e_g \sim (1p_{x,A} - 1p_{x,B}$ or $1p_{y,A} - 1p_{y,B})$. Identical observations can be made for sodium. The a_{1g}, a_{2u}, e_g, and e_u orbitals imitate the σ_g, σ_u, π_g, π_u orbitals of homonuclear diatomics.

PECs as a function of the distance between the two monomers for Li are plotted in Fig. 5. At every Li–Li distance, we optimize all other geometrical parameters with B3LYP for the ground state but impose the D_{3d} symmetry of the global minimum. We use these geometries to obtain the PECs of the excited states at CASPT2. The large computational cost constrained us to use only the 1s and 1p super-atomic orbitals of each monomer (see Fig. 1) in the CASSCF active space. All valence electrons are correlated at CASPT2.

The lowest two asymptotic channels are $1^2A_1(1s^1) + 1^2A_1(1s^1)$ and $1^2A_1(1s^1) + 1^2T_2(1p^1)$. The former generates one singlet (1^1A_{1g})

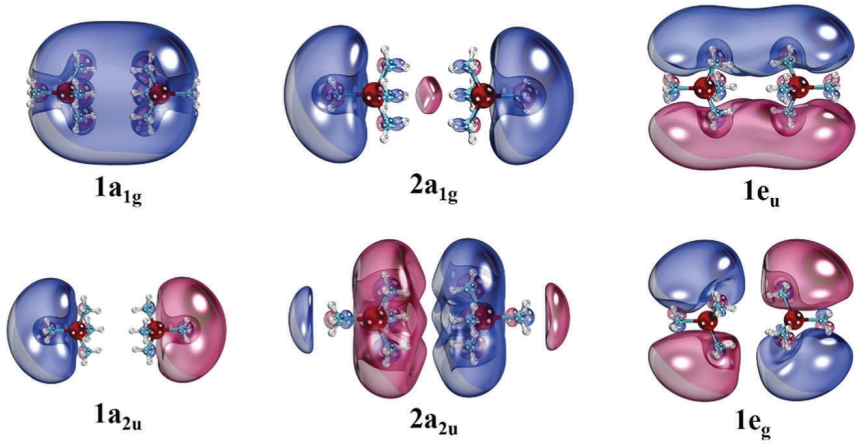

Fig. 4 Selected molecular orbitals of $[Li(NH_3)_4]_2$.

Table 3 CASPT2 excitation energies (eV) of $[Li(NH_3)_4]_2$ and $[Na(NH_3)_4]_2$

		$[Li(NH_3)_4]_2$		$[Na(NH_3)_4]_2$
State	E.C.[a]	CASPT2[b]	CASPT2[c]	CASPT2[c]
1^1A_{1g}	$1a_{1g}^2$	0.00	0.00	0.00
1^3E_u	$1a_{1g}^1 1a_{2u}^1$	0.63	0.59	0.42
1^3A_{2u}	$1a_{1g}^1 1e_u^1$	0.77	0.66	0.59
1^1A_{2u}	$1a_{1g}^1 1a_{2u}^1$	1.00	0.92	0.78
1^3A_{1g}	$1a_{1g}^1 2a_{1g}^1$	1.19	1.14	0.96
2^1A_{1g}	$1a_{1g}^1 2a_{1g}^1$	1.18	1.13	0.82
1^1E_g	$1a_{1g}^1 1e_g^1$	1.42	1.30	1.21
1^1E_u	$1a_{1g}^1 1e_u^1$	1.31	1.39	1.03
1^3E_g	$1a_{1g}^1 1e_g^1$	1.53	1.46	1.27
2^3A_{2u}	$1e_g^1 1e_u^1$	1.81	1.76	1.55

[a] Electronic configuration. [b] CASPT2 optimal geometry used. [c] DFT/B3LYP optimal geometry used.

and one triplet (1^3A_{2u}). These states resemble the $^1\Sigma_g^+$ and $^3\Sigma_u^-$ states of H_2 arising from the ground state fragments $H(^2S)$ + $H(^2S)$ and their equilibrium configurations are $1a_{1g}^2$ and $1a_{1g}^1 1a_{2u}^1$. The next channel is the analogue of $H(^2S)$ + $H(^2P)$, which gives singlets and triplets of $\Sigma_{g,u}$ and $\Pi_{g,u}$ symmetry. In our case we obtained the corresponding D_{3d} representations: $^{1,3}A_{1g}$, $^{1,3}A_{2u}$, $^{1,3}E_u$, and $^{1,3}E_g$. The $^1A_{2u}(1^1A_{2u})$ state is the open-singlet counterpart of 1^3A_{2u}. The equilibrium electronic configurations of the remaining states are given in Table 3. The global minima of all of our PECs occur at 6–8 Å, but have shoulders (or shallow minima in some cases) in the typically repulsive region around 4 Å. These features may arise from the complex electrostatics of the system or from avoided crossings with higher channels (see below).

The next dissociation channel should be $1^2A_1(1s^1) + 2^2T_2(1d^1)$ at 1.40 eV followed by $1^2T_2(1p^1) + 1^2T_2(1p^1)$ at 1.44 eV (see Table 2). Because of our 1s1p active space, we were not able to capture the $2^2T_2(1d^1)$ channel. We managed however to locate one of the PECs of $^1A_{1g}$ symmetry stemming from the ionic fragments $Li(NH_3)_4^+(^1A_1)$ + $Li(NH_3)_4^-(^1A_1)$; see Fig. 5. There is

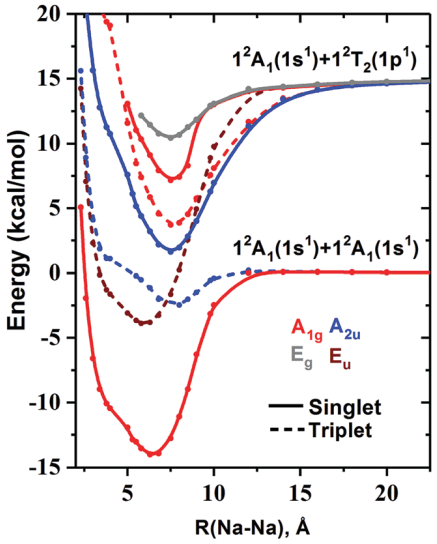

Fig. 6 CASPT2 PECs of $[Na(NH_3)_4]_2$ for its dissociation to two $Na(NH_3)_4$ monomers.

one more $^1A_{1g}$ state in between coming from $1^2T_2(1p^1) + 1^2T_2(1p^1)$ which undergoes an avoided crossing with the ionic one. We cannot rule out the possibility that the shoulders of our PECs at 4 Å are related to different ionic channels.

Identical conclusions can be deduced from the more demanding calculations performed on $[Na(NH_3)_4]_2$. Due to technical issues we were able to construct a smaller number of PECs shown in Fig. 6. The PECs of the states in common are of similar shape and have almost identical potential well depths.

Vertical excitation energies for the two dimers are listed in Table 3. These energies are slightly different from those of Fig. 5 and 6 because of the different number of states averaged at the CASSCF level. In Fig. 5 and 6, we included more states to ensure the smoothness of the PECs, but in Table 3 we have state-averaged only those listed and these values are more accurate. For $[Li(NH_3)_4]_2$ we used both the CASPT2 and DFT/B3LYP optimal structures of the ground state. The values differ by less than 0.13 eV. The excitation energies for sodium are lower than those of lithium, as happens for the monomers. The energy difference is consistently lower by 0.2–0.3 eV for the states studied here.

V. Conclusions

Ground and excited electronic states of the lithium and sodium tetra-ammonia complexes were investigated by means of high-level quantum chemical calculations. We found that a neutral complex has an $M(NH_3)_4^+$ core and one electron orbiting in its periphery that occupies s, p, d, or higher l-type orbitals. The orbital sequence is the same for both metals and identical to that which we found for $Be(NH_3)_4^{0,\pm}$ complexes and which resembles that of the jellium or nuclear shell model.[2] We demonstrated that the central metal acts more like a point charge and that it does not affect the shell model of the corresponding SEP. For both metals, the $M(NH_3)_4^+$ core can bind a second electron by 0.45 eV to form an anion.

We finally show that two $M(NH_3)_4$ complexes can form a single covalent σ-bond by coupling their unpaired electrons into a closed shell singlet. The binding energy for the two metals is practically identical implying that SEP dimers will be formed in both cases at similar concentrations. Excited states of the dimer involve electronic excitations to other σ- or π-type orbitals similar to those of typical diatomic molecules. The electronic spectrum of these dimers is also largely independent of the central metal. Our results reveal the ability of SEPs to form covalently bound aggregates which can lead to novel liquid–metal materials or chemical compounds made of SEPs.

Conflicts of interest

There are no conflicts to declare.

Acknowledgements

IRA and EM are indebted to Auburn University for financial support. This work was completed in part with resources

provided by the Auburn University Hopper Cluster. JVO acknowledges the support of the National Science Foundation through grant CHE-1565760 to Auburn University.

References

1 E. Zurek, P. P. Edwards and R. Hoffmann, *Angew. Chem., Int. Ed.*, 2009, **48**, 8198–8232.
2 I. R. Ariyarathna, S. N. Khan, F. Pawłowski, J. V. Ortiz and E. Miliordos, *J. Phys. Chem. Lett.*, 2018, **9**, 84–88.
3 U. Pinsook and S. Hannongbua, *J. Chem. Phys.*, 2006, **124**, 074702.
4 G. N. Chuev and P. Quémerais, *J. Chem. Phys.*, 2008, **128**, 144503.
5 E. Zurek, X.-D. Wen and R. Hoffman, *J. Am. Chem. Soc.*, 2011, **133**, 3535–3547.
6 A. G. Seel, E. Zurek, A. J. Ramirez-Cuesta, K. R. Ryan, M. T. J. Lodge and P. P. Edwards, *Chem. Commun.*, 2014, **50**, 10778–10781.
7 A. G. Seel, H. Swan, D. T. Bowron, J. C. Wasse, T. Weller, P. P. Edwards and C. A. Howard, and N Skipper, *Angew. Chem., Int. Ed.*, 2017, **56**, 1561–1565.
8 I. R. Ariyarathna and E. Miliordos, *Int. J. Quantum Chem.*, 2018, DOI: 10.1002/qua.25673.
9 I. V. Hertel, C. Hüglin and C. Nitsch, *Phys. Rev. Lett.*, 1991, **67**, 1767–1770.
10 R. Takasu, K. Hashimoto and K. Fuke, *Chem. Phys. Lett.*, 1996, **258**, 94–100.
11 R. Takasu, F. Misaizu, K. Hashimoto and K. Fuke, *J. Phys. Chem. A*, 1997, **101**, 3078–3087.
12 C. Steinbach and U. Buck, *J. Chem. Phys.*, 2005, **122**, 134301.
13 K. Hashimoto and K. Morokuma, *J. Am. Chem. Soc.*, 1995, **117**, 4151–4159.
14 Y. Ferro, A. Allouche and V. Kempter, *J. Chem. Phys.*, 2004, **120**, 8683–8691.
15 G. Gao and Z.-F. Liu, *J. Chem. Phys.*, 2007, **126**, 084501.
16 K. Hashimoto and K. Daigoku, *Phys. Chem. Chem. Phys.*, 2009, **11**, 9391–9400.
17 K. Hashimoto and K. Daigoku, *Chem. Phys. Lett.*, 2009, **469**, 62–67.
18 H. Zhang and Z.-F. Liu, *J. Chem. Phys.*, 2012, **136**, 124314.
19 N. V. Kryzhevoi, F. Tarantelli and L. S. Cederbaum, *Chem. Phys. Lett.*, 2015, **626**, 85–89.
20 K. Raghavachari, G. W. Trucks, J. A. Pople and M. Head-Gordon, *Chem. Phys. Lett.*, 1989, **157**, 479–483.
21 C. Lee, W. Yang and R. G. Parr, *Phys. Rev. B: Condens. Matter Mater. Phys.*, 1988, **37**, 785–789.
22 A. D. Becke, *J. Chem. Phys.*, 1993, **98**, 5648–5652.
23 H. H. Corzo and J. V. Ortiz, *Adv. Quantum Chem.*, 2017, **74**, 267–298.
24 M. H. Palmer, S. V. Hoffmann, N. C. Jones, M. Coreno, M. de Simone and C. Grazioli, *J. Chem. Phys.*, 2018, **148**, 214304.
25 T. H. Dunning, *J. Chem. Phys.*, 1989, **90**, 1007–1023.
26 R. A. Kendall, T. H. Dunning and R. J. Harrison, *J. Chem. Phys.*, 1992, **96**, 6796–6806.
27 H.-J. Werner, P. J. Knowles, G. Knizia, F. R. Manby, M. Schütz, *et al.*, MOLPRO, version 2015.1, a package of ab initio programs, see http://www.molpro.net [Accessed: 5/24/2018].
28 M. J. Frisch, G. W. Trucks, H. B. Schlegel, G. E. Scuseria, M. A. Robb, *et al.*, *Gaussian 16, Revision A.03*, Gaussian Inc., Wallingford CT, 2016.
29 *CRC Handbook of Chemistry and Physics*, ed. W. M. Haynes, CRC Press, USA, 92nd edn, 2012.
30 T. Sommerfeld and K. M. Dreux, *J. Chem. Phys.*, 2012, **137**, 244302.

Aufbau Rules for Solvated Electron Precursors: $Be(NH_3)_4^{0,\pm}$ Complexes and Beyond

THE JOURNAL OF PHYSICAL CHEMISTRY Letters

Letter

Cite This: J. Phys. Chem. Lett. 2018, 9, 84–88

pubs.acs.org/JPCL

Aufbau Rules for Solvated Electron Precursors: $Be(NH_3)_4^{0,\pm}$ Complexes and Beyond

Isuru R. Ariyarathna, Shahriar N. Khan, Filip Pawłowski, Joseph Vincent Ortiz, and Evangelos Miliordos*

Department of Chemistry and Biochemistry, Auburn University, Auburn, Alabama 36849-5312, United States

Supporting Information

ABSTRACT: Tetra-amino beryllium complexes and ions, $Be(NH_3)_4^{0,\pm}$, have a tetrahedral $Be(NH_3)_4^{2+}$ core with one, two, or three outer electrons orbiting its periphery. Our calculations reveal a new class of molecular entities, solvated electron precursors, with Aufbau rules (1s, 1p, 1d, 2s, 1f, 2p, 2d) that differ from their familiar hydrogenic counterparts and resemble those of jellium or nuclear-shell models. The core's radial electrostatic potential suffices to reproduce the chief features of the *ab initio* results. Wave function and electron-propagator methods combined with diffuse basis sets are employed to calculate accurate geometries, ionization energies, electron affinities, and excitation energies.

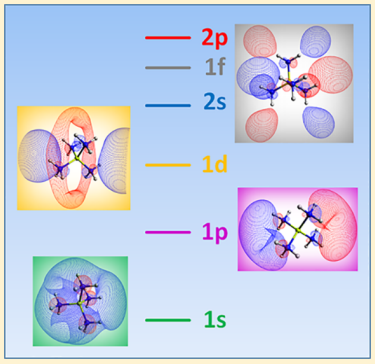

Ammonia's ability to abstract and solvate the loosely bound electrons of alkali and alkaline-earth metals[1] has inspired experimental[2−7] and theoretical[8−13] studies of $M(NH_3)_x$ clusters with $x = 1-11$ that provide insights into microsolvation processes[8−12] wherein valence electrons gradually migrate from the metal M to remote solvent molecules. In sodium−ammonia complexes, excited states feature promotion of the least bound electron to higher orbitals.[11,12] Are there Aufbau rules for electrons that occupy the periphery of these complexes? Calculations on complexes with only their first solvation shells provide the answer.

Here we study the $Be(NH_3)_4$ complex, whose ground state consists of a $Be(NH_3)_4^{2+}$ core and an electron pair in an s-type orbital delocalized over the core's periphery (see rightmost pictures of Figure 1). This system can be seen as a tetrahedral analogue of He, where $Be(NH_3)_4^{2+}$ has replaced the spherical nucleus. We also consider the singly charged ions $Be(NH_3)_4^{\pm}$, which contain the same core, but with one or three outer electrons. The lowest energy outer orbitals for the unpaired electron of the cation are found to be 1s, 1p, 1d, 2s, 1f, 2p, and 2d. This order is different from the traditional series of H and the hydrogenic ions and resembles that of jellium or nuclear-shell models.[14,15] We attribute this contrast to the effective electrostatic potential experienced by the outer electrons, which differs from its Coulombic counterpart.

Similar potentials bind two diffuse electrons to a molecular cationic core in double Rydberg anions.[16,17] According to electron-propagator calculations, $Be(NH_3)_4$ has a highly diffuse Dyson orbital for electron detachment and is isoelectronic to the tetrahedral $Li(NH_3)_4^-$ double-Rydberg anion.[18] Recently discovered examples of $N_xH_{3x+1}^-$ and $O_xH_{2x+1}^-$ double Rydberg anions have a diffuse electron pair that surrounds cores with ammonium or hydronium cations and varying numbers of ammonia or water molecules.[16,17]

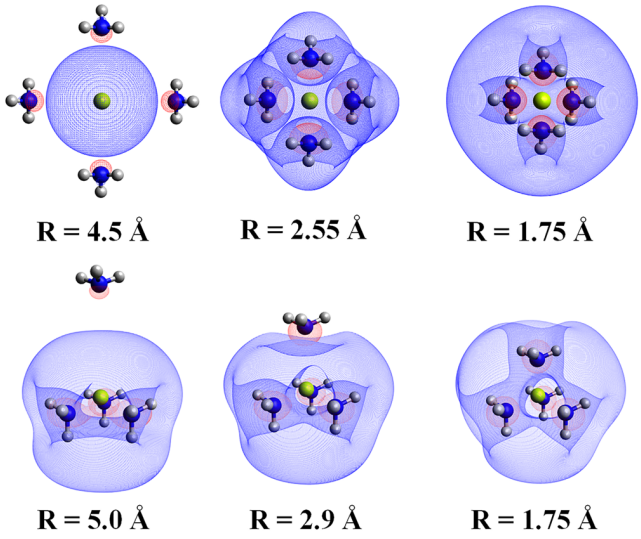

Figure 1. Contours of the highest occupied molecular orbital of $Be(NH_3)_4$ for the simultaneous $4NH_3 \rightarrow Be$ (upper diagrams) and the $NH_3 \rightarrow Be(NH_3)_3$ (lower diagrams) approaches. R is the Be−N distance of the incoming ammonia molecules, and the isosurfaces correspond to a wave function value of 0.015.

Received: November 11, 2017
Accepted: December 12, 2017
Published: December 12, 2017

DOI: 10.1021/acs.jpclett.7b03000
J. Phys. Chem. Lett. 2018, 9, 84−88

Several *ab initio* methods have been applied to the ground and excited states of $Be(NH_3)_4^{0,\pm}$. Ground state structures were optimized with coupled-cluster singles, doubles, and perturbative triples [CCSD(T)][19] total energies. B3LYP[20,21] provided harmonic vibrational frequencies, which were real and positive in all cases. Complete-active-space second-order perturbation theory (CASPT2) produced accurate excitation energies. Electron binding energies were calculated with the renormalized partial third-order quasiparticle (P3+) electron propagator method;[22] excitation energies were inferred from differences of electron binding energies. Several basis sets were tested, from plain correlation consistent cc-pVTZ (VTZ) and cc-pVQZ (VQZ) to the diffuse aug-cc-pVTZ (ATZ), d-aug-cc-pVTZ (DTZ), t-aug-cc-pVTZ (TTZ), and q-aug-cc-pVTZ (QTZ) basis sets.[23−25] All calculations were done under C_{2v} symmetry. The MOLPRO[26] and Gaussian[27] electronic structure codes were invoked. The full set of computational results is given in the Supporting Information (SI).

CCSD(T)/ATZ optimizations produce tetrahedral minima for the nondegenerate molecular ($1s^2$) and cationic ($1s^1$) configurations, but a slightly distorted (D_{2d}) structure emerges for the anionic ($1s^21p^1$) configuration. Therefore, two different N−H bond lengths are obtained for the anion (see Table 1 and SI). Complexation to Be^{2+} elongates N−H bonds by 0.002 Å; adding one or two electrons also has a small effect. As electrons are added to the dication, the Be−N length drops significantly.

Table 1. CCSD(T)/ATZ Distances (Å) and Relative Energies Δ*E* (eV)

species	Be−N	N−H	N−H	Δ*E*
$Be(NH_3)_4$	1.733	1.030	1.030	0.0
$Be(NH_3)_4^+$	1.741	1.027	1.027	3.91
$Be(NH_3)_4^{2+}$	1.764	1.023	1.023	11.23
$Be(NH_3)_4^-$	1.737	1.027	1.030	−0.26

The simultaneous approach of four ammonia ligands is expected to be dissociative because of repulsions between $2s_{Be}$ electrons in the metal atom's ground ^1S state and the lone pairs of ammonia (see Figure 1). The potential energy curve (PEC) as a function of the common Be−N distance *R* is shown in Figure 2. It is indeed repulsive for $R \geq 2.55$ Å and then turns highly attractive after a barrier of 18.2 kcal/mol. As the ammonia lone pairs approach the Be^{2+} nucleus (see Figure 1), the $2s_{Be}$ orbital gradually turns into the outer 1s function. For the approach of NH_3 to $Be(NH_3)_3$, only a small barrier is observed because of the already diffuse nature of the peripheral electron pair (see Figures 1 and 2).

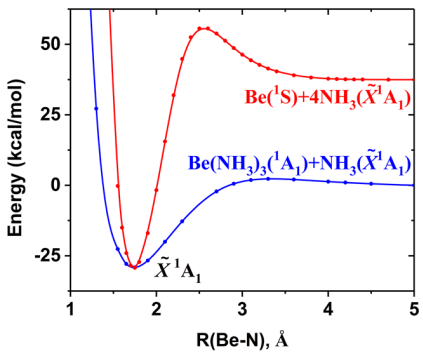

Figure 2. CCSD(T)/ATZ PECs for the $4NH_3 \rightarrow Be$ and $NH_3 \rightarrow Be(NH_3)_3$ approaches.

The ionization energy (IE) of Be to Be^{2+} is the sum of the IEs of Be and Be^+: 9.32 + 18.21 eV = 27.53 eV.[28] The formation of the $Be(NH_3)_4^{2+}$ core in $Be(NH_3)_4$ is driven by various electrostatic effects, including: (1) solvation of the outer electrons by the N−H bond dipoles, (2) $Be^{2+}-NH_3$ dative bonding, and (3) attraction between Be^{2+} and diffuse electrons. The IEs of $Be(NH_3)_4$ drop by about half compared to Be (see Table 1). Be^- is not stable,[28] but $Be(NH_3)_4$ has an electron affinity of 0.26 eV.

The first excited state of $Be(NH_3)_4^+$ is hextuply degenerate, as the diffuse electron may occupy any of three 1p spin−orbitals. Higher states involve orbitals with s, p, d, and f shapes (see Figure 3). Based on the shapes of the orbitals, we have assigned states to approximate ^2S, ^2P, ^2D, and ^2F terms, although T_d symmetry implies that states within each term are not necessarily degenerate.

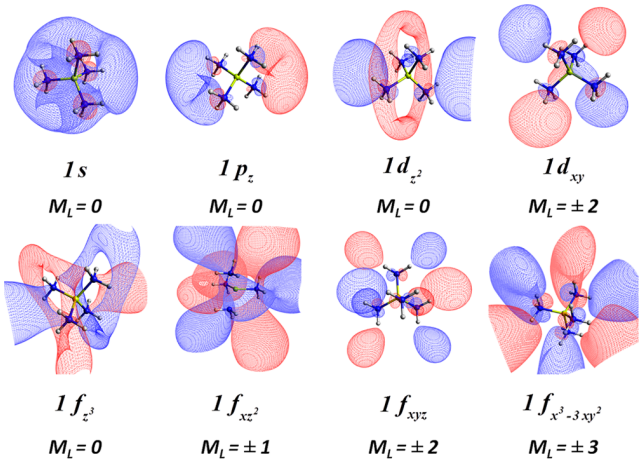

Figure 3. Contours of selected outer electron orbitals.

Table 2 lists the excitation energies for the lowest component of each approximate term for a series of basis sets at the CASPT2 level. The active space of the reference multiconfigurational self-consistent-field wave function includes two electrons in 25 outer orbitals. All of the valence electrons of the $Be(NH_3)_4^{2+}$ core are correlated in CASPT2 except those corresponding to the Be−N bonds (i.e., those assigned to the four lowest valence orbitals). Their contribution was less than 0.05 eV (see SI). Differences of P3+ electron affinities of the dication are in close agreement with CASPT2 results with the $VTZ/_{Be,N}$ $DTZ/_H$ basis, and the corresponding Dyson orbitals strongly resemble their CASSCF counterparts in Figure 3. Basis-set saturation with the latter choice is demonstrated in successive columns of Table 2. The first three columns of numerical data indicate that addition of two sets of diffuse functions to the VTZ H basis is necessary. The next two columns imply that additional diffuse functions on N and Be nuclei and a quadruple ζ basis for H are not needed. The last three columns confirm that addition of two sets of diffuse functions to the VTZ H basis is sufficient for all the considered states, except the highest 2^2D term, where a third set of diffuse functions is necessary to achieve saturation. These conclusions resemble those of Gutowski and Simons for double-Rydberg anions: "Computational effort should be focused on correlating

DOI: 10.1021/acs.jpclett.7b03000
J. Phys. Chem. Lett. 2018, 9, 84−88

Table 2. CASPT2 and P3+ Excitation Energies (eV) of $Be(NH_3)_4^+$ for Several Basis Sets[a]

atom	basis sets							
Be	VTZ	VTZ	VTZ	ATZ	VTZ	VTZ	VTZ	VTZ
N	VTZ	VTZ	VTZ	DTZ	VTZ	VTZ	VTZ	VTZ
H	VTZ	ATZ	DTZ	DTZ	DQZ	DTZ	TTZ	QTZ
state	**CASPT2**	**CASPT2**	**CASPT2**	**CASPT2**	**CASPT2**	**P3+**	**P3+**	**P3+**
1^2S	0.00	0.00	0.00	0.00	0.00	0.00	0.00	0.00
1^2P	1.55	1.40	1.39	1.40	1.40	1.34	1.34	1.34
1^2D	2.95	2.41	2.37	2.38	2.38	2.30	2.30	2.30
2^2S	4.78	3.50	3.34	3.33	3.34	3.27	3.26	3.26
1^2F	4.78	3.88	3.72	3.72	3.72	3.64	3.63	3.63
2^2P	6.50	4.30	3.91	3.91	3.91	3.85	3.84	3.84
2^2D	6.96	4.90	4.57	4.55	4.55	4.50	4.43	4.43

[a]For P3+, all valence electrons were correlated, whereas for CASPT2, eight electrons corresponding to the Be−N bonds in four inner valence MOs were frozen.

the outermost one or two electrons, whereas the closed-shell cation core can probably be considered more approximately".[29]

To explain the observed orbital sequence, we consider a simple quantum mechanical model where the electrostatic potential produced by the $Be(NH_3)_4^{2+}$ core (with a B3LYP/ATZ electron density) along three directions serves as an effective radial potential acting on the outer electron of $Be(NH_3)_4^+$. In the T_d structure of Figure 4, axes connect the Be nucleus with a N vertex (blue), the center of a N−N edge (green), or the center of a N−N−N face (red).

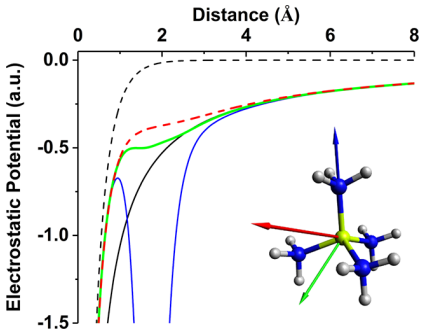

Figure 4. Electrostatic potentials along the three directions of the arrows. Solid and dashed black lines correspond to −2/R and $Be(NH_3)_4$ potentials, respectively.

These potentials as a function of the distance R from the Be nucleus are shown in Figure 4, which also depicts the electrostatic potential produced by a 2+ point charge and that of $Be(NH_3)_4$ with solid and dashed black lines, respectively. The blue line traces a typical, double-well, Coulombic potential. However, the red and green lines are steeper than the solid black one for short distances. The red and green lines also exhibit a curvature change at 1 Å, with a shallow local minimum for the latter. All three colored lines have Coulombic asymptotes.

The radial equation of the three-dimensional, one-electron Schrödinger equation, whose solutions read

$$\psi_{nlm}(r, \theta, \varphi) = R_{nl}(r)Y_{lm}(\theta, \varphi)$$

was solved numerically with the red and green potentials. The Numerov−Cooley integration scheme was employed.[30] Figure 5 depicts the energy levels and radial wave functions, $rR_{nl}(r)$, for the red line. The corresponding scheme for the green line is very similar (the two plots are compared in the SI). In both

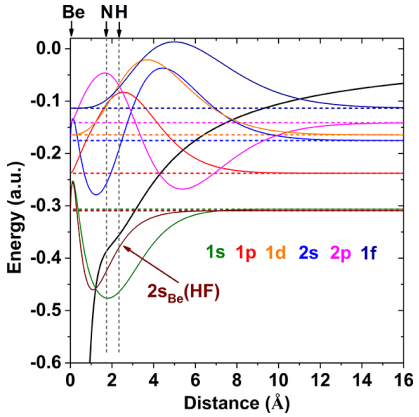

Figure 5. Energy levels and radial wave functions of the outer orbitals for the electrostatic potential of $Be(NH_3)_4^{2+}$ (red line of Figure 4) acting on an electron. The radial wave function of 2s of the beryllium atom at the Hartree−Fock (HF) level is also shown for comparison.

cases, there is an energy level at about −2.8 au, which is attributed to $1s_{Be}$, for it is almost identical with the 1s of atomic beryllium. The next six levels in both cases are 1s, 1p, 1d, 2s, 2p, and 1f. Their wave functions are diffuse with maxima near or beyond R = 2 Å, which is about equal to the radius of the $Be(NH_3)_4^{2+}$ core, as defined by the Be−H distance. The energy order of this simple model closely resembles that of Table 2. Only the fifth and sixth levels are permuted. In fact, the highest-energy state assigned to the 1^2F term lies above the 2^2P states (see Tables S4 and S14 in the SI). The nearly identical order of energy levels in Figure 5 and Table 2 indicates that (1) the source of the observed electron shell pattern is the electrostatic potential created by the $Be(NH_3)_4^{2+}$ core, and (2) the selected basis set describes properly the outer orbitals. Whereas the 1p, 1d, and 1f orbitals have no radial nodes, the 1s orbital has a node that enforces orthogonality to the Be core. Therefore, the 2s and 2p orbitals respectively have two and one radial nodes; both nodes occur beyond the H nuclei.

CASPT2 calculations on the excited states of $Be(NH_3)_4$ employ the same $VTZ/_{Be,N}$ $DTZ/_H$ basis set and have an active space with two electrons in 20 outer orbitals; all but the eight Be−N bonding electrons in the four lowest valence orbitals are correlated in the perturbative part of CASPT2 calculations. The ground term is 1^1S ($1s^2$), followed by the 1^3P and 1^1P ones ($1s^1 1p^1$), which are 0.81 and 1.62 eV higher. The 1^1D and 1^3D terms with mostly $1s^1 1d^1$ character are next at 1.65−1.82 and

DOI: 10.1021/acs.jpclett.7b03000
J. Phys. Chem. Lett. 2018, 9, 84−88

1.93−2.11 eV, respectively. The 1^1D term has partial $1p^2$ character, which stabilizes it further compared to 1^3D. The 2^3P ($1p^2$), 1^3S ($1s^12s^1$) and 2^1S ($1s^12s^1$) terms are almost all degenerate at 2.24−2.30 eV. The multireference 1^3F term follows and has mixed $1s^11f^1$ and $1p^11d^1$ character at 2.73−2.80 eV. The 3^3P and 2^1P ($1s^12p^1$) terms are the last ones with single-reference electronic configurations at 2.62 and 2.71 eV. The remaining terms (3^1S, 2^1D, 1^1F, 3^1D) are highly multireference in character and blend the $1p^2$, $1p^11d^1$, $1s^11f^1$, and $1s^11d^1$ configurations. Their excitation energies are in the 2.83−3.14 eV range. A complete list of energies for individual components of each term is given in the SI.

Preliminary density-functional calculations indicate that the Aufbau rules reported here might carry over to other metal-ammonia complexes. Indeed, $M(NH_3)_x$ structures with an $M(NH_3)_x^{n+}$ core and n outer electrons are stable for many metals. Whereas $Al(NH_3)_6$ hosts three outer electrons, $Ti(NH_3)_6$ has two inner unpaired d-electrons and an electron pair in its outer 1s orbital. These solvated electron precursors (SEP) can bind covalently to form aggregates such as $[Be(NH_3)_4]_4$.

High-level *ab initio* calculations on the ground and excited states of neutral and charged beryllium tetra-ammonia complexes disclose that these systems consist of a $Be(NH_3)_4^{2+}$ core surrounded by one, two, or three electrons. Dyson orbitals of electron detachment from the molecular complex resemble those of an isoelectronic double Rydberg anion, $Li(NH_3)_4^-$. Aufbau rules (1s, 1p, 1d, 2s, ...) pertain to orbitals that resemble those of a jellium or nuclear shell model. The effective electrostatic potential produced by the core and acting on the outer electrons reproduces the observed shell structure. The exploration of more metal-ammonia complexes and the construction of a new periodic table of SEPs are underway.

■ ASSOCIATED CONTENT

Supporting Information

The Supporting Information is available free of charge on the ACS Publications website at DOI: 10.1021/acs.jpclett.7b03000.

Optimal geometries, harmonic vibrational frequencies, electron binding energies, and vertical excitation energies, as well as a depiction of the energy levels and radial wave functions for the potentials of Figure 4 (PDF)

■ AUTHOR INFORMATION

Corresponding Author

*E-mail: emiliord@auburn.edu.

ORCID

Joseph Vincent Ortiz: 0000-0002-9277-0226

Evangelos Miliordos: 0000-0003-3471-7133

Notes

The authors declare no competing financial interest.

■ ACKNOWLEDGMENTS

I.R.A., S.N.K., and E.M. are indebted to Auburn University for financial support. We are grateful to Professor James E. Jackson, Michigan State University, for the valuable discussions that triggered the present study. J.V.O. acknowledges the support of the National Science Foundation through Grant CHE-1565760 to Auburn University. This work was completed in part with resources provided by the Auburn University Hopper Cluster.

■ REFERENCES

(1) Zurek, E.; Edwards, P. P.; Hoffmann, R. A Molecular Perspective on Lithium−Ammonia Solutions. *Angew. Chem., Int. Ed.* **2009**, *48*, 8198−8232.

(2) Hertel, I. V.; Hüglin, C.; Nitsch, C.; Schulz, C. P. Photoionization of $Na(NH_3)_n$ and $Na(H_2O)_n$ Clusters: A Step Towards the Liquid Phase? *Phys. Rev. Lett.* **1991**, *67*, 1767−1770.

(3) Misaizu, F.; Tsukamoto, K.; Sanekata, M.; Fuke, K. Photoionization of Clusters of Cs Atoms Solvated with H_2O, NH_3 and CH_3CN. *Chem. Phys. Lett.* **1992**, *188*, 241−246.

(4) Takasu, R.; Hashimoto, K.; Fuke, K. Study on Microscopic Solvation Process of Li Atom in Ammonia Clusters: Photoionization and Photoelectron Spectroscopies of $M(NH_3)_n$ (M = Li, Li^-). *Chem. Phys. Lett.* **1996**, *258*, 94−100.

(5) Takasu, R.; Misaizu, F.; Hashimoto, K.; Fuke, K. Microscopic Solvation Process of Alkali Atoms in Finite Clusters: Photoelectron and Photoionization Studies of $M(NH_3)_n$ and $M(H_2O)_n$ (M = Li, Li^-, Na^-). *J. Phys. Chem. A* **1997**, *101*, 3078−3087.

(6) Steinbach, C.; Buck, U. Ionization Potentials of Large Sodium Doped Ammonia Clusters. *J. Chem. Phys.* **2005**, *122*, 134301.

(7) Kryzhevoi, N. V.; Tarantelli, F.; Cederbaum, L. S. Tracing Electron Solvation in $Li^-(NH_3)_n$ Clusters with K-shell Photodetachment Spectroscopy. *Chem. Phys. Lett.* **2015**, *626*, 85−89.

(8) Hashimoto, K.; Morokuma, K. Ab Initio MO Study of $Na(NH_3)_n$ (n = 1−6) Clusters and Their Ions: A Systematic Comparison with Hydrated Na Clusters. *J. Am. Chem. Soc.* **1995**, *117*, 4151−4159.

(9) Gao, B.; Liu, Z.-F. Ionization Induced Relaxation in Solvation Structure: a Comparison Between $Na(H_2O)_n$ and $Na(NH_3)_n$. *J. Chem. Phys.* **2007**, *126*, 084501.

(10) Ferro, Y.; Allouche, A.; Kempter, V. Electron Solvation by Polar Molecules: the Interaction of Na Atoms with Solid Methanol Films Studied with MIES and Density Functional Theory Calculations. *J. Chem. Phys.* **2004**, *120*, 8683−8691.

(11) Hashimoto, K.; Daigoku, K. Formation and localization of a Solvated Electron in Ground and Low-lying Excited States of $Li(NH_3)_n$ and $Li(H_2O)_n$ Clusters: a Comparison with $Na(NH_3)_n$ and $Na(H_2O)_n$. *Phys. Chem. Chem. Phys.* **2009**, *11*, 9391−9400.

(12) Hashimoto, K.; Daigoku, K. Ground and Low-lying Excited States of $Na(NH_3)_n$ and $Na(H_2O)_n$ Clusters: Formation and Localization of Solvated Electron. *Chem. Phys. Lett.* **2009**, *469*, 62−67.

(13) Zhang, H.; Liu, Z.-F. The Solvation of Two Electrons in the Gaseous Clusters of $Na^-(NH_3)_n$ and $Li^-(NH_3)_n$. *J. Chem. Phys.* **2012**, *136*, 124314.

(14) Knight, W. D.; Clemenger, K.; deHeer, W. A.; Saunders, W. A.; Chou, M. Y.; Cohen, M. L. Electronic Shell Structure and Abundances of Sodium Clusters. *Phys. Rev. Lett.* **1984**, *52*, 2141−2143.

(15) Mayer, M. G.; Jensen, J. H. D. *Elementary Theory of Nuclear Structure*; Wiley: New York, 1955.

(16) Radisic, D.; Stokes, S. T.; Bowen, K. H. Two New Double Rydberg Anions Plus Access to Excited States of Neutral Rydberg Radicals via Anion Photoelectron Spectroscopy. *J. Chem. Phys.* **2005**, *123*, 011101.

(17) Melin, J.; Ortiz, J. V. OH_3^- and $O_2H_5^-$ Double Rydberg Anions: Predictions and Comparisons with NH_4^- and $N_2H_7^-$. *J. Chem. Phys.* **2007**, *127*, 014307.

(18) Hashimoto, K.; Daigoku, K.; Kamimoto, T.; Shimosato, T. Microscopic Solvation and Spontaneous Ionization of Li in Small Polar Solvent Clusters: Theoretical Analysis of Photoelectron Spectra for $Li^-(NH_3)_n$ and $Li^-(H_2O)_n$ (n = 1−4). *Internet Electron. J. Mol. Des.* **2002**, *1*, 503−526.

(19) Raghavachari, K.; Trucks, G. W.; Pople, J. A.; Head-Gordon, M. A Fifth-order Perturbation Comparison of Electron Correlation Theories. *Chem. Phys. Lett.* **1989**, *157*, 479−483.

(20) Becke, A. D. Density-functional Thermochemistry. III. The Role of Exact Exchange. *J. Chem. Phys.* **1993**, *98*, 5648−5652.

(21) Lee, C.; Yang, W.; Parr, R. G. Development of the Colle-Salvetti Correlation-energy Formula into a Functional of the Electron Density. *Phys. Rev. B: Condens. Matter Mater. Phys.* **1988**, *37*, 785−789.

DOI: 10.1021/acs.jpclett.7b03000
J. Phys. Chem. Lett. 2018, 9, 84−88

(22) Corzo, H. H.; Ortiz, J. V. Electron Propagator Theory: Foundations and Predictions. *Adv. Quantum Chem.* **2017**, *74*, 267−98.
(23) Dunning, T. H., Jr. Gaussian Basis Sets for Use in Correlated Molecular Calculations. I. The Atoms Boron Through Neon and Hydrogen. *J. Chem. Phys.* **1989**, *90*, 1007−1023.
(24) Kendall, R. A.; Dunning, T. H., Jr.; Harrison, R. J. Electron Affinities of the First-Row Atoms Revisited. Systematic Basis Sets and Wave Functions. *J. Chem. Phys.* **1992**, *96*, 6796−6806.
(25) Dunning, T. H., Jr.; Woon, D. E. Gaussian Basis Sets for Use in Correlated Molecular Calculations. IV. Calculation of static electrical response properties. *J. Chem. Phys.* **1994**, *100*, 2975−2988.
(26) Werner, H.-J.; Knowles, P. J.; Knizia, G.; Manby, F. R.; Schütz, M.; et al. *MOLPRO*, version 2015.1, a package of ab initio programs; see http://www.molpro.net (Accessed 11/29/2017).
(27) Frisch, M. J.; Trucks, G. W.; Schlegel, H. B.; Scuseria, G. E.; Robb, M. A. et al. *Gaussian 16*, revision A.03; Gaussian, Inc.: Wallingford, CT, 2016.
(28) Haynes, W. M., Ed. *CRC Handbook of Chemistry and Physics*, 92nd ed.; CRC Press: Boca Raton, FL, 2012.
(29) Gutowski, M.; Simons, J. Double-Rydberg Anions: Ground-state Electronic and Geometric Stabilities. *J. Chem. Phys.* **1990**, *93*, 3874−3880.
(30) Numerov, B. V. Note On The Numerical Integration Of $d^2x/dt^2 = f(x,t)$. *Astron. Nachr.* **1927**, *230*, 359−364.

DOI: 10.1021/acs.jpclett.7b03000
J. Phys. Chem. Lett. 2018, 9, 84−88

Stability and Electronic Features of Calcium Hexa–, Hepta–, and Octa–Coordinated Ammonia Complexes: A First–Principles Study

THE JOURNAL OF PHYSICAL CHEMISTRY A

Article

Cite This: J. Phys. Chem. A 2019, 123, 6744−6750

pubs.acs.org/JPCA

Stability and Electronic Features of Calcium Hexa-, Hepta-, and Octa-Coordinated Ammonia Complexes: A First-Principles Study

Isuru R. Ariyarathna, Nuno M. S. Almeida, and Evangelos Miliordos*

Department of Chemistry and Biochemistry, Auburn University, Auburn, Alabama 36849-5312, United States

Supporting Information

ABSTRACT: Neutral and positively charged calcium ammonia complexes are investigated by means of high-level quantum chemical calculations. We report optimal structures, binding energies, and vibrational spectra for $Ca(NH_3)_{1-8}^{0,+}$. The bigger $Ca(NH_3)_{6-8}^{0,+}$ complexes can be classified as solvated electron precursors (SEPs) and are best described as a $Ca(NH_3)_{6-8}^{2+}$ core with two or one peripheral electrons. In their ground state, only ∼10% of the outer electron density is estimated to be within the calcium van der Waals radius. For these systems, we calculated several low-lying electronic states, where electrons populate diffuse outer orbitals. The Aufbau principle for the outer electrons is found to be identical to previously studied SEPs: 1s, 1p, 1d, 1f, 2s, and 2p. We show that going from $Ca(NH_3)_5$, which has an incomplete first coordination shell and the two valence electrons that are mainly in the valence sphere of calcium, to $Ca(NH_3)_6$, both the vibrational and electronic features change abruptly. Infrared, visible, and ultraviolet spectroscopy can be used to identify and characterize calcium SEPs.

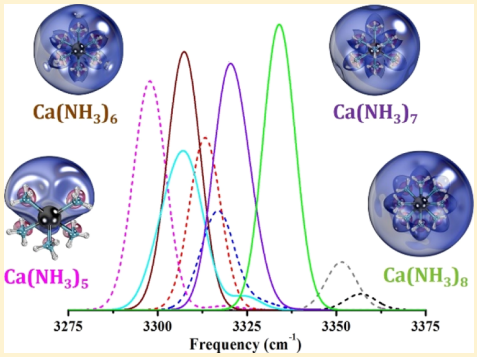

1. INTRODUCTION

Solvated electron precursors (SEPs) are the class of coordination metal complexes, where the ligands promote the relocation of metallic valence electrons to the "outer sphere" of the complex. We discovered that ammonia and water SEPs display diffuse electrons in peripheral hydrogenic-type orbitals which obey the jellium-type Aufbau rules (1s, 1p, 1d, 2s, 1f, 2p, 2d, and so forth.), instead of the typical hydrogenic model.[1−6] Such species are present in concentrated metal solutions.[5]

The properties of "free" electron solutions have been investigated since the beginning of the 19th century. The interest in the solvated species present in these solutions, including SEPs, has recently been revived.[1−5,7−13] Ammonia has received most of the interest among the solvents chosen in the published reports. Its ability to abstract and solvate electrons was first observed by Sir Humphry Davy (1807).[5] In his attempt to make potassium react with gaseous ammonia, he noticed a "fine blue color", which was only later associated to the solvation of electrons by ammonia. Recent studies found that the color and appearance of metal ammonia solutions vary with different metal concentrations. When the concentration of the solution reaches the saturation point at about 20 mol % metal, it becomes a liquid metal displaying bronze color.[5,14−16] A liquid metal can be represented by several positive metal cores coordinated by ammonia and electrons moving "freely" in the interstitial space. At low temperature (∼100 K), liquid metals become solids (expanded metals), the structure of which has been determined by means of X-ray and neutron scattering for Li, Na, and Ca.[15−19] Calcium has been reported to form such species with $Ca(NH_3)_6^{2+}$ cores.[17]

In the gas-phase regime, lithium, sodium, and magnesium ammonia complexes have been produced experimentally, and photoelectron spectra of their anions have been analyzed.[20−25] From the theoretical viewpoint, few studies exist in the past literature, focusing mainly on the microsolvation process, in which electrons migrate from the metal center to the solvent.[5,11,26−31] More recently, our group has published a series of theoretical studies on different metal ammonia complexes, and specifically for lithium, sodium, beryllium, vanadium, and yttrium, showing unique electronic features for each single species.[1−4] Transition metals were found to be way more challenging systems because of the dual shell nature (inner valence d-orbitals and outer diffuse orbitals) and the multireference nature of their wavefunction. The second-row transition metal yttrium forms an octa-coordinated system, $Y(NH_3)_8^{0,\pm}$, which preserves no inner shell electrons: a $Y(NH_3)_8^{3+}$ core hosts up to four electrons orbiting in its periphery.[1] Multiconfigurational techniques were proven to be essential for the study of such demanding systems.

Very recently, calcium ammonia complexes were produced by Albaqami and Ellis and their infrared (IR) spectra were recorded.[7] Based on MP2 calculations, the authors assigned the IR spectra and found that the first coordination sphere is saturated with eight ammonia ligands. They observed that the

Received: May 24, 2019
Revised: July 9, 2019
Published: July 15, 2019

DOI: 10.1021/acs.jpca.9b04966
J. Phys. Chem. A 2019, 123, 6744−6750

Table 1. Detachment Energy of a Single Ammonia Ligand from $Ca(NH_3)_n^{0,+}$ (kcal/mol) at Different Levels of Theory

	$Ca(NH_3)_n^+$			$Ca(NH_3)_n$			
n	D_e(MP2)[a]	D_e(C-MP2)[a]	D_0(C-MP2)[b]	D_e(MP2)[a]	D_e(C-MP2)[a]	D_0(C-MP2)[b]	D_e(MP2)[c]
1	28.4	28.5	26.7	8.1	6.6	5.6	9.6
2	24.1	27.3	25.6	9.9	11.8	10.7	9.6
3	18.2	20.4	19.1	8.7	9.6	8.6	12.5
4	17.4	19.9	18.4	11.6	12.8	11.7	13.8
5	17.2	18.6	17.7	12.4	11.1	9.8	15.3
6	16.1	18.1	17.1	13.9	19.5	18.0	17.5
7	11.4	13.7	11.3	9.9	12.2	9.8	10.2
8	9.3	4.9	3.5	7.7	3.3	1.8	9.1

[a] $D_e = E[Ca(NH_3)_{n-1}^{0,+}] + E[NH_3] - E[Ca(NH_3)_n^{0,+}]$. [b] $D_0 = D_e + ZPE[Ca(NH_3)_{n-1}^{0,+}] + ZPE[NH_3] - ZPE[Ca(NH_3)_n^{0,+}]$; ZPE values obtained at B3LYP. [c] MP2/6-311++G(d,p); ref 7.

main peak at ~3130 cm^{-1} (N−H stretches) is accompanied by a satellite peak at ~3280 cm^{-1} going from $Ca(NH_3)_8$ to $Ca(NH_3)_9$. This suggests that the lowest energy isomers for $Ca(NH_3)_{1-8}$ have all direct bonds with the ligands, and that the ninth ammonia populates the second shell of the complex, which is in agreement with their calculated relative energies of the involved isomers.

Although these gas-phase experiments isolated the $Ca(NH_3)_{8-10}$ complexes, the calcium ammonia expanded metals consist primarily of $Ca(NH_3)_6$.[17] To shed more light on the properties of calcium ammonia complexes, we carry out higher level calculations including core valence electron correlation, which affects considerably the Ca−N bond lengths and energetics of the system. In addition, we investigate for the first time the electronic structure of their ground and several low-lying electronic states for both the neutral and cationic species. Our findings make available accurate excitation energies to future experimental studies and provide additional means to identify and assign the spectra of calcium−ammonia complexes.

2. COMPUTATIONAL DETAILS

Geometry optimization for $Ca(NH_3)_{n=1-8}^{0,+}$ was performed at restricted and unrestricted MP2 for the neutral and cationic species, respectively. Spin contamination for the cation was minimal (~0.0005). We also considered the effect of core-correlation by unfreezing all the electrons from calcium and nitrogen, but 1s (C-MP2). To ensure all optimized complexes were minima on the potential energy surface and to get an estimate of zero-point energy (ZPE) corrections, frequency calculations were performed for all structures at the density functional theory (DFT)/B3LYP.[32,33] The MP2 structures were re-optimized at this level of theory. Cartesian coordinates, and frequencies are provided in the Supporting Information.

Considering the basis set selection, for calculations without core-correlation, we used cc-pVTZ[34,35] for calcium, and nitrogen, and aug-cc-pVTZ[34,35] for hydrogen. The use of augmented functions is necessary to describe the diffuse nature of the outer orbitals.[4] The C-MP2 calculations were done with the more balanced cc-pCVTZ[36] basis set for calcium. For the excited state calculations, doubly augmented bases were centered on hydrogen atoms to properly describe the nature of different outer orbitals.[34,37]

The methodology chosen for vertical excited state calculations was the complete active space self-consistent filed (CASSCF), followed by second-order perturbation theory (CASPT2), including both static and dynamic electron correlation effects. The MP2 optimal geometries of the ground state were used. The neutral and cationic hexacoordinated species bear C_1 symmetry, which was found to be computationally demanding. To bypass this technical issue, we imposed C_{2v} symmetry through small rotations of selected ammonia ligands and re-optimized the complex, as we did for $V(NH_3)_6$.[2] The energy difference between C_{2v} and C_1 geometries is only 0.10 (cation) and 0.06 (neutral) kcal/mol. Considering $Ca(NH_3)_7^{0,+}$, we used C_s as the largest abelian point subgroup of the actual C_{3v} symmetry of the complex. Similarly, for the octa-coordinated species, we used C_{2v} (full point group is D_{4d}). The CASPT2 excitation energies are obtained with cc-pVTZ for calcium and nitrogen, but d-aug-cc-pVTZ for hydrogen for penta-, hexa-, hepta- and octa-coordinated complexes. C-CASPT2 calculations were also carried out with the cc-pCVTZ basis set for calcium and the C-MP2 geometries for the ground state.

For the $Ca(NH_3)_6^+$ cationic case, CASSCF wavefunctions were constructed by allocating one outer electron in 20 orbitals: two s-type (1s and 2s), six p-type (1p and 2p), five d-type (1d), and seven f-type (1f) active orbitals. Considering $Ca(NH_3)_7^+$ and $Ca(NH_3)_8^+$, we used one electron in one s-type (1s), three p-type (1p), and five d-type (1d) (nine active orbitals). We performed the calculations for each irreducible representation separately. For the neutral species, we used the same active space as the cation for each of the species, but all irreducible representations were state-averaged for technical reasons.

Regarding CASPT2, we also took into consideration excitations from inner orbitals. For $Ca(NH_3)_6^{0,+}$, we activated 24 orbitals ($9a_1$, $5b_1$, $7b_2$, and $3a_2$) and for $Ca(NH_3)_7^{0,+}$ 28 (17a′, 11a″), which correspond to all ammonia valence orbitals in the system. For $Ca(NH_3)_8^{0,+}$, we could only include excitations out of 24 "sub-valence" orbitals ($7a_1$, $6b_1$, $6b_2$, and $5a_2$), which correspond to N−H bonding orbitals. For C-CASPT2 (done only for $Ca(NH_3)_6^{0,+}$), we included all electrons but the 1s and 2s of calcium and 1s of nitrogen.

To render these calculations feasible, we had to consider the internally contracted version of CASPT2, which is implemented in MOLPRO 2015.1 (RS2C).[38] To avoid intruder states instabilities in our calculations, we also considered a level shift of 0.02 and an IPEA value of 0.02.[38,39] Geometry optimizations were performed with Gaussian 16[40] and multireference calculations with MOLPRO 2015.1.[41]

3. RESULTS AND DISCUSSION

3.1. Ground-State Properties of $Ca(NH_3)_{n=1-8}^{0,+}$. The MP2 and C-MP2 optimized geometries and DFT harmonic vibrational frequencies are reported in the Supporting

DOI: 10.1021/acs.jpca.9b04966
J. Phys. Chem. A 2019, 123, 6744−6750

Information. The detachment energy D_e of a single ammonia from $Ca(NH_3)_n^{0,+}$ for $n = 1-8$ given by

$$D_e = E[Ca(NH_3)_{n-1}^{0,+}] + E[NH_3] - E[Ca(NH_3)_n^{0,+}]$$

is listed in Table 1. The $Ca(^1S)$ and $Ca^+(^2S)$ states are used for $n = 1$. The ZPE-corrected D_e values are also provided in Table 1 at the C-MP2 level as D_0

$$D_0 = D_e + ZPE[Ca(NH_3)_{n-1}^{0,+}] + ZPE[NH_3] - ZPE[Ca(NH_3)_n^{0,+}]$$

More detailed tables are provided in the Supporting Information. Here, we consider only complexes with ammonia ligands directly attached to calcium because they have been shown to be the lowest energy isomers. In the case of cationic complexes, D_e(MP2), D_e(C-MP2), and D_0(C-MP2) are all monotonically decreasing series of n ranging from ∼28 to ∼4 kcal/mol. Core correlation effects generally strengthen metal ammonia interactions by ∼2 kcal/mol, while ZPE corrections reduce the detachment energy by slightly smaller amounts. The two effects nearly cancel each other out. The same cancelation is generally seen for the neutral species, for which no specific trend is found for different n values.

A common feature for $Ca(NH_3)_n^{0,+}$ is the sudden drop of D_0 going from $n = 6$ to 7 and from $n = 7$ to 8. Especially, for $n = 8$, both the core correlation and ZPE effects are synergistic decreasing the detachment energy from 9.3 and 7.7 to just 3.5 and 1.8 kcal/mol for $Ca(NH_3)_8^+$ and $Ca(NH_3)_8$. The important drop in $D_0[Ca(NH_3)_n]$ for $n > 6$ by 8.2 ($n = 6-7$) and 8.0 ($n = 7-8$) kcal/mol and its sudden increase going from $n = 1-5$ (5.6−11.5 kcal/mol) to 6 (18.0 kcal/mol) explains why saturated calcium ammonia solutions prefer the $Ca(NH_3)_6$ entities (see Introduction).

D_e(MP2) values for $Ca(NH_3)_n$ are reported by Albaqami and Ellis, albeit with a smaller basis set.[7] Their 6-311++G(d,p) basis set consists of 4s1p (H) 5s4p1d (N) 9s8p2d (Ca) functions, while the composition of the present basis set (cc-pVTZ for Ca and N and aug-cc-pVTZ for H) is 5s4p3d (H) 4s3p2d1f (N) 6s5p3d1f (Ca). In addition, the 6-311++G(d,p) basis set has considerably less diffuse s- and p-type functions for hydrogen (smallest exponents: 0.025 vs 0.036 for s-type and 0.750 vs 0.102 for p-type), while no d-functions are present. Despite the significant size difference of the two sets, the D_e values agree within 3.8 kcal/mol with an average discrepancy over n of 1.9 kcal/mol (see Table 1). The 6-311++G(d,p) values are always larger (except for $n = 2$) as expected by Albaqami and Ellis. In the $n = 6-8$ cases, our ZPE-corrected C-MP2 detachment energies differ appreciably from the plain MP2 ones, stressing the importance of the vibrational and core correlation effects.

Another significant effect of the calcium core electron correlation is the significant shortening of the Ca−N bond lengths. For the highly symmetric $Ca(NH_3)_{6,8}$ complexes, the MP2 Ca−N bond lengths are 2.625 and 2.725 Å contracting by ∼0.12 Å to 2.508 and 2.529 Å at C-MP2, respectively. The same differences are seen for $Ca(NH_3)_{6,8}^+$. The N−H bonds elongate in all four systems by 0.007−0.0104 Å compared to free NH_3 at MP2. Core correlation affects them by less than 0.001 Å. The N−H elongation is because of the attraction from the outer electrons.

In Figure 1, the highest occupied molecular orbital (HOMO) of $Ca(NH_3)_n^+$ is displayed. For $n = 0$, the HOMO corresponds to the 4s atomic orbital of Ca. It is

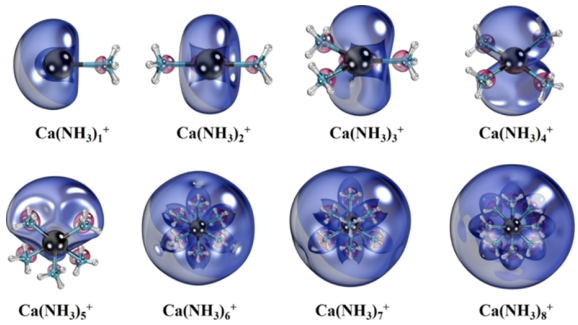

Figure 1. Contours of the highest molecular orbital of the $Ca(NH_3)_{n=1-8}^+$ species, which gradually gets converted from the atomic 4s orbital of calcium to the pseudo-spherical outer 1s orbital, which is clearly formed for $n = 6-8$.

apparent that the electron lone pairs of each attacking ammonia ligand displaces the $4s^1$ electron, which gradually shifts to the periphery of the $Ca(NH_3)^{2+}$ core. For $n = 6-8$, 4s transforms to the pseudo-spherical outer 1s orbital observed for Be, Li, and Na ammonia complexes.[3,4] Identical schemes are observed for the neutral species and they can rationalize the D_0 trends discussed in the previous paragraph.

Sommerfeld and Dreux have shown for the similar $Li(NH_3)_4$ complex that in terms of electronic density, only 6% of the excess electron's density is closely associated with the atoms and that the outer electron is best characterized as Rydberg-like electron of the whole cluster.[42] In this report, we employ a more practical approach to provide a semiquantitative measure of the transformation of $4s_{Ca}$ to the superatomic 1s orbital. We calculated the electronic density based solely on the HOMO (φ_{HOMO}) along specific directions as

$$\rho(r) = r^2 \varphi_{HOMO}^2(r) \quad (1)$$

The chosen direction always follows the line that is further from all ammonia ligands. For example, in the case of $Ca(NH_3)$, this line goes to the opposite direction from NH_3, while for $Ca(NH_3)_6$, this line goes through the middle of three neighboring nitrogen atoms. The density $\rho(r)$ for all calcium ammonia complexes with up to eight ammonias including the naked atom, $Ca(NH_3)_{n=0-8}$, is plotted in Figure 2. It is observed that its maximum is around 1.8 Å for $n = 0-4$. Although it is getting more diffuse going from $n = 0$ to 4, it is at

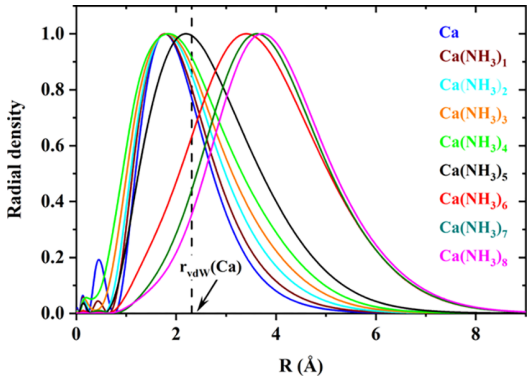

Figure 2. Radial distribution of the electronic density corresponding to the HOMO (eq 1) for the $Ca(NH_3)_{n=0-8}$ species. The van der Waals radius (r_{vdW}) for the calcium atom is shown with the dashed vertical line. The maximum of all curves is adjusted to be equal to one.

DOI: 10.1021/acs.jpca.9b04966
J. Phys. Chem. A 2019, 123, 6744−6750

n = 5 that the density maximum shifts to longer distance (~2.2 Å), which finally shifts another 1.2 Å going to n = 6. The maxima for n = 7, 8 shift only another 0.3 Å. This plot provides a clear indication for the displacement of calcium valence electrons. We further obtained the percentage of the density from the van der Waals distance of the calcium atom (2.31 Å)[43] and beyond by integrating the density along the chosen direction. For naked calcium, we obtained a value of 35%, which changed to 39, 43, 45, 47, 60, 86, 92, and 93% for n = 1−8, respectively. It is obvious that for $Ca(NH_3)_{6-8}$, the HOMO can clearly be characterized as an orbital of the whole complex in agreement with the observations of Sommerfeld and Dreux.

Albaqami and Ellis reported IR spectra in the N−H stretching region for $Ca(NH_3)_{8-10}$, focusing on the transition between $Ca(NH_3)_8$ (complete first solvation shell) and $Ca(NH_3)_7@NH_3$ (complete first shell plus one ammonia placed in the second shell). Here, we report theoretical IR spectra for $Ca(NH_3)_{1-8}$ to cover the other end too, where the first solvation shell is "incomplete". By that, we mean the $Ca(NH_3)_{1-5}$ cases, where valence electrons are still largely in the valence sphere of calcium (see Figure 1).

The 3275−3350 cm^{-1} region corresponds to symmetric N−H stretches of all coordinated ammonia ligands and is shown in Figure 3. The main peak of $Ca(NH_3)$ is at 3357 cm^{-1} red

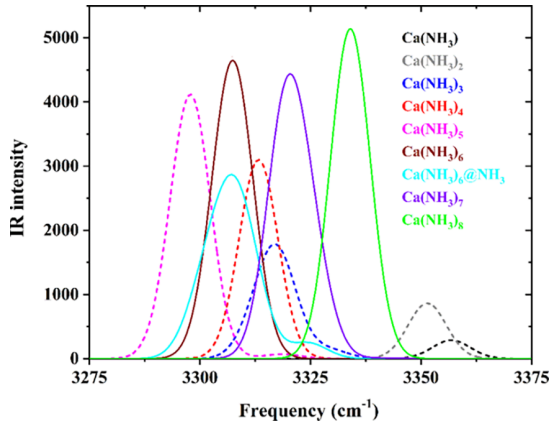

Figure 3. IR spectrum between 3275 and 3375 cm^{-1} for $Ca(NH_3)_{1-8}$. B3LYP harmonic frequencies and intensities are used. The HMHW for all peaks is set to 10 cm^{-1}.

shifted by ~100 cm^{-1} with respect to free NH_3 (see Supporting Information). The position of the main peak moves to lower frequencies all the way to $Ca(NH_3)_5$ with an average step of 15 cm^{-1}. Going from $Ca(NH_3)_5$ to $Ca(NH_3)_6$, the peak changes direction and shifts to higher frequencies by ~10 cm^{-1}. The same happens for $Ca(NH_3)_7$ and $Ca(NH_3)_8$ with steps of 14 and 12 cm^{-1}, respectively. Apparently, this change is a direct reflection of the "total" displacement of the valence calcium electrons to the periphery when the sixth ammonia enters the coordination sphere. The addition of more ligands makes the N−H bonds "stronger" (blue shift of harmonic frequencies). The reason is that the same two electrons are shared among more N−H bonds. As a result, a smaller effective negative charge corresponds to each hydrogen terminal causing a smaller N−H bond elongation.

Finally, we included the IR peaks for the $Ca(NH_3)_6@NH_3$ species, which has a completely different spectrum from its $Ca(NH_3)_7$ isomer. The main peak of the former is at the same position of $Ca(NH_3)_6$ having a smaller satellite peak 20 cm^{-1} higher in frequency. This is identical with the observation by Albaqami and Ellis relative to the $Ca(NH_3)_8$ and $Ca(NH_3)_7@NH_3$ complexes.[7] Recall that these authors identified the $Ca(NH_3)_8$ complex, while solid-state calcium ammonia systems prefer the $Ca(NH_3)_6$ arrangement. The spectra of $Ca(NH_3)_7$ and $Ca(NH_3)_6@NH_3$ can be used to confirm that the seventh ammonia indeed enters the first solvation shell confirming the observations of Albaqami and Ellis.

3.2. Excited States of $Ca(NH_3)_{n=6-8}^+$. The excited states for the $Ca(NH_3)_{6-8}^+$ species are examined in this section. As discussed earlier, the ground state of these species bears one electron in a pseudo-spherical (s-type) orbital covering almost evenly the periphery of the $Ca(NH_3)_{6-8}^{2+}$ core. Similar electronic structure features were observed in other metal−ammonia complexes by our group (see Introduction). The next excited states occupy orbitals of p-, d-, and f-type orbitals, forming a hydrogenic-type shell model.

For the smaller and computationally less-demanding $Ca(NH_3)_6^+$ complex, we studied the first 20 electronic states. Their excitation energies at CASSCF, CASPT2, and C-CASPT2 are reported in Table 2 and the Supporting Information. Based on the angular and radial distribution of the occupied orbital in each case, the states have been assigned using atomic electronic terms. Specifically, we studied the 1^2S, 1^2P, 1^2D, 1^2F, 2^2S, and 2^2P states, which have one electron in the 1s, 1p, 1d, 1f, 2s, and 2p outer diffuse orbitals (see Figure 4). The individual components of each state are not necessarily degenerate, that is, the three components of 1^2P span an energy range of a few hundredths of eV. A detailed list of the energies and irreducible representations under the actual point group of the complex for all individual components is given in the Supporting Information.

In all cases, the CASSCF excitation energies fall short of the CASPT2 ones by 0.17−0.44 eV. Similar observations were

Table 2. Electronic Configuration and Vertical Excitation Energies (eV) for $Ca(NH_3)_{n=5-8}^+$

	$Ca(NH_3)_5^+$	$Ca(NH_3)_6^+$			$Ca(NH_3)_7^+$	$Ca(NH_3)_8^+$
state	CASPT2	CASSCF	CASPT2	C-CASPT2	CASPT2	CASPT2
1^2S ($1s^1$)	0.00	0.00	0.00	0.00	0.00	0.00
1^2P ($1p^1$)[a]	1.33−1.40	0.69	0.86	0.90	0.83	0.81
1^2D ($1d^1$)[a]	2.30−2.57	1.52	1.85	1.90	1.75	1.70
1^2F ($1f^1$)[a]		2.34	2.78	2.82		2.50
2^2S ($2s^1$)		2.21	2.63	2.70		2.65
2^2P ($2p^1$)[a]		2.53	2.95	3.05		2.81

[a]State-averaged values over all "spherical" quasi-degenerate components for $Ca(NH_3)_{6-8}^+$, but a full range of energies for $Ca(NH_3)_5^+$. More detailed tables are given in the Supporting Information.

DOI: 10.1021/acs.jpca.9b04966
J. Phys. Chem. A 2019, 123, 6744−6750

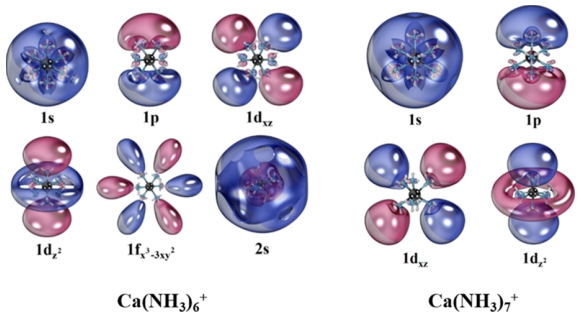

Figure 4. Selected outer orbitals for $Ca(NH_3)_6^+$ and $Ca(NH_3)_7^+$.

made for other metal−ammonia complexes by the authors.[1,2] C-CASPT2 increases the excitation energies further by less than 0.1 eV. Both valence and sub-valence electron correlations are more important for higher states. Identical conclusions were found for vanadium ammonia complexes.[2] For bigger complexes, we did not include the core correlation, and thus, our CASPT2 values of Table 2 should be considered as a lower bound. More accurate excitation energies can be estimated by adding 0.05−0.1 eV.

Moving to larger systems, we see that the excitation energy drops. Because of its lower symmetry, only the first three states were technically feasible for $Ca(NH_3)_7$. For these three states, the $^2P \leftarrow {}^2S/{}^2D \leftarrow {}^2S$ excitation energies decrease by 0.03/0.10 (n = 6 → 7) and 0.02/0.05 eV (n = 7 → 8) eV, exhibiting an asymptotic pattern. This trend can be explained by the larger number of ligands, which displace further the outer electrons (see Figure 2), increasing the radius of the peripheral orbitals. The larger radius is directly connected to the energy drop, as happens in the case of the simple particle-on-a-sphere model. Similarly, the excitation energies for the remaining states decrease going from n = 6 to 8.

For all the three systems, the energy order of the outer orbitals is 1s, 1p, 1d, 1f, 2s, and 2p. The energy difference between successive energy levels is nearly equal up to the 1f level (see Table 2). The 2s level is within 0.2 eV from 1f, and 2p is ∼0.3 eV higher than 2s. The first two excited states of Ca^+ are ^2D ($3d^1$) and ^2P ($4p^1$) 1.70 and 3.14 eV (M_J-averaged)[44] higher than the ground ^2S ($4s^1$) state. An interesting observation is that the order of the p- and d-type orbitals is reversed going from plain Ca^+ to $Ca(NH_3)_6^+$. Moreover, the energy order of the outer orbitals is identical for all metals studied so far by our group. Both observations suggest that the outer shell is independent of the central metal. Therefore, interpreting them as Rydberg orbitals of the central metal perturbed by the ligands is a less natural viewpoint. The metallic nature is rather suppressed, and only its ionization energy seems to make the difference among different metals.[1] The outer orbitals should be better viewed as the result of the complex electrostatics of the system and the central metal acts more like a central charge.[3]

Finally, we calculated the excited states of $Ca(NH_3)_5^+$ in an attempt to show how an incomplete first solvation shell affects the electronic spectrum. In this case, only the 1s, 1p, and 1d orbitals are considered. Table 2 indicates that the ^2P components retain their degeneracy but ^2D components are spread out in the 2.30−2.57 eV energy range. In all cases, the excitation energies are clearly larger by about ∼0.40 eV compared to the $Ca(NH_3)_{6-8}^+$ species because of closer proximity of the calcium valence electrons to the calcium nucleus. The sudden change of the excitation energy could be a clean indicator of the completion of the first coordination sphere.

3.3. Excited States of $Ca(NH_3)_{n=6-8}$. The addition of an electron renders the wavefunction of the low-lying electronic states quite multiconfigurational. The ground state for all $Ca(NH_3)_{6-8}$ species has a dominant $1s^2$ character (^1S), followed by the triplet $1s^11p^1$ state (^3P). The next state has mixed $1p^2$-$1s^11d^1$ (^1D) nature, which is followed by the open-shell singlet $1s^11p^1$ (^1P) counterpart of ^3P. Then, both electrons are promoted to the 1p level (^3P; $1p^2$) or one electron of the ground state moves to 1d (^3D; $1s^11d^1$). The excitation energies are registered in Table 3, while a more detailed list of the energies and symmetries of the individual components for each state is given in the Supporting Information. As in the cationic complexes, the energy order of the Rydberg states of Ca is very different. The energy order for the calcium atom is $4s^2$ (^1S), $4s^14p^1$ (^3P), $4s^13d^1$ (^3D), $4s^13d^1$ (^1D), $4s^14p^1$ (^1P), while the $4p^2$ (^3P) state is ranked fifteenth. This is another indication that the outer orbitals should not be seen as Rydberg orbitals of the metal.

Table 3 lists CASSCF, CASPT2, and C-CASPT2 excitation energies for $Ca(NH_3)_6$. In addition to the previously mentioned states, we did calculations to 30 more states of extremely multireference wavefunctions, which involve the higher energy 1f, 2s, and 2p orbitals. Table 3 reports only the energy range covered by these states; more details are provided in the Supporting Information. Similar to cations, the CASPT2

Table 3. Electronic Configuration and Vertical Excitation Energies (eV) for $Ca(NH_3)_{n=5-8}$

	$Ca(NH_3)_5$	$Ca(NH_3)_6$			$Ca(NH_3)_7$	$Ca(NH_3)_8$
state	CASPT2	CASSCF	CASPT2	C-CASPT2	CASPT2	CASPT2
1^1S ($1s^2$)	0.00	0.00	0.00	0.00	0.00	0.00
1^3P ($1s^11p^1$)[a]	0.46, 0.64 (2)	0.37	0.49	0.52	0.44	0.42
1^1D ($1p^2/1s^11d^1$)[a]	1.08−1.41[b]	0.92	1.18	1.22	1.05	1.04
1^1P ($1s^11p^1$)[a]	1.08−1.41[b]	0.97	1.15	1.18	1.04	0.98
2^3P ($1p^2$)[a]	1.54, 1.63 (2)	1.26	1.52	1.56	1.40	1.34
1^3D ($1s^11d^1$)[a]	1.67−1.81	1.30	1.51	1.55	1.50[c]	1.45
MC[d]		1.51−1.92	1.87−2.18			

[a]State-averaged values over all "spherical" quasi-degenerate components for $Ca(NH_3)_{6-8}^+$, but a full range of energies for $Ca(NH_3)_5$. More detailed tables are given in the Supporting Information. [b]The two manifolds of states are highly mixed. [c]Only two (out of five) components were feasible at CASPT2. The average CASSCF values for all five components were improved by adding the average CASPT2−CASSCF shift of the two former components (see the Supporting Information). [d]Multi-configurational wavefunctions: Mixture of $1s^12s^1$, $1p^11d^1$, $1s^12p^1$, and $1s^11f^1$. A range of values is given; see the Supporting Information.

DOI: 10.1021/acs.jpca.9b04966
J. Phys. Chem. A 2019, 123, 6744−6750

values are higher than CASSCF ones by 0.2−0.3 eV, and C-CASPT2 values are ∼0.05 eV higher than CASPT2 ones. Referring to the two larger clusters $Ca(NH_3)_{7,8}$, we see again that the excitation energies decrease asymptotically. Compared to the cationic counterparts, the neutral species reveal a much denser energy level pattern. For example, $Ca(NH_3)_6$ has 53 states within 2.2 eV, while $Ca(NH_3)_6^+$ has 20 states within 3.1 eV.

Finally, as in the cationic species, we calculated the excitation energies of $Ca(NH_3)_5$. In contrast to the $1p^1$ components of $Ca(NH_3)_5^+$, the $1s^11p^1$ ones of $Ca(NH_3)_5$ are not nearly degenerate. One of them lies at 0.46 eV and is 0.18 eV more stable than the other two components. A possible reason is that the 1s orbital shown in Figure 1 is polarized toward a specific direction ruining the spatial isotropy. Their degeneracy is recovered when going to larger complexes, where the two electrons become peripheral. The same is true for the three $1p^2$ components, as well as with the 1^1D, 1^1P, and 1^3D states (see Table 3). As in the cationic case, electronic spectroscopy can signify the electron delocalization and the formation of a SEP.

4. CONCLUSIONS

Neutral and cationic calcium ammonia complexes were studied using single and multireference quantum chemical approaches. For all of them, we report structures and binding energies. For the hexa-, hepta- and octa-coordinated complexes, we found that the valence electrons of calcium have been displaced in the periphery of the $Ca(NH_3)_{6-8}^{2+}$ skeleton and are thus classified as SEPs. The N−H stretching region of the IR spectrum is highly affected by the electronic structure changes. For the neutral series, we observe some red shift for the main peak of species with up to five ammonia ligands, which becomes blue shifted for larger systems.

We further examined the low-lying electronic states of these SEPs. As in other alkali and alkaline earth metal SEPs, the outer electrons populate diffuse orbitals resembling those of hydrogenic atoms but bearing a different Aufbau principle. The ranking for the first few peripheral orbitals is confirmed as 1s, 1p, 1d, 1f, 2s, and 2p. Excitation energies are quite insensitive to the number of coordinated ammonias for the three SEPs. Going from $Ca(NH_3)_5$, which has an incomplete first shell, to $Ca(NH_3)_{6-8}$, the pattern of the electronic spectrum is modified considerably. Both the vibrational and electronic features of the calcium ammonia complexes can reveal experimentally the unique personality of SEPs.

■ ASSOCIATED CONTENT

Supporting Information

The Supporting Information is available free of charge on the ACS Publications website at DOI: 10.1021/acs.jpca.9b04966.

Cartesian coordinates, harmonic vibrational frequencies, IR intensities of all optimized structures, more detailed tables on the binding energies of $Ca(NH_3)_{n=1-8}^{0,+}$, and vertical excitation energies of $Ca(NH_3)_{n=5,6,7,8}^{0,+}$ (PDF)

■ AUTHOR INFORMATION

Corresponding Author

*E-mail: emiliord@auburn.edu.

ORCID

Isuru R. Ariyarathna: 0000-0002-5259-4248

Nuno M. S. Almeida: 0000-0002-6091-7289

Evangelos Miliordos: 0000-0003-3471-7133

Notes

The authors declare no competing financial interest.

■ ACKNOWLEDGMENTS

The authors are indebted to Auburn University for financial support. This work was completed in part with resources provided by the Auburn University Hopper Cluster and in part with resources provided by the National Energy Research Scientific Computing Center (NERSC), a U.S. Department of Energy Office of Science User Facility operated under contract no. DE-AC02-05CH11231.

■ REFERENCES

(1) Almeida, N. M. S.; Miliordos, E. Electronic and Structural Features of Octa-Coordinated Yttrium-Ammonia Complexes: The First Neutral Solvated Electron Precursor with Eight Ligands and Three Outer Electrons. *Phys. Chem. Chem. Phys.* **2019**, *21*, 7098−7104.

(2) Almeida, N. M. S.; Pawłowski, F.; Ortiz, J. V.; Miliordos, E. Transition-Metal Solvated-Electron Precursors: Diffuse and 3d Electrons in $V(NH_3)_6^{0,\pm}$. *Phys. Chem. Chem. Phys.* **2019**, *21*, 7090−7097.

(3) Ariyarathna, I. R.; Khan, S. N.; Pawłowski, F.; Ortiz, J. V.; Miliordos, E. Aufbau Rules for Solvated Electron Precursors: $Be(NH_3)_4^{0,\pm}$ Complexes and Beyond. *J. Phys. Chem. Lett.* **2018**, *9*, 84−88.

(4) Ariyarathna, I. R.; Pawłowski, F.; Ortiz, J. V.; Miliordos, E. Molecules Mimicking Atoms: Monomers and Dimers of Alkali Metal Solvated Electron Precursors. *Phys. Chem. Chem. Phys.* **2018**, *20*, 24186−24191.

(5) Zurek, E.; Edwards, P. P.; Hoffmann, R. A Molecular Perspective on Lithium-Ammonia Solutions. *Angew. Chem., Int. Ed.* **2009**, *48*, 8198−8232.

(6) Ariyarathna, I. R.; Miliordos, E. Superatomic Nature of Alkaline Earth Metal−Water Complexes: The Cases of $Be(H_2O)_4^{0,+}$ and $Mg(H_2O)_6^{0,+}$. *Phys. Chem. Chem. Phys.* **2019**, *21*, 15861−15870.

(7) Albaqami, M. D.; Ellis, A. M. Infrared Spectroscopy of $Ca(NH_3)_n$ Complexes. *Chem. Phys. Lett.* **2018**, *706*, 736−740.

(8) Gunina, A. O.; Krylov, A. I. Probing Electronic Wave Functions of Sodium-Doped Clusters: Dyson Orbitals, Anisotropy Parameters, and Ionization Cross-Sections. *J. Phys. Chem. A* **2016**, *120*, 9841−9856.

(9) Hattab, A.; Dhaouadi, Z.; Malloum, A.; Fifen, J. J.; Lahmar, S.; Russo, N.; Sicilia, E. Structures, Binding Energies, Temperature Effects, Infrared Spectroscopy of $[Mg(NH_3)_{n=1-10}]^+$ Clusters from DFT and MP2 Investigations. *J. Comput. Chem.* **2019**, *40*, 1707−1717.

(10) Kumar, A.; Walker, J. A.; Bartels, D. M.; Sevilla, M. D. A Simple Ab *Initio* Model for the Hydrated Electron that Matches Experiment. *J. Phys. Chem. A* **2015**, *119*, 9148−9159.

(11) Mauksch, M.; Tsogoeva, S. B. Spin-Paired Solvated Electron Couples in Alkali-Ammonia Systems. *Phys. Chem. Chem. Phys.* **2018**, *20*, 27740−27744.

(12) Walker, J. A.; Bartels, D. M. A Simple Ab *Initio* Model for the Solvated Electron in Methanol. *J. Phys. Chem. A* **2016**, *120*, 7240−7247.

(13) Ariyarathna, I. R.; Miliordos, E. Dative Bonds Versus Electron Solvation in Tri-Coordinated Beryllium Complexes: $Be(CX)_3$ [X = O, S, Se, Te, Po] and $Be(PH_3)_3$ Versus $Be(NH_3)_3$. *Int. J. Quantum Chem.* **2018**, *118*, No. e25673.

(14) Martyna, G. J.; Deng, Z.; Klein, M. L. Quantum Simulation Studies of Singlet and Triplet Bipolarons in Liquid Ammonia. *J. Chem. Phys.* **1993**, *98*, 555−563.

(15) Seel, A. G.; Swan, H.; Bowron, D. T.; Wasse, J. C.; Weller, T.; Edwards, P. P.; Howard, C. A.; Skipper, N. T. Electron Solvation and the Unique Liquid Structure of a Mixed-Amine Expanded Metal: The

DOI: 10.1021/acs.jpca.9b04966
J. Phys. Chem. A 2019, 123, 6744−6750

Saturated Li-NH_3-$MeNH_2$ System. *Angew. Chem., Int. Ed.* **2017**, *56*, 1561−1565.
(16) Zurek, E.; Wen, X.-D.; Hoffmann, R. (Barely) Solid $Li(NH_3)_4$: The Electronics of an Expanded Metal. *J. Am. Chem. Soc.* **2011**, *133*, 3535−3547.
(17) *Metal-Ammonia Solutions*; Lagowski, J. J., Sienko, M. J., Eds.; Butterworth-Heinemann, 1970.
(18) Ibberson, R. M.; Fowkes, A. J.; Rosseinsky, M. J.; David, W. I. F.; Edwards, P. P. Structure and Phase Behavior of the Expanded-Metal Compound $^7Li(ND_3)_4$. *Angew. Chem., Int. Ed.* **2009**, *48*, 1435−1438.
(19) Seel, A. G.; Zurek, E.; Ramirez-Cuesta, A. J.; Ryan, K. R.; Lodge, M. T. J.; Edwards, P. P. Low Energy Structural Dynamics and Constrained Libration of $Li(NH_3)_4$, The Lowest Melting Point Metal. *Chem. Commun.* **2014**, *50*, 10778−10781.
(20) Hertel, I. V.; Hüglin, C.; Nitsch, C.; Schulz, C. P. Photoionization of $Na(NH_3)_n$ and $Na(H_2O)_n$ Clusters: A Step Towards the Liquid Phase? *Phys. Rev. Lett.* **1991**, *67*, 1767−1770.
(21) Kryzhevoi, N. V.; Tarantelli, F.; Cederbaum, L. S. Tracing Electron Solvation in $Li^-(NH_3)_n$ Clusters with K-Shell Photodetachment Spectroscopy. *Chem. Phys. Lett.* **2015**, *626*, 85−89.
(22) Misaizu, F.; Tsukamoto, K.; Sanekata, M.; Fuke, K. Photoionization of Clusters of Cs Atoms Solvated with H_2O, NH_3 and CH_3CN. *Chem. Phys. Lett.* **1992**, *188*, 241−246.
(23) Steinbach, C.; Buck, U. Ionization Potentials of Large Sodium Doped Ammonia Clusters. *J. Chem. Phys.* **2005**, *122*, 134301.
(24) Takasu, R.; Hashimoto, K.; Fuke, K. Study on Microscopic Solvation Process of Li Atom in Ammonia Clusters: Photoionization and Photoelectron Spectroscopies of $M(NH_3)_n$ (M = Li, Li^-). *Chem. Phys. Lett.* **1996**, *258*, 94−100.
(25) Takasu, R.; Misaizu, F.; Hashimoto, K.; Fuke, K. Microscopic Solvation Process of Alkali Atoms in Finite Clusters: Photoelectron and Photoionization Studies of $M(NH_3)_n$ and $M(H_2O)_n$ (M = Li, Li^-, Na^-). *J. Phys. Chem. A* **1997**, *101*, 3078−3087.
(26) Combellas, C.; Kanoufi, F.; Thiébault, A. Solutions of Solvated Electrons in Liquid Ammonia: Part 1. Chemical Properties of Magnesium Solutions. *J. Electroanal. Chem.* **2001**, *499*, 144−151.
(27) Borodin, A.; Höfft, O.; Kahnert, U.; Kempter, V.; Ferro, Y.; Allouche, A. Electron Solvation by Polar Molecules: The Interaction of Na Atoms with Solid Methanol Films Studied with MIES and Density Functional Theory Calculations. *J. Chem. Phys.* **2004**, *120*, 8692−8697.
(28) Gao, B.; Liu, Z.-F. Ionization Induced Relaxation in Solvation Structure: A Comparison Between $Na(H_2O)_n$ and $Na(NH_3)_n$. *J. Chem. Phys.* **2007**, *126*, 084501.
(29) Hashimoto, K.; Daigoku, K. Formation and Localization of a Solvated Electron in ground and Low-Lying Excited States of $Li(NH_3)_n$ and $Li(H_2O)_n$ Clusters: A Comparison with $Na(NH_3)_n$ and $Na(H_2O)_n$. *Phys. Chem. Chem. Phys.* **2009**, *11*, 9391−9400.
(30) Hashimoto, K.; Daigoku, K. Ground and Low-Lying Excited States of $Na(NH_3)_n$ and $Na(H_2O)_n$ Clusters: Formation and Localization of Solvated Electron. *Chem. Phys. Lett.* **2009**, *469*, 62−67.
(31) Hashimoto, K.; Morokuma, K. Ab *Initio* MO Study of $Na(NH_3)_n$ (n = 1-6) Clusters and Their Ions: A Systematic Comparison with Hydrated Na Clusters. *J. Am. Chem. Soc.* **1995**, *117*, 4151−4159.
(32) Becke, A. D. Density-Functional Thermochemistry. III. The Role of Exact Exchange. *J. Chem. Phys.* **1993**, *98*, 5648−5652.
(33) Lee, C.; Yang, W.; Parr, R. G. Development of the Colle-Salvetti Correlation-Energy Formula Into a Functional of the Electron Density. *Phys. Rev. B: Condens. Matter Mater. Phys.* **1988**, *37*, 785−789.
(34) Dunning, T. H. Gaussian Basis Sets for Use in Correlated Molecular Calculations. I. The Atoms Boron Through Neon and Hydrogen. *J. Chem. Phys.* **1989**, *90*, 1007−1023.
(35) Kendall, R. A.; Dunning, T. H.; Harrison, R. J. Electron Affinities of the First-Row Atoms Revisited. Systematic Basis Sets and Wave Functions. *J. Chem. Phys.* **1992**, *96*, 6796−6806.
(36) Koput, J.; Peterson, K. A. *Ab Initio* Potential Energy Surface and Vibrational-Rotational Energy Levels of $X^2\Sigma^+$ CaOH. *J. Phys. Chem. A* **2002**, *106*, 9595−9599.
(37) Woon, D. E.; Dunning, T. H. Gaussian Basis Sets for Use in Correlated Molecular Calculations. IV. Calculation of Static Electrical Response Properties. *J. Chem. Phys.* **1994**, *100*, 2975−2988.
(38) Ghigo, G.; Roos, B. O.; Malmqvist, P.-Å. A Modified Definition of the Zeroth-Order Hamiltonian in Multiconfigurational Perturbation Theory (CASPT2). *Chem. Phys. Lett.* **2004**, *396*, 142−149.
(39) Roos, B. O.; Andersson, K. Multiconfigurational Perturbation Theory with Level Shift - The Cr_2 Potential Revisited. *Chem. Phys. Lett.* **1995**, *245*, 215−223.
(40) Frisch, M. J.; Trucks, G. W.; Schlegel, H. B.; Scuseria, G. E.; Robb, M. A.; Cheeseman, J. R.; Scalmani, G.; Barone, V.; Petersson, G. A.; Nakatsuji, H.; et al. *Gaussian 16*; Gaussian, Inc.: Wallingford CT, 2016.
(41) Werner, H.-J.; Knowles, P. J.; Knizia, G.; Manby, F. R.; Schütz, M.; Celani, P.; Györffy, W.; Kats, D.; Korona, T.; Lindh, R.; et al. *MOLPRO*, version 2015.1, A Package of Ab Initio Programs, 2015.
(42) Sommerfeld, T.; Dreux, K. M. Characterizing the Excess Electron of $Li(NH_3)_4$. *J. Chem. Phys.* **2012**, *137*, 244302.
(43) *CRC Handbook of Chemistry and Physics*; CRC Press, 2012.
(44) Kramida, A.; Yu, R.; Reader, J.; NIST ASD Team. *NIST Atomic Spectra Database*, (ver. 5.5.2) [online]. Available: https://physics.nist.gov/asd; NIST, (accessed July 9, 2019).

DOI: 10.1021/acs.jpca.9b04966
J. Phys. Chem. A 2019, 123, 6744−6750

Aufbau Principle for Diffuse Electrons of Double–Shell Metal Ammonia Complexes: The Case of $M(NH_3)_4@12NH_3$, M = Li, Be^+, B^{2+}

JPCAFH

JANUARY 23, 2020
VOLUME 124
NUMBER 3
pubs.acs.org/JPCA

THE JOURNAL OF PHYSICAL CHEMISTRY A

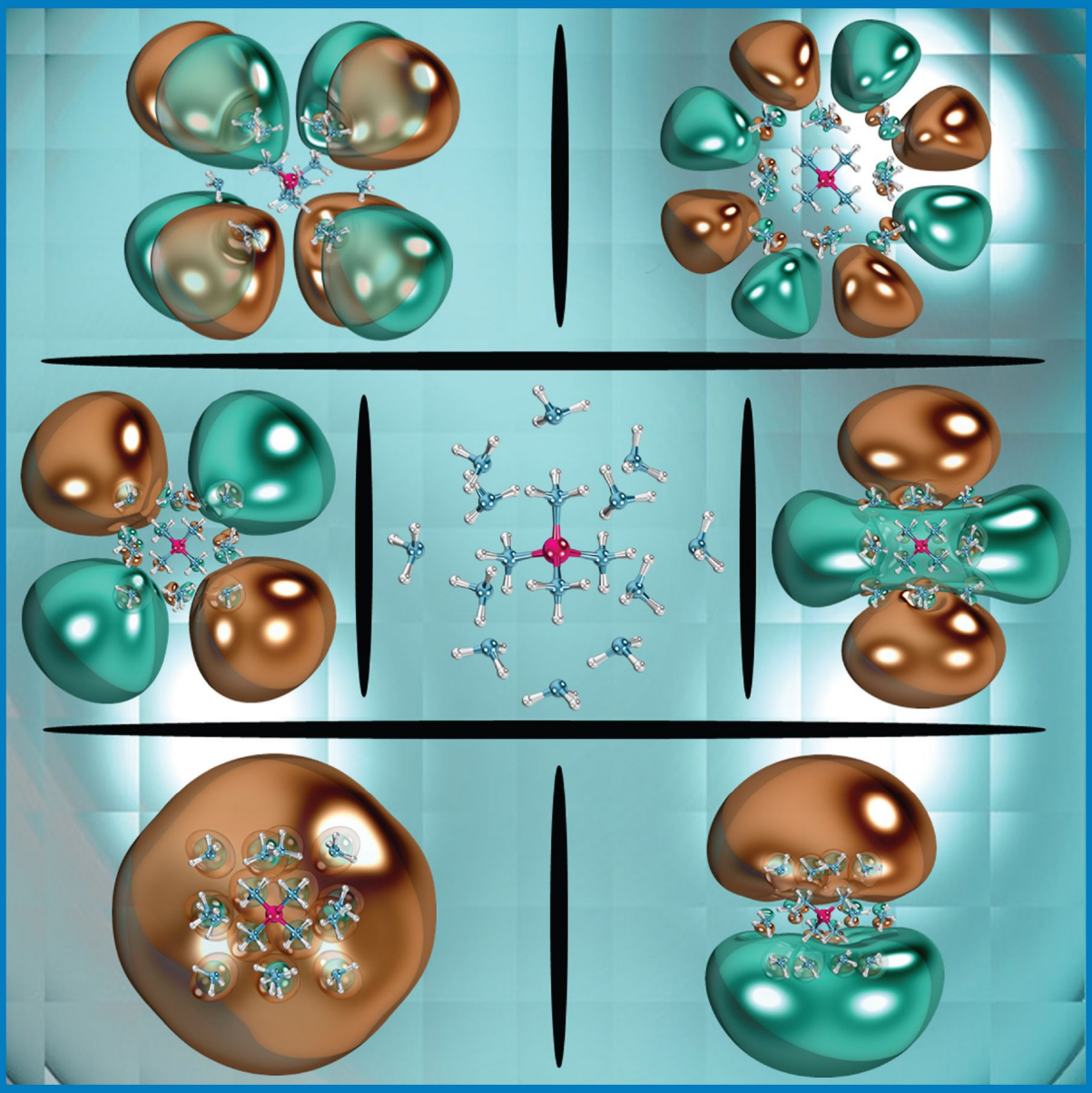

Dual-Solvation-Shell Metal–Ammonia Complexes Act Like Superatoms

ISOLATED MOLECULES, CLUSTERS, RADICALS, AND IONS; ENVIRONMENTAL CHEMISTRY, GEOCHEMISTRY, AND ASTROCHEMISTRY; NEW TOOLS AND METHODS

ACS Publications
Most Trusted. Most Cited. Most Read.

www.acs.org

THE JOURNAL OF PHYSICAL CHEMISTRY A

Article

Cite This: J. Phys. Chem. A 2020, 124, 505−512

pubs.acs.org/JPCA

Aufbau Principle for Diffuse Electrons of Double-Shell Metal Ammonia Complexes: The Case of $M(NH_3)_4@12NH_3$, M = Li, Be^+, B^{2+}

Isuru R. Ariyarathna, Filip Pawłowski,* Joseph Vincent Ortiz, and Evangelos Miliordos*

Department of Chemistry and Biochemistry, Auburn University, Auburn, Alabama 36849-5312, United States

Supporting Information

ABSTRACT: Positively charged or neutral metal ammonia complexes can form molecular species called solvated electron precursors (SEPs) that accommodate peripheral electrons in approximately hydrogenic diffuse orbitals. This work expands the notion of SEPs to metal ammonia complexes wherein a second coordination shell with 12 ammonia molecules is attached to $M(NH_3)_4$ (M = Li, Be^+, B^{2+}) SEPs via hydrogen bonding. In such complexes, denoted $M(NH_3)_4@12NH_3$, the 12 outer ammonia molecules displace the peripheral electrons even further away from the first shell of ammonia molecules. We have benchmarked several density functional methods against CCSD(T) results and found that CAM-B3LYP provides the best $M(NH_3)_4@12NH_3$ structures. The electron attachment energies of the closed-shell cores calculated with electron-propagator methods and the corresponding Dyson orbitals reveal the Aufbau principle for the ground and excited states of $M(NH_3)_4@12NH_3$ to be 1s, 1p, 1d, 1f, 2s, 2p, 1g, 2d. These orbitals are diffuse and delocalized over the periphery of the second solvation shell.

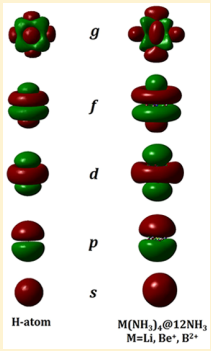

1. INTRODUCTION

A variety of solvent molecules can coordinate to metal atoms, detach their valence electrons, and generate solvated electrons. The first report of this effect dates back to 1807, when Sir Humphry Davy observed "a fine blue color" produced during the interaction of potassium with gaseous ammonia.[1] It was only later in 1916 that Gibson and Argo coined the term "solvated electrons" when they assigned this brilliant blue color to "free" electrons in ammonia.[2] Besides ammonia, water, alcohols, ethers, methylamine, and acetonitrile are also known to solvate electrons.[3−6] The longer lifetime of ammoniated electrons has motivated a plethora of studies on metal ammonia systems in gaseous, solution, and solid states.[7−12] These electrons even suffice to reduce an aromatic ring in a reaction known as the Birch reduction.[13]

Increasing metal concentration in alkali metal ammonia solutions causes a diminution of electrical conductivity due to the production of $M_s^+e_s^-$ ion pairs.[14] Further increasing the metal concentration to 1 mol % results in closer proximity of electrons, facilitating their coupling.[14] Subsequent increases (1 to 8 mol %) yield a bronze-gold metallic solution with delocalized solvated electrons and improved conductivity.[14,15] At ∼21 mol %, the solution is identified as a liquid or expanded metal that possesses the highest possible electrical conductivity.[14] Liquid metals have been mooted as high-temperature superconductors.[10]

We recently introduced a new perspective for neutral or partially oxidized metal ammonia complexes, dubbed solvated electron precursors (SEPs), that consist of a $M(NH_3)_n^{q+}$ core (M = metal) and a number of peripheral electrons. A critical number of ammonia molecules is necessary to displace the valence electrons of a metal.[16,17] Our first reported SEP was $Be(NH_3)_4$, which can be seen as a tetrahedral $Be(NH_3)_4^{2+}$ core surrounded by two electrons.[16] We discovered that the pseudospherical s-type orbital that extends over the whole complex (and is therefore termed superatomic) hosts two exterior electrons in the ground state and is followed by higher angular momentum (i.e., p-, d-, or f-shaped) superatomic orbitals that are populated in low-lying electronic states. On the basis of the excitation energies of the single peripheral electron system $Be(NH_3)_4^+$, we disclosed the Aufbau principle for SEPs, which reads 1s, 1p, 1d, 2s, 1f, 2p.[16] This orbital series resembles those of nuclear shell or jellium models. As electrons are added in the sequence $Be(NH_3)_4^{2+}$, $Be(NH_3)_4^+$, $Be(NH_3)_4$, and $Be(NH_3)_4^-$, the Be−N distances shorten and the N−H distances lengthen gradually in the ground states.

The two isovalent SEPs $Li(NH_3)_4$ and $Na(NH_3)_4$ have a single outer electron,[18] while the species $Ca(NH_3)_6$, $Ca(NH_3)_7$, and $Ca(NH_3)_8$ were all identified as SEPs with two outer electrons.[19] As the number of ammonia molecules bound to Ca increases by one, the first excitation energy drops only by ∼0.02 eV. Very recently, the largest one, $Ca(NH_3)_8$, has also been identified spectroscopically.[9] Transition metal ammonia complexes were also shown to form SEPs:[20] $V(NH_3)_6$ bears a $V(NH_3)_6^{2+}$ core and two outer electrons that are spin-coupled only weakly to the inner 3d electrons of vanadium. The outer 1s orbital was shown to be more diffuse than the 4s atomic orbital of vanadium. On the other hand, the second-row transition metal yttrium allows the "solvation" of all three valence electrons on the periphery of the $Y(NH_3)_8^{3+}$ skeleton.[21]

Received: August 13, 2019
Revised: October 12, 2019
Published: October 22, 2019

DOI: 10.1021/acs.jpca.9b07734
J. Phys. Chem. A 2020, 124, 505−512

Metal aqua complexes also behave as SEPs,[22−26] although they are less stable and tend to release hydrogen, depleting the system of outer electrons. For example, $Mg(H_2O)_6^+$ has one outer electron, and its high symmetry (D_{2h}) permitted us to expand the previously introduced Aufbau principle for SEPs beyond the 2d level. The observed shell model for this complex is 1s, 1p, 1d, 2s, 2p, 1f, 2d, 3s, 1g.[27]

According to mass spectra for n = 6−14, the $Mg(H_2O)_n^+$ structure is less favorable than the $MgOH^+(H_2O)_{n-1}$ structure, where a hydrogen atom is released and no solvated electrons are present.[23,28] However, for larger n values (n = 15−20), the $Mg^+(H_2O)_n$ structure becomes more stable.[23,28] Density functional theory (DFT) calculations on $Mg(H_2O)_n^+$ (n = 20−60) species studied by the Beyer group suggest that the valence electron of Mg^+ migrates further from $Mg(H_2O)_6^{2+}$.[29] Bigger clusters for $Na(H_2O)_n$ (n < 32),[30,31] $Al^+(H_2O)_n$ (n > 38),[32] and $M^+(H_2O)_n$ (n < 41; M = V, Cr, Mn, Fe, Co, Ni, Cu, Zn)[33,34] were also found in the literature. These results demonstrate that the stability of solvated electrons is recovered with a sufficiently large number of solvent molecules.

To our knowledge, the only report of metal ammonia systems with two coordination shells is that by Zurek, Edwards, and Hoffman.[14] They focused on the ground state of $Li(NH_3)_4@12NH_3$ and found that the valence electron is forced to move further from Li^+ beyond the first shell of ammonia molecules. A naturally emerging question is how the second solvation shell affects the electronic structure of the system. Specifically, do dual-layer SEPs possess similar types of superatomic s, p, d, etc. orbitals and what is their Aufbau principle? In an attempt to address these questions, in the present work we performed high-level excited-state calculations on the isoelectronic systems $M(NH_3)_4@12NH_3$ (M = Li, Be^+, B^{2+}).

2. COMPUTATIONAL DETAILS

The geometries of $M(NH_3)_4@12NH_3$ (M = Li, Be^+, B^{2+}) species are sensitive to three factors: (1) the correct description of the outer diffuse electron density, (2) the electrostatic potential of the complex experienced by the peripheral electrons, and (3) the hydrogen-bonding network. Therefore, we employed the $[Be(NH_3)_4]^{0,+,2+}$ and $(NH_3)_2$ systems to assess the ability of different methodologies to describe these effects. The reference structures of $[Be(NH_3)_4]^{0,+,2+}$ and $(NH_3)_2$ were obtained at the most reliable, but tractable, level of theory, namely, coupled-cluster singles, doubles, and perturbative triples [CCSD(T)][35] with the aug-cc-pVTZ[36−38] correlation-consistent basis set on all atoms. Møller−Plesset second-order perturbation theory (MP2)[39] and DFT structures were benchmarked against CCSD(T). The CAM-B3LYP,[40] B97D3,[41] B3LYP-D3,[42] CAM-B3LYP-D3,[40,42] LC-wPBE-D3,[42,43] wB97XD,[44] B3LYP,[45−48] LC-wPBE,[43] and M06-2X[49] density functionals were probed. CAM-B3LYP gave structures that were the most consistent with CCSD(T), and therefore, $M(NH_3)_4@12NH_3$ (M = $Li^{+,0,-}$, $Be^{2+,+,0}$, $B^{3+,2+,+}$) species were optimized with CAM-B3LYP/aug-cc-pVTZ. To render our calculations manageable, a high-symmetry arrangement (T point group) was imposed while expanding the T_d structure of the $M(NH_3)_4$ core. In this structure, the ammonia molecules of the second shell form hydrogen bonds only with first-shell ammonias and not with their peers. CAM-B3LYP geometries were used to perform single-point MP2/aug-cc-pVTZ calculations and obtain ionization energies and electron affinities. Unrestricted Hartree−Fock spin contamination for these open-shell systems was minor (∼0.0003).

Excited-state calculations were performed using the CAM-B3LYP geometries and exploiting the largest Abelian subgroup, D_2. To this end, we used the complete-active-space self-consistent field (CASSCF) and quasiparticle electron propagator theory (EPT) methods: Koopmans's theorem (KT),[50] diagonal second-order (D2),[51] and renormalized partial third-order (P3+).[52−54]

For calculations on excited states, various basis sets were employed. Since the correct description of the outer electronic density is more important and the contribution of the inner electrons to the electronic excitations is minor, we decided to employ plain basis sets for all of the inner atomic centers and diffuse sets for the outer 36 hydrogen atoms. Specifically, the following combinations were applied: cc-pVDZ/d-aug-cc-pVDZ, cc-pVDZ/t-aug-cc-pVDZ, and cc-pVTZ/d-aug-cc-pVTZ, denoted as dadz, tadz, and datz, respectively.

The CASSCF wave function consists of one electron in 20 (five a, five b_3, five b_2, and five b_1) active orbitals. These 20 active orbitals represent the 1s-, 1p-, 1d-, 1f-, 2s-, and 2p-type orbitals. Vertical electron attachment energies to $M(NH_3)_4@12NH_3$ (M = Li^+, Be^{2+}, B^{3+}) were calculated with the hierarchy of the EPT methods (KT, D2, and P3+), and excitation energies for M = Li, Be^+, B^{2+} were inferred from the differences of the electron attachment energies. The KT and D2 vertical electron binding energies (ω) were calculated with the datz basis, while the P3+/datz ones were estimated from the D2/datz, D2/dadz, and P3+/dadz results as

$$\omega(\text{P3+/datz}) \approx \omega(\text{P3+/dadz}) + [\omega(\text{D2/datz}) - \omega(\text{D2/dadz})] \quad (1)$$

The results of this composite P3+ method are denoted as cP3+/datz.

Geometry optimizations and EPT calculations were carried out using the Gaussian 16 package,[55] and CASSCF excited-state calculations were performed with MOLPRO 2015.1.[56] Plots of Dyson orbitals were obtained using Molden[57] and GaussView.[58]

3. RESULTS AND DISCUSSION

3.1. Ground-State Properties. For the structures considered in this paper, the tetrahedral $M(NH_3)_4$ core accommodates 12 ammonia molecules attached via hydrogen bonds (see Figure 1a). Geometry optimization at the highly accurate CCSD(T) level for the substantially large $M(NH_3)_4@12NH_3$ system is nearly an impossible task, and MP2 geometry optimizations were also found to be computationally demanding. In this regard, we decided to identify a suitable density functional method that can accurately describe the $M(NH_3)_4@12NH_3$ system.

$[Be(NH_3)_4]^{0,+,2+}$ and $(NH_3)_2$, with their diffuse outer electrons and hydrogen-bonding interactions, served as our reference models. Parameters optimized with various methods are listed in Table 1. Reference data are given for CCSD(T), whereas deviations from these values are reported for the rest of the methods.

MP2 is in excellent agreement with CCSD(T) in all instances. Among the functionals, only CAM-B3LYP has comparable accuracy: all of the bond lengths differ by less than 0.01 Å, and φ_{hb} deviates by 0.2°. The rest of the functionals are less accurate in reproducing the structures of either the

DOI: 10.1021/acs.jpca.9b07734
J. Phys. Chem. A 2020, 124, 505−512

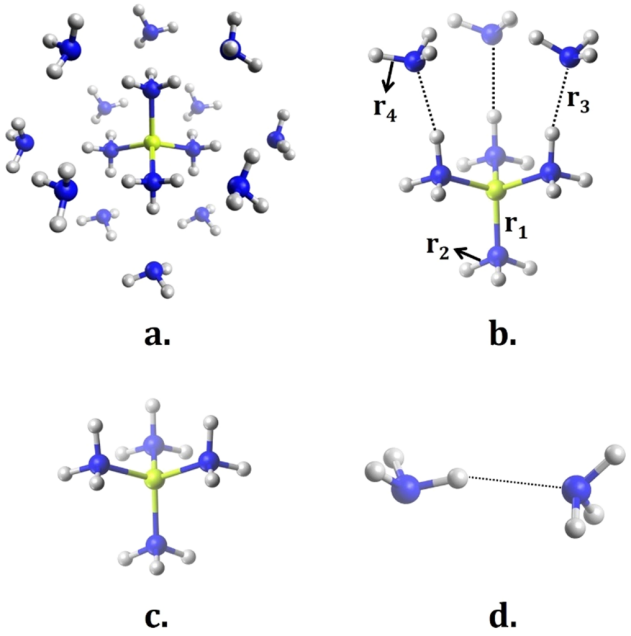

Figure 1. (a) Arrangement of 12 NH_3 molecules around $Be(NH_3)_4^+$. (b) Hydrogen bonds (black dashed lines) between the inner $Be(NH_3)_4^+$ complex and outer NH_3 molecules (for clarity, only three outer NH_3 molecules are displayed). (c) Tetrahedral geometry of $Be(NH_3)_4^+$. (d) Test structure of the $(NH_3)_2$ dimer.

hydrogen-bonding interaction or the chemically bound metal ammonia complexes. The CAM-B3LYP/aug-cc-pVTZ optimal geometrical parameters for $M(NH_3)_4@12NH_3$ are given in Table 2, and the Cartesian coordinates are reported in Tables S14−S16 in the Supporting Information. The M−N distances of the $Be(NH_3)_4@12NH_3^+$ system are 0.003 Å shorter than those of $Be(NH_3)_4^+$, indicating that the latter remains practically intact when the second solvation shell is added.

Table 2 also reports relative energies (ΔE) inferred from the MP2/aug-cc-pVTZ energy calculations along with the corresponding vertical electron binding energies (VEBE) calculated directly as electron propagator poles with cP3+/datz (see Table S13). The discrepancies between the MP2 ΔE values and the cP3+ VEBE values in Table 2 are much smaller than 0.1 eV (except for $Li(NH_3)_4@12NH_3^-$), indicating that second-order perturbation theory is a good approximation for the studied cases. The largest difference (0.1 eV) is encountered for the electron detachment energy from $Li(NH_3)_4@12NH_3^-$. Because of its anionic character, this system is the most demanding with respect to the need for diffuse functions in the basis set. The MP2 calculations used the aug-cc-pVTZ basis, whereas the cP3+ calculations employed a doubly diffuse set on the outer hydrogens. Additional calculations of the vertical electron detachment energy (VEDE) from $Li(NH_3)_4@12NH_3^-$ with D2/tadz (0.33 eV) indicated that the corresponding basis with a doubly diffuse set (D2/dadz VEDE of 0.30 eV) is practically saturated and that the datz set (D2/datz VEDE of 0.33 eV) used to produce the cP3+ results presented in Table 2 has the same effect as tadz. These observations substantiate the necessity of using a doubly diffuse set when diffuse electrons are present.

The ionization energy (IE) and electron affinity (EA) of $Li(NH_3)_4$ are 2.92 and 0.45 eV at the CCSD(T) level of theory.[18] The corresponding experimental values are 3.025[59] and 0.45 eV.[60] According to the cP3+/datz results in Table 2, the layer of 12 ammonia molecules around $Li(NH_3)_4$ leads to IE and EA values that are decreased by 1.21 and 0.13 eV, respectively, compared with the CCSD(T) results for $Li(NH_3)_4$. For $Be(NH_3)_4$, the CCSD(T) first and second IEs are 3.91 and 11.23 eV,[16,18] and the second shell of NH_3 lowers the first and second IEs of $Be(NH_3)_4$ to 2.40 and 6.68 eV, respectively.

In all cases, adding one electron to $M(NH_3)_4@12NH_3$ (M = Li^+, Be^{2+}, B^{3+}) makes the M−N distances shorter by ∼0.004 Å. Adding a second electron leads to an additional shortening by ∼0.002 Å. The corresponding values pertaining to adding electrons to $Be(NH_3)_4^{2+}$ are ∼0.02 and ∼0.008 Å, respectively, as revealed by CCSD(T) calculations.[16] It should be noted that the H···N distances become shorter as well by 0.03, 0.02, and 0.01 Å for $Li^+ \rightarrow Li$, $Be^{2+} \rightarrow Be^+$, and $B^{3+} \rightarrow B^{2+}$, respectively.

The N−H bonds in the outer NH_3 molecules are longer for the more electron-rich $M(NH_3)_4$ species. The CAM-B3LYP-optimized Be−N distances of $Be(NH_3)_4^{2+,+,0}$ are 1.758, 1.734, and 1.725 Å, respectively (see Table 1). In the $Be(NH_3)_4@12NH_3^+$ and $Be(NH_3)_4@12NH_3$ cases, the Be−N distances

Table 1. CCSD(T)-Optimized Parameters for $(NH_3)_2$ and $Be(NH_3)_4^{0/+/2+}$ and Deviations from the CCSD(T) Values for Other Methodologies[a]

	$NH_3\cdots NH_3$		$Be(NH_3)_4$		$Be(NH_3)_4^+$		$Be(NH_3)_4^{2+}$	
method	r_{hb} (Å)[b]	φ_{hb} (deg)[c]	r_{BeN} (Å)[d]	r_{NH} (Å)[e]	r_{BeN} (Å)[d]	r_{NH} (Å)[e]	r_{BeN} (Å)[d]	r_{NH} (Å)[e]
CCSD(T)	2.281	162.7	1.733	1.030	1.741	1.027	1.764	1.023
MP2	−0.006	−0.1	−0.002	−0.001	0.001	−0.001	0.000	−0.002
CAM-B3LYP	−0.007	0.2	−0.008	−0.002	−0.007	−0.002	−0.006	−0.003
B97D3	0.009	0.1	0.012	0.004	0.013	0.004	0.015	0.000
B3LYP-D3	−0.013	0.1	0.002	0.000	0.004	0.000	0.005	−0.001
CAM-B3LYP-D3	−0.035	0.1	−0.009	−0.002	−0.007	−0.002	−0.006	−0.002
LC-wPBE-D3	0.016	1.0	−0.004	−0.004	−0.003	−0.003	−0.003	−0.003
wB97XD	−0.031	2.7	−0.003	−0.003	0.000	−0.002	0.003	−0.004
B3LYP	0.036	3.4	0.002	0.000	0.003	0.000	0.003	−0.001
LC-wPBE	0.054	4.6	−0.004	−0.005	−0.003	−0.003	−0.003	−0.003
M06-2X	−0.001	−19.4	−0.013	−0.001	−0.012	0.000	−0.012	−0.001

[a]The aug-cc-pVTZ basis set was used for all of the methods. [b]r_{hb} is the N···H distance between the N and H atoms that are hydrogen-bonded; see Figure 1d. [c]φ_{hb} is the N−H···N angle that involves the two N atoms and the bridging H atom; see Figure 1d. [d]r_{BeN} is the bond length for each of the four equivalent Be−N bonds; see Figure 1c. [e]r_{NH} is the bond length for each of the 12 equivalent N−H bonds; see Figure 1c.

DOI: 10.1021/acs.jpca.9b07734
J. Phys. Chem. A 2020, 124, 505−512

Table 2. Relative Energies (ΔE, in eV) Obtained with MP2/aug-cc-pVTZ, Optimized Bond Distances (in Å; See Figure 1) of Neutral and Charged $M(NH_3)_4@12NH_3$ (M = Li, Be, B) Species Obtained with CAM-B3LYP/aug-cc-pVTZ, and Negatives of the Vertical Electron Binding Energies (−VEBE, in eV) Obtained Directly as Electron Propagator Poles with cP3+/datz (see Equation 1 and Table S13)

			bond distances			
species	ΔE (MP2)	−VEBE (cP3+)	r_1(M−N)[a]	r_2(N−H)[b]	r_3(H···N)[c]	r_4(N−H)[d]
$Li(NH_3)_4@12NH_3^+$	1.74	1.71	2.094	1.018	2.397	1.012
$Li(NH_3)_4@12NH_3$	0.00		2.087	1.017	2.366	1.012
$Li(NH_3)_4@12NH_3^-$	−0.22	0.32[e]	2.085	1.017	2.361	1.013
$Be(NH_3)_4@12NH_3^{2+}$	6.70	6.68	1.736	1.027	2.160	1.013
$Be(NH_3)_4@12NH_3^+$	2.40	2.40	1.731	1.027	2.139	1.014
$Be(NH_3)_4@12NH_3$	0.00		1.729	1.027	2.125	1.015
$B(NH_3)_4@12NH_3^{3+}$	12.27	12.18	1.562	1.046	1.958	1.015
$B(NH_3)_4@12NH_3^{2+}$	5.04	4.98	1.558	1.045	1.948	1.016
$B(NH_3)_4@12NH_3^+$	0.00		1.555	1.044	1.935	1.017

[a] r_1(M−N) is the M−N bond length for each of the four equivalent M−N bonds; see Figure 1b. [b] r_2(N−H) is the bond length for each of the 12 equivalent inner N−H bonds; see Figure 1b. [c] r_3(H···N) is the length of the hydrogen bond between the H atom of an inner ammonia molecule and the N atom of an outer ammonia molecule; see Figure 1b. [d] r_4(N−H) is the N−H bond distance in the outer NH_3 molecules; see Figure 1b. [e] Calculated directly as a vertical electron detachment energy from $Li(NH_3)_4@12NH_3^-$, hence the sign difference compared with the MP2 ΔE value.

Table 3. Fifteen Lowest Vertical Excitation Energies (in eV) for $Li(NH_3)_4@12NH_3$ at the CASSCF, KT, D2, and P3+ Levels of Theory with the dadz and datz Basis Sets; The States Are Ordered According to the cP3+/datz Excitation Energies and Collected into Quasi-degenerate Superatomic Shells

	dadz[a]				datz[b]			
neutral final state	CASSCF	KT	D2	P3+	KT	D2	cP3+[c]	quasi-degenerate superatomic shell
1^2A	0.000	0.000	0.000	0.000	0.000	0.000	0.000	1^2S
1^2T	0.161	0.162	0.222	0.224	0.161	0.228	0.230	1^2P
1^2E	0.405	0.404	0.540	0.547	0.399	0.554	0.561	1^2D
2^2T	0.422	0.419	0.546	0.552	0.414	0.559	0.565	1^2D
2^2A	0.701	0.699	0.859	0.867	0.679	0.861	0.869	1^2F
3^2T	0.701	0.699	0.874	0.882	0.685	0.883	0.891	1^2F
4^2T	0.694	0.693	0.872	0.881	0.678	0.883	0.892	1^2F
3^2A	0.955	0.956	0.965	0.969	0.860	0.898	0.902	2^2S
5^2T	0.945	0.944	1.082	1.090	0.886	1.021	1.029	2^2P
6^2T		1.118	1.208	1.214	1.051	1.193	1.199	1^2G
7^2T		0.992	1.199	1.210	0.959	1.193	1.204	1^2G
2^2E		0.995	1.201	1.212	0.962	1.194	1.205	1^2G
4^2A		1.059	1.260	1.271	1.005	1.235	1.246	1^2G
8^2T		1.169	1.296	1.304	1.077	1.222	1.230	2^2D
3^2E		1.150	1.289	1.298	1.064	1.225	1.234	2^2D

[a] cc-pVDZ on all inner atoms and d-aug-cc-pVDZ on the 36 external hydrogens. [b] cc-pVTZ on all inner atoms and d-aug-cc-pVTZ on the 36 external hydrogens. [c] Composite P3+ approach defined by eq 1.

vary only within 0.004 Å compared to their first-shell SEPs, but $Be(NH_3)_4@12NH_3^{2+}$ has Be−N distances that are 0.02 Å longer than those of $Be(NH_3)_4^{2+}$ at the CAM-B3LYP level of theory.

3.2. Excited States of $M(NH_3)_4@12NH_3$ (M = Li, Be^+, B^{2+}). CASSCF/dadz excitation energies for $M(NH_3)_4@12NH_3$ (M = Li, Be^+, B^{2+}) are presented in the second columns in Tables 3−5. The dadz basis comprises 766 basis functions, making dynamic electron correlation calculations based on the CASSCF reference nearly an impossible task. Therefore, to describe dynamic electron correlation contributions to the excitation energies, we employed EPT methods and carried out vertical electron attachment energy calculations for $M(NH_3)_4@12NH_3$ (M = Li^+, Be^{2+}, B^{3+}) with the KT, D2 and P3+ methods using the dadz basis set (the electron attachment energies are reported in Tables S1, S5, and S9). The excitation energies for M = Li, Be^+, and B^{2+} were inferred from the differences of the electron attachment energies (Tables 3−5). We initially note that all of the pole strengths related to the electron attachment energies are 0.97 or higher, which is far above the limiting value of 0.85 and therefore substantiates the applicability of the employed quasiparticle EPT methods.

For the KT and D2 calculations, we were also able to use the datz basis set. This basis set, which comprises 1806 basis functions, is expected to provide the same results as the tadz basis, as shown for $Li(NH_3)_4@12NH_3^-$ in section 3.1, and thus should be practically saturated. The KT and D2 vertical electron attachment energies obtained with the datz basis set are reported in Tables S3, S7, and S11 (again, pole strengths above 0.97 should be noted), and the excitation energies inferred from them are collected in Tables 3−5.

The differences between the P3+/dadz and D2/dadz excitation energies are 0.01 eV or smaller (see Tables 3−5),

DOI: 10.1021/acs.jpca.9b07734
J. Phys. Chem. A 2020, 124, 505−512

Table 4. Fifteen Lowest Vertical Excitation Energies (in eV) for $[Be(NH_3)_4@12NH_3]^+$ at the CASSCF, KT, D2, and P3+ Levels of Theory with the dadz and datz Basis Sets; The States Are Ordered According to the cP3+/datz Excitation Energies and Collected into Quasi-degenerate Superatomic Shells

	dadz[a]				datz[b]			
cation final state	CASSCF	KT	D2	P3+	KT	D2	cP3+[c]	quasi-degenerate superatomic shell
1^2A	0.000	0.000	0.000	0.000	0.000	0.000	0.000	1^2S
1^2T	0.303	0.305	0.407	0.406	0.304	0.416	0.415	1^2P
1^2E	0.724	0.718	0.959	0.960	0.718	0.985	0.986	1^2D
2^2T	0.781	0.769	0.985	0.985	0.768	1.007	1.007	1^2D
3^2T	1.206	1.200	1.527	1.530	1.201	1.563	1.566	1^2F
2^2A	1.244	1.233	1.563	1.566	1.236	1.601	1.604	1^2F
4^2T	1.275	1.263	1.577	1.579	1.262	1.609	1.611	1^2F
3^2A	1.389	1.384	1.645	1.658	1.365	1.668	1.681	2^2S
5^2T	1.566	1.562	1.848	1.860	1.545	1.877	1.889	2^2P
4^2A		1.704	2.046	2.051	1.693	2.077	2.082	1^2G
2^2E		1.740	2.127	2.135	1.734	2.158	2.166	1^2G
6^2T		1.736	2.124	2.130	1.739	2.171	2.177	1^2G
7^2T		1.725	2.125	2.133	1.729	2.175	2.183	1^2G
8^2T		1.865	2.183	2.193	1.833	2.208	2.218	2^2D
3^2E		1.830	2.193	2.203	1.815	2.239	2.249	2^2D

[a]cc-pVDZ on all inner atoms and d-aug-cc-pVDZ on the 36 external hydrogens. [b]cc-pVTZ on all inner atoms and d-aug-cc-pVTZ on the 36 external hydrogens. [c]Composite P3+ approach defined by eq 1.

Table 5. Fifteen Lowest Vertical Excitation Energies (in eV) for $[B(NH_3)_4@12NH_3]^{2+}$ at the CASSCF, KT, D2, and P3+ Levels of Theory with the dadz and datz Basis Sets; The States Are Ordered According to the cP3+/datz Excitation Energies and Collected into Quasi-degenerate Superatomic Shells

	dadz[a]				datz[b]			
dication final state	CASSCF	KT	D2	P3+	KT	D2	cP3+[c]	quasi-degenerate superatomic shell
1^2A	0.000	0.000	0.000	0.000	0.000	0.000	0.000	1^2S
1^2T	0.446	0.448	0.578	0.570	0.445	0.589	0.581	1^2P
1^2E	1.025	1.012	1.313	1.304	1.009	1.341	1.332	1^2D
2^2T	1.137	1.110	1.368	1.357	1.103	1.389	1.378	1^2D
3^2T	1.675	1.660	2.063	2.052	1.653	2.093	2.082	1^2F
4^2T	1.838	1.809	2.193	2.179	1.801	2.224	2.210	1^2F
2^2A	1.786	1.761	2.182	2.172	1.754	2.225	2.215	1^2F
3^2A	1.966	1.960	2.265	2.276	1.942	2.215	2.226	2^2S
5^2T	2.325	2.317	2.714	2.721	2.311	2.732	2.739	2^2P
4^2A		2.217	2.543	2.543	2.210	2.552	2.552	1^2G
6^2T		2.421	2.890	2.878	2.413	2.926	2.914	1^2G
7^2T		2.445	2.957	2.946	2.438	3.002	2.991	1^2G
2^2E		2.491	2.970	2.965	2.486	2.999	2.994	1^2G
3^2E		2.681	3.142	3.141	2.681	3.166	3.165	2^2D
8^2T		2.777	3.217	3.220	2.771	3.238	3.241	2^2D

[a]cc-pVDZ on all inner atoms and d-aug-cc-pVDZ on the 36 external hydrogens. [b]cc-pVTZ on all inner atoms and d-aug-cc-pVTZ on the 36 external hydrogens. [c]Composite P3+ approach defined by eq 1.

indicating that second-order perturbation theory captures the majority of the correlation effects for the diffuse excited states considered here. Furthermore, the small difference between the P3+/dadz and D2/dadz results substantiates the use of the cP3+/datz composite model introduced in section 2 for estimating P3+/datz excitation energies (see eq 1). The cP3+/datz excitation energies are our best estimate and are reported in the eighth columns of Tables 3−5. In addition, these tables display the symmetry label of each state and group the individual states into quasi-degenerate superatomic shells. This grouping is based on the energy and symmetry of the individual states and on the shapes of the Dyson orbitals corresponding to these states. Some examples of Dyson orbitals for $Be(NH_3)_4@12NH_3^{2+}$ are shown in Table 6 and compared to orbitals of the hydrogen atom obtained using the d-aug-cc-pV6Z basis in D_{2h} computational symmetry. Table 6 leaves no doubts about the assignment of individual P3+ states for $Be(NH_3)_4@12NH_3^{2+}$ to a given superatomic shell. The Dyson orbitals for electron attachment to $Li(NH_3)_4@12NH_3^+$ and $B(NH_3)_4@12NH_3^{3+}$ look the same.

The CASSCF/dadz excitation energies in Tables 3−5 should be compared against those obtained from Koopmans's theorem (KT/dadz values are presented in the third columns of Tables 3−5). The differences are very small, in particular much smaller than the differences between the KT/dadz and D2/dadz results (see Tables 3−5). This indicates that all of the considered systems have single-configuration character and that the orbital relaxation effects are smaller than the electron correlation effects.

DOI: 10.1021/acs.jpca.9b07734
J. Phys. Chem. A 2020, 124, 505−512

Table 6. Representative Superatomic Dyson Orbitals for Vertical Electron Attachment to $Be(NH_3)_4@12NH_3^{2+}$ (D_2 Computational Symmetry and the dadz Basis Set) and Corresponding cP3+/datz Excitation Energies (in eV; see Table 4) versus the Dyson orbitals for the Hydrogen Atom (D_{2h} Computational Symmetry and the d-aug-cc-pV6Z Basis Set)[a]

$Be(NH_3)_4@12NH_3^{2+}$		H		$Be(NH_3)_4@12NH_3^{2+}$		H	
				1^2F 1.566	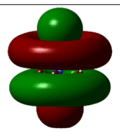	4f	
1^2S 0.000		1s		1^2F 1.611	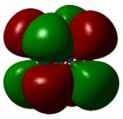	4f	
1^2P 0.415	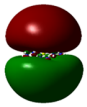	2p		1^2G 2.082	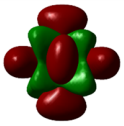	5g	
1^2D 0.986	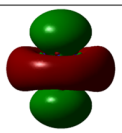	3d		1^2G 2.177	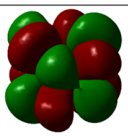	5g	
1^2D 1.007	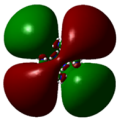	3d		1^2G 2.183	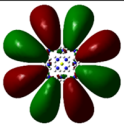	5g	

[a]An isovalue of 0.02 was used for all of the plots. The Dyson orbitals for $Li(NH_3)_4@12NH_3^{+}$ and $B(NH_3)_4@12NH_3^{3+}$ have identical shapes. The change from dadz to datz did not influence the qualitative features of the orbitals.

In several cases (e.g., the 3^2A and 5^2T states of $Li(NH_3)_4@12NH_3$; see Table 3), the energetic order of states calculated with CASSCF/dadz is different from that obtained with cP3+/datz. At the same time, KT/dadz, KT/datz, D2/dadz, and even P3+/dadz sometimes have a different ordering of states than D2/datz and cP3+/datz (see Tables 3−5). The components of the 1^2G shell for $Be(NH_3)_4@12NH_3^{+}$ constitute a good example (Table 4). The proper ordering of states thus requires not only a description of electron correlation but also a basis set of at least triple-ζ quality combined with a doubly diffuse set. Since the CASSCF calculations were possible for just a few of the lowest states and that only in the dadz basis, the D2/datz level of theory emerges as a particularly attractive tool for capturing a majority of orbital relaxation and electron correlation effects for systems such as those considered here, especially in light of the low arithmetic scaling of the D2 method (N^3, where N is the number of basis functions) and its recent efficient implementations.[55]

The cP3+/datz results in Tables 3−5 imply the following Aufbau principle for the diffuse electrons of the present second-solvation-shell complexes: 1s, 1p, 1d, 1f, 2s, 2p, 1g, 2d. Compared with that for the first solvation shell analogues (e.g., for $Be(NH_3)_4^{+}$, we found the Aufbau principle 1s, 1p, 1d, 2s, 1f, 2p, 2d),[16] the Aufbau principle reported here is slightly different and contains a new qualitative feature: the g shell. For the present second-solvation-shell complexes, the 1g shell occurs before the 2d shell, contrary to results for the single-solvation-shell complex $Mg(H_2O)_6^{+}$.[27] It should be noted that particularly for higher-lying states, components of neighboring shells interleave with each other, e.g., the energetically highest component of the 1^2G shell of $Li(NH_3)_4@12NH_3$ has an excitation energy above the components of the 2^2D shell. Similarly, the 2^2P shell of $B(NH_3)_4@12NH_3^{2+}$ lies energetically higher than the lowest component of the 1^2G shell. Such interleaving has been observed previously. For example, in our recent study of the $V(NH_3)_6^{+}$ complex, the $2^{3,5}S$ shells were higher in energy than the lowest component of the $1^{3,5}F$ shell.[20]

Let us finally consider the trends of the excitation energies as we move from lithium to beryllium to boron, where the central cations are Li^+, Be^{2+}, and B^{3+}, respectively. The highest charge results in the contraction of the metal−ammonia sphere. Both the metal−ammonia r_1(M−N) and hydrogen bond r_3(H···N) distances shorten in going from Li^+ to Be^{2+} and B^{3+} by approximately 0.2 Å (see Figure 1 and Table 2). The smaller size of the complex (and thus the smaller radius of the diffuse outer orbitals) and the higher central charge act synergistically in increasing the excitation energies by factors of ∼1.8 ($Li^+ \rightarrow Be^{2+}$) and ∼1.4 ($Be^{2+} \rightarrow B^{3+}$). The increase in the excitation energies due to the smaller size and higher charge can be rationalized by invoking the particle on a sphere and hydrogenic models. The former model can account for the decrease in the excitation energies by a factor of about 3 for the

DOI: 10.1021/acs.jpca.9b07734
J. Phys. Chem. A 2020, 124, 505−512

lowest-lying states when the second shell is added to $Li(NH_3)_4$ and $Be(NH_3)_4^+$.[16,18]

4. CONCLUSIONS

The present study focuses on the effect of the second solvation shell on the structural and electronic properties of metal ammonia solvated electron precursors. Specifically, the lithium, beryllium, and boron nuclei were employed to construct the $M(NH_3)_4@12NH_3$ complexes (M = Li, Be^+, B^{2+}). In their ground states, the Li^+, Be^{2+}, and B^{3+} cores accommodate two coordination shells and one diffuse peripheral electron occupying a 1s-type superatomic orbital. Among several functionals, CAM-B3LYP was identified to best describe the geometry of metal ammonia species, accounting properly for the hydrogen-bonding and other electrostatic interactions. The large number of correlated electrons was treated efficiently by means of electron propagator methods, such as D2 and P3+. We were able to calculate excitation energies of 15 energy levels associated with s-, p-, d-, f-, and g-type superatomic shells. The observed Aufbau principle is 1s, 1p, 1d, 1f, 2s, 2p, 1g, 2d. The excitation energies increase in going from lithium to boron but decrease in going from the single-shell to double-shell metal ammonia complexes. Besides the chemical insights for the systems presented here, our results are expected to serve as benchmark data for other methodologies targeting the calculation of accurate excitation energies on these large systems.

■ ASSOCIATED CONTENT

Supporting Information

The Supporting Information is available free of charge on the ACS Publications website at DOI: 10.1021/acs.jpca.9b07734.

Electron propagator results for $Li(NH_3)_4@12(NH_3)$, $Be(NH_3)_4@12(NH_3)^+$, and $B(NH_3)_4@12(NH_3)^{2+}$; lowest vertical electron attachment and detachment energies for the studied species; and Cartesian coordinates for the studied species (PDF)

■ AUTHOR INFORMATION

Corresponding Authors

*E-mail: emiliord@auburn.edu.
*E-mail: flp0008@auburn.edu.

ORCID

Isuru R. Ariyarathna: 0000-0002-5259-4248
Filip Pawłowski: 0000-0002-5928-2140
Joseph Vincent Ortiz: 0000-0002-9277-0226
Evangelos Miliordos: 0000-0003-3471-7133

Notes

The authors declare no competing financial interest.

■ ACKNOWLEDGMENTS

The National Science Foundation supported this work through Grant CHE-1565760 to Auburn University. We thank Dr. M. Díaz-Tinoco (Auburn University) for technical advice on plotting Dyson orbitals. This work was completed with resources provided in part by the Auburn University Hopper Cluster, in part by the Alabama Supercomputer Authority (ASA), and in part by the National Energy Research Scientific Computing Center (NERSC), a U.S. Department of Energy Office of Science User Facility operated under Contract DE-AC02-05CH11231. Technical support given by ASA's Dr. David Young is greatly appreciated.

■ REFERENCES

(1) Thomas, S. J. M.; Edwards, P. P.; Kuznetsov, V. L. Sir Humphry Davy: Boundless Chemist, Physicist, Poet and Man of Action. *ChemPhysChem* **2008**, *9* (1), 59−66.
(2) Gibson, G. E.; Argo, W. L. The Absorption Spectra of the Blue Solutions of Sodium and Magnesium in Liquid Ammonia. *Phys. Rev.* **1916**, *7* (1), 33−48.
(3) Abel, B.; Buck, U.; Sobolewski, A. L.; Domcke, W. On the Nature and Signatures of the Solvated Electron in Water. *Phys. Chem. Chem. Phys.* **2012**, *14* (1), 22−34.
(4) Herbert, J. M.; Coons, M. P. The Hydrated Electron. *Annu. Rev. Phys. Chem.* **2017**, *68* (1), 447−472.
(5) Abramczyk, H.; Kroh, J. Spectroscopic Properties of the Solvated Electron in Water, Alcohols, Amines, Ethers and Alkanes. *Radiat. Phys. Chem.* **1994**, *43* (3), 291−297.
(6) Singh, A.; Gesser, H. D.; Scott, A. R. Solvated Electron in Acetonitrile. *Chem. Phys. Lett.* **1968**, *2* (5), 271−273.
(7) Mammano, N.; Sienko, M. J. Low-Temperature X-ray Study of the Compound Tetraaminelithium(O). *J. Am. Chem. Soc.* **1968**, *90* (23), 6322−6324.
(8) Seel, A. G.; Zurek, E.; Ramirez-Cuesta, A. J.; Ryan, K. R.; Lodge, M. T. J.; Edwards, P. P. Low Energy Structural Dynamics and Constrained Libration of $Li(NH_3)_4$, the Lowest Melting Point Metal. *Chem. Commun.* **2014**, *50* (74), 10778−10781.
(9) Albaqami, M. D.; Ellis, A. M. Infrared Spectroscopy of $Ca(NH_3)_n$ Complexes. *Chem. Phys. Lett.* **2018**, *706*, 736−740.
(10) Edwards, P. P. Superconductivity in Metal-Ammonia Solutions. *J. Supercond.* **2000**, *13* (6), 933−946.
(11) Thompson, H.; Wasse, J. C.; Skipper, N. T.; Hayama, S.; Bowron, D. T.; Soper, A. K. Structural Studies of Ammonia and Metallic Lithium−Ammonia Solutions. *J. Am. Chem. Soc.* **2003**, *125* (9), 2572−2581.
(12) Yoshida, S.; Okai, N.; Fuke, K. Photodissociation of $Mg^+(NH_3)$ Ion. *Chem. Phys. Lett.* **2001**, *347* (1−3), 93−100.
(13) Zimmerman, H. E. A Mechanistic Analysis of the Birch Reduction. *Acc. Chem. Res.* **2012**, *45* (2), 164−170.
(14) Zurek, E.; Edwards, P. P.; Hoffmann, R. A Molecular Perspective on Lithium-Ammonia Solutions. *Angew. Chem., Int. Ed.* **2009**, *48* (44), 8198−8232.
(15) Cady, H. P. The Electrolysis and Electrolytic Conductivity of Certain Substances Dissolved in Liquid Ammonia. *J. Phys. Chem.* **1897**, *1* (11), 707−713.
(16) Ariyarathna, I. R.; Khan, S. N.; Pawłowski, F.; Ortiz, J. V.; Miliordos, E. Aufbau Rules for Solvated Electron Precursors: $Be(NH_3)_4^{0,\pm}$ Complexes and Beyond. *J. Phys. Chem. Lett.* **2018**, *9* (1), 84−88.
(17) Ariyarathna, I. R.; Miliordos, E. Dative Bonds versus Electron Solvation in Tri-Coordinated Beryllium Complexes: $Be(CX)_3$ [X = O, S, Se, Te, Po] and $Be(PH_3)_3$ versus $Be(NH_3)_3$. *Int. J. Quantum Chem.* **2018**, *118* (18), No. e25673.
(18) Ariyarathna, I. R.; Pawłowski, F.; Ortiz, J. V.; Miliordos, E. Molecules Mimicking Atoms: Monomers and Dimers of Alkali Metal Solvated Electron Precursors. *Phys. Chem. Chem. Phys.* **2018**, *20* (37), 24186−24191.
(19) Ariyarathna, I. R.; Almeida, N. M. S.; Miliordos, E. Stability and Electronic Features of Calcium Hexa-, Hepta-, and Octa-Coordinated Ammonia Complexes: A First-Principles Study. *J. Phys. Chem. A* **2019**, *123* (31), 6744−6750.
(20) Almeida, N. M. S.; Pawłowski, F.; Ortiz, J. V.; Miliordos, E. Transition-Metal Solvated-Electron Precursors: Diffuse and 3d Electrons in $V(NH_3)_6^{0,\pm}$. *Phys. Chem. Chem. Phys.* **2019**, *21* (13), 7090−7097.
(21) Almeida, N. M. S.; Miliordos, E. Electronic and Structural Features of Octa-Coordinated Yttrium−Ammonia Complexes: The First Neutral Solvated Electron Precursor with Eight Ligands and

DOI: 10.1021/acs.jpca.9b07734
J. Phys. Chem. A 2020, 124, 505−512

Three Outer Electrons. *Phys. Chem. Chem. Phys.* **2019**, *21* (13), 7098−7104.
(22) Harms, A. C.; Khanna, S. N.; Chen, B.; Castleman, A. W. Dehydrogenation Reactions in $Mg^+(H_2O)_n$ Clusters. *J. Chem. Phys.* **1994**, *100* (5), 3540−3544.
(23) Misaizu, F.; Sanekata, M.; Fuke, K.; Iwata, S. Photodissociation Study on $Mg^+(H_2O)_n$, n = 1−5: Electronic Structure and Photo-induced Intracluster Reaction. *J. Chem. Phys.* **1994**, *100* (2), 1161−1170.
(24) Berg, C.; Achatz, U.; Beyer, M.; Joos, S.; Albert, G.; Schindler, T.; Niedner-Schatteburg, G.; Bondybey, V. E. Chemistry and Charge Transfer Phenomena in Water Cluster Cations. *Int. J. Mass Spectrom. Ion Processes* **1997**, *167−168* (11), 723−734.
(25) Reinhard, B. M.; Niedner-Schatteburg, G. Co-Existence of Hydrated Electron and Metal Di-Cation in $[Mg(H_2O)_n]^+$. *Phys. Chem. Chem. Phys.* **2002**, *4* (8), 1471−1477.
(26) Reinhard, B. M.; Niedner-Schatteburg, G. Ionization Energies and Spatial Volumes of the Singly Occupied Molecular Orbital in Hydrated Magnesium Clusters $[Mg,nH_2O]^+$. *J. Chem. Phys.* **2003**, *118* (8), 3571−3582.
(27) Ariyarathna, I. R.; Miliordos, E. Superatomic Nature of Alkaline Earth Metal−Water Complexes: The Cases of $Be(H_2O)_4^{0,+}$ and $Mg(H_2O)_6^{0,+}$. *Phys. Chem. Chem. Phys.* **2019**, *21* (28), 15861−15870.
(28) Sanekata, M.; Misaizu, F.; Fuke, K.; Iwata, S.; Hashimoto, K. Reactions of Singly Charged Alkaline-Earth Metal Ions with Water Clusters: Characteristic Size Distribution of Product Ions. *J. Am. Chem. Soc.* **1995**, *117* (2), 747−754.
(29) van der Linde, C.; Akhgarnusch, A.; Siu, C.-K.; Beyer, M. K. Hydrated Magnesium Cations $Mg^+(H_2O)_n$, $n \approx 20-60$, Exhibit Chemistry of the Hydrated Electron in Reactions with O_2 and CO_2. *J. Phys. Chem. A* **2011**, *115* (36), 10174−10180.
(30) Schulz, C. P.; Bobbert, C.; Shimosato, T.; Daigoku, K.; Miura, N.; Hashimoto, K. Electronically Excited States of Sodium−Water Clusters. *J. Chem. Phys.* **2003**, *119* (22), 11620−11629.
(31) Bewig, L.; Buck, U.; Rakowsky, S.; Reymann, M.; Steinbach, C. Reactions of Sodium Clusters with Water Clusters. *J. Phys. Chem. A* **1998**, *102* (7), 1124−1129.
(32) van der Linde, C.; Beyer, M. K. The Structure of Gas-Phase $[Al{\cdot}nH_2O]^+$: Hydrated Monovalent Aluminium $Al^+(H_2O)_n$ or Hydride−Hydroxide $HAlOH^+(H_2O)_{n-1}$? *Phys. Chem. Chem. Phys.* **2011**, *13* (15), 6776−6778.
(33) van der Linde, C.; Beyer, M. K. Reactions of $M^+(H_2O)_n$, n < 40, M = V, Cr, Mn, Fe, Co, Ni, Cu, and Zn, with D_2O Reveal Water Activation in $Mn^+(H_2O)_n$. *J. Phys. Chem. A* **2012**, *116* (44), 10676−10682.
(34) van der Linde, C.; Höckendorf, R. F.; Balaj, O. P.; Beyer, M. K. Reactions of Hydrated Singly Charged First-Row Transition-Metal Ions $M^+(H_2O)_n$ (M = V, Cr, Mn, Fe, Co, Ni, Cu, and Zn) toward Nitric Oxide in the Gas Phase. *Chem. - Eur. J.* **2013**, *19* (11), 3741−3750.
(35) Raghavachari, K.; Trucks, G. W.; Pople, J. A.; Head-Gordon, M. A Fifth-Order Perturbation Comparison of Electron Correlation Theories. *Chem. Phys. Lett.* **1989**, *157* (6), 479−483.
(36) Dunning, T. H. Gaussian Basis Sets for Use in Correlated Molecular Calculations. I. The Atoms Boron through Neon and Hydrogen. *J. Chem. Phys.* **1989**, *90* (2), 1007−1023.
(37) Kendall, R. A.; Dunning, T. H.; Harrison, R. J. Electron Affinities of the First-row Atoms Revisited. Systematic Basis Sets and Wave Functions. *J. Chem. Phys.* **1992**, *96* (9), 6796−6806.
(38) Prascher, B. P.; Woon, D. E.; Peterson, K. A.; Dunning, T. H.; Wilson, A. K. Gaussian Basis Sets for Use in Correlated Molecular Calculations. VII. Valence, Core-Valence, and Scalar Relativistic Basis Sets for Li, Be, Na, and Mg. *Theor. Chem. Acc.* **2011**, *128* (1), 69−82.
(39) Møller, C.; Plesset, M. S. Note on an Approximation Treatment for Many-Electron Systems. *Phys. Rev.* **1934**, *46* (7), 618−622.
(40) Yanai, T.; Tew, D. P.; Handy, N. C. A New Hybrid Exchange−Correlation Functional Using the Coulomb-Attenuating Method (CAM-B3LYP). *Chem. Phys. Lett.* **2004**, *393* (1−3), 51−57.
(41) Grimme, S.; Ehrlich, S.; Goerigk, L. Effect of the Damping Function in Dispersion Corrected Density Functional Theory. *J. Comput. Chem.* **2011**, *32* (7), 1456−1465.
(42) Grimme, S.; Antony, J.; Ehrlich, S.; Krieg, H. A Consistent and Accurate Ab Initio Parametrization of Density Functional Dispersion Correction (DFT-D) for the 94 Elements H-Pu. *J. Chem. Phys.* **2010**, *132* (15), 154104.
(43) Vydrov, O. A.; Scuseria, G. E. Assessment of a Long-Range Corrected Hybrid Functional. *J. Chem. Phys.* **2006**, *125* (23), 234109.
(44) Chai, J.-D.; Head-Gordon, M. Long-Range Corrected Hybrid Density Functionals with Damped Atom−Atom Dispersion Corrections. *Phys. Chem. Chem. Phys.* **2008**, *10* (44), 6615.
(45) Lee, C.; Yang, W.; Parr, R. G. Development of the Colle-Salvetti Correlation-Energy Formula into a Functional of the Electron Density. *Phys. Rev. B: Condens. Matter Mater. Phys.* **1988**, *37* (2), 785−789.
(46) Becke, A. D. Density-functional Thermochemistry. III. The Role of Exact Exchange. *J. Chem. Phys.* **1993**, *98* (7), 5648−5652.
(47) Stephens, P. J.; Devlin, F. J.; Chabalowski, C. F.; Frisch, M. J. Ab Initio Calculation of Vibrational Absorption and Circular Dichroism Spectra Using Density Functional Force Fields. *J. Phys. Chem.* **1994**, *98* (45), 11623−11627.
(48) Vosko, S. H.; Wilk, L.; Nusair, M. Accurate Spin-Dependent Electron Liquid Correlation Energies for Local Spin Density Calculations: A Critical Analysis. *Can. J. Phys.* **1980**, *58* (8), 1200−1211.
(49) Zhao, Y.; Truhlar, D. G. The M06 Suite of Density Functionals for Main Group Thermochemistry, Thermochemical Kinetics, Noncovalent Interactions, Excited States, and Transition Elements: Two New Functionals and Systematic Testing of Four M06-Class Functionals and 12 Other Functionals. *Theor. Chem. Acc.* **2008**, *120* (1−3), 215−241.
(50) Koopmans, T. Über Die Zuordnung von Wellenfunktionen Und Eigenwerten Zu Den Einzelnen Elektronen Eines Atoms. *Physica* **1934**, *1* (1−6), 104−113.
(51) Linderberg, J.; Öhrn, Y. *Propagators in Quantum Chemistry*; John Wiley & Sons: Hoboken, NJ, 2004.
(52) Ortiz, J. V. An Efficient, Renormalized Self-Energy for Calculating the Electron Binding Energies of Closed-Shell Molecules and Anions. *Int. J. Quantum Chem.* **2005**, *105* (6), 803−808.
(53) Ortiz, J. V. Electron Propagator Theory: An Approach to Prediction and Interpretation in Quantum Chemistry. *Wiley Interdiscip. Rev.: Comput. Mol. Sci.* **2013**, *3* (2), 123−142.
(54) Corzo, H. H.; Ortiz, J. V. Electron Propagator Theory: Foundations and Predictions. *Adv. Quantum Chem.* **2017**, *74*, 267−298.
(55) Frisch, M. J.; Trucks, G. W.; Schlegel, H. B.; Scuseria, G. E.; Robb, M. A.; Cheeseman, J. R.; Scalmani, G.; Barone, V.; Petersson, G. A.; Nakatsuji, H.; et al. *Gaussian 16*, revision A.03; Gaussian, Inc.: Wallingford, CT, 2016.
(56) Werner, H.-J.; Knowles, P. J.; Knizia, G.; Manby, F. R.; Schütz, M.; Celani, P.; Györffy, W.; Kats, D.; Korona, T.; Lindh, R.; et al. *MOLPRO: A General-Purpose Quantum Chemistry Program Package*, version 2015.1; http://www.molpro.net.
(57) Schaftenaar, G.; Noordik, J. H. Molden: A Pre- and Post-Processing Program for Molecular and Electronic Structures. *J. Comput.-Aided Mol. Des.* **2000**, *14*, 123−134.
(58) Dennington, R.; Keith, T. A.; Millam, J. M. *GaussView*, version 6; Semichem: Shawnee Mission, KS, 2016.
(59) Salter, T. E.; Ellis, A. M. Structures of Small $Li(NH_3)_n$ and $Li(NH_3)_n^+$ Clusters (n = 1−5): Evidence from Combined Photoionization Efficiency Measurements and Ab Initio Calculations. *J. Phys. Chem. A* **2007**, *111* (23), 4922−4926.
(60) Takasu, R.; Misaizu, F.; Hashimoto, K.; Fuke, K. Microscopic Solvation Process of Alkali Atoms in Finite Clusters: Photoelectron and Photoionization Studies of $M(NH_3)_n$ and $M(H_2O)_n$ (M = Li, Li^-, Na^-). *J. Phys. Chem. A* **1997**, *101* (17), 3078−3087.

DOI: 10.1021/acs.jpca.9b07734
J. Phys. Chem. A 2020, 124, 505−512

Appendix C

Supporting material for Chapter 4: *"Superatomic nature of ground and excited states of neutral and partially oxidized metal–aqua complexes"*

Appendix C contains the full copies of following articles. Reprints were made with permissions from the publisher.

- Ariyarathna, I. R.; Miliordos, E. *Phys. Chem. Chem. Phys.* **2019**, *21*, 15861–15870.
- Ariyarathna, I. R.; Miliordos, E. *Phys. Chem. Chem. Phys.* **2020**, *22*, 22426–22435.

Superatomic nature of alkaline earth metal–water complexes: the cases of $Be(H_2O)_4^{0,+}$ and $Mg(H_2O)_6^{0,+}$

PCCP

PAPER

View Article Online
View Journal | View Issue

Cite this: *Phys. Chem. Chem. Phys.*, 2019, **21**, 15861

Superatomic nature of alkaline earth metal–water complexes: the cases of $Be(H_2O)_4^{0,+}$ and $Mg(H_2O)_6^{0,+}$†

Isuru R. Ariyarathna and Evangelos Miliordos *

Received 4th April 2019,
Accepted 2nd July 2019

DOI: 10.1039/c9cp01897b

rsc.li/pccp

Beryllium– and magnesium–water complexes are shown to accommodate peripheral electrons around their $Be^{2+}(H_2O)_4$ and $Mg^{2+}(H_2O)_6$ cores in hydrogenic type orbitals. The lowest energy state of these tetra- and hexa-coordinated complexes possess one (cationic species) and two electrons (neutral species) in a pseudo spherical s-orbital, and populate p-, d-, f-, and g-type orbitals in their low-lying excited electronic states. High level quantum chemical calculations are performed to study the electronic structure of these complexes belonging to the category of solvated electrons precursors (SEPs). The observed Aufbau principle is in harmony with the previously introduced series for metal–ammonia complexes. In the current study we are able to expand the previously proposed shell model of SEPs beyond the 2d level. The observed shell model for $Mg(H_2O)_6^+$ is found to be 1s, 1p, 1d, 2s, 2p, 1f, 2d, 3s, and 1g. The stability of the $Be(H_2O)_m^{0/+}$ and $Mg(H_2O)_n^{0/+}$ systems with m = 1–4 and n = 1–6 is also examined and the higher stability of metal–ammonia SEPs over metal–water SEPs is explained in terms of the metal–ligand binding energies, hydrogen bonding, and the activation energy barrier leading to H_2 release.

I. Introduction

The stability and reactivity of metal water clusters has received a lot of interest in the literature. The number of water molecules change the properties of the formed metal–water complex. For example, we found in the past that a critical coordination number is necessary to stabilize a metal di- or tri-cationic complex.[1] The neutral alkali and positively (+1) charged alkaline earth metals have accrued special attention with several studies focusing on the micro-solvation process of the present unpaired metallic valence electron.[2–15] A critical number of solvent molecules is necessary to displace this electron from the metal's valence space. For example, lithium and sodium need four water or ammonia ligands to switch from the quasi-valence type to the surface-type complex,[10,11] following the terminology introduced in ref. 16. Alkaline earth metal–water systems express additional complexity, since a peripheral electron in the near vicinity of the coordinated water molecules facilitates the release of a hydrogen atom.[17] As a result, complexes of intermediate sizes, $M(H_2O)_n^+$, tend to relax to the lower energy $HOM(H_2O)_{n-1}^+$ structure.

The present work focuses on the first two members of the alkaline earth metal water species. The first member, beryllium, displays different characteristics from its group IIa partners.[18] Despite its distinct personality, the literature on Be is limited possibly because of its high toxicity, and we are aware of only one very recent work, which examines the reaction of beryllium cations with a single water molecule.[19] On the other hand, magnesium has been the choice of many older and recent publications.[5,12,16,17,20–32] A comprehensive literature review has been recently given by Ončák and Beyer.[5,27] A summary of the main findings is provided herein. The first experiments of Fuke and co-workers produced complexes with up to twenty water molecules using laser evaporation.[28,33] Their mass spectra indicated that the smallest ($n \leq 5$) and largest ($n \geq 15$) systems prefer the $Mg(H_2O)_n^+$ structure. The intermediate sizes prefer the magnesium hydroxyl unit ($Mg^{2+}OH^-$), but $Mg(H_2O)_{6,7}^+$ were also present in smaller quantities. Employing deuterated water, these authors found a larger $Mg(D_2O)_{6,7}^+$ portion with the $Mg(D_2O)_6^+$: $DOMg(D_2O)_5^+$ ratio being almost 1 : 1. In the same year, Castleman and co-workers identified n = 5 as the critical size where hydrogen elimination occurs,[22] in agreement with later work of Niedner-Schatteburg and co-workers, who observed exclusively $HOMg(H_2O)_{4,5}^+$ for n = 5, 6.[24] The different observations emphasize the strong dependence of the nature of the products of metal–water chemical processes on the experimental conditions.[17] The theoretical (Hartree–Fock) calculations of Watanabe *et al.* showed that complexes with six and more water ligands are prone to hydrogen elimination,[29] while the more accurate work of Siu and Liu (Density Functional Theory = DFT with the PW91 functional) explained the experimental observations in terms of the activation barrier for the hydrogen release (or O–H activation) process.[17]

Another important aspect about the structure of the pure $Mg(H_2O)_n^+$ systems is that the first three water molecules attach

Department of Chemistry and Biochemistry, Auburn University, Auburn, AL 36849-5312, USA. E-mail: emiliord@auburn.edu

† Electronic supplementary information (ESI) available. See DOI: 10.1039/c9cp01897b

directly to the metal atom, but the fourth one is placed in the second shell of the $Mg(H_2O)_3^+$ core, as indicated by infrared photo-dissociation spectra.[30] Binding energy measurements seem to support this view.[26] The theoretical (HF) work of Watanabe *et al.* confirmed this observation and extended it for up to $n = 6$, *i.e.*, $Mg(H_2O)_6^+$ has a $Mg(H_2O)_3^+$ core and three other water molecules hydrogen bonded to this core.[29,34] The more recent and accurate DFT/BLYP study of Reinhard and Niedner-Schatteburg, however, indicated that $Mg(H_2O)_6^+$ is a hexa-coordinated complex with one electron delocalized in its periphery.[16] The same is true for systems as large as $Mg(H_2O)_{17}^+$, after which the Mg^{2+} and e^- are solvent separated entities.[16,31] These structural changes affect dramatically the ionization energy (IE) of the system. The IE goes from $\sim$8.5 eV to $\sim$5 eV moving from $n = 5$, $Mg^+(H_2O)_3@(H_2O)_2$ (@ indicates the second shell), to $n = 6$, $Mg^{2+}(H_2O)_6^-$.[31] Surprisingly, according to the same authors, the situation is very different for $Mg(H_2O)_6^-$, where the six water molecules form a book-type cluster[35] attached to the metal atom.[32] Finally, recent photo-dissociation experiments have turned the interest to the electronically excited states of magnesium water clusters.[5,27]

Metal ammonia complexes have generally received less attention in the literature. We are aware of a few studies on alkali metal–ammonia complexes,[36–40] and only one for magnesium ammonia species.[41] Our group has very recently revealed that metal–ammonia complexes form readily surface type complexes or solvated electron precursors (SEPs). Specifically, beryllium, sodium, lithium, vanadium, and yttrium were shown to create a $Be(NH_3)_4^{2+}$, $Na(NH_3)_4^+$, $Li(NH_3)_4^+$, $V(NH_3)_6^{2+}$, and $Y(NH_3)_6^{3+}$ core accompanied by up to three,[42] two,[43] three,[44] and four[45] peripheral electrons, respectively. We further found that these outer electrons populate diffuse hydrogenic-type orbitals, the energy ranking of which is similar to the jellium or nuclear shell model: 1s, 1p, 1d, 2s, 1f, 2p, 2d.[42–46] Presently, we perform a computational investigation of the two lightest alkaline-earth metal–water complexes in order to examine if the same superatomic nature can be observed, and compare the relative stability of ammonia *vs.* water SEPs in the case of beryllium.

We indeed found that metal water complexes can also create SEPs and they follow a nearly identical Aufbau principle. In addition, the highly symmetric $Mg(H_2O)_6^+$ complex allowed us to extend our calculations to higher excited states and reach g-type orbitals. Based on our present $Be(H_2O)_4$ and past $Be(NH_3)_4$ results, we reach the following conclusions: (1) because of the single lone electron pair of ammonia, the metal–ammonia bond is more directional making firm (libration-free) structures; (2) ammonia as a stronger Lewis-base than water makes stronger metal–ligand bonds; (3) ammonia as weaker acid makes complexes less prone to H_2 release; (4) the stronger hydrogen bond in water clusters compared to ammonia clusters (660 *vs.* 1244 cm^{-1})[47,48] tends to favor the migration of water to the second solvation shell of the metal.

II. Computational details

Geometry optimization for the ground state of all $Mg(H_2O)_n^{0/+}$ (n = 1–6) coordination complexes were performed using two sets of MP2 calculations, where the electron correlation of the $2s^22p^6$ electrons of Mg is included (C-MP2) or ignored (MP2). For $Be(H_2O)_n^{0/+}$ (n = 1–4) only plain MP2 calculations were done ($1s^2$ subvalence electron correlation was not included). It should be mentioned that the focus of our work is not locating the most stable structure of the titled species, but instead studying the migration process of the valence electrons to the periphery of the complex. Therefore, we limit our geometry optimizations to the complexes where all water ligands are directly coordinated to the metal, unless such a structure is unstable. The used basis sets for MP2 calculations are cc-pVTZ for Be, Mg and O, and aug-cc-pVTZ for H. For C-MP2 we employed the cc-pCVTZ basis set of Mg. We further carried out frequency calculations to confirm the stability of the located minima and to correct our binding energies for the zero-point energy (ZPE). The frequencies were obtained at the DFT/B3LYP level of theory after re-optimizing the MP2 geometries using the same basis set. All our numerical results are listed in Tables S1–S7 of the ESI.†

Contrary to the highly symmetric (T_h point group) $Mg(H_2O)_6^+$ optimal structure, optimal $Mg(H_2O)_6$ and $Be(H_2O)_4^{0/+}$ structures bear C_1 symmetry, which makes the multi-reference calculations for the excited states of the system computationally extremely demanding. We were able to conduct the calculations for beryllium, but to render our calculations for $Mg(H_2O)_6$ manageable, we re-optimized these complexes imposing C_s symmetry by rotating the water ligands around the Mg–O bonds (see Fig. S1 of ESI†), and employed the obtained structure to calculate vertical excitation energies. The energy difference between C_1 and C_s is 1.18 kcal mol^{-1} at MP2 or 0.20 kcal mol^{-1} per ligand. The first 1s $\rightarrow$ 1p excitation energy under MP2 for C_s/C_1 structures are 0.69/0.65 eV indicating that our values are accurate within 0.05 eV.

For the vertical excitation energy calculations of $Mg(H_2O)_6^+$, the D_{2h} subgroup of T_h was considered. The active space for the complete active space self-consistent field (CASSCF) wavefunction consists of 35 orbitals ($10a_g$, $4b_{3u}$, $4b_{2u}$, $4b_{1g}$, $4b_{1u}$, $4b_{2g}$, $4b_{3g}$, $1a_u$). For $Mg(H_2O)_6$ and $Be(H_2O)_4^{0/+}$, the CASSCF space has two (for neutral) or one (for the cation) in 9 orbitals (6a′ and 3a″ for magnesium, and 9a for beryllium). These orbitals represent the outer orbitals occupied in the considered electronic states.

We performed second-order perturbation theory level (CASPT2) calculations on top of the CASSCF wavefunction to account for the dynamic correlation. This approach has been benchmarked against very accurate electron propagator calculations for the metal–ammonia complexes,[42–44] and are currently compared to the electron attachment equation of motion coupled cluster singles and doubles, EOM-EA-CCSD, method for $Be(H_2O)_4^+$ and $Mg(H_2O)_6^+$ species by attaching an electron to the corresponding dications.[49] Excitations from all inner electrons except the $1s^22s^22p^6$ electrons of Mg and $1s^2$ of Be and all O atoms are allowed.

The used basis sets for these calculations are cc-pVTZ (Mg), cc-pVTZ (O), d-aug-cc-pVTZ (H). For $Mg(H_2O)_6^+$ we also did C-CASPT2 calculations, which include excitations from all inner electrons except the $1s^2$ electrons of Mg and $1s^2$ of all O atoms. The tuned cc-pCVTZ basis set of Mg was used for the latter

calculations and the corresponding C-MP2 geometries were used. Moreover, we tested the basis set effect on the excited states of $Mg(H_2O)_6^+$. To this end, we also performed C-CASPT2 excited state calculations using the d-aug-cc-pVQZ (= DAQZ), t-aug-cc-pVTZ (= TATZ), and t-aug-cc-pVQZ (= TAQZ), besides the d-aug-cc-pVTZ (= DATZ), basis set for all hydrogen centers. In all cases the cc-pVTZ basis set was still used for Mg and O, which have been shown to be less important for excitation energies in the metal–ammonia complexes.[25,42] We don't expect them to play role in the metal–water ones either because of the similar nature of the two types closed-shell ligands. For all the CASPT2 calculations a 0.02 shift value was used. For the EOM-EA-CCSD two basis set combinations were employed: the smaller cc-pVDZ(Mg,O) d-aug-cc-pVDZ(H) and the bigger cc-pVTZ(Mg,O) d-aug-cc-pVTZ(H). The excitation energies are found highly insensitive in the basis sets employed.

Finally, we calculated the transition dipole moments for the excitations from the ground state Ψ_0 to every excited state Ψ_{exc}. The $\mu_k = \langle \Psi_0 | \hat{\mu}_k | \Psi_{exc} \rangle$ integral was calculated at CASSCF/DATZ for $k = x, y$, and z, and the $\mu_T = \sqrt{\mu_x^2 + \mu_y^2 + \mu_z^2}$ value is reported.

Gaussian16 was implemented for the geometry optimizations and frequency calculations,[50] multi-reference calculations were performed with MOLPRO 2015.1,[51] and EOM-EA-CCSD calculations were done with Q-CHEM5.1.[52]

III. Results and discussion

III-A. Ground states properties

For specific n, the C-MP2 total binding energy ($D_{e,tot}$) of $Mg(H_2O)_m^+$ with respect to $Mg^+ + nH_2O$ is higher than the corresponding MP2 value (see Table 1). Moreover, as the number of bound H_2O molecules increases, the $D_{e,tot}$ difference between C-MP2 and MP2 becomes larger: for n = 1 to 6 it is 0.8, 1.4, 1.9, 2.3, 2.9, and 3.8 kcal mol^{-1}. The zero-point-energy reduces the binding energy in larger quantities canceling out the core-correlation effects. The C-MP2 binding per metal–water bond ($D_{0,tot}/n$) decreases monotonically from 30.7 (n = 1) to 20.6 (n = 6) kcal mol^{-1}. On the other hand, the C-MP2 detachment energy (D_0) of one water molecule decreases from n = 1 (30.7 kcal mol^{-1}) to n = 4 (14.6 kcal mol^{-1}) but then increases to the 16.8 kcal mol^{-1} value for n = 6. The inclusion of core-correlation and ZPE corrections do not change these trends. Our best D_0(C-MP2) values are in good agreement with the experimental values of Armentrout and co-workers,[26] ours being always towards or above the upper boundary (by less than 1.5 kcal mol^{-1}) of the experimental error (see Table 1).

One additional electron destabilizes the system considerably and water molecules are generally unable to displace the valence electrons of Mg. The smaller complexes instead prefer to populate the second shell making hydrogen bonds with the existing coordinated ligands. The binding energy for the first water is minimal (less than 1.0 kcal mol^{-1}; see Table 1), and we were not able to locate stable $Mg(H_2O)_{2,3}$ minima with all water molecules directly attached to Mg. Observe also the long Mg–O distances for n = 1–3 in Table 1 and that $Mg(H_2O)_4$ is metastable with respect to $Mg@3(H_2O) + H_2O$ (negative binding energy).

The addition of more than four water molecules in the system inverts the situation, and some sort of concerted action doubles the total binding energy going from n = 4 to 5 ($D_{0,tot}$ = 12.8 to 23.5 kcal mol^{-1}), and we finally get $D_{0,tot}$ = 38.4 kcal mol^{-1} for n = 6. The detachment energy of one water ligand from $Mg(H_2O)_5$ and $Mg(H_2O)_6$ is 10.7, 14.8 kcal mol^{-1} which are much higher

Table 1 Average M–O distance r_e (Å) of optimized structures, total binding energy $D_{e,tot}$ (kcal mol^{-1}), and detachment energy D_e (kcal mol^{-1}) of a single H_2O ligand for $M(H_2O)_n^{0/+}$, M = Be (n = 1–4), Mg (n = 1–6)

	r_e		$D_{e,tot}$[a]		$D_{0,tot}$[a,b]		D_e[c]		D_0[b,c]		D_0
Species	MP2	C-MP2	MP2	C-MP2	MP2	C-MP2	MP2	C-MP2	MP2	C-MP2	Expt.[d]
$Mg(H_2O)_1^+$	2.065	2.046	31.1	31.9		30.7	31.1	31.9		30.7	28.4 ± 3.0
$Mg(H_2O)_2^+$	2.091	2.073	57.0	58.4		55.6	25.9	26.5		24.9	22.4 ± 1.6
$Mg(H_2O)_3^+$	2.120	2.101	79.5	81.4		76.9	22.5	23.0		21.3	17.3 ± 2.1
$Mg(H_2O)_4^+$	2.151	2.129	94.8	97.1		91.5	15.2	15.6		14.6	11.5 ± 2.1
$Mg(H_2O)_5^+$	2.138	2.114	109.0	111.9		106.7	14.2	14.8		15.2	
$Mg(H_2O)_6^+$	2.086	2.067	125.9	129.7		123.5	16.9	17.8		16.8	
$Mg(H_2O)_1$	2.842	2.927	0.9	1.0		1.0	0.9	1.0		1.0	
$Mg(H_2O)_2$[e]	2.284	2.275	9.1	9.2		7.1	8.2	8.2		6.1	
$Mg(H_2O)_3$[f]	3.972	3.901	16.9	17.2		12.5[g]	7.8	7.9		5.5	
$Mg(H_2O)_4$	2.183	2.158	16.3	16.1		12.8	−0.7	−1.1		0.3	
$Mg(H_2O)_5$	2.080	2.061	25.1	25.9		23.5	8.9	9.8		10.7	
$Mg(H_2O)_6$	2.106	2.088	42.3	43.6		38.4	17.2	17.7		14.8	
$Be(H_2O)_1^+$	1.571		61.2		59.4		61.2		59.4		
$Be(H_2O)_2^+$	1.615		103.5		99.2		42.2		39.8		
$Be(H_2O)_3^+$	1.694		132.0		125.1		28.5		25.9		
$Be(H_2O)_4^+$	1.646		149.1		143.8		17.1		18.7		
$Be(H_2O)_1$	1.701		1.8		1.2		1.8		1.2		
$Be(H_2O)_2$	1.644		8.9		7.0		7.1		5.8		
$Be(H_2O)_3$	1.698		25.0		21.1		16.1		14.1		
$Be(H_2O)_4$	1.648		45.4		41.1		20.4		20.0		

[a] $D_{e,tot}$: with respect to $M(H_2O)_n^{0/+} \rightarrow M^{0/+} + nH_2O$. [b] ZPE corrected values. [c] With respect to $M(H_2O)_n^{0/+} \rightarrow M(H_2O)_{n-1}^{0/+} + H_2O$. [d] Experimental values from ref. 26. [e] Only $Mg(H_2O)@(H_2O)$ was found stable. The r_e value corresponds to the nearest (to Mg) water molecule. [f] Only $Mg@(H_2O)_3$ was found stable. The r_e value corresponds to the nearest (to Mg) water molecule. [g] MP2 frequencies are used in this case, since B3LYP couldn't locate a minimum.

than any of the smaller complexes. At the same time, the Mg–O bond lengths contract by almost 0.1 Å from n = 4 to n = 5. Overall, the simultaneous attack of five and six ligands is necessary to displace the two valence electrons in the periphery of the complex. The Mg–O distances of $Mg(H_2O)_6$ is longer by 0.02 Å than in $Mg(H_2O)_6^+$ under both MP2 and C-MP2. This differs from what we have seen earlier for $Be(NH_3)_4$ and $Li(NH_3)_4$,[42,43] where the metal–ligand distances of $Be(NH_3)_4$ and $Li(NH_3)_4$ were found 0.008 and 0.031 Å shorter than their corresponding cations.

Beryllium water complexes are considerably more stable. The total binding energy $D_{e,tot}$ of $Be(H_2O)_m^+$ is at least 1.5 times larger than the corresponding magnesium water complex (see Table 1). For example, our MP2 $Be(H_2O)^+ \rightarrow Be^+ + H_2O$ dissociation energy (D_e) is 61.2 kcal mol^{-1} (in good agreement with the recent MRCI value of 64.1 kcal mol^{-1} [19]) *vs.* the 31.1 kcal mol^{-1} value of $Mg(H_2O)^+$. On the other hand, the binding energy for neutral $Be(H_2O)_1$ and $Mg(H_2O)_1$ are very small (1–2 kcal mol^{-1}). D_e remains small (7.1 kcal mol^{-1}) for $Be(H_2O)_2$, but increases to 16.1 and 20.4 kcal mol^{-1} for $Be(H_2O)_3$ and $Be(H_2O)_4$. The corresponding values for $Mg(H_2O)_{3,4}$ are smaller than 10 kcal mol^{-1}. The reason can be assigned to the larger charge density of the Be^{2+} core, and possibly to the fact that three and four water molecules complete the first shell of beryllium acting in the same way that the fifth and sixth water ligands act for magnesium (see above).

Comparing the beryllium–water and beryllium–ammonia complexes, the following comments are in order.[42,46] Although the Be–O bond lengths are shorter than Be–N (~1.65 *vs.* ~1.74 Å; Table 1 and ref. 42), the binding energies are at least 30% bigger for beryllium–ammonia complexes. Specifically, for $Be(H_2O)_m$/$Be(NH_3)_m$ (MP2/CCSD(T)) we have D_e = 1.8/5.2, 7.1/11.4, 16.1/21.7, 20.4/29.1 kcal mol^{-1} for m = 1, 2, 3, and 4, respectively (see Table 1 and ref. 42 and 46). In addition, going from $Be(NH_3)_4^+$ to $Be(NH_3)_4$, the Be–N distance drops by ~0.01 Å from 1.741 to 1.733 Å,[42] but the Be–O distance going from $Be(H_2O)_4^+$ to $Be(H_2O)_4$ is only slightly affected and actually increases by 0.002 Å (see Table 1).

A last comment on the differences between metal–water and metal–ammonia complexes pertains to the hydrogen dissociation reaction. The relative energetics for the $Be(H_2O)^+ \rightarrow Be^+ + H_2O$ and $BeOH^+ + H$ channels were recently studied,[19] and presently we investigate the H_2 release from $Be(H_2O)_4$ and $Be(NH_3)_4$. Specifically, we located the intermediates and transition states for the $Be(H_2O)_4 \rightarrow Be(OH)_2(H_2O)_2 + H_2$ and $Be(NH_3)_4 \rightarrow Be(NH_2)_2(NH_3)_2 + H_2$ reaction pathways at the DFT/CAM-B3LYP/d-aug-cc-pVTZ level. The full CCSD(T)//CAM-B3LYP energy landscape is shown in Fig. 1. Observe that the mechanism is stepwise for ammonia with one proton detached first from an ammonia ligand, which attracts the diffuse outer electrons to form H^-, which then drags a second proton almost spontaneously (small activation barrier ~2 kcal mol^{-1}). Two protons are detached at the same time in the case of $Be(H_2O)_4$ with a three times smaller activation barrier (23.9 *vs.* 8.0 kcal mol^{-1}). All structures and frequencies are given in the ESI† (Tables S8 and S9).

Conclusively, both the metal identity and the ligand type affect considerably the properties of the complexes. Beryllium/ammonia were found to make more stable SEPs compared to magnesium/water. The reasons are detected to the larger charge density of beryllium, the stronger metal–ammonia bonds, the smaller tendency of ammonia to release hydrogen gas, and the preference of water to populate the second coordination shell due to its stronger hydrogen bonding.

The orbital of the unpaired electron for $Mg(H_2O)_{n=1-6}^+$ and $Be(H_2O)_{m=1-4}^+$ is depicted in Fig. 2. For n = 1–5 or m = 1–3, it is highly localized on the metal atom (quasi-valence type), and six or four ligands are necessary to fully delocalize an electron in the periphery (surface type). The same contours for the neutral

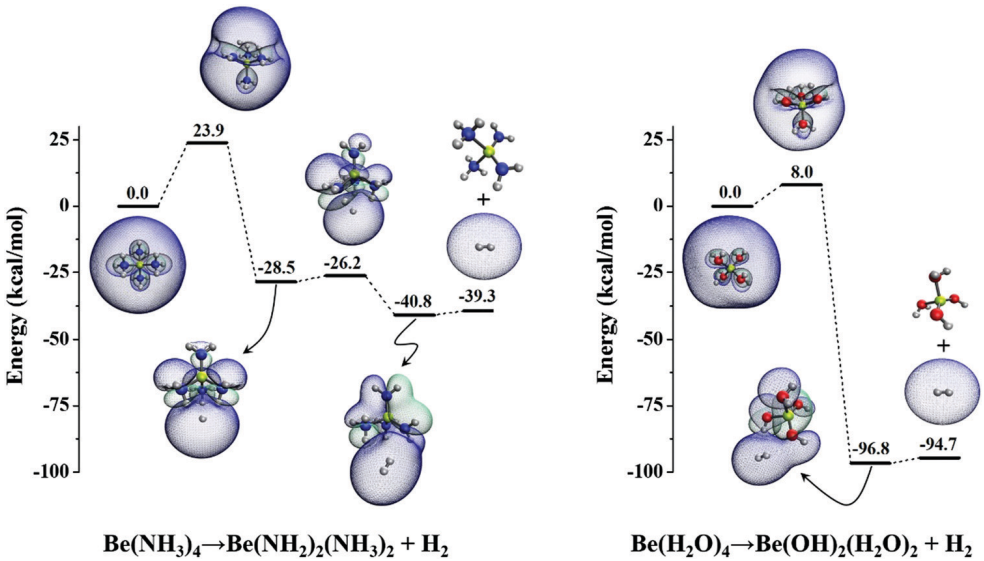

Fig. 1 CCSD(T)/ATZ//CAM-B3LYP/DATZ H_2-dissociation energy landscapes for $Be(NH_3)_4$ and $Be(H_2O)_4$. The contours show the evolution of the $Be(NH_3)_4$ and $Be(H_2O)_4$ highest occupied molecular orbital along the reaction path.

species are given in the ESI† (Fig. S2 and S3). It is apparent that the 3s atomic orbital of magnesium evolves to the outer 1s orbital of the SEP complexes. Moving from $n = 1$ to 4 the average Mg–O distances increases consistently by ~0.03 Å, but from $n = 4$ to 6 it actually drops quite substantially (~0.05 Å from $n = 5$ to 6). The exact same observation can be made for $Be(H_2O)_{m=1-3}$, where Be–O distance increase monotonically, *vs.* $Be(H_2O)_4$, where it drops by ~0.05 Å (see Table 1). This is consistent with our previous findings in $Be(NH_3)_4$ and $Li(NH_3)_4$ SEPs. The Coulombic attraction between the metal-core and the outer electron density pull the bound ligands towards the metal center. In the next section we examine the electronic states of the titled SEPs.

Finally, the MP2 (C-MP2) $Mg(H_2O)_6 \rightarrow Mg(H_2O)_6^+ + e^-$ ionization energy is 3.62 (3.63) eV, while the MP2 value for $Be(H_2O)_4$ is 4.31 eV.

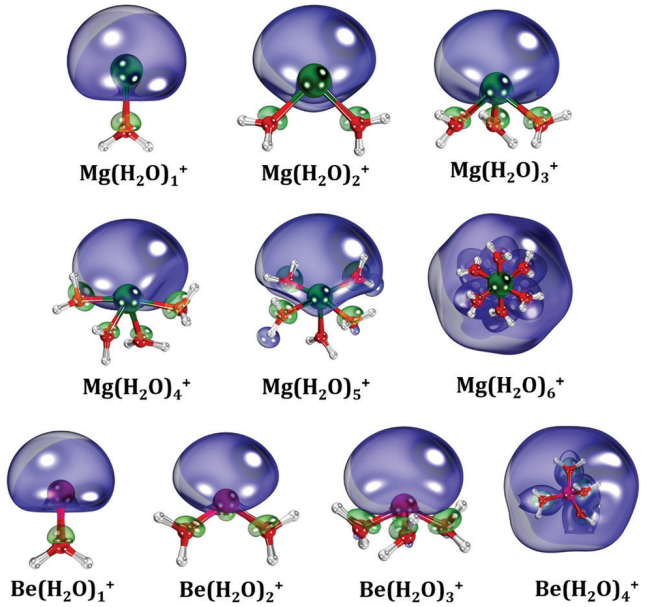

Fig. 2 Contours of the highest occupied molecular orbital (HOMO) of the $Mg(H_2O)_{n=1-6}^+$ and $Be(H_2O)_{m=1-4}^+$ series for their doublet ground state.

III-B. Excited electronic states of cationic species

In the ground state of $Mg(H_2O)_6^+$ and $Be(H_2O)_4^+$, one electron resides in the periphery in a quasi-spherical orbital resembling a 1s atomic orbital. Our previous studies on metal–ammonia complexes showed that the peripheral electron can be promoted to next higher energy 1p, 1d, 2s, 1f, 2p, and 2d-shaped orbitals.[42] To represent the diffuse nature of such outer orbitals, doubly augmented basis functions on the terminal H-atoms were deemed essential, whereas the contribution of diffuse functions centered on the inner atoms is minor. Presently, we have examined several excited states of $Mg(H_2O)_6^+$ and $Be(H_2O)_4^+$ to investigate whether a hydrated electron precursor reveals the same electronic structure features.

We start our discussion with $Mg(H_2O)_6^+$. Our calculated excitation energies are given in Table 2 (also represented schematically in Fig. 3) and selected orbitals populated in the excited states are depicted in Fig. 4. The Aufbau orbital series is identified as 1s, 1p, 1d, 2s, 2p, 1f, 2d, 3s, and 1g in this case. To examine the effect of the basis set on the accuracy of the calculated excitation energies, we employed four different diffuse basis sets on the hydrogen terminals (see Section II). The high symmetry of the system (D_{2h}) provides a unique opportunity to use larger basis sets for both plain CASPT2 and C-CASPT2 calculations. In some cases, CASPT2 calculations failed to converge and excitation energies are not reported in Table 2.

In all cases, CASSCF/DATZ underestimates the excitation energies with respect to CASPT2/DATZ by 0.21 (1s → 1p) to 0.51 (1s → 1g) eV. The contribution of core correlation to the

Table 2 Electronic configurations and vertical excitation energies (eV) at CASSCF, CASPT2, C-CASPT2, and EOM-CCSD of sixteen electronic states of $Mg(H_2O)_6^+$ under different basis sets and CASSCF/DATZ transition dipole moments (Debye) for the excitation from the ground state

Electronic configuration	State (T_h)	DATZ[a,b] CASSCF	DATZ[a,b] CASPT2	DATZ[a,b] C-CASPT2	DAQZ[a,b] C-CASPT2	TATZ[a,b] C-CASPT2	TAQZ[a,b] C-CASPT2	DADZ[b,c] EOM-EA-CCSD	DATZ[b,c] EOM-EA-CCSD	DATZ[a,d] CASSCF
1^2S ($1s^1$)	1^2A_g	0.00	0.00	0.00	0.00	0.00	0.00	0.00	0.00	
1^2P ($1p^1$)	1^2T_u	0.82	1.03	1.03	1.04	1.03	1.00	1.02	1.03	11.1
1^2D ($1d^1$)	1^2E_g	1.65	1.92	1.93	1.93	1.93	1.93	1.91	1.92	0.0
	1^2T_g	1.80	2.21	2.21	2.22	2.21		2.19	2.22	0.0
2^2S ($2s^1$)	2^2A_g	2.55	2.95	2.96	2.97	2.96	2.96	2.97	3.02	0.0
2^2P ($2p^1$)	2^2T_u	2.61	2.98	2.99	2.99	2.98		2.95	2.98	0.5
1^2F ($1f^1$)	1^2A_u	2.78	3.24	3.25	3.24	3.22	3.21	3.26	3.26	0.0
	3^2T_u	2.87	3.35	3.36	3.35	3.32	3.29	3.37	3.40	0.3
	4^2T_u	2.96	3.42	3.43	3.43	3.41	3.40	3.43	3.48	0.6
2^2D ($2d^1$)	2^2E_g	3.34	3.81	3.83	3.82	3.80	3.81	3.81	3.87	0.0
	2^2T_g	3.40	3.96	3.97	3.97	3.95		3.94	4.00	0.0
3^2S ($3s^1$)	3^2A_g	3.76	4.25	4.27	4.25	4.18	4.18	4.32	4.32	0.0
1^2G ($1g^1$)	3^2T_g	3.82	4.33	4.34	4.32	4.22		4.35	4.35	0.0
	3^2E_g	3.85	4.35	4.37	4.34	4.23	4.24	4.41	4.41	0.0
	4^2T_g	3.98	4.54	4.55	4.50	4.32		4.62	4.58	0.0
	4^2A_g	3.99						4.50	4.47	0.0

[a] Only the basis set on hydrogen centers changes as described in Section II: DADZ, DATZ, DAQZ, TATZ, TAQZ stand for d-aug-cc-pVDZ, d-aug-cc-pVTZ, d-aug-cc-pVQZ, t-aug-cc-pVTZ, t-aug-cc-pVQZ, respectively. The cc-pVTZ set is used for O, and cc-pVTZ or cc-pCVTZ for Mg. [b] Excitation energies. [c] DAXZ: the cc-pVXZ basis set for Mg and O, and the d-aug-cc-pVXZ set for H is used. [d] Transition dipole moments.

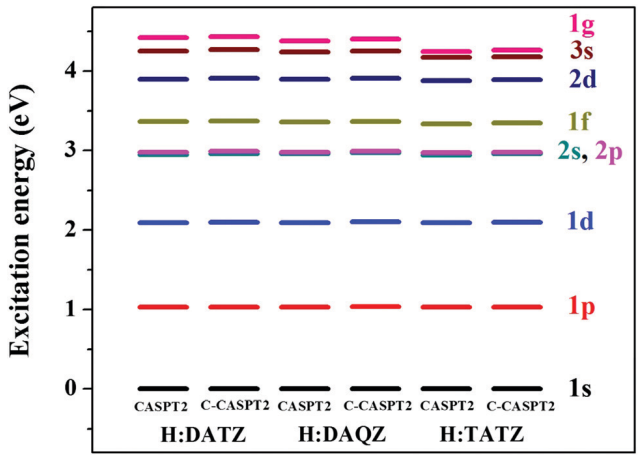

Fig. 3 Excitation energies of $Mg(H_2O)_6^+$ under different basis sets. The lowest energy component of each shell is shown.

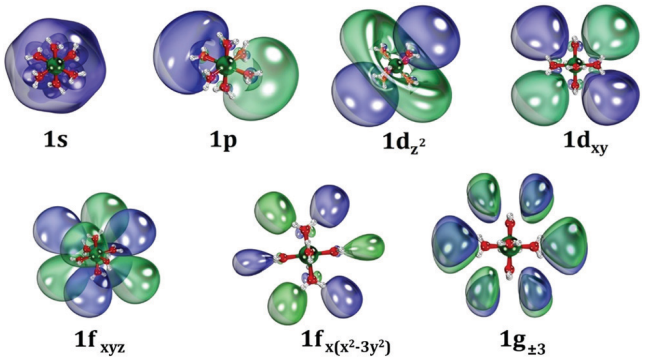

Fig. 4 Selected outer orbitals of $Mg(H_2O)_6^+$.

excitation energy is minor (0.00–0.03 eV); compare CASPT2/DATZ with C-CASPT2/DATZ. The difference in the excitation energy between our smallest and biggest basis sets (DATZ and TAQZ) is less than 0.13 eV for all the states calculated in common, confirming that DATZ is a good compromise between accuracy and efficiency. Especially for the lowest lying states involving 1s, 1p, 1d, and 2s, the discrepancy between the two sets is only 0.03 eV indicating that the complete basis set limit is practically reached. Finally, the incorporation of a third set of diffuse functions (DATZ to TATZ) is more important than going from triple-ζ (DATZ) to quadruple-ζ basis sets (DAQZ). This means that better valence functions (quadruple cardinality) do not affect much the excitation energies. These trends are summarized pictorially at the energy diagram of Fig. 3. Additionally, we employed the EOM-EA-CCSD approach to obtain the excitation energies (see Section II). The agreement between the EOM-EA-CCSD results with both DADZ and DATZ basis sets and CASPT2/DATZ is excellent, even for the highest energy states (see Table 2). The maximum discrepancy is 0.06 eV. The assignments of Table 2 are confirmed by the produced Dyson orbitals, which resemble closely those of Fig. 4 (see Fig. S4, ESI†).

The order of the orbitals within the shell model remains intact among the different basis sets. As in the ammonia SEPs, the lowest energy outer orbitals are 1s, 1p, 1d, 2s, 2p, 1f, 2d, but here we also revealed for the first time the 3s and 1g ones. The order of the shells in common with beryllium ammonia SEPs[42] is identical except for the switched 2p-1f shells. The nearly-octahedral (T_h) symmetry splits the 1d and 2d shells into e_g and t_g states. At C-CASPT2 the E_g–T_g energy difference for 1d is ~0.3 eV, which is twice larger than in 2d. The non-spherical symmetry causes the splitting in the 1f and 1g states. The splitting between the lowest and highest component of 1^2F ($1f^1$) is 0.18 eV which is almost equal to the 0.21 eV value of 1^2G ($1g^1$).

In the cases of $Be(NH_3)_4^+$ and $V(NH_3)_6^+$,[42,44] we demonstrated that the observed shell model can be rationalized by the complex electrostatics experienced by the outer electrons. To this end, we calculated the electrostatic potential generated by the $Be(NH_3)_4^{2+}$ or $V(NH_3)_6^{2+}$ core, and used it as the potential for an one-electron Hamiltonian of a hypothetic hydrogenic atom. This simple model was able to predict the lowest energy states. The same analysis is attempted here. The electrostatic potential produced by $Mg(H_2O)_6^{2+}$ along different directions is plotted in Fig. 5, and resembles closely that of $Be(NH_3)_4^{2+}$.[42] For the direction passing through the middle of an O–O–O face, we solved numerically the one-electron Schrödinger equation. The radial functions and the energies for the first nine levels are depicted in Fig. 6. With the exception of 1d–2s pair, the energy order is identical to that of Table 2. Also observe that the maximum of the outer 1s orbital at ~2 Å is shifted by about 0.5 Å with respect to its parent 3s atomic orbital of magnesium. Finally, this electrostatic model suggests that the central metal acts rather as a point charge. This explains why the orbital series is nearly the same for the metal–water and metal–ammonia complexes studied so far and rationalizes the presence of low-lying f- and g-type orbitals.

The absence of symmetry in $Be(H_2O)_4^+$ restricted our calculations in the first three shells. The CASSCF/DATZ, CASPT2/DATZ, and EOM-EA-CCSD vertical excitation energies are listed in Table 3 (see Fig. S5 and S6 of ESI† for selected outer and Dyson orbitals). As in the cationic magnesium water SEP, the

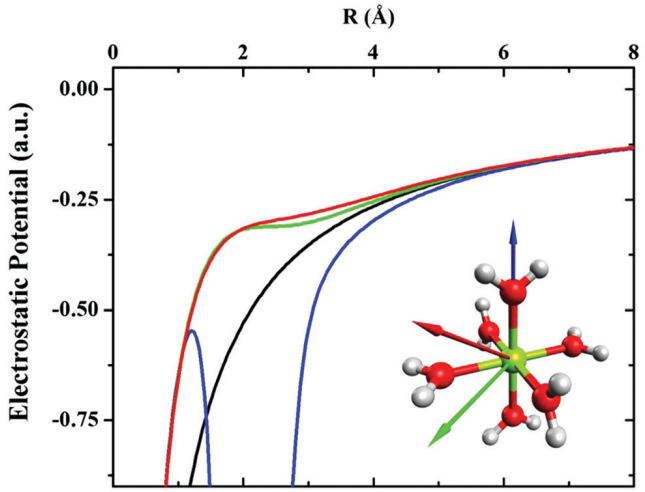

Fig. 5 Electrostatic potential along the three directions of the blue, red, and green arrows as a function of the distance R from Mg. The solid black line corresponds to $-2/R$.

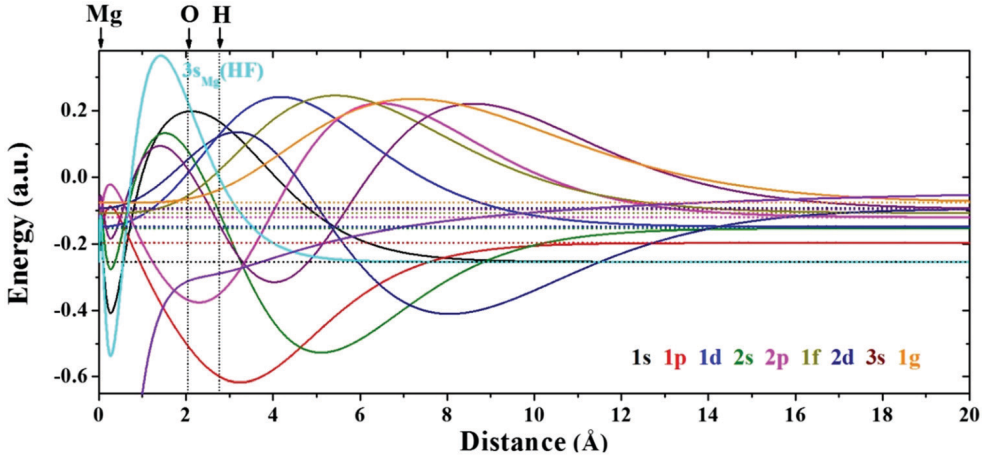

Fig. 6 Energy levels and radial wave functions of the outer orbitals for the electrostatic potential of $Mg(H_2O)_6^{2+}$ (red line of Fig. 5) acting on an electron. The radial wave function of 3s of the magnesium atom at the Hartree–Fock (HF) level is also shown for comparison.

Table 3 CASSCF/DATZ, CASPT2/DATZ, EOM-CCSD/DADZ and EOM-CCSD/DATZ vertical excitation energies (eV) for nine electronic state of $Be(H_2O)_4^+$ and CASSCF/DATZ transition dipole moments (Debye) for the excitation from the ground state

Electronic configuration	State (C_1)	CASSCF[a]	CASPT2[a]	EOM-EA-CCSD[a] DADZ	EOM-EA-CCSD[a] DATZ	CASSCF[b]
$1s^1$	1^2A	0.00	0.00	0.00	0.00	
$1p^1$	2^2A	1.21	1.40	1.36	1.37	9.1
	3^2A	1.51	1.71	1.66	1.66	7.4
	4^2A	1.57	1.72	1.68	1.68	7.3
$1d^1$	5^2A	2.38	2.62	2.58	2.58	1.1
	6^2A	2.72	3.11	3.05	3.06	0.8
	7^2A	2.74	3.12	3.11	3.11	0.4
	8^2A	2.94	3.37	3.32	3.33	0.5
	9^2A	3.04		3.47	3.44	1.1

[a] Excitation energies. [b] Transition dipole moments.

CASSCF-CASPT2 discrepancy ranges from 0.2 to 0.5 eV, while EOM-EA-CCSD is within 0.05 eV with respect to CASPT2. Compared to $Mg(H_2O)_6^+$, the 1s → 1p and 1s → 1d excitation energies are larger, while they cover a wider range of values: 1.0 *vs.* 1.4–1.7 eV, and 1.9–2.2 *vs.* 2.6–3.5 eV, respectively. The higher excitation energies for beryllium is a direct result of its smaller size as the particle-on-a-sphere system suggests.

The pseudo-spherical symmetry of $Mg(H_2O)_6^+$ suggests that only s → p or s → f transitions are allowed. The calculated μ_T values confirm this fact. The 1s → 1p transition has the largest value (11.1 D), while the 1s → 2p and 1s → 1f transition dipole moments are an order of magnitude smaller (see Table 2). All others states have zero μ_T values. The 1s → 1p transitions for $Be(H_2O)_4^+$ have also the largest μ_T values (7.3 to 9.1 D; see Table 3), but the C_1 symmetry allows non-zero values for the 1s → 1d transitions ($\mu_T \leq 1.1$ D)

III-C. Excited electronic states of neutral species

The excited states calculations for the neutral species were extremely challenging due to the rich multi-reference character of the system. Our numerical results along with the electronic composition of each state are listed in Tables 4 and 5 for Mg and Be, respectively. Recall that we imposed a C_s geometry for magnesium, but C_1 is used for beryllium. The C_s symmetry was imposed by rotating some water ligands around their Mg–O bonds (see Fig. S1 of ESI†). Based on our results for $Mg(H_2O)_6^+$ we employed only the DATZ basis set here and no core effects are considered, which is expected to affect mainly the highest energy states by ~0.1 eV. For all states and both species, CASSCF underestimates the excitation energies by 0.2–0.3 eV.

Table 4 CASSCF/DATZ and CASPT2/DATZ vertical excitation energies (eV) for twenty-one electronic state of $Mg(H_2O)_6$ and CASSCF/DATZ transition dipole moments (Debye) for the excitation from the ground state

Electronic configuration	State (C_s)	CASSCF[a]	CASPT2[a]	CASSCF[b]
$1s^2$	$1^1A'$	0.00	0.00	
$1s^11p^1$	$1^3A''$	0.45	0.66	0.0
$1s^11p^1$	$1^3A'$	0.46	0.66	0.0
$1s^11p^1$	$2^3A'$	0.52	0.74	0.0
$1s^11p^1/1s^11d^1$	$2^1A'$	0.91	1.16	10.6
$1s^11p^1/1s^11d^1$	$3^1A'$	1.01	1.28	9.0
$1s^11p^1/1s^11d^1$	$1^1A''$	1.09	1.34	10.2
$1s^11d^1/1p^2/1p^11p^1$	$4^1A'$	1.26	1.59	3.0
$1s^11d^1/1p^11p^1$	$2^1A''$	1.29	1.65	1.8
$1s^11d^1$	$3^3A'$	1.52	1.70	0.0
$1p^2/1s^11p^1$	$5^1A'$	1.54	1.73	7.0
$1s^11p^1/1p^11p^1/1s^11d^1$	$3^1A''$	1.53	1.74	6.9
$1s^11p^1/1p^11p^1/1s^11d^1$	$6^1A'$	1.63	1.80	7.2
$1s^11d^1$	$4^3A'$	1.62	1.83	0.0
$1s^11d^1$	$5^3A'$	1.67	1.83	0.0
$1s^11d^1$	$2^3A''$	1.67	1.88	0.0
$1p^11p^1$	$3^3A''$	1.60	1.93	0.0
$1s^11d^1/1p^11p^1$	$4^3A''$	1.75	1.97	0.0
$1s^11d^1/1p^11p^1$	$5^3A''$	1.73	2.02	0.0
$1p^11p^1$	$6^3A'$	1.75	2.04	0.0
$1p^11d^1$	$7^3A'$	2.32		0.0

[a] Excitation energies. [b] Transition dipole moments.

Only the ground and the first excited states have wavefunctions with a clean electronic configuration. Specifically, the ground $1^1A'$ or 1^1A ($1s^2$) states are followed by the triplets $1^3A''$, $1^3A'$, $2^3A'$ or 1^3A, 2^3A, 3^3A ($1s^11p^1$) at 0.66–0.74 or 0.68–1.13 eV for $Mg(H_2O)_6$ or $Be(H_2O)_4$, respectively. The next group of states consists of singlets with blended $1s^11p^1$, $1s^11d^1$, and $1p^2$ character covering excitation energies to about 1.8 eV (Mg)

Table 5 CASSCF/DATZ and CASPT2/DATZ vertical excitation energies (eV) for eighteen electronic states of $Be(H_2O)_4$ and CASSCF/DATZ transition dipole moments (Debye) for the excitation from the ground state

Electronic configuration	State (C_1)	CASSCF[a]	CASPT2[a]	CASSCF[b]
$1s^2$	1^1A	0.00	0.00	
$1s^1 1p^1$	1^3A	0.45	0.68	0.0
$1s^1 1p^1$	2^3A	0.70	0.92	0.0
$1s^1 1p^1$	3^3A	0.92	1.13	0.0
$1s^1 1p^1$	2^1A	1.19	1.39	8.0
$1s^1 1p^1$	3^1A	1.40	1.63	8.9
$1s^1 1p^1/1p^2$	4^1A	1.58	1.82	7.3
$1s^1 1d^1$	5^1A	1.64	1.94	4.5
$1s^1 1p^1/1p^1 1p^1/1s^1 1d^1$	6^1A	1.73	1.98	6.1
$1s^1 1d^1$	4^3A	1.85	1.98	0.0
$1s^1 1p^1/1p^2/1s^1 1d^1$	7^1A	1.88		6.6
$1p^2/1s^1 1d^1$	8^1A	1.88		4.2
$1s^1 1d^1$	5^3A	2.02	2.24	0.0
$1p^1 1p^1$	6^3A	2.07	2.29	0.0
$1p^1 1p^1/1s^1 1d^1$	7^3A	2.16	2.41	0.0
$1s^1 1d^1$	8^3A	2.18		0.0
$1p^2/1s^1 1d^1$	9^1A	2.23		4.1
$1p^1 1p^1$	9^3A	2.33		0.0

[a] Excitation energies. [b] Transition dipole moments.

and 2.0 eV (Be). The corresponding triplets come next reaching 2.0 eV (Mg) and ~2.5 eV (Be) energies with respect to the ground state. Selected orbitals for these systems are shown in Fig. S7 and S8 of the ESI.† As before, the beryllium–water complex has higher excitation energies than the magnesium–water one.

The transition dipole moments of Tables 4 and 5 indicate that the 1s → 1p transitions are the most probable for the neutral cases as happens for the cationic species. The difference between cationic and neutral complexes is that the multi-reference character of other excited states results in non-zero μ_T values. Therefore a richer electronic spectrum is predicted for neutral systems.

IV. Conclusions

In this work, we studied the stability of the $Mg(H_2O)_n^{0/+}$ and $Be(H_2O)_m^{+/0}$ clusters for n = 1–6 and m = 1–4, and focused on the electronic structure of the $Mg(H_2O)_6^{+/0}$ and $Be(H_2O)_4^{+/0}$ complexes, which can be categorized as solvated electron precursors (SEPs). One or two electrons reside at the periphery of $Mg(H_2O)_6^{2+}$ and $Be(H_2O)_4^{2+}$. Water ligands have larger difficulty than ammonia to displace the valence electrons of the metal and form SEPs, especially in the case of neutral magnesium complexes. The stronger metal–ammonia bonds, the weaker ammonia–ammonia hydrogen bonds, and the larger energy demands for H_2 release in the ammonia case account for this observation. In all cases, we detected enhanced stability of the metal–water complexes, when enough water ligands are present to complete the first solvation shell (four for Be and six for Mg). For example, the Mg–OH_2 binding energy suddenly increases when five or six water molecules occupy the first solvation shell of Mg.

We calculated excitation energies for $Mg(H_2O)_6^+$ with different basis sets confirming that the cc-pVTZ (Mg,O) and d-aug-cc-pVTZ (H) combination provides the best accuracy-efficiency compromise as in the case of metal–ammonia SEPs. The contribution of core correlation was found minimal.[44] The series of the outer orbitals was identified as 1s, 1p, 1d, 2s, 2p, 1f, 2d, 3s, and 1g, which is practically the same as for metal–ammonia complexes, except for the interchange of 2p and 1f. Finally, several excited states were investigated for $Be(H_2O)_4^+$, $Be(H_2O)_4$, and the less thermodynamically stable $Mg(H_2O)_6$. Our results will assist the identification of Mg–water SEPs not only in the gas-phase but also possibly in concentrated metal water solutions.

Conflicts of interest

There are no conflicts to declare.

Acknowledgements

The authors are indebted to Auburn University (AU) for financial support. This work was completed with resources provided by the Auburn University Hopper Cluster and the National Energy Research Scientific Computing Center (NERSC), a U.S. Department of Energy Office of Science User Facility operated under Contract No. DE-AC02-05CH11231. Finally, we would like to thank the two reviewers for their valuable comments, which improved considerably the quality of this article. The suggestion and instructions on the use of EOM-CCSD calculations by the editor Prof. Anna Krylov are greatly appreciated.

References

1 E. Miliordos and S. S. Xantheas, *Phys. Chem. Chem. Phys.*, 2014, **16**, 6886.
2 C. Steinbach and U. Buck, *Phys. Chem. Chem. Phys.*, 2005, **7**, 986.
3 C. P. Schulz, C. Bobbert, T. Shimosato, K. Daigoku, N. Miura and K. Hashimoto, *J. Chem. Phys.*, 2003, **119**, 11620–11629.
4 M. K. Beyer, *Mass Spectrom. Rev.*, 2007, **26**, 517–541.
5 M. Ončák, T. Taxer, E. Barwa, C. van der Linde and M. K. Beyer, *J. Chem. Phys.*, 2018, **149**, 044309.
6 U. Buck and C. Steinbach, *J. Phys. Chem. A*, 1998, **102**, 7333–7336.
7 L. Bewig, U. Buck, S. Rakowsky, M. Reymann and C. Steinbach, *J. Phys. Chem. A*, 1998, **102**, 1124–1129.
8 K. W. Chan, C.-K. Siu, S. Y. Wong and Z.-F. Liu, *J. Chem. Phys.*, 2005, **123**, 124313.
9 M. Sanekata, F. Misaizu and K. Fuke, *J. Chem. Phys.*, 1996, **104**, 9768–9778.
10 T. Tsurusawa and S. Iwata, *J. Chem. Phys.*, 2000, **112**, 5705–5710.
11 T. Tsurusawa and S. Iwata, *J. Phys. Chem. A*, 1999, **103**, 6134–6141.
12 E. H. Alsharaeh, *Int. J. Mol. Sci.*, 2011, **12**, 9095–9107.
13 C. van der Linde, A. Akhgarnusch, C.-K. Siu and M. K. Beyer, *J. Phys. Chem. A*, 2011, **115**, 10174–10180.
14 T.-W. Lam, C. van der Linde, A. Akhgarnusch, Q. Hao, M. K. Beyer and C.-K. Siu, *ChemPlusChem*, 2013, **78**, 1040–1048.
15 C. van der Linde, R. F. Höckendorf, O. P. Balaj and M. K. Beyer, *Chem. – Eur. J.*, 2013, **19**, 3741–3750.

16 B. M. Reinhard and G. Niedner-Schatteburg, *Phys. Chem. Chem. Phys.*, 2002, **4**, 1471–1477.
17 C.-K. Siu and Z.-F. Liu, *Phys. Chem. Chem. Phys.*, 2005, **7**, 1005.
18 M. L. Green, P. Jean and M. C. Heaven, *J. Phys. Chem. Lett.*, 2018, **9**, 1999–2002.
19 T. Yang, A. Li, G. K. Chen, C. Xie, A. G. Suits, W. C. Campbell, H. Guo and E. R. Hudson, *J. Phys. Chem. Lett.*, 2018, **9**, 3555–3560.
20 F. Misaizu, M. Sanekata, K. Tsukamoto, K. Fuke and S. Iwata, *J. Phys. Chem.*, 1992, **96**, 8259–8264.
21 K. F. Willey, C. S. Yeh, D. L. Robbins, J. S. Pilgrim and M. A. Duncan, *J. Chem. Phys.*, 1992, **97**, 8886–8895.
22 A. C. Harms, S. N. Khanna, B. Chen and A. W. Castleman, *J. Chem. Phys.*, 1994, **100**, 3540–3544.
23 C. Berg, M. Beyer, U. Achatz, S. Joos, G. Niedner-Schatteburg and V. E. Bondybey, *Chem. Phys.*, 1998, **239**, 379–392.
24 C. Berg, U. Achatz, M. Beyer, S. Joos, G. Albert, T. Schindler, G. Niedner-Schatteburg and V. E. Bondybey, *Int. J. Mass Spectrom. Ion Processes*, 1997, **167–168**, 723–734.
25 C. W. Bauschlicher and H. Partridge, *J. Phys. Chem.*, 1991, **95**, 9694–9698.
26 N. F. Dalleska, B. L. Tjelta and P. B. Armentrout, *J. Phys. Chem.*, 1994, **98**, 4191–4195.
27 T. Taxer, M. Oncak, E. Barwa, C. van der Linde and M. K. Beyer, *Faraday Discuss.*, DOI: 10.1039/C8FD00204E.
28 F. Misaizu, M. Sanekata, K. Fuke and S. Iwata, *J. Chem. Phys.*, 1994, **100**, 1161–1170.
29 H. Watanabe, S. Iwata, K. Hashimoto, F. Misaizu and K. Fuke, *J. Am. Chem. Soc.*, 1995, **117**, 755–763.
30 Y. Inokuchi, K. Ohshimo, F. Misaizu and N. Nishi, *J. Phys. Chem. A*, 2004, **108**, 5034–5040.
31 B. M. Reinhard and G. Niedner-Schatteburg, *J. Chem. Phys.*, 2003, **118**, 3571–3582.
32 B. M. Reinhard and G. Niedner-Schatteburg, *Phys. Chem. Chem. Phys.*, 2003, **5**, 1970–1980.
33 M. Sanekata, F. Misaizu, K. Fuke, S. Iwata and K. Hashimoto, *J. Am. Chem. Soc.*, 1995, **117**, 747–754.
34 H. Watanabe and S. Iwata, *J. Chem. Phys.*, 1998, **108**, 10078–10083.
35 E. Miliordos, E. Aprà and S. S. Xantheas, *J. Chem. Phys.*, 2013, **139**, 114302.
36 T. E. Salter and A. M. Ellis, *J. Phys. Chem. A*, 2007, **111**, 4922–4926.
37 R. Takasu, F. Misaizu, K. Hashimoto and K. Fuke, *J. Phys. Chem. A*, 1997, **101**, 3078–3087.
38 L. Varriale, N. M. Tonge, N. Bhalla and A. M. Ellis, *J. Chem. Phys.*, 2010, **132**, 161101.
39 W. S. Hopkins, A. P. Woodham, N. M. Tonge, A. M. Ellis and S. R. Mackenzie, *J. Phys. Chem. Lett.*, 2011, **2**, 257–261.
40 P. Brockhaus, I. V. Hertel and C. P. Schulz, *J. Chem. Phys.*, 1999, **110**, 393–402.
41 J. I. Lee, D. C. Sperry and J. M. Farrar, *J. Chem. Phys.*, 2004, **121**, 8375.
42 I. R. Ariyarathna, S. N. Khan, F. Pawłowski, J. V. Ortiz and E. Miliordos, *J. Phys. Chem. Lett.*, 2018, **9**, 84–88.
43 I. R. Ariyarathna, F. Pawłowski, J. V. Ortiz and E. Miliordos, *Phys. Chem. Chem. Phys.*, 2018, **20**, 24186–24191.
44 N. M. S. Almeida, F. Pawłowski, J. V. Ortiz and E. Miliordos, *Phys. Chem. Chem. Phys.*, 2019, **21**, 7090–7097.
45 N. M. S. Almeida and E. Miliordos, *Phys. Chem. Chem. Phys.*, 2019, **21**, 7098–7104.
46 I. R. Ariyarathna and E. Miliordos, *Int. J. Quantum Chem.*, 2018, **118**, e25673.
47 A. S. Case, C. G. Heid, S. H. Kable and F. F. Crim, *J. Chem. Phys.*, 2011, **135**, 084312.
48 L. C. Ch'ng, A. K. Samanta, G. Czakó, J. M. Bowman and H. Reisler, *J. Am. Chem. Soc.*, 2012, **134**, 15430–15435.
49 M. Nooijen and R. J. Bartlett, *J. Chem. Phys.*, 1995, **102**, 3629–3647.
50 M. J. Frisch, G. W. Trucks, H. B. Schlegel, G. E. Scuseria, M. A. Robb, J. R. Cheeseman, G. Scalmani, V. Barone, G. A. Petersson, H. Nakatsuji, X. Li, M. Caricato, A. V. Marenich, J. Bloino, B. G. Janesko, R. Gomperts, B. Mennucci, H. P. Hratchian, J. V. Ortiz, A. F. Izmaylov, J. L. Sonnenberg, D. Williams-Young, F. Ding, F. Lipparini, F. Egidi, J. Goings, B. Peng, A. Petrone, T. Henderson, D. Ranasinghe, V. G. Zakrzewski, J. Gao, N. Rega, G. Zheng, W. Liang, M. Hada, M. Ehara, K. Toyota, R. Fukuda, J. Hasegawa, M. Ishida, T. Nakajima, Y. Honda, O. Kitao, H. Nakai, T. Vreven, K. Throssell, J. A. Montgomery Jr., J. E. Peralta, F. Ogliaro, M. J. Bearpark, J. J. Heyd, E. N. Brothers, K. N. Kudin, V. N. Staroverov, T. A. Keith, R. Kobayashi, J. Normand, K. Raghavachari, A. P. Rendell, J. C. Burant, S. S. Iyengar, J. Tomasi, M. Cossi, J. M. Millam, M. Klene, C. Adamo, R. Cammi, J. W. Ochterski, R. L. Martin, K. Morokuma, O. Farkas, J. B. Foresman and D. J. Fox, *Gaussian 16, Revision B.01*, Gaussian, Inc., Wallingford CT, 2016.
51 H.-J. Werner, P. J. Knowles, G. Knizia, F. R. Manby, M. Schütz and M. W. P. Celani, W. Györffy, D. Kats, T. Korona, R. Lindh, A. Mitrushenkov, G. Rauhut, K. R. Shamasundar, T. B. Adler, R. D. Amos, A. Bernhardsson, A. Berning, D. L. Cooper, M. J. O. Deegan, A. J. Dobbyn, F. Eckert, E. Goll, C. Hampel, A. Hesselmann, G. Hetzer, *MOLPRO, version2015.1, a Package ab initio programs*, see http//www.molpro.net.
52 Y. Shao, Z. Gan, E. Epifanovsky, A. T. B. Gilbert, M. Wormit, J. Kussmann, A. W. Lange, A. Behn, J. Deng, X. Feng, D. Ghosh, M. Goldey, P. R. Horn, L. D. Jacobson, I. Kaliman, R. Z. Khaliullin, T. Kuś, A. Landau, J. Liu, E. I. Proynov, Y. M. Rhee, R. M. Richard, M. A. Rohrdanz, R. P. Steele, E. J. Sundstrom, H. L. Woodcock, P. M. Zimmerman, D. Zuev, B. Albrecht, E. Alguire, B. Austin, G. J. O. Beran, Y. A. Bernard, E. Berquist, K. Brandhorst, K. B. Bravaya, S. T. Brown, D. Casanova, C.-M. Chang, Y. Chen, S. H. Chien, K. D. Closser, D. L. Crittenden, M. Diedenhofen, R. A. DiStasio, H. Do, A. D. Dutoi, R. G. Edgar, S. Fatehi, L. Fusti-Molnar, A. Ghysels, A. Golubeva-Zadorozhnaya, J. Gomes, M. W. D. Hanson-Heine, P. H. P. Harbach, A. W. Hauser, E. G. Hohenstein, Z. C. Holden, T.-C. Jagau, H. Ji, B. Kaduk, K. Khistyaev, J. Kim, J. Kim, R. A. King, P. Klunzinger, D. Kosenkov, T. Kowalczyk, C. M. Krauter, K. U. Lao, A. D. Laurent, K. V. Lawler,

S. V. Levchenko, C. Y. Lin, F. Liu, E. Livshits, R. C. Lochan, A. Luenser, P. Manohar, S. F. Manzer, S.-P. Mao, N. Mardirossian, A. V. Marenich, S. A. Maurer, N. J. Mayhall, E. Neuscamman, C. M. Oana, R. Olivares-Amaya, D. P. O'Neill, J. A. Parkhill, T. M. Perrine, R. Peverati, A. Prociuk, D. R. Rehn, E. Rosta, N. J. Russ, S. M. Sharada, S. Sharma, D. W. Small, A. Sodt, T. Stein, D. Stück, Y.-C. Su, A. J. W. Thom, T. Tsuchimochi, V. Vanovschi, L. Vogt, O. Vydrov, T. Wang, M. A. Watson, J. Wenzel, A. White, C. F. Williams, J. Yang, S. Yeganeh, S. R. Yost, Z.-Q. You, I. Y. Zhang, X. Zhang, Y. Zhao, B. R. Brooks, G. K. L. Chan, D. M. Chipman, C. J. Cramer, W. A. Goddard, M. S. Gordon, W. J. Hehre, A. Klamt, H. F. Schaefer, M. W. Schmidt, C. D. Sherrill, D. G. Truhlar, A. Warshel, X. Xu, A. Aspuru-Guzik, R. Baer, A. T. Bell, N. A. Besley, J.-D. Chai, A. Dreuw, B. D. Dunietz, T. R. Furlani, S. R. Gwaltney, C.-P. Hsu, Y. Jung, J. Kong, D. S. Lambrecht, W. Liang, C. Ochsenfeld, V. A. Rassolov, L. V. Slipchenko, J. E. Subotnik, T. Van Voorhis, J. M. Herbert, A. I. Krylov, P. M. W. Gill and M. Head-Gordon, *Mol. Phys.*, 2015, **113**, 184–215.

Geometric and electronic structure analysis of calcium water complexes with one and two solvation shells

PCCP

PAPER

View Article Online
View Journal | View Issue

Cite this: *Phys. Chem. Chem. Phys.*, 2020, **22**, 22426

Geometric and electronic structure analysis of calcium water complexes with one and two solvation shells†

Isuru R. Ariyarathna and Evangelos Miliordos *

Received 13th August 2020,
Accepted 18th September 2020

DOI: 10.1039/d0cp04309e

rsc.li/pccp

Neutral and cationic calcium water complexes are studied by means of high-level quantum calculations. Both the geometric and electronic structure of these species is investigated. We study complexes with up to eight water molecules in the first solvation sphere of calcium $Ca(H_2O)_{n=1-8}^{0,+}$, and examine their stability with respect to $Ca(H_2O)_{n-k}@kH_2O^{0,+}$, where a number k of water molecules resides at the second solvation shell. For the cationic species, we find that five water molecules readily attach to calcium and the sixth water molecule goes to the second shell. The hexa-coordinated calcium core is restored after the addition of a seventh water molecule. For neutral species, zero-point energy corrections are critical in stabilizing structures with water ligands directly bound to calcium for up to six water ligands. The (one or two) valence electrons of Ca^+ and Ca are displaced gradually from the valence space of calcium to the periphery of the complex forming solvated electron precursors (SEPs). For example, in the ground state of $Ca(H_2O)_6^+$ one electron occupies an s-type diffuse peripheral orbital, which can be promoted to higher energy p-, d-, f-, g-atomic-type orbitals (1s, 1p, 1d, 2s, 1f, 2p, 2d, 1g, 3s) in the excited states of the system. Finally, we considered the effect of a complete second solvation shell using the $Ca(H_2O)_6^+@12H_2O$ cluster, which is shown to have significantly lower excitation energies compared to the $Ca(H_2O)_6^+$.

1. Introduction

Although studies on solvated electron systems have a history of two centuries, their chemical and physical properties are still poorly understood.[1] The studies on solvated electron systems have focused mainly on the ammonia and water solvents. NH_3 and H_2O force valence electron(s) to detach from the metal core and solvate in their cavities.[1] In ammonia, solvated electrons last for days before vanishing with the release of H_2, but in water their lifetime is about 300 μs.[2] Hence, macro-scale studies on solvated electrons have been carried out exclusively in metal ammonia solutions.

A dilute metal ammonia solution has a brilliant blue color consisting of ion-pairs formed by metal cations and solvated electrons.[1] As the metal concentration increases, the density of solvated electrons in the solution rises causing spin-pairing between solvated electrons.[3] At 0.1 mol% metal concentration, more than 90% of the solvated electrons are paired.[3] In the 1–8 mol% range of metal concentration, the blue solution transforms into a bronze-gold colored liquid metal with an increased electrical conductivity.[3] At the saturation limit (21 mol% metal) the conductivity of this liquid metal goes beyond that of liquid mercury.[3] The metal-like conductivity of the formed species is attributed to their structure: "free" electrons orbit around positively charged metal ammonia complexes.

Solid-state studies of such metal–ammonia or metal–water species are rare. Edwards reports that solid $Li(NH_3)_4$ shows superconductivity around 180–190 K.[3] Further Seel *et al.* identified $Li(NH_3)_4$ as the lowest melting point metal.[4] A comprehensive solid-state computational study which focuses $Li(NH_3)_4$ has been conducted by the Hoffman group.[5]

At the opposite end, several gas phase studies on metal–ammonia and metal–water complexes can be found in the literature. Among those, studies on $Al(H_2O)_n^+$,[6–10] $Na(H_2O)_n$,[11–19] and $Mg(H_2O)_n^+$[20,21–33] are common. Some reports about $Na(NH_3)_n$,[13,34,35] $Mg(NH_3)_n^+$,[36,37] $Sr(NH_3)_n^+$,[38,39] $Sr(H_2O)_n^+$,[32,38,40,41] $Ba(H_2O)_n^{0,+}$,[42,43] and $Ca(H_2O)_n^+$[32,44,45] are also available. Cationic alkaline earth metal–water complexes adopt either a $M(H_2O)_n^+$ or a $M(OH)(H_2O)_{n-1}^+$ structure. For example, when n = 1–5 or $n > 14$ $Mg(H_2O)_n^+$ is favored, but for n = 6–14 $Mg(OH)(H_2O)_{n-1}^+$ is dominant.[21,22] For n = 6 both $Mg(H_2O)_n^+$ and $Mg(OH)(H_2O)_{n-1}^+$ have been detected in 1 : 6 ratio by Misaizu *et al.*[21] Sperry *et al.* found that deuterium substitution causes $Mg(D_2O)_n^+$ to be the

Department of Chemistry and Biochemistry, Auburn University, Auburn, AL 36849-5312, USA. E-mail: emiliord@auburn.edu

† Electronic supplementary information (ESI) available. See DOI: 10.1039/d0cp04309e

main structure for n = 1–6.[41] Deuterium substitution can also determine the chief isomer of cationic Sr^+–H_2O clusters. According to Sperry *et al.*, $Sr(H_2O)_n^+$ is dominant for n = 1–4, while $Sr(D_2O)_n^+$ dominates for n = 1–5.[41]

Calcium water clusters produced by laser evaporation and their photo-dissociation spectra have been recorded by Fuke and co-workers.[44] Their mass spectrum points to $Ca(H_2O)_n^+$ structures for n = 1–4 or $n > 12$, whereas $Ca(OH)(H_2O)_{n-1}^+$ has been identified exclusively for n = 5–12. The isotopic substitution of hydrogen showed that $Ca(D_2O)_n^+$ persists for every n value including n = 5–12. Therefore, they recorded the photo-dissociation spectrum of $Ca(H_2O)_n^+$ for n = 1–5, but they used $Ca(D_2O)_6^+$ instead of $Ca(H_2O)_6^+$. These authors supported that the spectrum is not affected by the deuterium substitution since the $Ca(D_2O)_6^+$ fragments used to record the spectrum are hot and should be identical to that of $Ca(H_2O)_6^+$. Their photo-dissociation results suggest that the first solvation shell of Ca^+ may be filled up with $\sim$6 water molecules, as opposed to Mg^+ which is saturated with 3 water molecules.[27] We are aware of one more gas phase mass spectrometry study reporting water detachment energies for $Ca(H_2O)_{1-5}^+$.[45]

From the theoretical side, little is known about the geometric and electronic structure of the calcium water clusters. The Monte Carlo simulations of Kochanski and Constantin for $Ca(H_2O)_{1-10}^+$ suggest that the first solvation shell fills up with six water molecules, and that the most stable structure for $Ca(H_2O)_{6-10}^+$ has a $Ca(H_2O)_6^+$ core.[45] Their statistically averaged coordination number for $Ca(H_2O)_6^+$ is 5.29 indicating that arrangements with a $Ca(H_2O)_5^+$ core and one H_2O in the second solvation shell are also encountered. This average coordination number increases to 5.63 for $Ca(H_2O)_{10}^+$. The later work of Watanabe and Iwata, however, suggests that the lowest energy structure of $Ca(H_2O)_6^+$ has a $Ca(H_2O)_4^+$ core with two hydrogen bonded water molecules, with the hexa-coordinated complex to be 13.65 kcal mol^{-1} higher (free energy at room temperature).[46] Bauschlicher *et al.* studied the smallest three clusters, $Ca(H_2O)_{1-3}^+$ reporting water detachment energies. Given that all of these studies are at the Hartee–Fock level, a more accurate and systematic theoretical investigation is necessary. Presently, we examine the lowest energy structures at the second-order Møller–Plesset perturbation theory (MP2) level of theory.

For specific n values, $M(H_2O)_n$ or $M(NH_3)_n$ systems can be pictured as a solvent separated electron from a metal–ammonia or metal–water core, $qe^-@M(H_2O/NH_3)_n^{q+}$. We named such species solvated electron precursors (SEPs).[35] $Be(NH_3)_4$ is our first reported SEP, where two electrons rest in the periphery of $Be(NH_3)_4^{2+}$.[47] The two outer electrons (q = 2) of $Be(NH_3)_4$ occupy a diffuse s-type orbital in the ground state and can be promoted to higher energy hydrogenic type orbitals. Specifically, the outer electron of excited $Be(NH_3)_4^+$ populates (in energy order) the 1p, 1d, 2s, 1f, 2p, 2d orbitals. A similar shell model has been observed for $Li(NH_3)_4$, $Na(NH_3)_4$, and $Ca(NH_3)_8$ species.[35,48] We also discovered that transition metal ammonia complexes, $Sc(NH_3)_6$, $V(NH_3)_6$ and $Y(NH_3)_8$ behave as SEPs.[49–51] In $Sc(NH_3)_6$ and $V(NH_3)_6$, in addition to the peripheral orbitals, one and three inner d-electrons remain in the t_{2g} and/or e_g orbitals.[50,51] On the other hand, all $5s^24d^1$ valence electrons of Y solvate in the periphery of $Y(NH_3)_8$.[49] Recently, we reported our first H_2O-based SEPs, $Be(H_2O)_4^{0,+}$ and $Mg(H_2O)_6^{0,+}$.[52] We were able to expand the previously introduced Aufbau principle for SEPs beyond the 2d shell exploiting its higher D_{2h} symmetry. In the ground state of $Mg(H_2O)_6^+$ and $Mg(H_2O)_6$ one and two outer electron(s) occupy a quasi s-orbital.[52] The outer electron of $Mg(H_2O)_6^+$ can advance to one of the 1p, 1d, 2s, 2p, 1f, 2d, 3s, or 1g outer orbitals in energy order.[52] The observed series of $Mg(H_2O)_6^+$ is slightly different from that of $Be(NH_3)_4^+$. The first four shells are identical in both $Mg(H_2O)_6^+$ and $Be(NH_3)_4^+$, but 1f of the former falls in between 2p and 2d, and it rests in between 2s and 2p in the latter.[47,52]

The present report is devoted to the characterization of the geometric and electronic structure of the $Ca(H_2O)_n^{+,0}$ (n = 1–8) species, and are compared with the corresponding magnesium–water and calcium–ammonia species.[48,52] We focus on the more symmetric hexa- and octa-coordinated complexes, which can be characterized as SEPs, and investigate their excited states. Do these systems follow the same Aufbau principle introduced for $Mg(H_2O)_6^+$? How will the excitation energies be affected going from Mg to Ca or from hexa- to octa-coordinated complexes or from water to ammonia complexes? To answer these questions, we have performed high-level quantum calculations and our findings are discussed in this article. In addition, we see the effect of a second shell of H_2O molecules on the excitation energies for a SEP such as $Ca(H_2O)_6@12H_2O^+$ and compare with our recent findings on $M(NH_3)_4@12NH_3$, M = Li, Be^+, B^{2+}.[53]

2. Computational details

Initially, we optimized the lowest energy structures for $[Ca,nH_2O]^+$ (n = 1–7) at the MP2 level of theory using aug-cc-pVTZ basis sets[54–56] for all atoms and correlating all valence electrons. The diffuse functions for calcium were obtained by multiplying the smallest exponents of each shell of cc-pVTZ by 0.3. The diffuse functions on hydrogen and oxygen are needed for the accurate description of possible hydrogen bonds and the diffuse outer orbitals of SEPs. Two kinds of structures are considered, these with all water molecules attached directly to calcium denoted as $Ca(H_2O)_n^+$, and these with a number (k) of water molecules hydrogen bonded to the first solvation shell water ligands denoted as $Ca(H_2O)_n@kH_2O^+$. For the $Ca(H_2O)_{1-8}^{+,0}$ species, we performed additional calculations correlating the sub-valence $2s^22p^63s^23p^6$ electrons of Ca as well (C-MP2). The core-valence cc-pCVTZ basis set for Ca,[57] the cc-pVTZ for O, and the aug-cc-pVTZ for H were used in this case.

Harmonic vibrational frequencies were obtained at the Density Functional Theory (DFT/B3LYP) level of theory for the $Ca(H_2O)_{n=0-8}^{0,+}$ complexes using the cc-pVTZ(Ca,O) and aug-cc-pVTZ(H) basis set. The structures were re-optimized at B3LYP starting from the corresponding optimal MP2 structures. Frequency calculations confirmed the stability of the structures and are used to obtain zero-point energies (ZPE). For the relative

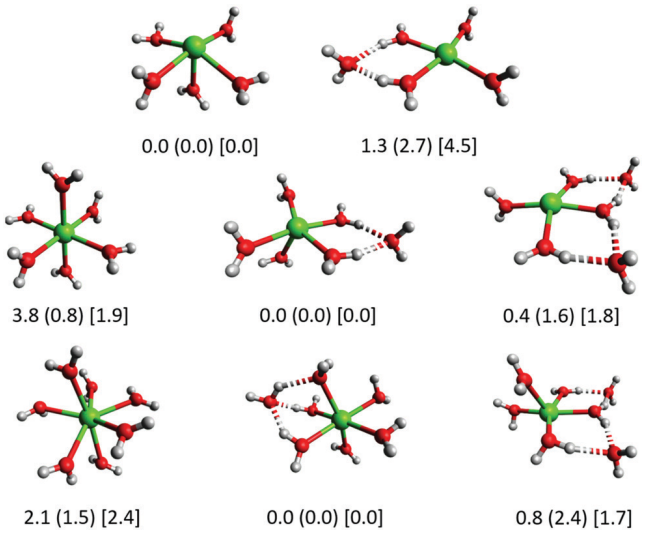

Fig. 1 MP2/aug-cc-pVTZ relative energies (kcal mol^{-1}) for the more stable structures of positively charged calcium water species with five to seven water molecules. ZPE-corrected and free energy corrected (at 20 °C temperature and 1 atm pressure) values (using MP2 frequencies) are shown in parenthesis and square brackets, respectively; CAM-B3LYP frequencies are used for the case of seven water molecules.

MP2 energetics of the $Ca(H_2O)_n$ and $Ca(H_2O)_m@kH_2O$ structures of Fig. 1 and 4, the ZPE and free energy corrections are calculated with MP2/aug-cc-pVTZ harmonic vibrational frequencies.

$Ca(H_2O)_6$ bears no symmetry rendering the multi-reference excited state calculations impractical. To provide excitation energies, we optimized the $Ca(H_2O)_6$ under C_s symmetry and used this geometry to calculate vertical excitations. The C_s structure of $Ca(H_2O)_6$ is 1.10 kcal mol^{-1} higher than its C_1 minimum at the MP2 level of theory. The first excitation energy at MP2 under C_1 and C_s symmetry are 0.64 and 0.60 eV, respectively. Therefore, we believe that the accuracy of our vertical excitation energies is affected by the constrained C_s optimization by less than 0.1 eV. We have used the original D_{2h} structure of $Ca(H_2O)_6^+$ to obtain its vertical excitation energies. Both $Ca(H_2O)_8^+$ and $Ca(H_2O)_8$ have S_8 symmetry. We have used their largest abelian sub-point group, C_2, for the excited state calculations. All optimized structures, their energies, and their frequencies are listed in the ESI.†

Vertical excitation energies for $Ca(H_2O)_{6,8}^+$ were studied at CASSCF and CASPT2 levels of theory. A single active electron is allocated in 35 ($10a_g$, $4b_{3u}$, $4b_{2u}$, $4b_{1g}$, $4b_{1u}$, $4b_{2g}$, $4b_{3g}$, $1a_u$) and 9 (5a, 4b) active orbitals for $Ca(H_2O)_6^+$ and $Ca(H_2O)_8^+$ CASSCF calculations, respectively. For the calculations of $Ca(H_2O)_6$ and $Ca(H_2O)_8$, two active electrons are distributed in 9 (6a′, 3a″ and 5a, 4b) active orbitals, respectively. CASPT2 calculations were performed on top of the CASSCF wave function and correlating all electrons except $1s^22s^22p^63s^23p^6$ of Ca and $1s^2$ of O. We have also performed C-CASPT2 calculations, where all electrons except $1s^2$ of Ca and O are correlated, for the $Ca(H_2O)_6^+$ and $Ca(H_2O)_8^+$ species. For the CASPT2 and C-CASPT2 calculations, the corresponding MP2 and C-MP2 structures were utilized. Unless otherwise stated, excitation energies are calculated with the following basis sets: cc-pVTZ or cc-pCVTZ (Ca) for CASPT2 or C-CASPT2, and cc-pVTZ (O), d-aug-cc-pVTZ (H) for both. A doubly diffuse basis set on hydrogenic centers suffices to provide excitations energies with better than 0.1 eV accuracy.[47]

Excitation energies of $Ca(H_2O)_6^+$ and $Ca(H_2O)_8^+$ systems were also studied using the EOM-EA-CCSD method.[58] For the $Ca(H_2O)_6^+$ we used two series of basis sets, a small double-ζ quality [cc-pVDZ (Ca), cc-pVDZ (O), d-aug-cc-pVDZ (H)] and a bigger triple-ζ quality [cc-pVTZ (Ca), cc-pVTZ (O), d-aug-cc-pVTZ (H)]. We show that the results with the two basis sets are in remarkable agreement. Therefore, due to the technical difficulties the $Ca(H_2O)_8^+$ was only studied with the small cc-pVDZ (Ca), cc-pVDZ (O), d-aug-cc-pVDZ (H) basis set. Furthermore, the excited states of $Ca(H_2O)_6^+$ and $Ca(H_2O)_8^+$ species were investigated through the partial third-order quasiparticle (P3+) electron propagator method[59,60] and core-P3+ (C-P3+) levels of theory using cc-pVTZ (Ca)/cc-pCVTZ (Ca), cc-pVTZ (O), d-aug-cc-pVTZ (H) basis set. For the C-P3+ calculations we correlated all electrons except $1s^2$ of Ca and O.

The $Ca(H_2O)_6@12H_2O^+$ structure was optimized at CAM-B3LYP/aug-cc-pVTZ under constrained S_6 symmetry (the highest abelian group is C_i). We recently showed that CAM-B3LYP provides geometries with MP2-level accuracy for similar systems.[53] There is no strong evidence that this is the lowest energy structure, but the electronic structure and excitation energies are not expected to depend significantly on the orientation of the outer water molecules. The CAM-B3LYP optimized geometry was used to study the excited states of the system with CASSCF, MP2, D2, and P3+. The CASSCF wave-function consists of one electron in 9 active orbitals ($6a_g$, $3a_u$). We used d-aug-cc-pVDZ basis set for all H atoms and cc-pVDZ basis set for Ca and O. Several electronic states of $Ca(H_2O)_6@12H_2O^+$ were studied with MP2, where the use of d-aug-cc-pVTZ for H atoms and cc-pVTZ for the rest atoms was feasible. The excited states were finally investigated using the diagonal second-order approximation (D2) and P3+ methods.[59,60] We introduced the d-aug-cc-pVDZ (H), cc-pVDZ (Ca,O) basis set (DADZ) in both D2 and P3+ calculations. For D2, the use of the d-aug-cc-pVTZ (H), cc-pVTZ (Ca,O) basis set (DATZ) combination was also possible. To get an estimate of the P3+ values with the triple-ζ basis set, we added the difference of the D2 excitation energies (ΔE) between the two basis sets to the P3+ double-ζ values. This quasi-P3+/DATZ method is reported as qP3+:

$$\Delta E(\text{qP3+}) = \Delta E(\text{P3+/DADZ}) + \Delta E(\text{D2/DATZ}) - \Delta E(\text{D2/DADZ})$$

Gaussian16 suite was used to perform geometry optimizations and frequency calculations,[61] MOLPRO 2015.1 was implemented to carry out multi-reference calculations,[62] and QChem was invoked for the EOM-EA-CCSD calculations.[63]

3. Results and discussion

3A. Cationic complexes

Ground state of $Ca(H_2O)_{n=1-8}^+$. According to the Hartree–Fock work of Watanabe and Iwata, the first four water

molecules bind directly to the calcium center,[46] while one to three more water molecules stay in the second solvation shell attaching to the first four with hydrogen bonds. Interestingly, the addition of one more water molecule (totally eight) leads to a penta-coordinated calcium complex. These results are in contrast with our MP2 calculations, which indicate that the first five water molecules bind directly to calcium. The sixth molecule stays in the second solvation shell, $Ca(H_2O)_5@H_2O^+$, with the hexa-coordinated complex being higher by less than 1 kcal mol^{-1} after correcting for ZPE. The addition of a seventh water molecule stabilizes the $Ca(H_2O)_6^+$ core. The most stable structure is $Ca(H_2O)_6@H_2O^+$ with the $Ca(H_2O)_7^+$ isomer being 1.5 kcal mol^{-1} higher in energy (ZPE applied). All of these structures along with their relative energetics are shown in Fig. 1. The structures reported with one or two water molecules in the second solvation shell form at least two hydrogen bonds with the first-shell water ligands. According to our calculations, these are the lowest energy isomers. Notice that structures with two or more water molecules in the second solvation shell are less stable, and that ZPE and free energy corrections at 20 °C and 1 atm favor the $Ca(H_2O)_n^+$ (n water ligands attached to calcium) ions. Our findings are in agreement with the Monte Carlo study of Kochanski and Constantin (see Section 1), who suggested that $Ca(H_2O)_6^+$ complexes dominate in solution phase. These observations are different from calcium ammonia complexes, where the first eight molecules for the (more weakly bound) neutral species bind directly to calcium.[48,64]

Presently we investigate further both the hexa- and octa-coordinated water species for comparison with ammonia. Although, the geometric structure for calcium water complexes has been studied in the literature, their electronic structure remains largely unknown. Our calculations indicate that there is the Ca^+ center present for the smaller species becomes a Ca^{2+} center and an unpaired electron is displaced in the periphery of the $Ca(H_2O)_{n=6-8}^{2+}$ skeleton. Fig. 2 shows the contour for the orbital of this unpaired electron. Every additional water ligand ''pushes'' away this electron from the valence space of calcium more and more.

Table 1 lists the detachment energies (D_e) of one water molecule from the $Ca(H_2O)_n^+$ species (all n water ligands attached to calcium). D_e MP2 values start from 20.7, 20.8 kcal mol^{-1} for n = 1, 2 and gradually reduce to 17.3 kcal mol^{-1} for n = 5. There is a sudden drop for n = 6 to 10.9 kcal mol^{-1}. Interestingly, D_e increases for n = 7 back to 17.1 kcal mol^{-1} and for n = 8 decreases again to 11.5 kcal mol^{-1}. The interaction energy (hydrogen bonding) between a second- and first-shell water molecule is around 14 kcal mol^{-1}, calculated as the average of the MP2 energy differences between $Ca(H_2O)_{1,4,5}@H_2O^+$ and $Ca(H_2O)_{1,4,5}^+$ (at the geometry of $Ca(H_2O)_{1,4,5}@H_2O^+$) + H_2O (13.1, 14.1, 15.1 kcal mol^{-1}, respectively). This interaction is stronger than the H_2O–$Ca(H_2O)_5$ binding. Considering that the hydrogen bonding interactions are slightly affected by the nature of the first coordination sphere, the two numbers (10.9 *vs.* ~14 kcal mol^{-1}) can explain why the sixth water balances between the first and second solvation shell. The hydrogen bonding interaction between a second- and first-shell weakens considerably after the inclusion of ZPE (6.6 kcal mol^{-1} for $Ca(H_2O)_{@}H_2O^+$), which rationalizes why ZPE favors the $Ca(H_2O)_n^+$ over $Ca(H_2O)_{n-k}@kH_2O^+$ complexes.

The core electron correlation effect enhances the binding energy by up to 5.7 kcal mol^{-1} (n = 1). The second larger increase belongs to n = 6 (4.9 kcal mol^{-1}), while the increase is smaller than 3.2 kcal mol^{-1} for the rest species and actually negative (−0.4 kcal mol^{-1}) for n = 8. Finally, ZPE reduces the detachment energies by up to 2.2 kcal mol^{-1} (n = 7). Our final D_0 values at C-MP2 compare favorably with the experimental data of ref. 45 with an average discrepancy of 1.7 kcal mol^{-1} (our values are always smaller); see Table 1. Table 1 reveals also that C-MP2 shortens appreciably the Ca–O distances (~0.1 Å).

Comparing calcium–water, magnesium–water,[52] and calcium–ammonia[48] complexes, we see that C-MP2 predicts comparable D_0 energies for all cases and n = 2–6. There is no specific trend going from Mg to Ca; for n = 2, 3, 6 values Mg–water binding energies are larger and for n = 4, 5 Ca–water ones are larger. The differences are within 3.2 kcal mol^{-1}. Ca–ammonia binding energies are always larger by 1.3 kcal mol^{-1} on average over all n = 2–6 values. These observations indicate that neither the identity of the metal nor the nature of the ligand plays an important role to the stability of the coordination complexes.

Excited states of $Ca(H_2O)_{6,8}^+$. In this section we study the excited states of the dominant (in condensed phase or bigger clusters) $Ca(H_2O)_6^+$ species. The $Ca(H_2O)_8^+$ is also studied as the largest complex with all ligands attached to the metal. Tables 2 and 3 collect the vertical excitation energies at different methodologies including CASSCF, CASPT2, P3+, and EOM-EA-CCSD. Fig. 3 depicts the contours of representative orbitals populated in the low-lying electronic states of $Ca(H_2O)_6^+$; those of $Ca(H_2O)_8^+$ have identical morphology.

The ground state in both cases has a $1s^1$ configuration, which is followed by the $1p^1$, $1d^1$, $2s^1$, $1f^1$, $2p^1$, $1g^1$, $3s^1$ states. The expected degeneracy for states with same configuration is lifted because of the lower symmetry of the complexes compared to hydrogen atom. The T_h point group of $Ca(H_2O)_6^+$ keeps the degeneracy of p-type orbitals, but splits the d-orbitals to the e_g and t_g groups, the f-orbitals to a_u, and two t_u groups, and the g-orbitals to a_g, e_g, and two t_g groups. The S_8 point group of $Ca(H_2O)_8^+$ allows up to doubly degenerate groups (see Table 3).

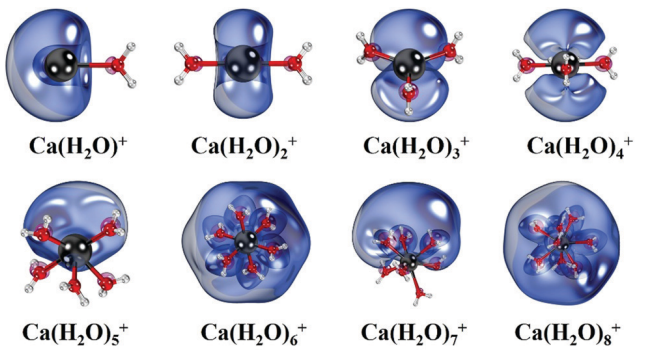

Fig. 2 Contours of the highest (singly occupied) occupied molecular orbital of $Ca(H_2O)_{n=1-8}^+$ for their doublet ground state.

Table 1 Average equilibrium Ca–O distances r_e (Å), and detachment energy of one water ligand D_e and D_0 (kcal mol^{-1}) for $Ca(H_2O)_{n=1-8}^{+,0}$ at MP2 and C-MP2 levels[a]

	$Ca(H_2O)_n^+$						$Ca(H_2O)_n$				
	r_e		D_e[b]		D_0[c]		r_e		D_e[b]		D_0[c]
n	MP2	C-MP2	MP2	C-MP2	C-MP2	Expt[d]	MP2	C-MP2	MP2	C-MP2	C-MP2
1	2.452	2.344	20.7	26.4	25.3	28	2.565	2.431	5.7	7.1	7.0
2	2.448	2.348	20.8	24.0	22.9	24	2.506	2.389	7.0	9.6	9.1
3	2.458	2.354	16.5	19.0	18.1	21.5	2.518	2.420	8.9	10.4	10.0
4	2.476	2.380	17.4	18.6	17.7	18.7	2.541	2.421	10.3	11.9	11.1
5	2.501	2.404	17.3	17.6	17.3	17.5	2.555	2.425	10.1	13.1	14.3
6	2.442	2.367	10.9	15.8	15.4		2.504	2.401	10.1	13.4	11.1
7	2.529	2.421	17.1	19.2	17.0		2.500	2.431	13.1	14.8	12.2
8	2.517	2.448	11.5	11.1	9.8		2.521	2.455	11.2	10.8	9.1

[a] The basis set is cc-pVTZ(Ca) or cc-pCVTZ(Ca) for MP2 or C-MP2 and cc-pVTZ(O), aug-cc-pVTZ(H) for both methods. [b] $D_e = E_e[H_2O] + E_e[Ca(H_2O)_{n-1}^{0,+}] - E_e[Ca(H_2O)_n^{0,+}]$, where E_e is the optimized equilibrium energy. [c] $D_0 = E_0[H_2O] + E_0[Ca(H_2O)_{n-1}^{0,+}] - E_0[Ca(H_2O)_n^{0,+}]$, where $E_0 = E_e$ + ZPE(B3LYP/cc-pVTZ(Ca,O) and aug-cc-pVTZ(H)). [d] Ref. 26.

Table 2 Electronic states, electronic configurations (Config.), and vertical excitation energies (eV) at CASSCF, CASPT2, C-CASPT2, P3+, C-P3+, and EOM-EA-CCSD of the first sixteen states of $Ca(H_2O)_6^+$

State (T_h)	Config.	CASSCF (DATZ)[a]	CASPT2 (DATZ)[a]	C-CASPT2 (DATZ)[a]	P3+ (DATZ)[a]	C-P3+ (DATZ)[a]	EOM-EA-CCSD (DADZ)[b]	EOM-EA-CCSD (DATZ)[a]
1^2A_g	$1s^1$	0.00	0.00	0.00	0.00	0.00	0.00	0.00
1^2T_u	$1p^1$	0.76	0.97	1.04	0.93	0.95	0.96	0.98
1^2E_g	$1d^1$	1.50	1.74	1.73	1.69	1.71	1.74	1.74
1^2T_g	$1d^1$	1.72	2.13	2.12	2.07	2.10	2.15	2.18
2^2A_g	$2s^1$	2.34	2.73	2.76	2.69	2.70	2.76	2.80
2^2T_u	$1f^1$	2.44	2.86	2.92	2.79	2.82	2.86	2.89
1^2A_u	$1f^1$	2.61	3.09	3.08	3.06	3.09	3.13	3.14
3^2T_u	$1f^1$	2.76	3.23	3.29	3.25	3.27	3.27	3.30
4^2T_u	$2p^1$	2.67	3.16	3.22	3.11	3.13	3.18	3.23
2^2E_g	$2d^1$	3.12	3.59	3.59	3.52	3.55	3.60	3.66
2^2T_g	$2d^1$	3.17	3.60	3.73	3.59	3.60		
3^2T_g	$1g^1$	3.45	3.66	3.87	3.71	3.63		
3^2A_g	$1g^1$	3.49	3.99	4.00				
3^2E_g	$1g^1$	3.59	4.10	4.11				
4^2T_g	$1g^1$	3.65	4.05	4.16				
4^2A_g	$3s^1$	3.74						

[a] DATZ = cc-pVTZ (Ca,O), d-aug-cc-pVTZ (H). [b] DADZ = cc-pVDZ (Ca,O), d-aug-cc-pVDZ (H).

Focusing on the excitation energies of $Ca(H_2O)_6^+$ and how the different methods perform, we make the following comments. The low CASSCF values by 0.5 eV in some cases (compared to CASPT2) indicate that dynamic electron correlation is certainly important. The dynamic correlation coming from the sub-valence electrons of calcium generally increase our values on average by only 0.05 eV (CASPT2 *vs.* C-CASPT2) or 0.01 eV (P3+ *vs.* C-P3+). Our values seem to be highly insensitive to the level of dynamic electron correlation treatment.

Due to the high symmetry of $Ca(H_2O)_6^+$, the three 1p and three 2p components are degenerate. The smallest range of excitation energies within the d, f, and g-type states belongs to $2d^1$ (2^2E_g and 2^2T_g). The components of 1d, 1f, and 1g of $Ca(H_2O)_6^+$ are within 0.39, 0.37, and 0.44 eV at CASPT2, but that of the more diffuse 2d is only within 0.01 eV. For $Ca(H_2O)_8^+$, The P3+ splitting for the 1p, 1d, and 1f states is 0.30, 0.39, and 0.28 eV, but that of 2p is only 0.09 eV. The smaller splitting of 2d and 2p is because these orbitals have an additional node compared to the 1p, 1d, 1f, or 1g orbitals, expand further in space, and experience the $Ca(H_2O)_{6,8}^{2+}$ core more as an isotropic structure.

Next, we compare the weighted (according to degeneracy) averaged P3+ excitation energies of the states studied in common for the two species. The excitation energies for 1p, 1d, 2s, 1f, and 2p are (n = 6/8) 0.93/0.81, 1.92/1.70, 2.69/2.55, 3.03/2.61, and 3.11/2.92 eV, respectively. The excitation energies are always lower for n = 8 by at least 0.12 eV as expected due to the more diffuse nature of the outer electron of $Ca(H_2O)_8^+$. Very similar observations were made for the $Ca(NH_3)_{6-8}^+$ sequence.[48] Finally, the excitation energies of the $Ca(H_2O)_6^+$, $Mg(H_2O)_6^+$, and $Ca(NH_3)_6^+$ for the different states agree within 0.2 eV (compare present Table 2 with Table 2 of ref. 52 and 48). The excitation energies are generally higher for $Mg(H_2O)_6^+$, but no obvious trend is observed between the calcium water and ammonia complexes.

3B. Neutral complexes

Ground state of $Ca(H_2O)_{n=1-8}$. No experimental or theoretical information is found in the literature about the stability and

Table 3 Electronic states, electronic configurations (Config.), and vertical excitation energies (eV) at CASSCF, CASPT2, C-CASPT2, P3+, C-P3+, and EOM-EA-CCSD of thirteen states of $Ca(H_2O)_8^+$

State (S_8)	Config.	CASSCF (DATZ)[a]	CASPT2 (DATZ)[a]	C-CASPT2 (DATZ)[a]	P3+ (DATZ)[a]	C-P3+ (DATZ) [a]	EOM-EA-CCSD (DADZ) [b]
1^2A	$1s^1$	0.00	0.00	0.00	0.00	0.00	0.00
1^2E_1	$1p^1$	0.56	0.74	0.73	0.71	0.72	0.74
1^2B	$1p^1$	0.84	1.04	1.03	1.01	1.02	1.04
1^2E_2	$1d^1$	1.29	1.61	1.59	1.57	1.58	1.62
1^2E_3	$1d^1$	1.45	1.74	1.72	1.70	1.71	1.74
2^2A	$1d^1$	1.59	2.00	1.99	1.96	1.97	2.03
3^2A	$2s^1$				2.55	2.56	2.62
2^2E_3	$1f^1$				2.47	2.48	2.53
2^2E_2	$1f^1$				2.57	2.58	2.63
2^2E_1	$1f^1$				2.72	2.74	2.78
2^2B	$1f^1$				2.75	2.77	2.81
3^2E_1	$2p^1$				2.89	2.90	2.96
3^2B	$2p^1$				2.98	3.00	3.04

[a] DATZ = cc-pVTZ (Ca,O), d-aug-cc-pVTZ (H). [b] DADZ = cc-pVDZ (Ca,O), d-aug-cc-pVDZ (H).

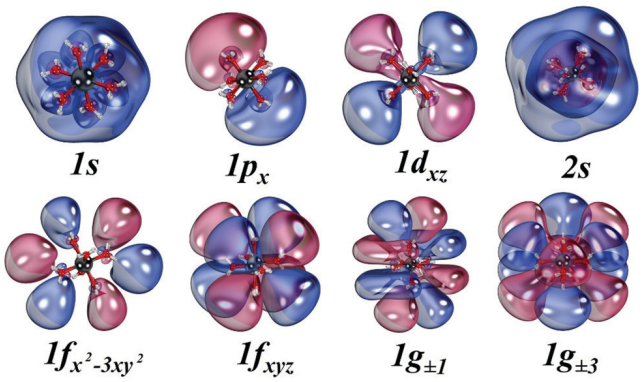

Fig. 3 Selected outer orbitals of $Ca(H_2O)_6^+$.

structure of the neutral calcium water complexes. To this end, we first optimized the geometry of the complexes from two to six water molecules. Besides the complexes with all water ligands coordinated to calcium, $Ca(H_2O)_n$, we also considered the complexes with one water molecule hydrogen bonded to one of the first coordination sphere water ligands, $Ca(H_2O)_n@H_2O$. Compared to cationic complexes, the presence of a second electron in the valence shell of calcium is expected to further deter water ligands from binding to calcium. Indeed, the binding energies are smaller and the equilibrium Ca–O distances longer by ~0.1 Å (see Table 1).

At the same time, the placement of a water ligand to the second coordination sphere is also less favorable for the neutral systems. For example, the neutral $Ca(H_2O)_5$ and $Ca(H_2O)_6$ complexes are more stable than $Ca(H_2O)_4@H_2O$ and $Ca(H_2O)_5@H_2O$ by 1.5 and 1.7 kcal mol^{-1} (ZPE corrected values; see Fig. 4) as opposed to the cations where the latter structures are slightly more stable (compare Fig. 1 and 4). Free energy corrections at 20 °C and 1 atm make little difference from ZPE corrected values. Actually they favor further $Ca(H_2O)_5$. The $Ca(H_2O)_n$ and $Ca(H_2O)_{n-1}@H_2O$ isomers are practically isoenergetic for n = 2 with or without the ZPE/free energy correction, while

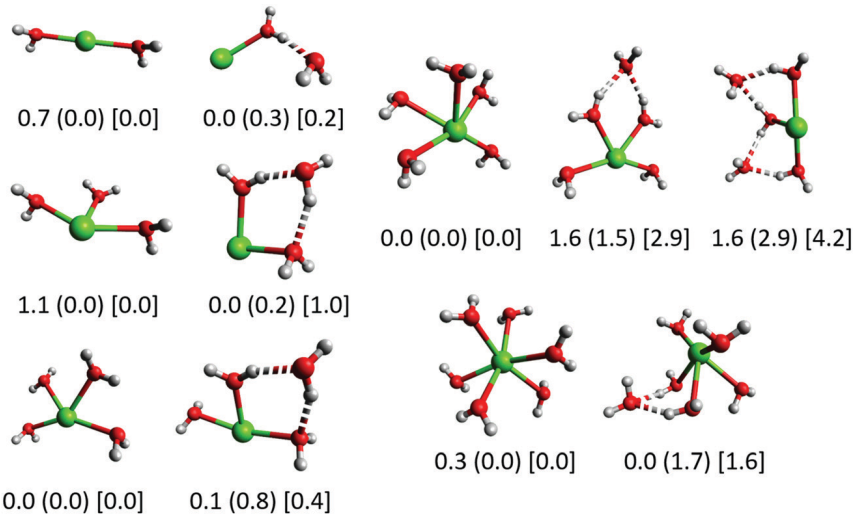

Fig. 4 MP2/aug-cc-pVTZ relative energies (kcal mol^{-1}) for the more stable structures of neutral calcium water species with two to six water molecules. ZPE-corrected and free energy corrected (at 20 °C temperature and 1 atm pressure) values (using MP2 frequencies) are shown in parenthesis and square brackets, respectively.

their energy difference for n = 3 is completely inverted when ZPE/thermal corrections are included (see Fig. 4). For n = 3–6, ZPE corrections clearly favor the $Ca(H_2O)_n$ structure. These observations indicate that going from the cationic to the neutral species the Ca–water interaction becomes weaker not only for the directly connected (to Ca) water ligands, but also for the second sphere water molecules. Actually, the latter interactions attenuate faster enhancing the stability of the $Ca(H_2O)_n$ species.

Focusing on the $Ca(H_2O)_n$ complexes, the attachment of a water molecule to calcium stabilizes the system by 5.7–11.2 kcal mol^{-1} at MP2. This range becomes 7.1–14.8 kcal mol^{-1} at C-MP2 and 7.0–14.3 kcal mol^{-1} when ZPE is added (see Table 1). Interestingly, the binding energy of the additional water is increasing, albeit only slightly, for bigger complexes in contrast with the cationic species where the binding energy decreases with the size. On the other hand, in both cationic and neutral species the sub-valence electron correlation (C-MP2) shortens the Ca–O bond lengths by ~0.1 Å.

Excited states of $Ca(H_2O)_{n=6,8}$. The binding energies for the larger neutral complexes are smaller, but still comparable to the energies of the experimentally observed cationic complexes (see Table 1) and these of the experimentally observed neutral calcium–ammonia complexes.[64] $Ca(H_2O)_6$ is the smallest complex where the electronic density of the two valence electrons is evenly distributed in the periphery of the $Ca^{2+}(H_2O)_6$ core (see Fig. S1 of the ESI†), and can be characterized as an SEP. We presently study the excited states of $Ca(H_2O)_6$, as well as the highly-symmetric $Ca(H_2O)_8$ complex.

The ground state of both systems has $1s^2$ configuration, which is followed by the three $1s^11p^1$ components of triplet spin multiplicity. These correspond to two $^3A'$ and one $^3A''$ states (C_s symmetry) for $Ca(H_2O)_6$, and to ^3B and $^3E_1$ states (S_8 symmetry) for $Ca(H_2O)_8$. The analogous ^3P atomic term is listed in Table 4 along with the range of CASPT2 excitation energies of 0.60–0.92 eV and 0.33–0.69 eV for $Ca(H_2O)_6$ and $Ca(H_2O)_8$, respectively. The corresponding CASSCF excitation energies are 0.10–0.24 eV lower as happens for the cationic systems. Additionally, the excitation energies drop going from $Ca(H_2O)_6$ to $Ca(H_2O)_8$. The same effect was observed for $Ca(NH_3)_{6,8}$ and was attributed to the more diffuse electronic density in the case of the octa-coordinated complex.[48] The more distant (from the Ca^{2+} core) electrons of $Ca(NH_3)_8$ can easier be excited or removed. Specifically, the first ionization energy of $Ca(NH_3)_6$ and $Ca(NH_3)_8$ are 3.43 eV and 3.24 eV, respectively.

The next states are of both singlet and triplet spin multiplicities. The triplets have pure $1p^2$ (^3P) and $1s^11d^1$ (^3D) configurations, while the singlets are of heavily mixed character mingling the $1s^11p^1$ (^1P), $1p^2$ (^1D), and $1s^11d^1$ (^1D) configurations. The energy order is unclear for the different groups of components, and a detailed list of the calculated energy spectrum is provided in the ESI.† Generally, the excitations are lower in energy for octa-coordinated species, and the order of ^3D and ^3P groups is reverse for the two complexes.

3C. Dual solvation shell species

The consideration of a second solvation shell of water molecules for the $Ca(H_2O)_6^+$ complex is the topic of this section. Similar theoretical studies have been reported for transition metal cations with oxidation states (2+ or 3+)[65,66] that do not afford an outer electron, as opposed to Ca^+. Although the $Ca(H_2O)_5@H_2O^+$ isomer is more stable for the $Ca/6H_2O$ system by just 0.8 kcal mol^{-1} (see Fig. 1), the addition of more water molecules will stabilize the $Ca(H_2O)_6^{2+}$ core as happens for the Mg–water complexes.[28] Therefore, we extended our study to the $Ca(H_2O)_6@12H_2O^+$ complex to see the effect of the second solvation shell for a water complex, as we did recently for the $M(NH_3)_4@12NH_3$ ammonia complexes with M = Li, Be^+, and B^{2+}.[53] The optimized structure was obtained at the CAM-B3LYP level (see Fig. 5) and the excitations energies with various electronic structure approaches (see Table 5). The obtained $Ca(H_2O)_6@12H_2O^+$ polyhedron has S_6 symmetry.

The large computational cost allowed us to explore only the $1s^1$, $1p^1$, and $1d^1$ electronic states. For the calculation of their excitation energies we employed the CASSCF (practically Hartree–Fock), MP2, D2, and P3+ methodologies combined with either double- or triple-ζ basis sets. The calculated

Table 4 Electronic configurations (Config.), electronic terms (State) and vertical excitation energies (eV) at CASSCF and CASPT2 for several low-lying states of $Ca(H_2O)_{6,8}$ at cc-pVTZ (Ca,O), d-aug-cc-pVTZ (H) basis set

		$Ca(H_2O)_6$		$Ca(H_2O)_8$	
Config.	State[a]	CASSCF	CASPT2	CASSCF	CASPT2
$1s^2$	^1S	0.00	0.00	0.00	0.00
$1s^11p^1$	^3P	0.44–0.69	0.60–0.92	0.23–0.56	0.33–0.69
$1s^11d^1$	^3D	1.41–1.66	1.64–1.89	1.31–1.54	1.33–1.64
$1p^2$	^3P	1.71–2.00	1.98–2.29	0.99–1.21	1.21–1.43
$1s^11p^1$/ $1s^11d^1/1p^2$	$^1P/^1D/^1D$	0.92–2.33	1.14–2.56	0.70–1.68	0.93–1.81

[a] The atomic terms corresponding to the assigned configuration is reported here. A more detailed list and the actual electronic terms are given in Tables S21 and S22 of the ESI.

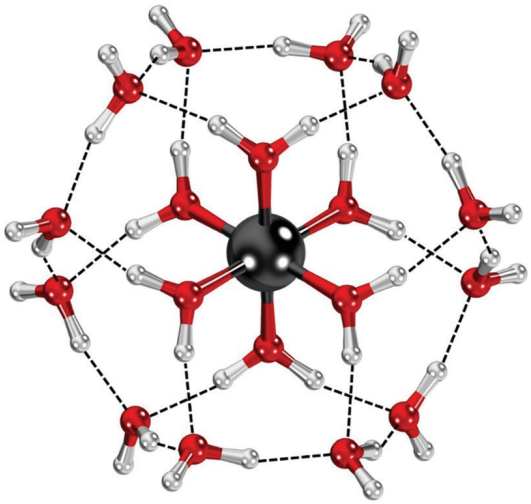

Fig. 5 Optimized geometry of $Ca(H_2O)_6^+@12H_2O$. The dashed black lines show hydrogen bonds between water molecules.

Table 5 Electronic terms, electronic configurations (Config.), and vertical excitation energies (eV) at the CASSCF, MP2, D2, and P3+ levels of theory for the first six states of $[Ca(H_2O)_6@12H_2O]^+$

State (S_6)	Config.	CASSCF (DADZ)[a]	MP2 (DATZ)[b]	D2 (DADZ)[a]	P3+ (DADZ)[a]	D2 (DATZ)[b]	qP3+ (DATZ)[c]
1^2A_g	$1s^1$	0.00	0.00	0.00	0.00	0.00	0.00
1^2E_u	$1p^1$	0.24	0.35	0.32	0.32	0.33	0.33
1^2A_u	$1p^1$	0.46	0.70	0.65	0.65	0.66	0.66
1^2E_g	$1d^1$	0.64	0.86	0.80	0.80	0.82	0.82
2^2E_g	$1d^1$	0.75	1.03	0.96	0.96	0.98	0.98
2^2A_g	$1d^1$	0.94		1.22	1.23	1.25	1.26

[a] Basis set: cc-pVDZ (Ca,O), d-aug-cc-pVDZ (H). [b] Basis set: cc-pVTZ (Ca,O), d-aug-cc-pVTZ (H). [c] Quasi-DATZ. See Section 2.

excitation energies seem largely insensitive to the method or basis set used, except for the dynamic-correlation-free CASSCF level. Specifically, the highest deviation among the non-CASSCF methods of 0.07 eV in the relatively high energy $2^2E_g(1d^1)$ state. As in the $Ca(H_2O)_6$ complex, the first excited state is of $1p^1$ character. However, the three components are not triply degenerate any more due to the anisotropy of the $Ca(H_2O)_6@12H_2O^+$ polyhedron, with the relative 1^2E_u and 1^2A_u states being separated by $\sim$0.33 eV (see Table 5). Similarly, the next five $1d^1$ components are grouped as 1^2E_g, 2^2E_g, and 2^2A_g covering a range of about 0.45 eV. Overall, the $1p^1$ and $1d^1$ states lie at 0.33–0.66 (weighted average 0.44) and 0.82–1.26 (weighted average 0.97) eV, respectively, at the composite qP3+ level of theory. The corresponding P3+ numbers for $Ca(H_2O)_6$ are 0.93 and 1.69–2.07 (weighted average 1.92) eV (see Table 2), about double of the previous numbers.

4. Conclusions

Presently we performed high level quantum chemical calculations to characterize the geometric and electronic structure of cationic and neutral calcium water complexes. Neutral complexes favor the coordination of water ligands directly to the metal more than the corresponding positively charged complexes. For example, $Ca(H_2O)_6$ is more stable than $Ca(H_2O)_5@H_2O$, but $[Ca,6H_2O]^+$ composition prefers $Ca(H_2O)_5@H_2O^+$. The $Ca(H_2O)_6^+$ core is formed however for $[Ca,7H_2O]^+$. The dissociation of a water molecule is easier for neutral species, and especially for the smaller of them. The dissociation of a water ligand for cations is easier for the bigger members. For six or more water ligands, the valence calcium electrons are displaced to the periphery of the complex as has been previously observed for a series of species called SEPs.

The energy pattern for the excited states of the "one-electron" $Ca(H_2O)_{6,8}^+$ follows the same Aufbau principle observed for the previously reported SEPs: 1s, 1p, 1d, 2s, 1f, 2p, 2d, 1g, 3s. The excitation energies drop going from the hexa- to the octa-coordinated complexes as expected because the electronic density of the latter is more remote from the metal center. Compared to magnesium water and calcium ammonia complexes, the excitation energies follow the order Mg–water > calcium–water $\sim$ calcium ammonia. The electronic spectrum of the neutral complexes is quite complex with the relative excited states being of multi-reference nature. Finally, we saw that a second solvation shell of water molecules around $Ca(H_2O)_6^+$ reduces the excitation energies by a factor of almost two.[47,53]

Our findings are expected to benefit future experimental studies aiming at the elucidation of the geometric and electronic structure of the calcium water complexes.

Conflicts of interest

There are no conflicts to declare.

Acknowledgements

The authors are indebted to Auburn University (AU) for financial support. This work was completed with resources provided by the Auburn University Hopper Cluster, Alabama Supercomputer, and the National Energy Research Scientific Computing Center, a DOE Office of Science User Facility supported by the Office of Science of the U.S. Department of Energy under Contract No. DE-AC02-05CH11231. This material is based upon work supported by the National Science Foundation under Grant No. CHE-1940456. Any opinions, findings, and conclusions or recommendations expressed in this material are those of the author(s) and do not necessarily reflect the views of the National Science Foundation.

References

1 E. Zurek, P. P. Edwards and R. Hoffmann, *Angew. Chem., Int. Ed.*, 2009, **48**, 8198–8232.
2 J. M. Herbert and M. P. Coons, *Annu. Rev. Phys. Chem.*, 2017, **68**, 447–472.
3 P. P. Edwards, *J. Supercond.*, 2000, **13**, 933–946.
4 A. G. Seel, E. Zurek, A. J. Ramirez-Cuesta, K. R. Ryan, M. T. J. Lodge and P. P. Edwards, *Chem. Commun.*, 2014, **50**, 10778–10781.
5 E. Zurek, X.-D. Wen and R. Hoffmann, *J. Am. Chem. Soc.*, 2011, **133**, 3535–3547.
6 C. V. D. Linde and M. K. Beyer, *Phys. Chem. Chem. Phys.*, 2011, **13**, 6776–6778.
7 M. Beyer, C. Berg, H. W. Görlitzer, T. Schindler, U. Achatz, G. Albert, G. Niedner-Schatteburg and V. E. Bondybey, *J. Am. Chem. Soc.*, 1996, **118**, 7386–7389.

8 B. M. Reinhard and G. Niedner-Schatteburg, *J. Phys. Chem. A*, 2002, **106**, 7988–7992.
9 C.-K. Siu, Z.-F. Liu and J. S. Tse, *J. Am. Chem. Soc.*, 2002, **124**, 10846–10860.
10 M. Beyer, U. Achatz, C. Berg, S. Joos, G. Niedner-Schatteburg and V. E. Bondybey, *J. Phys. Chem. A*, 1999, **103**, 671–678.
11 T. Tsurusawa and S. Iwata, *J. Phys. Chem. A*, 1999, **103**, 6134–6141.
12 T. Tsurusawa and S. Iwata, *J. Chem. Phys.*, 2000, **112**, 5705–5710.
13 B. Gao and Z.-F. Liu, *J. Chem. Phys.*, 2007, **126**, 084501.
14 C. P. Schulz, R. Haugstätter, H. U. Tittes and I. V. Hertel, *Phys. Rev. Lett.*, 1986, **57**, 1703–1706.
15 C. P. Schulz, R. Haugstätter, H. U. Tittes and I. V. Hertel, *Z. Phys. D: At., Mol. Clusters*, 1988, **10**, 279–290.
16 C. Steinbach and U. Buck, *Phys. Chem. Chem. Phys.*, 2005, **7**, 986–990.
17 U. Buck and C. Steinbach, *J. Phys. Chem. A*, 1998, **102**, 7333–7336.
18 C. J. Mundy, J. Hutter and M. Parrinello, *J. Am. Chem. Soc.*, 2000, **122**, 4837–4838.
19 L. Bewig, U. Buck, S. Rakowsky, M. Reymann and C. Steinbach, *J. Phys. Chem. A*, 1998, **102**, 1124–1129.
20 K. F. Willey, C. S. Yeh, D. L. Robbins, J. S. Pilgrim and M. A. Duncan, *J. Chem. Phys.*, 1992, **97**, 8886–8895.
21 F. Misaizu, M. Sanekata, K. Fuke and S. Iwata, *J. Chem. Phys.*, 1994, **100**, 1161–1170.
22 A. C. Harms, S. N. Khanna, B. Chen and A. W. Castleman, *J. Chem. Phys.*, 1994, **100**, 3540–3544.
23 T. Taxer, M. Ončák, E. Barwa, C. van der Linde and M. K. Beyer, *Faraday Discuss.*, 2019, **217**, 584–600.
24 C. van der Linde, A. Akhgarnusch, C.-K. Siu and M. K. Beyer, *J. Phys. Chem. A*, 2011, **115**, 10174–10180.
25 C. Berg, M. Beyer, U. Achatz, S. Joos, G. Niedner-Schatteburg and V. E. Bondybey, *Chem. Phys.*, 1998, **239**, 379–392.
26 C. Berg, U. Achatz, M. Beyer, S. Joos, G. Albert, T. Schindler, G. Niedner-Schatteburg and V. E. Bondybey, *Int. J. Mass Spectrom. Ion Processes*, 1997, **167-168**, 723–734.
27 Y. Inokuchi, K. Ohshimo, F. Misaizu and N. Nishi, *J. Phys. Chem. A*, 2004, **108**, 5034–5040.
28 B. M. Reinhard and G. Niedner-Schatteburg, *J. Chem. Phys.*, 2003, **118**, 3571–3582.
29 C.-K. Siu and Z.-F. Liu, *Phys. Chem. Chem. Phys.*, 2005, **7**, 1005–1013.
30 B. M. Reinhard and G. Niedner-Schatteburg, *Phys. Chem. Chem. Phys.*, 2003, **5**, 1970–1980.
31 T.-W. Lam, C. van der Linde, A. Akhgarnusch, Q. Hao, M. K. Beyer and C.-K. Siu, *ChemPlusChem*, 2013, **78**, 1040–1048.
32 C. W. Bauschlicher, M. Sodupe and H. Partridge, *J. Chem. Phys.*, 1992, **96**, 4453–4463.
33 M. Ončák, T. Taxer, E. Barwa, C. van der Linde and M. K. Beyer, *J. Chem. Phys.*, 2018, **149**, 044309.
34 K. Hashimoto and K. Daigoku, *Phys. Chem. Chem. Phys.*, 2009, **11**, 9391–9400.
35 I. R. Ariyarathna, F. Pawłowski, J. V. Ortiz and E. Miliordos, *Phys. Chem. Chem. Phys.*, 2018, **20**, 24186–24191.
36 T. E. Salter, V. Mikhailov and A. M. Ellis, *J. Phys. Chem. A*, 2007, **111**, 8344–8351.
37 S. Yoshida, K. Daigoku, N. Okai, A. Takahata, A. Sabu, K. Hashimoto and K. Fuke, *J. Chem. Phys.*, 2002, **117**, 8657–8669.
38 M. H. Shen and J. M. Farrar, *J. Chem. Phys.*, 1991, **94**, 3322–3331.
39 S. G. Donnelly and J. M. Farrar, *J. Chem. Phys.*, 1993, **98**, 5450–5459.
40 M. H. Shen, J. W. Winniczek and J. M. Farrar, *J. Phys. Chem.*, 1987, **91**, 6447–6449.
41 D. C. Sperry, A. J. Midey, J. I. Lee, J. Qian and J. M. Farrar, *J. Chem. Phys.*, 1999, **111**, 8469–8480.
42 I. Cabanillas–Vidosa, M. Rossa, G. A. Pino and J. C. Ferrero, *Phys. Chem. Chem. Phys.*, 2011, **13**, 13387–13394.
43 I. Cabanillas-Vidosa, M. Rossa, G. A. Pino, J. C. Ferrero and C. J. Cobos, *Phys. Chem. Chem. Phys.*, 2012, **14**, 4276–4286.
44 M. Sanekata, F. Misaizu and K. Fuke, *J. Chem. Phys.*, 1996, **104**, 9768–9778.
45 E. Kochanski and E. Constantin, *J. Chem. Phys.*, 1987, **87**, 1661–1665.
46 H. Watanabe and S. Iwata, *J. Phys. Chem. A*, 1997, **101**, 487–496.
47 I. R. Ariyarathna, S. N. Khan, F. Pawłowski, J. V. Ortiz and E. Miliordos, *J. Phys. Chem. Lett.*, 2018, **9**, 84–88.
48 I. R. Ariyarathna, N. M. S. Almeida and E. Miliordos, *J. Phys. Chem. A*, 2019, **123**, 6744–6750.
49 N. M. S. Almeida and E. Miliordos, *Phys. Chem. Chem. Phys.*, 2019, **21**, 7098–7104.
50 N. M. S. Almeida, F. Pawłowski, J. V. Ortiz and E. Miliordos, *Phys. Chem. Chem. Phys.*, 2019, **21**, 7090–7097.
51 S. N. Khan and E. Miliordos, *J. Phys. Chem. A*, 2020, **124**, 4400–4412.
52 I. R. Ariyarathna and E. Miliordos, *Phys. Chem. Chem. Phys.*, 2019, **21**, 15861–15870.
53 I. R. Ariyarathna, F. Pawłowski, J. V. Ortiz and E. Miliordos, *J. Phys. Chem. A*, 2020, **124**, 505–512.
54 T. H. Dunning, *J. Chem. Phys.*, 1989, **90**, 1007–1023.
55 R. A. Kendall, T. H. Dunning and R. J. Harrison, *J. Chem. Phys.*, 1992, **96**, 6796–6806.
56 D. E. Woon and T. H. Dunning, *J. Chem. Phys.*, 1994, **100**, 2975–2988.
57 J. Koput and K. A. Peterson, *J. Phys. Chem. A*, 2002, **106**, 9595–9599.
58 M. Nooijen and R. J. Bartlett, *J. Chem. Phys.*, 1995, **102**, 3629–3647.
59 J. V. Ortiz, *Int. J. Quantum Chem.*, 2005, **105**, 803–808.
60 J. V. Ortiz, *Wiley Interdiscip. Rev.: Comput. Mol. Sci.*, 2013, **3**, 123–142.
61 M. J. Frisch, G. W. Trucks, H. B. Schlegel, G. E. Scuseria, M. A. Robb, J. R. Cheeseman, G. Scalmani, V. Barone, G. A. Petersson and H. Nakatsuji, *et al.*, *Gaussian 16 Rev. B.01*, Wallingford, CT, 2016.
62 H.-J. Werner, P. J. Knowles, G. Knizia, F. R. Manby, M. Schütz, P. Celani, W. Györffy, D. Kats and T. Korona,

R. Lindh, *et al.*, *MOLPRO, version 2015.1, a package of ab initio programs*, 2015.
63 Y. Shao, Z. Gan, E. Epifanovsky, A. T. B. Gilbert, M. Wormit, J. Kussmann, A. W. Lange, A. Behn, J. Deng and X. Feng, *et al.*, Advances in molecular quantum chemistry contained in the Q-Chem 4 program package, *Mol. Phys.*, 2015, **113**, 184–215.
64 M. D. Albaqami and A. M. Ellis, *Chem. Phys. Lett.*, 2018, **706**, 736–740.
65 M. Radoń and G. Drabik, *J. Chem. Theory Comput.*, 2018, **14**, 4010–4027.
66 M. Radoń, K. Gąssowska, J. Szklarzewicz and E. Broclawik, *J. Chem. Theory Comput.*, 2016, **12**, 1592–1605.

Appendix D

Supporting material for Chapter 5: *"Ab initio investigations of ground and excited states of transition metal monoxides and their catalytic strengths towards water and hydrogen sulfide activation"*

Appendix D contains the full copies of following articles. Reprints were made with permissions from the publisher.

- Ariyarathna, I. R.; Miliordos, E. *J. Quant. Spectrosc. Radiat. Transf.* **2020**, *255*, 107265.
- Ariyarathna, I. R.; Miliordos, E. Radical abstraction vs. oxidative addition mechanisms for the activation of the S−H, O−H, and C−H bonds using early transition metal oxides, Under review PCCP.
- Ariyarathna, I. R.; Miliordos, E. *Phys. Chem. Chem. Phys.* **2018**, *20*, 12278–12287.
- Ariyarathna, I. R.; Almeida, N. M. S.; Miliordos, E. *Phys. Chem. Chem. Phys.* **2020**, *22*, 16072–16079.

Ab initio investigation of the ground and excited states of ZrO^+ and NbO^+

Journal of Quantitative Spectroscopy & Radiative Transfer 255 (2020) 107265

Contents lists available at ScienceDirect

Journal of Quantitative Spectroscopy & Radiative Transfer

journal homepage: www.elsevier.com/locate/jqsrt

Ab initio investigation of the ground and excited states of ZrO^+ and NbO^+

Isuru R. Ariyarathna, Evangelos Miliordos*

Department of Chemistry and Biochemistry, Auburn University, Auburn, AL 36849

ARTICLE INFO

Article history:
Received 28 July 2020
Revised 16 August 2020
Accepted 16 August 2020
Available online 17 August 2020

Keywords:
Ab initio calculations
Potential energy curves
Multi-reference configuration interaction
valence-bond-Lewis diagrams
Spectroscopic parameters

ABSTRACT

High-level *ab initio* quantum calculations were performed to study thirteen and sixteen low-lying electronic states of ZrO^+ and NbO^+. We report their potential energy curves, electronic configurations, bond distances, harmonic vibrational frequencies, anharmonicities, spin–orbit splittings, and excitation energies. Chemical bonding patterns for low-lying electronic states are also proposed. The removal of one electron from the ~$5s_{Zr}$ of ZrO creates the first three states of ZrO^+ ($X^2\Delta$, $1^2\Sigma^+$, $1^2\Pi$). These three states bear oxo ($Zr^{3+}O^{2-}$) character and the remaining states show oxyl ($Zr^{2+}O^{\cdot-}$) nature. Similarly, the detachment of one electron from ~$5s_{Nb}$ of nine low-lying states of NbO generate the nine lowest energy states of NbO^+ that possess oxo ($Nb^{3+}O^{2-}$) character. Low-lying electronic states of ZrO^+ and NbO^+ are very similar to their isovalent TiO^+ and VO^+ partners. The current study rectifies spectroscopic assignments made for ZrO^+ and NbO^+ in the literature.

1. Introduction

Transition metal oxides are efficient heterogenous catalysts owing to their rich redox chemistry [1–3], and have a wide scope of industrial applications [4,5]. From the theoretical point of view, to understand the catalytic processes on metal oxide surfaces, periodic boundary conditions are commonly applied. Metal oxide molecular compounds are also common homogeneous catalysts. The deeper comprehension originating from the electronic structure calculations of naked metal oxides offers a starting point for a bottom-up approach to predict and synthesize more efficient metal oxide catalysts [6,7].

To this end, the electronic structure of ground and excited states of first-row transition metal monoxides (TMOs) have been studied extensively in the past [8–10]. First-row TMOs are found to bear strong ionic nature with minor radical character on oxygen [8–10]. On the other hand, the electronic structure of ground and excited states of many second-row TMOs is yet to be explored. The present study is an extension to our ongoing work to disclose the electronic structure of second-row transition metal monoxides [11–16]. In the past we explored the ground and low-lying electronic states of $MoO^{+,0,-}$ [11], $RuO^{0,+,2+,-}$ [15,16], NbO [13], and ZrO [14]. The current work focuses on ZrO^+ and NbO^+.

The pattern of the ground and low-lying electronic states of ZrO^+ is unclear in the literature, and a systematic high-level theoretical work is necessary. Early experimental studies in 1980 and 1993 (near-IR rotational and electron spin resonance spectroscopy) identified $^2\Sigma^+$ ($1\sigma^2 1\pi^4 2\sigma^1$) as the ground state of ZrO^+ [17,18]. Five years ago, Luo et al. assigned the ground state as $^2\Delta$ by rotationally resolved photoelectron spectroscopy [19]. This finding is consistent with the assignment made by the Hu et al. in 2009 [7] in terms of density functional and coupled cluster theory, and has been adopted by Lam et al. in 2018 [20] who provided a very accurate binding energy and ionization energy at the complete basis set limit and using up to quadruple replacements in the CI expansion. However, the theoretical density functional work of Rondinelli et al. in 2006 predicted a $^2\Sigma^+$ ground state [21]. Finally, the $^2\Sigma^+$ assignment was adopted by Sievers and Armentrout, who studied the $Zr^+/ZrO^+ + CO_2 \longleftrightarrow ZrO^+/ZrO_2^+ + CO$ reaction pathways by ion beam mass spectrometry. The authors "assuming that there are no barriers in excess of the endothermicity of these reactions" identified two excited states of ZrO^+ with excitation energies of 1.99 ± 0.08 and 2.93 ± 0.14 eV [22]. These energies were assigned to $^2\Delta/^2\Pi$ and $^4\Phi$ states.

The first experimental study of NbO^+ belongs to Dyke et al. [23]. They identified its ground and first excited state as $^3\Sigma^-$ and $^3\Delta$, respectively. Using Hartree-Fock calculations they assigned them to $2\sigma^2 1\pi^4 1\delta^2$ and $2\sigma^2 3\pi^4 1\delta^1 3\sigma^1$ electronic configurations. The vertical ionization energy of $NbO(^4\Sigma^-)$ to the $^3\Sigma^-$ and $^3\Delta$ states of NbO^+ are equal to 7.91 ± 0.02 and 10.34 ± 0.02 eV. Their corresponding Hartree-Fock values were estimated as 5.95

* Corresponding author.
E-mail address: emiliord@auburn.edu (E. Miliordos).

https://doi.org/10.1016/j.jqsrt.2020.107265
0022-4073/

and 6.88 eV, appreciably smaller than the experimental values. Using these ionization energies, the experimental and theoretical first excitation energy of NbO^+ can be estimated as 2.43 and 0.93 eV, respectively. Their photoelectron spectrum displayed two more unassigned bands at 11.43 ± 0.04 and 12.64 ± 0.04 eV. In 1998 Sievers and Armentrout suggested that these two bands correlate to $^5\Pi$ and $^5\Sigma^-$ [24]. Moreover, they predicted a $^1\Gamma$ or $^1\Sigma^+$ low-lying excited state of NbO^+ between $^3\Sigma^-$ and $^3\Delta$ [24]. They further tested the ability of $Nb^+(^5D)$ and $NbO^+(^3\Sigma^-)$ to activate carbon dioxide [24]. The $NbO(^3\Sigma^-) + CO_2 \longrightarrow NbO_2^+ (^1A_1) + CO$ reaction was found to be an endothermic barrierless process [25]. Based on the existing literature, high-level quantum calculations studying the complete spectrum of the low-lying states of NbO^+ are necessary.

In the present study we perform high-level electronic structure calculations on ZrO^+, NbO^+ and report accurate bond distances, chemical bonding patterns, spectroscopic constants, excitation energies, and spin-orbit splittings of several low-lying electronic states. We compare these results with the findings of recently studied ZrO and NbO species [13,14] and the corresponding first row TiO^+ and VO^+ counterparts [8,10]. We discuss our computational details and results in sections II and III, respectively. The conclusions of our study is given in section IV.

2. Computational details

The internally contracted multi-reference configuration interaction (MRCI) [26–28] method implemented in MOLPRO 2015.1 [29] was used to construct potential energy curves (PECs) and compute spectroscopic parameters of all reported electronic states. The highest possible Abelian point group (C_{2v}) was used in all cases. All MRCI calculations are built on top of the complete active space self-consistent field (CASSCF) wavefunctions. In both ZrO^+ and NbO^+ cases reference CASSCF wavefunctions consist of nine active orbitals ($4a_1$, $2b_1$, $2b_2$, $1a_2$) with seven and eight electrons, respectively. At far distances nine active orbitals correspond to 2p of O and 4d and 5s of metal. To minimize size extensivity errors Davidson correction (MRCI+Q) was applied.

For ZrO^+, we state-averaged $18A_1$, $16B_1$, $16B_2$, and $16A_2$ states of doublet and quartet spin states (each spin group separately) in order to get the correct orbitals in the active space. Especially the second b_1 and b_2 orbitals tend to become $3p_{x,y}$(O) orbitals instead of $4d_{xz,yz}$(Zr). The same observation was made for neutral ZrO [14]. For the three lowest energy states of ZrO^+, we also employed a larger active space including three more orbitals of symmetries a_1, b_1, and b_2 under C_{2v}, but state-averaging only the first three states. This calculation placed both $4d_{xz,yz}$(Zr) and $3p_{x,y}$(O) in the active space. These MRCI and MRCI+Q calculations are referred as MRCI-L and MRCI-L+Q, and the two sets of calculations are compared below. We didn't encountered such an issue for NbO^+, for which each spin multiplicity was studied separately with the small active space with the following state-averaged scheme: $4A_1$, $3B_1$, $3B_2$, $2A_2$/singlets ; $1A_1$, $4B_1$, $4B_2$, $2A_2$/triplets ; $1A_1$, $1B_1$, $1B_2$, $2A_2$/quintets.

Spectroscopic parameters of low-lying single reference states were also obtained at coupled cluster single, double and perturbative triples [CCSD(T)] method. For coupled cluster calculations restricted Hartree-Fock orbitals were used. Furthermore, the effect of outer core electron correlation was evaluated by performing core-MRCI (C-MRCI) and core-CCSD(T) [C-CCSD(T)] calculations. Core calculations include $4s^2$ and $4p^6$ electron correlation of metal at the MRCI and CCSD(T) levels.

Quadruple-ζ quality correlation consistent basis sets were applied for all ZrO^+ and NbO^+ calculations. Specifically, aug-cc-pVQZ basis set was used for the electronegative oxygen [30]. For the metal atom cc-pVQZ-PP basis set with Stuttgart relativistic pseudopotential (replacing the $1s^2$ through $3d^{10}$ twenty-eight inner electrons) was utilized [31]. For the core calculations weighted-core cc-pwCVQZ-PP basis set of metal was adopted [31].

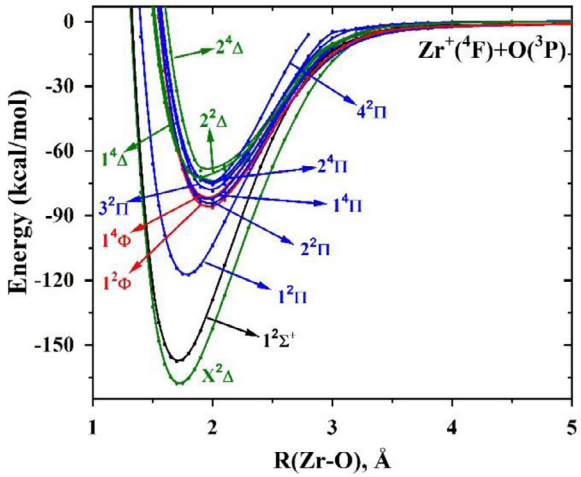

Fig. 1. MRCI PECs of ZrO^+ with respect to the Zr–O distance.

The ro-vibrational Schrödinger equation was solved to calculate harmonic frequencies ω_e and anharmonicities $\omega_e x_e$. To calculate spin-orbit coupling constants, the spin-orbit part of the pseudopotential was coupled with the MRCI wavefunctions via the Breit-Pauli Hamiltonian. All MRCI and CCSD(T) calculations were performed using MOLPRO 2015.1 package [29].

3. Results and discussion

This section is composed of two sub-sections (IIIA and IIIB). Sections IIIA and IIIB discuss the electronic structure of low-lying states and spectroscopic constants of ZrO^+ and NbO^+, respectively.

3.1. IIIA. ZrO^+

The ground state of Zr^+ (a^4F) bears $4d^25s^1$ electron configuration [32]. The first excited state of Zr^+ is another ^4F state (b^4F; $4d^3$) and lies ~2,000 cm^{-1} higher [32]. The combination of $Zr^+(a^4F)$ with $O(^3P;2s^22p^4)$ creates twenty-one (sextet + quartet + doublet) electronic states (two Σ^+, one Σ^-, three Π, three Δ, two Φ, one Γ). To identify the lowest energy states of ZrO^+, we produced the potential energy curves (PECs) as a function of Zr–O distance dissociating to the $Zr^+(a^4F)$ + $O(^3P;2s^22p^4)$ channel. All PECs except that of $4^2\Pi$ dissociate to the ground state fragments. The thirteen lowest energy PECs are shown in the Fig. 1, the first three of which are well separated from the rest ones and produce minima at around 1.8 Å. The higher energy PECs are congested between −69 and −87 kcal mol^{-1} with longer equilibrium distances at around 2 Å.

The prevailing electronic configurations at the equilibrium bond distance of all of these states of are listed in the Table 1, and the corresponding molecular orbitals are given in the Fig. 2. Only the valence orbitals, except for the 2s of oxygen, are numbered. The 1σ and 3σ orbitals correspond to the metal-oxygen σ-bonding and anti-bonding molecular orbitals, while the 2σ is largely a distorted 5s atomic orbital of Zr. The $1\pi_x$ and $1\pi_y$ ones are the metal-oxygen π-bonds highly polarized towards O, composed mostly of $2p_x$ and $2p_y$ orbitals with smaller contribution of $4d_{xz}$ and $4d_{yz}$ metallic orbitals. The $2\pi_x$ and $2\pi_y$ are antibonding orbitals with major contribution from $4d_{xz}$ and $4d_{yz}$ of Zr, respectively. Finally, the $4d_{xy}$ and $4d_{x^2-y^2}$ orbitals of Zr (or 1δ) do not overlap with any of the oxygen atomic orbitals.

Table 1
Dominant electronic configurations at the equilibrium distance of the thirteen lowest energy electronic states of ZrO^+.

State	Coefficient	1σ	2σ	3σ	$1\pi_x$	$2\pi_x$	$1\pi_y$	$2\pi_y$	$1\delta_{xy}$	$1\delta x^2\text{-}y^2$
$X^2\Delta$	0.94	2	0	0	2	0	2	0	α	0
$1^2\Sigma^+$	0.93	2	α	0	2	0	2	0	0	0
$1^2\Pi$	0.85	2	0	0	2	α	2	0	0	0
$1^2\Phi$	0.64	2	α	0	β	0	2	0	0	α
	0.64	2	α	0	2	0	β	0	α	0
$2^2\Pi$	0.64	2	α	0	β	0	2	0	0	α
	-0.64	2	α	0	2	0	β	0	α	0
$1^4\Pi$	-0.64	2	α	0	α	0	2	0	0	α
	0.64	2	α	0	2	0	α	0	α	0
$1^4\Phi$	0.68	2	α	0	α	0	2	0	0	α
	0.68	2	α	0	2	0	α	0	α	0
$3^2\Pi$	0.64	2	0	0	2	0	β	0	α	α
	-0.64	2	0	0	2	0	α	0	β	α
$2^4\Pi$	0.91	2	0	0	2	0	α	0	α	α
$4^2\Pi$	0.62	2	2	0	α	0	2	0	0	0
	-0.48	2	0	0	α	0	2	0	0	2
	-0.48	2	0	0	α	0	2	0	2	0
$1^4\Delta$	0.95	α	α	0	2	0	2	0	0	α
$2^2\Delta$	0.68	α	β	0	2	0	2	0	0	α
	0.68	α	α	0	2	0	2	0	0	β
$2^4\Delta$	0.66	2	0	0	2	0	α	α	0	α
	0.66	2	0	0	α	α	2	0	0	α

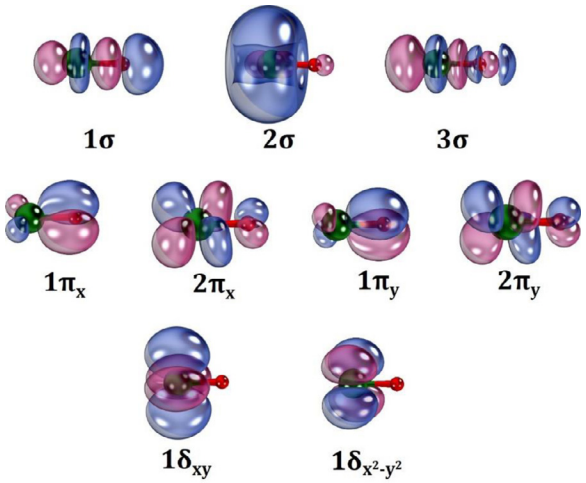

Fig. 2. Selected CASSCF orbitals of ZrO^+.

The first three states have the three 1σ and 1π bonding orbitals doubly occupied and one electron in 1δ ($X^2\Delta$), 2σ ($1^2\Sigma^+$), or 2π ($1^2\Pi$). In the next states one 1π orbital is singly occupied and there are two electrons in the 1δ, 2σ, and 2π orbitals. Doublet and quartet states are present, depending on the spin coupling of the three electrons. The $2\sigma^1\ 1\delta^1$ combination generates $2^2\Pi$, $1^2\Phi$, $1^4\Pi$, and $1^4\Phi$; $1\delta^2$ creates $3^2\Pi$ and $2^4\Pi$; $4^2\Pi$ is a mixture of $2\sigma^2$ and $1\delta^2$; $2\pi^1\ 1\delta^1$ gives our highest energy $2^4\Delta$ state. All of these states are of multi-reference character (except for $2^4\Pi$) with at least two major components. Finally, there are two states with the σ-bonding orbital (1σ) being singly occupied ($2^2\Delta$, $1^4\Delta$) with a $1\sigma^1\ 2\sigma^1 1\pi^4 1\delta^1$ electronic configuration.

Based on their electronic configurations, the first three states are of oxo ($Zr^{3+}O^{2-}$) character, while the rest of them are of profound oxyl ($Zr^{2+}O^{\cdot-}$) nature. It should be mentioned that the notation $Zr^{3+}O^{2-}$ for the oxo character is rather conventional. A better description could be $Zr^{3+}O^{2-} \leftrightarrow Zr^{2+}{-}O^{-}$, where a resonance of a pure ionic bond and a covalent bond between Zr^{2+} and O^- is in effect. The two 1π orbitals are essentially localized on oxygen and the contribution of each picture depends highly on how we interpret the σ-bonding orbital 1σ. In any case the $Zr^{3+}O^{2-}$ notation expresses directly that the oxygen terminal is saturated with electrons and will be used throughout this work. The proposed valence-bond-Lewis (vBL) diagrams of the three lowest electronic states of ZrO^+ are illustrated in Fig. 3. The Zr^{3+} center holds one unpaired electron in one of the metallic 2σ, 2π, or 1δ orbitals. On the other hand, the higher energy states have a single electron in one of the 1π, which clearly suggests an unpaired electron in the proximity of the oxygen center. As before, the bonding in this case could be described as $Zr^{2+}O^{\cdot-} \leftrightarrow Zr^{+}{-}O^{\cdot}$.

Compared to ZrO [14], the first three states of ZrO^+ can be generated by just removing one 2σ ~ 5s orbital. Specifically, the ground state of ZrO is $^1\Sigma^+$, the first two excited states $^{1,3}\Delta$ and the subsequent $^{1,3}\Pi$ pair are related to the $^2\Sigma^+$, $^2\Delta$, $^2\Pi$ states of ZrO^+. The energy order of Σ^+ and Δ states is reverse, and the Π states lie at least 10,000 cm^{-1} higher. The next dozen of states of ZrO keep the oxo character ($1\sigma^2 1\pi^4$), and only the quintet states (~30,000 cm^{-1} higher than the ground $^1\Sigma^+$ state) present oxyl ($1\sigma^2 1\pi^3$) character. ZrO^+ oxyl states lie at approximately the same energy difference from the ground state, but besides the first three states, there are no other low-lying oxo states.

Comparing ZrO^+ to TiO^+ [10], we see a very similar pattern. Both have a $^2\Delta$ ground state, followed by the $^2\Sigma^+$ and $^2\Pi$, well separated from the rest oxyl states. The main difference is the excitation energy of $^2\Sigma^+$ (~3,000 cm^{-1} for ZrO^+ vs. ~11,000 cm^{-1} for TiO^+). The $^2\Pi$ states are at ~15,500 cm^{-1} in both cases. This difference can be attributed to the fact that $^2\Sigma^+$ originates from $Zr^{3+}(^2S;\ 5s^1)$ or $Ti^{3+}(^2S;\ 4s^1)$, as opposed to the other two states both coming from the ^2D ($4d^1$ or $3d^1$) states (see Fig. 3). The ^2S state of Zr^{3+} is lower than that of Ti^{3+} (38,258 vs. 80,389 cm^{-1}) [32].

Our calculated equilibrium bond lengths, harmonic frequencies, anharmonicities, and excitation energies obtained for the lowest thirteen electronic states of ZrO^+ are listed in the Table 2. The bond lengths and harmonic frequencies reflect the bonding pattern of the different states. The first two states have the shortest bonds and larger frequencies as a result of the non-bonding nature of the occupied metallic orbitals (2σ and 1δ). At our highest level of theory, the two r_e values are 1.695 and 1.685 Å, and the two ω_e values are ~1,000 cm^{-1}. The bond is elongated by 0.06 Å for $^2\Pi$ at MRCI and the frequency drops by ~150 cm^{-1}, due to the population of the 2π "anti-bonding" orbital. The bonds expand further for the

Table 2
Equilibrium energy E_e (hartrees), bond length r_e (Å), harmonic vibrational frequency ω_e (cm^{-1}), anharmonicity $\omega_e x_e$ (cm^{-1}), and excitation energy T_e (cm^{-1}) for the lowest thirteen electronic states of $^{90}Zr^{16}O^+$.

State	Method	$-E_e$	r_e	ω_e	$\omega_e x_e$	T_e
$X^2\Delta$	MRCI	121.376673	1.723	925	1.7	0
	MRCI+Q	121.392612	1.724	924	1.3	0
	MRCI-L	121.388395	1.719	944	2.5	0
	MRCI-L+Q	121.397169	1.719	943	2.3	0
	C-MRCI	121.689376	1.693	999	3.2	0
	C-MRCI+Q	121.738701	1.695	990	3.4	0
	CCSD(T)	121.396943	1.723	950	2.1	0
	C-CCSD(T)	121.746951	1.695	992	3.2	0
	Expt. [19] ($^2\Delta_{3/2}$)		1.691 (2)	991.2 (8)	3.5 (8)	
	Expt. [19] ($^2\Delta_{5/2}$)		1.688 (1)	991.9 (8)	3.6 (8)	
$1^2\Sigma^+$	MRCI	121.360033	1.711	955	2.2	3652
	MRCI+Q	121.376337	1.712	955	2.3	3572
	MRCI-L	121.372364	1.707	975	3.9	3518
	MRCI-L+Q	121.382020	1.707	976	3.9	3325
	C-MRCI	121.672186	1.681	1030	3.7	3773
	C-MRCI+Q	121.723729	1.686	1016	3.8	3286
	CCSD(T)	121.382578	1.712	980	2.6	3153
	C-CCSD(T)	121.732414	1.685	1019	3.7	3191
$1^2\Pi$	MRCI	121.296206	1.784	829	3.1	17660
	MRCI+Q	121.320611	1.775	854	2.9	15802
	MRCI-L	121.316102	1.766	860	2.9	15866
	MRCI-L+Q	121.326645	1.768	865	2.9	15478
$1^2\Phi$	MRCI	121.246847	1.971	682	3.1	28494
	MRCI+Q	121.260876	1.974	681	3.4	28913
$2^2\Pi$	MRCI	121.244458	1.974	682	3.0	29018
	MRCI+Q	121.258593	1.978	678	3.3	29414
$1^4\Pi$	MRCI	121.241257	1.964	675	2.0	29720
	MRCI+Q	121.257984	1.970	683	3.7	29547
$1^4\Phi$	MRCI	121.239974	1.965	687	3.9	30002
	MRCI+Q	121.256721	1.970	705	4.3	29825
$3^2\Pi$	MRCI	121.234269	1.982	683	2.9	31254
	MRCI+Q	121.248906	1.988	673	2.4	31540
$2^4\Pi$	MRCI	121.229580	1.989	636	-1.3	32283
	MRCI+Q	121.246593	1.999	619	-1.5	32047
$4^2\Pi$	MRCI	121.228559	1.979	687	1.4	32507
	MRCI+Q	121.244660	1.984	680	1.8	32472
$1^4\Delta$	MRCI	121.227532	2.028	440	5.4	32733
	MRCI+Q	121.247108	2.041	544	6.7	31934
	CCSD(T)	121.247599	1.981	559	3.2	32777
$2^2\Delta$	MRCI	121.224683	1.900	555	4.4	33358
	MRCI+Q	121.240997	1.898	630	4.9	33276
$2^4\Delta$	MRCI	121.222803	1.970	830	23.5	33771
	MRCI+Q	121.238416	1.928	901	25.1	33842

higher energy oxyl states to about 2.0 Å and the frequencies drop to 550-700 cm^{-1}. The first two states are within 3,500 cm^{-1} depending on the level of theory, the $1^2\Pi$ state is at ~16,000 cm^{-1}, and the rest states fall in the 28913-29825 cm^{-1} range at MRCI+Q.

Looking at the different methods applied for the ground and first excited state, the following observations can be made. The Davidson correction affects only slightly on the bond lengths (of the 0.001 Å order) and vibrational frequencies (of the 10 cm^{-1} order). The larger active space calculations (MRCI-L and MRCI-L+Q) provide practically identical results to MRCI and MRCI+Q. The bond lengths are shorter by ~0.005 Å, the frequencies are higher by 10-20 cm^{-1}, and the excitation energies agree within 350 cm^{-1} at the MRCI+Q and MRCI-L+Q. The biggest difference is the excitation energy of $1^2\Pi$ at the MRCI level; the MRCI-L/MRCI-L+Q difference is about 400 cm^{-1} but the MRCI/MRCI+Q one is of the 2,000 cm^{-1} order. Overall, the use of the smaller active space with more states averaged together provides similar accuracy with the use of larger active space and averaging only the first three states.

On the other hand, the $4s^24p^6$ electron correlation is a more important effect to consider. It decreases r_e by 0.03 Å and increases frequencies by ~70/40 cm^{-1} at MRCI/CCSD(T) levels. Our best estimates are r_e = 1.695 and 1.685 Å and ω_e = 992 and 1019 cm^{-1} (C-CCSD(T)) for $X^2\Delta$ and $1^2\Sigma^+$. The experimental r_e and ω_e values for the $X^2\Delta_{5/2}$ and $X^2\Delta_{3/2}$ components are in excellent agreement with our C-MRCI+Q and C-CCSD(T) values (see Table 2). The bond length is predicted within 0.005 Å and the frequencies within a couple of cm^{-1}. Our $\omega_e x_e$ values are within the experimental error bars. As a result, a correction of 0.03 Å and ~50 cm^{-1} is suggested for the rest of the states, where the $4s^24p^6$ electron correlation effects are not considered. As far as the excitation energy of $1^2\Sigma^+$ is concerned, the Davidson correction "pushes" the MRCI values towards the CCSD(T) ones. For example, C-MRCI gives 3773 cm^{-1}, C-MRCI+Q reduces it to 3286 cm^{-1}, which is closer to the C-CCSD(T) value of 3191 cm^{-1}. The MRCI+Q values for the rest of the states should be considered quite accurate.

According to our results, the ground state is definitely a $^2\Delta$ state, and the $^2\Sigma^+$ state (claimed as the ground state in the past) is the first excited state. The 1.99 ± 0.08 eV (or 16,050 ± 645 cm^{-1}) excitation energy measured by Sievers and Armentrout [22] matches very well our value for $1^2\Pi$, but their 2.93 ± 0.14 eV (or 23,632 ± 1129 cm^{-1}) value does not match with any of our values and falls short of the $^4\Phi$ state assumed by them. Their excitation energies are estimated indirectly (not spectroscopically) through the reaction of Zr^+ with CO_2 assuming barrier-free reactions. The invalidity of their assumption may be the reason of this discrepancy. Finally, the spin-orbit coupling constant A for $X^2\Delta$ is

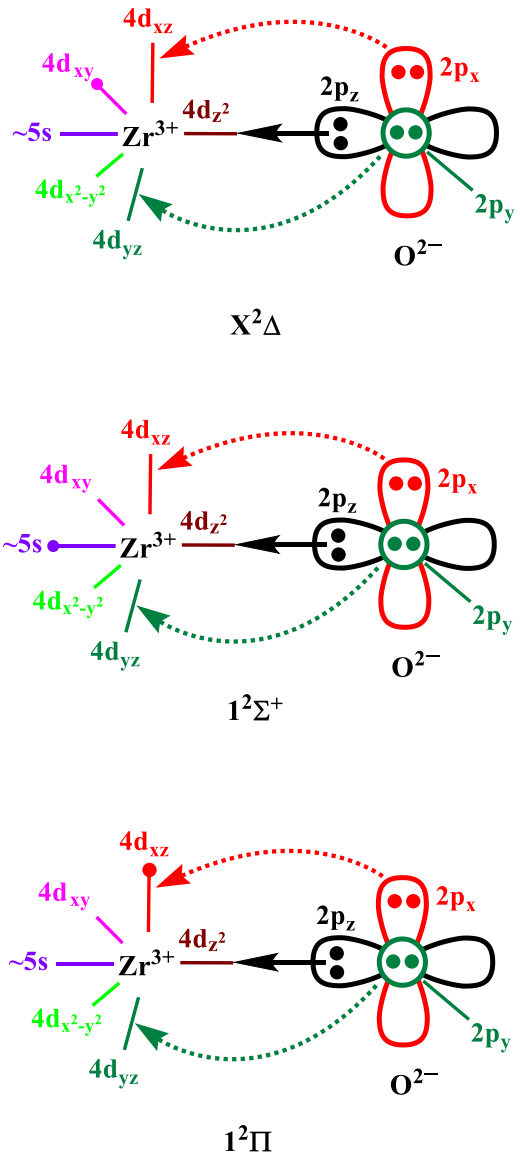

Fig. 3. Proposed vbL diagrams for the lowest three electronic states of ZrO^+.

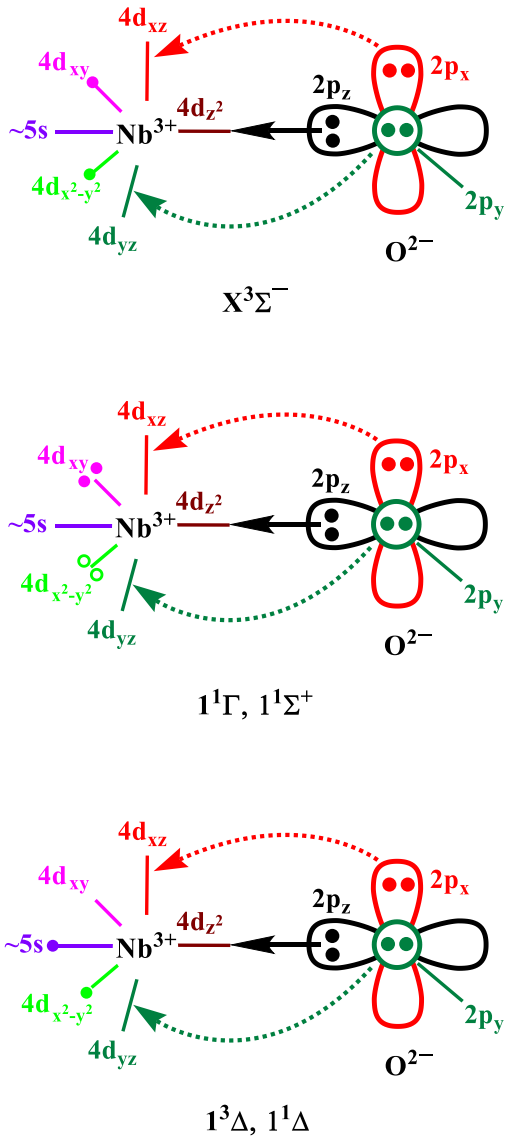

Fig. 4. Proposed vbL diagrams for the lowest three electronic states of NbO^+. The $(4d_{xy})^2 \pm (4d_{x^2-y^2})^2$ combinations of $1^1\Gamma$ and $1^1\Sigma^+$ states (see Table 3) are represented by electron pairs with solid ($4d_{xy}$) and open circles ($4d_{x^2-y^2}$). The two 5s and $4d_{x^2-y^2}$ electrons of $1^3\Delta$ and $1^1\Delta$ are same and have opposite spin.

calculated to be 364 cm^{-1} in good agreement with the experimental value of 349.7 ± 0.8 cm^{-1} [19]. Our MRCI A value for $1^2\Pi$ is 420.4 cm^{-1}.

3.2. IIIB. NbO^+

Adopting a $Nb^{3+}O^{2-}$ (oxo) character for the low-lying states of NbO^+ and the oxyl $Nb^{2+}O^{\cdot-}$ character for the higher energy states, we expect that $Nb^{3+}(4d^2$ or $4d^15s^1)$ singlet and triplet states are the most stable ones followed by quintets with a $Nb^{2+}(4d^3$ or $4d^25s^1)$ center. Indeed, this is exactly the case as can be seen in Table 3. Among the first sixteen states, there are seven singlet and six triplet states with a $1\sigma^21\pi^4(2\sigma 2\pi 1\delta)^2$ electronic configurations. The molecular orbitals are similar to those of ZrO^+ (see Figure 2) and the 2σ, 2π, and 1δ orbitals are rather localized on niobium with 2σ pertaining to 5s and 2π, 1δ to 3d. Finally, there are three quintet states of $1\sigma^21\pi^3(2\sigma 2\pi 1\delta)^3$ signifying oxyl-type states.

The lowest three states are of $1\sigma^21\pi^41\delta^2$ nature with the two 1δ orbitals coupled into a triplet ($X^3\Sigma^-$) or a singlet ($1^1\Gamma$ and $1^1\Sigma^+$). All three pertain to a $4d^2$ niobium center, while the next two states ($1^{1,3}\Delta$) have a $1\sigma^21\pi^42\sigma^11\delta^1$ configuration corresponding to $4d^15s^1$. The latter states are higher in energy for Nb^{3+} [32] and this is reflected to the NbO^+ states. In the next four states, there are two unpaired electrons in the 2π and 1δ orbitals generating $1^{1,3}(\Pi,\Phi)$. The major component of the second $^{1,3}\Pi$ and $^1\Sigma^+$ states bears a $2\sigma^12\pi^1$ and $2\sigma^2$ combination, respectively. Then, the quintet states follow with $2\pi^11\delta^2$, $2\sigma^11\delta^2$, and $2\sigma^11\pi^11\delta^1$ metallic electrons coupled into a quartet and ferromagnetically with the oxygen 1π electron. Proposed vbL diagrams for the first five states of NbO^+ are illustrated in Fig. 4.

The PECs of all of these states are plotted in Fig. 5. The first two asymptotic channels $Nb^+(^5D;\ 4d^4)+O(^3P)$ and $Nb^+(^5F;\ 4d^35d^1)+O(^3P)$ produce triplets, quintets, and septets, and thus the PECs of the singlet states dissociate to the next two channels $Nb^+(^3P;\ 4d^4)+O(^3P)$ and $Nb^+(^3F;\ 4d^4)+O(^3P)$. Considering the spin-orbit splitting, the energy ranges for these channels are 0–1224.8 cm^{-1}, 2356.8–4146.0 cm^{-1}, 5562.2–7261.3 cm^{-1}, and 7505.8–8320.4 cm^{-1} [32]. Specifically, these asymptotes create ^{3,5,7}(one Σ^+, two Σ^-, three Π, two Δ, one Φ), ^{3,5,7}(two Σ^+, one

Table 3
Dominant electronic configurations at the equilibrium distance of the sixteen lowest energy electronic states of NbO^+. Orbitals of NbO^+ have identical shapes as ZrO^+. See Fig. 2.

State	Coefficient	1σ	2σ	3σ	$1\pi_x$	$2\pi_x$	$1\pi_y$	$2\pi_y$	$1\delta_{xy}$	$1\delta x^2\text{-}y^2$
$X^3\Sigma^-$	0.94	2	0	0	2	0	2	0	α	α
$1^1\Gamma$	0.67	2	0	0	2	0	2	0	2	0
	-0.67	2	0	0	2	0	2	0	0	2
$1^1\Sigma^+$	0.63	2	0	0	2	0	2	0	2	0
	0.63	2	0	0	2	0	2	0	0	2
$1^3\Delta$	0.94	2	α	0	2	0	2	0	0	α
$1^1\Delta$	-0.66	2	α	0	2	0	2	0	0	β
	0.66	2	β	0	2	0	2	0	0	α
$1^3\Phi$	0.67	2	0	0	2	0	2	α	α	0
	0.67	2	0	0	2	α	2	0	0	α
$1^3\Pi$	-0.65	2	0	0	2	0	2	α	α	0
	0.65	2	0	0	2	α	2	0	0	α
$1^1\Pi$	-0.44	2	0	0	2	α	2	0	0	β
	0.44	2	0	0	2	β	2	0	0	α
	-0.44	2	0	0	2	0	2	β	α	0
	0.44	2	0	0	2	0	2	α	β	0
$1^1\Phi$	0.46	2	0	0	2	α	2	0	0	β
	-0.46	2	0	0	2	β	2	0	0	α
	-0.46	2	0	0	2	0	2	β	α	0
	0.46	2	0	0	2	0	2	α	β	0
$2^3\Pi$	0.85	2	α	0	2	α	2	0	0	0
	-0.26	2	α	0	2	0	β	0	α	α
$2^1\Sigma^+$	0.87	2	2	0	2	0	2	0	0	0
	0.20	2	0	0	2	0	2	0	2	0
	0.20	2	0	0	2	0	2	0	0	2
$1^5\Sigma^-$	0.66	2	0	0	α	α	2	0	α	α
	0.66	2	0	0	2	0	α	α	α	α
$2^1\Pi$	-0.60	2	β	0	2	α	2	0	0	0
	0.60	2	α	0	2	β	2	0	0	0
$1^5\Pi$	0.90	2	α	0	2	0	α	0	α	α
$1^5\Delta$	0.65	2	α	0	2	0	α	α	0	α
	0.65	2	α	0	α	α	2	0	0	α
$3^3\Pi$	0.68	2	α	0	2	α	2	0	0	0
	0.44	2	α	0	2	0	β	0	α	α

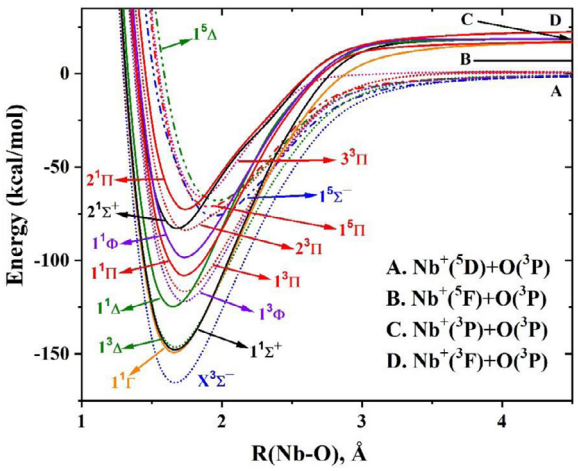

Fig. 5. MRCI PECs of NbO^+ with respect to the Nb–O distance.

Σ^-, three Π, three Δ, two Φ, one Γ), ^{1,3,5}(one Σ^+, two Σ^-, two Π, one Δ), and ^{1,3,5}(one Σ^+, two Σ^-, three Π, three Δ, two Φ, one Γ) states. All triplet and quintet states dissociate to $Nb^+(^5D; 4d^4)+O(^3P)$, while some singlets ($1^1\Sigma^+$, $1^1\Delta$, $1^1\Pi$, $2^1\Pi$) dissociate to the third and some others ($1^1\Gamma$, $1^1\Phi$, $2^1\Sigma^+$) to the fourth channel.

Table 4 lists our calculated equilibrium bond lengths, harmonic frequencies, anharmonicities, and excitation energies. Regarding bond lengths, the states can be divided in three groups depending on the populated orbitals. The $1\sigma^2 1\pi^4(2\sigma 1\delta)^2$, $1\sigma^2 1\pi^4 2\pi^1(2\sigma 1\delta)^1$, and $1\sigma^2 1\pi^3(2\pi^1 2\sigma 1\delta)^1$ groups have MRCI bond lengths of 1.67, 1.73, and >1.95 Å, respectively. The first five states and $2^1\Sigma^+$ belong to the first group, the quintets to the third one, and the remaining states to the second group. The population of the 2π orbital elongates the bond by ~0.05 Å as a result of its anti-bonding nature, and the depopulation of the bonding 1π orbital increases the internuclear distance by more than 0.2 Å. The same trend is observed for the harmonic frequencies, which range as >1020, 850–1000, 650–700 cm^{-1} for the three groups. The ground state is well separated (by ≥5,000 cm^{-1}) from the first three excited states, which lie close to each other in the 5,800–6,400 cm^{-1} region (MRCI excitation energies). The next twelve states have an average energy separation of 1,900 cm^{-1}. Both MRCI and MRCI+Q predicted the same ranking for the states from $X^3\Sigma^-$ to $2^1\Sigma^+$ ($X^3\Sigma^-$, $1^1\Gamma$, $1^1\Sigma^+$, $1^3\Delta$, $1^1\Delta$, $1^3\Phi$, $1^3\Pi$, $1^1\Pi$, $1^1\Phi$, $2^3\Pi$, $2^1\Sigma^+$). According to MRCI, the last five states are $1^5\Sigma^-$, $2^1\Pi$, $1^5\Pi$, $1^5\Delta$, $3^3\Pi$, but are arranged as $2^1\Pi$, $1^5\Sigma^-$, $1^5\Pi$, $3^3\Pi$, $1^5\Delta$ at MRCI+Q.

As in ZrO^+, the $4s^24p^6$ electron correlation effects reduce the metal-oxygen bond length, but the impact is smaller in the NbO^+ case. In the first three states the shortening is of the 0.01 Å order as opposed to 0.03 Å for ZrO^+. Similar changes have been observed for the first row transition metal counterparts [8,10]. As in the ZrO^+, the Davidson correction does not affect the bond lengths or frequencies much, but generally reduces the excitation energies. This energy drop approaches the 2,000 cm^{-1} in some cases; see for example $1^{1,3}(\Phi,\Pi)$.

Using the vertical ionization energies of NbO reported by Dyke et al. [23], 7.91 ± 0.02, 10.34 ± 0.02, 11.43 ± 0.04, and 12.64 ± 0.04 eV, we estimated the following excitation energies of NbO^+: 19,599, 28.391, and 38,150 cm^{-1} with uncertainties which can reach ~500 cm^{-1} (0.04 + 0.02 = 0.06 eV). The first two values

Table 4
Equilibrium energy E_e (hartrees), bond length r_e (Å), harmonic vibrational frequency ω_e (cm^{-1}), anharmonicity $\omega_e x_e$ (cm^{-1}), and excitation energy T_e (cm^{-1}) for the lowest sixteen electronic states of $^{93}Nb^{16}O^+$.

State	Method	$-E_e$	r_e	ω_e	$\omega_e x_e$	T_e
$X^3\Sigma^-$	MRCI	131.214545	1.665	1025	3.4	0
	MRCI+Q	131.230187	1.666	1031	5.5	0
	C-MRCI	131.535141	1.653	1008	1.2	0
	C-MRCI+Q	131.593787	1.654	1035	3.4	0
	CCSD(T)	131.230878	1.667	1029	3.5	0
	C-CCSD(T)	131.603955	1.652	1050	3.6	0
$1^1\Gamma$	MRCI	131.187965	1.661	1042	4.7	5834
	MRCI+Q	131.204258	1.661	1046	5.9	5691
	C-MRCI	131.511022	1.649	1038	0.8	5294
	C-MRCI+Q	131.571156	1.650	1046	2.9	4967
$1^1\Sigma^+$	MRCI	131.185660	1.667	1026	4.7	6340
	MRCI+Q	131.203269	1.667	1030	5.0	5908
	C-MRCI	131.504425	1.656	1021	1.0	6741
	C-MRCI+Q	131.566148	1.656	1031	3.1	6066
$1^3\Delta$	MRCI	131.185602	1.667	1021	5.5	6352
	MRCI+Q	131.201058	1.667	1028	6.9	6393
	CCSD(T)	131.203485	1.669	1021	4.0	6012
$1^1\Delta$	MRCI	131.150392	1.653	1060	5.8	14080
	MRCI+Q	131.169682	1.654	1071	7.8	13279
$1^3\Phi$	MRCI	131.144132	1.727	930	1.6	15454
	MRCI+Q	131.169284	1.722	940	2.5	13367
$1^3\Pi$	MRCI	131.135662	1.732	913	1.8	17313
	MRCI+Q	131.160207	1.727	924	2.6	15359
$1^1\Pi$	MRCI	131.121771	1.726	931	1.4	20362
	MRCI+Q	131.147166	1.719	945	2.2	18221
$1^1\Phi$	MRCI	131.106175	1.732	905	2.1	23784
	MRCI+Q	131.130277	1.723	922	2.7	21928
$2^3\Pi$	MRCI	131.084494	1.735	867	3.7	28543
	MRCI+Q	131.107912	1.727	927	8.2	26836
$2^1\Sigma^+$	MRCI	131.083370	1.679	980	5.3	28790
	MRCI+Q	131.106841	1.675	1004	7.9	27071
$1^5\Sigma^-$	MRCI	131.069606	1.956	676	5.6	31810
	MRCI+Q	131.087873	1.955	669	1.3	31234
$2^1\Pi$	MRCI	131.066439	1.738	907	2.0	32506
	MRCI+Q	131.089302	1.737	916	2.9	30921
$1^5\Pi$	MRCI	131.064425	1.914	673	6.8	32948
	MRCI+Q	131.080241	1.917	665	5.7	32909
	CCSD(T)	131.083058	1.914	686	3.4	32443
$1^5\Delta$	MRCI	131.054798	1.962	651	1.8	35060
	MRCI+Q	131.072437	1.965	638	1.7	34622
$3^3\Pi$	MRCI	131.054427	1.872	947	4.5	35142
	MRCI+Q	131.072724	1.889	914	3.9	34559

match well with our excitation energies for $1^1\Pi$ and $2^3\Pi$ or $2^1\Sigma^+$. The last value is beyond our larger excitation energy. Conclusively, the assignments by Dyke are incorrect, but the suggestion of Sievers and Armentrout [24] of low-lying $^1\Gamma$ or $^1\Sigma^+$ states is confirmed by our results. The latter authors estimated a vibrational frequency for NbO^+ as 1067 cm^{-1}, which is larger than our C-MRCI+Q and C-CCSD(T) values of 1035 and 1050 cm^{-1}.

The lowest lying states of NbO^+ can be easily produced by those of NbO [13] by just removing one 2σ (~$5s_{Nb}$) electron. For example, the lowest nine states of NbO are $X^4\Sigma^-$, $1^2\Delta$, $1^2\Sigma^-$, $1^2\Gamma$, $1^2\Sigma^+$, $1^4\Phi$, $1^4\Pi$, $1^2\Phi$, $1^2\Pi$, which correlate to the first nine states of NbO^+. $X^4\Sigma^-$ and $1^2\Sigma^-$ generate $X^3\Sigma^-$, $1^2\Delta$ gives $1^3\Delta$ and $1^1\Delta$, and the rest relate to $1^1\Gamma$, $1^1\Sigma^+$, $1^3\Phi$, $1^3\Pi$, $1^1\Phi$, $1^1\Pi$. Compared to VO^+ [8], all of these nine states are in common, but they follow different energy ranking. The first three lowest energy states of VO^+ ($X^3\Sigma^-$, $1^1\Gamma$, $2^1\Sigma^+$) are identical to that of NbO^+. The next four states of VO^+ are $^3\Phi$, $^3\Delta$, $^3\Pi$, and $^1\Delta$ and this order is different from that of NbO^+ ($1^3\Delta$, $1^1\Delta$, $1^3\Phi$, $1^3\Pi$) [8].

4. Conclusions

Several low-lying electronic states of ZrO^+ and NbO^+ are analyzed performing high-level *ab initio* calculations. We report electronic configurations, bond distances, spectroscopic constants, potential energy curves, and excitation energies for the considered states. The first three electronic states of ZrO^+ ($X^2\Delta$, $1^2\Sigma^+$, $1^2\Pi$) generate by removing one electron from the ~$5s_{Zr}$ of $ZrO(^1\Sigma^+)$. Similarly, the lowest nine states of NbO^+ produced by detaching one electron from ~$5s_{Nb}$ of nine low-lying states of NbO. These electronic states of ZrO^+ and NbO^+ possess oxo ($M^{3+}O^{2-}$) character.

Our theoretical calculations set definitely the $^2\Delta$ and $^2\Sigma^+$ states as the ground and first excited state of ZrO^+ in agreement with the most recent work of Luo et al [19]. Our numerical values for the ground state are in very good agreement with the latter experimental values. The excitation energy reported by Sievers and Armentrout [22] matches our $1^2\Pi$ value, but their 2.93 ± 0.14 eV (or 23,632 ± 1129 cm^{-1}) value does not match with any of our states and falls short of the $^4\Phi$ state assumed by them. Concerning NbO^+, our excitation energies reassign the recorded excitation energies by Dyke et al. [23] and confirm the assignment for low-lying $^1\Gamma$ or $^1\Sigma^+$ states made by Sievers and Armentrout [24]. We believe that our findings will aid future spectroscopic studies of titled species.

Declaration of Competing Interest

There are no conflicts to declare.

CRediT authorship contribution statement

Isuru R. Ariyarathna: Conceptualization, Methodology, Investigation, Visualization, Writing - original draft. **Evangelos Miliordos:** Validation, Formal analysis, Resources, Writing - review & editing, Supervision, Funding acquisition.

Acknowledgements

The financial support provided by the Auburn University is greatly appreciated. Computational resources are provided by the Auburn University Hopper Cluster.

References

[1] Védrine JC. Heterogeneous catalysis on metal oxides. Catalysts 2017;7:341. doi:10.3390/catal7110341.
[2] Védrine JC. Metal oxides in heterogeneous oxidation catalysis: state of the art and challenges for a more sustainable world. Chem Sus Chem 2019;12:577–88. doi:10.1002/cssc.201802248.
[3] Védrine JC. Metal oxides in heterogeneous catalysis. Elsevier; 2018. doi:10.1016/C2016-0-01790-4.
[4] Kumar S, Saralch S, Jabeen U, Pathak D. Metal oxides for energy applications. In: Colloid. met. oxide nanoparticles. Elsevier; 2020. p. 471–504. doi:10.1016/B978-0-12-813357-6.00017-6.
[5] Rodríguez JA, Fernández-García M. Synthesis, properties, and applications of oxide nanomaterials. Hoboken, NJ, USA: John Wiley & Sons, Inc.; 2007. doi:10.1002/0470108975.
[6] Kirkland JK, Khan SN, Casale B, Miliordos E, Vogiatzis KD. Ligand field effects on the ground and excited states of reactive FeO^{2+} species. Phys Chem Chem Phys 2018;20:28786–95. doi:10.1039/C8CP05372C.
[7] Hu D-B, Yang X-M, Yao L-F, Zhang L-X, Ma S-Y, Yu S-W, et al. Theoretical study on the reaction of the $^2\Delta$ ground state of ZrO^+ with CS_2 in the gas phase. J Mol Struct Theo Chem 2009;915:188–92. doi:10.1016/j.theochem.2009.08.038.
[8] Miliordos E, Mavridis A. Electronic structure of vanadium oxide. neutral and charged species, $VO^{0,\pm}$. J Phys Chem A 2007;111:1953–65. doi:10.1021/jp067451b.
[9] Sakellaris CN, Miliordos E, Mavridis A. First principles study of the ground and excited states of FeO, FeO^+ , and FeO^-. J Chem Phys 2011;134:234308. doi:10.1063/1.3598529.
[10] Miliordos E, Mavridis A. Electronic structure and bonding of the early 3d-transition metal diatomic oxides and their ions: $ScO^{0,\pm}$, $TiO^{0,\pm}$, $CrO^{0,\pm}$, and $MnO^{0,\pm}$. J Phys Chem A 2010;114:8536–72. doi:10.1021/jp910218u.
[11] Ariyarathna IR, Miliordos E. Ab initio investigation of the ground and excited states of $MoO^{+,2+,-}$ and their catalytic strength on water activation. Phys Chem Chem Phys 2018;20:12278–87. doi:10.1039/C8CP01676C.
[12] Almeida NMS, Ariyarathna IR, Miliordos E. Ab initio calculations on the ground and excited electronic states of neutral and charged palladium monoxide, $PdO^{0,+,-}$. Phys Chem Chem Phys 2018;20:14578–86. doi:10.1039/C8CP01251B.

[13] Claveau EE, Miliordos E. Quantum chemical calculations on NbO and its reaction with methane: ground and excited electronic states. Phys Chem Chem Phys 2019;21:26324–32. doi:10.1039/C9CP05408A.
[14] Jackson BA, Miliordos E. Weak-field ligands enable inert early transition metal oxides to convert methane to methanol: the case of ZrO. Phys Chem Chem Phys 2020;22:6606–18. doi:10.1039/C9CP06050B.
[15] Almeida NMS, Ariyarathna IR, Miliordos E. O–H and C–H bond activations of water and methane by RuO^{2+} and $(NH_3)RuO^{2+}$: ground and excited states. J Phys Chem A 2019;123:9336–44. doi:10.1021/acs.jpca.9b05910.
[16] Ariyarathna IR, Almeida NMS, Miliordos E. Ab initio investigation of the ground and excited states of $RuO^{+,0,-}$ and their reaction with water. Phys Chem Chem Phys 2020;22:16072–9. doi:10.1039/D0CP02468F.
[17] Van Zee RJ, Li S, Weltner W. Ground electronic states of ZrO^+, HfO^+, and Nb_2^+. ESR spectra of the matrix-isolated ions. Chem Phys Lett 1994;217:381–6. doi:10.1016/0009-2614(93)E1412-A.
[18] Balfour WJ, Lindgren B. Rotational analysis of the near-infrared system of the ZrO^+ molecule. Phys Scr 1980;22:36–44. doi:10.1088/0031-8949/22/1/005.
[19] Luo Z, Chang Y-C, Zhang Z, Ng CY. Rotationally resolved state-to-state photoelectron study of zirconium monoxide cation (ZrO^+). Mol Phys 2015;113:2228–42. doi:10.1080/00268976.2015.1021726.
[20] Lam C-S, Lau K-C, Ng C-Y. High-level ab initio predictions for the ionisation energy, bond dissociation energies and heats of formation of zirconium oxide and its cation (ZrO/ZrO^+). Mol Phys 2018;116:2709–18. doi:10.1080/00268976.2018.1434906.
[21] Rondinelli F, Russo N, Toscano M. CO2 activation by Zr^+ and ZrO^+ in gas phase. Theo Chem Acc 2006;115:434–40. doi:10.1007/s00214-006-0124-2.
[22] Sievers MR, Armentrout PB. Oxidation of CO and reduction of CO_2 by gas phase Zr^+, ZrO^+, and ZrO_2^+. Int J Mass Spectrom 1999:185–7 117–29. doi:10.1016/S1387-3806(98)14074-5.
[23] Dyke JM, Ellis AM, Fehèr M, Morris A, Paul AJ, Stevens JCH. High-temperature photoelectron spectroscopy. A study of niobium monoxide and tantalum monoxide. J Chem Soc, Faraday Trans 1987;2:1555–65 83. doi:10.1039/F29878301555.
[24] Sievers M, Armentrout P. Gas phase activation of carbon dioxide by niobium and niobium monoxide cations. Int J Mass Spectrom 1998:179–80 103–15. doi:10.1016/S1387-3806(98)14064-2.
[25] Di Tommaso S, Marino T, Rondinelli F, Russo N, Toscano M. CO_2 activation by Nb^+ and NbO^+ in the gas phase. A case of two-state reactivity process. J Chem Theo Comput 2007;3:811–15. doi:10.1021/ct700014k.
[26] Knowles PJ, Werner H-J. An efficient method for the evaluation of coupling coefficients in configuration interaction calculations. Chem Phys Lett 1988;145:514–22. doi:10.1016/0009-2614(88)87412-8.
[27] Werner H-J, Knowles PJ. An efficient internally contracted multiconfiguration–reference configuration interaction method. J Chem Phys 1988;89:5803–14. doi:10.1063/1.455556.
[28] Shamasundar KR, Knizia G, Werner H-J. A new internally contracted multi-reference configuration interaction method. J Chem Phys 2011;135:054101–17. doi:10.1063/1.3609809.
[29] Werner H-J, Knowles PJ, Knizia G, Manby FR, Schütz M, Celani P, Györffy W, Kats D, Korona T, Lindh R, Mitrushenkov A, Rauhut G, Shamasundar KR, Adler TB, Amos RD, Bernhardsson A, Berning A, Cooper DL, Deegan MJO, Dobbyn AJ, Eckert F, Goll E, Hampel C, Hesselmann A, Hetzer G. MOLPRO, Version 2015;1. see http// www.molpro.net .
[30] Kendall RA, Dunning TH, Harrison RJ. Electron affinities of the first-row atoms revisited. Systematic basis sets and wave functions. J Chem Phys 1992;96:6796–806. doi:10.1063/1.462569.
[31] Peterson KA, Figgen D, Dolg M, Stoll H. Energy-consistent relativistic pseudopotentials and correlation consistent basis sets for the 4d elements Y–Pd. J Chem Phys 2007;126:124101. doi:10.1063/1.2647019.
[32] Kramida A, Ralchenko Y, Reader J, NIST ASD team. NIST atomic spectra database (version 5.4), national institute of standards and technology, Gaithersburg, 2016. http://physics.nist.gov/asd (accessed December 13, 2019).

Radical abstraction vs. oxidative addition mechanisms for the activation of the S–H, O–H, and C–H bonds using early transition metal oxides

PCCP

ROYAL SOCIETY OF CHEMISTRY

PAPER

View Article Online
View Journal | View Issue

Cite this: *Phys. Chem. Chem. Phys.*, 2021, **23**, 1437

Radical abstraction *vs.* oxidative addition mechanisms for the activation of the S–H, O–H, and C–H bonds using early transition metal oxides†

Isuru R. Ariyarathna and Evangelos Miliordos *

Received 21st October 2020,
Accepted 18th December 2020

DOI: 10.1039/d0cp05513a

rsc.li/pccp

Quantum chemical calculations are performed to study the S–H, O–H, and C–H bond activation of H_2S, H_2O, and CH_4 by bare and ligated ZrO^+ and NbO^+ units. These representative oxides bear low energy oxo and higher energy oxyl units. S–H and C–H bonds are readily activated by metal oxyl states (radical mechanism), but the O–H bond is harder to activate with either the oxyl or oxo states. Our results suggest that known practices for the C–H bond activation can be applied to S–H, but not to O–H bonds. The identified trends are rationalized in terms of the HS–H, HO–H, and H_3C–H dissociation energies to the homolytic or heterolytic fragments. We also found that these dissociation energies drop to about half after coordination of H_2S or H_2O to the metal oxide unit. In addition, chlorine ligands are shown to stabilize the higher energy oxyl states of the transition metal oxygen unit enhancing the reactivity of the formed complexes.

1. Introduction

The activation of the H–OH and H–SH bonds is a topic of intense research. On one hand, water splitting leads to the production of H_2 (fuel for green energy applications),[1,2] and on the other hand, the removal of H_2S as elemental sulfur (desulfurization) from oil and natural gas streams is necessary in industrial applications for the prevention of catalyst poisoning and corrosion.[3,4] Among the common H_2S sorbents, metal oxides have been used widely.[4–10] The overall reaction is summarized as $H_2S + M_mO_n + [O] \rightarrow H_2O + M_mO_{n-1}S + [O] \rightarrow M_mO_n + (1/k)S_k$, where [O] is some oxygen source. The initial catalytic step involves the MO + H–SH reaction, which leads to S/O exchange in the metal vicinity.[6] This reaction step is analogous to the first step (MO + H–CH_3) of methane conversion to methanol or that of the O–H bond activation of H_2O facilitated by a metal oxide. Is the activation mechanism the same for these three bonds? Theoretical calculations are able to answer such questions and provide companion to experimental studies.[11] Our present goal is to shed light on the activation mechanism of the O–H and S–H chemical bonds in electronic structure terms and compare them with the well-explored C–H activation process. The same direction was suggested a decade ago by Piers, who proposed the use of organometallic approaches for the manipulation of C–H bonds to water splitting.[12] Within this context, we demonstrate that the S–H bond, as opposed to O–H, bears similar activity to C–H.

Terminal metal oxides are mentioned in the literature either as oxo or oxyl units depending on the nature of the oxygen terminus. Oxo compounds bear a closed-shell O^{2-} end, while oxyl compounds feature a radical $O^{\bullet -}$ nature.[13] Generally the lowest energy electronic states of early transition metals (prior to the oxo-wall)[13] have oxo character. Oxyl states are higher in energy and have longer metal-oxygen bond lengths (see for example ref. 14–16). Therefore, the oxyl character increases in the region of the M–O$\cdots$H–CR_3 transition state (R = some alkyl group).[17]

The reaction of C–H bonds with the higher energy oxyl units bear lower activation energy barriers, which are nearly independent of the substrate.[18] Therefore, oxyl units provide more efficient but less selective catalytic pathways.[18] We recently demonstrated that ammonia and halide ligands stabilize the oxo and oxyl states, respectively.[15,17] Our results open an avenue for a bottom-up systematic approach to tune the catalytic activity of molecular transition metal compounds through a proper combination of weak (halogen) or strong (ammonia) field ligands. Do these observations apply to the activation of S–H and O–H bonds?

To answer this question, we employed the model reactions between NbO^+ or ZrO^+ and H_2S or H_2O. These two oxides are typical representatives with low energy oxo and higher energy

Department of Chemistry and Biochemistry, Auburn University, Auburn, AL 36849-5312, USA. E-mail: emiliord@auburn.edu

† Electronic supplementary information (ESI) available. See DOI: 10.1039/d0cp05513a

oxyl states. In addition, the small number of valence metallic electrons makes the calculations tractable and, as it will be shown later, they are ideal cases to demonstrate the role of the employed ligands (Cl and NH_3).

2. Computational details

Density functional theory (DFT) calculations are carried out within the Gaussian 16 suite of codes.[19] The MN15 functional is selected combined with the aug-cc-pVTZ(O,S), cc-pVTZ(H), and cc-pVTZ-PP(Zr,Nb) basis sets. The stuttgart relativistic pseudopotential for Zr and Nb replaces their twenty-eight inner electrons.[20–22] Harmonic frequencies are calculated to assess the stability of the potential energy minima for the reactants and products, to ensure that the located transition states are first order saddle points, and to estimate zero-point and free energies (at 25 °C and 1 atm).

To assess our DFT calculations, we also employed multi-reference configuration interaction methods. We performed multi-reference configuration interaction (MRCI) for the smallest $MO^+ + H_2X$ systems (M = Zr, Nb and X = S, O) in their ground and excited states, using the same basis set. The active space of the reference CASSCF (complete active space self-consistent field) calculations are composed of seven active orbitals with five and six electrons in M = Zr and M = Nb cases, respectively. All valence electrons are correlated at the MRCI level. The Davidson correction was also applied for more accurate energetics (MRCI + Q). MOLPRO 2015 was used for the MRCI calculations.[23]

3. Results and discussion

The three lowest states of ZrO^+ are doublet states with a $Zr^{3+}O^{2-}$ character. The unpaired electron occupies one of the five 4d-orbitals of the metal: $X^2\Delta$ ($4d_{xy}$, $4d_{x^2-y^2}$), $1^2\Sigma^+$ ($4d_{z^2}$ mixed with 5s), $1^2\Pi$ (d_{xz}, d_{yz}).[16] Six electrons occupy the three bonding molecular orbitals (σ, π_x, π_y) polarized towards oxygen ($\sigma \sim 2p_z$, $\pi_x \sim 2p_x$, $\pi_y \sim 2p_y$); see Fig. 2 of ref. 16. These states are well separated (by about 13 000 cm^{-1}) from the next group of states, which have $Zr^{2+}O^{\bullet-}$ (oxyl) character. In these states one of the electrons of the $\pi \sim 2p_{x,y}(O)$ bonding orbitals transfers to a 4d-metallic orbital creating a radical oxygen terminus. The three unpaired electrons couple to an overall quartet or doublet state. The lowest among them is the $1^2\Phi$ with two α and one β electrons and excitation energy of about 29 000 cm^{-1}.[16] The antiferromagnetic coupling in this state generates spin contamination in the DFT calculations. Therefore, for the purpose of our investigation we focused on the first oxyl quartet state $1^4\Pi$, which is just ~600 cm^{-1} above $1^2\Phi$ and ~29 600 cm^{-1} higher than the ground $X^2\Delta$ state. The bond lengths in the oxo ($X^2\Delta$) and oxyl ($1^4\Pi$) states are 1.72 and 1.97 Å, respectively.[16]

A very similar situation is seen for NbO^+.[16] The low-lying states are described as $Nb^{3+}O^{2-}$ with two electrons localized on Nb. There are eleven such states (singlet and triplet) before the lowest $Nb^{2+}O^{\bullet-}$ state ($1^5\Sigma^-$) at around 32 000 cm^{-1}. The latter state has an unpaired electron in one $\pi \sim 2p_x(O)$ or $2p_y(O)$ bonding orbital, and three electrons in the $4d_{xy}$, $4d_{x^2-y^2}$, $4d_{xz}$ or $4d_{yz}$ orbitals of Nb.

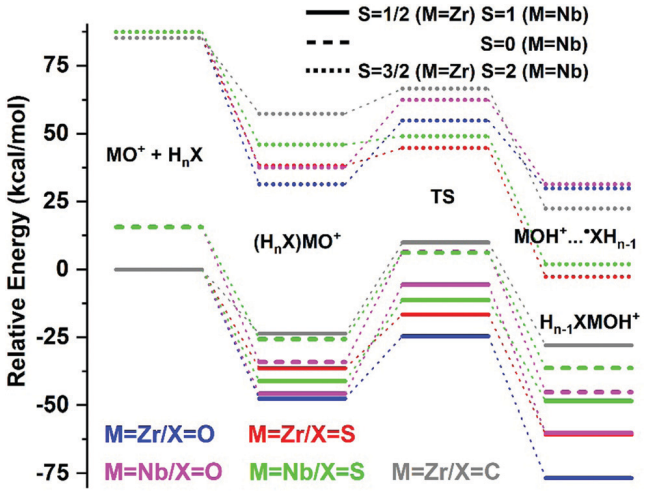

Fig. 1 Energy diagram for the $ZrO^+/NbO^+ + H_2O/H_2S/CH_4$ reactions (n = 2 except for X = C where n = 4). The zero of the energy scale is set to the energy of the ground state fragments.

To see the electronic structure effect of the metal oxide to the reaction energetics and activation of the H–OH and H–SH bonds, we first studied the reaction of "naked" ZrO^+ and NbO^+ with H_2S and H_2O. The lowest energy doublet and singlet/triplet oxo-states of zirconium and niobium, respectively, are employed. The lowest energy quartet and quintet states of the two metals are considered as representatives of oxyl states. The potential energy profiles for the four reactions ($ZrO^+/NbO^+ + H_2S/H_2O$) are plotted in Fig. 1. The leftmost energy levels correspond to the $MO^+ + H_2X$ fragments (M = Zr or Nb and X = O or S), followed by the coordination $(H_2X)MO^+$ complex, the transition state TS, and finally the $MOH^+\cdots{}^\bullet SH$ (high-spin) or $HSMOH^+$ (intermediate and low-spin) products. The $ZrO^+ + CH_4$ reaction has also been included for comparison.

The low (S = 1/2 for Zr and S = 0 for Nb) and intermediate spin (S = 1 for Nb) follow an oxidative addition (2+2) mechanism, where H^+ migrates from X to the O terminal of MO^+. The high-spin states (S = 3/2 for Zr and S = 2 for Nb) cause a homolytic cleavage of the H–XH and produce a $^\bullet XH$ radical, which finally attaches to M. The intrinsic activation energy barriers $\Delta E^\ddagger$ (energy difference between $(H_2X)MO^+$ and TS) is always lower for X = S independently of the mechanism or metal. In addition, in the case of niobium, the dependence of $\Delta E^\ddagger$ on the spin state is small when the 2+2 pathway occurs. Specifically, the $\Delta E^\ddagger$ values for triplet/singlet for X = O and S are 40.2/40.5 and 30.0/31.8 kcal mol^{-1}, respectively. However, $\Delta E^\ddagger$ drops significantly for the radical route and especially for X = S. The $\Delta E^\ddagger$ values for the quintet state are 25.0 (X = O) and 3.2 kcal mol^{-1} (X = S). The former is about 40% and the latter 90% smaller. In the case of zirconium, $\Delta E^\ddagger$ remains practically the same for X = O for the two mechanisms (23.0 and 23.4 kcal mol^{-1}), but becomes three times smaller in the radical case for X = S (19.8 *vs.* 6.5 kcal mol^{-1}). These results indicate that the radical mechanism is very efficient for the cleavage of the H–SH bond, as opposed to H_2O, and this is practically independent of the metal.

The intrinsic barrier of the radical mechanism for X = O and X = S is nearly the same for the two metals (23.4 *vs.* 25.0 kcal mol^{-1} and 6.5 *vs.* 3.2 kcal mol^{-1}).

These observations are direct consequence of two factors. First, the homolytic cleavage to HX$^{\bullet}$ + H$^{\bullet}$ (radical mechanism) is less energy demanding than the heterolytic products HX^{-} + H^{+} (2+2 mechanism). In addition, the binding energy of H–XH with respect to HX$^{\bullet}$ + H$^{\bullet}$ for X = O is significantly higher than X = S (124 *vs.* 96 kcal mol^{-1} at the MN15/aug-cc-pVTZ level of theory). The binding energy for H–CH_3 is in the middle of these values (111 kcal mol^{-1}). For comparison, we reproduced the energy profiles for the ZrO^+ + CH_4 reaction. The hydroxylation of the methane C–H bond with ZrO^+ resembles the ZrO^+ + H_2S reaction in the sense that the radical mechanism $\Delta E^{\ddagger}$ is more than three times smaller: 33.5 *vs.* 9.2 kcal mol^{-1}.

To put the above observations in a more quantitative context, we plotted $\Delta E^{\ddagger}$ of the ZrO^+ + H_2S/H_2O/CH_3 reactions with respect to the dissociation energy D_e of a H–SH/H–OH/H–CH_3 bond to either H$^{\bullet}$ + $^{\bullet}$SH/$^{\bullet}$OH/$^{\bullet}CH_3$ (radical mechanism) or H$^+$ + $^-$SH/$^-$OH/$^-CH_3$ (2+2 mechanism); see Fig. 2. We now see a clear correlation of $\Delta E^{\ddagger}$ to the two kinds of dissociation energies. The two D_e values for sulfur are the smallest ones and this reflects to the smallest activation energies for both mechanisms. On the other hand, water has the largest homolytic dissociation energy but not the largest heterolytic dissociation energy. Again, this reflects to the barriers of the two mechanisms: water has the largest activation barrier for the radical mechanism, but not the largest barrier for the 2+2 mechanism. Finally, methane bears the largest oxidative addition (2+2) activation barrier due to the large H$^+$ + CH_3^- dissociation energy. The latter can be attributed to the low stability of the CH_3^- anion, as expressed by the low electron affinity EA of CH_3: EA(OH) = 1.83 eV, EA(SH) = 2.31 eV, and EA(CH_3) = 0.08 eV.[24]

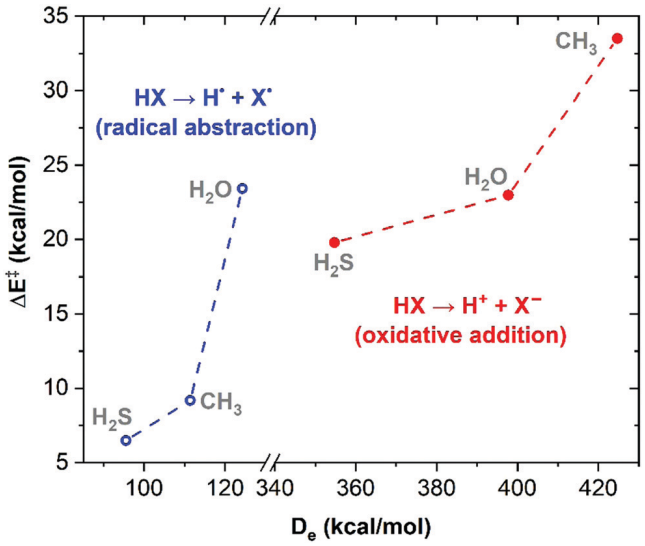

Fig. 2 Activation energy $\Delta E^{\ddagger}$ of the radical abstraction and oxidative addition mechanisms *vs.* the dissociation energy to the neutral and ionic fragments, respectively, for the ZrO^+ + HX reaction, where X = OH, SH, or CH_3.

A different approach (brought to our attention by one of the reviewers) is to consider the binding HO–H and HS–H binding energies within the initial $(H_2X)MO^+$ complex. Past infrared spectroscopic studies showed that the O–H stretch frequencies drop by about 50 cm^{-1}; see for example ref. 25 and 26 about $Nb^+(H_2O)$ and H_2O. Surprisingly, our calculated DFT/MN15 $(H_2X)ZrO^+$ (S = 3/2) → $(HX)ZrO^+$ (S = 1) + H and $(H_2X)ZrO^+$ (S = 1/2) → (HX)ZrO (S = 1/2) + H$^+$ dissociation energies were found to be nearly half of those for free H_2X (H_2X → X + H and H_2X → X$^-$ + H$^+$). Specifically, the homolytic/heterolytic dissociation energies for free H_2O are 124.3/397.8 and become 64.3/217.4 kcal mol^{-1}, while for free H_2S we obtained 94.7/353.9 becoming 47.8/210.6 kcal mol^{-1}. The trends remain exactly the same with both dissociation processes being "easier" for H_2S. Overall, this example indicates that coordination "pre-activates" chemical bonds, and that the use of the experimentally measurable binding energies of free species is a simpler, "first-order" criterion to identify chemical trends.

To assess the accuracy of our DFT calculations for these systems, we also performed accurate multi-reference calculations for the ground and excited states. The results of the two series of calculations are compared in more detail in the ESI.† The comparison for the bare metal oxides suggests that the used DFT scheme is appropriate for the states of interest and can be employed for the study of bigger ligated systems.

Recently, we showed for the ZrO + CH_4 reaction that the addition of ammonia ligands has a rather minor effect in the reactivity of the ZrO unit.[16] The energy landscape for the two mechanisms remains largely the same before and after adding ammonia, while in the past we found that ammonia favors the oxo character of FeO^{2+}.[17] On the other hand, halide ligands were shown to favor the radical pathway for ZrO + CH_4.[16] To see the action of these ligands for H_2O and H_2S, we started by adding two chlorine atoms to ZrO^+. The ground state of Cl_2ZrO^+ turns out to have an oxyl radical $Cl_2ZrO^{\bullet+}$ character in agreement with our previous findings. The oxyl quartet state of ZrO^+ has two electrons on the metal center, which can couple to the two electrons of the chlorine atoms and make two strong Zr–Cl bonds. The ground doublet state of ZrO^+ has only one electron on Zr and cannot facilitate the formation of these bonds. As a result, the oxyl state of ZrO^+ is stabilized further and becomes the global minimum of Cl_2ZrO^+. The same procedure was proved for H_3ZrO by constructing the 3H + ZrO potential energy curves. The H_3ZrO global minimum originates diabatically from an excited $Zr^+O^{\bullet-}$ electronic state. Alternatively, the (adiabatic) formation of $Cl_2ZrO^{\bullet+}$ from the ground oxo state of ZrO^+ can be seen as the initial formation of a covalent Zr–Cl bond with one of the Cl atoms. In order for the second Cl atom to bind to Zr, one electron has to migrate from oxygen to the metal. The early transition metal-chlorine bonds are quite polarized ($M^{\delta+}Cl^{\delta-}$)[27] and therefore it may be claimed that the second chlorine atom "steals" an oxygen electron. The two different bonding schemes along with contour of the singly occupied molecular orbital of Cl_2ZrO^+ are depicted in Fig. 3.

Conclusively, the equilibrium electronic structure of Cl_2ZrO^+ is better described $[(Cl^-)_2Zr^{4+}O^{\bullet-}]^+$, where the metal center is

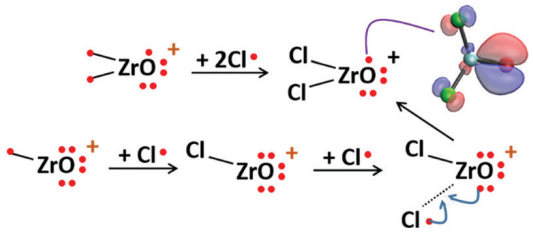

Fig. 3 Alternative formation pathways of Cl_2ZrO^+ from oxo (doublet) and oxyl (quartet) ZrO^+ states and two Cl atoms. The resulting doublet state bears an unpaired electron on oxygen (oxyl state).

closed-shell and fully stripped of electrons. The approach of a H_2S molecule causes the transfer of a hydrogen atom from H_2S to the radical oxygen center leaving sulfur an unpaired electron. Fig. 4 shows the molecular orbitals accommodating the unpaired electrons of Cl_2ZrO^+ (top left) and $Cl_2ZrOH(SH)^+$ (top right). The same figure depicts also the two molecular orbitals of the TS pertaining to the hydrogen atom transfer (top middle). The initially π_{ZrO} (singly occupied) and σ_{SH} (doubly occupied) orbitals are combined with a positive (doubly occupied) or negative (singly occupied) sign to finally make the σ_{OH} (doubly occupied) and p_S (singly occupied). The addition of ammonia ligands to the complex does not change the observed process (see bottom of Fig. 4). Ammonia molecules act as observers coordinating to "inert" (more like point-charge with no valence electrons) metal center.

The addition of the two chlorine ligands destabilizes both the reactive complex (interaction complex between H_2S and ZrO^+ or Cl_2ZrO^+) and the products ($HSZrOH^+$ or $HSZr(Cl)_2OH^+$) with respect to infinitely separated reactants by 5 kcal mol^{-1}; compare red and blue lines of Fig. 5 and see Table 1. The reaction energy barrier nearly doubles but remains minimal (from 6.5 to 12.0 kcal mol^{-1}). To complete the first coordination sphere of Zr, we added one to three ammonia molecules. The addition of ammonia ligands destabilized further the reactive complex and product, but reduced the intrinsic activation energy barrier to less than 6.5 kcal mol^{-1} (see Fig. 5 and Table 1). The reaction remains highly exothermic (by at least

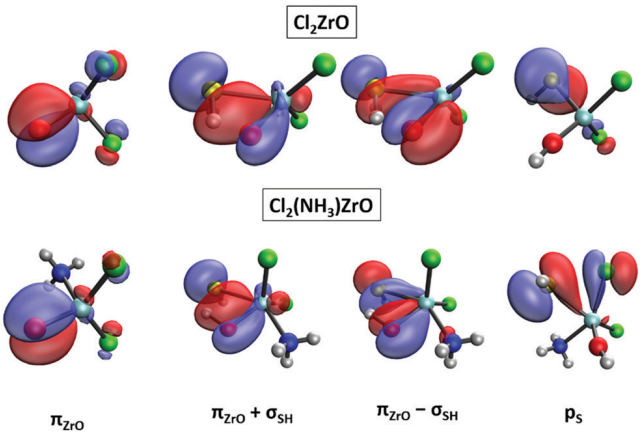

Fig. 4 Molecular orbitals involved in the HS–H activation process mediated by Cl_2ZrO and $Cl_2(NH_3)ZrO$.

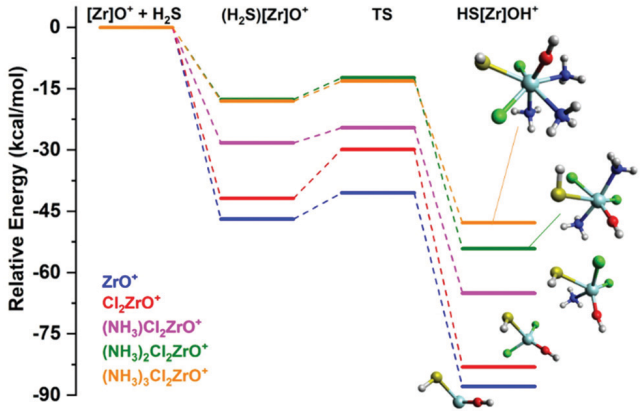

Fig. 5 Energy diagram for the reaction of $[Zr]O^{\bullet+}$ (S = 3/2 for ZrO and S = 1/2 otherwise) with H_2S, where [Zr] represents the transition metal complex $(NH_3)_mCl_nZr$ (m,n = 0,0; 0,2; 1,2; 2,2; 3,2).

Table 1 Relative energy (in kcal mol^{-1}) of all intermediate and transition state structures for the reaction of H_2S and H_2O with bare and ligated ZrO^+ and NbO^+ units. [Zr]/[Nb] denotes the metal-ligands combination, and A represents an ammonia molecule. The radical high-spin state is listed for the bare units

	[Zr]/[Nb] compound				
Species	Zr	Cl_2Zr	Cl_2ZrA	Cl_2ZrA_2	Cl_2ZrA_3
$[Zr]O^+ + H_2S$	0.0	0.0	0.0	0.0	0.0
$(H_2S)[Zr]O^+$	−46.9	−41.8	−28.3	−17.6	−18.0
TS	−40.5	−29.9	−24.5	−12.3	−13.1
$HS[Zr]OH^+$	−87.8	−83.0	−65.0	−54.2	−47.9

	[Zr]/[Nb] compound			
Species	Nb	Cl_3Nb	Cl_3NbA	Cl_3NbA_2
$[Nb]O^+ + H_2S$	0.0	0.0	0.0	0.0
$(H_2S)[Nb]O^+$	−41.4	−53.2	−37.2	−33.0
TS	−38.3	−47.5	−35.1	−30.8
$HS[Nb]OH^+$	−85.3	−62.5	−48.4	−41.9

	[Zr]/[Nb] compound				
Species	Zr	Cl_2Zr	Cl_2ZrA	Cl_2ZrA_2	Cl_2ZrA_3
$[Zr]O^+ + H_2O$	0.0	0.0	0.0	0.0	0.0
$(H_2O)[Zr]O^+$	−53.8	−52.2	−38.3	−26.1	−23.9
TS	−30.4	−28.2	−20.3	−12.1	−6.0
$HO[Zr]OH^+$	−55.3	−63.0	−50.2	−43.3	−21.2

	[Zr]/[Nb] compound			
Species	Nb	Cl_3Nb	Cl_3NbA	Cl_3NbA_2
$[Nb]O^+ + H_2O$	0.0	0.0	0.0	0.0
$(H_2O)[Nb]O^+$	−49.9	−36.6	−30.4	−22.2
TS	−24.9	−11.0	−6.4	−0.2
$HO[Nb]OH^+$	−56.3	−54.0	−47.8	−21.3

45 kcal mol^{-1}). The Zr–S distance of the products increases gradually with the attachment of ligands, from 2.665 Å of bare $HSZrOH^+$ to 2.731 Å in the case of the $Cl_2Zr(NH_3)_3$ complex.

Similar observations can be done for the reaction of NbO^+ with H_2S. The addition of three chlorine atoms is necessary to stabilize its high spin state with the oxyl character. The reaction

becomes clearly less exothermic by 23 kcal mol^{-1} and the intrinsic barrier nearly doubles but remains minimal (from 3.1 to 5.7 kcal mol^{-1}). The energetics are listed in Table 1 and all of the structures with more detailed energy information are given in the ESI.† The addition of two more ammonias (to complete the first coordination shell) reduced the exothermicity by another 21 kcal mol^{-1} but reduced the barrier to only 2.2 kcal mol^{-1}.

A noticeable difference between zirconium and niobium is that the produced SH unit is not attached to Nb but located at the second coordination shell hydrogen-bonded to OH, when at least one ammonia ligand is present (see Fig. S4 of ESI†). The Nb–S distance is longer than the Zr–S one even for bare ZrS^+ (2.665 Å) and NbS^+ (2.730 Å). Conclusively, niobium can activate easier H_2S and the fully coordinated $Cl_3(NH_3)_2NbO^+$ complex reveals the best performance among the presently studied species.

Finally, we performed the exact same analysis for the activation of H_2O by bare and ligated ZrO^+/NbO^+. The numerical results are reported in Table 1. As in H_2S, the reaction becomes less exothermic as more ligands are added and $\Delta E^{\ddagger}$ decreases by 5.5 and 3.0 kcal mol^{-1} going from bare ZrO^+/NbO^+ (high spin/oxyl) to fully coordinated oxides with two/three chlorine and three/two ammonia ligands, respectively. The barriers remain quite larger compared to those of H_2S: 17.9 and 22.0 kcal mol^{-1} for $(NH_3)_3Cl_2ZrO^+$ and $(NH_3)_2Cl_3NbO^+$ *vs.* 8.5 and 2.2 kcal mol^{-1} in the H_2S case.

To see the effect of the vibrational degrees of freedom at 0 K and the thermal contributions at 25 °C and 1 atm of the rovibrational/translational motions, we collected the zero-point and free energies of all intermediates and transition states in the ESI† (see Tables S4, S8, S12, S16, S19 and Fig. S5 and S6). The main observations are that zero-point corrections increase the energies of the interacting reactants and products on average by 2.0 kcal mol^{-1} with respect to separated reactants, while the free energies of them shift to the same direction by about 10 kcal mol^{-1}. The free energy of the transition states increases also by 10 kcal mol^{-1} but they are rather stabilized by about 0.5 kcal mol^{-1} at 0 K. The activation energies barriers in both cases are reduced (as expected) by about 2.0 kcal mol^{-1}.

4. Conclusions

Our theoretical calculations demonstrate that S–H and C–H bonds can be activated readily by a metal–oxygen oxyl unit *via* a radical mechanism. The activation energy barrier is nearly independent of the metal identity for the radical mechanism. The oxyl units of the early transition metal ZrO^+ and NbO^+ oxides are highly excited states, but can become the ground state with the proper number of chlorine ligands (two for Zr and three for Nb). The addition of ammonia ligands to complete the first coordination sphere of the metal does not change the ground state oxyl character. On the contrary, the O–H bond of water is a harder bond to activate with either the radical abstraction or oxidative addition pathways, and independently of the present ligands. The reason is the relatively large dissociation energy of water to both neutral and ionic products. Our findings suggest that the practices used for the activation of C–H bonds can be applied to the activation of S–H but not O–H bonds. For O–H bonds, metal oxide anions have shown superior performance.[28,29]

Conflicts of interest

There are no conflicts to declare.

Acknowledgements

The authors are indebted to Auburn University (AU) for financial support. This work was completed with resources provided by the Auburn University Hopper Cluster and Alabama Supercomputer Center. They are also grateful to one of the reviewers for suggesting us to calculate dissociation energies for the titled bonds after the coordination of the substrate molecules to the transition metal complex.

References

1 X. Li, L. Zhao, J. Yu, X. Liu, X. Zhang, H. Liu and W. Zhou, *Nano-Micro Lett.*, 2020, **12**, 131.
2 N. S. Lewis and D. G. Nocera, *Proc. Natl. Acad. Sci. U. S. A.*, 2006, **103**, 15729.
3 I. V. Babich and J. A. Moulijn, *Fuel*, 2003, **82**, 607–631.
4 S. Lew, K. Jothimurugesan and M. Flytzani-Stephanopoulos, *Ind. Eng. Chem. Res.*, 1989, **28**, 535–541.
5 R. Portela, F. Rubio-Marcos, P. Leret, J. F. Fernández, M. A. Bañares and P. Ávila, *J. Mater. Chem. A*, 2015, **3**, 1306–1316.
6 M.-Y. Jia, X.-L. Ding, S.-G. He and M.-F. Ge, *J. Phys. Chem. A*, 2013, **117**, 8377–8387.
7 Y.-X. Zhao, Q.-Y. Liu, M.-Q. Zhang and S.-G. He, *Dalton Trans.*, 2016, **45**, 11471–11495.
8 A. Junkaew, P. Maitarad, R. Arróyave, N. Kungwan, D. Zhang, L. Shi and S. Namuangruk, *Catal. Sci. Technol.*, 2017, **7**, 356–365.
9 M. Brancher, D. Franco and H. de Melo Lisboa, *Environ. Technol.*, 2016, **37**, 2852–2864.
10 R. Sadegh-Vaziri and M. U. Babler, *Appl. Sci.*, 2019, **9**, 5316.
11 D. Lupp, N. J. Christensen and P. Fristrup, *Dalton Trans.*, 2014, **43**, 11093–11105.
12 W. E. Piers, *Organometallics*, 2011, **30**, 13–16.
13 Y. Shimoyama and T. Kojima, *Inorg. Chem.*, 2019, **58**, 9517–9542.
14 E. E. Claveau and E. Miliordos, *Phys. Chem. Chem. Phys.*, 2019, **21**, 26324–26332.
15 B. A. Jackson and E. Miliordos, *Phys. Chem. Chem. Phys.*, 2020, **22**, 6606–6618.
16 I. R. Ariyarathna and E. Miliordos, *J. Quant. Spectrosc. Radiat. Transfer*, 2020, **255**, 107265.

17 J. K. Kirkland, S. N. Khan, B. Casale, E. Miliordos and K. D. Vogiatzis, *Phys. Chem. Chem. Phys.*, 2018, **20**, 28786–28795.
18 A. A. Latimer, A. Kakekhani, A. R. Kulkarni and J. K. Nørskov, *ACS Catal.*, 2018, **8**, 6894–6907.
19 M. J. Frisch, G. W. Trucks, H. B. Schlegel, G. E. Scuseria, M. A. Robb, J. R. Cheeseman, G. Scalmani, V. Barone, G. A. Petersson, H. Nakatsuji, *et al.*, *Gaussian 16, Rev. B.01*, Wallingford, CT, 2016.
20 T. H. Dunning, *J. Chem. Phys.*, 1989, **90**, 1007–1023.
21 D. E. Woon and T. H. Dunning, *J. Chem. Phys.*, 1994, **100**, 2975–2988.
22 K. A. Peterson, D. Figgen, M. Dolg and H. Stoll, *J. Chem. Phys.*, 2007, **126**, 124101.
23 H.-J. Werner, P. J. Knowles, G. Knizia, F. R. Manby, M. Schütz, P. Celani, W. Györffy, D. Kats, T. Korona, R. Lindh, *et al.*, *MOLPRO, version 2015.1, a package of ab initio programs*2015.
24 W. M. Haynes, *CRC Handbook of Chemistry and Physics*, Taylor & Francis, 93rd edn, 2012.
25 T. B. Ward, E. Miliordos, P. D. Carnegie, S. S. Xantheas and M. A. Duncan, *J. Chem. Phys.*, 2017, **146**, 224305.
26 T. Shimanouchi, Molecular Vibrational Frequencies, in *NIST Chemistry WebBook, NIST Standard Reference Database Number 69*, ed. P. J. Linstrom and W. G. Mallard, National Institute of Standards and Technology, Gaithersburg MD, 20899, DOI: 10.18434/T4D303, (retrieved November 1, 2020).
27 S. Kardahakis and A. Mavridis, *J. Phys. Chem. A*, 2009, **113**, 6818–6840.
28 I. R. Ariyarathna and E. Miliordos, *Phys. Chem. Chem. Phys.*, 2018, **20**, 12278–12287.
29 I. R. Ariyarathna, N. M. S. Almeida and E. Miliordos, *Phys. Chem. Chem. Phys.*, 2020, **22**, 16072–16079.

Ab initio investigation of the ground and excited states of $MoO^{+,2+,-}$ and their catalytic strength on water activation

PCCP

PAPER

Cite this: *Phys. Chem. Chem. Phys.*, 2018, **20**, 12278

Ab initio investigation of the ground and excited states of $MoO^{+,2+,-}$ and their catalytic strength on water activation†

Isuru R. Ariyarathna and Evangelos Miliordos*

Received 14th March 2018,
Accepted 16th April 2018

DOI: 10.1039/c8cp01676c

rsc.li/pccp

The charged molybdenum monoxides, $MoO^{+,2+,-}$ were studied by multireference configuration interaction and coupled cluster calculations in conjunction with large basis sets. Full potential energy curves were constructed and bonding patterns were proposed for several low-lying electronic states of the three species. Our numerical results involve accurate equilibrium bond lengths, harmonic vibrational frequencies, anharmonicities, excitation energies, and binding energies. This is the first high-level theoretical investigation and our results compare favorably with the limited existing experimental data. Nine states of MoO^{2+} are bound with respect to the lowest energy fragments $Mo^+ + O^+$, while MoO^- has five bound electronic states with respect to $MoO + e^-$. Energetics, including activation energies, are given for the reaction between the lowest lying electronic states of the titled species and water. It is shown that MoO^- is clearly more efficient at activating an OH bond.

I. Introduction

Coordination complexes of transition metal monoxides serve as homogeneous catalysts used for C–H activation or water splitting reactions.[1,2] Terminal metal–oxygen bonds are also found in natural metalloenzymes, such as cytochrome P450.[3] Although the presence of the ligands affects the catalytic activity, deeper knowledge on the electronic structure of the naked transition metal monoxides can provide useful insights about the metal–oxygen bonding. For example, different mechanisms on the methane activation by bare $FeO^{0,\pm}$ have been discussed depending on the nature of the iron–oxygen bond.[4] These mechanisms involve the transfer of hydrogen from carbon to oxygen as a proton or radical followed by the migration of CH_3 to iron. Another mechanism is the concerted detachment of one C–H bond and attachment of the fragments to iron and oxygen. The polarity of the metal–oxygen bond and the radical character of the terminal oxygen atom will determine the actual mechanism.

In the past we have found that the first row transition metal monoxides, $MO^{0,\pm}$ (M = Sc–Fe), prefer a highly ionic character represented by $M^{+,2+}$ and O^- or O^{2-}.[5–7] Minimal radical character was detected for the ground and several excited electronic states of these systems. Herein we study the charged molybdenum oxides, MoO^+, MoO^{2+}, and MoO^- in an attempt to extend our work to the second row transition metals and doubly charged cationic species. We perform multi-reference calculations to elucidate the chemical bonding for many low-lying electronic states. Our findings are expected to shed light on the underlying electronic structure transformations in catalytic processes such as H_2 production from water facilitated by $[(PY5Me_2)MoO]^{2+}$.[2] The MoO^+ and MoO^{2+} moieties have both been identified in the mechanism of this reaction.[8] Neutral MoO will not be considered here since has recently been studied at a high level of theory.[9]

Among the three titled systems only MoO^+ has been studied theoretically. First, Broclawik in 1995 employed density functional theory (DFT) and reported bond lengths, vibrational frequencies, and binding energies for four low-lying electronic states, $^4\Sigma^-$, $^4\Pi$, $^6\Pi$, and $^2\Delta$.[10] Two years later, Kretzschmar *et al.* used multi-reference perturbation theory to calculate bond lengths, excitation and binding energies for $^4\Sigma^-$, $^2\Delta$, and $^6\Sigma^-$.[11] These authors showed also that relativistic effects have a big impact on the binding energy which is 87.1 kcal mol^{-1} and becomes 106.1 kcal mol^{-1} before and after special relativity is considered. Loock *et al.* did DFT calculations including relativistic effects for four states ($^4\Sigma^-$, $^4\Pi$, $^2\Delta$, $^2\Sigma^+$) providing their excitation energies and the binding energy for the ground $^4\Sigma^-$ state.[12] In 1999, Broclawik *et al.* revisited MoO^+ reporting numerical data by means of DFT with the BPW91 functional this time for $^4\Sigma^-$, $^4\Pi$, and $^2\Delta$.[13] We are not aware of any other work between the latter work and the recent one by Luo *et al.* seventeen years later.[14] Highly accurate coupled-cluster calculations were carried out for the bond length, harmonic vibration frequency, and binding energy for the ground state of MoO^+. The ionization energy of MoO was also given.

Department of Chemistry and Biochemistry, Auburn University, Auburn, AL 36849, USA. E-mail: emiliord@auburn.edu

† Electronic supplementary information (ESI) available. See DOI: 10.1039/c8cp01676c

To our knowledge, three experimental works have been devoted to MoO^+. Sievers *et al.* report a very accurate binding energy for the ground state of 5.06 ± 0.02 eV or 116.7 ± 0.5 kcal mol^{-1}.[15] The electron affinity of MoO^+ (or ionization energy of MoO) of 7.4504 ± 0.0004 eV is reported by Loock *et al.*,[12] who provide experimental evidence for a $^4\Sigma^-$ ground state. Finally, Luo *et al.* report spectroscopic data for the $^4\Sigma^-$ and $^2\Delta$ states.[14]

No theoretical or experimental work seems to exist in the literature on MoO^{2+}, and we are knowledgeable of only one work on MoO^- by Gunion *et al.*[16] The electron affinity of MoO was found 1.290 ± 0.006 eV by means of photoelectron pectroscopy. The equilibrium bond distance was estimated 0.02 Å longer than that of MoO. The harmonic vibrational frequency for the ground $^4\Pi_{-1/2}$ state of MoO^- is 810 ± 40 cm^{-1} and its spin orbit splitting is 226 cm^{-1}.

Herein we present the first systematic high level computational study of the three titled charged species. We provide energetics, potential energy curves, and spectroscopic data for several electronic states of MoO^+ and MoO^{2+} and all bound states of MoO^-. For the lowest lying electronic states of the three species we studied the reaction with water. Our goal is to comprehend the role of the electronic configuration of a given state and the overall charge of the system in the OH activation process. The computational details of our calculations are given in Section II. Sections III, IV, and V pertain to our results on MoO^+, MoO^{2+}, and MoO^-, respectively. In Section VI we discuss the reaction of them with water and Section VII summarizes our findings.

II. Computational details

The internally contracted multi-reference configuration interaction (MRCI) approach was employed to construct full potential energy curves and calculate spectroscopic parameters for all of the electronic states. The reference wavefunction was provided by complete active space self-consistent field (CASSCF) calculations. The active space for $MoO^{+,2+}$ consists of the valence 5s and 4d orbitals of molybdenum and the 2p orbitals of oxygen. For MoO^- two series of calculations were performed. The first one has exactly the same active space as $MoO^{+,2+}$. The second one includes three additional orbitals, which are of $5p_{Mo}$ character at infinity but have larger contribution from diffuse p-basis functions of oxygen (not $2p_O$) at equilibrium. The two series are dubbed as MRCI and MRCI+p. The inclusion of these orbitals was deemed necessary for accurate results. The MRCI potential energy curves were done using state-average CASSCF orbitals averaging states of the same spin-multiplicity together. MRCI calculations based on state-specific CASSCF reference wavefunctions were then performed around equilibrium to extract accurate spectroscopic constants. Single and double excitations from the reference active space and the 2s orbital of oxygen to the virtual space were allowed at the MRCI level. The Davidson correction (MRCI+Q) was finally employed to reduce the size extensivity errors.

In cases of minimal multi-reference character, the single-reference coupled cluster methodology was also applied. The restricted Hartree–Fock orbitals were used and single, double and perturbative triples were included [CCSD(T)]. For selected states we also included the dynamic correlation of the semi-core $4s^24p^6$ electrons. These calculations are denoted as C-MRCI and C-CCSD(T).

The quadruple-ζ quality correlation consistent basis sets were generally employed. The all-electron aug-cc-pVQZ (6s5p4d3f2g) basis set was used for oxygen.[17,18] The cc-pVQZ-PP (7s7p6d4f3g2h) basis set combined with the appropriate relativistic pseudopotential (replacing 28 inner electrons $1s^2$ through $3d^{10}$) was used for molybdenum.[19] In the case of MoO^- a series of diffuse functions was added on Mo center (aug-cc-pVQZ-PP = cc-pVQZ-PP + 1s1p1d1f1g1h). For the calculations including core correlation effects we used the appropriately designed weighted-core cc-pwCVQZ-PP basis set for molybdenum.[19] For the three lowest electronic states of each species the MRCI, MRCI+Q or CCSD(T) calculations were also done with the corresponding quintuple-ζ quality basis sets denoted with a "-5Z" suffix.

For the $MoO^{+,2+,-} + H_2O$ reaction we did MRCI calculation for the lowest lying states using a triple-ζ quality basis set to optimize the geometries for the reactants, transition states and products. Specifically, the cc-pVTZ-PP(Mo)/cc-pVTZ(H)/aug-cc-pVTZ(O) basis sets combination was employed for $MoO^{+,2+} + H_2O$, and aug-cc-pVTZ-PP(Mo)/cc-pVTZ(H)/aug-cc-pVTZ(O) for $MoO^- + H_2O$ (MRCI/TZ). For these structures we performed single-point MRCI energy calculations using the corresponding quadruple-ζ quality (MRCI/QZ). The reference space (at CASSCF) for these reactions is smaller than the pure metal oxides: two and three electrons in five orbitals for $MoO^{+,2+}$ and five electrons in eight orbitals for MoO^-. This space includes only the valence orbitals localized on Mo plus (in the MoO^- case) three additional p-orbitals, as we did for single MoO^-. We made this choice because of technical difficulties, but we also observed that the states of our interest keep mainly these orbitals partially occupied along the reaction coordinate. All valence electrons are correlated at the MRCI level.

The harmonic frequencies ω_e and anharmonicities $\omega_e x_e$ were calculated by solving the ro-vibrational Schrödinger equation numerically. Spin–orbit coupling constants A were calculated at employing the spin–orbit part of the pseudopotential and coupling the MRCI wavefunctions *via* the Breit–Pauli Hamiltonian. All calculations were done with MOLPRO2015.1.[20]

III. MoO^+

The ground state of Mo^+ is the ^6S ($4d^5$) electronic state followed by ^6D ($5s^14d^4$) at around 12 000 cm^{-1}. Two nearly degenerate states ^4G and ^4P of $4d^5$ character follow at 15 000–16 000 cm^{-1}.[21] The reaction of $Mo^+(^6S)$ with $O(^3P)$ yields quartets, sextets, and octets of Σ^- and Π irreducible representations as shown by the valence-bond-Lewis (vbL) diagrams of Scheme 1.

In Scheme 1 the 4d orbitals of molybdenum are shown with straight lines. The $4d_{z^2}$ is of σ symmetry (horizontal blue line) and can mix with the $2p_z$ of oxygen. The $4d_{xz}$ and $4d_{yz}$ orbitals (red and orange lines) are of π symmetry and can mix with the $2p_x$ and $2p_y$ ones. Finally, the remaining 4d-orbitals on the *xy*

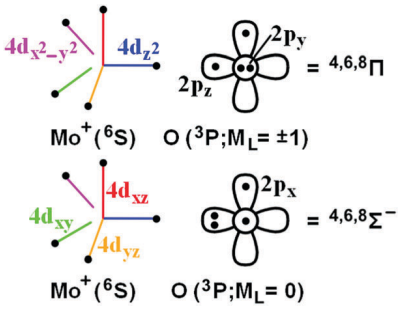

Scheme 1

plane (purple and green lines) are of δ symmetry and cannot be mixed with any of the valence orbitals of oxygen; they are always localized on molybdenum. According to Scheme 1 all Σ^- states are expected weakly bound (electrostatic forces) or unbound because of the repulsion between the $4d_{z^2}$ and $2p_z$ electrons in the σ frame. The $^8\Pi$ state should also be repulsive since no covalent bond can occur if all electrons bear parallel spins. On the contrary, $^6\Pi$ and $^4\Pi$ should be bound because they both can form a σ-bond and the latter can also make a π-bond. Therefore, $^4\Pi$ is expected more bound than the $^6\Pi$ one.

The potential energy curves (PECs) as a function of the Mo–O distance are shown in Fig. 1. Indeed, $^8\Sigma^-$ and $^8\Pi$ originating from $Mo^+(^6S)$ + $O(^3P)$ are repulsive and the $^4\Pi$, $^6\Pi$ states ($A^4\Pi$ and $1^6\Pi$) are attractive with $^4\Pi$ having more than three times larger binding energy. The potential energy curves for $^{4,6}\Sigma^-$ are unexpectedly strongly bound and $^4\Sigma^-$ becomes finally the ground state of MoO^+.

To understand the reason for the stabilization of these states, we resort to the dominant electronic configurations at equilibrium (see Table 1) and the corresponding molecular orbitals given in Fig. 2. We show that these states are coming diabatically from different channels. The 1σ molecular orbital

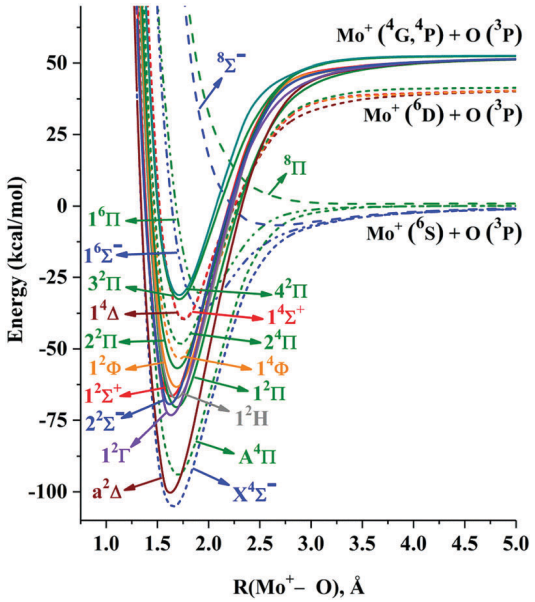

Fig. 1 MRCI PECs of MoO^+ with respect to the Mo–O distance.

Table 1 Dominant electronic configurations at the equilibrium distance of the electronic states of MoO^+

State	Coef.[a]	1σ	2σ	3σ	$1\pi_x$	$2\pi_x$	$1\pi_y$	$2\pi_y$	$1\delta_{xy}$	$1\delta_{x^2-y^2}$
$X^4\Sigma^-$	0.94	2	α	0	2	0	2	0	α	α
$a^2\Delta$	0.93	2	0	0	2	0	2	0	α	2
$A^4\Pi$	0.92	2	0	0	2	0	2	α	α	α
$1^2\Gamma$	0.84	2	α	0	2	0	2	0	α	β
	0.45	2	β	0	2	0	2	0	α	α
$1^2\Sigma^-$	−0.43	2	α	0	2	0	2	0	α	β
	0.84	2	β	0	2	0	2	0	α	α
$1^2\Pi$	0.70	2	0	0	2	0	2	β	α	α
	−0.41	2	0	0	2	0	2	α	α	β
$1^2\Sigma^+$	0.65	2	α	0	2	0	2	0	2	0
	0.70	2	α	0	2	0	2	0	0	2
1^2H	0.58	2	0	0	2	0	2	α	α	β
	0.47	2	0	0	2	α	2	0	2	0
	−0.47	2	0	0	2	α	2	0	0	2
	0.33	2	0	0	2	0	2	β	α	α
$1^2\Phi$	0.58	2	0	0	2	0	2	α	α	β
	−0.47	2	0	0	2	α	2	0	2	0
	0.47	2	0	0	2	α	2	0	0	2
	0.33	2	0	0	2	0	2	β	α	α
$2^2\Pi$	0.50	2	0	0	2	0	2	α	0	2
	0.47	2	0	0	2	0	2	α	2	0
$1^4\Phi$	0.66	2	α	0	2	0	2	α	0	α
	−0.66	2	α	0	2	α	2	0	α	0
$2^4\Pi$	−0.64	2	α	0	2	0	2	α	0	α
	0.64	2	α	0	2	α	2	0	α	0
$1^4\Delta$	0.90	2	0	0	2	α	2	α	α	0
$1^6\Sigma^-$	0.67	2	0	α	2	0	α	α	α	α
	0.67	2	0	α	α	α	2	0	α	α
$1^6\Pi$	0.97	2	0	0	α	α	2	α	α	α
$1^4\Sigma^+$	0.67	2	α	0	2	α	β	0	α	α
	0.62	2	α	0	β	0	2	α	α	α
$3^2\Pi$	0.61	2	α	0	2	β	2	0	α	0
	−0.61	2	α	0	2	0	2	β	0	α
$4^2\Pi$	0.62	2	α	0	2	0	2	β	α	0
	−0.59	2	α	0	2	β	2	0	0	α

[a] The coefficient for each configuration is given in this column.

points to a σ-bond between $4d_{z^2}$ and $2p_z$, the 2σ is mostly 5s, 1π orbitals correspond to $4d_\pi$ + $2p_\pi$ but is polarized towards oxygen, 2π orbitals pertain to $4d_\pi$ − $2p_\pi$ polarized towards molybdenum, and 1δ finally are pure 4d orbitals lying on the *xy* plane. The $1\sigma^2\ 2\sigma^1\ 1\pi^4\ 1\delta^2$ configuration for $X^4\Sigma^-$ suggests that

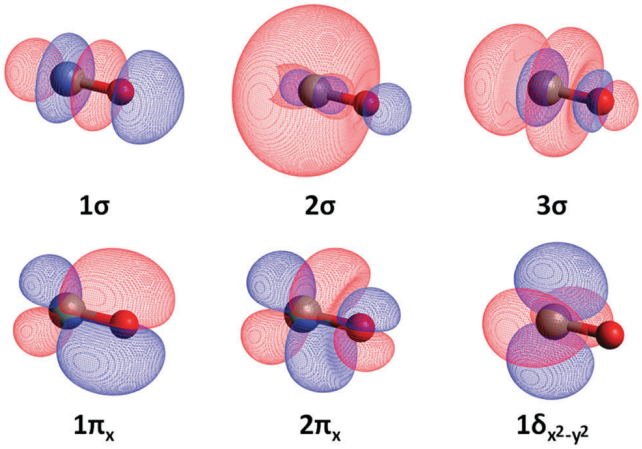

Fig. 2 Selected molecular orbitals of MoO^+: rotation of $1\pi_x$ and $2\pi_x$ by 90° around *z*-axis yields $1\pi_y$ and $2\pi_y$, while rotation of $1\delta_{x^2-y^2}$ by 45° yields $1\delta_{xy}$.

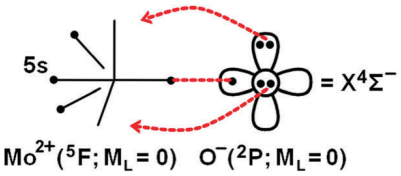

Scheme 2

it is actually coming from some state which has a $5s^1 \sim 2\sigma$ character and not from the $^6S(4d^5)$ state. We monitored the nature of 2σ at several distances and we saw that it transforms gradually from $4d_{z^2}$ to 5s. Considering the polarization of 1π towards oxygen, we finally suggest a formal $Mo^{2+}O^-$ picture of Scheme 2.

The vbL diagram of Scheme 2 describes a triple bond (one σ covalent and two π dative) between the excited state of $Mo^{2+}(^5F; 5s^14d^3)$ and $O^-(^2P)$. Three observer electrons localized on molybdenum remain unpaired producing a quartet spin multiplicity. This scheme is in complete agreement with the experimental evidence of a $\delta^2\sigma^1$ configuration.[12] Similarly, the $1^6\Sigma^-$ state bears also one 2σ electron and seems to come from the same fragments as $X^4\Sigma^-$ but created by different components of $Mo^{2+}(^5F; M_L = \pm1)$ and $O^-(^2P; M_L = \mp1)$.

Based on the CI vectors of Table 1 and the orbitals of Fig. 2 the bonding in the $a^4\Pi$ state, which comes from the ground state fragments, can also be described as "ionic" coming from $Mo^{2+}(^5D; 4d^4)$ and $O^-(^2P)$; see Scheme 3.

All of the excited states studied here, with the exception of $1^6\Pi$, have the $1\sigma^21\pi^4$ configuration in common and three electrons localized on different molybdenum orbitals (2σ, 2π, 1δ molecular orbitals) coupled to either a doublet or a quartet spin multiplicity. For example, the first excited state $a^2\Delta$ has three electrons on the two 1δ orbitals. We believe that all of them are rather described as $Mo^{2+}O^-$ combining some $4d^4$ or $5s^14d^3$ state of Mo^{2+} with the $M_L = 0$ component of O^-.

Table 2 reports equilibrium energies and spectroscopic constants for all of the examined states. The ground state has been suggested to be of $^4\Sigma^-$ symmetry both experimentally and theoretically.[11–13] The assignment of the first excited state is not consistent in the literature. The ionization energies of Loock *et al.*[12] and dissociation energies of Broclawik *et al.*[13] imply that $^4\Pi$ is the first excited state at 0.77 eV and 0.04 eV with the $^2\Delta$ following at 0.84 eV and 0.19 eV, respectively. Kretzschmar *et al.* report only the $^2\Delta$ state,[11] which has even been proposed to be the ground state by the early work of Broclawik.[10] The very recent experimental work of Luo and co-workers determined the excitation energies of $^2\Delta_{3/2}$ and $^2\Delta_{5/2}$ to be as small as

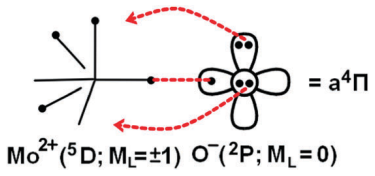

Scheme 3

Table 2 Equilibrium energy E_e (hartrees), bond length r_e (Å), harmonic vibrational frequency ω_e (cm^{-1}), and excitation energy T_e (cm^{-1}) for the lowest electronic states of $^{98}Mo^{16}O^+$

State	Method	$-E_e$	r_e	ω_e	$\omega_e x_e$	T_e
$X^4\Sigma^-$	MRCI	142.338531	1.645	986	5.0	0
	MRCI+Q	142.355118	1.647	980	5.0	0
	C-MRCI	142.650525	1.639	1006	5.0	0
	C-MRCI+Q	142.708738	1.642	999	4.9	0
	CCSD(T)	142.355176	1.643	1007	4.9	0
	C-CCSD(T)	142.719024	1.635	1033	4.6	0
	MRCI-5Z	142.346899	1.643	989	5.0	0
	MRCI+Q-5Z	142.363889	1.645	983	5.0	0
	C-MRCI-5Z	142.680498	1.636	1008	5.0	0
	C-MRCI+Q-5Z	142.741625	1.639	1000	4.8	0
	CCSD(T)-5Z	142.364370	1.642	1009	4.8	0
	C-CCSD(T)-5Z	142.753509	1.632	1034	4.6	0
$a^2\Delta$	MRCI	142.328650	1.619	1079	4.1	2169
	MRCI+Q	142.346475	1.621	1072	4.2	1897
	C-MRCI	142.638338	1.616	1088	4.1	2675
	C-MRCI+Q	142.698150	1.619	1079	4.2	2324
	CCSD(T)	142.347687	1.620	1085	4.1	1644
	C-CCSD(T)	142.708584	1.615	1098	4.1	2291
	MRCI-5Z	142.337946	1.617	1081	4.1	1965
	MRCI+Q-5Z	142.356231	1.619	1075	4.1	1681
	C-MRCI-5Z	142.669906	1.613	1091	4.1	2325
	C-MRCI+Q-5Z	142.732818	1.615	1082	4.1	1933
	CCSD(T)-5Z	142.357866	1.619	1088	4.1	1427
	C-CCSD(T)-5Z	142.744880	1.611	1101	4.1	1894
$A^4\Pi$	MRCI	142.314326	1.691	951	4.9	5312
	MRCI+Q	142.337428	1.689	956	4.8	3883
	C-MRCI	142.618902	1.686	957	4.9	6940
	C-MRCI+Q	142.684965	1.684	965	4.8	5218
	CCSD(T)	142.339205	1.683	984	4.1	3505
	C-CCSD(T)	142.698204	1.676	995	3.9	4570
	MRCI-5Z	142.322651	1.690	953	4.9	5321
	MRCI+Q-5Z	142.346100	1.687	959	4.8	3904
	C-MRCI-5Z	142.649562	1.684	960	4.8	6790
	C-MRCI+Q-5Z	142.718563	1.681	967	4.7	5061
	CCSD(T)-5Z	142.348609	1.681	987	4.1	3459
	C-CCSD(T)-5Z	142.733628	1.673	998	3.9	4363
$1^2\Gamma$	MRCI	142.285200	1.630	1029	4.8	11 705
	MRCI+Q	142.303094	1.632	1024	4.8	11 418
$2^2\Sigma^-$	MRCI	142.281294	1.617	1072	5.3	12 562
	MRCI+Q	142.301235	1.620	1061	4.9	11 826
$1^2\Pi$	MRCI	142.276307	1.684	972	4.4	13 657
	MRCI+Q	142.300094	1.682	976	4.3	12 076
$1^2\Sigma^+$	MRCI	142.274171	1.632	1023	5.0	14 125
	MRCI+Q	142.293984	1.635	1017	5.0	13 417
1^2H	MRCI	142.271547	1.680	986	4.2	14 701
	MRCI+Q	142.294718	1.680	987	4.2	13 256
$1^2\Phi$	MRCI	142.264280	1.684	973	4.6	16 296
	MRCI+Q	142.288084	1.682	977	4.8	14 712
$2^2\Pi$	MRCI	142.254552	1.691	954	4.4	18 431
	MRCI+Q	142.279363	1.689	957	4.4	16 626
$1^4\Phi$	MRCI	142.251770	1.706	905	5.4	19 042
	MRCI+Q	142.274548	1.705	909	5.3	17 683
$2^4\Pi$	MRCI	142.243798	1.713	876	6.1	20 792
	MRCI+Q	142.266617	1.711	882	6.0	19 424
$1^4\Delta$	MRCI	142.229776	1.744	850	1.5	23 869
	MRCI+Q	142.256609	1.741	862	1.9	21 620
	CCSD(T)	142.261123	1.736	926	0.9	20 642
$1^6\Sigma^-$	MRCI	142.226482	1.931	654	2.1	24 592
	MRCI+Q	142.246066	1.931	668	2.2	23 934
$1^6\Pi$	MRCI	142.223782	1.968	661	2.7	25 185
	MRCI+Q	142.244334	1.968	658	2.3	24 314
	CCSD(T)	142.244984	1.957	678	3.4	24 184
$1^4\Sigma^+$	MRCI	142.221401	1.750	896	2.7	25 707
	MRCI+Q	142.251958	1.787	906	2.5	22 641
$3^2\Pi$	MRCI	142.214805	1.715	888	5.6	27 155
	MRCI+Q	142.238551	1.712	897	5.5	25 584
$4^2\Pi$	MRCI	142.214207	1.712	906	4.9	27 286
	MRCI+Q	142.238414	1.711	909	4.9	25 614

408.5 cm^{-1} (0.05 eV) and 1570.3 cm^{-1} (0.19 eV).[14] Our results clearly assign $^2\Delta$ as the first excited state with the $^4\Pi$ being about 2000 cm^{-1} higher.

The equilibrium Mo–O distance of $X^4\Sigma^-$ is 1.645 and 1.647 Å at MRCI and MRCI+Q, respectively, which shortens by 0.006 and 0.005 Å after the inclusion of the $4s^24p^6$ correlation. Similar decrease of 0.008 Å occurs at the CCSD(T) level. Our C-MRCI+Q value of 1.642 Å is in complete agreement with the experimental r_e value of 1.642 ± 0.001 Å.[14] while C-CCSD(T) gives a shorter value of 1.635 Å. Our harmonic vibrational frequencies increase by 20 cm^{-1} when core correlation effects are included at the MRCI level. Our best ω_e value (C-MRCI+Q) is 999 cm^{-1} which is in excellent agreement with the experimental value of 1000 ± 9 cm^{-1}.[14] The same is true for our $\omega_e x_e$ of 4.9 cm^{-1} *vs.* 5 ± 3 cm^{-1}.[14] C-CCSD(T) seems to provide shorter distances and higher vibrational frequencies.

The first excited state $a^2\Delta$ lies at 1897 cm^{-1} at MRCI+Q, 2324 cm^{-1} at C-MRCI+Q, and 2291 cm^{-1} at C-CCSD(T). Luo *et al.* measured the ionization energies from MoO ($X^5\Pi$) to MoO^+ ($X^4\Sigma^-$), IE_0 = 60147.9 cm^{-1}, and from MoO ($X^5\Pi$) to MoO^+ ($a^2\Delta_{3/2,5/2}$), $IE_{3/2}$ = 60556.4 cm^{-1} and $IE_{5/2}$ = 61718.2 cm^{-1}, by means of photoelectron spectroscopy.[14] Using these values we estimate the excitation energy $T_e(a^2\Delta_{3/2}) = IE_{3/2} - IE_0$ = 408.5 cm^{-1} and $T_e(a^2\Delta_{5/2}) = IE_{5/2} - IE_0$ = 1570.3 cm^{-1}. Our theoretical values are larger than the experimental average of 989.4 cm^{-1}. MRCI+Q gives 1897 cm^{-1} and C-MRCI+Q increases this value to 2324 cm^{-1}. C-MRCI+Q-5Z reduces it slightly to 1933 cm^{-1} while C-CCSD(T)-5Z gives 1894 cm^{-1}. The experimental spin–orbit splitting of these two states is 1570.3–408.5 = 1161.8 cm^{-1} which compares favorable with our theoretical value of 1010 cm^{-1}. The bond length drops by 0.002–0.003 Å after core correlation is included and converges to 1.619 Å at the C-MRCI+Q level, which is in harmony with the experimental bond lengths of 1.613 and 1.616 Å for $a^2\Delta_{3/2}$ and $a^2\Delta_{5/2}$, respectively.

The next state is $A^4\Pi$ at about 5000 cm^{-1} with a bond length of 1.68 Å. The +Q correction increases the excitation energy by about 1500 cm^{-1}, while the core correlation shortens the bond length by 0.005 Å. Judging by the better agreement of the C-MRCI+Q *vs.* C-CCSD(T) harmonic frequencies with experiment in the ground state, we think that the C-MRCI+Q value of 965 cm^{-1} is more accurate.

For the first three states we also performed valence and core CI and CC calculations using the quintuple-ζ basis set. We found minimal differences from the quadruple-ζ suggesting that our numerical results are quite accurate. Specifically, there is a consistent trend for all computational approaches: bond lengths contract by 0.002–0.003 Å, harmonic frequencies increase by ~3 cm^{-1}, anharmonicities remain constant, and excitation energies drop by 200–300 cm^{-1} when moving from quadruple to quintuple basis set.

The first three electronic states are well separated from the higher electronic states. There are six doublets crowded within 11 418 ($1^2\Gamma$) and 14 712 ($1^2\Phi$) cm^{-1}, and seven more states of doublet and quartet spin multiplicity follow in the region 16 626 cm^{-1} and 25 614 cm^{-1}. All of these states have bond lengths between 1.62 Å ($1^2\Sigma^-$) and 1.75 Å ($1^4\Sigma^+$). The vibrational frequencies lie between 862 ($1^4\Delta$) and 1061 cm^{-1} ($1^2\Sigma^-$). The last two states we studied are the sextets $1^6\Sigma^-$ and $1^6\Pi$ which are both coming from the ground state fragments. Their bond distances are much longer (1.93 and 1.96 Å) and their frequencies are much smaller (around 660 cm^{-1}).

Table 3 Spin–orbit coupling constants A for the multiplet states of MoO^+, MoO^{2+}, and MoO^-

MoO^+				MoO^{2+}		MoO^-	
State	*A*	State	*A*	State	*A*	State	*A*
$a^2\Delta$	505	$1^4\Phi$	193	$1^3\Phi$	301	$X\ ^4\Pi$	351
$A^4\Pi$	179	$2^4\Pi$	219	$1^3\Pi$	377	$^2\Delta$	492
$1^2\Gamma$	10	$1^4\Delta$	188	$1^3\Delta$	326	$^6\Pi$	120
$1^2\Pi$	1004	$1^6\Pi$	12	$1^5\Delta$	56		
1^2H	110	$3^2\Pi$	837				
$1^2\Phi$	151	$4^2\Pi$	956				
$2^2\Pi$	530						

We are not aware of any previous theoretical or experimental work studying these fifteen excited states. C-MRCI calculations are not performed for them currently. Based on the trends in the first three states more accurate bond lengths can be obtained by reducing the MRCI+Q by approximately 0.005 Å and the MRCI+Q excitation energies should be accurate within 1000 cm^{-1}.

The PECs of Fig. 1 show that $X^4\Sigma^-$, $A^4\Pi$, $1^6\Sigma^-$ and $1^6\Pi$ states dissociate to the ground state fragments $Mo^+(^6S)$ + $O(^3P)$. The rest of the states dissociate either to $Mo^+(^6D)$, $Mo^+(^4G)$, or $Mo^+(^4P)$ with binding energies larger than 100 kcal mol^{-1}. The experimental binding energy for the ground state has been measured by Sievers *et al.*, D_0 = 116.7 ± 0.5 kcal mol^{-1}.[15] Our CCSD(T) binding energies using the cc-pVXZ-PP/$_{Mo}$ and cc-pVXZ/$_O$ basis sets are D_e = 96.4, 106.3, 109.5, 110.8 kcal mol^{-1} for X = D, T, Q, 5, respectively. Different extrapolation schemes consistently converged to the complete basis set (CBS) limit of 112 ± 1 kcal mol^{-1}. Our C-CCSD(T) value with the cc-pwCVQZ-PP/$_{Mo}$ and cc-pVQZ/$_O$ basis sets is 114.9 kcal mol^{-1} which means that the core-correlation enhances D_e by 114.9 − 109.5 = 5.4 kcal mol^{-1}. Adding this correction to the CCSD(T)/CBS limit we get a value of 117.4 ± 1 kcal mol^{-1}, which should reduced by the zero-point energy of 1.5 kcal mol^{-1}. Therefore, our best estimate is D_0 = 115.9 ± 1 kcal mol^{-1} in excellent agreement with the experiment. Spin–orbit effects are minimal because of the zero orbital angular momentum for the $^4\Sigma^-$ and ^6S states of MoO^+ and Mo^+.

Finally, the spin–orbit coupling constants for the multiplets are reported in Table 3 and they are as small as 10 cm^{-1} ($1^2\Gamma$) and as big as 1004 cm^{-1} ($1^2\Pi$).

IV. MoO^{2+}

The first ionization energy of Mo^+ to Mo^{2+} is 16.16 eV and that of O to O^+ is 13.62 eV.[22] Therefore, the lowest energy fragments are $Mo^+(^6S)$ + $O^+(^4S)$ and the $Mo^{2+}(^5D)$ + $O(^3P)$ channel is 16.16 − 13.62 = 2.54 eV above. Considering a simple electrostatic model for the Mo^+ and O^+ repulsion the two channels are expected to cross at 5.7 Å. Our state-averaged calculations predict

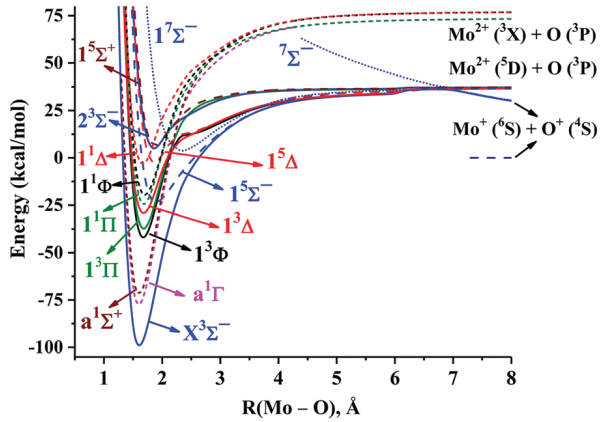

Fig. 3 MRCI PECs of MoO^{2+} with respect to the Mo–O distance. The ^3X states can be one of ^3P, ^3H, ^3F, or ^3G.

this crossing at around 7 Å. Within the energy gap of 2.54 eV other $Mo^+ + O^+$ channels are present corresponding to the ^6D, ^4G, ^4P, and ^4D excited states of Mo^+.[21] The first one, $Mo^+(^6D) + O^+(^4S)$, is 1.59 eV above $Mo^+(^6S) + O^+(^4S)$ and crosses with $Mo^{2+}(^5D) + O(^3P)$ at 25 Å. The complete PECs for distances shorter than 30 Å and for all of the states coming from the first two $Mo^+ + O^+$ and $Mo^{2+} + O$ channels are given in the ESI.† Fig. 3 depicts the PECs for Mo–O distances shorter than 8 Å of the lowest lying states, the equilibrium energy of which is below the $Mo^{2+}(^5D) + O(^3P)$ dissociation limit.

The $Mo^+(^6S) + O^+(^4S)$ asymptote produces the $^{3,5,7,9}\Sigma^-$ states, all of which bear repulsive PECs. The PECs of $^{3,5,7}\Sigma^-$ cross with those of the same symmetry coming from $Mo^{2+}(^5D) + O(^3P)$ which are attractive with the $^3\Sigma^-$ being finally the ground state of MoO^{2+}. The binding energies for $^3\Sigma^-$, $^5\Sigma^-$, and $^7\Sigma^-$ are 135, 61, and 40 kcal mol^{-1} with respect to $Mo^{2+}(^5D) + O(^3P)$. Based on the dominant configurations of Table 4, the bonding diagram for the ground state can be captured by Scheme 4.

The formation of a σ dative bond from oxygen to molybdenum and the two covalent π bonds stabilize $^3\Sigma^-$ over the $^5\Sigma^-$ and $^7\Sigma^-$ states where only one or none π-bonds are present. The bonding for $X^3\Sigma^-$ can also be represented by that of $MoO^+(X^4\Sigma^-)$ shown in Scheme 2 after removing the 5s electron localized on molybdenum. The latter picture implies an ionic $Mo^{3+}O^-$ character. The relative weights of the "covalent" $Mo^{2+}O$ *vs.* "ionic" $Mo^{3+}O^-$ bindings depend on the employed electronic density partition technique and will not be subject of the present study.

Our numerical values for the various equilibrium parameters for all of the electronic states examined here are listed in Table 5. The core correlation has a slightly smaller effect for the ground state compared to MoO^+. The bond length decreases by 0.003–0.004 Å, while harmonic frequencies increase by a few wavenumbers. Our suggested bond length is 1.60 Å which is considerably shorter than that of MoO^+ (~1.64 Å). It seems that the larger charge on the metal center and the absence of the 5s electron enables the closer proximity of the two atoms. The stronger binding in the MoO^{2+} case is also expressed by its larger vibrational frequency.

The first two excited states, $1^1\Gamma$ and $1^1\Sigma^+$, lie at about 7000 and 10 000 cm^{-1}, and they are well separated from the next

Table 4 Dominant electronic configurations at the equilibrium distance of the electronic states of MoO^{2+}

State	Coef.	1σ	2σ	3σ	$1\pi_x$	$2\pi_x$	$1\pi_y$	$2\pi_y$	$1\delta_{xy}$	$1\delta_{x^2-y^2}$
$X^3\Sigma^-$	0.94	2	0	0	2	0	2	0	α	α
$\alpha^1\Gamma$	0.67	2	0	0	2	0	2	0	2	0
	−0.67	2	0	0	2	0	2	0	0	2
$\alpha^1\Sigma^+$	0.67	2	0	0	2	0	2	0	2	0
	0.67	2	0	0	2	0	2	0	0	2
$1^3\Phi$	0.66	2	0	0	2	α	2	0	α	0
	0.66	2	0	0	2	0	2	α	0	α
$1^3\Pi$	−0.64	2	0	0	2	0	2	α	0	α
	0.64	2	0	0	2	α	2	0	α	0
$1^3\Delta$	0.92	2	0	α	2	0	2	0	0	α
$1^1\Pi$	0.66	2	0	0	2	0	2	α	0	β
	0.66	2	0	0	2	β	2	0	α	0
$1^5\Sigma^-$	0.61	2	0	0	2	0	α	α	α	α
	0.61	2	0	0	α	α	2	0	α	α
$1^1\Phi$	−0.62	2	0	0	2	0	2	α	0	β
	0.62	2	0	0	2	β	2	0	α	0
$1^1\Delta$	0.93	2	0	β	2	0	2	0	α	0
$1^5\Delta$	0.66	2	0	0	α	0	2	α	α	α
	−0.66	2	0	0	2	α	α	0	α	α
$1^7\Sigma^-$	0.99	2	0	0	α	α	α	α	α	α
$2^3\Sigma^-$	0.46	2	0	0	β	α	2	0	α	α
	0.46	2	0	0	2	0	β	α	α	α
	−0.35	2	0	0	α	α	2	0	α	β
	−0.35	2	0	0	2	0	α	α	α	β
$1^5\Sigma^+$	0.64	2	0	0	α	0	2	α	α	α
	0.64	2	0	0	2	α	α	0	α	α

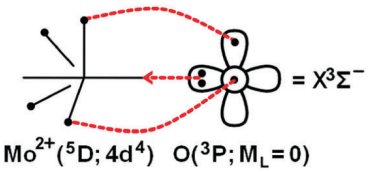

Scheme 4

excited states. We also performed C-MRCI calculations for these two states confirming the same trends. Therefore, for the rest of the states more accurate bond lengths can be obtained by subtracting a few mili-Å from the r_e and adding a few cm^{-1} to the ω_e values of Table 5. Going to the quinuple-ζ basis set for the first three states, we see the same minimal changes as in MoO^+ (see Section III). No experimental data exist for any of the MoO^{2+} states, all of which are stable with respect to the lowest energy $Mo^+ + O^+$ fragments.

The first three states have two spectator electrons (see Table 4) residing at the 1δ orbitals and can be seen as the sister states of MoO^+, $X^4\Sigma^-$, $1^2\Gamma$, $1^2\Sigma^+$, where an additional electron occupies $5s_{Mo}$. The next three states are $^3\Phi$, $^3\Pi$, and $^3\Delta$ followed by their singlet counterparts. The Φ and Π states have a $\pi^1\delta^1$ configuration and the Δ ones a $\sigma^1\delta^1$ character. All of these six states have bond lengths from 1.66 to 1.68 Å and they span an energy range of 19 000 to 33 000 cm^{-1}.

The remaining states are $1^5\Sigma^-$, $1^5\Delta$, $1^7\Sigma^-$, $2^3\Sigma^-$, and $1^5\Sigma^+$. The origin of $1^5\Sigma^-$ and $1^7\Sigma^-$ was discussed earlier, whereas the rest three states are coming from higher channels *via* avoided crossings. Finally, only four electronic states have non-zero first order spin–orbit splitting and the related constants are included in Table 3.

Table 5 Equilibrium energy E_e (hartrees), bond length r_e (Å), harmonic vibrational frequency ω_e (cm^{-1}), and excitation energy T_e (cm^{-1}) for the lowest electronic states of $^{98}Mo^{16}O^{2+}$

State	Method	$-E_e$	r_e	ω_e	$\omega_e x_e$	T_e
$X^3\Sigma^-$	MRCI	141.801408	1.603	1072	4.6	0
	MRCI+Q	141.813531	1.605	1066	4.5	0
	C-MRCI	142.110884	1.599	1079	4.3	0
	C-MRCI+Q	142.161204	1.602	1066	3.9	0
	CCSD(T)	141.811063	1.601	1106	4.7	0
	MRCI-5Z	141.809717	1.601	1077	5.6	0
	MRCI+Q-5Z	141.822180	1.603	1072	5.8	0
	C-MRCI-5Z	142.141249	1.596	1083	4.2	0
	C-MRCI+Q-5Z	142.194363	1.598	1071	4.3	0
	CCSD(T)-5Z	141.820041	1.599	1109	5.0	0
$a^1\Gamma$	MRCI	141.766509	1.594	1105	3.5	7659
	MRCI+Q	141.778531	1.595	1101	3.4	7682
	C-MRCI	142.079518	1.590	1114	3.8	6884
	C-MRCI+Q	142.130486	1.592	1107	3.6	6742
	MRCI-5Z	141.775464	1.592	1102	4.8	7518
	MRCI+Q-5Z	141.787857	1.593	1097	4.9	7533
	C-MRCI-5Z	142.110721	1.587	1122	3.5	6700
	C-MRCI+Q-5Z	142.164624	1.588	1110	3.8	6527
$a^1\Sigma^+$	MRCI	141.755721	1.599	1093	4.0	10 027
	MRCI+Q	141.769983	1.600	1085	3.5	9558
	C-MRCI	142.062109	1.595	1101	3.9	10 705
	C-MRCI+Q	142.115829	1.595	1088	3.1	9959
	MRCI-5Z	141.764649	1.597	1094	3.5	9891
	MRCI+Q-5Z	141.779293	1.598	1081	3.8	9412
	C-MRCI-5Z	142.093005	1.591	1109	3.8	10 588
	C-MRCI+Q-5Z	142.149610	1.591	1096	4.4	9822
$1^3\Phi$	MRCI	141.711105	1.673	969	5.4	19 819
	MRCI+Q	141.727604	1.673	971	5.2	18 859
$1^3\Pi$	MRCI	141.703626	1.680	948	5.7	21 461
	MRCI+Q	141.720287	1.679	949	5.5	20 465
$1^3\Delta$	MRCI	141.691106	1.674	880	6.0	24 209
	MRCI+Q	141.704083	1.675	876	6.0	24 021
	CCSD(T)	141.702611	1.667	921	5.1	23 802
$1^1\Pi$	MRCI	141.683105	1.676	952	5.7	25 965
	MRCI+Q	141.700589	1.673	957	5.1	24 788
$1^5\Sigma^-$	MRCI	141.678954	1.904	656	5.9	26 876
	MRCI+Q	141.692571	1.890	658	4.8	26 548
$1^1\Phi$	MRCI	141.675292	1.690	905	6.2	27 679
	MRCI+Q	141.691701	1.69	909	6.3	26 739
$1^1\Delta$	MRCI	141.648928	1.662	892	4.3	33 466
	MRCI+Q	141.663951	1.663	893	5.6	32 829
$1^5\Delta$	MRCI	141.645092	1.864	570	5.6	34 307
	MRCI+Q	141.660284	1.863	557	7.0	33 634
$1^7\Sigma^-$	MRCI	141.640187	2.332	344	1.1	35 384
	MRCI+Q	141.650564	2.330	345	0.6	35 767
$2^3\Sigma^-$	MRCI	141.631879	1.867	706	0.2	37 207
	MRCI+Q	141.648426	1.861	718	0.9	36 236
$1^5\Sigma^+$	MRCI	141.630664	1.880	621	3.9	37 474
	MRCI+Q	141.647399	1.878	640	4.1	36 462

V. MoO^-

The electron affinity of Mo (0.748 eV)[16] is smaller than that of oxygen (1.461 eV).[22] Therefore the lowest energy fragments are $Mo(^7S) + O^-(^2P)$ followed by $Mo^-(^6S) + O(^3P)$ 1.461 − 0.748 = 0.713 eV above. The ground state fragments produce the $^{6,8}\{\Sigma^+,\Pi\}$ states. The sextet states are strongly bound and their equilibrium energies are below the energy of the ground state of MoO ($X^5\Pi$).[9] The octet states create rather electrostatically driven minima. The full PECs for all of the states studied presently are shown in Fig. 4, while the PECs around equilibrium are given in Fig. 5. Overall, there are five electronic states of MoO^- bound with respect to MoO ($X^5\Pi$) + e^-: $X^4\Pi$, $1^2\Delta$, $1^6\Sigma^+$, $1^4\Sigma^-$, and $1^6\Pi$.

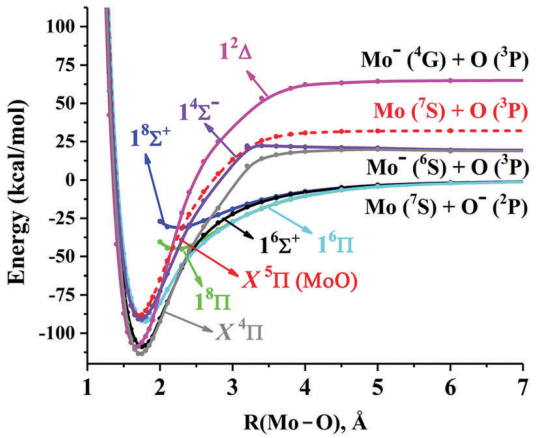

Fig. 4 MRCI+Q PECs of MoO^- with respect to the Mo–O distance. The PEC of $X^5\Pi$ for MoO is also shown with red dashed lines.

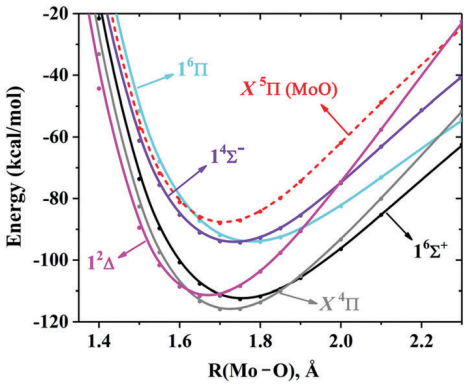

Fig. 5 CCSD(T) PECs of MoO^- with respect to the Mo–O distance at equilibrium. The energy zero is set to the energy of $Mo(^7S) + O^-(^2P)$.

The electron affinity (EA) of MoO has been determined experimentally equal to 1.290 ± 0.006 eV by Gunion *et al.*[16] Our adiabatic EA at the MRCI level (without the additional p-orbitals in the active space) is just 0.05 eV and becomes negative (−0.01 eV) at MRCI+Q. The MRCI+p and MRCI+p+Q numbers of 0.87 and 1.07 eV, respectively, are more reasonable. The CCSD(T) and C-CCSD(T) values of 1.198 and 1.197 eV are closer to the experimental value. Increasing the number of basis functions we get 1.218 eV at C-CCSD(T)-5Z. Given that harmonic vibrational frequencies at CCSD(T) of 897 cm^{-1} for MoO^- (see Table 6) and 934 cm^{-1} for MoO are very similar, the vertical EA is practically identical to the adiabatic one differing by less than 0.01 eV.

Table 6 lists our numerical results for all five bound states. Their small multi-reference character allowed us to perform CCSD(T) calculations for all of them. The core correlation effects were considered only at the CCSD(T) level. The first three states are nearly degenerate lying within 1500 cm^{-1}, while the two highest ones are also nearly degenerate at around 7600 cm^{-1}. MRCI predicts the $^6\Sigma^+$ state to be the ground state, with the $^2\Delta$ and $^4\Pi$ ones following at least 2500 cm^{-1} higher. The energy order changes dramatically at the MRCI+p level. The $^4\Pi$ state becomes ground state in agreement with the CCSD(T) results and the experimental assignment.[16]

Table 6 Equilibrium energy E_e (hartrees), bond length r_e (Å), harmonic vibrational frequency ω_e (cm^{-1}), and excitation energy T_e (cm^{-1}) for the lowest electronic states of $^{98}Mo^{16}O^-$

State	Method	$-E_e$	r_e	ω_e	$\omega_e x_e$	T_e
$X^4\Pi$	MRCI	142.589412	1.733	863	5.1	3505
	MRCI+Q	142.616922	1.730	853	5.0	6426
	MRCI+p	142.637761	1.725	898	4.3	0
	MRCI+p+Q	142.663881	1.726	902	4.6	0
	CCSD(T)	142.669643	1.724	897	3.8	0
	C-CCSD(T)	143.036036	1.717	909	3.7	0
	MRCI+p-5Z	142.646000	1.723	880	4.0	0
	MRCI+p+Q-5Z	142.672540	1.725	874	4.0	0
	CCSD(T)-5Z	142.678921	1.721	900	3.8	0
	C-CCSD(T)-5Z	143.070224	1.713	911	3.7	0
$1^6\Sigma^+$	MRCI	142.605383	1.758	825	2.9	0
	MRCI+Q	142.646203	1.750	855	5.0	0
	MRCI+p	142.634188	1.753	812	3.6	784
	MRCI+p+Q	142.659243	1.755	819	4.0	1018
	CCSD(T)	142.663996	1.754	823	3.5	1239
	C-CCSD(T)	143.029931	1.748	830	3.5	1340
	MRCI+p-5Z	142.642296	1.752	813	3.3	813
	MRCI+p+Q-5Z	142.667792	1.753	821	4.0	1042
	CCSD(T)-5Z	142.673062	1.750	825	3.5	1286
	C-CCSD(T)-5Z	143.064240	1.744	830	3.3	1313
$1^2\Delta$	MRCI	142.593348	1.655	1036	6.0	2641
	MRCI+Q	142.626943	1.658	1024	3.7	4227
	MRCI+p	142.630635	1.667	977	4.0	1564
	MRCI+p+Q	142.657316	1.675	979	4.0	1441
	CCSD(T)	142.662641	1.669	1000	3.9	1537
	C-CCSD(T)	143.029815	1.664	1013	3.6	1365
	MRCI+p-5Z	142.635374	1.652	1169	6.0	2332
	MRCI+p+Q-5Z	142.664385	1.654	1078	5.8	1790
	CCSD(T)-5Z	142.672595	1.667	1002	3.8	1388
	C-CCSD(T)-5Z	143.064762	1.659	1015	3.6	1199
$1^4\Sigma^-$	MRCI	142.566155	1.722	951	5.9	8610
	MRCI+Q	142.604359	1.720	946	3.5	9184
	MRCI+p	142.602292	1.732	783	2.7	7785
	MRCI+p+Q	142.628839	1.729	840	3.3	7691
	CCSD(T)	142.634951	1.735	845	3.6	7614
	C-CCSD(T)	143.001635	1.725	855	3.5	7550
$1^6\Pi$	MRCI	142.582393	1.778	766	3.8	5046
	MRCI+Q	142.621753	1.781	782	1.8	5366
	MRCI+p	142.606391	1.793	726	4.0	6885
	MRCI+p+Q	142.629558	1.800	744	5.6	7533
	CCSD(T)	142.634673	1.778	769	3.6	7675
	C-CCSD(T)	143.000943	1.770	781	3.6	7702

The optimal bond length for $X^4\Pi$ is 1.725 ± 0.001 Å at the MRCI+p, MRCI+p+Q, and CCSD(T) levels. C-CCSD(T) reduces it to 1.717 Å, which is in excellent agreement with the experimental value of 1.72 Å.[16] Our harmonic vibrational frequencies of around 900 cm^{-1} are larger than the experimental range of 810 ± 40 cm^{-1}.[16] Our spin–orbit coupling constant is A = 350 cm^{-1}. Increasing the basis set from quadruple to quintuple-ζ quality, we see the same trends as in the positively charged species.

No experimental data exist for any of the excited states. Identical comments to those of $X^4\Pi$ can be made on the trends followed by the different methodologies (see Table 6). Our suggested r_e values are 1.75 ($1^6\Sigma^+$), 1.66 ($1^2\Delta$), 1.73 ($1^4\Sigma^-$), and 1.77 ($1^6\Pi$) Å, and our suggested excitation energies are 1300 ($1^6\Sigma^+$), 1400 ($1^2\Delta$), 7600 ($1^4\Sigma^-$), and 7700 ($1^6\Pi$) cm^{-1}. The harmonic vibrational frequencies should be probably considered overestimated. Finally, our spin–orbit coupling constants for $X^4\Pi$, $1^2\Delta$, and $1^6\Pi$ are listed in Table 3.

The electronic configurations in terms of the orbitals of Fig. 2 are $1\sigma^2 2\sigma^2 1\pi^4 2\pi^1 1\delta^2$ ($X^4\Pi$), $1\sigma^2 2\sigma^1 1\pi^4 2\pi^2 1\delta^2$ ($1^6\Sigma^+$), $1\sigma^2 2\sigma^2 1\pi^4 1\delta^3$ ($1^2\Delta$), $1\sigma^2 2\sigma^2 3\sigma^1 1\pi^4 1\delta^2$ ($1^4\Sigma^-$), and $1\sigma^2 2\sigma^1 3\sigma^1 1\pi^4 2\pi^1 1\delta^2$ ($1^6\Pi$).

VI. Water activation

In this section we investigate the reaction between the lowest electronic states of MoO^{2+} (two states), MoO^+ (three states), and MoO^- (three states) and water. We obtained the structures for the interacting complex of the reactants, the transition state, and the produced $Mo(OH)_2^{2+,+,-}$.

Our MRCI/TZ optimal structures are given in the (ESI†) and some geometric features are collected in Table 7. The energy landscapes for all three species are compared in Fig. 6, where selected structures are also shown. It should be mentioned that the doubly degenerate states of the diatomic molybdenum oxide species split into two components when water is considered due to symmetry lowering. Therefore we calculated totally three energy pathways for MoO^{2+} and five for $MoO^{\pm}$, for which we use different colors in Fig. 6: $\alpha^1\Gamma$ (MoO^{2+}), $\alpha^4\Pi$ (MoO^+), and $X^4\Pi$ (MoO^-) split to the blue and purple lines, $\alpha^4\Pi$ (MoO^+), and $X^4\Pi$ (MoO^-) split to red and brown lines. The $X^3\Sigma^-$, $X^4\Sigma^-$, and $1^6\Sigma^+$ states for the dication, cation, and anion, respectively, are shown in black.

The interaction energy (E_{int}) between the charged oxides and water is larger for the dication (128–133 kcal mol^{-1}), followed by the cation (32–44 kcal mol^{-1}) and finally the anion (9–14 kcal mol^{-1}). To take into account the size extensivity issues of the MRCI methodology, we used the supermolecular approach. Specifically, we didn't use the energy of the individual fragments, but the energy of the two fragments at a distance of 1000 Å. For example, the size extensivity error for all species was 40–45 milihartrees at MRCI reduced to 15–18 milihartrees at MRCI+Q.

The intrinsic activation energies or energy barriers from the reactants (interacting complex) to the transition state (E_{act}) reveal the same trend: 85–89 (MoO^{2+}), 42–62 (MoO^+), and 14–32 (MoO^-) kcal mol^{-1} (see Table 7). The reaction is exothermic

Table 7 MRCI/TZ optimized distances (Å) at the transition state, and MRCI/QZ energetics for the $MoO^{+,2+,-}$ + H_2O reaction

Species	State	R_{OH}[a]	R_{OH}[b]	R_{MoO}[c]	$\Delta R(MoO)$[d]	E_{int}[e]	E_{act}[f]	E_{rx}[g]
MoO^{2+}	$X^3\Sigma^-$ (1^3A)	1.355	0.969	1.687	0.113	127.8	85.0	19.9
	$\alpha^1\Gamma$ (1^1A)	1.467	0.971	1.669	0.104	132.6	88.6	23.7
	$\alpha^1\Gamma$ (2^1A)	1.401	0.969	1.668	0.103	127.9	87.9	19.2
MoO^+	$X^4\Sigma^-$ (1^4A)	1.279	0.953	1.736	0.123	44.2	42.0	−12.9
	$a^2\Delta$ (1^2A)	1.301	0.954	1.720	0.123	41.0	61.6	−2.1
	$a^2\Delta$ (2^2A)	1.345	0.954	1.718	0.121	38.8	61.8	−4.0
	$A^4\Pi$ (1^4A)	1.294	0.955	1.746	0.090	39.9	46.7	−6.7
	$A^4\Pi$ (2^4A)	1.199	0.954	1.773	0.117	32.1	47.5	−7.3
MoO^-	$X^4\Pi$ (1^4A)	1.227	0.945	1.814	0.114	14.3	25.6	−28.9
	$X^4\Pi$ (2^4A)	1.170	0.951	1.790	0.090	9.1	27.5	−21.2
	$1^6\Sigma^+$ (1^6A)	1.142	0.950	1.848	0.107	9.1	14.4	−19.4
	$1^2\Delta$ (1^2A)	1.176	0.951	1.790	0.144	12.1	29.6	−19.2
	$1^2\Delta$ (2^2A)	1.136	0.951	1.797	0.151	12.5	32.2	−17.8

[a] Distance for the activated OH bond. [b] Distance for the inert OH bond. [c] Distance between Mo and O of water. [d] Elongation of the original MoO bond. [e] Interaction energy between the reactants. [f] Intrinsic activation energy. [g] Reaction energy.

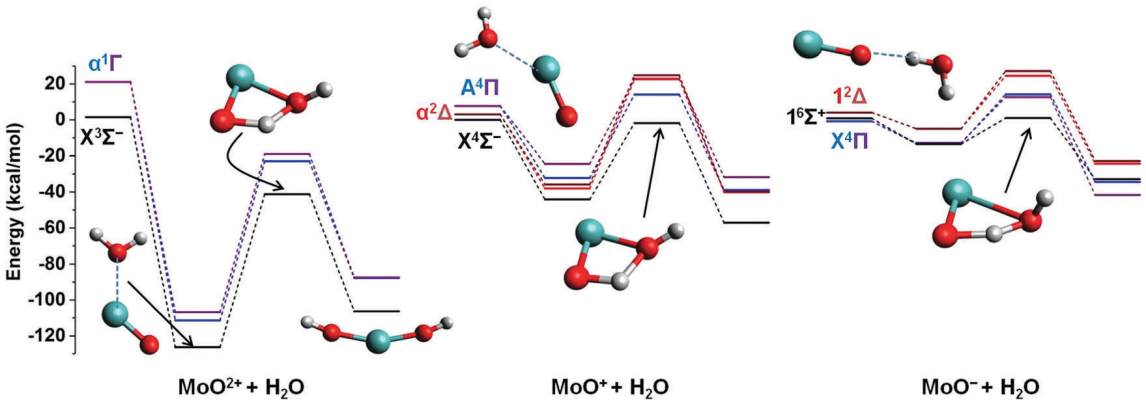

Fig. 6 MRCI+Q potential energy landscapes for the reaction between $MoO^{2+,+,-}$ and H_2O. The four energy levels for each case correspond (left to right) to infinitely separated reactants (showing the molybdenum oxide state), the interacting complex of them, the transition state, and the produced $Mo(OH)_2^{2+,+,-}$.

in all cases with respect to infinitely separated reactants. With respect to the interacting complex ($MoO^{2+,+,-}\cdots H_2O$) the reaction is endothermic for the dication by about 20 kcal mol^{-1} and the three energy pathways are nearly parallel (see Fig. 6). On the other hand, the reaction is exothermic for the cation and anion by 2–13 and 18–29 kcal mol^{-1}, respectively.

These trends are collectively depicted in Fig. 6. Overall, MoO^- provides the most efficient OH activation because it combines the low stability of the interacting complex ($MoO^-\cdots HOH$), the small activation energy, and the legitimate stability of the products. The products are stable enough to drive the reaction, but more stable products could trap the system and poison possible later steps of an extended catalytic cycle. The first excited state ($1^6\Sigma^+$) reveals the lowest intrinsic activation barrier (14.4 kcal mol^{-1}), which is about 10 kcal mol^{-1} lower than the next larger barrier (25.6 kcal mol^{-1} for $X^4\Pi$) and it's lower than the MoO^- + H_2O fragments. It's noteworthy that the reaction in the anionic case undergoes two spin crossovers. The ground state is a quartet which changes to sextet to overcome the barrier and switches back to quartet to produce the final hydroxide. In the cationic systems no spin changes are observed for the lowest energy pathway.

Fig. 6 shows also the structure for the lowest energy transition state. Observe that the distance between Mo and O of the incoming water molecules increases gradually from ~1.67–1.68 Å, to 1.72–1.77 Å, and 1.79–1.85 Å for the dication, cation, and anion. The closer proximity of water distorts the activated OH bond further and its length increases going from the anion, to the cation, and finally the dication (see Table 7). The inert OH bond length shortens by less than 0.005 Å in the case of $MoO^{\pm}$, but elongates by up to 0.016 Å for MoO^{2+}. In all cases the Mo–O distance of the oxide increases by about 0.1 Å.

The produced $Mo(OH)_2^{2+,+,-}$ species have a nearly linear O–Mo–O arrangement, but the Mo–O–H moiety is bent. On average, the Mo–OH distance is 1.74, 1.82, and 1.99 Å for the dication, cation, and anion, respectively. Considering that OH is anionic in the $Mo(OH)_2^{2+,+,-}$ species, we can explain the observed sequence: larger positive charge on Mo attracts stronger the OH^- terminals. This is an elongation of the initial Mo–O bond by at least 0.15 Å in all cases. Therefore, in addition to the cleavage of one O–H bond, the original Mo–O bond has to weaken too.

Finally, the following question is in order: what is special about the $1^6\Sigma^+$ state, which generates the smallest intrinsic activation barrier? A complete answer is beyond the scope of the present work, but we make the following observation. Among the three lowest states of the anion, this state has the longest Mo–O bond, because of its $1\sigma^2 2\sigma^1 1\pi^4 2\pi^2 1\delta^2$ configuration (see Section V): there are two electrons in the "anti-bonding" 2π orbitals, whereas the other two states have one ($X^4\Pi$) or none ($1^2\Delta$). The 2σ and 1δ are rather non-bonding orbitals localized on Mo (see Fig. 2). Accordingly, the bond lengths are 1.659 ($1^2\Delta$), 1.713 ($X^4\Pi$), and 1.744 ($1^6\Sigma^+$) Å following the 2π occupation for these states. Taking the average of the two components for $X^4\Pi$ and $1^2\Delta$ the activation energy for them is 30.9 ($1^2\Delta$), 26.5 ($X^4\Pi$), and 14.4 ($1^6\Sigma^+$) kcal mol^{-1}. Therefore it seems there is a correlation between the bond length of pure MoO and the energy needed to proceed to the products.

VII. Summary and conclusions

High level electronic structure calculations were performed to study several low-lying electronic states for the $MoO^{+,2+,-}$ charged species. Full potential energy curves and equilibrium molecular constants are reported for all of them. This is the first systematic work for these species and the majority of our numerical results appear for the first time in the literature. The ground states are found to be $^4\Sigma^-$, $^3\Sigma^-$, and $^4\Pi$ for MoO^+, MoO^{2+}, and MoO^-, respectively. The order of the low-lying excited states for MoO^+ is clarified and our numerical results compare favorably with the existing experimental data. The $4s^2 4p^6$ semi-core electron correlation effects decrease the bond lengths by about 0.005 Å, while they are important for the accurate calculation of the binding energy. MoO^{2+} is stable with respect to the lowest Mo^+ + O^+ asymptote and its electronic states originate from Mo^{2+} + O. MoO^- has five bound electronic states with respect to its ionization to MoO. The active space was found to be critical for accurate description of the wavefunction,

and the inclusion of three additional orbitals ($5p_{Mo}$ at infinite Mo–O separations) is necessary. Finally, we investigated the reaction of the lowest energy states of all three species with water. We found that the stability of the interacting complex of the reactants, the intrinsic activation energy barrier, and the stability of the products drop moving from the dication, to the cation, and the anion of molybdenum oxide. MoO^- serves overall as a better catalyst for the activation of OH bonds. The present work reports an entire collection of molecular properties and structures, bonding schemes, spectroscopic constants, and energetics which will aid the characterization of future experimental spectra for the titled charged MoO species and their reaction with water. Our work highlights the better catalytic behavior of anionic transition metal systems and suggests that future research should focus more on such systems.

Conflicts of interest

There are no conflicts to declare.

Acknowledgements

The authors are indebted to Auburn University for financial support. The computational resources were provided by the Auburn University Hopper Cluster.

References

1 A. Gunay and K. H. Theopold, C–H Bond Activations by Metal Oxo Compounds, *Chem. Rev.*, 2010, **110**(2), 1060–1081.
2 H. I. Karunadasa, C. J. Chang and J. R. Long, A Molecular Molybdenum-Oxo Catalyst for Generating Hydrogen from Water, *Nature*, 2010, **464**(7293), 1329–1333.
3 P. R. Ortiz de Montellano, Hydrocarbon Hydroxylation by Cytochrome P450 Enzymes, *Chem. Rev.*, 2010, **110**(2), 932–948.
4 Y. Wang, X. Sun, J. Zhang and J. Li, A Theoretical Study on Methane C–H Bond Activation by Bare $[FeO]^{+/0/-}$, *J. Phys. Chem. A*, 2017, **121**(18), 3501–3514.
5 E. Miliordos and A. Mavridis, Electronic Structure of Vanadium Oxide. Neutral and Charged Species, $VO^{0,\pm}$, *J. Phys. Chem. A*, 2007, **111**(10), 1953–1965.
6 E. Miliordos and A. Mavridis, Electronic Structure and Bonding of the Early 3d-Transition Metal Diatomic Oxides and Their Ions: $ScO^{0,\pm}$, $TiO^{0,\pm}$, $CrO^{0,\pm}$, and $MnO^{0,\pm}$, *J. Phys. Chem. A*, 2010, **114**(33), 8536–8572.
7 C. N. Sakellaris, E. Miliordos and A. Mavridis, First Principles Study of the Ground and Excited States of FeO, FeO^+, and FeO^-, *J. Chem. Phys.*, 2011, **134**(23), 234308.
8 J. Li and K. Yoshizawa, Computational Evidence for Hydrogen Generation by Reductive Cleavage of Water and α-H Abstraction on a Molybdenum Complex, *Angew. Chem., Int. Ed.*, 2011, **50**(50), 11972–11975.
9 J. C. Harms, K. A. Womack, L. C. O'Brien and W. Zou, Analysis of a New MoO Transition in the near-IR: A Combined Theoretical and Experimental Study, *J. Chem. Phys.*, 2014, **141**(13), 134310.
10 E. Broclawik, On the Electronic Structure of Transition-Metal Oxide cations: DFT Calculations for VO^+ and MoO^+, *Int. J. Quantum Chem.*, 1995, **56**(6), 779–785.
11 I. Kretzschmar, a. Fiedler, J. N. Harvey, D. Schroder and H. Schwarz, Effects of Sequential Ligation of Molybdenum Cation by Chalcogenides on Electronic Structure and Gas-Phase Reactivity, *J. Phys. Chem. A*, 1997, **101**(35), 6252–6264.
12 H.-P. Loock, B. Simard, S. Wallin and C. Linton, Ionization Potentials and Bond Energies of TiO, ZrO, NbO and MoO, *J. Chem. Phys.*, 1998, **109**(20), 8980–8992.
13 E. Broclawik, W. Piskorz and K. Adamska, On the Ground Electronic State of MoO^+: Upgrade Density Functional Theory Calculations, *J. Chem. Phys.*, 1999, **110**(24), 11685–11687.
14 Z. Luo, Y.-C. Chang, Y. Pan, K.-C. Lau and C. Y. Ng, Rotationally Resolved State-to-State Photoelectron Study of Molybdenum Monoxide Cation (MoO^+), *J. Phys. Chem. A*, 2016, **120**(27), 4643–4654.
15 M. R. Sievers, Y. Chen and P. B. Armentrout, Metal Oxide and Carbide Thermochemistry of Y^+, Zr^+, Nb^+, and Mo^+, *J. Chem. Phys.*, 1996, **105**(15), 6322–6333.
16 R. F. Gunion, S. J. Dixon-Warren, W. C. Lineberger and M. D. Morse, Ultraviolet Photoelectron Spectroscopy of Molybdenum and Molybdenum Monoxide Anions, *J. Chem. Phys.*, 1996, **104**(5), 1765–1773.
17 T. H. Gaussian Basis Dunning, Sets for Use in Correlated Molecular Calculations. I. The Atoms Boron through Neon and Hydrogen, *J. Chem. Phys.*, 1989, **90**(2), 1007–1023.
18 R. A. Kendall, T. H. Dunning and R. J. Harrison, Electron Affinities of the First-row Atoms Revisited. Systematic Basis Sets and Wave Functions, *J. Chem. Phys.*, 1992, **96**(9), 6796–6806.
19 K. A. Peterson, D. Figgen, M. Dolg and H. Stoll, Energy-Consistent Relativistic Pseudopotentials and Correlation Consistent Basis Sets for the 4d Elements Y–Pd, *J. Chem. Phys.*, 2007, **126**(12), 124101.
20 MOLPRO, version 2015.1, a package of ab initio programs, H.-J. Werner, P. J. Knowles, G. Knizia, F. R. Manby, M. Schütz, *et al.*, see http://www.molpro.net.
21 A. Kramida, Y. Ralchenko and J. Reader, NIST ASD Team. 2015. NIST Atomic SpectraDatabase (ver. 5.3), [Online]. Available: http://physics.nist.gov/asd [2017, September National Institute of Standards and Technology, Gaithersburg, MD].
22 *CRC Handbook of Chemistry and Physics*, ed. W. M. Haynes, Taylor and Francis, Boca Raton, FL, 93rd edn, 2012.

Ab initio investigation of the ground and excited states of $RuO^{+,0,-}$ and their reaction with water

PCCP

PAPER

View Article Online
View Journal | View Issue

Cite this: *Phys. Chem. Chem. Phys.*, 2020, **22**, 16072

Ab initio investigation of the ground and excited states of $RuO^{+,0,-}$ and their reaction with water†

Isuru R. Ariyarathna, Nuno M. S. Almeida ‡ and Evangelos Miliordos *

Received 6th May 2020,
Accepted 26th June 2020

DOI: 10.1039/d0cp02468f

rsc.li/pccp

High-level quantum chemical calculations on $RuO^{0,\pm}$ elucidate the electronic structure of their low-lying electronic states. For thirty-two states, we report the electronic configurations, bond lengths, vibrational frequencies, spin–orbit splittings, and excitation energies. The electronic states of RuO can be generated from those of RuO^+ by adding one electron to the σ non-bonding orbital closely resembling the 5s atomic orbital of Ru. The ground states for RuO and RuO^- are clearly identified as $^5\Delta$ and $^4\Delta$, but the two states ($^4\Delta$ and $^2\Pi$) compete for RuO^+. The difficulty of calculations is revealed by our small binding energies compared to the experimental values. In addition, we studied the reaction of the three species with water in their ground and selected low-lying electronic states. We found a consistent decrease of the activation energy barriers and higher exothermicity as we add electrons to the system. RuO^- is found to facilitate the reaction for both kinetic and thermodynamic reasons.

I. Introduction

Transition metal oxide units are commonly used to facilitate catalytic reactions of environmental and industrial importance.[1–5] Compared to solid-state catalysts, molecular complexes offer easier adjustment of the catalytic performance by appropriate selection of ligands. Quantum chemical calculations can guide these searches by providing a less expensive, safer, systematic, and far broader alternative approach.[6] Two of the currently most important chemical processes involve the activation of C–H (selective hydrocarbon functionalization) and O–H (water splitting) bonds.

Our recent efforts focus on the reaction of small transition metal–oxide compounds with methane and water.[7–11] A systematic path for the discovery of more efficient and selective catalysts is followed starting from the "naked" metal oxide unit and adding different numbers and types of ligands. This approach allows us to monitor both the role of the electronic structure of the metal and the effect of the ligands. Concerning the C–H activation, we recently found that the most efficient (but less selective) radical mechanism is promoted by weak field ionic ligands since they stabilize the oxyl form of the metal–oxygen unit ($MO^{\bullet-}$). Specifically, we were able to show that an appropriate number of halogen ligands (F^-, Cl^-) can stabilize highly excited electronic states of ZrO with oxyl character and render them the ground state of the complex.[7,9] In contrast, strong field ligands, such as ammonia, stabilize the oxo ($M^{4+}O^{2-}$) character of the metal oxide FeO^{2+} unit, which leads to larger activation energy barriers *via* an oxidative addition reaction step.[8]

These studies emphasize the necessity to comprehend the electronic structure of several low-lying electronic states of metal oxides with various charges. The application of our knowledge from organometallic chemistry to the activation chemistry of O–H bonds has been suggested in the past.[12] No encouraging progress has been observed in this direction. Inspired by the release of H_2 from H_2O in the (negatively charged) cathode of an electrochemical cell, we have studied in the past by both quantum computations and photoelectron spectroscopy the reaction of transition metal anionic compounds (Ni^-, Pd^-, Pt^-, and MoO^-) with water.[10,11] Our theoretical work on the $MoO^{2+,+,-}$ + H_2O reaction demonstrated the superior performance of anionic over cationic systems, offering lower activation barriers and more stable products.[10]

The electronic structure of first-row transition metal oxides is quite well investigated by high-level theoretical methods and spectroscopic measurements over the last fifty years.[13–15] On the other hand, the electronic structure of the second-row transition metals is poorly understood. The construction of suitable basis sets combined with relativistic pseudopotentials over the past decade has enabled the accurate description of the wave function for second-row transition metal compounds.[16]

In this study, we investigate the electronic structure of RuO and its singly charged counterparts. Accurate spectroscopic constants are calculated for several electronic states and compared with the existing (limited) values of the literature. The reaction between the lowest energy states of all three systems ($RuO^{0,\pm}$) and water is then examined. We confirm that the

Department of Chemistry and Biochemistry, Auburn University, Auburn, AL 36849, USA. E-mail: emiliord@auburn.edu

† Electronic supplementary information (ESI) available. See DOI: 10.1039/d0cp02468f

‡ Current Address: Department of Chemistry, Michigan State University, East Lansing, MI 48864, USA.

anionic species are advantageous over the cationic species as happens for MoO. Our results allow the generalization that metal oxide anions activate water easier, and that the nature of the metal plays a minor role, which suggests the use of earth abundant metals.

II. Computational details

The construction of full potential energy curves was carried out with the internally contracted multi-reference configuration interaction (MRCI) approach. The reference wave function was provided by complete active space self-consistent field (CASSCF) calculations. The active space for $RuO^{0,+}$ consists of the valence 5s and 4d orbitals of ruthenium and the 2p orbitals of oxygen. For RuO^- the active space was increased to include three more orbitals, which correspond to the 5p orbitals of Ru at long Ru–O distances, but they are highly localized on oxygen ($\sim$3p) at equilibrium distances. Our recent studies on MoO^- and PdO^- suggested that the inclusion of these orbitals is necessary for accurate results.[10,17] The MRCI potential energy curves were obtained using state-average CASSCF orbitals averaging states of the same spin-multiplicity together. MRCI calculations based on state-specific CASSCF reference wave functions were then performed around equilibrium to extract accurate spectroscopic constants by solving numerically the rovibrational Schrödinger equation. Single and double excitations from the reference active space and the 2s orbital of oxygen to the virtual space were allowed at the MRCI level. The Davidson correction (MRCI+Q) was finally employed to reduce the size extensivity errors.

In cases of minimal multi-reference character, the single-reference coupled cluster methodology was also applied. The restricted Hartree–Fock orbitals were used and single, double and perturbative triples were included [CCSD(T)]. For selected states, we also included the dynamic correlation of the semi-core $4s^24p^6$ electrons. These calculations are denoted as C-MRCI and C-CCSD(T).

The quintuple-ζ quality correlation consistent basis sets were employed. The all-electron aug-cc-pV5Z basis set was used for oxygen.[18] The cc-pV5Z-PP basis set combined with the appropriate relativistic pseudopotential (replacing 28 inner electrons $1s^2$ through $3d^{10}$) was used for ruthenium.[16] In the case of RuO^- a series of diffuse functions were added on the Ru center (aug-cc-pV5Z-PP = cc-pV5Z-PP + 1s1p1d1f1g1h). For the calculations including core correlation effects we used the appropriately designed weighted-core cc-pwCV5Z-PP basis set for ruthenium.[16]

For the $RuO^{0,+,-} + H_2O$ reaction we performed MRCI calculations for the lowest lying states using a triple-ζ quality basis set to optimize the geometries for the reactants, transition states and products. Specifically, the cc-pVTZ-PP(Ru) cc-pVTZ(H) aug-cc-pVTZ(O) basis set combination was employed for $RuO^{+,0} + H_2O$, and aug-cc-pVTZ-PP(Ru) cc-pVTZ(H)/aug-cc-pVTZ(O) for $RuO^- + H_2O$ (MRCI/TZ). For these structures, we performed single-point MRCI+Q energy calculations, which were used to construct the complete reaction energy diagrams. The zero of the scale is set to the energy of the reactants placed at a distance of 1000 Å to alleviate the size extensivity error of the truncated MRCI expansion. The reference space (at CASSCF) for these reactions is smaller than the pure metal oxides. We made this choice for technical reasons. We decided to rule out the Ru–O bonding 2σ and 1π orbitals since they are always doubly occupied, and the anti-bonding 4σ Ru–O orbital because it is always unoccupied in all dominant determinants of the low-lying states. These orbitals are still optimized at CASSCF and correlated at the MRCI level of theory. The active space is 5 or 6 electrons in 5 orbitals for the cation and neutral systems, and 7 electrons in 8 orbitals (we kept the 5p orbitals of Ru in the active space) for the anionic ones. All valence electrons are correlated at the MRCI level of theory.

Spin–orbit coupling constant A was calculated by employing the spin–orbit part of the used pseudopotential and coupling the MRCI wave functions *via* the Breit–Pauli Hamiltonian. All calculations were performed using MOLPRO2015.1.[19]

III. Results and discussion

In this section, we first analyze the electronic structure of the titled ruthenium monoxide species and we comment on their spectroscopic constants. Sections IIIA, IIIB, and IIIC correspond to RuO^+, RuO, and RuO^-, respectively. The last section (IIID) discusses the reaction of them in their ground and excited states, with water and we compare the reaction energetics.

IIIA. RuO^+

The ground state of Ru^+ is a ^4F with a $4d^7$ electronic configuration. Among the first seven states with excitation energies up to $\sim$15 000 cm^{-1}, only the third one (^6D) is of $5s^14d^6$ character at $\sim$10 000 cm^{-1}.[20] The $Ru^+(^4F) + O(^3P;2s^22p^4)$ combination gives rise to two Σ^+, one Σ^-, three Π, three Δ, two Φ, and one Γ states of doublet, quartet, and sextet spin multiplicities. The potential energy curves (PECs) as a function of the Ru–O distance for many of these states are shown in Fig. 1. As the atoms approach, all of the PECs follow a smooth energy decrease until a distance of about 2.3 Å, where there is a sudden slope change. At this distance, there are avoided crossings from higher energy $Ru^+ + O$ or other ionic channels, such as $Ru^{2+} + O^-$.

The dominant electronic configurations at the equilibrium bond length for sixteen electronic states are given in Table S1 of the ESI.† The lowest two states, $^2\Pi$ and $^4\Delta$, are nearly degenerate and well separated from the next state (see below) with electronic configurations $2\sigma^21\pi^42\pi^11\delta^4$ and $2\sigma^21\pi^42\pi^21\delta^3$, respectively. Contours of these molecular orbitals are depicted in Fig. 2 (only valence orbitals are numbered; 1σ is the 2s of oxygen and it is not shown). The 2σ and 1π orbitals can be better described as the σ- and π-bonds between the metal and oxygen atoms, 2π is an anti-bonding Ru–O π-orbital, while 1δ is a localized 4d orbital on Ru. The configurations of all doublet and quartet states have the $2\sigma^21\pi^4$ part in common with the

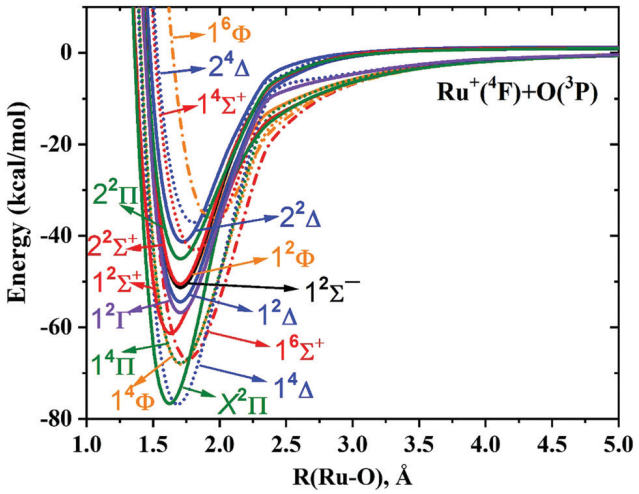

Fig. 1 Potential energy curves of RuO^+ as a function of the Ru–O distance at the MRCI level of theory.

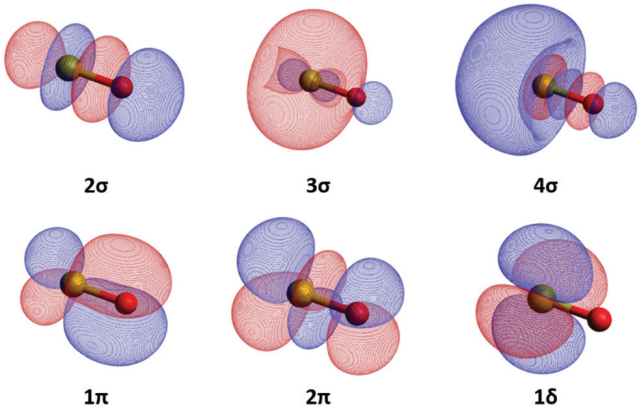

Fig. 2 State-averaged CASSCF molecular orbitals of RuO^+ at 1.7 Å.

remaining five valence electrons populating the 3σ, 2π, and 1δ orbitals. The 3σ is mostly composed of the 5s atomic orbital of Ru, and is singly occupied only in the $1^4\Phi$, $1^4\Pi$, $1^6\Sigma^+$, $1^2\Sigma^+$, $1^2\Phi$, $2^2\Pi$, $1^4\Sigma^+$, $2^4\Delta$, and $1^6\Phi$ states. The majority of the states are multi-reference, except for $X^2\Pi$, $1^4\Delta$, $1^6\Sigma^+$, and $1^2\Sigma^+$. The latter two are of $2\sigma^2 3\sigma^1 1\pi^4 2\pi^2 1\delta^2$ and $2\sigma^2 3\sigma^1 1\pi^4 1\delta^4$ characters.

Table 1 lists our numerical results for the electronic states of RuO^+, which include absolute energies, equilibrium bond lengths, harmonic frequencies, anharmonicities, and excitation energies. The first two states, $^2\Pi$ and $^4\Delta$, are nearly degenerate at every employed level of theory. In all cases, except CCSD(T), $^2\Pi$ is found lower by 7 (MRCI+Q) to 568 (C-MRCI) cm^{-1}. CCSD(T) predicts $^4\Delta$ to be lower by 230 cm^{-1}. The assignment of $^2\Pi$ as the ground state is based on the fact that our most accurate calculations, C-MRCI+Q and C-CCSD(T), place $^4\Delta$ higher than $^2\Pi$ by 525 and 116 cm^{-1}, respectively. The two states have distinct spectroscopic features: $^2\Pi$ has a shorter bond length by 0.05–0.06 Å and larger frequency by ~80 cm^{-1}. In both cases, the sub-valence electron correlation effects have minimal influence on the numerical results changing the bond

Table 1 Equilibrium energy E_e (hartrees), bond length r_e (Å), harmonic vibrational frequency ω_e (cm^{-1}), anharmonicity $\omega_e\chi_e$ (cm^{-1}), $\Delta G_{1/2}$ (cm^{-1}), and excitation energy T_e (cm^{-1}) for the lowest electronic states of $^{102}Ru^{16}O^+$

State	Method	$-E_e$	r_e	ω_e	$\omega_e\chi_e$	T_e
$X^2\Pi$	MRCI	168.859874	1.621	1013	4.3	0
	MRCI+Q	168.893645	1.620	1016	4.3	0
	C-MRCI	169.223081	1.629	1016	6.4	0
	C-MRCI+Q	169.307823	1.623	1017	5.1	0
	CCSD(T)	168.897934	1.609			230
	C-CCSD(T)	169.327238	1.609			0
$1^4\Delta$	MRCI	168.859232	1.680	940	4.8	141
	MRCI+Q	168.893614	1.682	942	4.6	7
	C-MRCI	169.220494	1.684	931	4.1	568
	C-MRCI+Q	169.305429	1.683	932	3.6	525
	CCSD(T)	168.898984	1.665			0
	C-CCSD(T)	169.326711	1.662			116
$1^6\Sigma^+$	MRCI	168.845517	1.755	783	5.7	3151
	MRCI+Q	168.879094	1.755	789	5.9	3194
	CCSD(T)	168.882147	1.741			3695
$1^4\Phi$	MRCI	168.845621	1.701	818	4.9	3128
	MRCI+Q	168.877563	1.701	818	4.8	3530
	C-MRCI	169.211013	1.695	834	4.7	2649
	C-MRCI+Q	169.293613	1.694	841	4.8	3119
$1^4\Pi$	MRCI	168.844030	1.705	808	4.6	3477
	MRCI+Q	168.876842	1.703	811	4.8	3688
$1^2\Sigma^+$	MRCI	168.835619	1.632	880	2.5	5323
	MRCI+Q	168.868361	1.628	901	3.0	5549
	CCSD(T)	168.873194	1.626			5660
$1^2\Gamma$	MRCI	168.826438	1.703	861	6.0	7338
	MRCI+Q	168.860501	1.699	868	5.8	7274
$1^2\Delta$	MRCI	168.822722	1.701	864	6.2	8154
	MRCI+Q	168.857423	1.697	874	5.8	7950
$1^2\Sigma^-$	MRCI	168.818299	1.703	866	5.8	9124
	MRCI+Q	168.852543	1.700	873	5.8	9021
$2^2\Sigma^+$	MRCI	168.816199	1.702	860	2.0	9585
	MRCI+Q	168.851496	1.696	877	2.4	9250
$1^2\Phi$	MRCI	168.815989	1.704	811	6.5	9631
	MRCI+Q	168.850298	1.699	821	1.4	9513
$2^2\Pi$	MRCI	168.807200	1.703	796	6.5	11 560
	MRCI+Q	168.840819	1.700	808	5.7	11 594
$1^4\Sigma^+$	MRCI	168.805237	1.814	659	5.6	11 991
	MRCI+Q	168.838688	1.811	660	4.9	12 061
$2^2\Delta$	MRCI	168.803669	1.719	809	6.7	12 335
	MRCI+Q	168.838249	1.714	820	6.7	12 158
$2^4\Delta$	MRCI	168.796905	1.805	686	3.2	13 820
	MRCI+Q	168.829752	1.802	686	2.9	14 023
$1^6\Phi$	MRCI	168.794358	1.950	547	15.8	14 379
	MRCI+Q	168.827053	1.951	530	21.1	14 615

lengths by ~0.001 Å and the frequencies by a few cm^{-1}. However, CCSD(T) predicts shorter bond lengths compared to MRCI or MRCI+Q by 0.015–0.02 Å.

The next three states are also very close to each other lying between 3000 and 3700 cm^{-1}. At MRCI+Q the order is $1^6\Sigma^+ < 1^4\Phi < 1^4\Pi$. The Ru–O distance of the sextet is ~0.05 Å longer than the other two states, which have similar electronic structures ($2\sigma^2 3\sigma^1 1\pi^4 2\pi^1 1\delta^3$; see Table S1, ESI†) and spectroscopic constants. All three states have considerably smaller vibrational frequencies compared to the first two states (~800 *vs.* >900 cm^{-1}).

Seven doublet states follow in the 5000–12 000 cm^{-1} range with various bond lengths and vibrational frequencies. The shorter bond length belongs to $1^2\Sigma^+$ (1.63 Å), which has no electrons in the 2π anti-bonding orbitals, while the rest of them have nearly equal bond lengths around 1.70 Å. It also has the largest vibrational frequency and it is energetically separated

from the rest doublets. Finally, we report four more states in Table 1 covering excitation energies up to 15 000 cm^{-1}. The last state ($1^6\Phi$) has the longest bond length and smaller vibrational frequency of all states, and it is the only state with only three electrons in the 1π bonding orbitals (see Table S1, ESI†).

The ground ^4F state of Ru^+ has a quite large spin–orbit splitting with the difference between $^4F_{9/2}$ (lowest energy component) and $^4F_{3/2}$ (highest energy component) being experimentally 3104.260 cm^{-1}.[20] Our theoretical splittings for the molecular states at equilibrium are of the same order: $X^2\Pi$ (1452 cm^{-1}), $1^4\Delta$ (2258 cm^{-1}), $1^4\Pi$ (2178 cm^{-1}), and $1^4\Phi$ (1129 cm^{-1}). A more detailed list of the exact energies is given in Table S2 of ESI.† The larger splitting for $^4\Delta$ sets the ground state to $^4\Delta_{7/2}$. The lowest energy $^2\Pi$ component ($^2\Pi_{1/2}$) is 0.09 eV or 726 cm^{-1} higher at MRCI. As expected, the $1^2\Sigma^+$ and $1^6\Sigma^+$ states have minimal splittings and thus their excitation energy increases with respect to the ''new'' ground state ($^4\Delta_{7/2}$) by about 2000 cm^{-1} (see Table S2 of ESI†).

We are aware of only one experimental and one theoretical work on RuO^+ in the literature. The mass spectrometric work of Chen and Armentrout yielded a bond dissociation energy of 3.81 ± 0.05 eV or 88 ± 1 kcal mol^{-1}.[21] Our MRCI/MRCI+Q binding energies (calculated using the energy of the fragments at 10.0 Å to avoid size extensivity issues) are 79.0/83.4 kcal mol^{-1}. The corresponding values including the sub-valence electron correlation energy are nearly identical, C-MRCI/C-MRCI+Q = 78.0/84.2 kcal mol^{-1}. The CCSD(T) and C-CCSD(T) numbers are 81.7 and 83.3 kcal mol^{-1}, respectively. Our best estimate for D_0 is $D_0 = D_e$(C-CCSD(T)) − ZPE(C-MRCI+Q) + SO(RuO^+) − SO(Ru^+) − SO(O) = 83.3 − 1.45 + 2.43 − 4.04 − 0.22 = 79.7 kcal mol^{-1}. ZPE(C-MRCI+Q) is the zero-point energy calculated as ω_e(C-MRCI+Q)/2 = 1017/2 cm^{-1} (see Table 1), and SO(X) is the energy lowering due to spin–orbit effects for system X. The SO(Ru^+) and SO(O) are taken from the experimental data of ref. 20, and SO(RuO^+) is calculated presently. Our estimate falls short of the experimental value by about 8 kcal mol^{-1}. Similar discrepancy was observed for FeO^+ (77.4 *vs.* 81.2 ± 0.5 kcal mol^{-1})[13,22] and it should be attributed to the missing higher order dynamic electron correlation.

The theoretical work of Carter and Goddard predicted a very different pattern of electronic states at the generalized valence bond (GVBCI) level of theory.[23] The authors predicted a ground $^4\Delta$ state followed by a group of doublet states ($^2\Gamma$, $^2\Delta$, $^2\Sigma^+$, $^2\Sigma^-$, $^2\Delta$) lying between 16.9 kcal mol^{-1} (5911 cm^{-1}) and 37.1 kcal mol^{-1} (12 976 cm^{-1}). No reference to our predicted $^2\Pi$ or the low-lying $^6\Sigma^+$ state was made in this article and the $^2\Sigma^+$ state was placed much higher in energy.

Comparing with the electronic states of the first row transition metal counterpart metal oxide FeO^+,[13] we see that some of the low-lying states are identical ($^6\Sigma^+$, $^4\Pi$, $^4\Phi$, and $^4\Delta$), but there is one striking difference. The ground state $^2\Pi$ ($2\sigma^2 1\pi^4 2\pi^1 1\delta^4$) of RuO^+ is not even among the low-lying states of FeO^+. There is one $^2\Pi$ state of FeO^+ at around 15 000 cm^{-1}, the bigger (31% or 0.56 coefficient, but not major) component of which has the same electronic configuration. On the other hand, $^6\Phi$ is the fourth excited state in the case of FeO^+ at around 9200 cm^{-1}, but the fifteenth excited state in the case of RuO^+ at ∼14 500 cm^{-1}. It seems that states with no 3σ (∼metallic valence s-orbital) electrons and $1\delta^4$ configurations are more stable for ruthenium. A similar observation was made for FeO^{2+} *vs.* RuO^{2+}.[24] In the RuO^{2+} case the ground state is a singlet state with $2\sigma^2 1\pi^4 1\delta^4$ configuration unlike FeO^{2+}, which prefers high spin states populating the 3σ and 2π orbitals.[8,24]

IIIB. RuO

The electronic structure of the low lying states of RuO has been studied theoretically earlier by Krauss and Stevens.[25] The ground state was identified as a $^5\Delta$ followed by a $^3\Pi$ and a series of closely spaced states lying between 6800 and 11 500 cm^{-1}: $^3\Pi < {}^3\Delta \leq {}^3\Sigma^- < {}^3\Phi < {}^7\Sigma^+ \leq {}^5\Sigma^+ < {}^3\Sigma^+ \leq {}^5\Pi \leq {}^5\Phi$. The average energy difference between two successive states is ∼600 cm^{-1}. Our more advanced calculations confirm this dense picture of states. We were actually able to locate five more states in this energy region: $1^1\Sigma^+$, $1^1\Pi$, $1^3\Gamma$, $2^3\Pi$, and $2^3\Sigma^-$, while we located the $^7\Sigma^+$ state higher than our highest lying state at ∼13 000 cm^{-1}. This energy series is completely different from the first-row transition metal counterpart FeO, where there is a competition between $^5\Delta$ and $^5\Sigma^+$ for the ground state and the $^7\Sigma^+$ is only ∼2000 cm^{-1} higher.[13] The next states are $^5\Pi$ and $^5\Phi$ at around 800 cm^{-1}.

The PECs for all of our states are plotted in Fig. 3, the numerical findings for them are listed in Table 2, and the dominant electronic configurations are listed in Table S3 of ESI.† Comparing the configurations of RuO^+ and RuO (Tables S1 and S3 of ESI†), we can see that the low-lying states of RuO are generated by adding an electron to the 3σ orbital (see Fig. 2). The 3σ orbital is composed mainly of the 5s orbital of Ru, and thus the transition from RuO^+ to RuO resembles that from Ru^+(^4F; $4d^7$) to Ru(^5F; $5s^1 4d^7$), where the additional electron goes to the 5s. Specifically, the $X^2\Pi$ state of RuO^+ generates the $1^3\Pi$ and $1^1\Pi$ states of RuO depending on the spin coupling between the $2\pi^1$ and $3\sigma^1$ electrons. Similarly, $1^4\Delta$ gives $X^5\Delta$ and $1^3\Delta$, $1^4\Pi/1^4\Phi$ gives $2^3\Pi/1^3\Phi$, and $1^2\Sigma^+/1^6\Sigma^+$ gives $1^1\Sigma^+/1^5\Sigma^+$. The rest of the states result from the doublet states of RuO^+ by again adding a $3\sigma^1$ electron.

The PECs of all triplets and quintets dissociate to the ground state fragments Ru(^5F) + O(^3P). This channel cannot generate singlet states, and thus $1^1\Sigma^+$ and $1^1\Delta$ have to dissociate to the first excited state of Ru(^3F). However, spin–orbit coupling will allow the dissociation of the $\Omega = 0^+$ ($1^1\Sigma^+$) and $\Omega = 2$ ($1^1\Delta$) components to the ground state fragments.

The addition of an electron elongates the Ru–O bond by at least 0.02 Å. For example, going from $1^5\Delta$ to $1^{1,3}\Delta$, the bond length changes from 1.68 to 1.70 or 1.73 Å. Similarly, the elongation is 0.04 and 0.05 Å for the $X^2\Pi$ and $1^1\Sigma^+$ states (see Tables 1 and 2). At the same time, the vibrational frequencies decrease significantly (∼50 cm^{-1} for the $X^2\Pi$ and ∼100 cm^{-1} for the $1^4\Delta$) going from RuO^+ to RuO. Finally, the addition of the 3σ electron favors the $1^4\Delta$ state and the $X^5\Delta$ state becomes clearly the ground state of RuO with the $1^3\Pi$ being nearly 5000 cm^{-1} higher at every level of theory. As in the case of RuO^+, the Ru($4s^2 4p^6$) sub-valence electron correlation changes

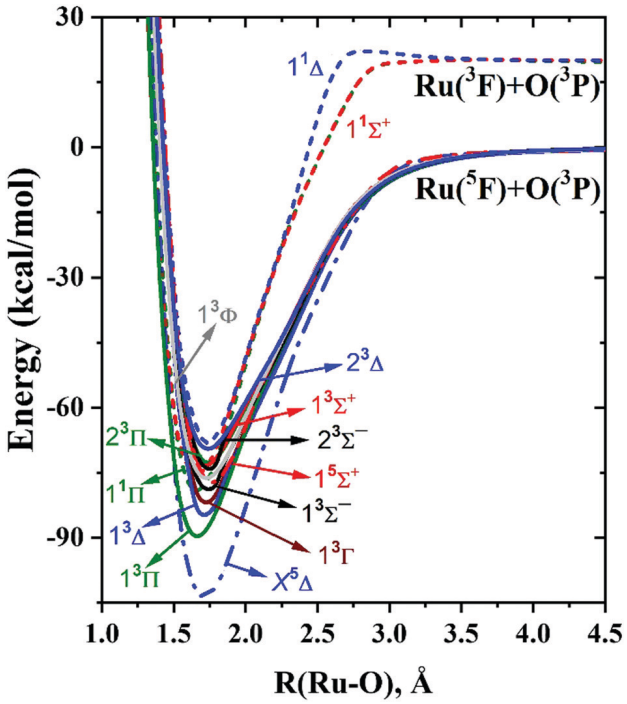

Fig. 3 Potential energy curves of RuO as a function of the Ru–O distance at the MRCI level of theory.

only slightly the numerical results for the first three states, and thus they are not considered for the rest of the states. Specifically, the bonds shorten by ~0.001 Å, the frequencies change by ~10 cm^{-1}, and the excitation energies by a few hundreds of cm^{-1}.

The bond length for the ground state at equilibrium varies from 1.703 to 1.711 Å depending on the employed method (see Table 2). The experimental values reported by Huber and Herzberg range from 1.7154 to 1.72 depending on the Ω-component.[26] For $\Omega = 3$, their given harmonic vibrational frequency is 855 cm^{-1}, which is in excellent agreement with our MRCI+Q value. Another experimental anharmonic frequency is 834.4 cm^{-1},[27] which compares favorably with our $\omega_e - 2\omega_e\chi_e = 852 - 2 \times 2.6 = 847$ cm^{-1}.

Our binding energy at the CCSD(T) and C-CCSD(T) levels of theory is 112.1 and 112.3 kcal mol^{-1}. The contribution of the electron correlation of the sub-valence ruthenium orbitals is minor. Our numbers are larger than the 110.6 kcal mol^{-1} of ref. 28, calculated at the modified coupled pair functional (MCPF) level and with double-ζ basis sets. Correcting for ZPE and spin–orbit splittings (see Section IIIA) we get $D_0 = D_e$ + SO(RuO) − SO(O) − SO(Ru) − ZPE(RuO) = 112.3 + 2.39 − 0.22 − 3.94 − 1.22 = 109.3 kcal mol^{-1}. The SO(X) stabilization energy is calculated at the MRCI level and ZPE is estimated as the half of the MRCI+Q vibrational frequency. Our value falls short of the experimental value reported by Huber and Herzberg of 5.3 eV or 122 kcal mol^{-1} [26] by more than 10 kcal mol^{-1} showing the importance of higher order electron correlation effects.

We calculated the dipole moment at the CCSD(T) level using the finite field approach. We applied a positive and negative electric field along the Ru–O axis of $f = 0.01$ a.u. and the two energies (E_+, E_-) were used to calculate numerically the dipole moment as the first derivative of the energy with respect to the external field: $\mu_e = (E_+ - E_-)/2f = 1.50$ a.u. or 3.81 Debye. Our value is larger than the theoretical value of 1.29 a.u. of ref. 25. Finally, we report spin–orbit energies and splittings for the first ten states at 1.70 Å (see Table S4 of ESI†). The ground $^5\Delta$ state splits into the $^5\Delta_4$, $^5\Delta_3$, $^5\Delta_2$, $^5\Delta_1$, and $^5\Delta_{0^\pm}$ components. The splitting between each pair is 419 cm^{-1} at MRCI, which is smaller than the 508 cm^{-1} value of ref. 25.

Table 2 Equilibrium energy E_e (hartrees), bond length r_e (Å), harmonic vibrational frequency ω_e (cm^{-1}), anharmonicity $\omega_e\chi_e$ (cm^{-1}), $\Delta G_{1/2}$ (cm^{-1}), and excitation energy T_e (cm^{-1}) for the lowest electronic states of $^{102}Ru^{16}O$

State	Method	$-E_e$	r_e	ω_e	$\omega_e\chi_e$	T_e
$X^5\Delta$	MRCI	169.152723	1.709	852	2.6	0
	MRCI+Q	169.195894	1.711	848	2.7	0
	C-MRCI	169.512182	1.707	858	2.5	0
	C-MRCI+Q	169.608120	1.710	854	2.6	0
	CCSD(T)	169.211389	1.707			0
	C-CCSD(T)	169.644185	1.703			0
$1^3\Pi$	MRCI	169.130577	1.663	858	3.2	4860
	MRCI+Q	169.174866	1.665	852	1.2	4615
	C-MRCI	169.490958	1.663	870	3.4	4658
	C-MRCI+Q	169.588640	1.667	865	1.0	4275
	CCSD(T)	169.188606	1.650			5000
	C-CCSD(T)	169.622610	1.650			4735
$1^3\Delta$	MRCI	169.116398	1.727	846	2.6	7972
	MRCI+Q	169.160844	1.728	843	3.3	7693
	C-MRCI	169.475422	1.731			8068
	C-MRCI+Q	169.572807	1.734	835	2.6	7750
$1^1\Sigma^+$	MRCI	169.113192	1.679	1046	3.8	8676
	MRCI+Q	169.154746	1.684	1141	3.9	9031
	CCSD(T)	169.168449	1.628			9424
$1^1\Pi$	MRCI	169.112910	1.656	917	8.0	8738
	MRCI+Q	169.157076	1.659	905	6.1	8520
$1^3\Gamma$	MRCI	169.111177	1.746	732	4.2	9118
	MRCI+Q	169.154614	1.742	752	4.8	9060
$1^3\Phi$	MRCI	169.111156	1.723	748	3.3	9123
	MRCI+Q	169.156132	1.715	763	2.5	8 727
$1^5\Sigma^+$	MRCI	169.110669	1.762	778	5.8	9230
	MRCI+Q	169.158108	1.757	793	5.2	8293
$1^3\Sigma^-$	MRCI	169.107893	1.734	786	8.4	9839
	MRCI+Q	169.153230	1.726	813	8.1	9364
$2^3\Pi$	MRCI	169.106372	1.708	774	5.6	10 173
	MRCI+Q	169.152088	1.701	796	4.8	9614
$2^3\Sigma^-$	MRCI	169.105687	1.762	799	7.2	10 323
	MRCI+Q	169.150538	1.771	689	8.4	9954
$1^3\Sigma^+$	MRCI	169.103349	1.738	795	10.1	10 836
	MRCI+Q	169.148186	1.734	800	7.9	10 471
$2^3\Delta$	MRCI	169.098140	1.735	722	10.0	11 980
	MRCI+Q	169.143262	1.728	741	7.5	11 551
$1^1\Delta$	MRCI	169.096560	1.725	970	10.7	12 326
	MRCI+Q	169.143598	1.723	1030	12.2	11 478

IIIC. RuO$^-$

The first two states of RuO^- are generated from the first two states of RuO by placing the additional electron to the 3σ (~$5s_{Ru}$) orbital. The lowest state is $X^4\Delta$ followed by $A^2\Pi$ at around 5000 cm^{-1}. Specifically, at MRCI (MRCI+Q) the excitation energy is 5267 (4686) cm^{-1}. In both cases the bonds are elongated only by 0.01–0.02 Å due to the additional electron in a rather non-bonding electron. The MRCI/MRCI+Q bond lengths for the two states are 1.735/1.735 ($X^4\Delta$) and 1.672/1.670 ($A^2\Pi$) Å. The corresponding harmonic vibrational frequencies for $^{102}Ru^{16}O^-$ are 834/837 and 898/907 cm^{-1}. The

MRCI PECs are shown in the ESI,† and the spin–orbit splitting for the ground state components is estimated as 527 cm^{-1} at MRCI. Finally, we calculated the electron affinity of RuO equal to 1.104 and 1.373 eV at the MRCI+Q and CCSD(T) levels, respectively.

IIID. The $RuO^{+,0,-}$ + H_2O reaction

In this section, we examine the reaction between charged and neutral RuO in their ground and excited states with water towards the formation of $Ru(OH)_2$. First, water coordinates with RuO and then the system goes through a transition state where the hydrogen atom migrates to the oxygen of RuO and the remaining OH attaches to Ru. The energy diagram for all three species is shown in Fig. 4, which also includes the structure of the interacting complex, transition state, and product of the lowest energy state (quartet for $RuO^{\pm}$ and quintet for RuO). The leftmost energy levels for each system pertain to the energy of the reactants, $RuO^{0,\pm}$ + H_2O. Note that the energy order of nearly degenerate states is different from that shown in Tables 1 and 2 because of the smaller active space used in this case (see Section II). Specifically, the order of the $1^3\Delta$ and $1^3\Pi$ states of RuO, and the order of the $X^2\Pi$–$1^4\Delta$ and $1^6\Sigma^+$–$1^4\Phi$ pairs of RuO^+ are switched in Fig. 4. The symmetry lowering caused by the coordination of water to $RuO^{0,\pm}$ lifts the double degeneracy of the Π, Δ, and Φ states generating two different energy routes for each of these states (see Fig. 4).

Fig. 4 reveals the following striking differences for the three systems. Water coordinates with the metal for RuO and RuO^+, but coordinates with oxygen in the case of RuO^-. The latter can be seen more as a hydrogen bond between one aquatic hydrogen and the oxygen terminal of RuO^-. This leads to strongly bound $(H_2O)RuO^{0,+}$ complexes with higher activation energy barriers than $RuO^-\cdots HOH$. In addition, the reaction for RuO^+ is endothermic with respect to the interaction complex and becomes increasingly exothermic for RuO and RuO^-. Overall, the reaction of anionic ruthenium oxide with water is promoted by both kinetic and thermodynamic factors.

Specifically, the intrinsic activation barrier (energy difference between the interaction complex and the transition state) decreases as we go from RuO^+ to RuO^-: 36.8 ± 18.5 (RuO^+), 21.4 ± 11.4 (RuO), and 18.5 ± 9.7 (RuO^-). Although the barrier is highly dependent on the electronic state of the system, we see a general trend that the barrier decreases by a factor of 1.7 and 1.2 every time one electron is added to the ruthenium oxide unit. Similarly, the energy difference between the interaction complex and the product increases rapidly. For RuO, all states pertain to an endothermic reaction except for one component of $X^2\Pi$ and that of $1^6\Sigma^+$ (black line of Fig. 4; see Table S10 (ESI†) for exact energies). In combination with the large activation energy barriers, this suggests that the positively charged system will likely get trapped in the $(H_2O)RuO^+$ configuration. On the other hand, all states of neutral and anionic species produce exothermic channels. On average, RuO and RuO^- channels are exothermic by 24.7 and 35.7 kcal mol^{-1}, respectively. The weaker binding of water to the oxygen terminal in the RuO^- case is partly the reason why the activation barrier is smaller and the reaction is more exothermic.

The energetics become even less favorable for RuO^{2+}.[24] Our previous study on the RuO^{2+} + H_2O reaction predicted higher stability of the $(H_2O)RuO^{2+}$ interaction complex (~80 kcal mol^{-1} with respect to RuO^{2+} + H_2O), and larger intrinsic activation barriers (~70 kcal mol^{-1}), and the products are exothermic with respect to $(H_2O)RuO^{2+}$ by ~40 kcal mol^{-1}.

The electronic structure of the produced metal di-hydroxides points to a Ru^{3+}, Ru^{2+}, or Ru^+ center combined with two OH^- groups for RuO^+, RuO, or RuO^-, respectively. Representative orbitals for the anion are shown in Fig. 5. In all of the low-lying states only the metallic σ, π, and δ orbitals are partially occupied. The highly polarized σ_{OH} and π_{OH} orbitals are always fully occupied ($\sigma_{OH}^2\pi_{OH}^4$) and correspond to the three OH electron pairs. In all cases, the nature of the occupied metallic orbitals does not change along the reaction coordinate. For example, the $RuO^+(1^4\Delta)$ state starts with an electronic configuration $2\sigma^2 1\pi^4 2\pi^2 1\delta^3$ (see Fig. 2) and ends up with a $Ru(OH)_2^+$ electronic configuration $\sigma_{OH}^2\pi_{OH}^4\pi^2\delta^3$. Comparing orbitals of Fig. 2 and 5, we see that the 3σ, 2π, and 1δ orbitals of monoxide species convert to σ, π, and δ orbitals of the di-hydroxide species. Therefore, the nearly "metallic" electrons remain intact, and the Ru–O σ and π bonds polarize further towards oxygen.

The electronic structure of the metal remains the same in all cases, except for the triplet states of the neutral species, where

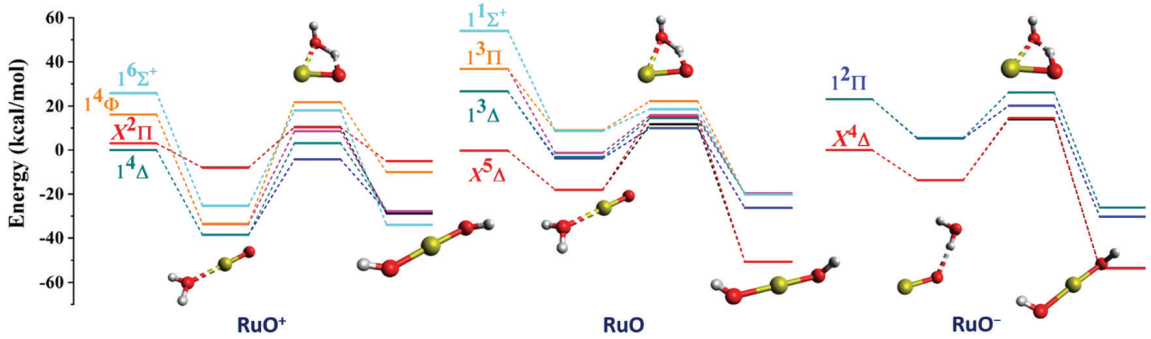

Fig. 4 Energy diagrams for the reaction of $RuO^{0,\pm}$ with water. The energy levels in each case from left to right correspond to the reactants, $RuO^{0,\pm}$ + H_2O, their interaction complex, the transition state, and the $Ru(OH)_2^{0,\pm}$ products. The depicted structures correspond to the lowest quartet and quintet states for the charged and neutral systems, respectively. Ru is depicted with yellow, oxygen with red, and hydrogen with white spheres.

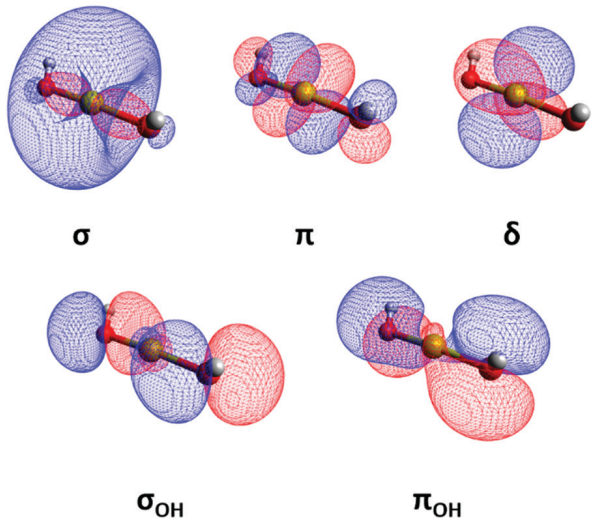

Fig. 5 Selected CASSCF orbitals for $Ru(OH)_2^-$. The upper three orbitals correspond mainly to Ru and the bottom two ones are localized mainly on the OH units.

higher states of RuO with $3\sigma^0$ configuration intervene. For example, the $2^3\Sigma^-$ ($2\sigma^2 1\pi^4 3\sigma^0 2\pi^2 1\delta^4$) state of RuO generates the ground state of $Ru(OH)_2$ ($\sigma_{OH}{}^2\pi_{OH}{}^4\sigma^0\pi^2\delta^4$). The higher complexity of RuO and the involvement of higher energy triplet states in the reaction are also demonstrated by the closer energy proximity of the transition states of RuO. For example, the seven transition states in RuO^+ span an energy range of 26.0 kcal mol^{-1}, as opposed to the 12.4 kcal mol^{-1} of the seven RuO transition states.

The above observations suggest a rather heterolytic dissociation of the activated OH bond, with a proton (H^+) being transferred to oxygen and the remaining OH^- to ruthenium. The Ru–O bond lengths elongate considerably by about 0.2 Å during the reaction. For example, it goes from 1.62 to 1.81 Å in the case of RuO^+. The Ru–O bond lengths for the neutral and anionic species are 1.92 and 1.99 Å, respectively.

Our recent calculated energy barriers of about 40 and 10 kcal mol^{-1} for the reaction of ground state MoO^+ and MoO^- with water[10] are in harmony with the present ones for $RuO^{\pm}$ (see above). This observation, along with the fact that the metallic nature remains highly unaffected during the reaction, indicates that the metal identity plays a minor role in this type of reaction ($MO + H_2O \rightarrow M(OH)_2$), but the overall charge of the system is more important. Anionic systems are shown to facilitate this reaction. For $MoO^{\pm}$, we attributed this effect to the weaker Mo–O bond (expressed by its longer bond length), which is also activated during the reaction.[10] Calculations with more metals are necessary for a more definitive conclusion and clearer explanation.

IV. Summary and conclusions

In this study, we have performed high-level electronic structure calculations on RuO, its cation and anion. Several electronic states have been investigated, and for all of them we report the electronic configurations, bond lengths, vibrational frequencies, and excitation energies. For the ground states we also provide binding energies and dipole moments. Spin–orbit splittings are also given for the lowest-lying ones. Our results are the first accurate results enriching the limited knowledge on these systems in the literature. We found that going from RuO^+, to RuO and RuO^- the additional electrons populate a molecular orbital with major $5s_{Ru}$ contribution for all low-lying electronic states. Every time the bond lengths increase by ~0.02 Å, the vibrational frequencies decrease by 50 cm^{-1} or more. The ground states for RuO and RuO^- are clearly identified as $^5\Delta$ and $^4\Delta$, but the two states ($^4\Delta$ and $^2\Pi$) compete for RuO^+. Our findings on the excited states for RuO agree with earlier computational studies, but those of RuO^+ are radically different from previous theoretical literature results. Our binding energies are significantly smaller (by ~10 kcal mol^{-1}) than the experimental values indicating the importance of higher order electron correlation effects. Finally, the comparison between iron and ruthenium oxides showed a completely different pattern of low-lying electronic states. The titled species are practically unexplored by experimental means and the present study will facilitate the assignments of future spectroscopic analyses.

In addition, we studied the reaction of the three species with water in their ground and low-lying electronic states. We found a consistent decrease of the activation energy barriers and higher exothermicity as we add electrons to the system. RuO^- is found to facilitate the reaction for both kinetic and thermodynamic reasons. This can be attributed to the weaker binding of water to RuO^- and the longer Ru–O bond of RuO^-, as opposed to RuO and RuO^+. Our results on RuO^+ will assist future experimental work to identify the products of RuO^+ with water by means of infrared and electronic spectroscopy, while our results on $RuO^{0,-}$ will enable the characterization of the RuO^- + H_2O products *via* photoelectron spectroscopy (see for example ref. 11).

The present findings suggest that electron rich metal oxide clusters are expected to activate O–H bonds and release H_2 easier. Over the past decade, there is high experimental interest in the reactions of anionic single metal centers or small metal oxide clusters with small molecules, such as water, methane, and carbon monoxide or dioxide (see for example ref. 29–36). The comparison of cationic and anionic V_2O_3 clusters has shown that the cation favors the association reaction with water, which hinders the dehydrogenation reaction.[37] Our present theoretical work is in agreement with this observation, and our ongoing efforts to study the reaction of neutral and charged metal oxides will provide insights into the effect that the nature of the metal has on their overall chemical activity.

Conflicts of interest

There are no conflicts to declare.

Acknowledgements

The authors are indebted to Auburn University for financial support. The computational resources were provided by the Auburn University Hopper Cluster.

References

1 A. Gunay and K. H. Theopold, *Chem. Rev.*, 2010, **110**, 1060–1081.
2 J. Védrine, *Catalysts*, 2017, **7**(11), 341.
3 J. C. Védrine, *ChemSusChem*, 2019, **12**, 577–588.
4 H. Dai, *Sci. Bull.*, 2015, **60**, 1708–1710.
5 A. Yusuf, C. Snape, J. He, H. Xu, C. Liu, M. Zhao, G. Z. Chen, B. Tang, C. Wang, J. Wang and S. N. Behera, *Catal. Rev.*, 2017, **59**, 189–233.
6 M. Jacoby, *Chem. Eng. News*, 2015, **93**, 8–11.
7 E. E. Claveau and E. Miliordos, *Phys. Chem. Chem. Phys.*, 2019, **21**, 26324–26332.
8 J. K. Kirkland, S. N. Khan, B. Casale, E. Miliordos and K. D. Vogiatzis, *Phys. Chem. Chem. Phys.*, 2018, **20**, 28786–28795.
9 B. A. Jackson and E. Miliordos, *Phys. Chem. Chem. Phys.*, 2020, **22**, 6606–6618.
10 I. R. Ariyarathna and E. Miliordos, *Phys. Chem. Chem. Phys.*, 2018, **20**, 12278–12287.
11 G. Liu, E. Miliordos, S. M. Ciborowski, M. Tschurl, U. Boesl, U. Heiz, X. Zhang, S. S. Xantheas and K. Bowen, *J. Chem. Phys.*, 2018, **149**, 221101.
12 W. E. Piers, *Organometallics*, 2011, **30**, 13–16.
13 C. N. Sakellaris, E. Miliordos and A. Mavridis, *J. Chem. Phys.*, 2011, **134**, 234308.
14 E. Miliordos and A. Mavridis, *J. Phys. Chem. A*, 2007, **111**, 1953–1965.
15 E. Miliordos and A. Mavridis, *J. Phys. Chem. A*, 2010, **114**, 8536–8572.
16 K. A. Peterson, D. Figgen, M. Dolg and H. Stoll, *J. Chem. Phys.*, 2007, **126**, 124101.
17 N. M. S. Almeida, I. R. Ariyarathna and E. Miliordos, *Phys. Chem. Chem. Phys.*, 2018, **20**, 14578–14586.
18 R. A. Kendall, T. H. Dunning and R. J. Harrison, *J. Chem. Phys.*, 1992, **96**, 6796–6806.
19 H.-J. Werner, P. J. Knowles, G. Knizia, F. R. Manby, M. Schütz and M. W. P. Celani, W. Györffy, D. Kats, T. Korona, R. Lindh, A. Mitrushenkov, G. Rauhut, K. R. Shamasundar, T. B. Adler, R. D. Amos, A. Bernhardsson, A. Berning, D. L. Cooper, M. J. O. Deegan, A. J. Dobbyn, F. Eckert, E. Goll, C. Hampel, A. Hesselmann and G. Hetzer, *MOLPRO, version 2015.1, a Package ab initio programs*, see http//www.molpro.net.
20 A. Kramida, Y. Ralchenko, J. Reader and NIST ASD Team, NIST Atomic Spectra Database (version 5.4), National Institute of Standards and Technology, Gaithersburg, MD, 2016, http://physics.nist.gov/asd, accessed 13 December 2019.
21 Y. Chen and P. B. Armentrout, *J. Chem. Phys.*, 1995, **103**, 618–625.
22 R. B. Metz, C. Nicolas, M. Ahmed and S. R. Leone, *J. Chem. Phys.*, 2005, **123**, 114313.
23 E. A. Carter and W. A. Goddard, *J. Phys. Chem.*, 1988, **92**, 2109–2115.
24 N. M. S. Almeida, I. R. Ariyarathna and E. Miliordos, *J. Phys. Chem. A*, 2019, **123**, 9336–9344.
25 M. Krauss and W. J. Stevens, *J. Chem. Phys.*, 1985, **82**, 5584–5596.
26 K. P. Huber and G. Herzberg, *Molecular Spectra and Molecular Structure*, Springer US, Boston, MA, 1979, pp. 8–689.
27 J. G. Kay, D. W. Green, K. Duca and G. L. Zimmerman, *J. Mol. Spectrosc.*, 1989, **138**, 49–61.
28 P. E. M. Siegbahn, *Chem. Phys. Lett.*, 1993, **201**, 15–23.
29 J. U. Reveles, G. E. Johnson, S. N. Khanna and A. W. Castleman, *J. Phys. Chem. C*, 2010, **114**, 5438–5446.
30 G. Liu, Z. Zhu, S. M. Ciborowski, I. R. Ariyarathna, E. Miliordos and K. H. Bowen, *Angew. Chem., Int. Ed.*, 2019, **58**, 7773–7777.
31 X.-N. Li, Z. Yuan and S.-G. He, *J. Am. Chem. Soc.*, 2014, **136**, 3617–3623.
32 R. O. Ramabhadran, J. E. Mann, S. E. Waller, D. W. Rothgeb, C. C. Jarrold and K. Raghavachari, *J. Am. Chem. Soc.*, 2013, **135**, 17039–17051.
33 E. Lim, S. K. Kim and K. H. Bowen, *J. Chem. Phys.*, 2015, **143**, 174305.
34 L. G. Dodson, M. C. Thompson and J. M. Weber, *J. Phys. Chem. A*, 2018, **122**, 2983–2991.
35 G. Liu, S. M. Ciborowski, Z. Zhu, Y. Chen, X. Zhang and K. H. Bowen, *Phys. Chem. Chem. Phys.*, 2019, **21**, 10955–10960.
36 M. L. Weichman, S. Debnath, J. T. Kelly, S. Gewinner, W. Schöllkopf, D. M. Neumark and K. R. Asmis, *Top. Catal.*, 2018, **61**, 92–105.
37 X.-N. Li, B. Xu, X.-L. Ding and S.-G. He, *Dalton Trans.*, 2012, **41**, 5562.